Imperial College
London

Optical and Computational Studies of Liquid-liquid Flows

Lan LIU

A dissertation submitted to University of London
in fulfilment of the requirements for the degree of
Doctor of Philosophy and the Diploma of Imperial College London

Department of Chemical Engineering and Chemical Technology
Imperial College London

February 2005

BIBL.
LONDIN.
UNIV.

Abstract

This thesis reports experimental and numerical investigations of liquid-liquid dispersions, both in the pipeline flows and in an agitated vessel.

The literature on liquid-liquid systems in pipe flow and agitated containers is reviewed with emphasis on phase inversion phenomena.

The laser-induced fluorescence (LIF) technique was used to directly visualize the dynamic evolution of dispersions and complex liquid-liquid structures in both pipe flows and agitated vessels. A green laser sheet was generated by a copper vapour laser and a high-speed digital video camera recorded the fluorescence. Exxol D80 Oil and 39 wt.% $CaCl_2$ solution with their refractive indices matched at 1.438 at 25°C were chosen as the liquid pair and Eosin Y (dissolved in the aqueous phase) was used as the fluorescent dyestuff. For pipeline flows, a vertical 18mm×18mm square cross-sectional duct was used with liquid-liquid flows in the downwards direction. For studies on phase inversion in agitated vessels, a 80mm high and 30 mm×30 mm square cross-sectional agitated vessel was used.

The experimental work on pipeline flows was carried out in two parts, one for high mixture velocity and the other for the low velocity. The flow structures in liquid-liquid flows were observed in detail using LIF. For the pipeline flows, an unstable region was found in the flow pattern map separating regions of oil-in-aqueous phase (o/w) and aqueous phase-in-oil (w/o) dispersed flows. Secondary w/o/w and o/w/o dispersions and multiple dispersions were observed, especially in flows in the unstable range. Compared with those in the agitated vessel system, the structures of the secondary dispersions in the pipeline flow were more complex and varied; the preponderance of o/w/o over w/o/w dispersions observed in agitated system was not found in the pipe flow experiments. Estimated were made of phase holdups both from the experimental data and from dispersed and annular flow models. Agreement between experiment and analysis was reasonably good. At low flow velocities, a dramatic flow pattern transition was observed between annular flow and a highly dispersed annular flow; this arose from wave growth and droplet entrainment at the interface.

The experimental work carried out in the agitated vessel was focused on phase inversion and associated phenomena, such as drop breakup and coalescence, secondary and multiple dispersion and the complex flow structures occurring during phase inversion. The experimental results suggested that phase inversion was a gradual phenomenon rather than a

catastrophic one; the process lasted for several seconds and during phase inversion both oil-in-aqueous phase and aqueous phase-in-oil dispersions could co-exist. The process may occur locally rather than globally, dependent on the local phase distribution. It was also found that the formation of secondary dispersions, with the associated inclusion and escape processes, was a dominant mechanism behind phase inversion.

A commercial CFD code (CFX4.4) was used to simulate oil-in-water dispersed pipeline flow and the results compared with experimental data. It was found that, to obtain agreement with the data for dense dispersed flows, values of the lift force coefficient, the turbulence dispersed force coefficient and the break-up coefficient at the lower end of the recommended range were needed. CFD modeling strategy was also applied to oil-in-water dispersed flows in a square cross-section duct. To predict the turbulence-induced secondary flow in the corners of the duct, it was necessary to use the Reynolds Stress Model.

Acknowledgements

First of all, I would like to acknowledge my deepest debt and gratitude to my supervisors, Prof. G.F. Hewitt, FRS, FREng, Dr. O.K. Matar and Dr. E.S. Ortiz. Without their infinite enthusiasm and great wisdom it would not be possible to produce this thesis. I am extremely grateful for their help and guidance not only in the academic field but also on how to become a successful person. I will benefit from what they teach me forever.

I must express my thanks to my collaborating supervisor Prof. A. R. Jones and Prof. C.J. Lawrence who put lots of excellent ideas into my head and help me solve many practical problems I met. I also owe a debt to Dr. C. P. Hale who always gives me a hand whenever I need help and lends me an ear whenever I feel low.

I want to express my thanks to all the members of electronics, technician services and Workshops, especially, Malcolm Dix, Richard Oxenham, Bob King, Nick Duggan, Fred Carleton and Patricia Carry who make my PhD study possible.

I am grateful to many friends and colleagues for their help and encouragement and would like to take this opportunity to say a large "thank you" to all of them with whom I share my laugh and tears during my whole PhD life. Particular, I would like to mention the various friends: Priscilla, Prash, Pooiling, Zuu, Wai-Lid, Florence, Tahsin, Ngugi, Tony, Liyun, Lina, Salihu, Jin, Jerry, James, Sandeep.

Last but not least, I would like to thank my husband, Mr. Bin Hu and my family back in China for their persistent encouragement, support and love throughout the duration of my studies in London and my whole life. (最后，我要把我真挚的感谢献给我的先生和家人，是他们无微不至的关怀和鼓励帮助我顺利地渡过了异国求学的岁月)。

Contents

Abstract 1

Acknowledgements 3

Contents 4

List of Figures 9

List of Tables 21

List of Movies 22

Nomenclature 23

1 Introduction 27

1.1 Liquid-liquid Pipe Flow 27

1.2 Objective of the Study 30

1.3 Structure of the Thesis 32

2 Literature Review 33

2.1 Liquid-liquid Pipe Flow 34

2.1.1 Flow Pattern 34

2.1.2 Pressure Gradient 45

2.1.3 Phase Distribution 49

2.1.4 Drop Size Distribution 52

2.2 The phase inversion process 57

2.2.1 Experimental Research on Phase Inversion 58

2.2.1.1 Phase Inversion in Agitated Vessels 58

2.2.1.2 Phase Inversion in Pipeline Flow 60

2.2.1.3 Prediction of the phase inversion point 62

2.2.1.4 Ambivalent Range 65

2.2.1.5 Effects of System Parameters on Phase Inversion 68

2.2.1.6 Review of the Experimental Methods for Liquid-Liquid Dispersed Flow and Phase Inversion 74

2.2.2 The Mechanisms of Phase Inversion 75

2.2.2.1 Postulated Mechanisms of Phase Inversion 75

2.2.2.2 Drop Coalescence & Breakup 76

2.2.2.3 Secondary Dispersions 77

2.2.3 Simulations for Phase Inversion 81
2.3 Summary 83
3 Experimental System 84
3.1 Introduction 84
3.2 Laser-induced Fluorescence technique 85
3.3 Laser and Digital Imaging Equipment 88
3.3.1 Laser and Associated Optics 88
3.3.2 High Speed Imager 90
3.4 Selection of Liquid Pair and Fluorescent Dyestuff 93
3.4.1 Selection of Liquid Pair 93
3.4.2 The Fluorescent Dyestuffs 95
3.5 Experimental Facilities 96
3.5.1 Agitated Vessel System 96
3.5.2 Pipe Flow Systems 97
3.5.2.1 Test Section 99
3.5.2.2 Experimental Flow Facility (a) for High Flow Velocities 100
3.5.2.3 Experimental Flow Facility (a) for Low Flow Velocities 104
4 Optical Studies of Liquid-liquid Pipe Flows: I. High Velocities 108
4.1 Experimental Procedure 108
4.2 Flow patterns 109
4.2.1 Flow Pattern Map 109
4.2.2 Flow Structures 110
4.3 Phase Inversion Process 115
4.4 Ambivalent Range 117
4.5 Secondary and Multiple Dispersion 119
4.6 Analysis and Discussion 125
4.6.1 Analysis of Data Using One–Dimensional Method 125
4.6.2 Annular Flow Analysis 139
4.6.2.1 Model and Equations 140
4.6.2.2 Analysis of experimental Annular Flow 144
4.7 Summary 148
***5* Optical Studies of Liquid-liquid Pipe Flows: II. Low Velocities** 150
5.1 Experimental Results 151
5.1.1 Steady State Flow 151

5.1.2 Transient Test 154
5.1.3 Secondary Dispersion 155
5.2 Discussions 156
5.3 Summary 159
6 Phase Inversion & Associated Phenomena in a Liquid-liquid Agitated Vessel System 160
6.1 Experimental Procedure 161
6.2 Ambivalence Range 162
6.3 The Phase Inversion Process 163
6.4 Drop Breakup and Coalescence 168
6.5 Secondary and Multiple Dispersions 170
6.6 Drop Size Distributions Before and After Phase Inversion 174
6.7 Discussion 178
6.7.1 Film Formation on the Impeller 178
6.7.2 Local Occurrence of Phase Inversion 179
6.7.3 The Route to Phase Inversion 180
6.8 Summary 181
7 CFD Models for Liquid-liquid Dispersed Pipe Flows 182
7.1 Governing Equations 183
7.2 Turbulent Flow and Its Modelling 184
7.2.1 Turbulent Flow 184
7.2.2 Turbulent Modelling 185
7.2.2.1 Eddy Viscosity Models 185
7.2.2.2 The k- ε Model Turbulence Model 186
7.2.2.3 Reynolds Stress Model 187
7.3 Boundary Conditions 189
7.3.1 Wall Boundary Conditions for Turbulent Flow 189
7.3.2 Flow Boundaries 191
7.3.3 Symmetry Boundary 191
7.3.4 Periodic Boundaries 191
7.4 Multi-phase Flow 191
7.4.1 Multi-fluid Model 192
7.4.1.1 Inter-phase Drag 192
7.4.1.2 Inter-phase Non-drag Forces 195
7.4.2 Multiple-size-group (MUSIG) Model 197

7.4.2.1 Theory and Modelling of Drop Size Distribution 197
7.4.2.2 Population Balance 198
7.4.2.3 Break-up Model 199
7.2.4.4 Coalescence Model 200
7.5 Introduction of CFX®-4.4 202
8 Computational Results for Liquid-liquid Dispersed Flows 204
8.1 CFX Simulations of Oil-Water dispersed Flows in Circular Pipe 204
8.1.1 Experiments 205
8.1.2 Numerical Methods 205
8.1.3 Results Comparison and Discussion 208
8.1.3.1 Non-drag Forces Coefficients 209
8.1.3.2 Break-up and Coalescence Model Coefficients 210
8.1.3.3 Drop Size Distribution 213
8.1.4 Summary 218
8.2 CFX Simulations of Oil-Water Dispersed Flows in Non-circular Duct 219
8.2.1 Turbulence-induced Secondary Flow in Non-circular Duct 219
8.2.2 Numerical Methods 221
8.2.3 Calculated Results and Discussions 222
8.2.4 Summary 230
9 Conclusions & Recommendations 231
9.1 Conclusions 231
9.1.1 Conclusions from Experiments 231
9.1.2 Conclusions from Numerical Calculations 235
9.2 Recommendations for the Future Work 236
Reference 238
Appendix A Photochromic Dye Tracing 248
A.1 The Mechanism of Photochromic Dye Tracing 248
A.2 Application of Photochromic Dye Tracing to Flow Visualisation 250
A.3 The Trail Experiments using Photochromic Dye Tracing 252
Appendix B Refractive Indices of Liquid Pair 257

	B.1	Refractive Indices	257
	B.2	Heat Capacity of the Liquid Pair	258
	B.3	The Procedure of Making 39% wt. $CaCl_2$ solution	259
Appendix C	**Fluorescent Dyestuff Selection**		260
Appendix D	**Light Diffraction and Reflection**		264
Appendix E	**Preliminary Experimental Circuits and Results**		267
	E.1	The 1st experimental Circuit	267
	E.2	The 2nd Experimental Circuit	268
		E.2.1 The objective and design the 2nd experimental circuit	268
		E.2.2 Experimental results using the 2nd experimental circuit	271
	E.3	The 3rd Experimental Circuit	276
Appendix F	**Proposed Experimental Circuit**		279
Appendix G	**In-situ Phase Volume Fraction and Drop Size Measurement Program**		280
Appendix H	**Location of File on CD**		281

List of Figures

Chapter 1

Figure 1.1 Schematic representations of possible flow regimes in a horizontal pipe (Arirachakaran et al. 1989). 28

Figure 1.2 Flow regime map in liquid-liquid flow in a horizontal pipe (Soleimani, 1999). 29

Chapter 2

Figure 2.1 Flow patterns for a 16.8 mPa s, 998 kg/m^3 oil and water system in a 0.026 m ID pipe based on observations of Charles *et al.* (1961). Map as published by Govier and Aziz (1972). 35

Figure 2.2 Flow patterns for a 0.82 mPa s, 1020 kg/m^3 kerosene-perchlorethylene solution and water system in a 1.26 cm ID glass tube based on observations of Hasson *et al.* (1970). 37

Figure 2.3 Flow patterns for a 21.7 mPa s, 896 kg/m^3 oil and water system in a 0.0394 m pipe based on observations of Guzhov *et al.* (1973), as revised and presented by Oglesby *et al.* (1979). 38

Figure 2.4 Flow patterns for an 84.0 mPa s oil and water system in a 0.041 m pipe based on observations of Oglesby *et al.* (1979). 39

Figure 2.5 Experimental oil-water system flow pattern map by Arirachakaran *et al.* (1989). 40

Figure 2.6 Flow patterns by Angeli & Hewitt (2000a) in the (a) stainless steel test section. (b) actylic test section. ○, stratified wavy (SW); ▬, three layers (3L); Δ, stratified mixed/oil (SM/oil); - - -, phase continuity boundaries; ▲, stratified wavy/drops (SWD); ●, stratified mixed/water(SM/water); +, mixed (M). 41

Figure 2.7 Flow regime map (Nädler and Mewes, 1997) for the two-phase flow of water and oil based on input water fraction. 42

Figure 2.8 The Brauner & Ullmann (2001) predictions for transition to Do/w (boundary 4) and transition to Dw/o (boundary 5) in (a) horizontal oil-water system (Trallera, 1995) and (b) vertical upwards oil-water flow (Flores, et al., 1997). 43

Figure 2.9 Flow pattern map (Lovick & Angeli, 2004) with the results from Laflin and Oglesby (1976) (solid lines). (I) dual continuous flow; (II) 44

dispersion of oil in water and water; (III) dispersion of oil in water; (IV) dispersion of water in oil.

Figure 2.10 Flow pattern maps obtained by Hussain (2004); (a) without mixer and (b) with a 5-element Kenics™ mixer at the tube inlet. 45

Figure 2.11 Non-dimensional pressure gradient in the steel and acrylic pipes at mixture velocity 3.0 m/s by Angeli and Hewitt (1998). 47

Figure 2.12 Pressure gradient data by Soleimani (1999) showing peak at phase inversion. 48

Figure 2.13 Comparison of non-dimensional pressure gradient in the acrylic and steel pipes at the mixture velocity 4.5 m/s starting with oil dominated mixture. (Ioannou *et al.* 2004b). 49

Figure 2.14 Phase distribution in a pipe cross section at 3.5 m/s mixture velocity at (a) before phase inversion, 72% oil input fraction; (b) after phase inversion, 70% oil input fraction. Scale is of oil volume fraction ranging from zero (blue) to 100% (red) (Ioannou *et al.*, 2004a). 51

Figure 2.15 Comparison of measured cross-sectional phase distributions at a distance of (a) 1.0 m and (b) 7.72 m from the inlet with those calculated using CFX using the measured water fraction data at 1.0 m as input (input water fraction 40%, mixture velocity 2.76 m/s) by Hussain (2004). 52

Figure 2.16 Typical photomicrograghs for surfactant-stabilized emulsions by Pal (1993). (a) stable 25.85% W/O emulsion; (b) multiple emulsions (water concentration is 25.85% vol.); (c) 68.44% O/W emulsion; and (d) 44.9% O/W emulsion. 55

Figure 2.17 Sauter mean diameter (D_{32}) as a function of water concentration (Pal, 1993). 55

Figure 2.18 Phase inversion process for an oil-water dispersion system (Arirachakaran *et al.*, 1989). 58

Figure 2.19 Pressure gradient in liquid-liquid flow (Soleimani, 1999). 60

Figure 2.20 Mixture viscosity vs. input water fraction for low-viscosity oil (Arirachakaran *et al.*, 1989). 61

Figure 2.21 General ambivalence behaviour for a benzene-water system (Kumar *et al.*, 1991). 66

Figure 2.22 Region of ambivalence as affected by a change in the liquids/wall wetting-effect of the mixture velocity and contact angle on the critical oil cut for the oil-water system (Brauner & Ullmann, 2002). 67

Figure 2.23 Pressure gradient in the steel pipe for the two initial conditions used at 4 m/s and 4.5 m/s mixture velocities (Ioannou *et al*. 2004b). 68
Figure 2.24 Simplified representation of multi-body collisions producing secondary dispersions (Kumar, 1996). 78
Figure 2.25 Schematic presentation of internal droplet formation by drop deformation mechanism. (a) Droplet formation and (b) Satellite droplet formation (Sajjadi *et al*., 2002). 79

Chapter 3

Figure 3.1 Schematic energy-level diagram for a diatomic molecule (Guilbault, 1973). 87
Figure 3.2 Schematic diagram of Laser and optics; dimensions in mm; (a). the kit for UV light; (b). the kit for green light. 89
Figure 3.3 (a) Schematic description of trigger system and (b) trigger box working mechanism 92
Figure 3.4 The four mechanisms of light attenuation through drop 93
Figure 3.5 (a) A schematic representation of the experimental setup for the agitated system; (b) The position of the laser light 97
Figure 3.6 (a) The test section and (b) Visualization section 100
Figure 3.7 A schematic description of the experimental circuit; aqueous phase flows in 'blue' loop through the text section and oil phase in 'yellow' loop. The green route is for oil-water mixture. 103
Figure 3.8 Calibration plot of turbine flow sensor. 104
Figure 3.9 (a) Liquid-liquid flow facility; (b) The photo of gear pump (Model 75211-30, Cole-Parmer Ltd). 105
Figure 3.10 Flow rate calibration plot of the gear pump. 107

Chapter 4

Figure 4.1 Flow pattern map based on the oil input fraction for the liquid-liquid flow in a vertical pipe. 109
Figure 4.2 O/W dispersed flow at mixture velocity U_m = 0.7 m/s and oil input volume fraction ε^o_{input} = 40%. 110
Figure 4.3 W/O dispersed flow at mixture velocity U_m = 0.824 m/s and oil input volume fraction ε^o_{input} = 77.4%. 111
Figure 4.4 Time series photographs about aqueous phase-continuous transitional 114

flow with mixture velocity U_m = 1.46 m/s and ε^o_{input} = 48%.

Figure 4.5 Time series photographs about water-continuous transitional flow with mixture velocity U_m = 2.1 m/s and oil holdup ε_{oil} = 49%. 115

Figure 4.6 Time series of photographs shown phase inversion process of transient flow at mixture velocity decreased from 1.28 m/s to 0.53 m/s and oil fraction increased from 30% to 83%. 117

Figure 4.7 The unstable range observed in the experiments 118

Figure 4.8 The ambivalent range obtained in Benzene-water stirred system by Kumar *et al.* (1991). 119

Figure 4.9 W/O/W secondary dispersions; (a) – (d) at mixture velocity U_m = 1.5 m/s and oil holdup ε_{oil} = 31%; (e) U_m = 1.16 m/s and ε_{oil} = 67.7%. 121

Figure 4.10 O/W/O secondary dispersions; (a) U_m = 1.3 m/s and ε_{oil} = 48%; (b) U_m = 1.22 m/s and ε_{oil} = 55%; (c) U_m = 0.68 m/s and ε_{oil} = 42%; (d) – (e) U_m = 1.17 m/s and ε_{oil} = 67%; (f) U_m = 1.34 m/s and ε_{oil} = 80.9%. 122

Figure 4.11 O/W/O dispersions are rupturing from the water films; (a) at U_m = 1.2 m/s and ε_{oil} = 56%; (b) at U_m = 1.2 m/s and ε_{oil} = 62.8%; (c) at U_m = 1.22 m/s and ε_{oil} = 69%. 122

Figure 4.12 Time-series photographs of coalescing process of two water waves including water drop inside oil phase at U_m = 1.46 m/s and ε_{oil} = 16%. 123

Figure 4.13 W/O/W dispersions are formed by two coalescing water waves; (a) at U_m = 1.02 m/s and ε_{oil} = 45%; (b) at U_m = 0.68 m/s and ε_{oil} = 42%. 123

Figure 4.14 O/W/O/W Multiple dispersions; (a) at U_m = 1.5 m/s and ε_{oil} = 31%; (b) at U_m = 0.68 m/s and ε_{oil} = 42%. 124

Figure 4.15 W/O/W/O Multiple dispersions; (a) at U_m = 1.12 m/s and ε_{oil} = 59%; (b) at U_m = 1.2 m/s and ε_{oil} = 62.8%; (c) at U_m = 1.11 m/s and ε_{oil} = 71.7%; (d) at U_m = 1.85 m/s and ε_{oil} = 61.8%; (e) at U_m = 1.34 m/s and ε_{oil} = 80.9%; (f) at U_m = 1.45 m/s and ε_{oil} = 78.2%. 124

Figure 4.16 Complex drop structures at U_m = 1.11 m/s and ε_{oil} = 71.9%. 124

Figure 4.17 Shape regimes and subregimes for liquid drops and gas bubbles rising or falling freely through liquids under gravity (Grace *et al.*, 1976); adapted from Clift *et al.* (1978). 129

Figure 4.18 Graphical solution of oil in-situ volume fraction $\varepsilon^o_{in-situ}$ of Eqs. (4-1) and (4-2) for various drop diameters in the oil-in-water dispersed flow with mixture velocity of V_m = 1.5 m/s and input oil volume fraction ε^o_{input} = 31%. 131

Figure 4.19 Predicted in-situ volume fractions of oil phase $\varepsilon^{o}_{in-situ,p}$ for different oil drop diameters, calculated from Eqs. (4-1) and (4-2) in the oil-in-water dispersed flow with mixture velocity of V_m = 1.5 m/s and input oil volume fraction ε^{o}_{input} = 31%. 132

Figure 4.20 The processed images for obtaining $\varepsilon^{o}_{in-situ,m}$ in an oil-in-water dispersed flow with mixture velocity of V_m = 1.5 m/s and input oil volume fraction ε^{o}_{input} = 31%; (a) original image; (b) processed black-white image (white represents dispersed phase). 133

Figure 4.21 The drop size distribution for the oil-in-water dispersed flow with mixture velocity of V_m = 1.5 m/s and input oil volume fraction ε^{o}_{input} = 31%. 134

Figure 4.22 Predicted in-situ volume fractions of oil phase $\varepsilon^{o}_{in-situ,p}$ for d^{o}_{32} =2.4 mm in the oil-in-water dispersed flow with mixture velocity of V_m = 1.5 m/s and oil input volume fraction ε^{o}_{input} = 31%. 133

Figure 4.23 Graphical solution of aqueous phase in-situ volume fraction $\varepsilon^{w}_{in-situ}$ of Eq. (4-1) and (4-2) for various drop diameters in aqueous phase-in-oil dispersed flow with the mixture velocity of V_m = 0.824 m/s and the input aqueous phase volume fraction of ε^{w}_{input} = 22.6%. 136

Figure 4.24 Predicted water in-situ volume fraction $\varepsilon^{w}_{in-situ,p}$ for different aqueous phase drop diameters, calculated from Eqs. (4-1) and (4-2) in aqueous phase-in-oil dispersed flow with the mixture velocity of V_m = 0.824 m/s and the input aqueous phase volume fraction of ε^{w}_{input} = 22.6%. 137

Figure 4.25 The processed images for obtaining $\varepsilon^{w}_{in-situ,m}$ in an aqueous phase-in-oil dispersed flow with mixture velocity of V_m = 0.824 m/s and input aqueous phase volume fraction ε^{w}_{input} = 22.6%; (a) original image; (b) processed black-white image (white represents dispersed phase). 138

Figure 4.26 Predicted in-situ volume fractions of oil phase $\varepsilon^{w}_{in-situ,p}$ for d^{w}_{32} = 4.4 mm in the water-in-oil dispersed flow with mixture velocity of V_m = 0.824 m/s and input water volume fraction ε^{o}_{input} = 22.6%. 138

Figure 4.27 The drop size distribution for the water-in-oil dispersed flow with 139

mixture velocity of V_m = 0.824 m/s and input oil volume fraction ε^{w}_{input} = 22.6%.

Figure 4.28 The schematic diagram of the co-current downward lamina annular flow. 140

Figure 4.29 The relationship of the interface position, a, and dimensionless the oil input volume fraction, $\hat{Q}_o$, with $m = 0.14$ and $V_m = 0.65$ m/s. 145

Figure 4.30 The relationship of the dimensionless driving force, α, and the dimensionless oil input volume fraction, $\hat{Q}_o$, with $m = 0.14$ and $V_m = 0.65$ m/s. 145

Figure 4.31 The cross sectional dimensionless velocity profile for the aqueous phase-annulus annular flow under conditions of mixture velocities of V_m = 0.65 m/s and the input oil volume fraction of ε^{o}_{input} = 69%. 146

Figure 4.32 The typical image of water-annulus annular flow with the mixture velocity of V_m = 0.69 m/s and input oil volume fraction ε^{o}_{input} = 69%; (a) original image; (b) processed black-white image (white represents oil phase). 147

Figure 4.33 Annular flow behaviour, (a) entrainment of film phase into core phase, (b) propagation of wave. 148

Chapter 5

Figure 5.1 A time-series of photographs taken over 2.046 seconds, showing annular wavy flow (51 % oil holdup). The mixure velocity is 0.0417 m/s. 152

Figure 5.2 A time-series of photographs of the annular flow with water dispersion in the oil core. The mixture velocity is 0.0572 m/s and other parameters are the same as those described in Figure 5.1. 153

Figure 5.3 A time-series of photographs taken over 5.546 seconds, which shows the oil-in-water dispersed flow. The mixture velocity is 0.0594 m/s and other parameters are the same with those in Figure 5.1. 154

Figure 5.4 A time-series of photographs of the transiant flow. The mixture velocity varied from 0.0594 m/s to 0.05 m/s and the other parameters are the same as those in Figure 5.1. 154

Figure 5.5 A time-series of photographs showing two oil drops undergoing coalescence. Here, the mixture velocity varied from 0.0572 m/s to 0.05 155

m/s and the other parameters are the same as those in Figure 5.1.

Figure 5.6 W/O/W dispersions observed in the transition flow regime and other parameters are the same as those in Figure 5.1. 156

Figure 5.7 The formation of w/o/w dispersion in transient flow, here, the mixture velocity varied from 0.059 m/s to 0.0 m/s and other parameters are the same as those in Figure 5.1. 156

Figure 5.8 The prediction of oil in-situ volume fraction from one dimensional dispersed flow model and laminar annular flow model, in comparisons with the experimental data. 158

Figure 5.9 An example image in annular-mist flow, (a) original image; (b) processed black-white image (white represents oil phase). 158

Chapter 6

Figure 6.1 Variation of the organic phase holdup with stirrer speed for a 39%wt. $CaCl_2$ solution and Exxol oil showing the ambivalence range. 163

Figure 6.2 A time-series of photographs taken over 5.458 seconds, showing the dynamic evolution of an o/w emulsion (45 % aqueous solution holdup) to a w/o emulsion using the LIF technique. 164

Figure 6.3 A time-series of photographs taken over 1.365 seconds, showing the transition from an o/w emulsion (38% aqueous solution holdup) to a w/o emulsion using the LIF technique. 167

Figure 6.4 A time-series of photographs taken over 1.365 seconds, showing the dynamic evolution of the w/o emulsion (38% aqueous solution holdup) resulting from the phase inversion shown in Figure 6.3 using the LIF technique. 168

Figure 6.5 Photographic evidence for the coalescence of two relatively large oil drops before phase inversion for the same parameters as in Figure 6.3. 169

Figure 6.6 A series of photographs showing an elongated oil drop undergoing deformation and breakup. Subsequently, one of the daughter drops is seen to coalesce with neighbouring oil drops before phase inversion for the same parameters as in Figures 6.3. 169

Figure 6.7 A large water drop undergoing breakup after phase inversion. Coalescence of regions of the continuous phase is also visible for the same parameters in Figure 6.4. 170

Figure 6.8 An example of an o/w/o secondary dispersion observed after phase inversion had taken place for the same parameters as in Figures 6.3. 171

Figure 6.9 Examples of a w/o/w dispersion observed before phase inversion; (a)-(b) for the same parameters as in Figures 6.3; (c)-(e) for 62% oil holdup at 706 rpm. 171

Figure 6.10 Photographic evidence for the formation of relatively large oil droplets in water drops for the same parameter as in Figure 6.4. 172

Figure 6.11 A schematic illustration of a possible mechanism for the formation of large oil droplets in water drops secondary dispersions following the collision of dispersed phase drops. The yellow and black regions designate the aqueous and organic phases, respectively. 172

Figure 6.12 Multi-dispersions o/w/o/w. (a)-(b) the same parameters as in Figures 6.3; (c)-(d) 62% oil holdup at 706 rpm. 173

Figure 6.13 A time-series of photographs showing the formation of an o/w/o/w multiple-dispersion for the same parameters as in Figures 6.3. 173

Figure 6.14 Complex structures directly visualized to accompany phase inversion of o/w to w/o for the same parameter as Figure 6.3; (a) 1.112s and (b) 1.342s. 174

Figure 6.15 Photographs during phase inversion showing the dynamic evolution of an o/w emulsion (45 % aqueous solution holdup) to a w/o emulsion 176

Figure 6.16 Oil drop section diameter distributions before phase inversion 177

Figure 6.17 Water drop section diameter distribution after phase inversion 177

Figure 6.18 The Sauter mean diameter vs. time 178

Figure 6.19 Water-in-oil dispersion; 19% aqueous phase holdup and 588 rpm impeller speed. 178

Figure 6.20 A time series of photographs show that dispersion changes between o/w and w/o dispersions during phase inversion; (a), (d) and (e) o/w dispersions; (b), (c) and (f) w/o dispersions. 179

Figure 6.21 Phase inversion in a liquid-liquid system (Chesters and Issa, 2004) (Courtesy of O. Masbernat, ENSIACET, Toulouse) 180

Chapter 8

Figure 8.1 Mesh in the XY plane of the quarter tube geometry 206

Figure 8.2 Grid sensitivity tests on dispersed phase distributions with oil volume quality q= 20%; (a) 100 and 150 grids in the longitudinal direction; (b) 12 and 15 grids in radial direction of block 2 and 3. The parameter values are taken as, lift force coefficient C_L = 0.01, the turbulent dispersion force coefficient C_{TD} = 0, break-up coefficient f_B = 0.1 and 207

coalescence coefficient f_C =1.

Figure 8.3 Comparisons of experimental dispersed phase distributions, ε(r), with the calculation results using Reynolds stress model and k– ε model. 208

Figure 8.4 The effect of varying C_L on the radial phase distribution with q = 20%. The rest of the parameter values are taken as, the turbulent dispersion force coefficient C_{TD} = 0, break-up coefficient f_B = 0.1 and coalescence coefficient f_C =1. 209

Figure 8.5 The effect of varying C_{TD} on the radial phase distribution. (a) q = 10%; the rest of the parameter values are C_L = 0.01, f_B = 1 and f_C =1. (b) q = 30%; the rest of the parameter values are taken as, C_L = 0.01, f_B = 0.1 and f_C =1. 210

Figure 8.6 The effect of varying f_C on the radial phase distributions with q = 30%. The rest of the parameter values are taken as, C_{TD} = 0, C_L = 0.01 and f_B = 0.1. 211

Figure 8.7 The effect of varying f_B on radial phase distributions; (a) q = 10%; the rest of the parameter values are taken as, C_L = 0.01, C_{TD} = 0.1 and f_C = 1; (b) q = 20%; the rest of the parameter values are taken as, C_L = 0.01, C_{TD} = 0 and f_C = 1; 211

Figure 8.8 Comparison of the CFX-predicted ε(r) with the experimental data of Farrar and Bruun (1996). C_{TD} = 0.1, f_B = 1.0 and f_C = 1.0 for q= 5%, 10% and 15%; C_{TD} = 0, f_B = 0.1 and f_C = 1 for q = 20%, 25% and 30%. 212

Figure 8.9 A comparison of experimentally determined bubble cut chord length c(r) with drop Sauter mean diameter obtained from the CFX simulations. The rest of the parameters are the same as those in Figure 8.8. 213

Figure 8.10 Drop size distributions with q = 20%; (a) at the inlet and the entire volume; (b) at different planes. The rest of the parameters are the same as those in Figure 8.8. 215

Figure 8.11 The effect of varying f_B and f_C, shown in (a) and (b) on the drop size distributions with q = 30%. The rest of the parameters are the same as those in Figure 8.8. 216

Figure 8.12 Drop size distribution for different oil holdup. The rest of the parameters are the same as those in Figure 8.8. 216

Figure 8.13 Drop size distributions with q = 20%; (a) at the inlet and the entire volume; (b) at different planes. The rest of the parameters are the same as those in Figure 8.8. 217

Figure 8.14 Mesh in the XY plane of the quarter tube geometry 222

Figure 8.15 Grid sensitivity tests on dispersed phase distributions with oil volume quality q= 20% with 2000 and 9000 grids; (a) oil phase distribution; (b) drop Sauter mean diameter. 222

Figure 8.16 Aqueous (continuous) phase volume fraction profile; (a) Reynolds stress model with secondary flow vectors and (b) k– ε model. Oil input volume fraction ε^{o}_{input} =20%. Calculated mixture velocity U_m= 1.81m/s for k– ε model and U_m= 2.13 m/s for Reynolds stress model. 224

Figure 8.17 Oil volume fraction profile; (a) Reynolds stress model with secondary flow vectors and (b) k– ε model. Oil input volume fraction ε^{o}_{input} =20%. Calculated mixture velocity U_m= 1.81 m/s for k– ε model and U_m= 2.13m/s for Reynolds stress model. 225

Figure 8.18 Comparison of the oil volume fractions obtained using different turbulence models; (a) along the diagonal plane; (b) along the side wall (see inset). 226

Figure 8.19 Volume fraction profiles ε^{o}_{input} =30% oil-in-water dispersed flow (a) aqueous phase volume fraction; (b) oil volume fraction. Calculated axial velocity U_m= 2.27 m/s. 227

Figure 8.20 Volume fraction profiles for ε^{o}_{input} =10% oil-in-water dispersed flow; (a) aqueous phase volume fraction; (b) oil volume fraction. Calculated axial velocity U_m= 2.01 m/s. 228

Figure 8.21 Axial variations of the oil volume fraction distribution along the plane indicated in the inset for 10%, 20% and 30% oil input holdup. 229

Appendix

Figure A.1 Typical Behaviour of Photochemical Compound (Brown, 1971). 249

Figure A.2 Absorption Spectra of Coloured (Dotted Line) and Colourless (Solid Line) Solutions of 5,7-DiChloro-6-NitroBPS in Ethanol at 20°C (Brown, 1971). 250

Figure A.3 DNBP – Tautomeric shift. 250

Figure A.4 TMINBPS-Heterolytic cleavage. 251

Figure A.5 Structure of Acid Violet 19 (Acid Magenta – Monomethyl Magenta). 252

Figure A.6 Aqueous and organic phase dyestuffs test (static); (a) aqueous phase with 0.1% Acid Violet 19; (b) aqueous phase with 1% Acid Violet 19; (c) organic phase with TNSB; (d) aqueous solution (upper) and Freon 254

113 (lower and drops) with photochromic dyestuff-TNSB.

Figure A.7 Boundary Layer of Single- phase Flow - aqueous solution with Acid Violet 19 (0.1%) (Re=9033). 255

Figure A.8 The dispersion during the separation process after the pump turned off; the red region is Freon drop with activated TNSB (25% holdup) and yellow region is NaCl solution. 256

Figure B.1 Refractive indices of calcium chloride solution under different concentrations. 257

Figure B.2 Refractive indices of the different concentration calcium chloride solution under different temperature. 258

Figure B.3 Heat capacities of water, calcium chloride solution (39% wt.) and Exxsol D80 oil. 259

Figure C.1 Rhodamine B Test in Two-phase Static liquids. Exxol Oil (upper) and Water (lower and drops) with Rhodamine B. 260

Figure D.1 'Oil tail' in oil-in-water dispersions (a) in the pipe; (b) in agitated vessel. 264

Figure D.2 'Oil tail' in water-in-oil dispersions in agitated vessel. 264

Figure D.3 The electromagnetic fields surrounding a particle by Prof. Alan Jones (December, 2003). 265

Figure D.4 The reflection loss in the calcium chloride solution and oil dispersed system. 266

Figure E.1 The schematic description of the 1st experimental circuit. 268

Figure E.2 Operating Principle of the 2nd flow Circuit. 269

Figure E.3 Schematic description of the 2nd experimental circuit. 270

Figure E.4 The chamber with a bellows. 271

Figure E.5 The process of two aqueous drops (with activated Eosin Y) coalescence during transient period after the pump start-up; in this and subsequent Figures, the yellowish green and black regions designate the aqueous and organic phases, respectively. 273

Figure E.6 Time series photographs of two oil-droplets coalescence, during transient period after the pump start-up. The drop moved at 0.0375 m/s. 274

Figure E.7 Time series photographs of two oil-droplets coalescence, during transient period after the pump start-up. The drop moved at 0.03125 m/s. 275

Figure E.8 The collide and separate process of two aqueous drops (with oil 276

droplets inside).

Figure E.9 (a) The Grandfos pump for the aqueous phase in the 3rd experimental rig; (b) The pump for the aqueous phase in the 4th experimental rig. 277

Figure E.10 Liquid-liquid dispersed flow using the 3rd experimental circuit. 278

Figure F.1 The schematic description of the proposed experimental circuit. 279

List of Tables

Table 2.1	Studies of phase inversion in agitated vessels.	59
Table 2.2	Studies of phase inversion in pipe flow.	62
Table 2.3	Empirical correlation of phase inversion.	64
Table 2.4	Measurement techniques for phase inversion. (Application is to agitated vessel unless otherwise stated).	75
Table 3.1	Physical Properties of the Selected Liquid Pair.	95
Table 4.1	Solutions for volume fraction in vertical flow using the one-dimensional analysis method (Butterworth & Hewitt, 1977).	127
Table 7.1	The standard values of the constants used in the Reynolds stress model.	188
Table 8.1	The physical properties of the two phases.	205
Table A.1	Physical Properties of the Selected Liquid Pair.	253
Table A.2	Photochromic Dyestuffs	254
Table C.1	Fluorescence dyestuffs.	261
Table H.1	Locations of files on CD	281

List of Movies

Movie 4.1 Time series photographs about aqueous phase-continuous transitional flow with mixture velocity U_m = 1.46 m/s and ε^o_{input} = 48%.

Movie 4.2 Time series of photographs shown phase inversion process of transient flow at mixture velocity decreased from 1.28 m/s to 0.53 m/s and ε^o_{input} increased from 30% to 82%.

Movie 5.1 A time-series of photographs of the annular flow with water dispersion in the oil core. The mixture velocity is 0.0572 m/s and 51 % oil input fraction.

Movie 6.1 A time-series of photographs taken over 5.458 seconds, showing the dynamic evolution of an o/w emulsion (45 % aqueous solution holdup) to a w/o emulsion using the LIF technique.

Movie 6.2 A time-series of photographs taken over 1.365 seconds, showing the transition from an o/w emulsion (38% aqueous solution holdup) to a w/o emulsion using the LIF technique.

Nomenclature

Roman

Symbol	
A	Area of a single particle projected in the flow direction,
A_i	Interfacial area
B	Body force, [N]
C_1, C_2	Constants in Eq. (2-12) and (2-17)
C_1 , C_2	Constants in wall lubrication force
$c_{\alpha\beta}^{(d)}$	Inter-phase drag terms
C_D	Drag coefficient
C_H	Tunable constant
C_L	Lift force coefficient
C_{TD}	Turbulence dispersed force coefficient
C_w	Wall lubrication force coefficient
$C_w^{'}$, $C_o^{'}$	Multiplier in the Blasius type equation described in Eq. (2-14).
C_μ, $C_{1\varepsilon}$, $C_{2\varepsilon}$	Constants of standard k- ε model
C_{1s} C_{2s} C_{3s} $c_1^{'}$ $c_2^{'}$ C_s c_d c_w $C_{1\varepsilon}$ $C_{2\varepsilon}$	Constants of the Reynolds Stress model
d	Internal pipe diameter, Eq.(2-17) or drop diameter, [m]
d	Volume equivalent mean diameter, [m]
d_I , d_{II}	Diameters (corresponding to volume v_I and v_{II}) of the daughter particles in the binary breakage of a parent particle with diameter d (corresponding to volume v)
d_{max}	Maximum drop diameter, [m]
d_s, d_{32}	Drop Sauter mean diameter, [m]
D	Pipe diameter, [m]
$D_{\alpha\beta}$	Inter-phase drag force, [N]
D_H	Mixer hydraulic diameter, [m]
D_I	Impeller diameter, [m]
Eo	Eotvos number
f	Friction factor
f_B	Break-up coefficient
f_{BV}	Dimensionless variable describing the sizes of daughter drops
f_C	Coalescence coefficient

$\mathbf{F}_{\alpha}$	Inter-phase non-drag forces, [N]
Fr	Froude number
g	Gravity acceleration, [m s^{-2}]
h	Film thickness, [m]
i	Turbulence intensity
k	Turbulent kinetic energy, m^2 s^{-2}
k_1, k_2	Parameter in Eq. (2-19)
l_k	Kolmogorov length scale
m	Refractive index
$\dot{m}_{\alpha\beta}$	Mass flow rate per unit volume into phase α from phase β, [kg m^{-3}]
$\mathbf{n}$	Normal to the wall
n_i	Particle number density, [m^{-3}]
n_l	Unit normal to the wall
n_w, n_o	Multiplier in the Blasius type equation described in Eq. (2-10).
N	Rotation speed of impeller, [rpm]
N_P	Number of phases
p	Pressure, [Pa]
P	Power input (W), Eq.(2-9)
Q_{ij}	Coalescence rate
Q	Volumetric flow rate
r	Radial coordinate
r_i, r_j, r_{ij}	Radius of drop i and drop j and the equivalent radius
R	Reflectivity.
Re	Reynolds number
s	Solid surface area per unit volume in Eq. (2-15), [m^2/m^3]
$S_{ij}^{\ 2}$	Collision cross-sectional area of the particle
S_M	Source includes the overall effect of body force
$\mathbf{T}$	Stress tensor
t_c	Circulation time of an inclusion in the dispersed droplet
$\mathbf{U}$	Velocity vector given by $\mathbf{u}$ = [u, v, w], [m s^{-1}]
$u_{ti(tj)}$	Turbulent velocity
u_{in}	Normal velocity at inlet, [m s^{-1}]
$\mathbf{U}$	Fluid (mean) velocity of phase, [m s^{-1}]

v_i	Drop volume, [m^3]
v_I, v_{II}	Volume of the daughter drops in the binary breakage of a parent drop with volume v
v_m	Superficial liquid mixture velocity, [$m\ s^{-1}$]
v_T	Total velocity of the dispersion, [$m\ s^{-1}$]
V	Volume of a single drop
We	Weber number
x_n	Normal distance to the wall
y_w	Distance from the wall, [m]

Greek Symbol

α	Constant in Eq. (2-9)
χ_c	Critical dimensionless energy for break-up
δ_{ij}	Kronecker delta
ε	Turbulent energy dissipation rate, [$m^2\ s^{-3}$]
ε	Phase holdup or volume fraction.
$\phi_{o,i}$'	Constant value at high impeller speeds, Eq. (2-9)
η_{ij}	Collision efficiency
κ	von Karman constant
μ	Liquid viscosity, [Pa s]
μ_T	turbulent viscosity
θ	Contact angle (rad)
σ_k, σ_ε	constants of standard k- ε model
ρ	Density, [kg/m^3]
$\Delta\rho$	Density difference, [kg/m^3]
σ	Interfacial tension or surface tension, [N/m]
σ_t	Turbulent Prandtl/Schmidt number
τ	Wall shear stress
τ_{ij}	Contact time of two drops
ξ	Turbulence dimensionless size of eddies in the inertial sub-range of isotropic
Γ_t	Turbulent diffusivity
δ_{film}	Thickness of the film

ν	Kinematic viscosity
μ_t	Turbulent or eddy viscosity
δ_{ij}	Kronecker delta, $\delta_{ij} = 1$ if $i = j$ and $\delta_{ij} = 0$ if $i \neq j$

Subscript

1,2	Continuous and dispersed phases, respectively, or core and annulus phase, respectively in Section 4.6.2.1.
a	Aqueous phase
c	Continuous phase
d	Dispersed phase
i	Inversion point
I	Impeller, Eq. (2-10) –(2-11)
m	Mixture liquids or measured value
o/w, w/o	Oil-in-water dispersion and water-in-oil dispersion
o	Oil phase or organic phase
p	Prediction
w	Water phase
α	Continuous phase
β	Dispersed phase

CHAPTER 1

Introduction

Multiphase flow is the simultaneous flow of two or more immiscible phases (gas, liquid or solid) in direct contact in a given system. These flows are encountered in a wide range of industries ranging from the petroleum and chemical industries to nuclear and geothermal power plants. Thus, the study of multiphase flows is pertinent to the design and operation of industrial processes and the equipment associated with these processes.

1.1 Liquid-liquid Pipe Flow

In the petroleum industry, two-phase oil-water flows are of central importance in production wells and sub-sea pipeline systems. As an oil well becomes older, de-natured water is often injected into the well to push oil from the reservoir. In these cases, the well may be economically operated even for "water cuts" (volumetric flow fractions of water) as high as 90%. The presence of water in the pipe will affect the transport of oil from the reservoir to the processing unit in the sense that when two immiscible liquids flow together in a pipe the mixture will behave differently from a single-phase flow. The pipeline flow of water-oil mixture presents unique and complex problems due to its complicated rheological behaviour and the vast difference in pressure gradients encountered for different flow patterns. Transport of mixtures with certain flow patterns might influence strongly the input power required to pump the mixture. Figures 1.1 and 1.2 show a schematic description and map (Soleimani, 1999) of the liquid-liquid flow regimes, respectively. The main flow

patterns observed in liquid-liquid flow can be classified into five categories as follows (Arirachakaran *et al.* 1989):



(i) Segregated (or stratified) Flow – The two fluid phases flow in separate stratified layers separated by either a smooth or a wavy surface depending on the velocities of the phases.



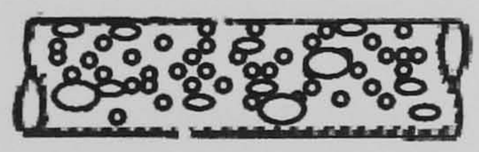
(ii) Mixed Flow – This regime can be divided into several sub-regimes, such as a flow with separated layers of dispersion (water-in-oil or oil-in-water) and a 'free' phase or a dual continuous flow which with water-in-oil dispersion and oil-in-water at the bottom and top of the pipe, respectively.



(iii) Slug Flow – One liquid phase flows as a large spherical or elongated slug in another liquid phase.



(iv) Annular Flow – One of the liquids forms an annular core in the centre of the pipe while the other liquid flows in the annulus surrounding it. This flow regime is common when the two liquids have similar densities or when one liquid has a large viscosity compared to the other.



(v) Dispersed Flow – One fluid forms a dispersion of drops within the continuous phase of the other fluid.

Figure 1.1 Schematic representations of possible flow regimes in a horizontal pipe (Arirachakaran *et al.* 1989)

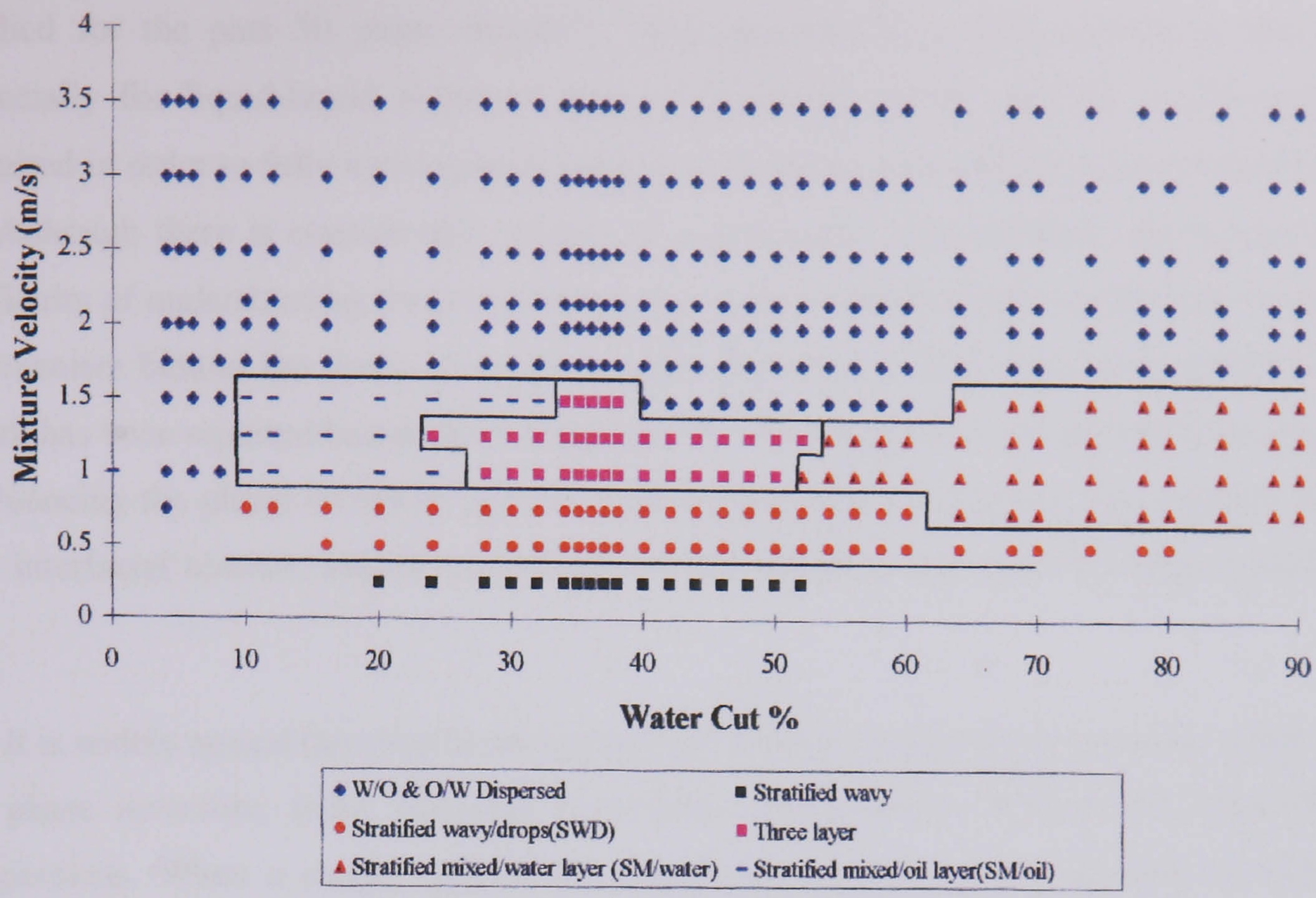


Figure 1.2 Flow regime map in liquid-liquid flow in a horizontal pipe (Soleimani, 1999)

The work described in this thesis mainly concentrates on one form of two-phase flow, namely the dispersed flow of two immiscible liquid phases. Two-phase liquid-liquid dispersed flow, where one phase is usually an aqueous phase (e.g. water) and the other one is organic (e.g. oil), and where one phase is dispersed as droplets in the other, is a flow pattern which is often observed in liquid-liquid systems.

Liquid-liquid two-phase dispersed flows are found in a wide range of applications, in both continuous flow (e.g. production wells and pipeline transportation) or in batch systems (e.g. two-phase reactors). Compared to gas-liquid two-phase flows, which have been the subject of much attention, the experimental data and theoretical models for liquid-liquid dispersed flows cover only a restricted range of flow configurations and fluid properties. Much of the previous work on liquid-liquid systems has been concentrated on liquid-liquid dispersions in agitated vessels. There is substantially less material on liquid-liquid pipeline flow systems.

In oil-water two-phase flows, both water-in-oil (w/o) and oil-in-water (o/w) dispersions may occur depending on the phase fractions. *Phase inversion* occurs when, in a liquid dispersion, the continuous phase changes. For example, with a change of water fraction or other conditions in an oil-in-water dispersion, the system changes from a dispersion of oil drops in water to a dispersion of water drops in oil. Little is known about the detailed mechanism of the phase inversion phenomenon despite the fact that phase inversion has been

studied for the past 50 years. Recently, there has been a revived interest in this area especially for liquid-liquid dispersed flow. Nevertheless, much research is still urgently required in order to fully understand the phase inversion process and the mechanisms behind it. Although there is considerable amount of experimental data available, the fundamental difficulty of understanding the phenomenon lies in the problem of conceptualising the actual mechanism behind the phase inversion process. However, a large amount of experimental work has been reported based on investigating the various physical and geometry parameters influencing the phase inversion process, such as, the density difference, the viscosity ratio, the interfacial tension, impeller speed (or mixture velocity) and vessel (or pipe) geometry, etc.

It is widely agreed that drop break-up and coalescence are important processes which lead to phase inversion; these processes accompany the evolution of turbulent liquid-liquid dispersions. When a steady state of the dispersion is reached, breakage and coalescence reach a dynamic equilibrium, and they control the steady state drop size distribution. After a decrease in the stirrer speed and/or an increase in the dispersed phase holdup, the coalescence rate becomes increasingly dominant over that of break-up, resulting in an overall increase in drop sizes, which promotes phase inversion. Pacek *et al.* (1994a) postulated that simultaneous break-up of the continuous phase is required to explain the inversion process. By monitoring the change in the full drop size distribution and the mean drop size, they showed that, both continuous phase break-up to produce droplets-within-drops (i.e. secondary dispersions) and enhanced coalescence of the dispersed phase to give larger drops, play a significant role in phase inversion.

In spite of the many studies conducted on phase inversion, a fundamental understanding of the mechanism leading to phase inversion has not yet been achieved. The development of such an understanding requires direct visualisation of the dynamic evolution of the phase inversion process in concentrated liquid-liquid dispersions. The main aim of the work described in this thesis was therefore to apply non-intrusive visualization techniques to the investigation of liquid-liquid dispersed flow and the phase inversion process.

1.2 Objective of the Study

The work presented in this thesis was performed as part of a joint project carried out by teams at Imperial College London (ICL), University College London (UCL) and the University of Edinburgh (EU). The work was aimed at combining leading-edge experimental

and theoretical efforts in order to gain a fundamental understanding at the mesoscale level and to derive models for the prediction of phase inversion at the process level. Experimental studies are being undertaken at the mesoscale by teams at both ICL and UCL, whilst a process-level analytical study is also being undertaken at UCL. A theoretical study of phase inversion at mesoscale level is being conducted at EU using explicit numerical simulation (ENS) based on the lattice gas automata (LGA) method. This work will be validated against the experimental data obtained from the mesoscale experiments. Applied models for use at the process level have been derived and parameterized on the basis of the mesoscale simulation and experimental work, and validated against the data obtained from the process-level experiments (undertaken jointly by ICL and UCL).

The experimental work described in this thesis aims to exploit novel visualization techniques, which involve the use of matched refractive index liquids, fluorescence (or photochromic) dyestuffs dissolved in these liquids and the activation of the dyestuffs (with subsequent observation of the flow) by illumination with a laser sheet.

The work described here had the following main objectives:

1. To search for a liquid pair whose refractive indices matched and for the appropriate dyestuffs.

2. To design and build a flow facility to perform experiments.

3. To utilize modern instrumentation techniques, in particular laser-induced fluorescence and laser photochromic dye tracing, to produce a better phenomenological understanding of liquid-liquid dispersed flow and phase inversion.

4. To study liquid-liquid systems, in pipe flow and in agitated vessels, paying particular attention to the phenomena associated with phase inversion.

5. To simulate the liquid-liquid dispersed flow by using CFD software and compare the drop size distribution and phase distribution with the experimental results.

Specific issues addressed by the work included:

(a) Whether the deciding factor for phase inversion is enhanced dispersed phase coalescence and/or the formation of secondary dispersions;

(b) The time scale of the phase inversion phenomenon;

(c) Whether phase inversion appears in the whole system globally or locally; whether the appearance of local phase inversion depends on the concentration distribution in the dispersed system;

(d) Differences, in the phase inversion mechanism in pipeline flow and in a stirred vessel, between the case where the system approaches phase inversion from the aqueous continuous side and the case when phase inversion is approached from the oil continuous side.

1.3 Structure of the Thesis

This thesis is organised as follows. A detailed literature review of liquid-liquid pipe flow and phase inversion and associated phenomena is given in Chapter 2. Chapter 3 then introduces the chosen experimental method (laser-induced fluorescence) and the experimental apparatus used. The physical properties of the chosen liquids are also presented. Chapter 4 and 5 described the experiments on visualisation of pipe flows for high and low mixture velocities respectively. Chapter 6 describes the experiments in agitated vessel. As was mentioned above, studies of the use of photochromic dye tracing for visualisation of phase inversion phenomena were also planned for the present work; a limited amount of work was done on this technique and this is described in Appendix A. However, laser-induced fluorescence was found to give much more useful information and the work was focussed on the application of this latter technique.

Numerical simulations of liquid-liquid pipe flows were also carried out as part of the work described in this thesis. There are implemented using a commercial Computational Fluid Dynamics (CFD) code (CFX4.4). Calculations were carried out for both a circular tube and also for a square cross-section duct (the geometry used in the present experiments). The basic equations and the calculations for the circular tube and square duct cases are presented in Chapter 7 and 8 respectively. The CFD predictions of dispersed flow in a circular pipe were compared with the published experimental results (Farrar & Bruun, 1996). The aim of the simulations on the dispersed flow in a square duct was to understand the influence of the turbulence-induced secondary (corner vortex) flows. Finally, the conclusions and recommendations for the future work are presented in Chapter 9.

CHAPTER 2

Literature Review

This chapter reviews significant developments over the past fifty years in the study of the behaviour of liquid-liquid mixtures in agitated containers and pipelines, with a focus on the phase inversion phenomenon. Section 2.1 reviews liquid-liquid pipe flow and focuses on flow pattern, pressure gradient, phase distribution and drop size distribution. Section 2.2 reviews the phase inversion process for both pipe flows and agitated vessels; in this section, the experimental and theoretical work on phase inversion and associated phenomena, such as the ambivalent range, the critical holdup for phase inversion, the influence of parameters on phase inversion, etc., are introduced. Experimental methods are also reviewed. Drop coalescence and breakup, which are postulated mechanisms for phase inversion, are also discussed in Section 2.2 and a brief review of simulation methods for phase inversion is also given in this section. A short summary is then given in Section 2.3.

2.1 Liquid-liquid Pipe Flow

Multiphase flows are defined as the simultaneous flow of two or more phases in a system. The phases are liquid, gas or solid and a whole range of combinations of phases is possible. Two-phase flows (gas/liquid, liquid/liquid, gas/solid and liquid/solid) are the simplest and the most common of the multiphase flow systems. However, they are still fundamentally complex. It is not surprising that fundamental research in multiphase flow has focussed on understanding two-phase flows. Compared to the vast amount of work on gas-liquid flows, experimental data and theoretical studies on liquid-liquid pipe flows, especially vertical pipe flows, have covered only a very restricted range of geometries and flow rates. The flow characteristics of liquid-liquid (e.g. oil–water) mixtures are generally different from liquid–gas systems, so the results of liquid–gas flow cannot be applied directly to liquid-liquid flow in most cases. Most work on liquid-liquid flows has focused on horizontal pipes, with comparatively little in vertical pipe flows.

2.1.1 Flow Pattern

When two immiscible liquids flow together in a pipe, the interfaces between them distribute in a variety of "flow patterns". Each individual flow pattern has its unique hydrodynamic properties. The occurrence of a particular flow pattern depends on a number of parameters, such as phase input fractions, mixture velocities, pipe wettability and liquids physical properties, etc. The regions of occurrence of flow patterns are usually delineated in terms of areas on a graph demonstrating the effect of two independent parameters, e.g. the mixture velocity and the input volume flow fraction.

Russel *et al.* (1959) studied the flow of a white mineral oil (18 mPa s viscosity and 834 kg/m^3 density) and water in a smooth transparent 25.4 mm diameter horizontal pipe, for oil-water flow ratio values ranging from 0.1 to 10 and for water velocities ranging from 0.0350 to 1.08 m/s. They measured pressure drop and described the flow patterns at different input rates of each phase (generally classified as stratified and mixed). Charles *et al.* (1961) carried out oil-water flow experiments using three kinds of oil. Carbon tetrachloride was added to the oils, so that the density of the oil phase increased to 998 kg/m^3, close to that of water. Three oil were used with different viscosities 6.29, 16.8 and 65.0 mPa·s at 25 °C and with oil-water interfacial tensions of 0.044,0.045 and 0.30 N/m respectively. The flow patterns

observed were oil drops in water, oil slugs in water, oil in water concentric flow (i.e. water annulus and oil core) and water drops in oil (dispersed). The flow pattern map derived from these observations is shown in Figure 2.1. Interestingly, the only form of annular flow found was the water-annulus/ oil-core. Oil-annulus annular flow was not recorded.

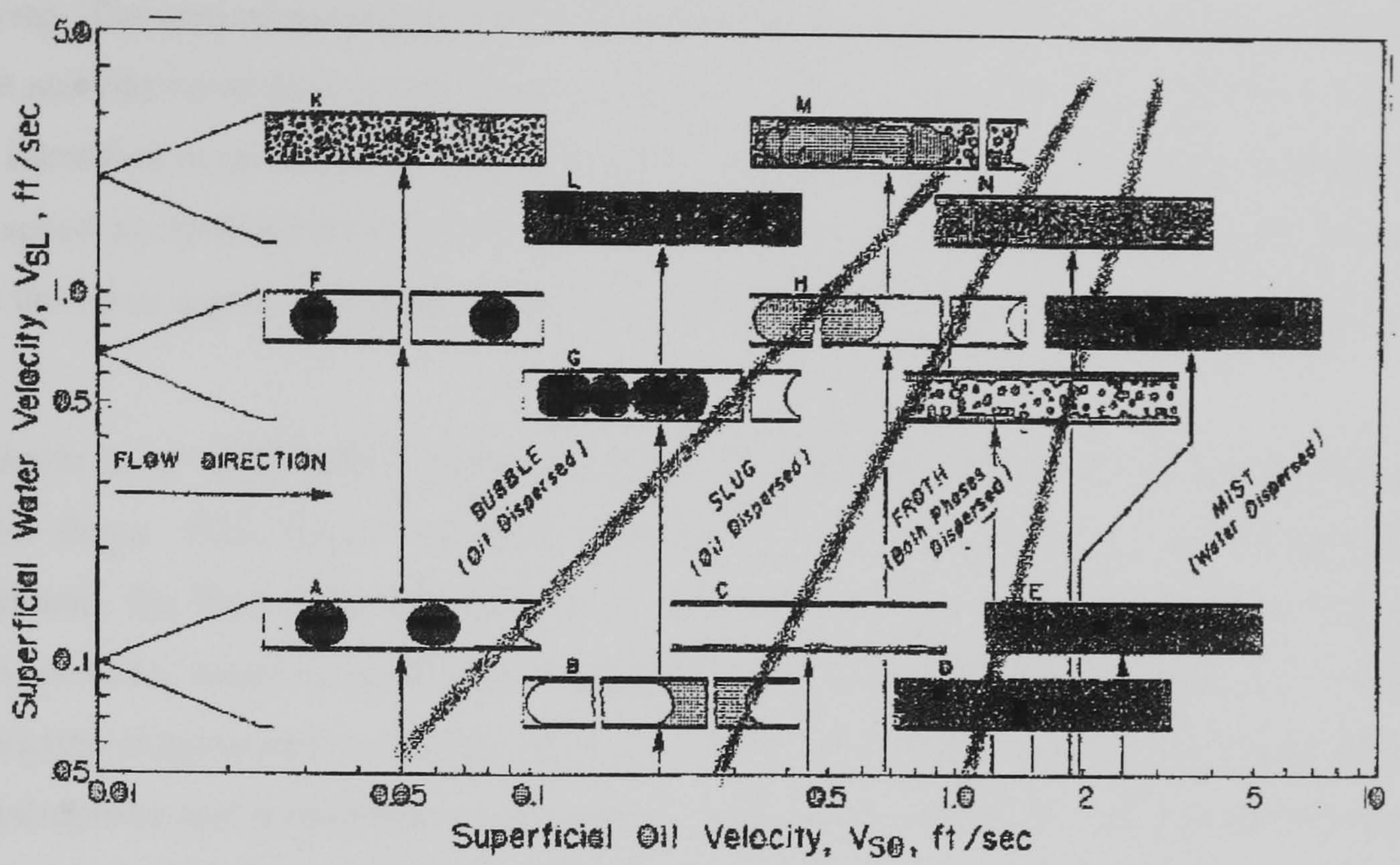


Figure 2.1 Flow patterns for a 16.8 mPa s, 998 kg/m^3 oil and water system in a 0.026 m ID pipe based on observations of Charles *et al.* (1961). Map as published by Govier and Aziz (1972).

Hasson *et al.* (1970) studied the flow mechanisms of core-annular flow of two immiscible liquids with similar densities: distilled water and a kerosene-perchlorethylene solution mixed to get a density of 1020 kg/m^3 in a horizontal 12.6 mm internal diameter, 2.7 m long glass pipe. The viscosity and surface tension of these fluids at 30 °C, were respectively 1.0 mPa·s, and 0.067 N/m for the water phase and 0.82 mPa·s and 0.0285 N/m for the organic phase. In the experiments, a concentric flow, with the lighter and more viscous water phase as the core and the heavier and less viscous organic phase as the annulus, was initially found at the inlet. Break-up of this initial configuration then occurred; water tended to be in contact with the whole pipe periphery because of its preferential wetting properties. In the final configuration the heavier organic liquid accumulating at the bottom of the pipe either formed a body of revolution separated from the wall by a water film or, if the glass was not sufficiently clean, spread in to a stratified layer. The break-up mechanisms were observed to be of two types: either a wall film rupture, (a low speed phenomenon) or core breakup due to the growth of

interfacial waves (a high speed phenomenon). The occurrence of the film rupture was considered to be strongly related to the relative wall wetting properties of the two liquids. The water core exerted a potentially disruptive influence on the wall film due to its tendency to preferentially wet the walls. To demonstrate this influence, a hydrophobic treatment using silicone was applied to the walls and stable core-annular flows were obtained without film break-up. The second mechanism of core flow break-up was attributed to the appearance of waves and ripples at the interface between fluids in the annulus and in the core. These waves were identified to be Rayleigh-type waves, which were originally observed in the studies of slow speed jet disintegration. Break-up of the annular flow through this mechanism occurred when the wave amplitude reached the core centre and this led to the formation of slug flow.

Hasson *et al.* (1970) also studied the stable flow patterns that followed the break-up of annular flows. They found that these patterns were mainly determined by the break-up mechanism, the flow rates and the wetting properties of the pipe wall. The flow patterns observed were: water-in-organic and organic-in-water dispersions; water slugs in organic and organic slugs in water; stratified flow and stable annular flow. Flow pattern maps drawn for hydrophilic and hydrophobic wall wetting conditions showed that the hydrophobic pipe provided the maximum length of the annular regime because it prevented the occurrence of film break-up, while the area of occurrence for all the other flow patterns remained more or less constant as illustrated in Figure 2.2. It was also found that for low organic to water flowrate ratios and a hydrophilic pipe surface, film break-up yielded flow patterns in which water remained as a continuous phase, with the organic phase forming either a dispersion or slugs or a stratified layer. At high organic to water flowrate ratios, core break-up was followed by patterns in which the organic liquid was the continuous phase, with water broken-up either in slugs or as a dispersion irrespective of the pipe-surface.

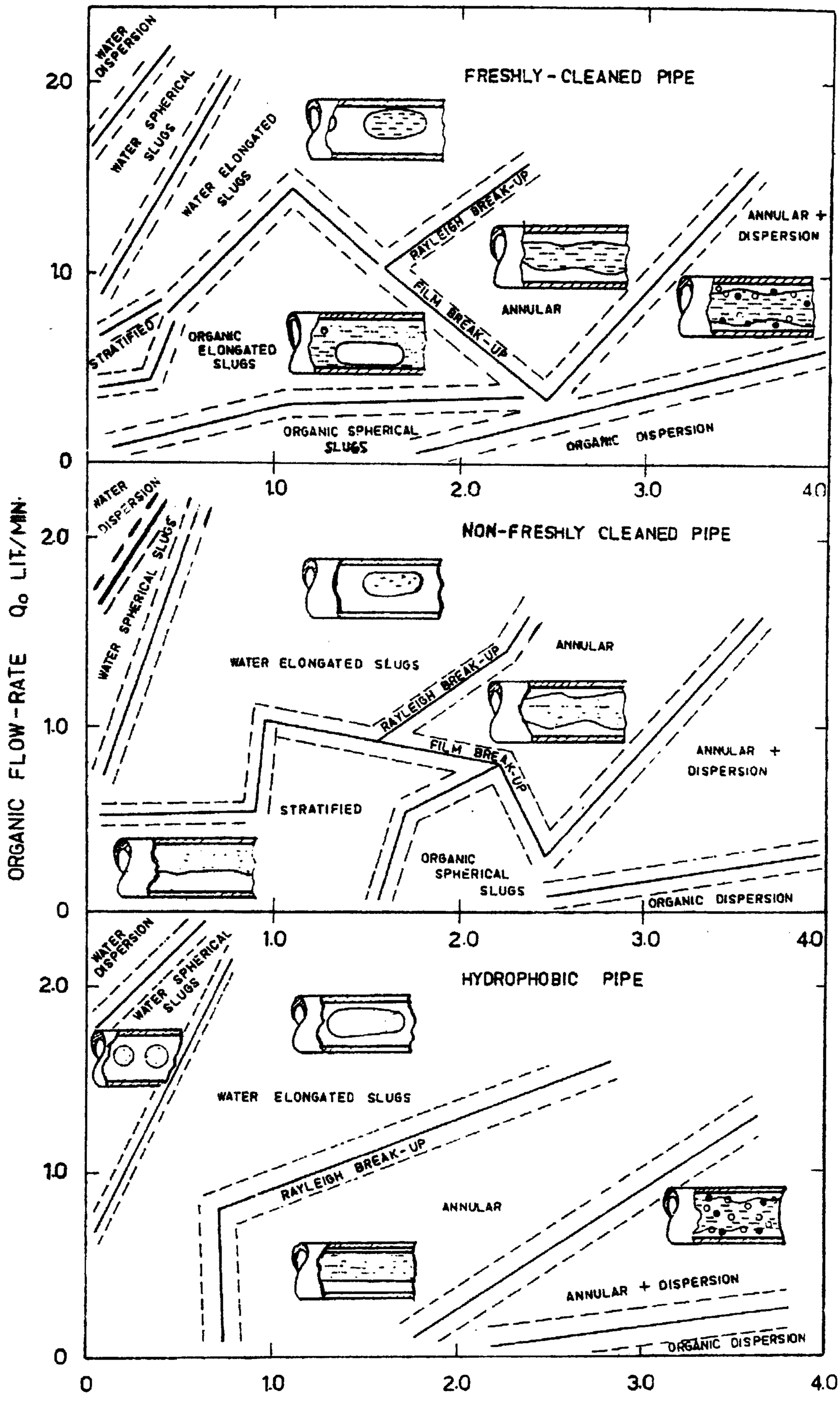
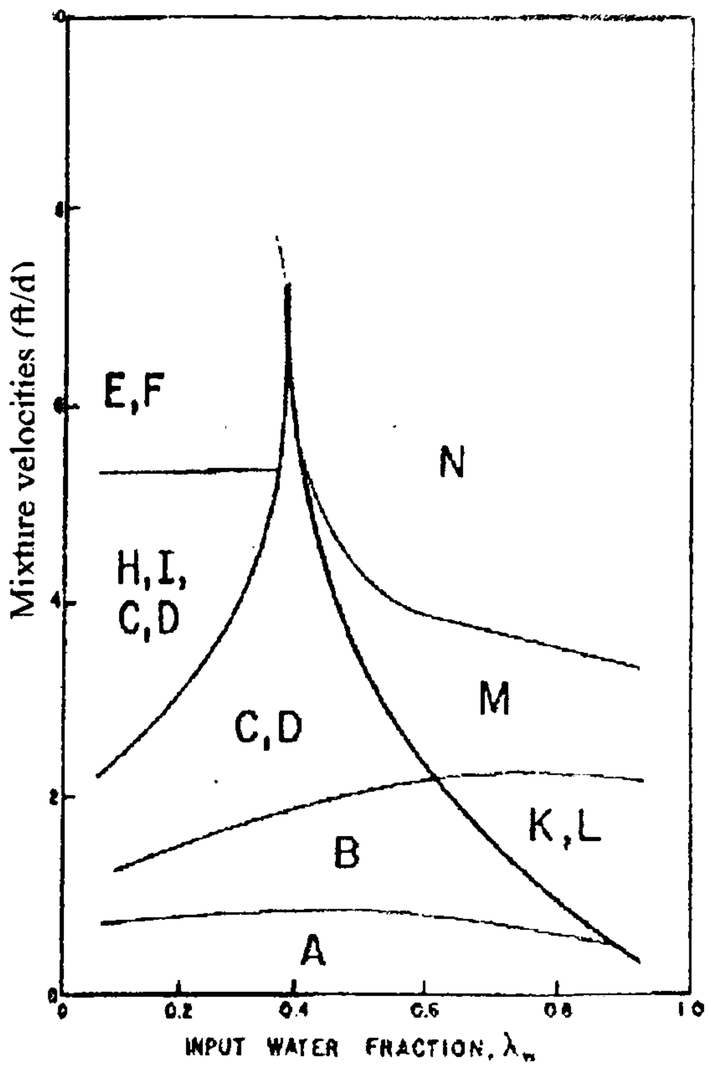


Figure 2.2 Flow patterns for a 0.82 mPa s, 1020 kg/m^3 kerosene-perchlorethylene solution and water system in a 1.26 cm ID glass tube based on observations of Hasson *et al.* (1970).

Guzhov *et al.* (1973) determined the flow patterns (see Figure 2.3) and pressure drops for an oil-water system where a transformer oil with a viscosity of 21.7 mPa s and a density of 896 kg/m^3 at 20°C was used as the non-aqueous phase.



A- Segregated : (no mixing at the interface)
B- Semi-segregated: (some mixing at the interface)

Oil dominant

C- semi-mixed: layers of free oil and oil in water dispersion. The layer of the dispersion occupies less than 50% of the pipe diameter.
D- Mixed: layers of free oil and oil in water dispersion. The layer of the dispersion occupies more than 50% of the pipe diameter.
E- Semi-dispersed: Non-homogeneous water in oil dispersion.
F- Dispersed: Homogeneous fully dispersed flow
G – Annular: water core and oil film
H- Slug: Water slugs in oil.

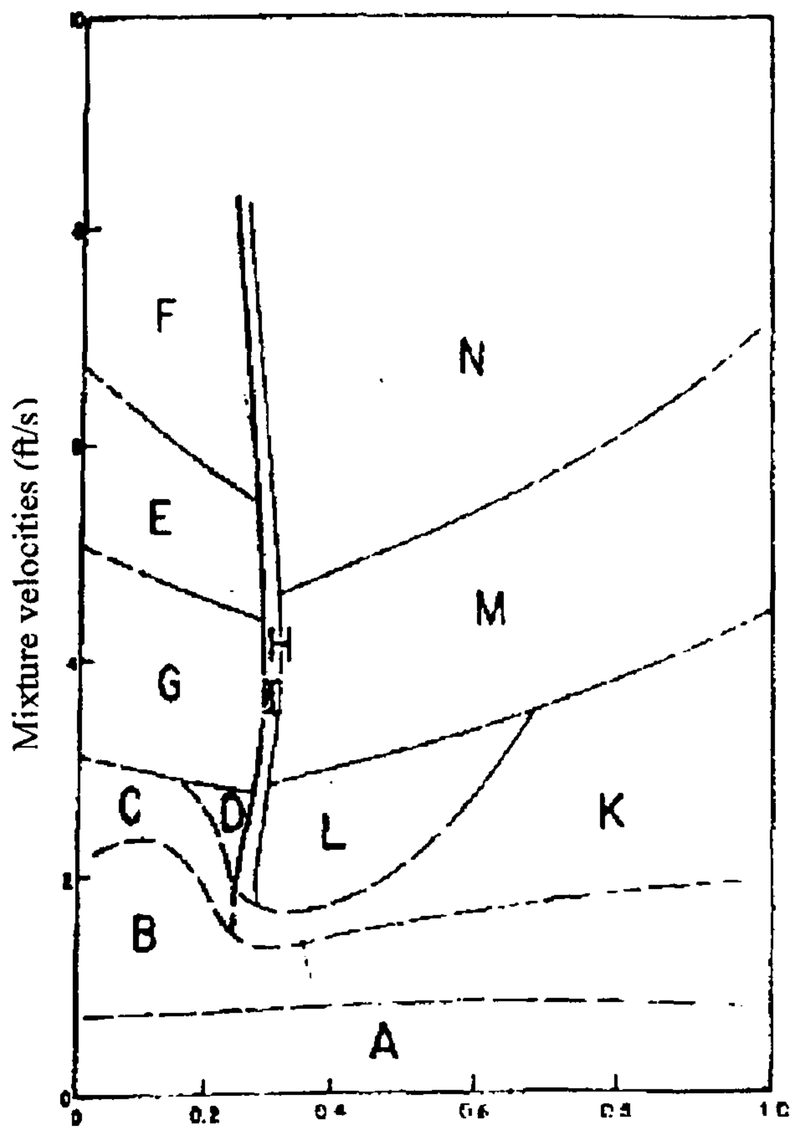
Water dominant

I- Slug: oil slugs in water
J- Annular: oil core and water film
K- Semi-mixed: layers of free water and water in oil dispersion. The layer of the dispersion occupies less than 50% of the pipe diameter.
L – Mixed: layers of free water and water in oil dispersion. The layer of the dispersion occupies more than 50% of the pipe diameter.
M- semi-dispersed: Non-homogeneous water in oil dispersion.
N- dispersed: homogeneous fully dispersed flow.

Figure 2.3 Flow patterns for a 21.7 mPa s, 896 kg/m^3 oil and water system in a 0.0394 m pipe based on observations of Guzhov *et al.* (1973), as revised and presented by Oglesby *et al.* (1979).

Oglesby (1979) conducted a study on horizontal oil-water pipe flow for three oils with viscosities of 58.0, 84.0 and 115.0 mPa s at 21 °C. The observed oil-water flow patterns, classified according to the definitions of Oglesby (1979), are shown in Figure 2.4. Three basic flow patterns previously described by other researchers (stratified, dispersed and intermittent) were also observed in this work. However Oglesby (1979) was the only investigator to report the extra flow configuration of an annular flow with a core of water rather than oil. This apparently contradicted the *minimum viscous dissipation principle* used in the works of MacLean (1973) and Joseph *et al.* (1984), in which it was hypothesised that in a pipe flow of two liquids with different viscosities under an applied pressure drop, the low-viscosity liquid would tend to encapsulate the high-viscosity liquid. This contradiction could possibly be overcome if one could consider that the water core would be in turbulent flow, while the oil annulus would be in laminar flow. By this means the apparent viscosity of

the water would be greater than that of the oil and the principle would still hold. A similar explanation could also be extended to gas-liquid annular flows where the less viscous gas core is surrounded by a liquid film. The flow pattern maps for the other two oils had very similar trends, with the main difference in the diminishing size of the region of occurrence for the uncommon more viscous annulus/less viscous core flow pattern when the oil viscosity was lowered; to the point of its complete extinction for the 32 mPa s viscosity oil. In Oglesby (1979)'s flow pattern map, there is a long and narrow area in which intermittent flow occurs and Oglesby (1979) related the occurrence of this intermittent flow to the phase inversion point.



A- Segregated: (no mixing at the interface)
B- Semi-segregated: (some mixing at the interface)

Oil dominant

C- semi-mixed: layers of free oil and oil in water dispersion. The layer of the dispersion occupies less than 50% of the pipe diameter.
D- Mixed: layers of free oil and oil in water dispersion. The layer of the dispersion occupies more than 50% of the pipe diameter.
E- Semi-dispersed: Non-homogeneous water in oil dispersion.
F- Dispersed: Homogeneous fully dispersed flow
G – Annular: water core and oil film
H- Slug: Water slugs in oil.

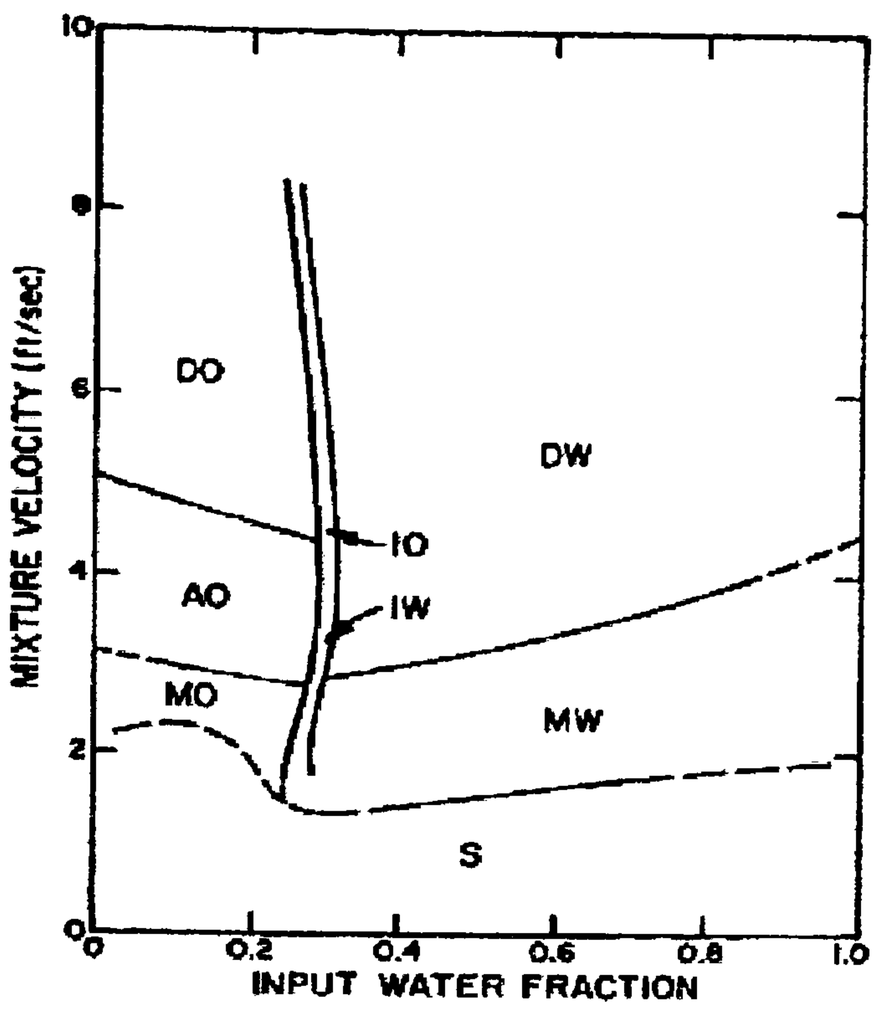
Water dominant

I- Slug: oil slugs in water
J- Annular: oil core and water film
K- Semi-mixed: layers of free water and water in oil dispersion. The layer of the dispersion occupies less than 50% of the pipe diameter.
L – Mixed: layers of free water and water in oil dispersion. The layer of the dispersion occupies more than 50% of the pipe diameter.
M- semi-dispersed: Non-homogeneous water in oil dispersion.
N- dispersed: homogeneous fully dispersed flow.

Figure 2.4 Flow patterns for an 84.0 mPa s oil and water system in a 0.041 m pipe based on observations of Oglesby *et al.* (1979).

Arirachakaran *et al.* (1989) studied flow patterns in a 1.5-in horizontal pipe using four types oils with viscosities of 4.7, 58, 84 and 115 mPa s respectively (Figure 2.5). Mixture velocities were varied from 0.45 to 3.6 m/s, while the input water fraction range was between 0.05 and 0.9. Water-annular flow was not observed for any of the oils in their flow pattern study. It was believed that the oils used in their studies were not viscous and heavy enough to sustain a stable oil core in the water-annulus annular flow. Thus the flow type was predominately water-continuous dispersed and mixed flow pattern. An intermittent region was also delineated in the flow pattern map and Arirachakaran *et al.* (1989) considered that

the two phases alternately occupied the pipe as the continuous phase or as a dispersion in this region.



Stratified flow (S): Possibly with some mixing at the interface.

Mixture flow (MO, MW): With separated layers of a dispersion and 'free' phase.

Annular flow (AO): Core of one phase within the other phase.

Intermittent flow (IO, IW): Phases alternatively occupying the pipe as a free phase or as a dispersions

Dispersed flow (DO, DW): Homogeneous mixture

Figure 2.5 Experimental oil-water system flow pattern map by Arirachakaran *et al.* (1989).

Flores *et al.* (1997) studied oil-water flow in vertical and inclined 0.05 m pipes. They observed water holdup to be strongly affected by flow pattern and inclination and proposed a mechanistic model to predict holdup in vertical wells. They found that a homogeneous model was adequate for flow patterns showing negligible slippage and a drift-flux approach gave reasonable results for the high slippage flow patterns.

Angeli (1996) and Angeli & Hewitt (2000a) studied the flow structure occurring during the co-current flow of oil (1.6 mPa s viscosity and 801 kg/m^3 density) and water in two 25.4 mm horizontal test sections made from stainless steel and acrylic resin respectively. Two methods were used for the flow pattern identification, namely high speed video recording and determination of the local phase fractions with a high frequency impedance probe. In dispersed flows, the identity of the continuous phase was recognized with a conductivity needle probe. Measurements were made for mixture velocities varying from 0.2 to 3.9 m/s and input water volume fractions from 6% to 86%. Over this range of conditions, different flow patterns were observed (Figure 2.6), ranging from stratified to fully mixed. However,

annular flow did not appear. In certain ranges of conditions the distribution of the phases differed dramatically between the stainless steel and the acrylic pipes. In general, the mixed flow pattern appeared in the steel pipe at lower mixture velocities than in the acrylic pipe, where oil was the continuous phase for a wider range of conditions. The average in-situ velocity ratios of the two phases in the acrylic pipe calculated from the phase distribution measurements were in general lower than unity. In Figure 2.6, an undefined region is included between the dotted lines in the fully dispersed flow pattern (Figure 2.6). To the left of this region oil was the continuous phase and to the right of this region water was the continuous phase. It is suggested that an intermediate flow pattern where both phases were periodically continuous in waves exists in this region and between the two dispersed regimes a stratification of the flow possibly happens. Results from the conductivity probe also showed that the change from one continuous phase to the other (phase inversion) is not instantaneous.

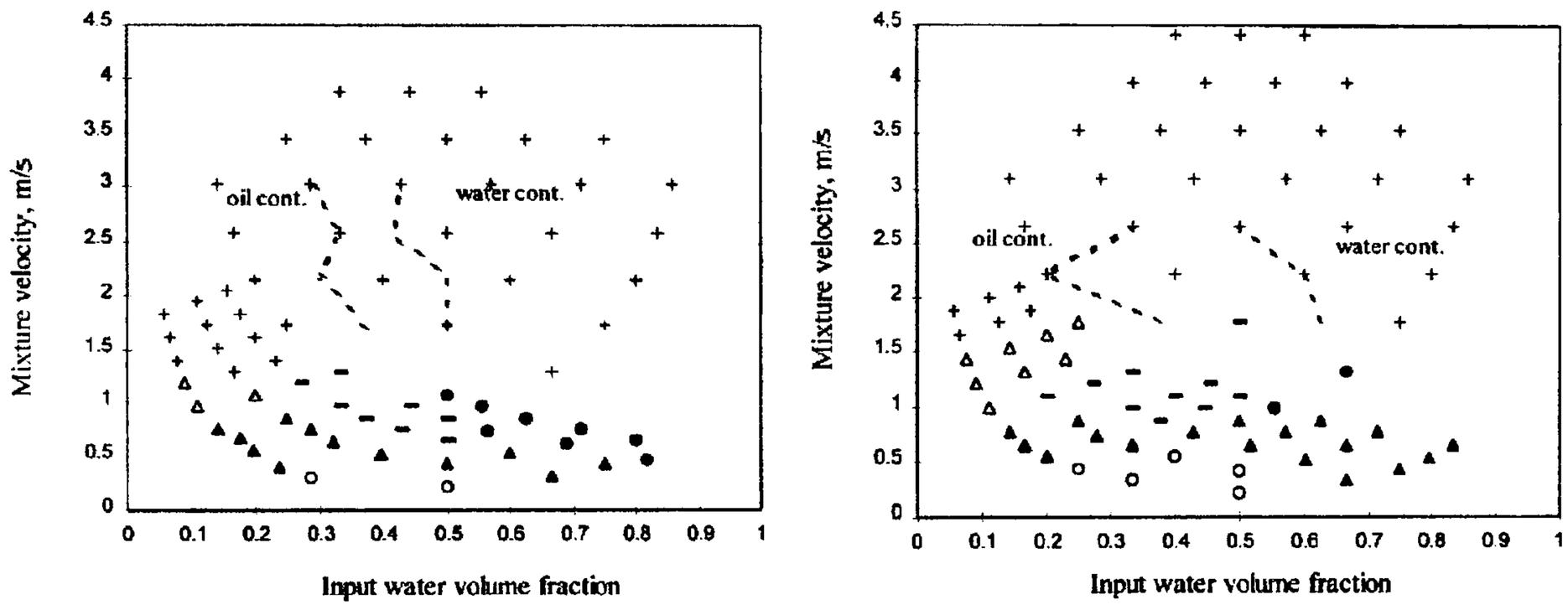


Figure 2.6 Flow patterns by Angeli & Hewitt (2000a) in the (a) stainless steel test section. (b) actylic test section. ○, stratified wavy (SW); ═, three layers (3L); Δ , stratified mixed/oil (SM/oil); - - -, phase continuity boundaries; ▲, stratified wavy/drops (SWD); ●, stratified mixed/water(SM/water); +, mixed (M).

Nädler and Mewes (1997) investigated the flow of oil and water in a horizontal pipe with an inner diameter of 59 mm and a total length of 48 m. Their results presented the effect of emulsification and phase inversion on the pressure drop for different flow regimes of oil-water mixtures. The measurements were conducted for oil viscosities of 22, 27 and 35mPa s, which were obtained by changing the temperature of the liquids. The flow regimes are given in Figures 2.7. Nädler and Mewes (1997) observed that phase inversion took place within the

dispersion layer and hence only in a restricted part of the cross-section. The location of phase inversion within the dispersion layers is given the boundary between regions IIIa and IIIb in Figure 2.7. In region IIIa, the flow is in the form of a water-in-oil dispersion above a water layer. In region IIIb, the flow changes to one in which there are three layers, water-in-oil, oil-in-water and (at the bottom of the pipe) water alone. The input water fraction for the transition from region IIIa to region IIIb changes with mixture velocity as shown in Figure 2.7.

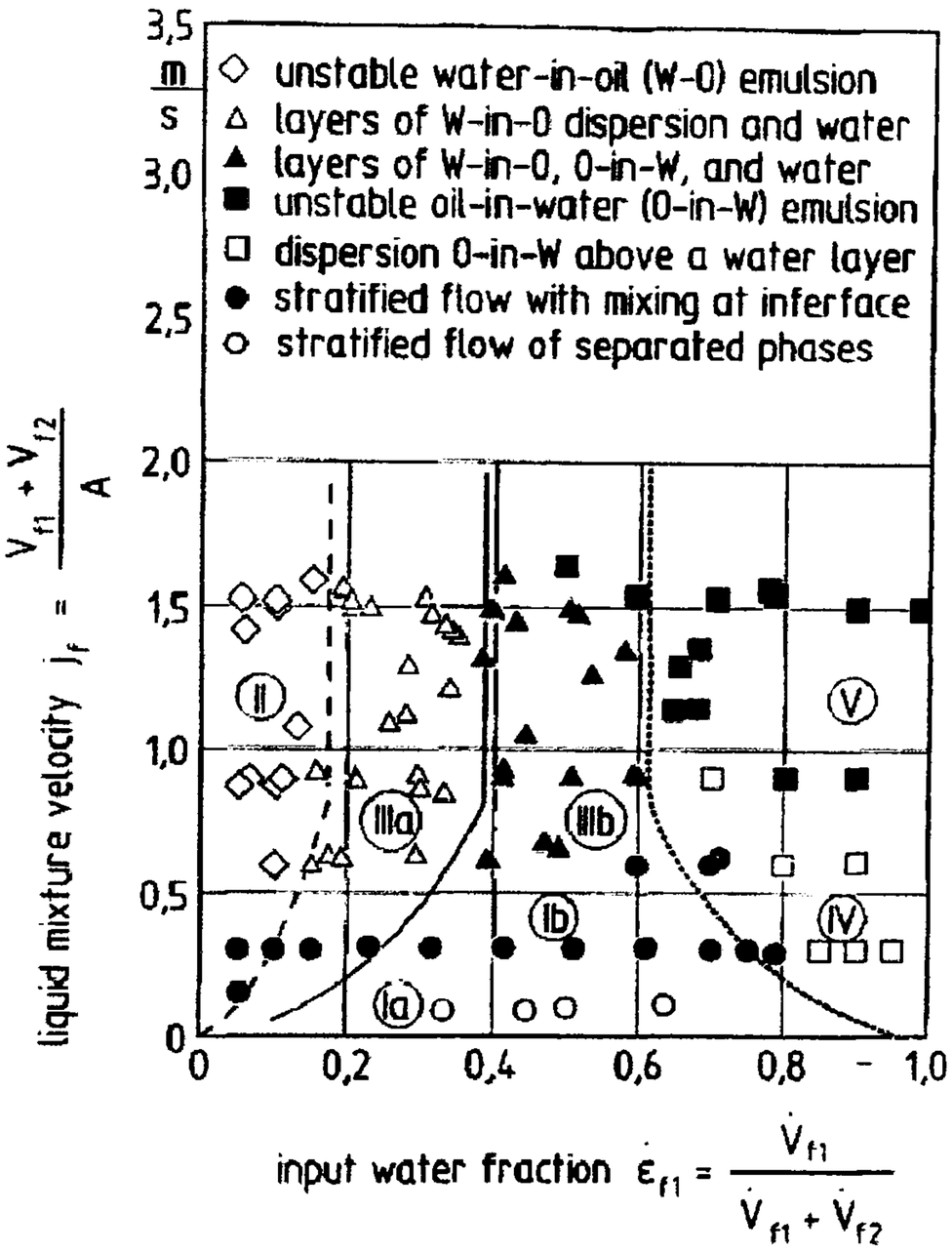
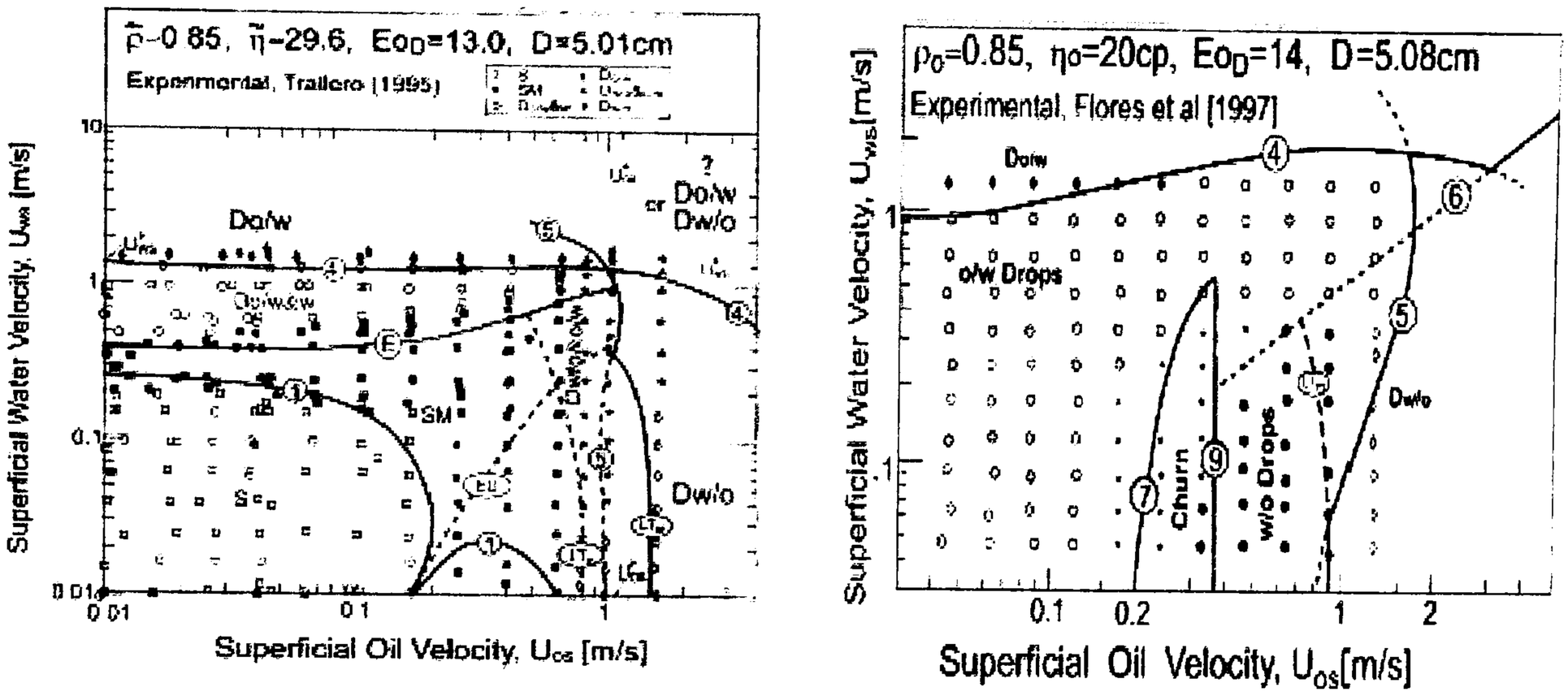


Figure 2.7 Flow regime map (Nädler and Mewes, 1997) for the two-phase flow of water and oil based on input water fraction.

The work of Angeli (1996) was extended by Soleimani (1999) who used a high-speed video camera to identify the water-oil flow pattern (see Figure 1.2); the oil viscosity and density were 1.6 mPa s and 801 kg/m^3 respectively (as in Angeli's work). On the basis of results obtained with a high frequency probe/gamma densitometer system, Soleimani redefined the flow patterns for 1.25 m/s mixture velocity; and concluded that stratified flow of oil and water dispersions rather than a three-layer pattern existed at this velocity.

Brauner (2001) provided an approach for predicting the transition to dispersed flow patterns in liquid-liquid systems. The boundaries between the o/w and w/o dispersion regions

were also considered. In their predictions, the Kolmogorov (1949)–Hinze (1955) model for break-up drops in turbulent flow was revised and for the drop size larger than 0.1D, the relations proposed by Hughmark (1971) and Kubie & Gardner (1977) were employed. Comparisons with experimental data available from the literature indicated that the models were capable of predicting the dispersed flow boundaries in a variety of two-fluid systems over a wide range of fluid physical properties, pipe diameter and inclination (Figure 2.8).



(a) (b)

Figure 2.8 The Brauner (2001) predictions for transition to Do/w (boundary 4) and transition to Dw/o (boundary 5) in (a) horizontal oil-water system (Trallera, 1995) and (b) vertical upwards oil-water flow (Flores, *et al.*, 1997).

Oddie *et al.* (2003) have investigated kerosene-water flow in a 10.9 m long, 152 mm internal diameter pipe inclined at various angels (θ) from the vertical. It was seen that for 0° (upward) $\leq \theta \leq$ 45° (upward 45°), only dispersed and homogeneous flows were observed, indicating that oil and water mix relatively easily at these inclinations. In addition, the flow pattern map changes very little over $0° \leq \theta \leq 45°$. As the pipe deviates further, oil and water tend to become stratified, with two semi-mixed flows observed at low oil and water flow rates for $\theta = 70°$. As the pipe approaches horizontal, most of the flow patterns, including segregated, semi-segregated, semi-mixed, mixed, dispersed, and homogeneous, were observed. For downward flow ($\theta = 92°$), most flows were stratified, with only one dispersed flow observed at high oil and water flow rates.

The dual continuous flow pattern (where both phases retain their continuity at the top and bottom of the pipe while there is inter-dispersion near the middle) was studied by Lovick & Angeli (2004) (Figure 2.9). The experimental work was performed with a 38 mm diameter, horizontal, stainless steel test section, using water and oil (6 mPa s viscosity and 828 kg/m3 density) as test fluids. The identification of the dual continuous flow pattern boundaries was achieved with the use of an impedance and a conductivity probe. Measurements were made for mixture velocities from 0.8 to 3 m/s and input oil volume fractions from 10% to 90%. Dual continuous flow appeared at intermediate mixture velocities between stratified and dispersed flows and resulted in pressure gradients less than those of single phase oil flow. The velocity ratio increased with increasing input oil fraction, and was above 1 at high oil fractions apart from the highest mixture velocities where it reduced to values below 1.

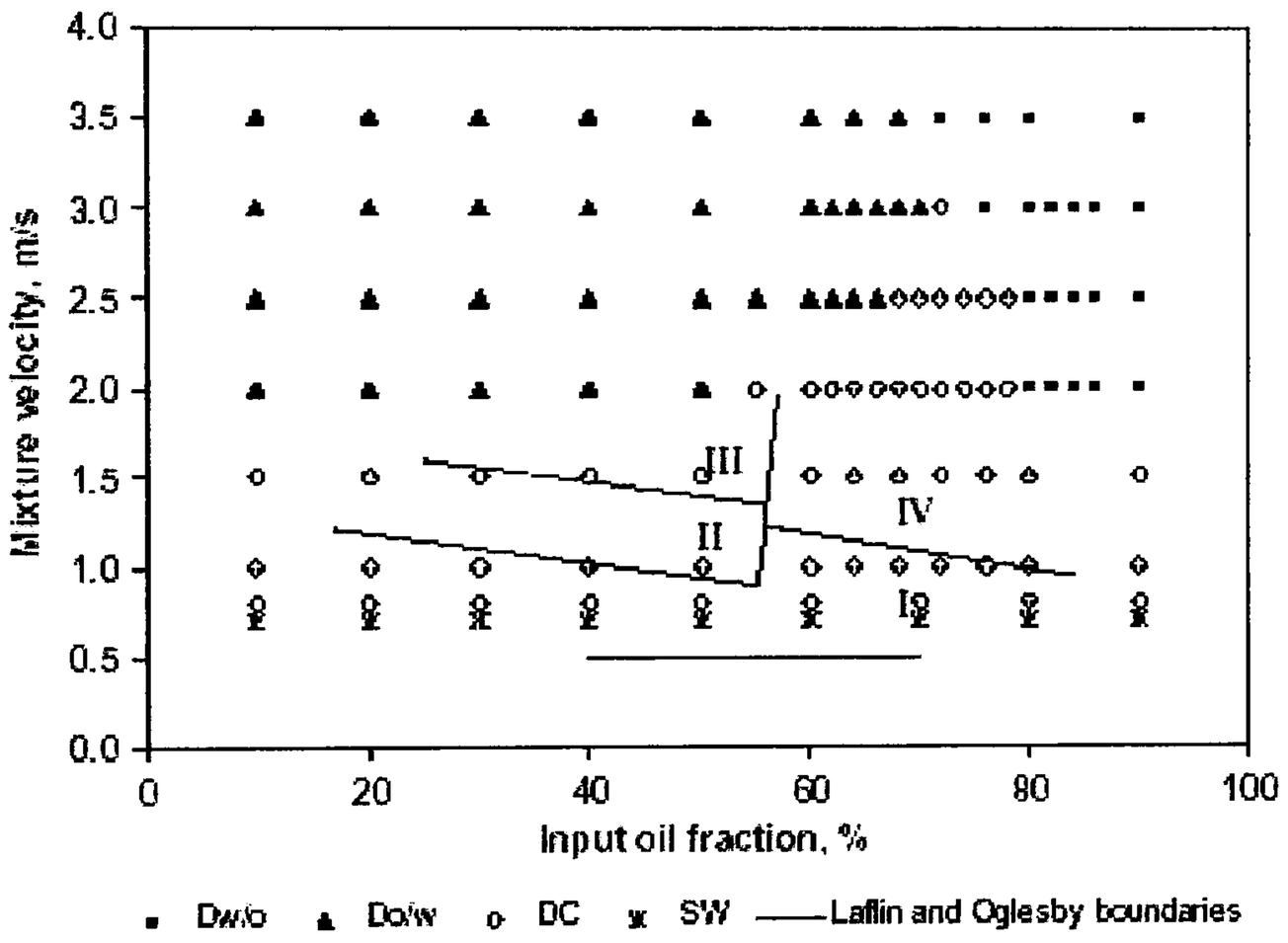


Figure 2.9 Flow pattern map (Lovick & Angeli, 2004) with the results from Laflin and Oglesby (1976) (solid lines). (I) dual continuous flow; (II) dispersion of oil in water and water; (III) dispersion of oil in water; (IV) dispersion of water in oil.

Hussain (2004) extended the work of Angeli (1996) and Soleimani (1999) using the same facility and the same fluids. Similar flow patterns to the previous work were obtained (Figure 2.10a). However, flow patterns were also observed for the case where a five-element KENICS^{TM} mixer was placed immediately downstream of the tube inlet. When the mixer was in place, only four flow regimes were observed named wavy-flow, dispersed oil-in-water, dispersed water-in-oil and fully dispersed flow (Figure 2.10b).

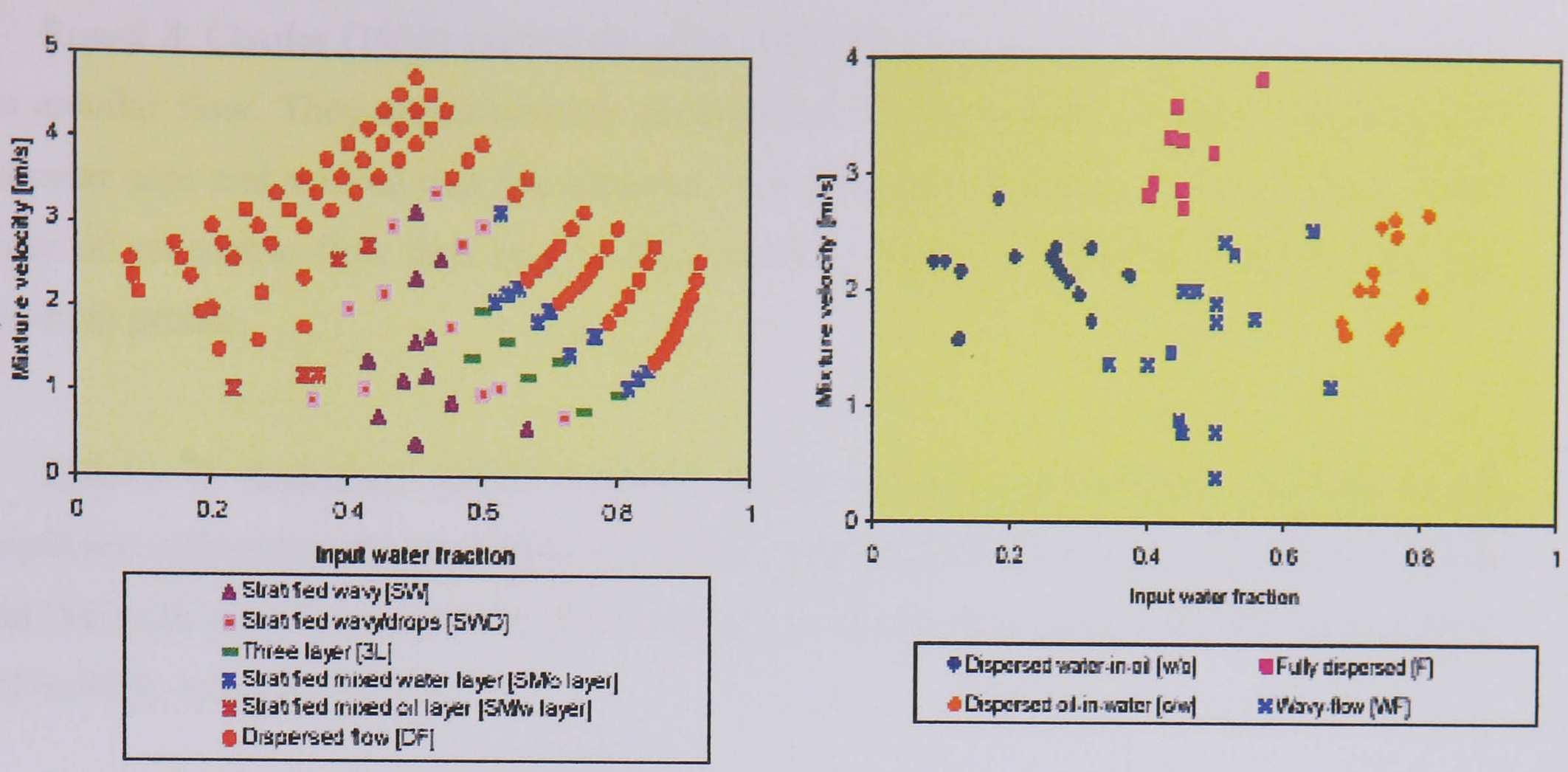


Figure 2.10 Flow pattern maps obtained by Hussain (2004); (a) without mixer and (b) with a 5-element Kenics™ mixer at the tube inlet.

2.1.2 Pressure Gradient

Pressure gradient in liquid-liquid two-phase flow can be quite different from that in single-phase flows and also vastly different for different flow patterns. For instance, annular flow with water as the annulus is perhaps the most useful flow pattern in co-current liquid-liquid flow since it can be used to transport high viscous crude oil with a very low pressure gradient. According to previous investigations, the pressure gradient reduction factor is larger for annular flow (water annulus and oil core) in comparison with other flow patterns. On the other hand, for the dispersed flow pattern, the pressure drop in the pipeline could differ greatly between an oil-in-water and a water-in-oil system. The phase inversion phenomenon, in which the dispersed phase switches to the continuous phase, can cause very high pressure gradient reflecting a dramatic increase in mixture viscosity at the phase inversion point (Arirachakaran *et al.*, 1989; Angeli & Hewitt, 1998; Soleimani, 1999; Ioannou *et al.*, 2004 and 2005). Thus, it is highly recommended that the operation of an oil-water pipeline should be avoided at these flow conditions.

Russel & Charles (1959) studied the effect of less viscous liquid on the pressure gradient in annular flow. They considered the annular flow of two liquids of equal densities in a circular pipe and noticed that the reduction in the pressure gradient is much greater in the case of concentric flow than in a parallel stratified flow, as might be expected from the velocity profile.

Charles & Redberger (1962) reported on the reduction of pressure gradients in oil pipelines with water addition. They measured a maximum reduction between 12% and 31% for different oils. The pressure gradient reductions occurred at water contents ranging from 12 to 93%, respectively.

Pressure drop in dispersed flow has been investigated by a number of researchers. Guzhov *et al.* (1973) observed two peaks in the graph of pressure drop against water cut for dispersed water-oil pipeline flow; their oil had a viscosity of 21.7 mPa s. They attributed the first peak to the turbulence in the oil layer while the second peak was said to be due to phase inversion. Guzhov *et al.* (1973) also observed a peak at the transition from water continuous dispersed flow to dual continuous flow (water-in-oil dispersion and oil-in-water dispersion at the top and bottom of the pipe respectively).

Martinez *et al.* (1988) found that the pressure gradient for a dispersion was a function of mixture velocity, input water fraction and temperature. They observed that the pressure drop increased with increasing water fraction and that, at the phase inversion point, it has a value higher than that of the single-phase oil flow.

Arirachakaran *et al.* (1989) studied pressure drop in 25.4 and 38.1 mm diameter tubes and found that pressure drop was a function of mixture velocity, input water fraction, oil viscosity and temperature. For an oil-in-water dispersion, temperature and oil viscosity have a small effect on the mixture pressure drop, which was the same order of magnitude as a single-phase water pressure drop at the same flow conditions. For a water-in-oil dispersion, pressure drop was highly affected by temperature, since the oil viscosity was very sensitive to changes in temperature. Pressure drop changes dramatically at the phase inversion point, and the magnitude of this change varied with the mixture velocity and the oil viscosity.

Pal (1993) observed a reduction of pressure gradient (relative to both the oil-alone and water-alone pressure gradients) for water-in-oil dispersions. He stated that the size of the

dispersed drops could affect the pressure drop and noted that the pressure drop increased as the size of the drops decreased in the dispersed flow regime. This drag reduction phenomenon was also observed by Angeli & Hewitt (1998) as illustrated in Figure 2.11.

Nädler & Mewes (1997) investigated the effect of emulsification and phase inversion on the pressure drop for different flow regimes of oil-water mixtures. Oil viscosities of 22, 27 and 35 mPa s were obtained by changing the temperature of the liquids. The maximum pressure drops were measured in the region of phase inversion. The minimum pressure drop for the flow of dispersions was of the order of the pressure drop of the pure water phase flowing alone in the pipe. In the case of oil-in-water emulsions filling the whole cross-sectional area of the pipe the pressure drop was between the pressure drop of the pipeline flow of the pure oil phase and the flow of the pure water phase.

Angeli & Hewitt (1998) found that the material of the pipe wall had a strong influence on the pressure gradient during liquid-liquid flow. Pressure gradients under all conditions were higher in the steel pipe than in the acrylic pipe for the same mixture velocities and flow volume fractions. The authors suggested that the different wettability characteristics were also responsible for the large difference between pressure drops for the respective tube materials in addition to the effect of different roughness (Figure 2.11).

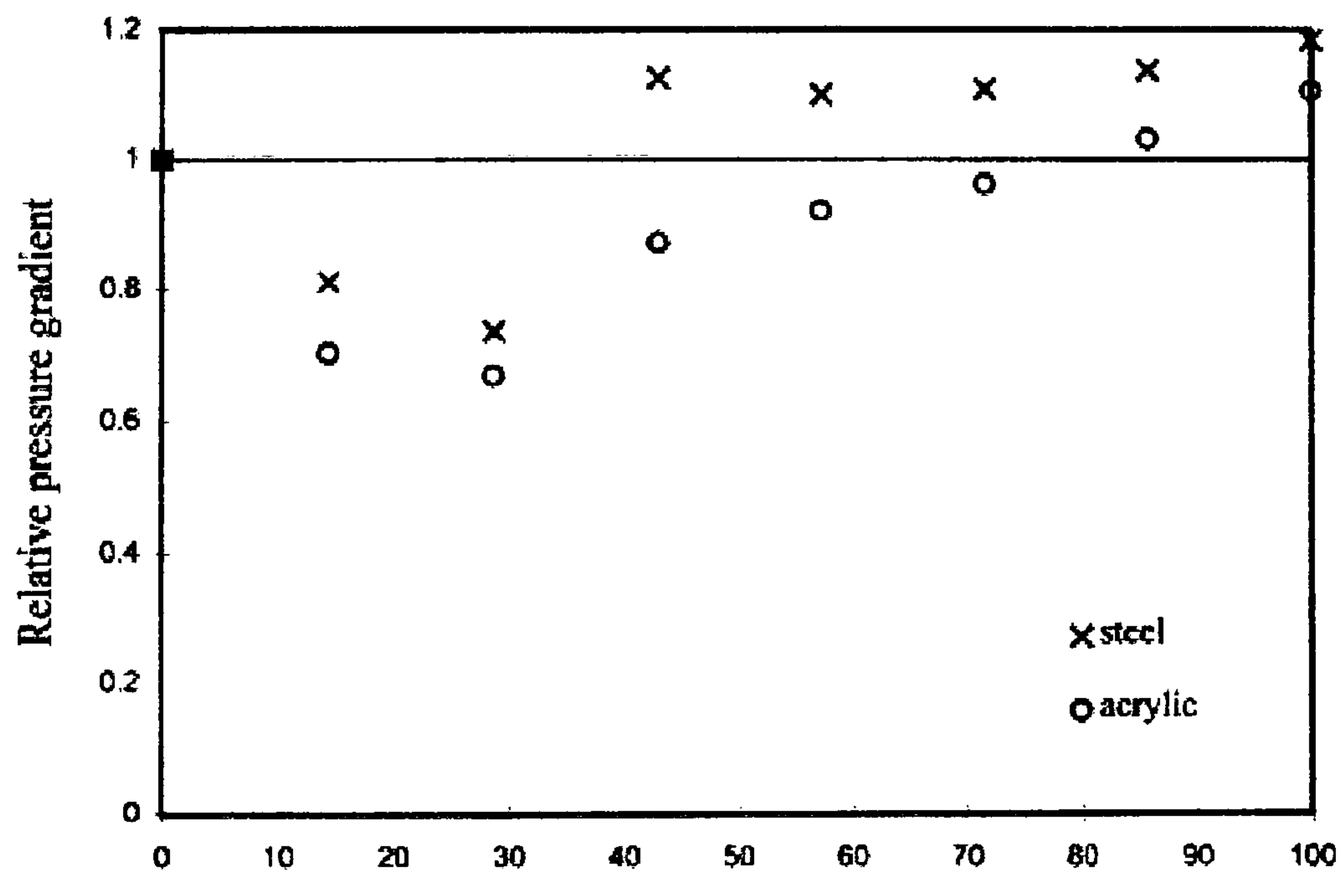


Figure 2.11 Non-dimensional pressure gradient in the steel and acrylic pipes at mixture velocity 3.0 m/s by Angeli & Hewitt (1998).

Soleimani (1999) used the same system as that used by Angeli & Hewitt (1998) to investigate the pressure drop in water-oil pipeline flow and also found a characteristic peak in the pressure gradient in the region of flow inversion of the dispersed flow regime (Figure 2.12). Soleimani also observed the drag reduction effect for water-in-oil emulsions, referred to above. He postulated that this was related to the drop coalescence and breakup processes. The influence of an inline mixer at the tube inlet on pressure gradient was also studied. A swirl flow produced by a mixer in the pipe resulted in a sharpening of the pressure gradient peak over a range of conditions.

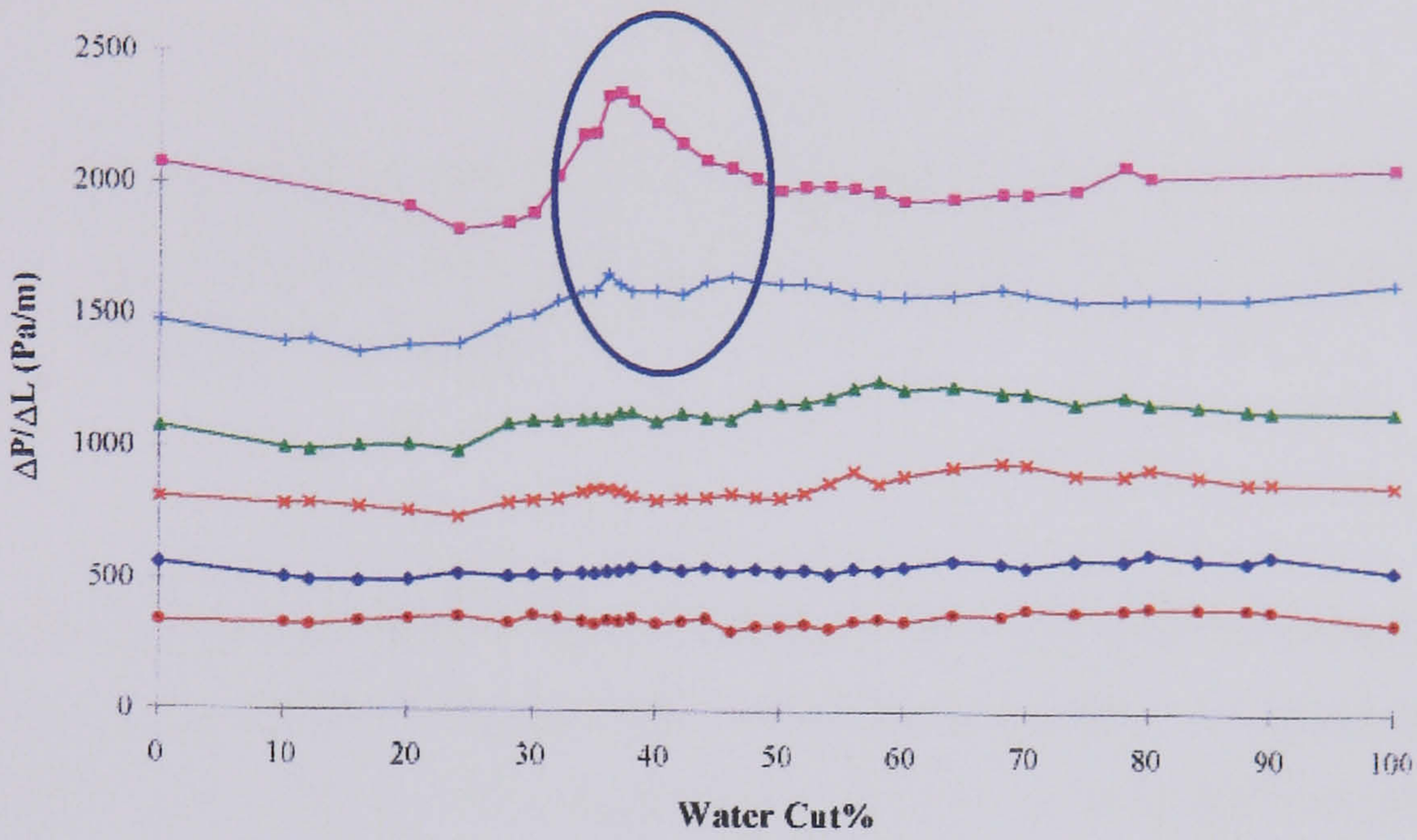


Figure 2.12 Pressure gradient data by Soleimani (1999) showing peak at phase inversion.

Ioannou *et al.* (2005) studied phase inversion and its effect on pressure gradient during dispersed flow of oil-water for two pipe materials (steel and acrylic) and two pipe sizes (60 and 32 mm ID). As in previous studies, these workers also found that phase inversion was accompanied with a large increase in pressure gradient in all cases. However, a much sharper and larger pressure gradient peak was observed in the acrylic pipe than in the steel one (Figure 2.13).

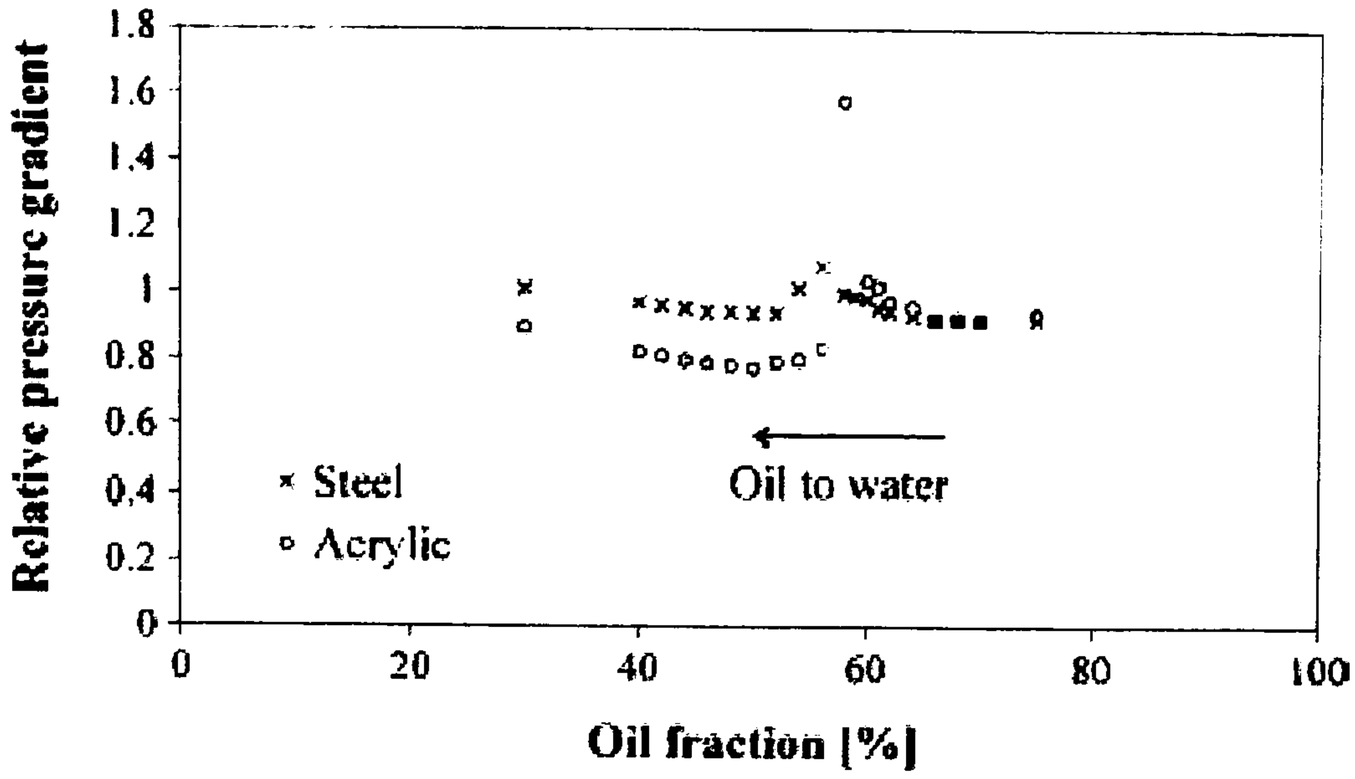


Figure 2.13 Comparison of non-dimensional pressure gradient in the acrylic and steel pipes at the mixture velocity 4.5 m/s starting with oil dominated mixture. (Ioannou *et al*. 2005).

Hussain (2004) investigated the effects of distance from inlet, mixture velocity and inlet water fraction on pressure gradient. The characteristic peaks in pressure gradient corresponding to phase inversion were again observed. The pressure gradient was found to fall towards a constant value with distance from the inlet and increased, as expected, with increasing phase velocity (though the net effect of velocity is smaller at greater distances from the inlet). It was suggested that the effect of position probably reflects the progressive mixing of the fluids and the results indicate that the flows are reaching equilibrium states towards the end of the pipe.

2.1.3 Phase Distribution

The flow of equal density oil-water mixtures in a horizontal pipeline, was investigated by Charles *et al*. (1961) using oils with viscosities of 6.29, 16.8 and 65 mPa s. They found that the resulting oil-water flow patterns were mostly independent of the oil viscosities and the in-situ holdup was higher than the no-slip holdup when the oil phase was in contact with the pipe wall.

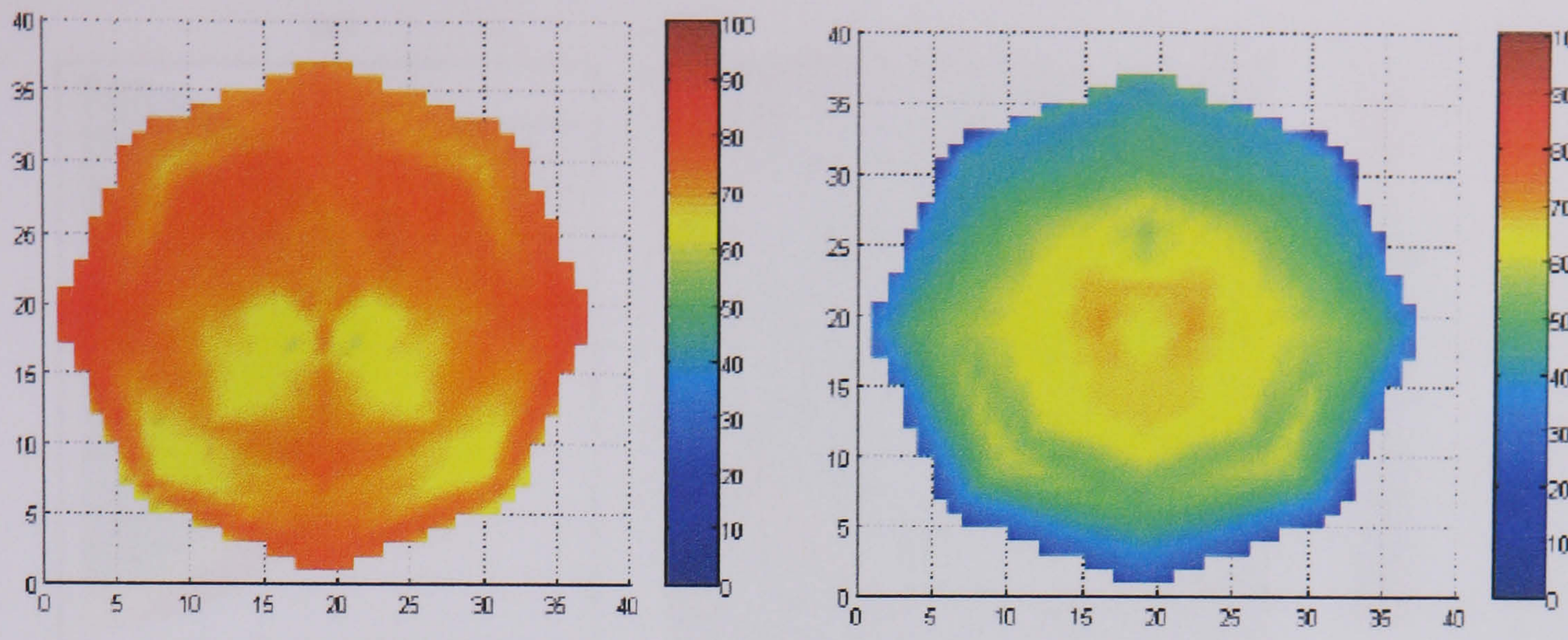
Angeli (1996) and Angeli & Hewitt (2000a) used a high frequency impedance probe to clarify the flow pattern and obtain phase distribution data for oil-water flow in steel and

BIBL. -49- DIB.

acrylic tubes. The results showed that the phases were more uniformly distributed as the mixture velocity increased and the distributions were more homogeneous at low oil fractions than at high ones for the same mixture velocity. Comparing the results between the acrylic and the steel tubes, the volume fraction distribution has a strong gradient in the acrylic pipe, where the flow pattern was *Three Layer*, while it was almost uniform in the steel pipe, where the flow pattern was *Mixed*.

Soleimani (1999) combined a high frequency probe and a gamma densitomenter system to quantify the phase distribution and identified the flow pattern of liquids in the cross section of the pipe in liquid-liquid co-current flow. He was the first investigator to use the gamma densitometer system in this field. These methods provided a comprehensive knowledge of the liquid fraction distribution for different superficial velocities. Experiments were carried out at three different mixture velocities 1.25 m/s, 2.12 m/s and 3 m/s for a range of water cuts from 20% to 70%. A high concentration of water was observed around the upper periphery of the pipe for flow at low speed (1.25 m/s) with high water cut. Soleimani suggested four explanations for this finding: hydrophilic pipe material, viscous instability (the lower viscosity fluid tends to move towards regions of high shear stress), the action of waves in the water layer and secondary flow in the oil core. Phase inversion of liquid-liquid dispersed flow was also studied by comparing the phase distribution of the two liquids for different water fractions in the ambivalent range; it was found that phase inversion could occur at different locations across the cross section even for the mixed flow regime. For example, phase inversion could happen in the water-in-oil layer at the bottom part of pipe.

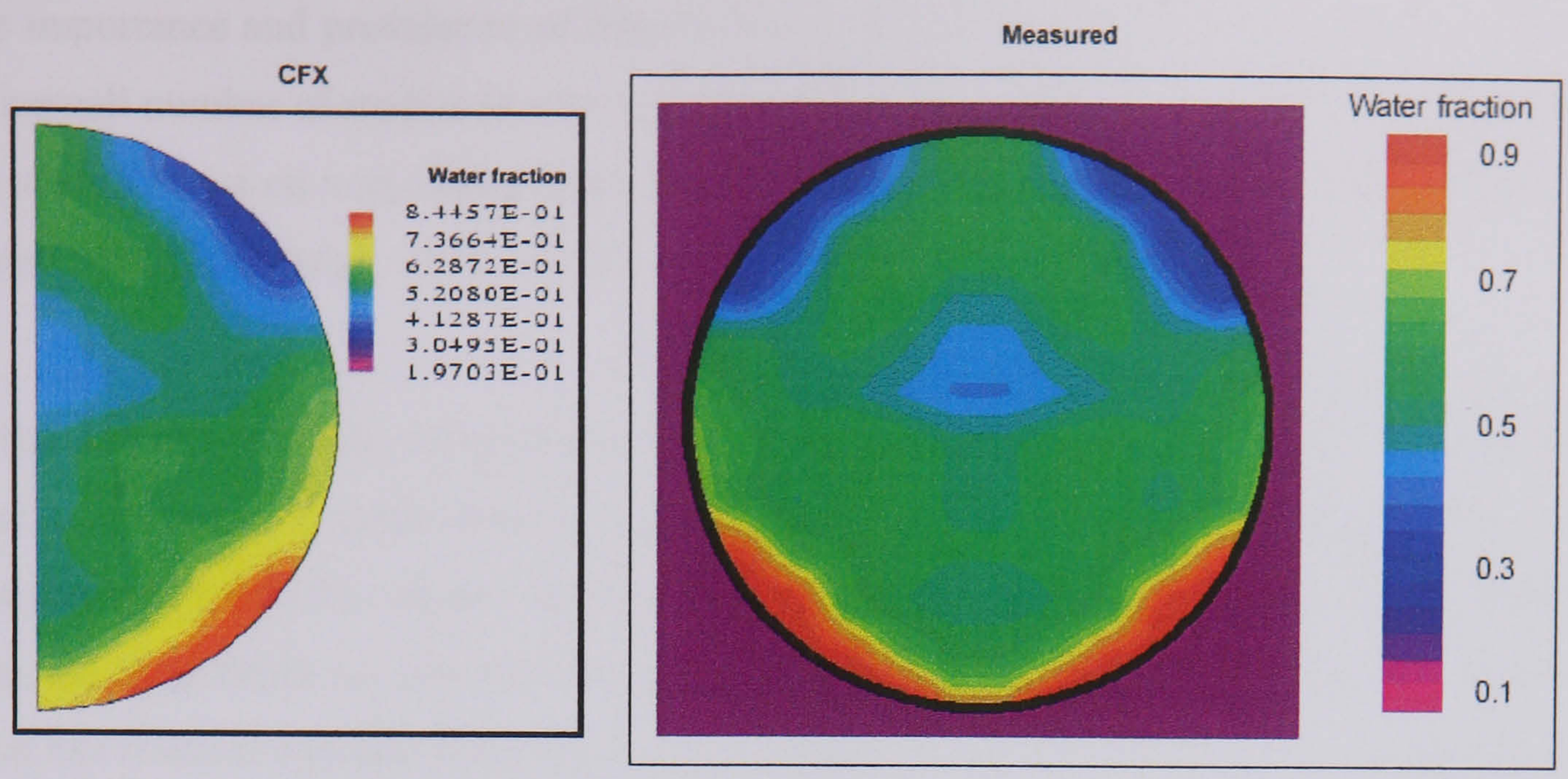
Ioannou *et al.* (2004) used an impedance probe to make phase distribution measurements before and after phase inversion for 3.5 m/s mixture velocity in liquid-liquid dispersed flow. In these experiments, phase inversion occurred between 70 and 72% input oil volume fraction; the local oil fraction was close to the input value, with some indication of liquid concentration of water at the bottom of the pipe. At 70% input oil volume fraction, a dramatic change has occurred with the oil now being dispersed and concentrated near the centre of the pipe.



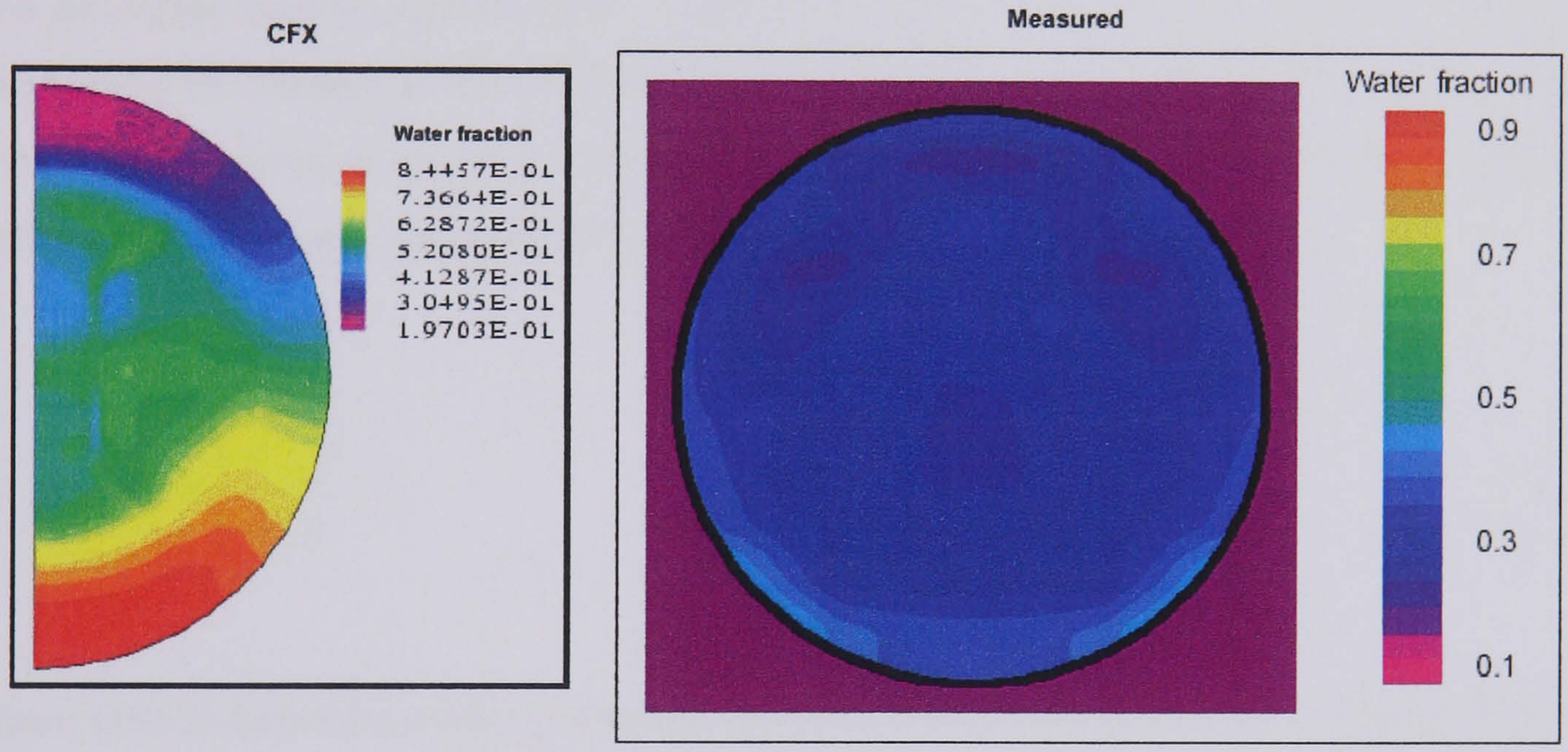
(a) (b)

Figure 2.14 Phase distribution in a pipe cross section at 3.5 m/s mixture velocity at (a) before phase inversion, 72% oil input fraction; (b) after phase inversion, 70% oil input fraction. Scale is of oil volume fraction ranging from zero (blue) to 100% (red) (Ioannou *et al.*, 2004).

Though interesting results may be obtained with impedance probes (as demonstrated in Figure 2.14), there are some uncertainties in measurements with such probes when the drop size is small. A more quantitative method is to use gamma densitometry, as developed by Soleimani (1999). Hussain (2004) used the gamma densitomenter system developed by Soleimani (1999) to measure the phase distributions over the pipe cross-section. The effects of the phase volume fraction, mixture velocities and the distance from the inlet on phase distribution investigated. In Hussain's experiments, the oil was fed at the bottom and water at the top of the inlet section. As expected, the experimental results showed that as the mixture velocity was increased from 1.8 to 2.76 m/s, the two-phase flows changed from partially separated to fully mixed. Distance from the inlet was also found to play an important role on the phase distributions. The results demonstrated that as the fluids flow along the pipe, the phases tend to mix and approach a uniform distribution. However, interestingly, the tendency of the fluids to mix along the pipe could not be predicted by numerical simulation using a computational fluid dynamic code (CFX 4) (Figure 2.15). Using the measured phase distribution at 1m from the inlet as an initial condition and then predicting the downstream evolution of the flow, the computations indicated a tendency for the phases to separate whereas the experiments indicated a tendency for them to mix! It was suggested by the author that perhaps Kelvin-Helmholtz instability could play a role for the mixing process which would not be predicted by CFD.



(a)



(b)

Figure 2.15 Comparison of measured cross-sectional phase distributions at a distance of (a) 1.0 m and (b) 7.72 m from the inlet with those calculated using CFX using the measured water fraction data at 1.0 m as input (input water fraction 40%, mixture velocity 2.76 m/s) by Hussain (2004).

2.1.4 Drop Size Distribution

In liquid-liquid dispersed flow the drop size and its distribution are important factors that determine flow rheology and stability of a dispersion and have a very significant effect upon equipment performance, for example, in liquid-liquid contactors or phase separators. In spite

of the importance and prevalence of dispersions in liquid-liquid pipe flows, there have only been a small number of studies in which drop size distributions have been measured. Most of these studies focus on very dilute dispersed flow (≤ 1%) (Ward & Knudsen, 1967; Kubie & Gardner, 1977; Karabelas, 1978; El-Hamouz & Stewart, 1995 & 1996).

Drop size is a function of the rate of break-up of large droplets into smaller ones, and the rate of coalescence of small droplets to form large ones. Moreover, in dispersed flows the interactions between the drops and the turbulent eddies of the continuous phase further affects the drop break-up and coalescence processes (Serizawa & Kataoka, 1992). Once a system has reached a steady state, there is a constant break-up and coalescence of drops with a theoretical maximum and minimum drop size. In a turbulent flow field, the minimum drop size is governed by the Kolmogorov length scale l_k (the length scale of turbulence which gives a Reynolds number equal to one). Larger drops are deformed by the dynamic pressure forces, caused by changes in the continuous phase velocity over a distance equal to the drop size, and may be broken up. The Kolmogorov length scale is a function of the kinematic viscosity ν and the energy dissipation rate ε as follows.

$$l_k = \left(\frac{\nu^3}{\varepsilon}\right)^{\frac{1}{4}} \tag{2-1}$$

Hinze (1955) derived a model giving the maximum drop size in a dilute turbulent flow as follows:

$$d_{\max} = C\left(\frac{\rho_c}{\sigma}\right)^{-0.6} \varepsilon^{-0.4} \tag{2-2}$$

where C is a constant, ρ_c is the continuous phase density and σ is the interface tension. If ε is set equal to the rate of the mean energy dissipation per unit mass, then in a pipe flow

$$\varepsilon = \frac{f U_c^3}{2D} \tag{2-3}$$

where f is the friction factor, $f = \frac{0.046}{\mathrm{Re}_c^{0.2}}$, U_c is the average axial velocity of the continuous phase and D is the pipe diameter.

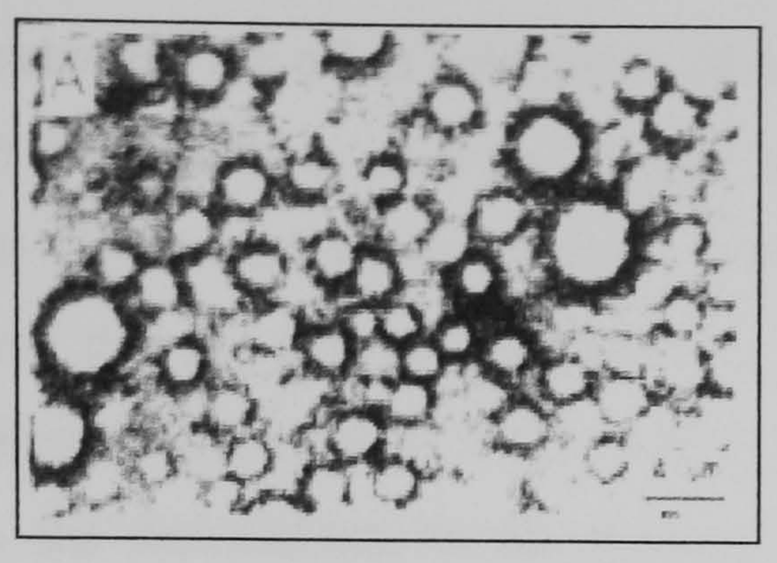
Brauner and Ullmann (2002) gave the maximum drop size for dilute and dense dispersions, respectively as the following:

$$(d_{\max})_{dilute} = 0.55\left(\frac{\rho_c U_c^2 D}{\sigma}\right)^{-0.6}\left[\frac{\rho_m}{\rho_c(1-\varepsilon_d)}f\right]^{-0.4} D \qquad (2\text{-}4)$$

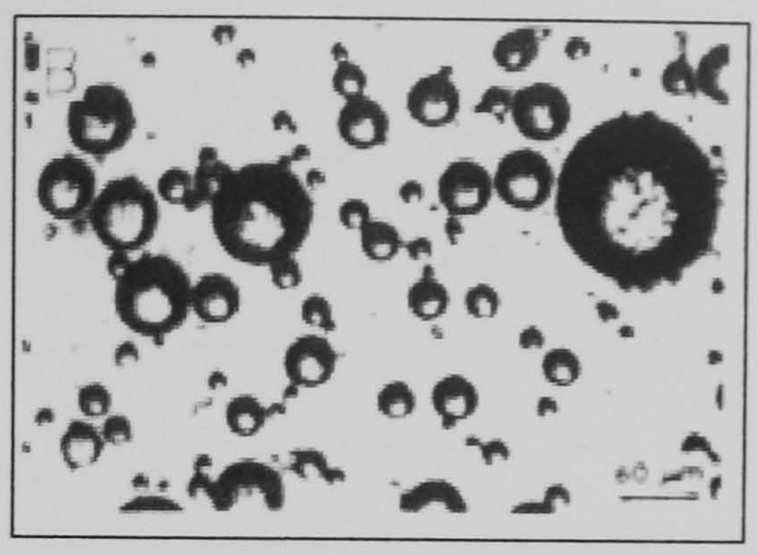
$$(d_{\max})_{dense} = 2.22 C_H\left(\frac{\rho_c U_c^2 D}{\sigma}\right)^{-0.6}\left[\frac{\rho_m}{\rho_c(1-\varepsilon_d)}f\right]^{-0.4}\left(\frac{\varepsilon_d}{1-\varepsilon_d}\right)^{0.6} D \qquad (2\text{-}5)$$

where C_H is a tunable constant, ρ_m is the mixture density, ε_d is the dispersed phase fraction.

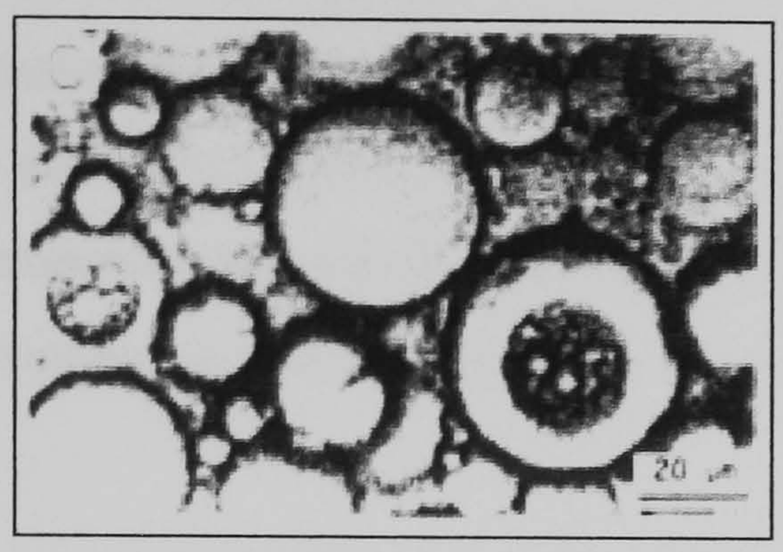
Pal (1993) measured the drop size before and after phase inversion of the oil-water dispersion with added surfactant. Direct microscopic observations indicated that significant changes in drop sizes occurred near the inversion point. Figure 2.16 shows the photomicrographs of emulsion before and after phase inversion. The drops of stable 25.85% water-in-oil emulsion (Figure 2.16 a) are quite small. The multiple emulsion drops (Figure 2.16 b) were very large before phase inversion and upon inversion to an oil-in-water emulsion, the drop size decreased (Figure 2.16 c) and continued to decrease with a further increase in water concentration (figure 2.16 d). The dramatic variation in the drop sizes with the water concentration is illustrated in Figure 2.17.



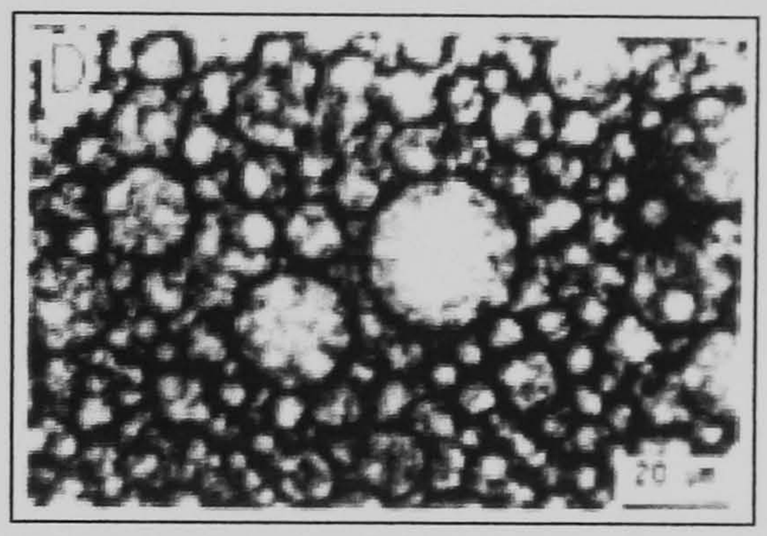
(a)



(b)



(c)



(d)

Figure 2.16 Typical photomicrograghs for surfactant-stabilized emulsions by Pal (1993). (a) stable 25.85% W/O emulsion; (b) multiple emulsions (water concentration is 25.85% vol.); (c) 68.44% O/W emulsion; and (d) 44.9% O/W emulsion.

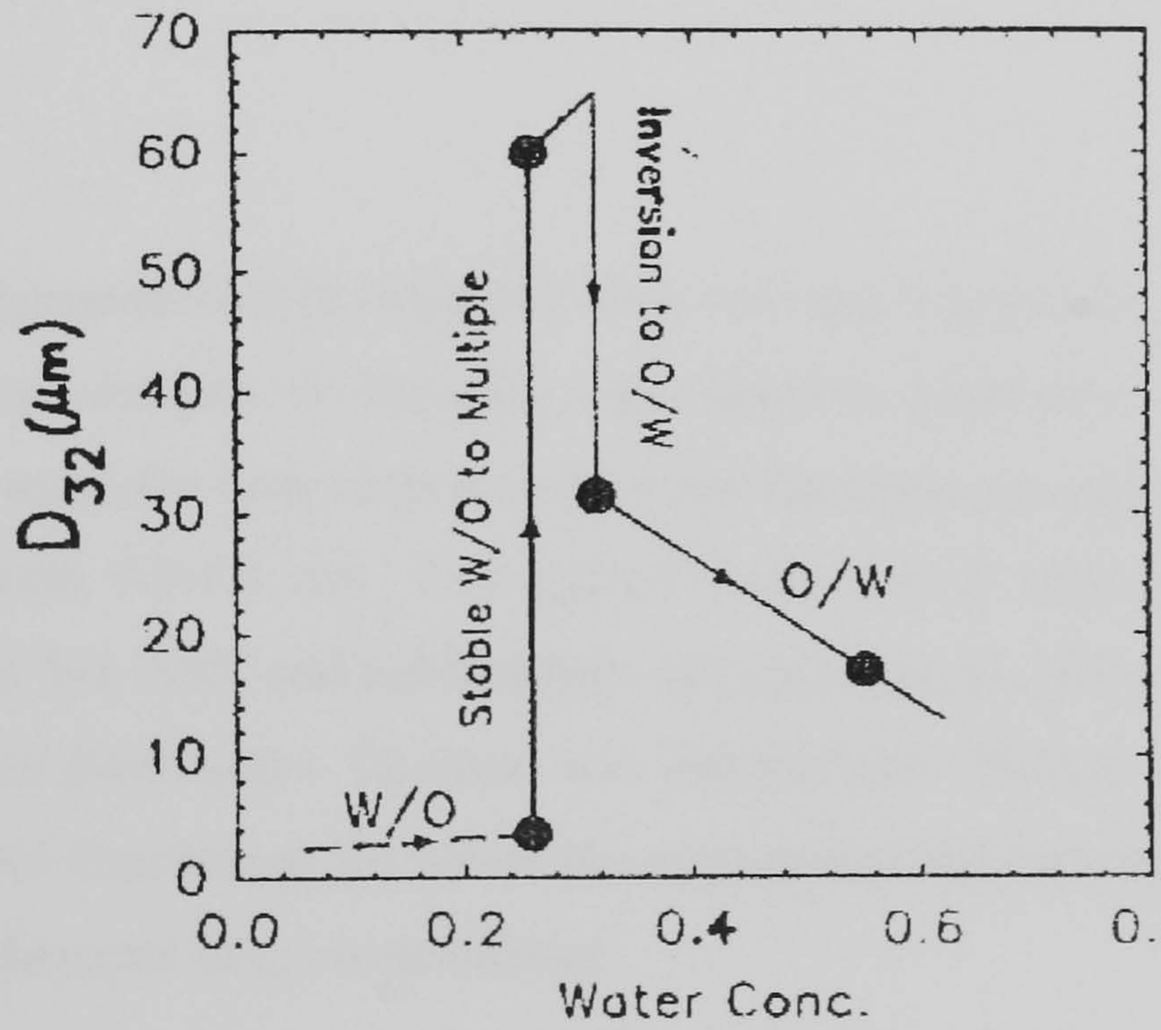


Figure 2.17 Sauter mean diameter (D_{32}) as a function of water concentration (Pal, 1993).

Angeli & Hewitt (2000b) obtained drop size distributions formed during oil-water flows using a video recording technique which employed an endoscope; the oil had a viscosity of 1.6 mPa s viscosity and a density of 801 kg/m^3. The experiments were performed with both

the water and the oil as continuous phases, in two 1-in nominal bore horizontal test sections, made from stainless steel and acrylic resin, respectively. Continuous phase velocities from 1.1 to 1.7 m/s and dispersed phase volume fractions from 3.4 to 9% were used. The results showed that the drop size distributions were strongly influenced by the pipe material, with the drops being smaller in the steel than in the acrylic pipe for the same flow conditions. Also, the distributions in the steel pipe were more uniform than in the acrylic one. The identity and the velocity of the continuous phase influenced drop size distributions and increasing the continuous phase velocity resulted in a shift of the distributions to smaller drop sizes. Two correlations for d_{max} and d_{32} (in m) were found to satisfactorily represent the experimental data which took account for the influence of the pipe material and the nature of the continuous phase by using the friction factors (f):

$$d_{max} U_c^{1.8} = 4.2 \times 10^{-2} \times f^{-3.13} \times 10^3 \tag{2-6}$$

$$d_{32} U_c^{1.8} = 2 \times 10^{-2} \times f^{-3.12} \times 10^3 \tag{2-7}$$

where $d_{32} = \dfrac{\sum_{j=1}^{n} P(j) d_j^3}{\sum_{j=1}^{n} P(j) d_j^2}$ as $P(j)$ is number density of drop group j and U_c is continuous phase velocity, m/s.

Simmons and Azzopardi (2001) examined drop size distributions in a 0.063 m diameter pipe for a two-phase mixture of kerosene and aqueous potassium carbonate solution. Measurements were made for both vertical upflow and horizontal geometries and for mixture velocities ranging from 0.8-3.1 m/s. Two optical measurement techniques, a backscatter technique using a Par-Tec 300C and a diffraction technique using a Malvern 2600, were used to obtain the drop size distribution. The drop size distributions obtained were found to fit an upper limit log-normal distribution for which the relationship between Sauter mean diameter (d_{32}) and maximum diameter (d_{max}) is as follows:

$$d_{32} = \frac{d_{\max}}{1 + a \exp\left(\dfrac{1}{4\delta^2}\right)} \tag{2-8}$$

The constants δ and a were fitted as 0.61 and 1.35, respectively. Simmons and Azzopardi also found that the theory of Hinze (1955) could not be applied to data taken at high concentrations.

2.2 The phase inversion process

After introducing liquid-liquid pipe flow in general, we now focus our attention on one particular flow regime: liquid-liquid dispersed flow. This regime exists not only in pipe flow but also in agitated vessels. The liquid phases involved are usually an aqueous phase (water or an aqueous solution) and an organic phase (e.g. an oil). There are two types of dispersion, namely oil drops (dispersed phase) in water (continuous phase) or water drops in oil; which type exists on system parameters (phase fraction, velocity or agitator speed etc.). The transition from oil-in-water (o/w) to water-in-oil (w/o) dispersions and *vice versa* is known as *phase inversion*.

Phase inversion is the phenomenon whereby the phases of a liquid-liquid dispersion interchange so that the dispersed phase inverts to become the continuous phase and *vice versa* under conditions determined by the system properties, phase volume ratio and energy input. This process is illustrated in Figure 2.18. Phase inversion can be regarded as a form of instability of a system, with the stability of the dispersion being at its lowest at the point of phase inversion.

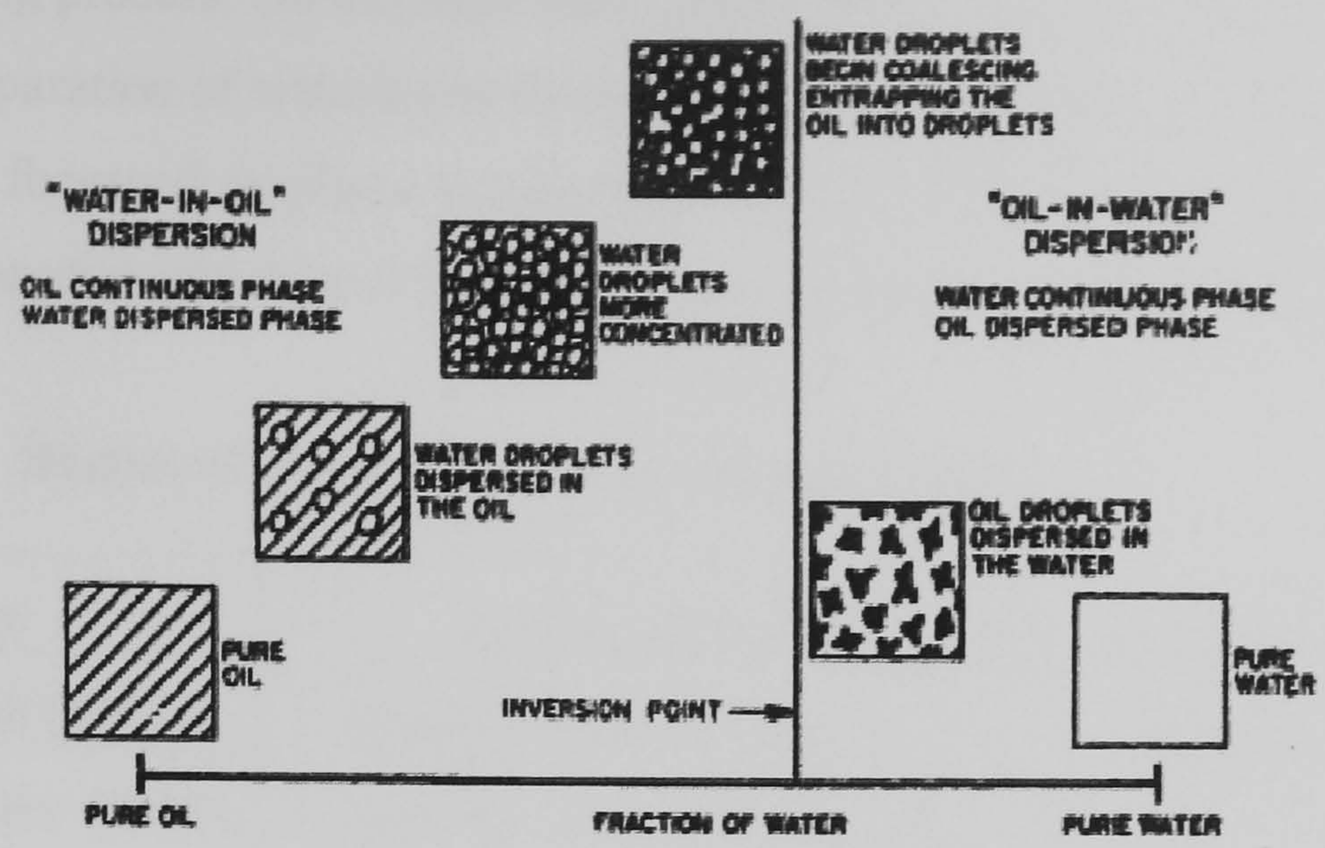


Figure 2.18 Phase inversion process for an oil-water dispersion system (Arirachakaran *et al.*, 1989).

The phenomenon of phase inversion was first reported by Rodger *et al.* in 1956. Since then, it has been the subject of a considerable amount of experimental and theoretical research. However, until now, there is no generic description (or analytical model) which describes the process. The fundamental difficulty in understanding phase inversion lies in the problem of conceptualising the actual mechanism behind the phase inversion processes. A large range of experiments have indicated that phase inversion is affected by a number of physical and physicochemical parameters, such as liquid properties, container geometry and the initial conditions of flow systems. A comprehensive review of the published work on phase inversion is given by Yeo *et al.* (2000).

2.2.1 Experimental Research on Phase Inversion

2.2.1.1 Phase Inversion in Agitated Vessels

Liquid-liquid dispersions in agitated (or stirred) vessels are frequently employed in the chemical industry for conducting operations such as solvent extraction, chemical reactions, etc. Phase inversion occurs, for instance, when the dispersed phase holdup is increased in order to obtain higher interfacial areas. In some chemical processes, such as solvent extraction in mixer-settlers, phase inversion can be extremely undesirable because it can

delay the settling process. On the other hand, phase inversion is desirable in some operations, such as the preparation of waterborne dispersions of polymer resin. Therefore, most research work has been focussed on phase inversion in agitated vessels, rather than in pipeline flow. Table 2.1 lists studies which have been carried out on phase inversion in agitated vessels.

Table 2.1 Studies of phase inversion in agitated vessels.

Author	System parameters and/or phenomena studied
Quinn and Sigloh (1963)	1. Impeller geometry and position; 2. Agitation speed.
Selker and Sleicher (1965)	1. Impeller and tank geometry; 2. Viscosity ratio; 3. Agitation speed; 4. Manner of initial dispersions.
Luhning and Sawistowski (1971)	1. Agitation speed; 2. Interfacial tension; 3. Mass transfer.
Clark and Sawistowski (1978)	1. Agitation speed; 2. Mass transfer
McClarey & Mansoori (1978)	1. Agitation speed; 2. Temperature; 3. Viscosity difference.
Arashmid and Jeffreys (1980)	1. Agitation speed. 2. Modelling of phase inversion
Guilinger *et al.* (1988)	1. Viscosity of dispersed phase; 2. Agitation speed; 3. Tank geometry; 4. Impeller wetting characteristics.
Gilchrist *et al.* (1989)	1. Delay time; 2. Tank geometry; 3. Agitation speed.
Kumar *et al.* (1991)	1.Impeller wetting characteristics; 2. Agitation speed.
Chiang and Chen (1994)	1. Density Difference; 2. Agitation speed; 3. Surfactants; 4. Mass Transfer.
Brooks *et al.* (1994)	1. Oil viscosity; 2. Drop size.
Nienow *et al.* (1994)	1. Viscosity; 2. Delay time; 3. Batch & Semi-batch.
Pacek *et al.* (1994a)	1. Agitation speed; 2. Changes of Drop size; 3. Secondary droplets[1].
Pacek *et al.* (1994b)	1. Secondary droplets; 2. Drop size; 3. Delay time; 4. Critical phase inversion holdup.
Norato *et al.* (1998)	1. Density; 2. Viscosity; 3. Interfacial tension; 4. Agitation speed; 5. Impeller geometry; 6. Delay time.
Yang *et al.* (2000)	1. Emulsifier concentration; 2. Temperature.
Dong and Tsouris (2001)	1. Effects of applied electric fields
Deshpande and Kumar (2003)	1. Impeller and tank geometry; 2. Electrolytes.
Hu *et al.* (2004)	1. Modelling of phase inversion.

[1] The term 'droplet' is used in this thesis for drops within drops, while the term "drop" is used to denote the entire compound drop, including any ingested droplets.

2.2.1.2 Phase Inversion in Pipeline Flow

In the phase inversion region an increase in pressure gradient may occur in pipeline flows as already mentioned in Section 2.1.1 above. The data may be plotted as the ratio of pressure gradient to that pure oil flow as exemplified in Figure 2.19 (Soleimani, 1999) which shows the substantial peak in pressure gradient associated with phase inversion in dispersed flow. Failure to account for the abnormally high pressure drops in this region may result in substantial decreases in the oil productivity in wells and in the capacity of pipelines. Arirachakaran *et al*. (1989) calculated the mixture viscosity in a homogeneous flow pattern from the pressure drop and found that at the phase inversion point, the apparent mixture viscosity exhibited a peak (Figure 2.20). Phase inversion also causes a decrease of the heat transfer coefficient (Lang & Auracher, 1996), which may be important in process industry applications. Therefore, knowing the critical phase holdup (phase inversion point) at which phase inversion occurs, and understanding the mechanism of phase inversion, is an important requirement.

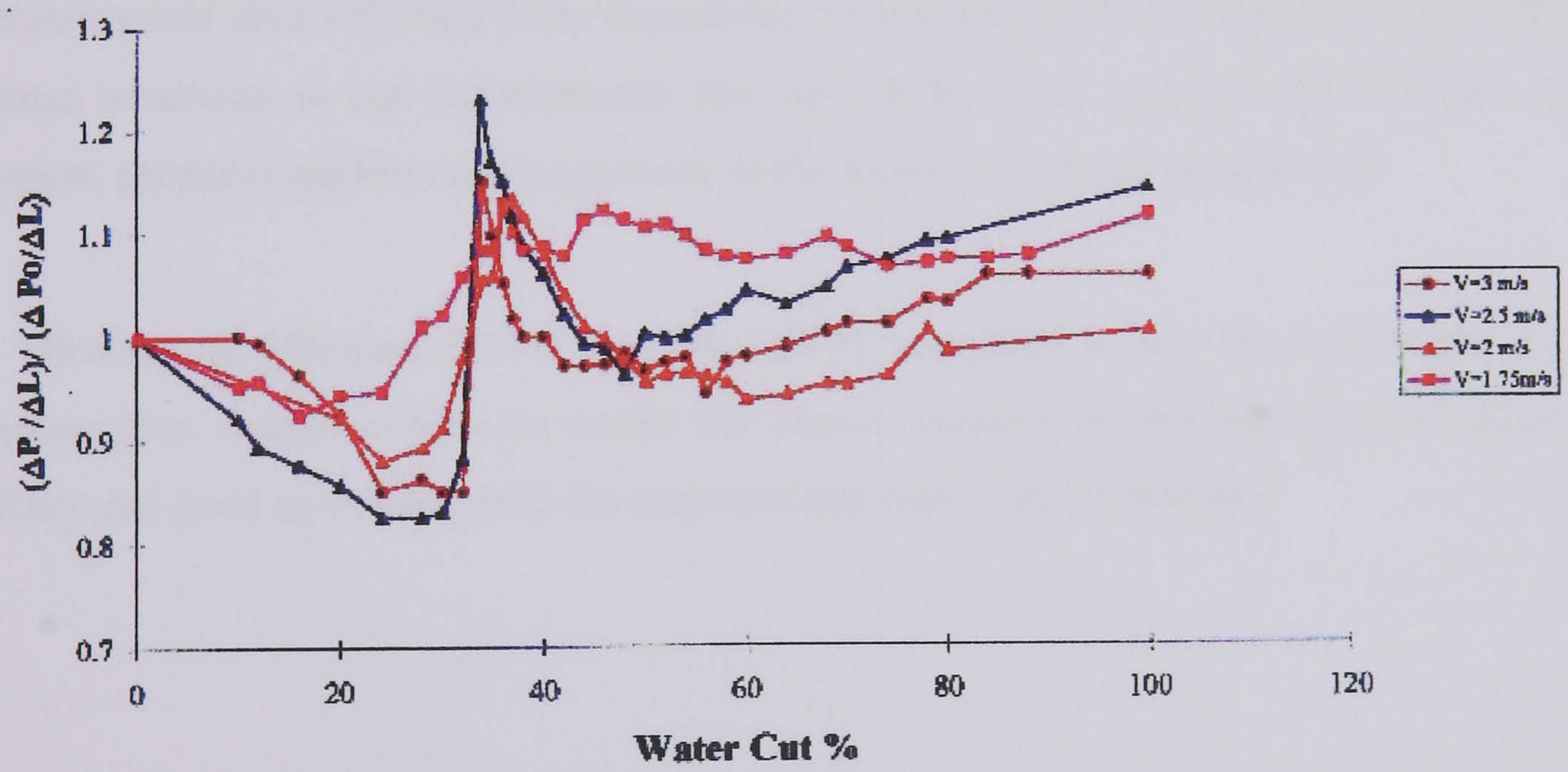


Figure 2.19 Pressure gradient in liquid-liquid flow (Soleimani, 1999).

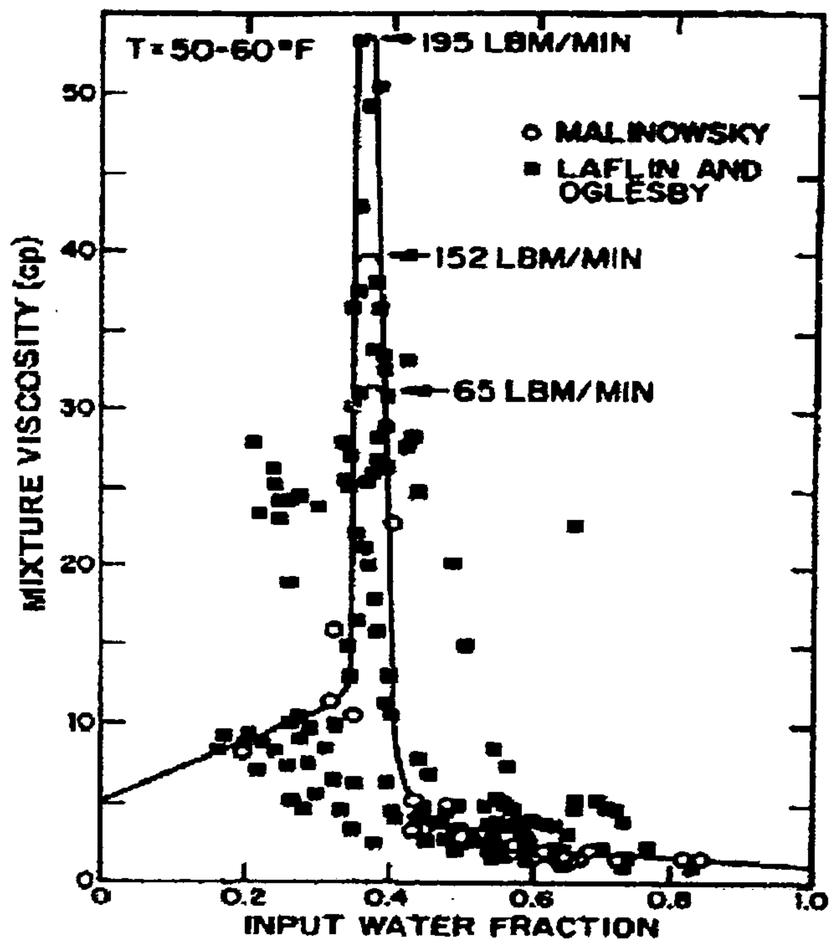


Figure 2.20 Mixture viscosity vs. input water fraction for low-viscosity oil (Arirachakaran *et al.*, 1989).

Ioannou *et al.* (2005) investigated phase inversion in dispersed liquid-liquid flows in horizontal pipes and analyzed the effect of phase inversion on pressure gradient. The experimental data obtained from impedance probes and pressure transducers indicated that phase inversion is not instantaneous but takes place over a significant distance. In this region, pressure gradient and impedance of the mixture fluctuate significantly.

Brauner & Ullmann (2002) and Hu (2004) attempted to use the minimization of the system free energy criteria to model the phase inversion phenomenon in two-phase pipe flows and good agreement with the experimental data were all obtained.

Table 2.2 Studies of phase inversion in pipe flow.

Author	Focal Point of the Study
Arirachakaran et al., (1989)	1. Pressure drop; 2. Mixture viscosity; 3. Flow patterns; 4. Phase inversion point correction; 5. Stratified pressure-gradient prediction model
Pal (1993)	1. Surfactants; 2. Drag Reduction.
Luo *et al.* (1997)	1. Mixture velocity; 2. Temperature; 3. Pressure; 4. Emulsion viscosity; 5. Pressure loss; 6. Phase Inversion Point (PIP)
Nädler and Mewes (1997)	1. Oil viscosity; 2. Temperature; 3. Pressure drop.
Angeli and Hewitt (1998, 2000a,b)	1. Wettability of pipe materials; 2. Mixture velocity; 3. Pressure gradient.
Soleimani (1999)	1. Pressure drop; 2. Flow pattern
Gillies et al. (2000)	1. Surfactants; 2. Intensity and nature of Shear Process; 3. Solids Content of the Oil (A rotated pipe toroid simulate pipe flow)
Brauner and Ullmann (2002)	1. Modelling of phase inversion
Ioannou et al. (2004)	1. Pressure gradient; 2. Phase distributions.
Hu (2004)	1. Modelling of phase inversion
Ioannou et al. (2005)	1. Pressure gradient; 2. Mixture velocities; 3. Initial conditions; 4.Pipe diameter; 5. Pipe materials; 6. Ambivalent range.

2.2.1.3 Prediction of the Phase Inversion Point

A controlled phase inversion is a desirable and essential step in certain industrial processes; uncontrolled phase inversion can lead to undesirable consequences and need to be avoided in some circumstances. Thus, the experimental and modelling work has been focussed on finding the phase inversion point (or the critical dispersed phase holdup) (Quinn & Sigloh, 1963; Clark & Sawistowski, 1978; Selker & Sleicher, 1965; Norato *et al.*, 1998; Brauner & Ullmann, 2002; Yeo, *et al.* 2002b; Hu *et al.* 2004). Most of the knowledge on phase inversion, as well as of the critical phase holdup, stems from experiments. The critical phase holdup (ϕ_{crit}) varies between systems. In general, any factor that affects phase inversion may also change ϕ_{crit}. One proposal for the prediction of phase inversion is based on calculating these conditions where the total energy of the system (kinetic energy plus interfacial energy) is a minimum. (Luhning & Sawistowski, 1971; Tidhar *et al.*, 1986).

Observations indicate that no measurable change in the power delivered to the system occurs during phase inversion. However, there is always a reduction in the interfacial energy at the point at which phase inversion occurs (Fakhr-Din, 1973); the minimization of the total system energy would, therefore, correspond to a condition at which the interfacial energy and the total system kinetic energy are redistributed. As the magnitude of the change in the interfacial energy is comparable to that of the total system, the change in kinetic energy would be small compared to the change in the interfacial energy upon inversion. Thus, the modelling of phase inversion by minimising the interfacial energy closely satisfies the criterion that the total system energy has to be minimised. The simplified criterion has been used in some models (Yeo, *et al.*, 2002b; Brauner & Ullmann, 2002, Hu *et al.*, 2004, Hu, 2004).

An alternative proposal based on geometric considerations assumes that drops can be represented by uniform hard spheres and thus, if a monodispersion was additionally assumed, then phase inversion would occur by complete coalescence of the dispersed phase when the volume fraction representing the optimum packing efficiency of the spheres has been exceeded. This volume fraction is given by Ostwald's ratio that corresponds to the packing efficiency of a rhombohedral face centred cubic structure i.e. 74.06%. However, dispersed phase volume fractions for phase inversion exceeding 74.06% and even exceeding 90% have been reported (McClarey & Mansoori, 1978; Arashmid &Jeffreys, 1980; Pal *et al.*, 1986; Guilinger *et al.*, 1988; Plegue *et al.*, 1989; Mewes *et al.*, 1997). It has been suggested that dispersed phase concentrations at phase inversion may exceed 74.06% because of the deformation that the dispersed drops experience (Nädler & Mewes, 1997) or the influence of surfactants or contaminants in inhibiting coalescence (Brauner &Ullmann, 2002).

Extensive research has been carried out on phase inversion leading to many empirical and semi-empirical relationships for the prediction of phase inversion as summarized in Table 2.3.

Table 2.3 Empirical correlation of phase inversion.

Author	Empirical Correlations	Remarks
Agitated Vessels		
Quinn and Sigloh (1963)	$\phi_{o,i} = \phi_{o,i}' + \frac{\alpha}{P}$ (2-9) α is a constant, $\phi_{o,i}'$ is constant value at high impeller speeds; P is the power input	
Luhning and Sawistowski (1971)	Upper inversion curve: $\phi_{o,i} = 0.160 + 6.0\times10^{-5}\ We_I$ (2-10a) Lower inversion curve: $\phi_{o,i} = 0.470 + 2.0\times10^{-5}\ We_I$ (2-10b) $We_I = \frac{\rho_c N^2 D_I^3}{\sigma}$ (2-10c)	N > 680.85 r.p.m (Fakhr-Din, 1973)
Fakhr-Din (1973)	Upper inversion curve : $\phi_{o,i} = 1.32\times10^6 \left(\frac{\mu_d}{\mu_c}\right)^{0.32} \left(\frac{\Delta\rho}{\rho_c}\right)^{-0.11} Fr_I^{0.71}\,\mathrm{Re}_I^{1.06}\,We_I^{-0.25}$ (2-11a) Lower inversion curve: $\phi_{o,i} = 12.2 \left(\frac{\mu_d}{\mu_c}\right)^{0.31} \left(\frac{\Delta\rho}{\rho_c}\right)^{0.04} Fr_I^{0.13}\,\mathrm{Re}_I^{0.22}\,We_I^{-0.03}$ (2-11b) $\mathrm{Fr_I} = \frac{N^2 D_I^3}{g}$; $\mathrm{Re}_I = \frac{\rho_c N D_I}{\mu_c}$ (2-11c)	Based on the criterion that the total energy is minimised
Yeo *et al.* (2002b)	$\frac{\phi_{o,i}}{1-\phi_{o,i}} = \frac{d_{32_{o/w}}}{d_{32_{w/o}}}$ (2-12a) $d_{32} = C_1(1 + C_2\phi_d^m)We_I^{-n} D_I (\frac{\mu_d}{\mu_c})^p$ (dense) (2-12b) $d_{32} = C_1 We_I^{-n} D_I (\frac{\mu_d}{\mu_c})^p$ (dilute) (2-12c)	Based on as the criterion of minimisation of the interfacial energy;
Pipeline Flow		
Arirachakaran *et al.* (1989)	$\phi_{w,i} = 0.500 - 0.1108 \log \mu_o$ (2-13)	
Nädler and Mewes (1995)	$\phi_{w,i} = \frac{1}{1 + k_1 \left(\frac{C_o'}{C_w'} \frac{\rho_o^{(1-n_o)}}{\rho_w^{(1-n_w)}} \frac{\mu_o^{n_o}}{\mu_w^{n_w}} \frac{1}{[dv_m]^{(n_o - n_w)}} \right)^{\frac{1}{k_2}}}$ (2-14)	Assuming that the interfacial shear stress is zero and there is no slip.

Continued

Brauner and Ullmann (2002)	$\phi_o^i = \frac{[\sigma/d_{32}]_{w/o} + \frac{s}{6}\sigma\cos\theta}{[\sigma/d_{32}]_{w/o} + [[\sigma/d_{32}]_{o/w}]}$	(2-15)	Based on the criterion of the local minimum of the system-free energy
Other Systems			
Yeh *et al.* (1964)	$\frac{\phi_{d,i}}{1-\phi_{d,i}} = \sqrt{\frac{\mu_d}{\mu_c}}$	(2-16)	Hand-shaking Flask.
Tidhar et al. (1986)	$\phi_{o,i} = 0.5 + C_1 We^{-0.5}\,\mathrm{Re}^{0.15}(aD_H)\cos\theta$	(2-17a)	Static mixer;
	$We = \frac{\rho_m v_T^2 D_H}{\sigma}; \mathrm{Re} = \frac{\rho_m v_T D_H}{\mu_m}$	(2-17b)	

2.2.1.4 Ambivalent Range

Previous work has shown that in a system of two immiscible liquids, there is a so-called *ambivalent range* of volume fractions over which either component can be the stable dispersed phase (Selker & Sleicher, 1965; Luhning & Sawistowski, 1971; Clarke & Sawistowski, 1978; Efthimiadu *et al.*, 1994; McClarey & Mansoori, 1978; Tidhar *et al.*, 1986; Pacek *et al.*, 1994b; Dong & Tsouris, 2001; Deshpande & Kumar, 2003). The extent of the ambivalent range depends on how the dispersion is produced (Arashmid & Jeffreys, 1980). The ambivalent range is generally defined in terms of the volume fraction of the organic phase (or dispersed phase) and a quantity related to the level of energy input into the system (stirrer speed or mixture velocity). A typical graphical representation of the ambivalent region for the hexane-water system is shown in Figure 2.21. If the volume fraction of the organic phase is plotted as the ordinate, the system can exist as an organic phase continuous dispersion only above the upper ambivalence curve and as an aqueous phase continuous dispersion only below the lower ambivalence curve. In between the curves, either of the above two configurations are possible depending on the system's previous history. Another interesting characteristic is that in all cases the upper inversion curve of the ambivalence range (o/w-w/o) and the lower inversion curve (w/o-o/w) are asymmetric (Luhning & Sawistowski, 1971; McClarey & Mansoori, 1978; Kumar *et al.*, 1991; Pacek *et al.*, 1994b). In other words, the critical dispersed phase holdups for inversion from oil-in-

water dispersions to water-in-oil dispersions are much higher than those for the reverse inversion (Selker & Sleicher, 1965; Arashmid & Jeffreys, 1980; Guilinger *et al.*, 1988; Kumar *et al.*, 1991; Nienow *et al.*, 1994).

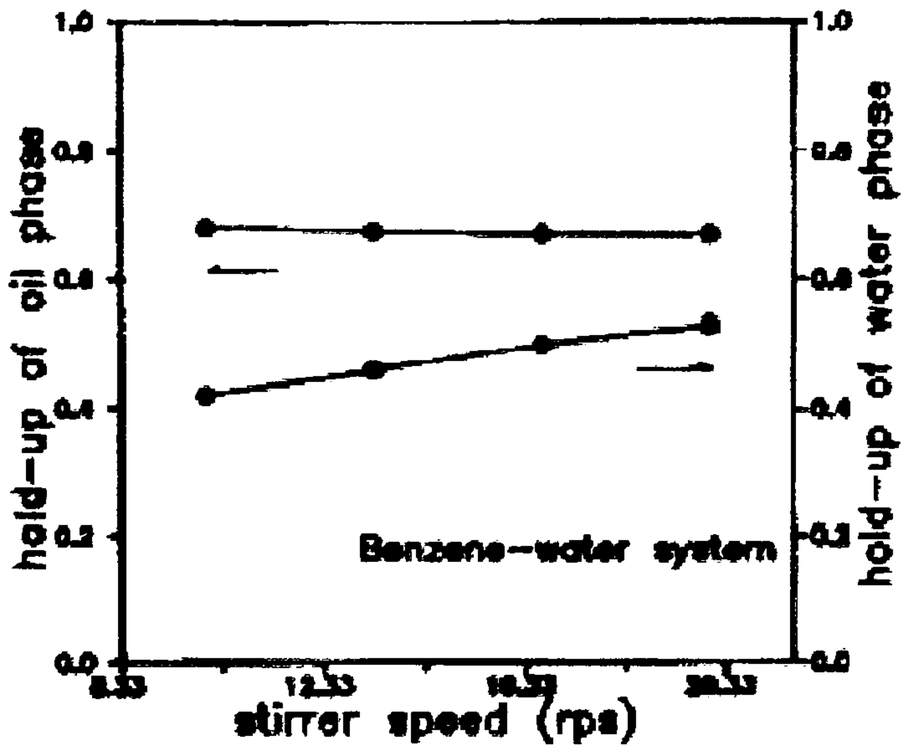


Figure 2.21 General ambivalence behaviour for a benzene-water system (Kumar *et al.*, 1991).

Many investigators have investigated the limits of the ambivalent range by obtaining experimental data and producing a physical model to interpret these data. Luhning & Sawistowski (1971), for instance, correlated the width of the ambivalent range with agitation speed and interfacial tension. They suggested that the asymptotic phase holdup of the dispersed organic phase at inversion (at high impeller speeds) for the upper and lower inversion curves could be related linearly to the impeller Weber number and they also suggested that interfacial tension is one of the principal factors affecting the width of the ambivalent region. An alternative method for plotting ambivalence behaviour was proposed by Deshpande and Kumar (2003). They plotted the volume fraction of the initially dispersed phase at phase inversion, regardless of which phase was initially dispersed, as a function of the stirrer speed; this method of plotting clearly illustrates the hysteresis effect that accompanies the inversion process (Norato *et al.*, 1998). Both Pacek *et al.* (1994b) and Kumar (1996) attribute ambivalent range to the effect of secondary dispersions; they suggest that, in water-in-oil dispersions, part of the oil continuous phase is trapped in the dispersed phase (droplet-in-drop structure), leading to an increase in the effective holdup of the dispersed phase. These authors further suggest that such secondary dispersions do not occur in oil-in-water dispersions, even close to the phase inversion point (the details of secondary dispersion will be introduced later). However, Brauner & Ullmann (2002) and Deshpande & Kumar (2003) also suggested that the inversion holdup for sufficiently intense turbulence is

independent of all the operational parameters (e.g. stirrer speed or mixture velocities), and depends only on the properties of the liquid-liquid system.

In contrast to the results for agitated vessels, an ambivalent range of phase inversion in dispersed pipe flow has not been widely reported. Brauner & Ullmann (2002) modelled the phase inversion phenomenon in two-phase pipe flows using a criterion of minimization of the system free energy. Though this criterion defines a single inversion curve, the authors still believed that an ambivalent range around the phase inversion curve existed due to characteristics such as surface rewetting. Their model indicated that, for a hydrophobic surface, the critical inversion holdup of the organic phase decreased, whereas for a hydrophilic surface, the critical holdup of the organic phase increased. Brauner and Ullman suggest that the effect of the wetting characteristics is more significant for large d/D (where d is drop size and D is pipe diameter). For sufficiently high mixture velocities, both curves approach the constant critical holdup obtained for $cos\theta = 0$ (θ is liquid-solid contact angle). Figure 2.22 implies that the preferred configuration is w/o dispersion above the upper curve and o/w dispersion below the lower curve, independent of the surface wetting characteristics. In the region between the two curves, either of the dispersions may exist depending on the wettabilility of the surface by the continuous liquid. Brauner & Ullmann also pointed out that, from a practical point of view, the time scale for complete rewetting of the wall after the inversion (which requires the removal of the old continuous phase film) is much longer than the time scale of the inversion.

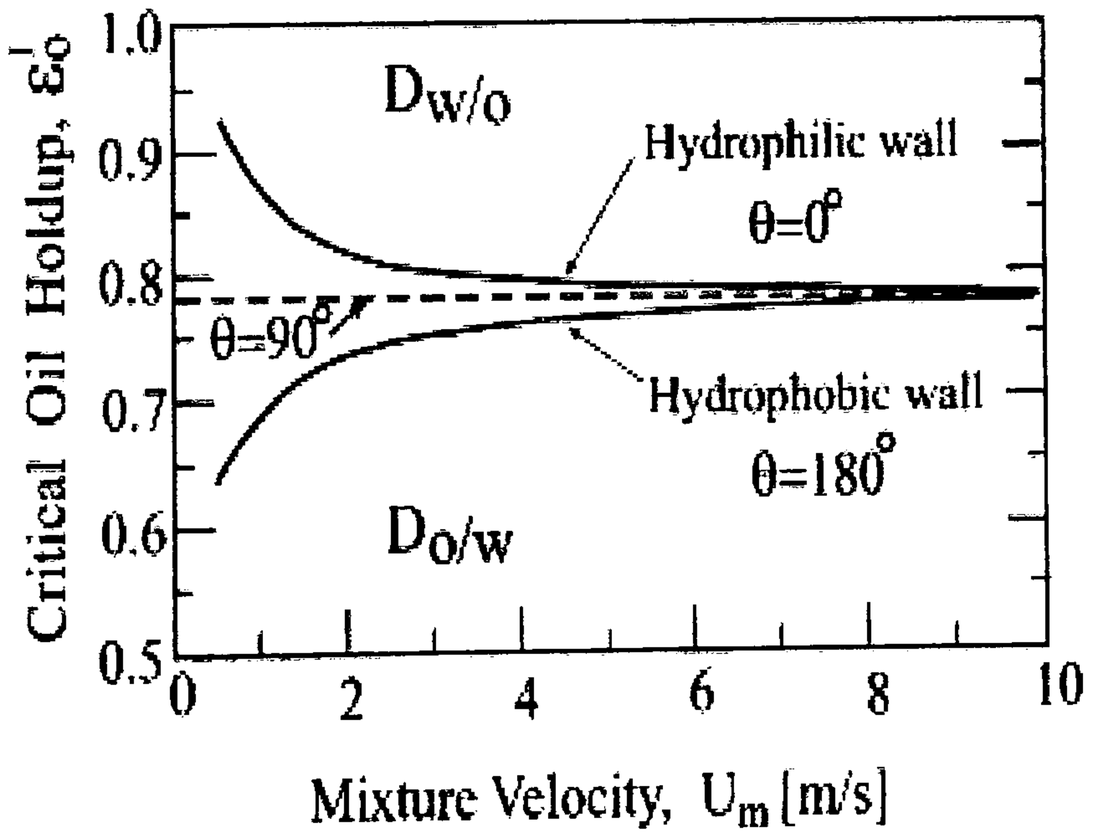


Figure 2.22 Region of ambivalence as affected the liquid/wall wetting characteristics for an oil-water system (Brauner & Ullmann, 2002).

An ambivalent range in pipeline flows has been found experimentally only by Ioannou *et al.* (2005); they obtained the ambivalent range between phase inversion from oil and water dominated mixtures by plotting the oil fraction where the maximum pressure gradient appeared against the mixture velocities (Figure 2.23). However, the ambivalent range was only observed for mixture velocities higher than 4 m/s in larger pipes (60 mm ID). No ambivalent range was found in a small diameter (32 mm ID) pipe; this is in conflict with the theoretical conclusion drawn by Brauner & Ullmann (2002). In addition, experiments carried out by Ioannou *et al.* (2005) also showed the ambivalent range increased with increasing velocity whereas the theoretical models predicted that two curves for the ambivalent range approached equal holdup as the mixture velocity increased (Brauner & Ullmann, 2002).

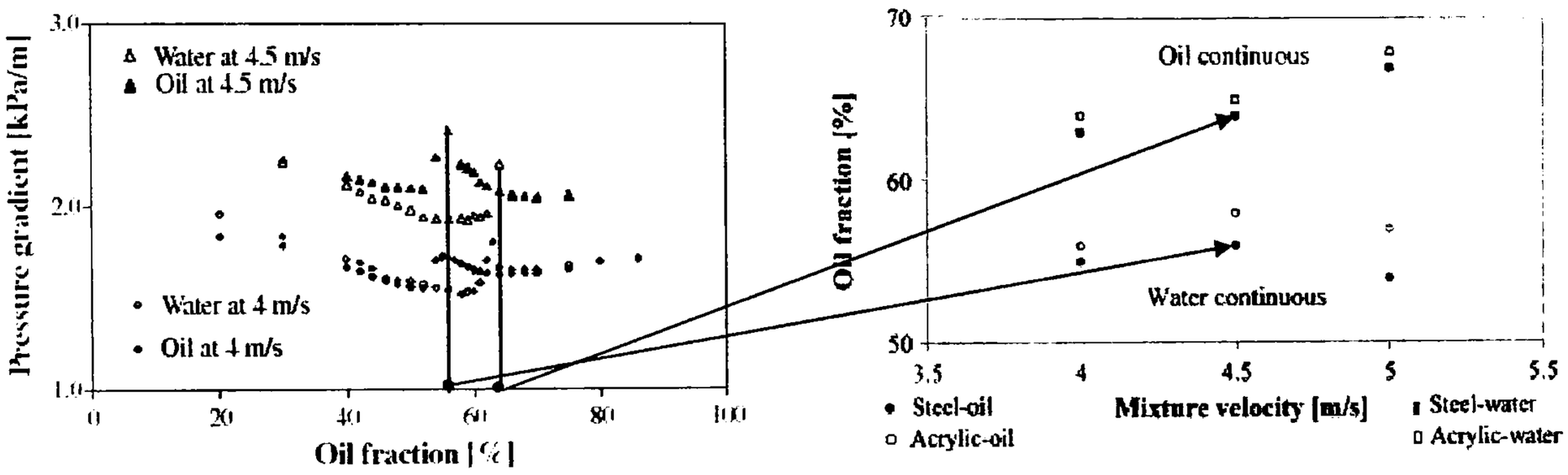


Figure 2.23 Pressure gradient in the steel pipe for the two initial conditions used at 4 m/s and 4.5 m/s mixture velocities (Ioannou *et al.* 2005).

It is noted that for both agitated vessels and for pipe flow, the ambivalence limits vary between systems. The physical phenomena defining these limits are extremely complex. Any factor that influences the phase inversion will affect the boundaries i.e. the width of the ambivalent range.

2.2.1.5 Effects of System Parameters on Phase Inversion

Phase inversion is a very complex phenomenon. Experiments have indicated that phase inversion can be affected by a number of physical and physicochemical parameters, (such as liquid properties), system geometry and system parameters, (such as, mixture velocities,

wettability and the initial conditions of flow systems, etc.). Some of the parametric effects on phase inversion are discussed in this section.

Electrolyte

Some work has proved that drop electric charge, concentration and the pH of the solution have effects on the coalescence and, furthermore, on the stability of liquid-liquid dispersions.

According to Coehn's (Becher, 1966) empirical rule, oil drops in water should carry negative charge due to the large difference of dielectric constant between water and oil. Thus, the oil drops dispersed in water experience a repulsive force because of overlapping of the electrical double layer (EDL). Tobin & Ramkrishna (1992) have reported that because of OH^- adsorption at the organic-water interface, oil drop coalescence was inhibited and the stability of the dispersions was increased, even in the absence of surfactants. Kumar (1996) also postulated that the drop electrostatic charges could explain the asymmetric ambivalence range phenomenon and the preponderance of o/w/o (oil droplets in water drops in an oil continuous phase) over w/o/w (water droplets in oil drops in a water continuous phase) dispersions. It is considered that oil drops in water experience electrostatic repulsion due to the EDL and thus have low coalescence efficiencies whereas water drops in oil have high coalescence efficiencies because no such repulsion exists.

According to the DLVO (Derjaguin & Landau, 1941; Verwey & Overbeek, 1948) theory, which describes the static forces between two drops of given radius as a function of the distance between their surfaces, increasing the electrolyte concentration in o/w dispersions would result in a reduction of the electric double layer thickness and decreasing electric repulsion, and hence, increasing coalescence rate. Howarth (1967) studied the effect of an electrolyte (0.05mole/L NaCl) on the coalescence frequency of an o/w dispersion. He concluded that the addition of small quantities of electrolytes to the continuous phase cause a marked reduction in coalescence rate. He attributed this phenomenon to the non-uniform distribution of sodium and chloride ions and the increase of neutralisation rate due to the addition of electrolyte. However, Tobin & Ramkrishna (1992) questioned Howarth's conclusion since Howarth had calculated average values of coalescence based on rate changes of the Sauter mean drop diameter rather than the full drop size distributions. Tobin & Ramkrishna (1992) also found that the coalescence rate decreased with increasing pH and decreasing ionic strength. Reddy & Fogler (1980) obtained similar results by adding NaCl and NaOH; i.e. the stability of the o/w dispersion increased, especially by addition of the

latter, and the stability decreased with the addition of HCl. Later work by Deshpande & Kumar (2003) also verified that increasing electrolyte content increased the drop size, i.e. increased the coalescence rate. The increasing coalescence is proportional to the electrolyte concentration.

For w/o dispersions, Cheesman & King (1939) and Pfenning *et al.* (1998) both found that the stability goes through a maximum with an increase in electrolyte concentration. Pfenning *et al.* (1998) attempted to explain this phenomenon using the DLVO theory. At low salt concentrations the forces between the drops are slightly repulsive. The maximum value of the repulsive force increases slowly with increasing electrolyte concentration up to an optimum point and then decreases relatively rapidly due to an increase in the attractive force.

Though electrolytes were used in many experiments on phase inversion, the results and conclusions are not consistent. Generally, coalescence and break-up are considered as two important processes which influence phase inversion, and so it is expected that the effect of electrolyte on coalescence should be similar to its effect on phase inversion. However, according to limited research work, the actual results do not confirm expectations. Selker & Sleicher (1965) performed phase inversion experiments in the presence of NaCl at various electrolyte concentrations. They found that, with an increase in electrolyte concentration, the inversion holdup of both o/w and w/o dispersions decreases. No explanations were offered for this finding.

The role of an electrolyte on phase inversion (w/o-o/w) was also investigated by Norato *et al.* (1998) who dissolved sodium chloride (1 mol/L NaCl) into the aqueous phase. They found that, in the system with NaCl, no large fluctuations occurred in the conductivity trace after phase inversion (compared with the systems without any NaCl). It was also demonstrated that phase inversion was delayed with NaCl. Norato *et al.* (1998) also observed that adding NaCl to the system reduced the separation time of the phases after phase inversion once agitation was stopped. It is thus apparent that increasing the ionic strength by adding NaCl eliminated the possibility of secondary dispersions being formed. As mentioned above, the presence of electrolyte could reduce the thickness of the electrical double layer so that repulsive forces are overlapped by van der Waals attraction forces. Therefore, the coalescence rates between oil droplets are increased both for those droplets, that appear in the water drops in w/o dispersions, and for those drops which have external continuous water in o/w dispersions. Increasing coalescence leads to oil droplets escaping from water drops and thus the secondary dispersion is eliminated. After phase inversion, the settling time was

shortened for o/w dispersions, also due to an increasing coalescence rate. The results obtained by Norato *et al.* (1998) are therefore similar to those exhibited for the effect of electrolyte on coalescence.

However, different results were obtained by Deshpande & Kumar (2003) who also studied phase inversion in the presence of an electrolyte (0.01M and 0.1M KI). They found that phase inversion for both w/o-o/w and o/w-w/o dispersions was delayed, i.e. the critical inversion holdup was increased. The delay of w/o-o/w could be explained by the elimination of secondary dispersion as mentioned above. However, the expected decrease in o/w inversion holdup due to increasing coalescence did not appear. To explain this phenomenon qualitatively, Deshpande (2001) attempted to use a modified DLVO theory, i.e. the Multi-Particle Interaction Model of SenGupta *et al.*, (1998). Deshpande (2001) suggested that the DLVO theory, which is derived for dilute dispersions, might not be suitable for the concentrated dispersions near the phase inversion point. Furthermore, he found that, at high salt concentration, the predictions of this theory conflicted with the experimental observations.

Agitation Speed or Mixture Velocity

Generally, in liquid-liquid dispersions, drop break-up and coalescence are the two major processes influencing phase inversion. Turbulence has a strong influence on both processes. Thus, the breakage of drops is due to turbulent shear forces and the turbulent motions acting to promote collision of drops determine the coalescence frequency. Therefore, varying the agitation speed or mixture velocity, (i.e., varying the energy input), has vital effects on phase inversion. Most recent research work has focussed on these effects. (Table 2.1 and 2.2)

At low speed, increasing the speed increases the critical holdup for the water continuous (o/w)/oil continuous (w/o) transition whereas it decreases the holdup for the oil continuous/water continuous transition. Once the speed is high enough, the o/w and w/o critical inversion holdups reach constant values and remain unchanged with increasing speed (Selker & Sleicher, 1965; Luhning & Sawistowski, 1971; Brauner & Ullmann, 2002; Deshpande & Kumar 2003).

Geometrical Considerations

Many experimental results demonstrate that geometrical conditions, such as impeller size, type and position, gap between impeller and vessel in agitated vessels and pipe diameter and shape in flow systems, do have effects on phase inversion. However, no systematic conclusions were obtained. However, according to the Deshpande (2001) and Brauner & Ullmann (2002) analyses, it is concluded that, as long as the turbulence, in the dispersed systems, is sufficiently intense to provide dynamically stable dispersions, and the container is large enough to diminish solid-liquid wettabilitty effects, the nature of the dispersion and phase inversion is determined by the fluid physical properties. Thus, the effect of the flow field on the critical holdup practically cancels out at high enough energy input rate, even if the system is a hand shaken flask (Yeh *et al.*,1964). This is consistent with the observations on the effects of agitator speed mentioned above, if the speed is high enough then the phase fraction at transition becomes independent of speed. The results for pipe flow may show more complex features, as also mentioned above.

Wetting Characteristics and Pipe Inlet Conditions

In large diameter pipes and containers, generally, the wetting characteristics of the solid surfaces can be neglected since the solid-liquid interfacial area is relatively small. In smaller vessels and pipes, the wettability should be considered. Guilinger *et al.* (1988), Groeneweg et al., (1998), Kumar *et al.* (1991), Angeli & Hewitt, (2000a) and Brauner & Ullmann, (2002) investigated the effects of wettability on phase inversion, using different surface materials. They all found that a hydrophobic surface, such as an acrylic resin, increased the critical aqueous phase fraction for the o/w transitions, whereas with hydrophilic surfaces, such as steel, reduce the critical aqueous phase holdup. For low mixture velocities, the effect of wetting characteristics is more significant. In addition, an oil-wetted surface could be considered as a hydrophobic surface and *vice versa*. Therefore, the initial and inlet conditions may also affect the effective liquid-surface wettability and thus, phase inversion. However, in Ioannou *et al.* (2005)'s experiments, the effects of the initial conditions on phase inversion were only observed in the larger diameter pipes rather than in the small diameter pipe; this may reflect differences in the nature of the oil for the two cases.

Viscosity

The viscosity plays an important role in phase inversion of liquid-liquid dispersions. Some experimental results indicated that as the viscosity of a phase increases, its tendency to be dispersed increases (Selker & Sleicher, 1965; Norato *et al.*, 1998). Some phase inversion models (Arirachakaran, *et al.* 1989; Yeh *et al.*, 1964; Brauner & Ullmann, 2002) have shown that the larger the oil viscosity, the wider the ambivalence range. However, for high viscosity ratio ($\frac{\nu_o}{\nu_w}$), the critical holdup becomes practically independent of the viscosity ratio. In addition, the apparent mixture viscosity undergoes a rather sudden and sharp increase when phase inversion occurs (Martinez *et al.*, 1988; Arirachakaran, *et al.*, 1989; Pal, 1993).

Density

Small density differences do not have marked effects on phase inversion (Selker & Sleicher, 1965; Norato *et al.*, 1998, Brauner & Ullmann, 2002) whereas large differences not only make it difficult to obtain dispersions, but also change the critical holdup. Kumar *et al.* (1991) and Chiang & Chen (1994) found that if the material impeller was hydrophobic and, at the same time, the oil density is larger than the water density, the oil drops fall on the impeller and form an oil film and, thus, the inversion holdup would decrease.

Interfacial Tension and the Presence of Contaminants or Surfactants

In general, interfacial tension has a significant influence on phase inversion. Decreasing interfacial tension gives rise to a wider ambivalence range. In other words, it would increase the dispersed phase inversion holdup (Luhning& Sawistowski, 1971; Clark & Sawistowski, 1978; Norato *et al.*, 1998). It is well known that contaminants or surfactants accumulate at the interface and lower the interfacial tension of the dispersed system. Hence, even the slightest impurities may change the phase inversion point, for instance, a significantly larger oil holdup may be required to invert a contaminated o/w dispersions into w/o dispersions compared to the critical oil holdup obtained in a pure system (Brauner & Ullmann, 2002).

2.2.1.6 Review of the Experimental Methods for Liquid-Liquid Dispersed Flow and Phase Inversion

One conclusion drawn from this literature review is that there is no single unified mechanism leading to phase inversion. Definitive information on the details of the drop coalescence and break-up processes, which govern the inversion process, remains elusive despite extensive investigations having been carried out. The difficulty in understanding phase inversion lies in the problem of conceptualising the actual mechanism behind the process.

Since the infancy of investigation of liquid-liquid dispersed flow and phase inversion, researchers have searched for better methods to 'visualize' the whole processes and, furthermore, to reveal the mechanism behind them. The simplest method is observing the change of brightness of different dispersions qualitatively by eye; water-in-oil was found to be dull in appearance whereas oil-in-water dispersion scatters light giving a milky coloured appearance (Yeh, *et al.*, 1964). A number of other techniques have been applied to investigate liquid-liquid dispersed flows and phase inversion (Table 2.4). Impedance probes have been applied in many experiments for measuring quantities such as local volume fraction and drop size, based on the large conductivity difference of the two liquids. These probes depend on the measurement of impedance between the insulated tip and the probe body. However, one disadvantage of such probes is signal processing; at higher velocities reliable results cannot be obtained due to the very fine dispersions formed. For such fine dispersions, no pronounced signal characteristics outside of the noise band are observed. The electric needle conductive probe depends on the measurement of conductivity between two needle tip placed at a sufficient distance apart such that the conduction between them is an indications of the continuous phase (high conductivity if the continuous phase is aqueous, low conductivity if it is oil).

Another method, which has been widely utilized in observing the flow pattern and drop size, is photography. However, due to the difference of refractive index between the two liquids and the materials of pipe or agitated vessel, it is difficult to obtain clear and reliable pictures for liquid-liquid dispersions, especially secondary dispersions. For the phase inversion phenomenon, visualization presents a formidable challenge. The problem is that phase inversion occurs at a high phase fraction where refraction and scattering preclude non-intrusive observations from outside of the vessel or pipe.

Table 2.4 Measurement techniques for dispersions. (Application is to agitated vessel unless otherwise stated).

Methods and Techniques	Authors	Concentration of dispersed (or oil) phase
Photography	Charles, et al., 1961	0.1-0.9
	Pal, et al., 1986. (Pipe)	0.55-0.86
	Gilchrist, et al., 1989	0.4-0.44
	Brooks, et al., 1994	0.2-0.8
	Pacek, et al., 1994	0-0.7
	Sajjadi, et al., 2002	0.06-0.17
Electric needle conductive probe	Yeh, et al., 1964	0.325-0.9
	Selker and Sleicher, 1965	0-0.9
	Guilinger, et al., 1988	0-0.9
	Nädler and Mewes, 1997. (Pipe)	Oil: 0.2-0.95
	Norato, et al., 1998. (Pipe)	0.8
	Angeli and Hewitt, 2000. (Pipe)	0.034-0.091
	Deshpande and Kumar, 2003	
High frequency impedance probe	Lang and Auracher, 1996	Oil: 0-1.0
	Angeli and Hewitt, 2000a and b. (Pipe)	0.034-0.091
	Lovick and Angeli, 2004. (Pipe)	0-0.7
Endoscopes	Angeli and Hewitt, 2000b. (Pipe)	0.034-0.091
Laser based Backscatter technique	Simmons and Azzopardi, 2001. (Pipe)	0.062-0.423
Laser-induced Fluorescence	Augier, et al., 2003 a and b. (Duct)	0-0.4 (Re = 10~100)
Hot film Anemometry	Farrar and Bruun, 1996. (Pipe)	0.05-0.3
	Hu, et al., 2004 (Pipe)	0-0.7

2.2.2 The Mechanisms of Phase Inversion

2.2.2.1 Postulated Mechanisms of Phase Inversion

The phenomenon of phase inversion is very complex and little is known about the actual mechanism governing the inversion process. Some researchers (Dickinson, 1981; Brooks, *et al.*, 1991 & 1994; Vaessen, et al., 1996; Zerfa *et al.*, 1999 & 2001) classified phase inversion into two types—'catastrophic' and 'transitional' inversion. A 'transitional' inversion is

induced by changing factors that affect the distribution of a surfactant between the phases. This is based on a thermodynamic framework and focussing on the role of the surfactant. On the other hand, a 'catastrophic' inversion occurs because of a change in volume fraction.

More recently, investigators such as Pacek *et al.* (1994a), Kumar (1996) and Groeneweg *et al.* (1998) have postulated mechanisms based on a kinetic approach, taking into account drop coalescence and break-up.

2.2.2.2 Drop Coalescence & Breakup

Drop breakup and coalescence are two basic processes in liquid-liquid turbulent dispersions. When a steady state of the dispersion is reached, breakup and coalescence reach a dynamic equilibrium, and they control the steady state drop size and the drop distribution. On the other hand, if the equilibrium is broken (e.g. if the dispersed phase holdup is increased) then the coalescence rate becomes increasingly dominant over the rate of drop break-up, and the drop sizes grow indefinitely, i.e. phase inversion occurs.

Generally, it is accepted that phase inversion is a function of the rates of drop coalescence and breakup. The breakup rate of drops in the turbulent flow is given by the following product (Prince & Blanch, 1990):

Breakup Rate = (Eddy-drop Collision Frequency) • (Breakage Efficiency).

Similarly, some researchers (Quinn & Sigloh, 1963; Coulaloglou & Tavlarides, 1977; Sovova, 1981; Tsouris & Tavlarides, 1994; Tobin & Ramkrishna, 1999.) have suggested that the coalescence rate should be given as:

Coalescence Rate = (Drop-drop Collision Frequency) • Coalescence Efficiency.

Drop breakup and coalescence are controlled by a number of mechanisms. Thus, drop elongation in a shear flow, turbulent intensity, drop-eddy interaction and interfacial tension all affect the drop breakage. On the other hand, coalescence can only occur if there is sufficient contact time to allow the drainage of the thin film of the continuous phase

separating the two colliding drops. The dispersed phase holdup and the viscosity of the continuous phase film are also two important factors for coalescence.

Pacek *et al.* (1994a) used a stereo microscope, with a very shallow depth of field, connected to a video camera to visualise the phase inversion process. On the basis of their observations, they postulated that a simultaneous mechanism of the breakup of the continuous phase is required to explain the inversion process. By monitoring the change in the full drop size distribution and the mean drop size, they show that both continuous phase breakup to produce droplets-within-drops (i.e. secondary dispersions) and enhanced coalescence of the dispersed phase to give larger drops play a significant role in phase inversion.

Yeung *et al.* (2003) investigated shear-induced coalescence of emulsified oil drops in water and found that when two oil drops were brought together to give direct (i.e., 'head on') approach, coalescence was rarely observed. Upon oblique approach, however, the same drops were seen to coalescence readily.

2.2.2.3 Secondary Dispersions

Generally, the inversion process is driven by the coalescence of the dispersed phase leading to larger drops. Phase inversion will be promoted significantly if, during coalescence, some volume of the continuous phase is included in the dispersed phase. This leads to the occurrence of so-called secondary dispersions (or double emulsions). Secondary dispersions have been observed from the earliest studies of liquid-liquid dispersions (Rodger *et al.*, 1956; Quinn & Sigloh, 1963; Luhning & Sawistowski, 1971; Pal, 1993; Pacek *et al.*, 1994 a and b; Pacek & Nienow, 1995; Yang *et al.*, 2000; Sajjadi *et al.*, 2002). Generally, it is considered that secondary dispersions form because of the drop deformation occurring during the collision and subsequent coalescence of pairs of drops or of multiple drops. At a low dispersed phase holdup, it has been suggested that during binary-drop coalescence, the film of continuous phase which separates the dispersed phase droplets from each other breaks, leading to the formation of small droplets (Davies, et al., 1970; Groeneweg et al., 1998). Sajjadi *et al.* (2002) also attributed the inclusion of small internal droplets to a binary-collision mechanism. On the other hand, the multi-drop collision becomes progressively

more important as the closest packed arrangement between the drops is reached; i.e. near the phase inversion point (Kumar, 1996). Inclusion is most probable when at least four water drops collide, so that the continuous phase enclosed by the colliding drops is entrained in the newly formed drop (Figure 2.24). Moreover, Sajjadi *et al.* (2002) has proposed that the drop deformation mechanism may explain the formation of the larger droplets which are observed in their experiments. They considered that at a low volume fraction of the dispersed phase, collision frequency is very low and the drop coalescence mechanism cannot significantly contribute to inclusion. The formation of a secondary dispersion could occur if a large deformation of the dispersed water phase under the high shear rate is applied by stirring. When a drop deformation propagates toward the inside of the drop, a thread of oil is formed. The thread gradually breaks into a rather large droplet and a few small as shown in Figure 2.25 below.

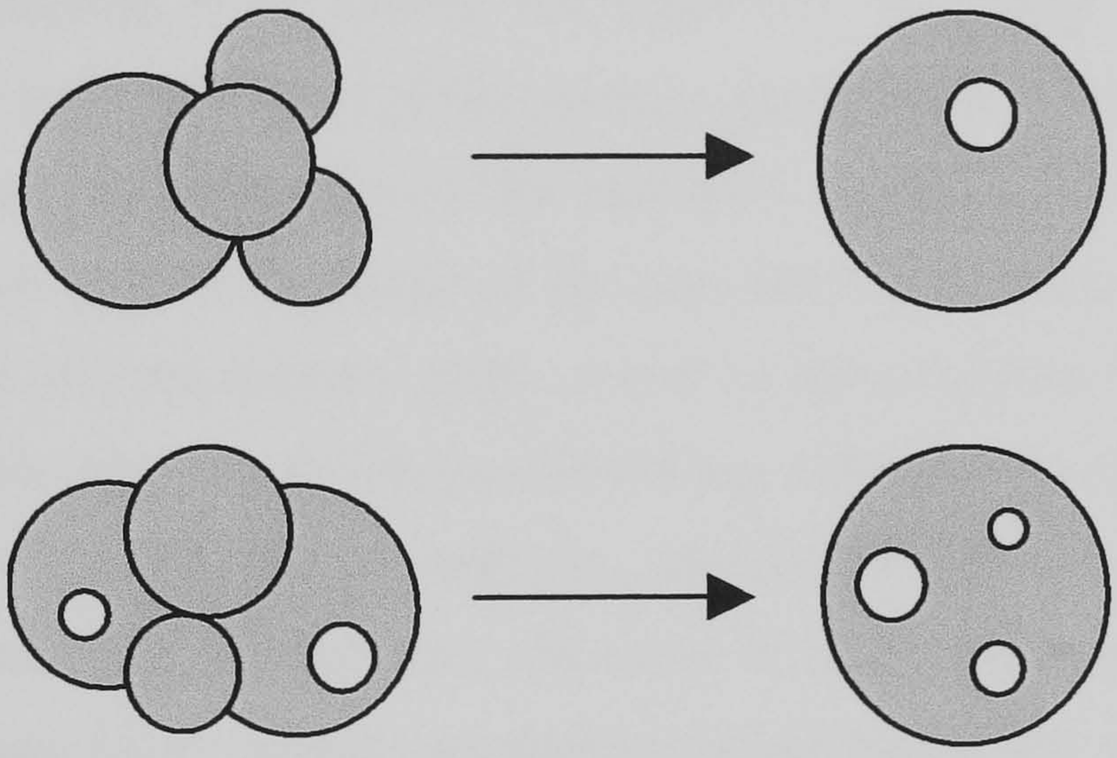
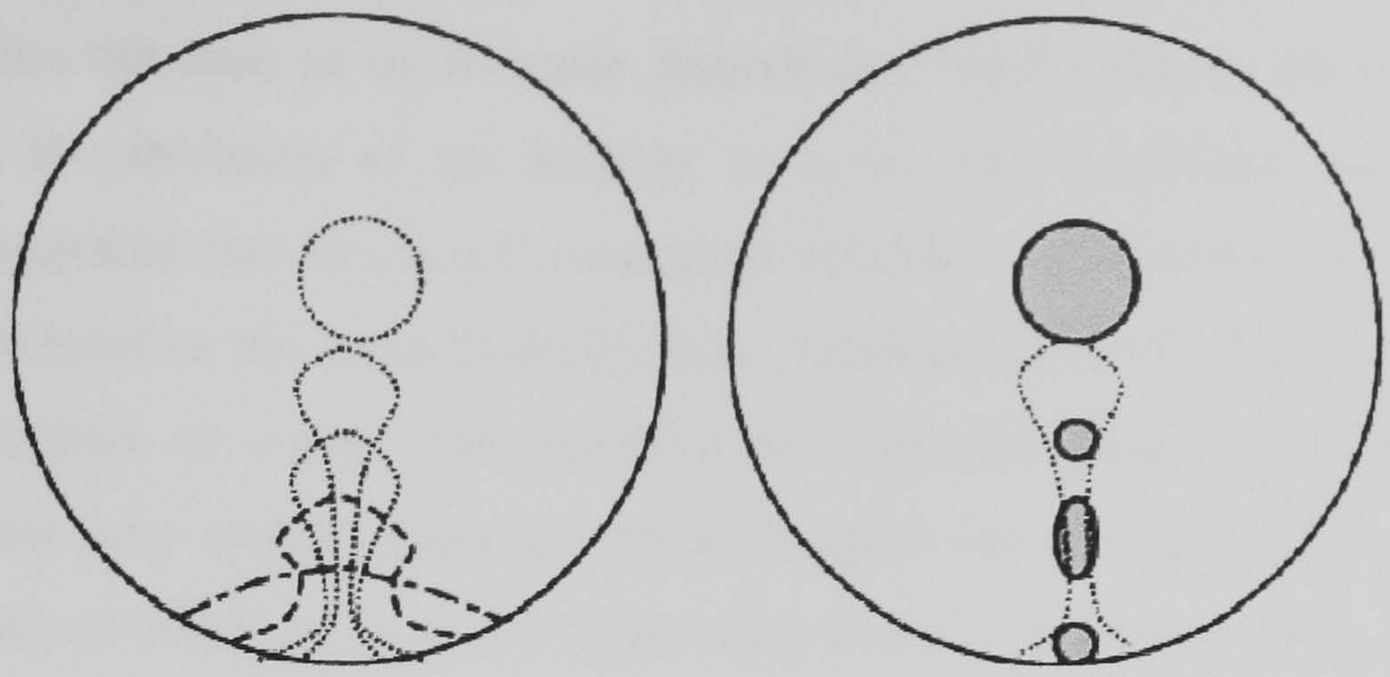


Figure 2.24 Simplified representation of multi-body collisions producing secondary dispersions (Kumar, 1996).



(a) (b)

Figure 2.25 Schematic presentation of internal droplet formation by drop deformation mechanism. (a) Droplet formation and (b) Satellite droplet formation (Sajjadi *et al.*, 2002).

According to Groeneweg *et al.* (1998) and Sajjadi *et al.* (2002), in addition to the processes of break-up and coalescence of the primary (host) drops, processes of *escape* and *inclusion* are occurring at the same time for the secondary droplets. Secondary drops escape from the host drops due to the deformation of the host drops in the shear field. Inclusion of the secondary droplets into the primary drops occurs by the processes illustrated in Figure 2.24 and 2.25. At steady state, these processes (break-up, coalescence, escape and inclusion) reach a state of dynamic equilibrium and the size distributions of both primary and secondary drops become invariant with time. However, as phase inversion is approached, an increase in the dispersed phase holdup can lead to an increase in the size of the multiple drops which, in turn, may lead to their coalescence and to their formation into a continuous phase in which the secondary drops are now the dispersed phase (i.e. phase inversion has taken place).

An interesting characteristic of secondary dispersions is that oil droplets in water-in-oil dispersions are much more likely to occur than water droplets in oil-in-water dispersions, even in the case of systems with equal phase densities and viscosities. Kumar (1996) attributed this asymmetric behaviour to drop charge because of the difference of the dielectric constants of the two immiscible phases. The oil drops in water experience repulsion due to the overlapping of the electrical double layers, leading to low coalescence efficiencies, whereas the water drops in oils of low dielectric constant do not experience such repulsions and are therefore associated with high coalescence. Therefore, the high

coalescence efficiencies of the water drops in oil lead to the possible formation of secondary dispersions that are not seen in oil-in-water dispersions. Later work by Pacek & Nienow (1995) observed the inclusion of oil droplets in many w/o emulsions but not in o/w emulsions and suggested that this non-symmetrical behaviour of oil-in-water and water-in-oil dispersions (subject to the same hydrodynamic conditions) is not dependent on which phase is more viscous or dense. The existence of secondary dispersions has also been invoked to explain why critical dispersed phase holdups for inversion from oil-in-water dispersions to water-in-oil dispersions are higher than in the reverse case. When a part of the oil continuous phase is entrapped in the water dispersed drops, secondary dispersions form and the effective dispersed phase holdup is greater than that suggested by the mass balance. However, this argument is based on the assumption that secondary dispersions only exist in water-in-oil dispersions and not in oil-in-water dispersions.

Luhning & Sawistowski (1971) and Groeneweg *et al.* (1998) suggested that a secondary dispersion does, in fact, occur in oil-in-water dispersions. Groeneweg *et al.* suggest that phase inversion is governed by the balance between drop break-up and coalescence, which is changed in favour of coalescence by the increase of the effective volume fraction on continuous stirring, resulting from inclusion of droplets from the continuous phase into the dispersed phase drops. This phenomenon is counteracted by the escape of these enclosed droplets to the continuous phase. The balance of these processes determines whether inversion takes place. In contrast to the usual finding discussed above, Groeneweg *et al.* (1998), using a microscope, observed inclusion of water droplets in emulsions of triglyceride oil-in-water and toluene-in-water systems, and found no inclusion in the reverse type of emulsions. Groeneweg *et al.* (1998) suggest that inclusion occurs in both types of emulsion but that for one type of emulsion the inclusion is efficiently counteracted by the escape process. With a sufficiently fast escape, included droplets will not be observed. Lang & Auracher (1996) also verified the existence of water-in-oil-in-water drops using impedance probes and photographic techniques. A new method of signal processing, using derivative thresholding rather than level thresholding, has been used which could better detect small fast-moving droplets.

Agterof *et al.* (2003) also pointed out that, in a phase inversion process secondary dispersions are often formed before inversion takes place. The kinetics of the inversion process is to some extent determined by the stability of the secondary dispersion. The instability of a secondary dispersion is governed by the external flow, which generates a flow in the dispersed droplet so that an included droplet is pushed against the interface of the host

drop. This results in a fluid film that starts to drain as in a traditional coalescence process. If the drainage is fast enough the included droplet will escape from the host drop and coalesce with the continuous phase. Thus, if the secondary dispersion is highly unstable, droplets escape very quickly; inversion can only be brought about by an increase of the volume fraction of the dispersed phase so that coalescence becomes faster. A stable secondary dispersion increases the effective volume fraction of the dispersed phase and increases the rate of coalescence and hence, promotes inversion.

2.2.3 Simulations for Phase Inversion

The phenomenon of phase inversion is very complex and determined by a large range of factors; the mechanisms behind it are still not clear. Thus, setting up a proper simulation model is very difficult.

Vaessen & Stein (1995) applied the catastrophe theory to catastrophic phase inversion. Catastrophic inversion is induced by increasing the fraction of the dispersed phase and has the characteristics of a catastrophe, i.e. a sudden change in behaviour of a system, as a result of gradually changing conditions. Catastrophe theory, (see, for instance Thom, 1989), is a mathematical framework to describe such catastrophes. The applicability of catastrophe theory to emulsion phase inversion was first suggested by Dickinson (1981). The most outstanding characteristic of catastrophe theory was the occurrence of hysteresis, which could not be explained by other theories at that time. However, it was proved that catastrophe theory could not be applied to predict phase inversion in coarse emulsions, which should instead be treated on a kinetic basis.

Juswandi (1995) and Yeo *et al.* (2002 a and c) have attempted to simulate phase inversion based on a stochastic model. A Monte Carlo technique was used to model the movement of the drops from their original positions in a lattice and the minimization of interfacial energy was used as the criterion for phase inversion. Juswandi (1995) simulated phase inversion of a dispersion of spherical drops existing in a thin annular liquid film flowing around a tube wall. The limitations of his model are that it does not accurately reflect the actual mechanisms behind the inversion process; secondary dispersions have not been considered. The model also does not take into account the hydrodynamics of the coalescence process;

film drainage times and contact times have not been incorporated into the coalescence model. Yeo *et al.* (2002 a and c) modified Juswandi's model for liquid-liquid dispersions in an agitated vessel. The hydrodynamics of drop coalescence were included. In addition, the model also included a framework for dealing with the interpenetration of drops. However, this model could not predict the presence of hysteresis effects, which often accompany phase inversion.

Brauner & Ullmann (2002) employed the criterion of minimum system free energy to predict conditions under which phase inversion will occur in dispersed liquid-liquid pipe flows. They assumed that the initial dispersion and the dispersion after inversion are stable within a range of operational conditions. After assuming that the system free energy should be represented by the total surface energy, they suggested that phase inversion will occur under a critical condition, where the sum of the wall-liquid and liquid-liquid surface energies in either of two possible dispersions are equal (Equations see Eq. 2-20). By taking account of the wettability of the pipe and the initial conditions, an ambivalent range could be predicted by Brauner & Ullmann (2002)'s model.

Hu *et al.* (2004) and Hu (2004) applied a novel form of population balance (PBE) model to investigate phase inversion in liquid-liquid dispersions in a stirred vessel and in pipe flow. The model includes sub-models for breakage and coalescence. Two alternative criteria are used to identify phase inversion. The first equates phase inversion with minimum interfacial energy. The second criterion is that, at phase inversion, the total volumetric breakage rate equals the total volumetric coalescence rate. The predictions by using PBE with a minimum interfacial energy and the new criterion are both investigated. Results show agreement with the experimentally determined drop size distributions. Good agreement is also found between theory and experiment in terms of the ambivalent ranges, which illustrate the feasibility of using the PBE model to study phase inversion.

Layfield (2003) discuss the use of lattice-gas automata (LGA), based on explicit numerical simulation methods (ENS), to study phase inversion in liquid-liquid systems. This work forms part of the University College London/ Imperial College London/ Edinburgh University project of which the present study also forms part (see Section 1.2). The aim is to elucidate for the first time the mechanisms of phase inversion at the micro and mesoscale levels; this work is still ongoing.

Chesters & Issa (2004) suggested using Computer Fluid Dynamic (CFD) techniques to simulate phase inversion process. They presented a mathematical model to describe the evolution of phase inversion processes in two-fluid systems. The model they used was cast within the framework of the 'two-fluid' model for dispersed flows. Transport equations for newly defined quantities that represent the fraction of dispersed drops and ingested secondary droplets are derived.

2.3 Summary

This Chapter reviewed the significant developments over the past fifty years on liquid-liquid systems, with emphasis on the phase inversion process in agitated vessels and pipelines. In chemical or food processes, phase inversion is either pursued in order to obtain higher interfacial areas or undesirable due to the delay of the settling process. Thus, much research work has focussed on phase inversion in agitated vessels to reveal the influence of phase inversion on the fluid physical properties, such as mixture viscosity, drop size distributions and mass and heat transfer, etc. Work on phase inversion in pipe flow is also important, since an increase of pressure gradient may occur in the phase inversion region for crude oil transportation. Therefore, much of the experimental and modelling work has been directed towards finding the critical dispersed phase holdup. Some empirical and semi-analytical correlations to predict the phase inversion point (the critical holdup) have been developed. However, it is found that a wide range of physical and physicochemical parameters influence phase inversion. Thus, it is not surprising that one conclusion drawn from the literature review is that there is no single unified mechanism behind phase inversion.

In spite of the many studies conducted, fundamental understanding of the mechanism leading to phase inversion has not yet been achieved. Hence, it is apparent that further studies on phase inversion and associated phenomena, especially direct visualization of the dynamic evolution of the liquid-liquid dispersion is still urgently required to reveal the mechanism of phase inversion. This has been the main aim of the present study.

CHAPTER 3

Experimental System

3.1 Introduction

As indicated in the literature review in Chapter 2, phase inversion in liquid-liquid dispersed flow is a complex phenomenon, whose driving mechanism has not yet been identified. Most experiments have focused on phase inversion in agitated vessels. Less attention has been given to pipe flow, despite the fact that it is very common in oil wells and in the petro-chemical and food industries etc.

The purpose of the experiments performed in the present work was to use Laser-Induced Fluorescence (LIF) to visualize liquid-liquid flows and especially to elucidate the phenomena associated with phase inversion, such as drop breakup and coalescence, secondary dispersion, etc.

Hydrodynamic flow visualisation is a direct and powerful aid to provide more details of the flow field and, furthermore, to reveal the mechanisms behind phase inversion. Since the first dye trace experiments by Reynolds, many flow visualisation techniques have been used in fluid mechanics. In particular, in recent decades, several new experimental instruments have been invented (such as high speed video imagers, lasers, computers, etc.) that could be used to improve flow visualization and the interpretation of results. In general, there are two types of flow visualisation methods: optical methods (including, shadowgraphs, Schlieren methods and holographic interferometry techniques) and tracer methods.

Tracer techniques, such as the addition of solid, liquid or gaseous tracers, floating agents (powders or light tracers spread over the free surface), wall methods (colours or air bubbles emitted from the walls) or chemical reaction methods (e.g. luminescent reactions), have been widely used in fluid mechanics experiments, with the main emphasis being on solid particle and dye tracers. In particular, since the laser has been invented, many new flow visualisation techniques using lasers have been reported. Some examples are PIV (Particle Imager Velocimetry), LIF (Laser-induced Fluorescence) and PDT or PDA (Photochromic Dye Tracing or Activation). However, when some tracers are injected into the flows, the physical properties of the system are changed and the flow patterns being studied will be disturbed, no matter how cautiously the injection procedure is performed. Therefore, the non-intrusive dye tracing techniques, LIF and PDT, are particularly attractive methods where they can be applied. In the work described in this thesis, both PDT and LIF were tested in initial experiments and it was found that the LIF technique was more suitable and so it was used for the further investigations. The preliminary work on the PDT technique is summarised in Appendix A.

In what follows, Section 3.2 describes the basis of LIF technique and Section 3.3 describes the visualization system used in the present work, starting with a description of the laser and associated optical system and continuing with a description of the high speed imaging equipment and its synchronisation with the laser pulses. Important requirements for the application of LIF to liquid-liquid systems are to match the refractive index of the two liquids and to choose a suitable dyestuff; these aspects are discussed in the context of the present experiments in Section 3.4. Experiments were carried out on liquid-liquid dispersions in both an agitated vessel and in vertical downwards flow in a pipe of square cross section; the equipment used for these tests is described in Section 3.5. Thus, Section 3.5.1 describes the test system for the agitated vessel and Section 3.5.2 the experimental systems for pipe flow.

3.2 Laser-Induced Fluorescence (LIF) Technique

The Laser-induced Fluorescence (LIF) technique is based on one of the oldest and most established analytical techniques, namely Luminescence. Luminescence is the emission of light from any substance and occurs from electronically excited states. Luminescence is formally divided into two categories, fluorescence and phosphorescence, depending on the

nature of the excited state. When light impinges upon matter, two things can happen: it can pass through the matter with no absorption taking place, or it can be absorbed either entirely or in part. In the latter case energy is transferred to the molecule in the absorption process. Every molecule possesses a series of closely spaced energy levels and can jump from a lower to a higher energy level by the absorption of a discrete quantum of light equal in energy to the difference between the two energy states. Only a few molecules are raised to this higher excited state and hence are capable of exhibiting luminescence. Between each main electronic state are the various vibration levels of the molecule. Figure 3.1 illustrates the schematic energy-level diagram for a diatomic molecule.

When a quantum of light impinges on a molecule, it is absorbed in about 10^{-15} second, and a transition to a higher electronic state takes place. During the time the molecule can spend in the excited state, 10^{-4} second, some energy in excess of the lowest vibration energy level is rapidly dissipated. If all the excess energy is not further dissipated by collisions with other molecules, the electron returns to the ground electronic state, with the emission of energy. This phenomenon is called fluorescence. In general, the fluorescence lifetimes are typically near 10^{-8} sec. Since some energy is lost in the brief period before emission can occur, the emitted energy (fluorescence) is of longer wavelength than the energy that was absorbed (the shorter the wavelength, the higher the energy the photons possess). Any fluorescence molecule has two characteristic spectra: the excitation spectrum (the relative efficiency of different wavelengths of exciting radiation to cause fluorescence) and the emission spectrum (the relative intensity of radiation emitted at various wavelengths). Emission spectra vary widely and are dependent upon the chemical structure of the fluorescence compound and the solvent in which it is dissolved. Every molecule possesses a characteristic property that is described by a number called the quantum yield, or quantum efficiency, Φ. The higher the value of Φ, the greater the fluorescence of a compound.

$$\Phi = \frac{\textit{Number of quanta emitted}}{\textit{Number of quanta absorbed}} = \textit{quantum yield}$$

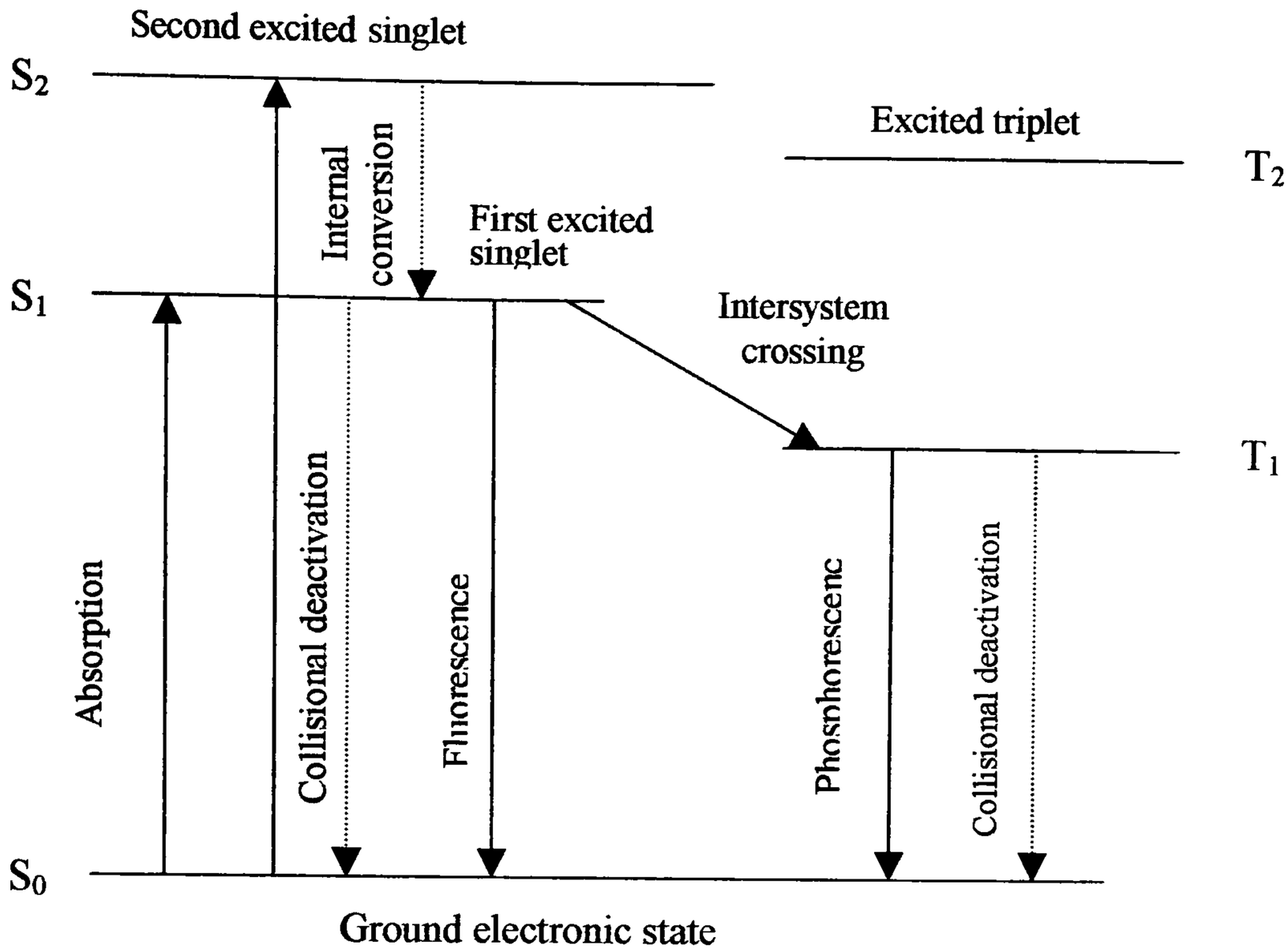


Figure 3.1 Schematic energy-level diagram for a diatomic molecule (Guilbault, 1973).

Fluorescence has been widely used in chemical and biochemical engineering, biological science, environmental engineering, etc. The first advantage of fluorescence is its extreme sensitivity. Fluorometric methods can detect concentrations of substances as low as one part in ten billion. For example, fluorescent substances, dissolved in organic liquids, have been used to detect quite low concentrations of crude oil/oil products or pesticide, which are encountered as pollutants, in water and soil (Pascu, *et al.*, 2001). Apart from the sensitivity, good specificity is another advantage. Different fluorescent substances that absorb the same wavelength radiation will probably not emit at the same wavelength. Even the same fluorescent substances that absorb the same wavelength radiation at different temperature will not emit at the same wavelength. This characteristic has been used to measure temperature distribution in fluids (Lavieill *et al.*, 2000).

The Laser-Induced Fluorescence technique is one of the most useful of modern visualization techniques; it takes advantage of the laser's specific characteristics – mono chromaticity, high light intensity, etc. In general, in most experiments, the laser sheet, which is focused by a series of optical components from a laser beam, excites a fluorescence dye dissolved in the fluids. The fluorescence dye will then emit a longer wavelength light. For example, Rhodamine B will emit orange and yellow light when it is excited by 514nm green

light. The Laser-induced Fluorescence technique is also a non-intrusive dye tracing technique that does not need background light.

In the last twenty years, many kinds of fluorescent dyestuffs and tracers have been used with aqueous soluble fluorescence, organic soluble fluorescence and gas fluorescence employed in the Laser-Induced Fluorescence technique to visualise flow fields. Among the large range of available fluorescence dyestuffs, Rhodamine B, Rhodamine 6G and sodium fluorescein have been most widely used in single phase and two-phase liquid-liquid flows.

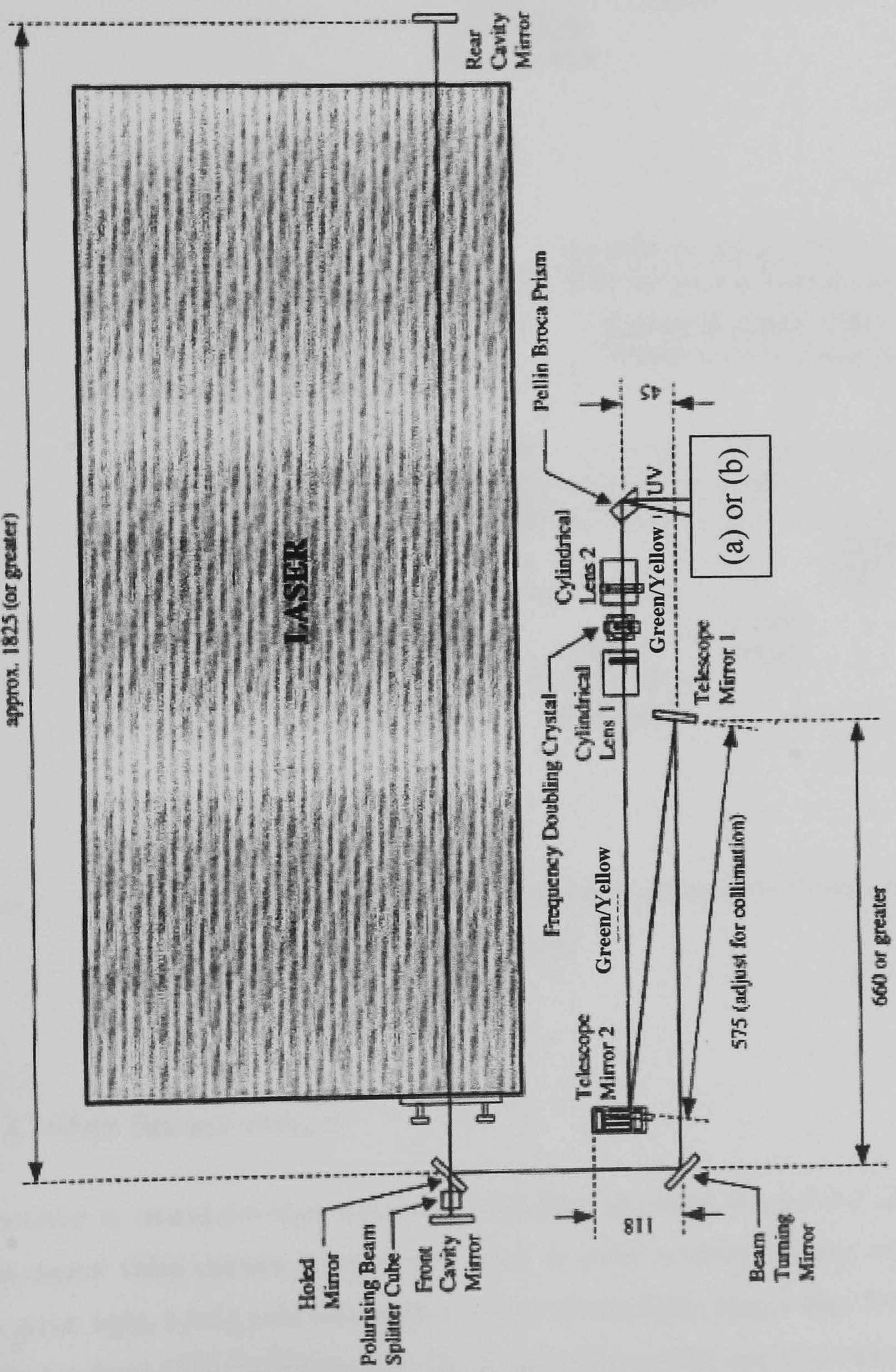
3.3 Laser and Digital Imaging Equipment

3.3.1 Laser and Associated Optics

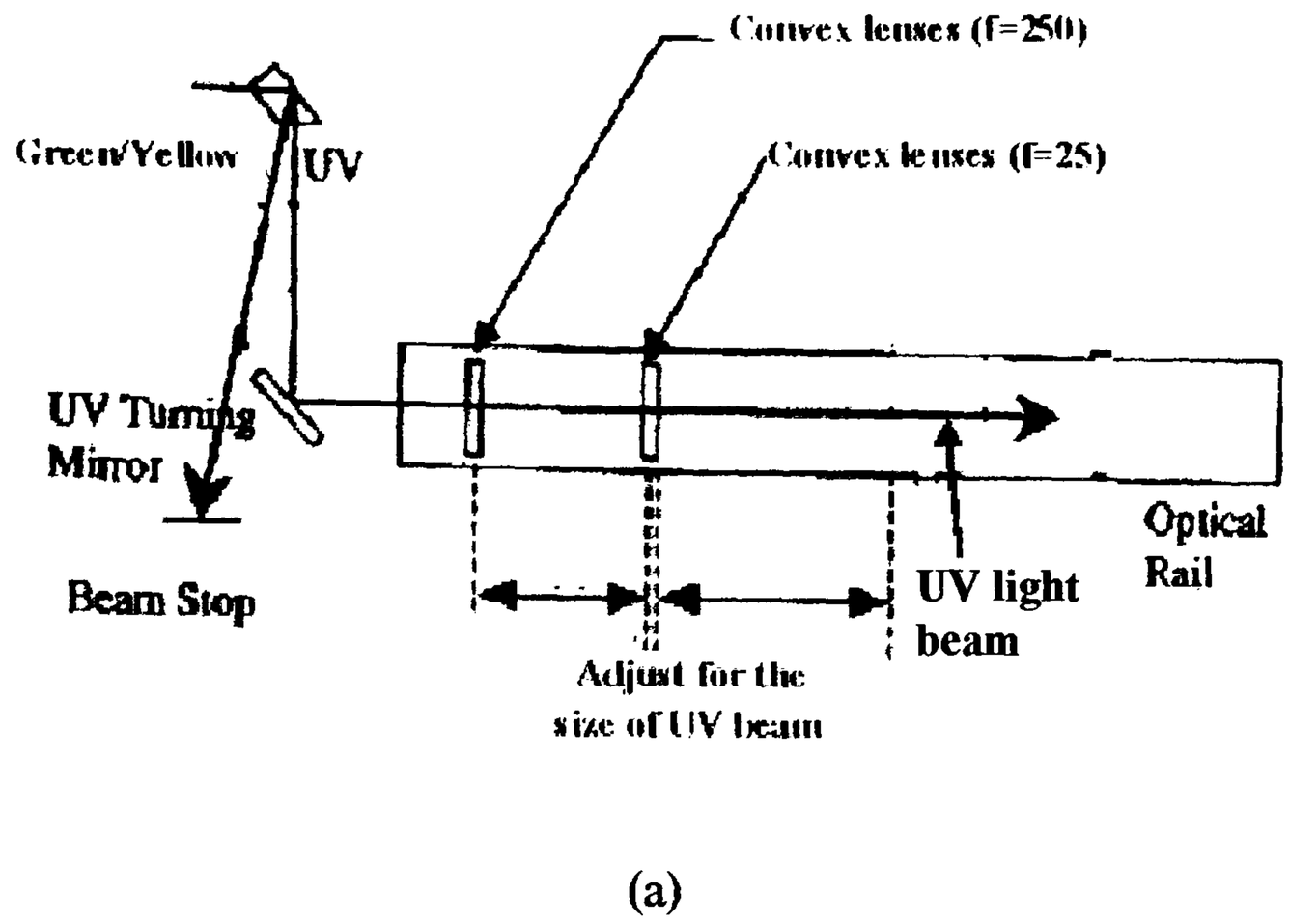
A 20-W nominal output pulsed copper vapour laser (Oxford Lasers LS20-10) was used as an ultraviolet light source for the PDT tests described in Appendix A and as a green light source for the main series of tests using LIF. The output spectrum is double-peaked at 510.6nm (green) and 578.2nm (yellow) and the laser is always pulsed (about 2mJ/pulse), with an internal clock frequency of 10kHz. Pulse Repetition Frequencies (PRFs) other than 10kHz (as low as 168Hz) can be achieved using an external trigger source. The pulse duration is dependent on the PRF and can have values between 10 nanoseconds and 60 nanoseconds.

The optical system is shown schematically in Figure 3.2. The beam from the laser is first passed through a series of mirrors which can be adjusted to obtain the appropriate collimation. If the required final beam is UV, a frequency doubling crystal can be inserted as shown which converts some of the source beam into UV radiation with wavelengths of 255nm, 271nm or 289nm. The main beam is labelled "green/yellow" in Figure 3.2 for simplicity through, as indicated above, it contains peak wavelengths at 510.6nm and 578.2nm, the latter being yellow. After the frequency doubling crystal (which has cylindrical lenses before and after it), the green and UV components are separated using a Pellin Broca Prism. For photochromic dye tracing (PDT), the non-UV components of the beam are either fed to a beam stop or are passed into a fibre-optics cable and used to illuminate the test section from behind so as to obtain synchronised images of the dye distributions in PDT –see Appendix A. The UV beam is then passed through a mirror and through convex lenses to produce the required 1-2mm diameter light beam (Figure 3.2a).

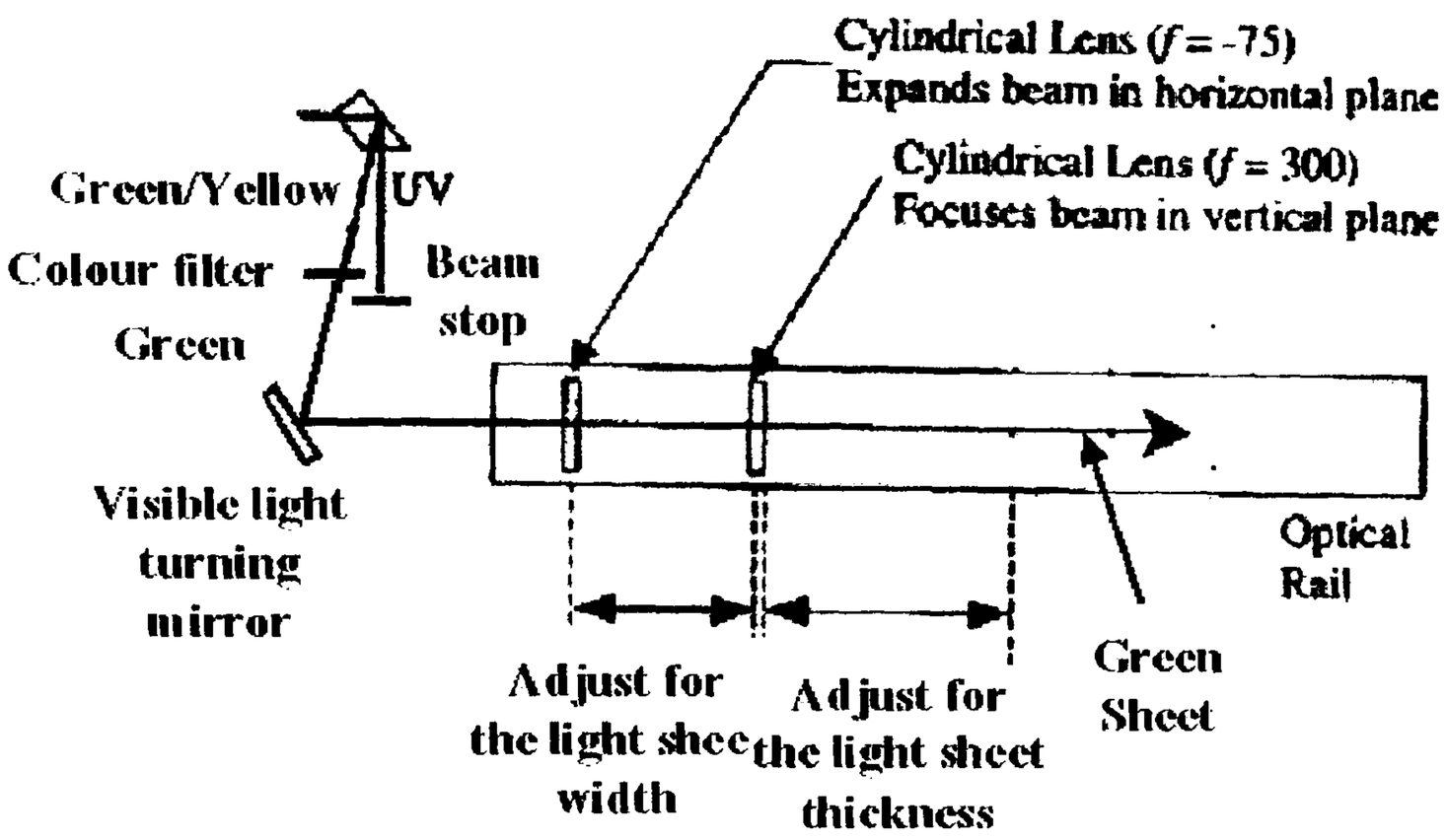
For the main series of LIF experiments reported here, the UV components are blocked by a beam stop and the yellow component is filtered out using a short-pass colour filter (green). Only the green (510.6 nm) component was then passed through the cylindrical lenses to produce a green light sheet which has a width controlled in the range 20 to 40mm and a thickness of 1-2mm (Figure 3.2b).



Continued



(a)



(b)

Figure 3.2 Schematic diagram of Laser and optics; dimensions in mm; (a). The kit for UV light; (b). The kit for green light

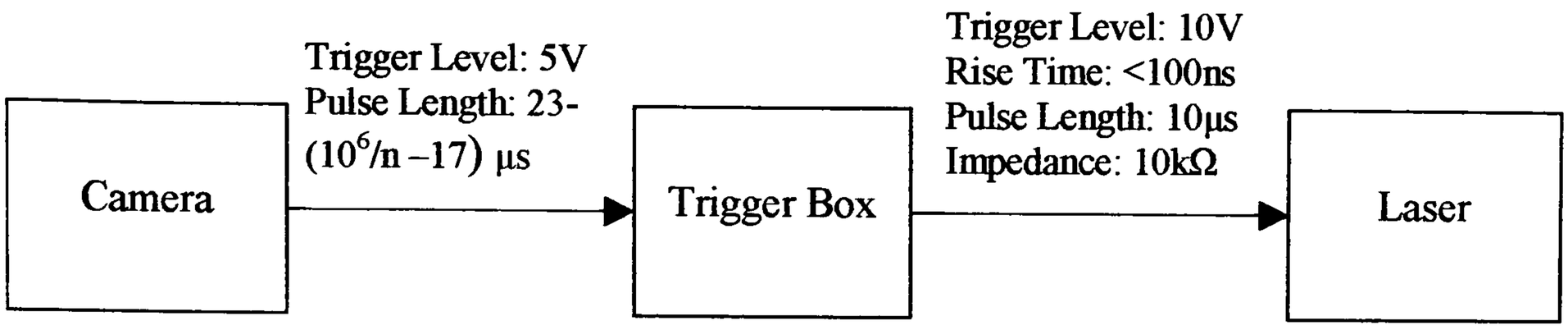
3.3.2 High Speed Imager

In order to record the high speed dispersed flow on video, one of two alternative high-speed digital video camera systems were used. In order to eliminate any reflections of the laser green light, a long pass colour filter, which allows lights longer than 530 nm to pass, is attached in front of the camera lenses. The digital video system employed were:

The Kodak Extapro HG Imager (Model 2000) System offers recording rates from 30 to 2000 frames per second (256×512 pixel resolution for 2000fps and 512×512 for 1000 fps and below). Digital images can be downloaded in a 24 bit colour TIFF file format. The camera is located perpendicularly to the laser light sheet activating the dyestuff and is focussed at the plane of the laser sheet.

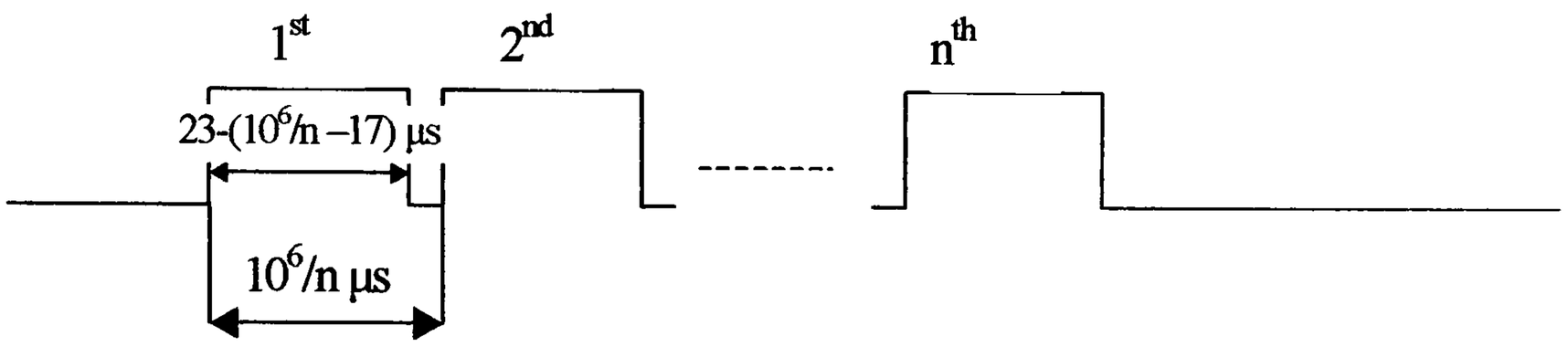
A Trigger Box was designed to synchronize the laser pulse with the digital camera so that each pulse illuminates one image. Each time the camera's shutter opens (and exposure starts), the camera 'Exposure out' connector outputs a TTL level signal that goes high at the start of each frame and is high for the length of the exposure. This signal is sent through a BNC cable to the trigger box whose frequency has been set to the camera's frequency (e.g. 2000 frame/s). After receiving the signal, the trigger box sends a signal to the laser. After receiving the external signal, the laser automatically drops its internal Pulse Repetition Frequency to that of the external signal. When the external signal stops, the laser adjusts its frequency to its original value. The synchronization system is illustrated in Figure 3.3.

The Phantom v7.1 system (Photo-sonics International Ltd.), was borrowed from the EPSRC Engineering Instrument Pool, and uses SR-CMOS sensors with a maximum resolution of 800 × 600 pixels at up to 4,800fps giving 1.2 seconds of recording time. Above 4,800 fps, the resolution decreases. Recording speeds of up to 150,000 fps are available. Recording time can be increased by reducing the resolution. Triggering is possible via switch closure or a TTL signal. Triggering is continuously variable pre and post recording. Shutter speeds down to 2 microseconds are available. The camera system includes a Nikon 24-85mm F2.8 macro zoom lens. Images can be saved in many formats including TIF, GIF, JPEG, BMP, AVI etc.

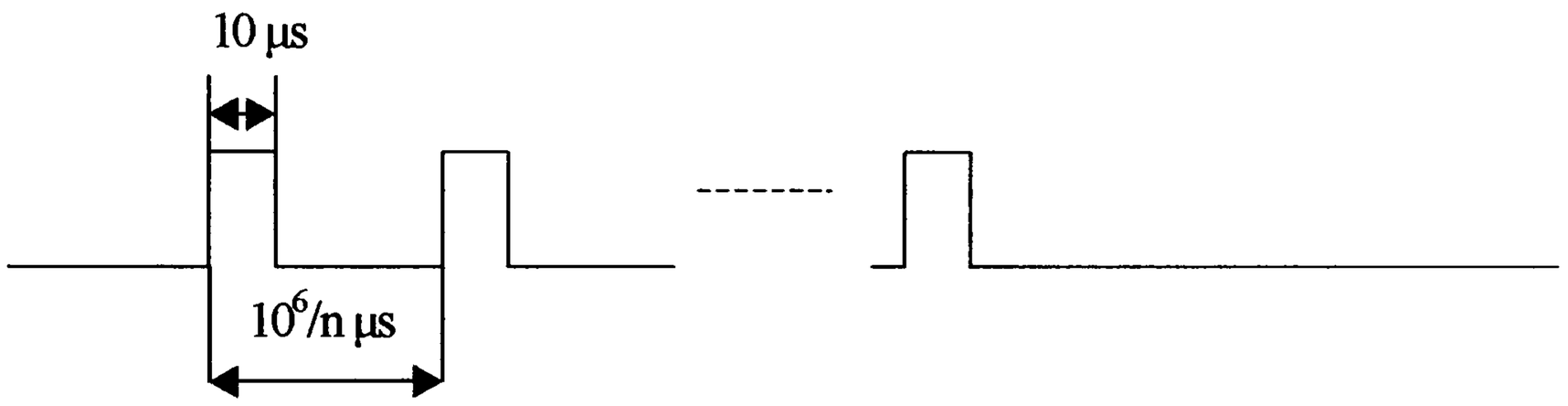


(a)

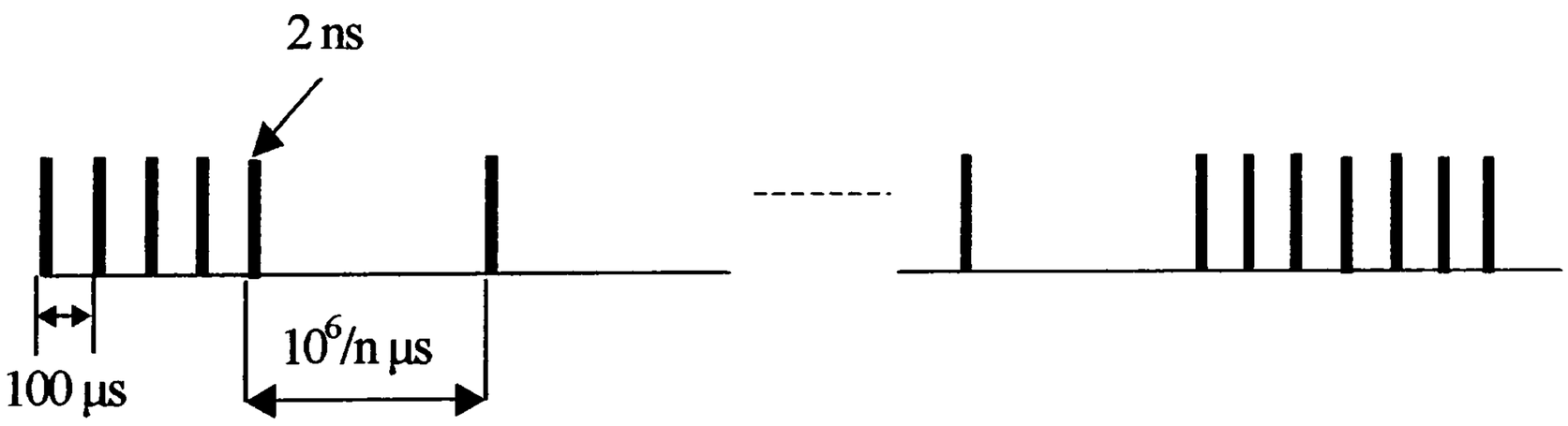
The signal camera send



The signal trigger box send



The laser pulse



(b)

Figure 3.3 (a) Schematic description of trigger system and (b) Trigger box working mechanism

3.4 Selection of Liquid Pair and Fluorescent Dyestuff

3.4.1 Selection of Liquid Pair

When a parallel beam of light passes through a dispersed system, its intensity is attenuated by diffraction, reflection, refraction and absorption. The contribution of the first three mechanisms is usually lumped together and termed scattering. If one drop is considered, the angular scattering of the parallel rays can be pictured as in Figure 3.4. As illustrated, each of the four scattering mechanisms prevents the rays from maintaining their original direction. Multiple scattering occurs when light which has been scattered by one drop, is scattered again by another drop. The transmitted light intensity is therefore a function of both position and direction.

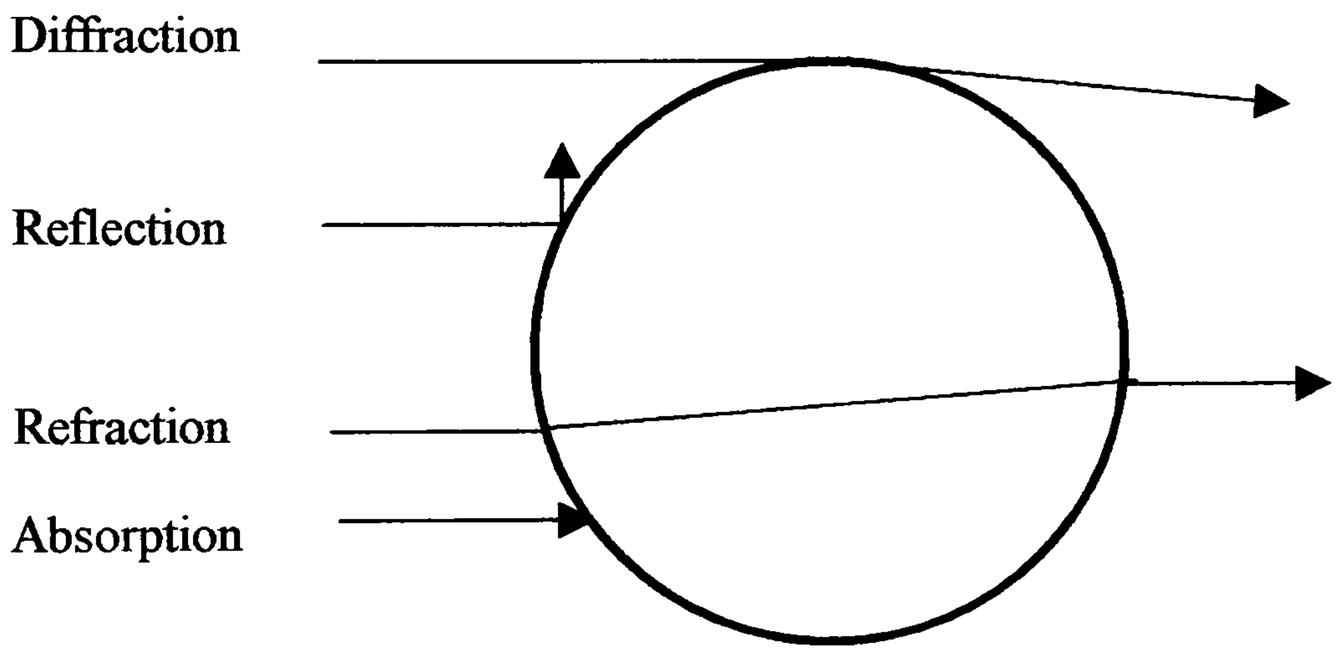


Figure 3.4 The four mechanisms of light attenuation through a drop

Three of the light attenuation mechanisms shown in Figure 3.4 (namely diffraction, refraction and reflection) can be eliminated by matching the refractive index of the two liquids; in the absence of such matching, it would be impossible for the activating laser sheet to penetrate the mixture and for the fluorescence to be observed through the mixture. Even if the refractive indices are matched, absorption still remains as an attenuating mechanism and it is important that the fluids are transparent to both the activating and generated light. By definition, however, the induction of the fluorescence causes absorption of the activating laser sheet and the intensity of the fluorescence decreases with distance along the sheet. Thus, in order to obtain clearer images to investigate dispersed two-phase flow, refractive index matching (RIM) is the most important characteristic required for a liquid-liquid pair. The search criteria for the liquid pair were as follows:

- Colourless/pale coloured and clear liquids with matched refractive indices to ensure that the liquids are optically transparent in order to facilitate viewing the coloured plane at which the dyes are activated;

- Good transmittance at excitation wavelengths; between 255 nm and 289 nm for the photochromic dye in PDT and 500-520nm for the fluorescent dye in LIF;

- Organic phase to be able to dissolve the spiropyran photochromic dyestuff for PDT;

- Since the inorganic phase (usually aqueous solution), normally have high dipole moments i.e. polar liquid, in order to keep the dyestuff in one phase, the organic phase should be with low dipole moment (between 0 to 0.5 debyes) i.e. non polar liquid;

- Inorganic phase to be able to dissolve Acid Violet 19 photochromic dye and the associated bleaches for PDT, and to dissolve the selected fluorescent dyestuff (Eosin Y) for LIF;

- Low toxicity;

- Low flammability;

- Low corrosiveness;

- Low cost.

The difficulty of finding a pair of liquids that satisfies each of the criteria above can easily be recognised. After searches and tests, the liquid pair-- Exxol D80 Oil and 39 wt.% calcium chloride ($CaCl_2$) was chosen for Laser-induced Fluorescence experiment. An refractometer was used to determine the refractive index of liquids. At 39%, the refractive index for calcium chloride and Exxol D80 are exactly matched at 1.438 at 25°C (see Appendix B). Data for the refractive index of calcium chloride solution as a function of temperature and concentration are presented in Appendix B. The physical properties for the liquid pairs are given in Table 3.1 below.

Table 3.1 Physical Properties of the Selected Liquid Pair

	Exxol D80	39 wt.% *Calcium Chloride* Solution with fluorescent dyestuff (Eosin Y)
Density (20°C)	803kg/m^3	1442 kg/m^3
Viscosity (25°C)	0.00162 Ns/m^2	0.01184 Ns/m^2
Refractive Index (25°C)	1.438	1.438
Interfacial Tension with Eosin Y (20°C)	0.0190 N/m	

3.4.2 The Fluorescent Dyestuffs

Ideally the fluorescence dye had to meet the following requirements:

1. The dye should be soluble in Exxol oil or aqueous solution;

2. The absorption wavelength of the dye should be around 510nm (green) or 578nm (yellow) and the emission wavelength should be in the range of visible light;

3. Where an interface exists in the system under study it is important that the surfactant properties of the water remain unchanged by the addition of the dye components. Also any disturbance to the flow caused by localised heating, due to the excitation radiation application, should be minimized;

4. The change of the refractive index of the liquids which is caused by the dye should be minimized;

5. The relative contrast between the solution in the excited and unexcited forms should be as high as possible;

6. Relatively stable;

7. Low toxicity, low flammability, low corrosiveness to the rig material (copper).

After investigating a large number of fluorescence dyestuffs (details shown in Appendix C), the fluorescence dyestuff Eosin Y was selected to use in the experiments described below, with the dyestuff being dissolved in the aqueous phase. The fluorescence emission of

Eosin Y, centred in the red-orange part of the visible spectrum[1], is strong. Furthermore, its fluorescence can be excited by green light (λ=510.6nm) of the Copper Vapour Laser. In the experiments, a 5% wt. solution of Eosin Y in water was prepared and 0.2 ml of the solution per litre of calcium chloride solution was used.

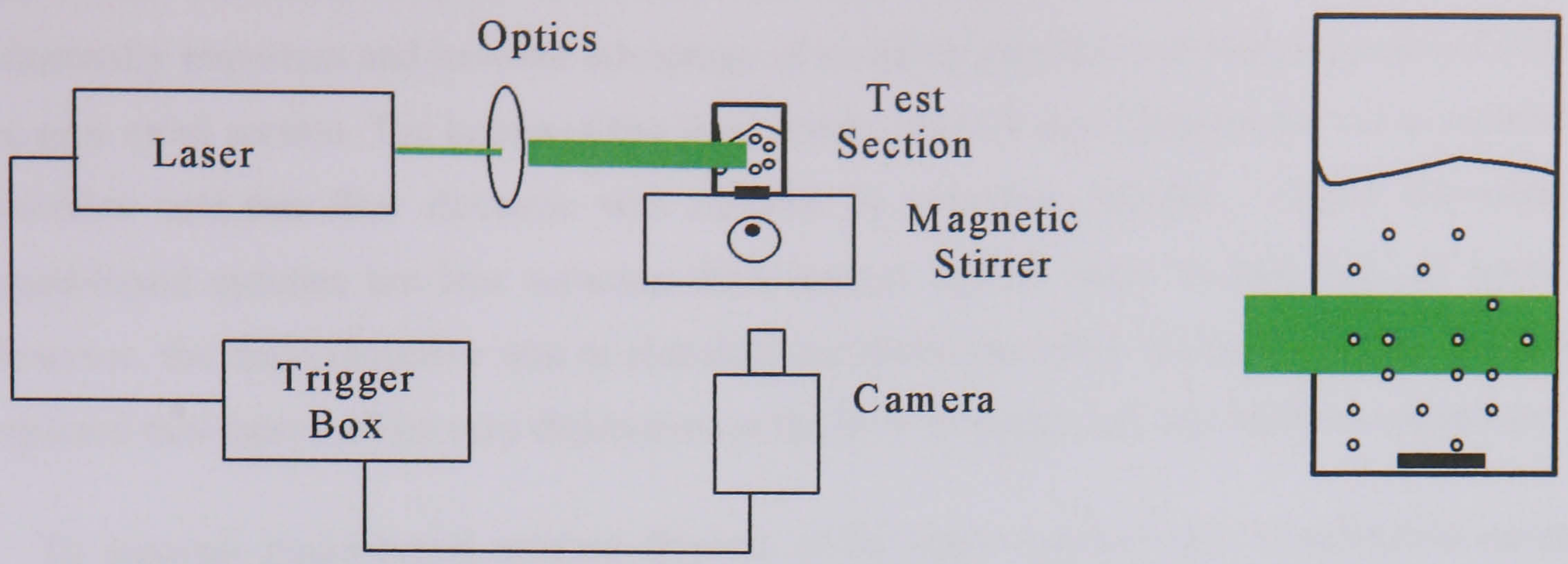
3.5 Experimental Facilities

Experiments for liquid-liquid dispersed systems were carried out in both an agitated vessel and a square cross section duct. The experimental arrangement for the agitated vessel is described in Section 3.5.1 and the systems used for the pipe flow experiments are described in Section 3.5.2

3.5.1 Agitated Vessel System

The first experiments using the LIF technique were carried out using a simple agitated vessel system as illustrated in Figure 3.5. The use of this system not only allowed validation of the methodology as a precursor to the more complex pipe flow experiments but was also of intrinsic interest since much of the work on phase inversion in liquid-liquid systems has been done with agitated vessel systems (see Chapter 2). The test section (shown in Figure 3.5) was a 80mm high and 30 mm×30 mm square cross section cell made of CaF_2 glass. A magnetic stirrer was used as an impeller. The impeller was a 20 mm long, 6 mm diameter cylinder with PTFE surface. It was located at the centre of the base of the cell by the influence of the rotating magnet placed under the cell shown. The configuration of the liquid-liquid dispersions in the cell could be determined by passing the (green) laser sheet through the cell (as shown in Figure 3.5b), causing the aqueous phase (containing Eosin Y) to fluorescence.

[1] In most of the photographs shown in Chapters 4-6, the aqueous phase are showing greenish colour rather than orange. This is because the photograph were taken by changing the "white balance" of the camera to achieve a better contrast.



(a) (b)

Figure 3.5 (a) A schematic representation of the experimental setup for the agitated system; (b) The position of the laser light sheet.

The results of the experiments on the stirred vessel are presented in Chapter 6.

3.5.2 Pipe Flow Systems

Ideally, the LIF visualization of liquid-liquid pipe flow would have been carried out on a flow facility such as the TOWER rig (Two-phase Oil-Water Experimental Rig) situated at Imperial College London and used by previous investigators there (Angeli, 1996; Soleimani, 1999; Hussain, 2004). This facility includes large scale pumping and phase separation facilities and accommodates long test sections. However, the rig is situated in an open laboratory and a special containment housing would have had to be build for the laser and its associated optics. At this first demonstration phase of the work, therefore, the laser was placed in a small laboratory at Imperial College London, with safety locks and warning systems installed. Ultimately (and particularly in view of the success of the present experiments), it is hoped to install the laser system on the TOWER rig by building a suitable containment. However, in the present work, a flow system had to be built which could be accommodated in the small laboratory.

In the TOWER facility, long horizontal test sections have been used and such test sections were clearly not feasible in the small laboratory. Short horizontal test sections could have been used but the earlier work on horizontal flows (Hussain, 2004) has shown that long tube lengths are required to reach equilibrium phase distribution. Also, horizontal flows are not axially symmetric due to the gravitational separation of the heavier phase. The decision

was made, therefore, to carry out the present tests using *vertical flows*. Such flows are industrially important and have the advantage of avoiding gravitational phase separation over the pipe cross section. The layout of the laser system made it more convenient to use *vertical downflow* and this flow direction was adopted. In industrial practice, vertical downflow liquid-liquid systems are less common than vertical upflow ones, though they do occur. However, the main objective was to elucidate the phase inversion mechanisms and it is not expected that these will be very dependent on the flow direction and test section orientation.

To separate liquid-liquid mixture flowing at the rates required (i.e. at velocities up to several meters per second) requires a large scale separator. For example, the separator vessel on the TOWER facility is 0.54 m ID and 1.94 m long. Such a large phase separator was clearly not possible in the small laboratory in which the laser was housed and two solutions were pursued:

(1) To pump a liquid-liquid mixture of known phase fraction around a closed loop including the LIF test section. It was found that, using a centrifugal pump, the dispersed phase was broken up into very small (and thus atypical) drops. Another problem was that there was a significant heating effect of the pump (though this could be solved using a heat exchanger). The pump-around system was therefore abandoned for high flow velocities. However, at very low velocities, a more gentle circulation could be achieved using a gear pump and a series of experiments were carried out using this system.

(2) To pump the two liquids separately into the test section at known rates and over a period of time which, though short, was sufficient to establish the flow and carry out the LIF visualization. In this system, small volumes of the liquids were sufficient and gravitational separation of the phases was carried out between tests.

In what follows, the test section is described in Section 3.5.2.1 and the high flow rate (two-pump) system is described in Section 3.5.2.2. The gear pump (pump-around) system is described in Section 3.5.2.3. It should be stated that considerable development work was carried out in evolving these two viable systems and this is summarised in Appendix E.

3.5.2.1 Test Section

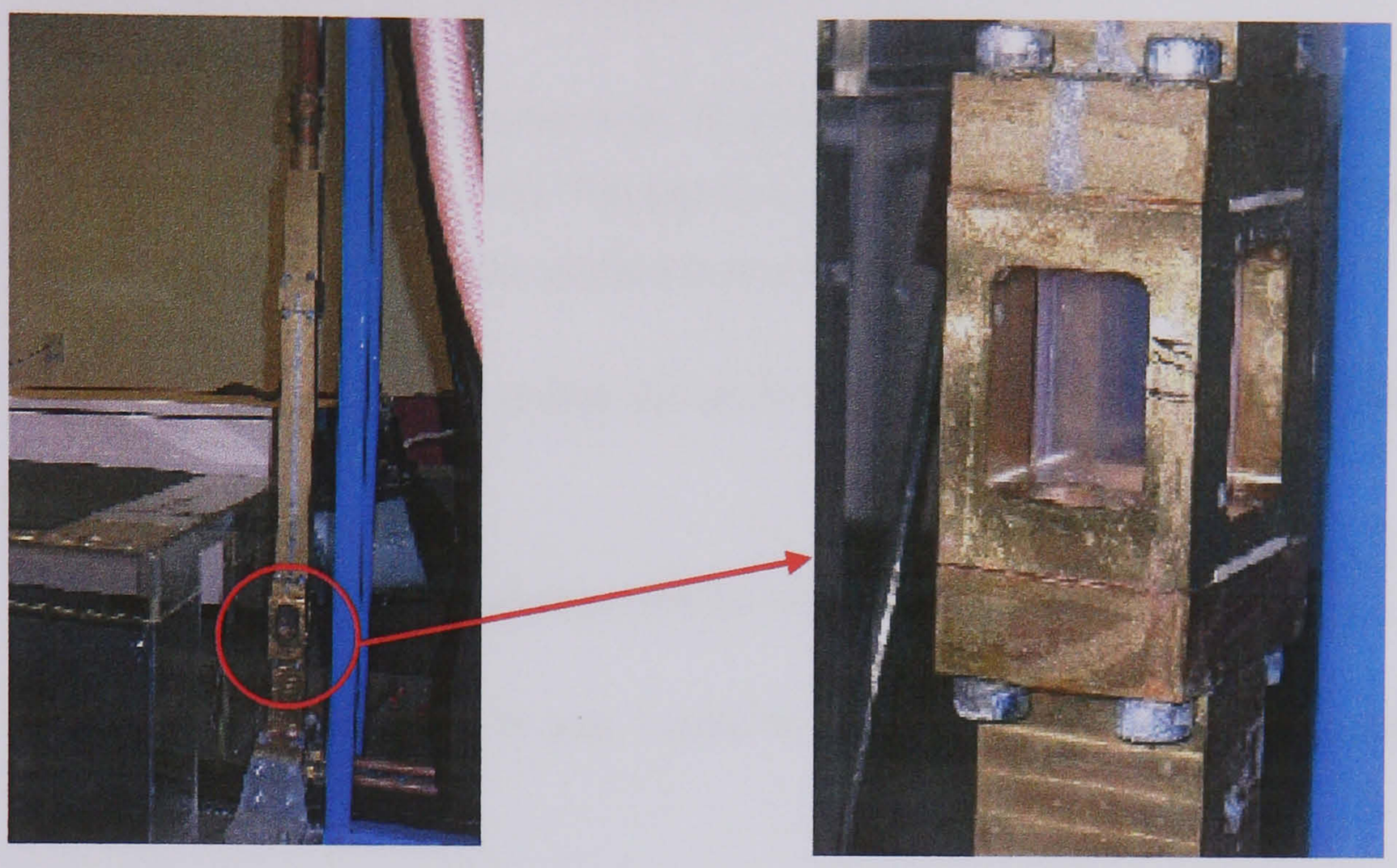
The design of the test section for the visualization of liquid-liquid flows was influenced by two main considerations:

(1) The need for transparency of the test section walls to *both* the UV and green components of the laser emission. The UV transparency was required in the evaluation work on photochromic dye tracing (see Appendix A). To achieve this UV transparency, a quartz test section was employed.

(2) The need to avoid distortion of the images by refraction effects in the test section walls. If a circular tube is used then the image is distorted; one way round this problem would be to have matching of the refractive index of the wall material and the fluids and to make the outer surface of the wall of, say, square cross section. In effect, this approach was followed by Hope (1990) in his photochromic dye tracing studies of air-water flows. Hope used an FEP (fluorinated ethylene propylene) tube which had a refractive index close to that of water. He surrounded this tube with water inside a rectangular tank and obtained excellent visualization of PDT traces. However, in the present studies, the approach was to use a section of square cross section quartz tube for visualization. It would have been preferable to have used a circular tube from the point of view of the hydrodynamics but it was felt that, since the visualization was in a plane passing through the centre of the wall and the tube axis, the effect of the corners would not be great. However, the corner effects were investigated using CFD analysis as is reported in Chapter 8.

The square cross section quartz cell used for visualization had 18mm internal width sides, a 2mm wall thickness and was 48.16mm long. The cell clamped from above and below between two precisely machined brass square channels of the same internal dimensions. Thus, a constant flow cross section was maintained between the brass channels and the quartz cell. A long brass test section (whose length was equivalent to approximately 20 diameters) preceded the cell with minimum disturbance at the junctions. To avoid stressing and breaking the (rather delicate) quartz section, it was mounted in a brass block which had windows cut into its sides as shown in Figure 3.6b. The brass square cross section tube above (i.e. upstream) of the visualization section had a length of 360 mm, i.e. 20 pipe diameters. The top of the upper brass section was attached to a 22 mm diameter circular pipe into which the fluids were pumped. A smooth transition was machined between the circular and square section. The total distance between the top of the circular tube and the

visualization section was 1440 mm, equal to 80 test section equivalent diameters. It is believed that this arrangement gave reasonably well-developed flows at the visualization section.



(a) (b)

Figure 3.6 (a) The test section and (b) Visualization section

3.5.2.2 Experimental Flow Facility (a) for High Flow Velocities

As was indicated in the introduction to Section 3.5.2 above, two flow arrangements were used for the main experiments:

(1) For the high mixture velocity experiments described in Chapter 4 below, a two-pump, once-through system was employed and

(2) For the low mixture velocity experiments described in Chapter 5 below, a recirculation system using a gear pump was used.

The high mixture velocity system is described in this present section whereas the low mixture velocity system is described in Section 3.5.2.3 below.

A schematic diagram of the experimental circuit for the high mixture velocity system is shown in Figure 3.7. The experimental circuit comprised the following components labelled A-R:

- Two 20 litres tanks for aqueous phase (A) and the oil phase (B) respectively;
- Two small pumps manufactured by Grundfos Pump Ltd. for the aqueous phase (C) and for the oil phase (D). The aqueous phase pump had a maximum capacity of 1 litre/s amd the oil phase pump a maximum capacity of 3 litre/s;
- A three- way valve (E) to switch the oil flow between tank B and the test section L;
- Two gate valves F and G used to provide control of the flows;
- Two turbine flowmeters H and I used to measure the aqueous phase and oil flowrates respectively;
- Two non-return valves J and K to prevent reverse flow of the aqueous phase and oil respectively;
- The test section L including the visualization section M;
- A tank N for collection of the effluent flow and subsequent separation. This was linked via a pipe to an emergency separator O;
- Two on/off valves, P and Q;
- A bypass valve R for the oil pump;
- A bypass valve S for the water flow.

The operational procedure for the rig was as follows:

(1) Tanks A and B were filled with the aqueous phase ($CaCl_2$ solution) and the oil phase (Exxol D80) respectively.

(2) With valve F open, with valves Q and G closed and with the three-way valve E positioned to return the oil phase to tank B, the pumps were switched on. The aqueous phase was pumped through the test section and, hence, into the separator vessel N at a rate measured by flowmeter H and controlled by adjustment of

valves F and S. The oil recirculation rate between the pump D and the tank B was adjusted by adjusting bypass valve R.

(3) When the experiment was about to begin, the three-way valve E was switched to pass the oil phase through valve G and flowmeter I and into the test section. The flows of the two phases were quickly adjusted to the required values by adjustments of valves G and S. In the meantime, tanks A and B were emptying and the mixture passing through the test section was collected in tank N.

(4) When the required flow rates were achieved, the laser (which had been previously warmed up and was operating at its full pulse frequency) and the camera were actuated.

(5) At the close of the recording sequence, the pumps were switched off and the two liquids in the separator tank N were allowed to separate and settle. The aqueous phase in tank N was then returned to the aqueous phase tank A by opening valve P and, when all the aqueous phase was transferred, valve P was closed and the oil phase in the separator tank was then drained into the oil tank B by opening valve Q. The rig was then ready to start a further test by repeating the above sequence.

Inter-contamination of the aqueous and oil phases occurs in the aqueous and oil phases occurs in the aqueous and oil tanks but is not a serious problem since the traces of oil phase entering the aqueous phase tank A float to the top and are not pumped during the run. Similarly, traces of the aqueous phase entering the oil phase tank B sink to the bottom and are pumped out quickly at the beginning of the run.

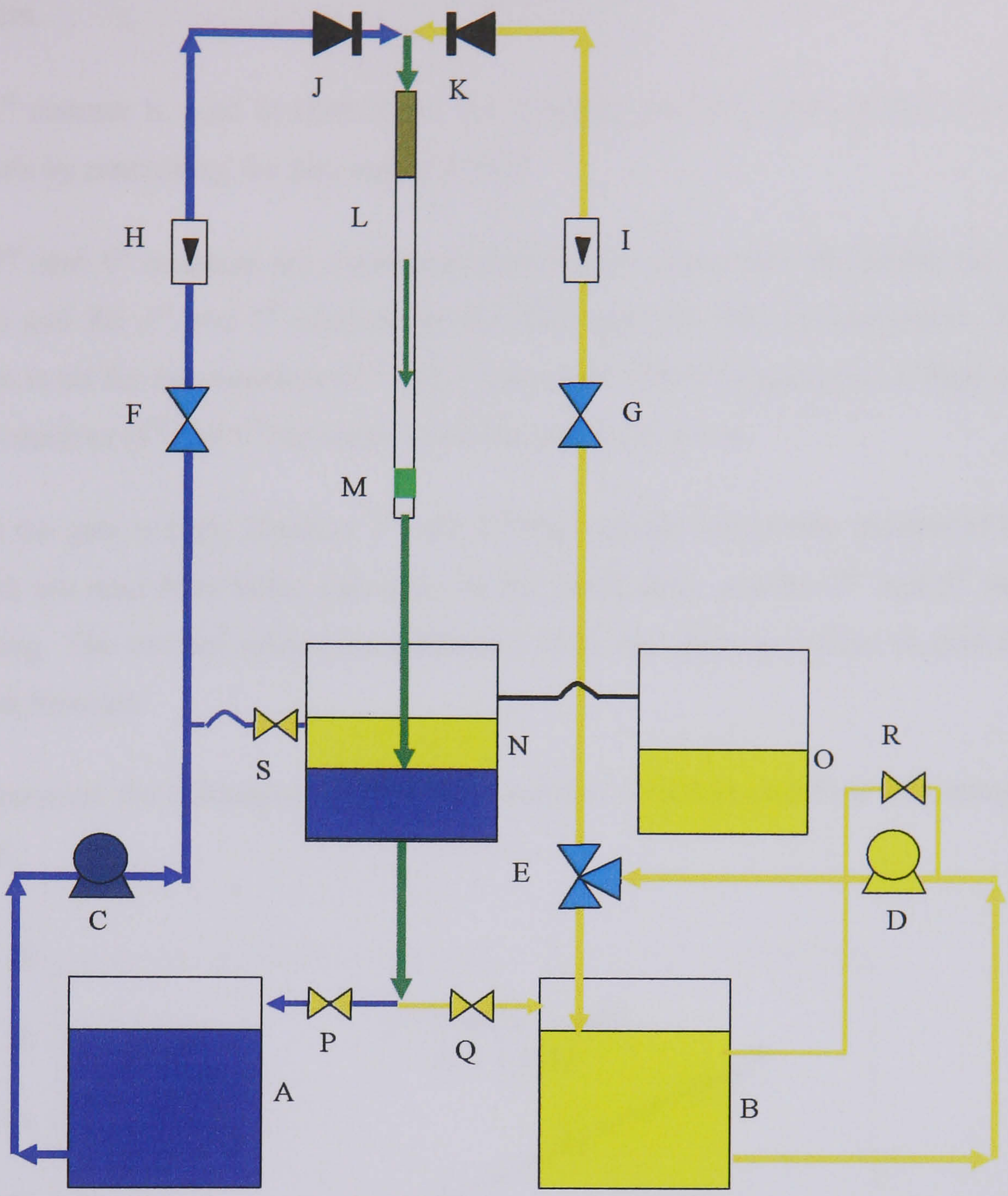


Figure 3.7 A schematic description of the experimental circuit; aqueous phase flows in 'blue' loop through the text section and oil phase in 'yellow' loop. The green route is for oil-water mixture.

Flow measurement was achieved using turbine flow rate sensors (Gems Sensors) which measured the volumetric flow over the range 2-30 litres/min. The pulse output signal is a square wave signal, whose frequency varies linearly with flow rate. The signals are sent to a counting card mounted in a PC. The counting card, plugged into the computer, has 5 count timers (type: CIO/CTR05, manufactured by Computer Boards) containing 5 × 16 bit time counters; two counters for each flowmeter and the other one for reference. The mechanism of the counting system was as follows:

1. Configure the digital board to initialize the time, counters and then configure the 5 counters.

2. The 1st counter is used to control for the counting period (1 sec) of the other 4 counters by controlling the gate inputs (volts).

3. The 2nd and 4th counters are connected to the same source (the flowmeter for oil phase) and the 3rd and 5th counters to the flowmeter for the aqueous phase. The system is set for two counters (2nd and 3rd) to count when the gate level is high and other counters (4th and 5th) to count when the gate level is low.

4. When the gate is high, counters 2nd and 3rd stop and the values (the number of the pulses) are read from these counters. At the same time, counter 4th and 5th start counting. The current values are subtracted from the previous values to give the current flowrate.

Figure 3.8 presents the calibration plot between number of pulses and flow rate using a volume method.

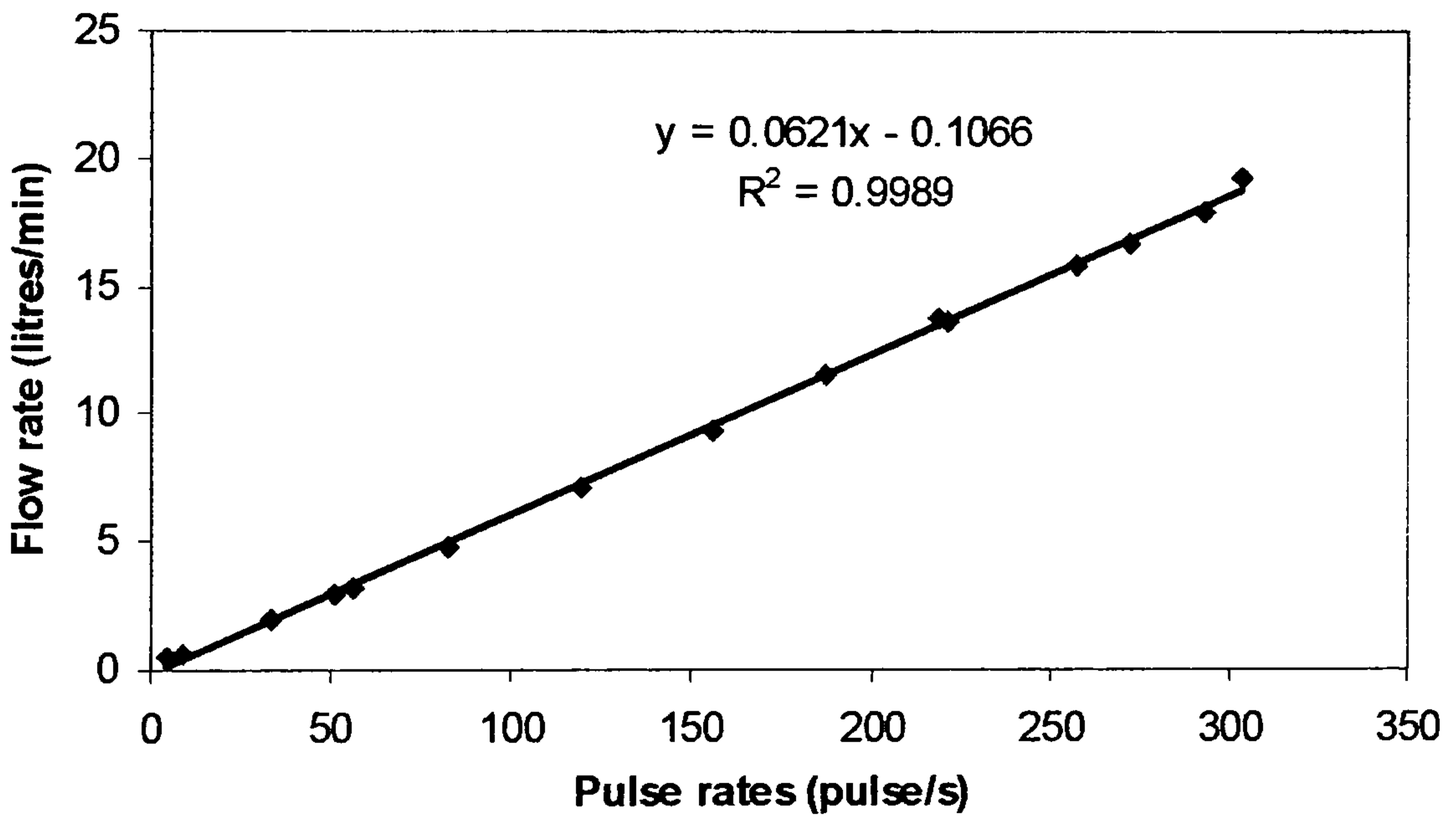


Figure 3.8 Calibration plot of turbine flow sensor.

3.5.2.3 Experimental Flow Facility (b) for Low Flow Velocities

For low liquid flow rates, a closed experimental circuit was used. The visualization section and test section were the same as those used for high flow velocities. The liquid-liquid flow facility used for the low flow tests is shown in Figure 3.9 (a). The facility was

designed to deliver a mixture of aqueous solution and oil of known composition. The test rig comprises the following components labelled 1-8:

- A graduated vessel [1] containing the two liquids and transparent tubing [2] which introduces the two liquids into the rig;
- A gear pump [3] (Model 75211-30, Cole-Parmer Ltd) (Figure 3.9b) is used to circulate and mix the two liquid phases in a closed loop;
- A test section [4] and a visualization section [5], which were described in Section 3.5.2.1 above;
- The rig also includes an air vent valve [6] to remove any air from the system and a drain valve [7] at the bottom;
- Valve [8] is used to introduce the liquids into the rig. The flow rate can be obtained directly from the calibrated gear pump display.

The two-phase mixture flows anti-clockwise in the closed loop, so that the mixture flows downwards through the test section.

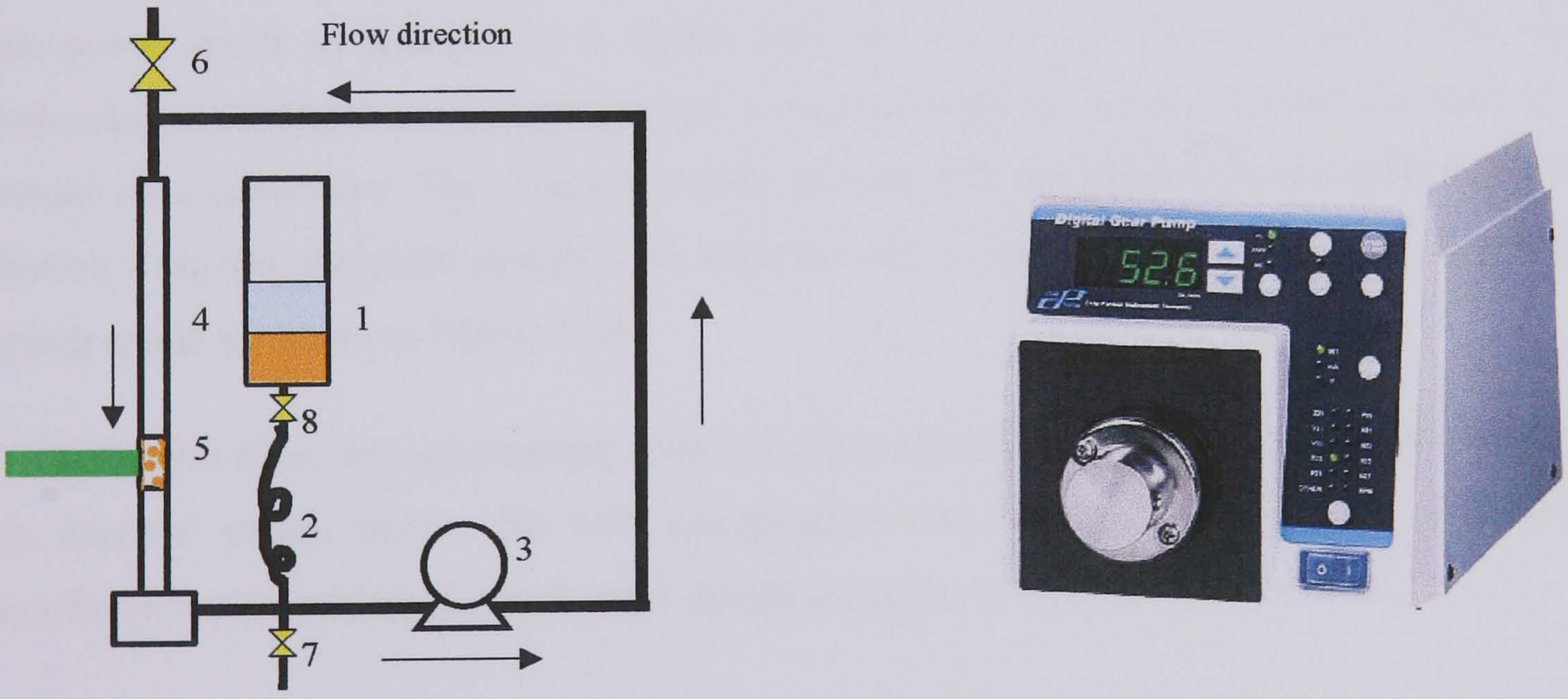


Figure 3.9 (a) Liquid-liquid flow facility; (b) The photo of gear pump (Model 75211-30, Cole-Parmer Ltd)

In the experiments, the two liquids were pumped round the circuit using the gear pump which also acted to mix the fluids, though much more gently (yielding drop sizes more representative of liquid-liquid pipe flows than a centrifugal pump, which was also tried). It is

vital to know the phase fractions of the respective liquids in the circuit and this was achieved by using the graduated vessel (1). Known volumes of the two liquids were fed into vessel (1), the liquid of higher density being introduced into the rig before the lighter liquid. At this stage, the circuit was empty and the total volume of liquid introduced into vessel (1) was sufficient to fill the circuit. The liquids were introduced into the circuit by opening valve (8) whilst venting the air in the circuit via valve (6). All of the heavier phase and some of the lighter phase passed into the circuit and, when the circuit was full, valve (8) was closed. By noting the level of the remaining lighter fluid in vessel (1), it was then possible to estimate the volumes of the two fluids in the circuit and hence the phase volume fractions. Reduction of the heavy phase volume fraction could be achieved by shutting off the pump, allowing the heavy fluid to settle to the bottom of the circuit and removing heavy fluid through the drain valve (7). The removed heavier fluid was replaced by the lighter fluid from vessel (1) entering the circuit via valve (8) which was opened for this purpose. Due to the mixing action of the gear pump, the fluids around the main circuit are expected to have a reasonably uniform flow phase fraction. The composition of the fluid in the connecting pipe (2) was assumed to be the same as that in the main circuit. Since the volume of pipe (2) was small compared to the circuit volume, the assumption is considered reasonable.

The gear pump pumps at a constant volumetric flow rate, and this flow rate is related to the pump speed as indicted by a digital indicator on the pump (see Figure 3.9b). The indicator was calibrated by pumping water at various pump speeds and feeding the water to a vessel for a know time. The volume of water delivered by the pump over this time could be known from the graduated cylinder. As expected, the volume flow rate varied linearly with pump speed as shown in Figure 3.10.

In the low flow rate experiments, a period of around 2-3 minutes was allowed for the flow to become steady before the LIF visualisation was initiated. Experiments were also conducted with transient flows. Further details are given in Chapter 5.

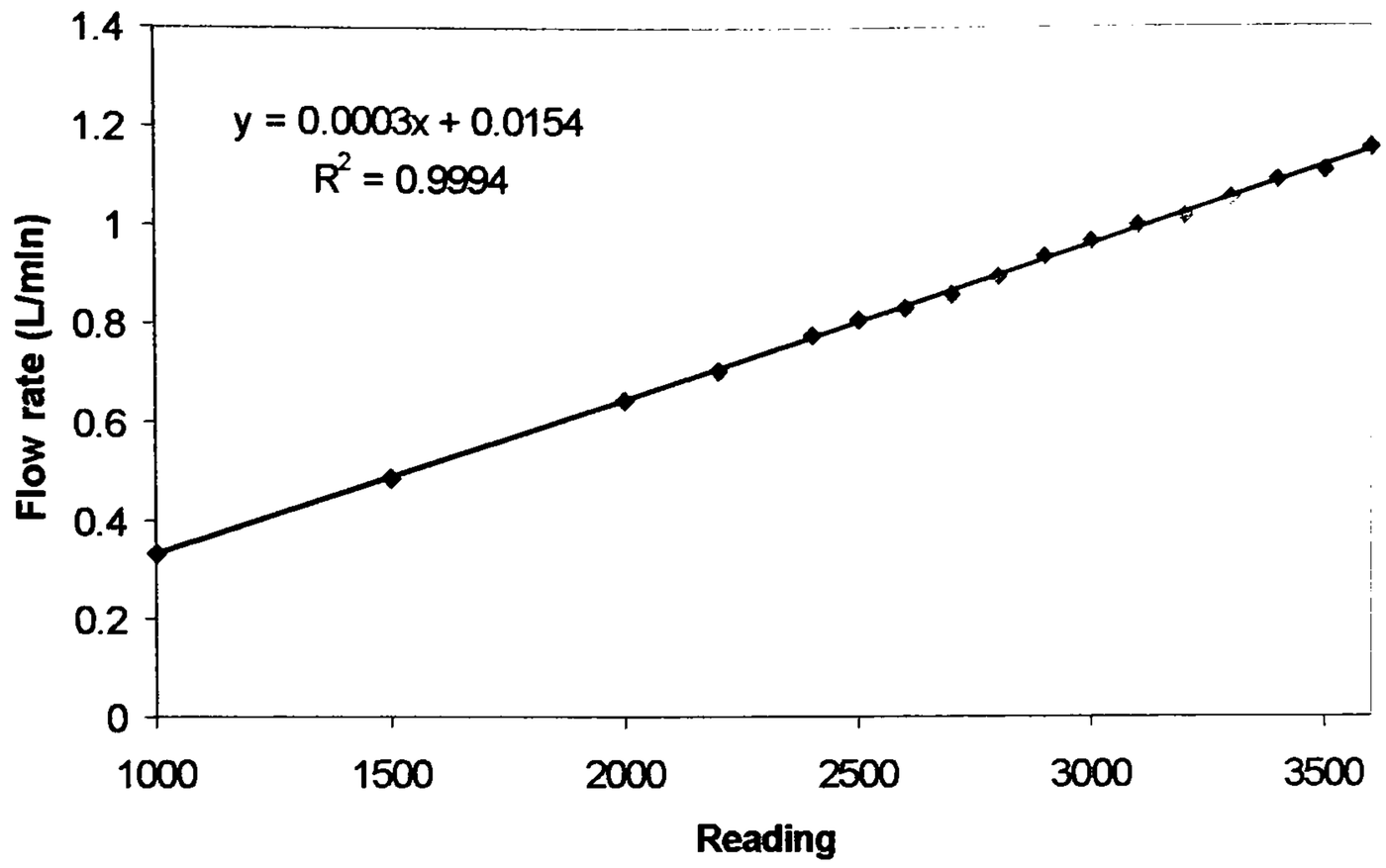


Figure 3.10 Flow rate calibration plot of the gear pump.

Chapter 4

Optical Studies of Liquid-liquid Pipe Flows: I. High Velocities

This Chapter describes the experimental results obtained using the once-through system described in Section 3.5.2.2. In these experiments, the aim was to visualize the flow patterns and flow structures in concentrated liquid-liquid pipeline flows at relatively high velocities. Section 4.1 describes the experimental procedure. Section 4.2 presents the flow pattern map obtained in the experiments and the flow structures observed in the various flow patterns. In Section 4.3, the phase inversion process observed in transient flows is discussed. In pipe flow, an unstable range is found during phase inversion. This unstable range is compared with the ambivalent range obtained in agitated systems in Section 4.4. Section 4.5 describes the complex structures in concentrated dispersed flow observed by this study, e.g. secondary dispersions and multi-dispersions. In Section 4.6, the experimental volume fractions in oil-in-aqueous phase and aqueous phase-in-oil dispersions are compared with the predicted values obtained from dispersed flow and annular flow models. Finally, a brief summary is given in Section 4.7.

4.1 Experimental Procedure

The two-pump and once-through flow circuit described in Section 3.5.2.2 was used to perform the experiments. The experimental procedure is also described in Section 3.5.2.2. Both steady flows and transient flows were studied.

For the steady flows, the oil gate valve and the aqueous phase by-pass valve remained in a fixed position during the recording of the video sequence so that the flowrates stayed constant during the sequence. For the transient flow, during the video sequence period, the flowrates were adjusted gradually. As was described in Section 3.5.2.2, the time-span of the experiment is governed by the volume of supply tanks A and B (see Figure 3.7) and is relatively short (around 15 seconds depending on the flow rates). However, this time-span is sufficient to give (for the steady state experiments) reasonably constant values of flowrates over the recording period. The flowrate of each phase before mixing was recorded in a PC. The photographs captured by a high-speed camera were stored by another PC, where the corresponding flowrates can be tracked by the flowrate PC.

4.2 Flow Patterns

4.2.1 Flow Pattern Map

A variety of flow patterns were formed in the co-current flow of oil and aqueous ($CaCl_2$ solution) phases in the 18 mm×18 mm vertical square duct. The flow pattern could be identified from the LIF outputs. The flow pattern map is shown in Figure 4.1 in terms of mixture velocity against oil input volume fraction.

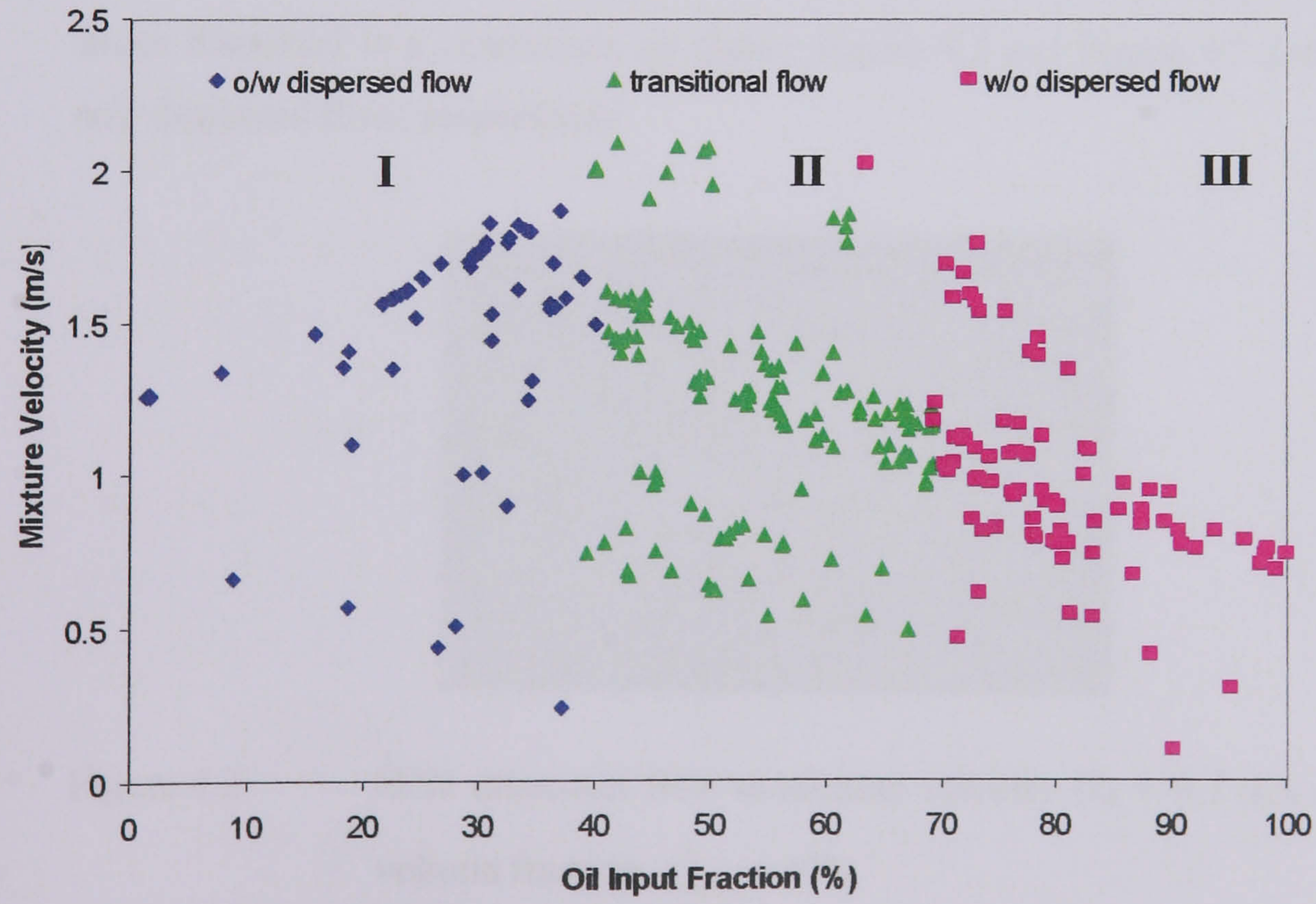


Figure 4.1 Flow pattern map based on the oil input fraction for the liquid-liquid flow in a vertical pipe.

The experimental results shown in Figure 4.1 show that the flows could be divided into stable dispersed flows (oil-in-aqueous phase dispersed flow, region I, and aqueous phase-in-oil dispersed flow, region III) and unstable transitional flows (region II). Under conditions where the input oil fraction (ε^{o}_{input}) is less than 35% a stable oil-dispersed, aqueous phase continuous (o/w) dispersed flow is found. On the other hand, when the input oil fraction is higher than 70% (or aqueous phase fraction is less than 30%) stable aqueous phase dispersed, oil-continuous (w/o) dispersions occur. Flows in region II (oil fraction is 35% ~ 70%) show instabilities of flow pattern in that o/w and w/o dispersions were found to co-exist in the pipe. The two types of dispersions appear alternatively in the visualization test section, which leads to the very complicated flow structure observed in the present studies. Here we define this flow regime as "unstable transitional flow".

4.2.2 Flow Structures

Figures 4.2-4.5 show more details of the flow structures of each flow pattern observed by the LIF technique:

(1) ***Dispersed flows.*** Dispersed flows are characterized as having one phase dispersed as drops in the other phase; thus, o/w dispersed flow corresponds to oil drops dispersed in a continuous aqueous phase and w/o dispersed flow corresponds to aqueous phase drops dispersed in a continuous oil phase. Figure 4.2 and Figure 4.3 present o/w and w/o dispersed flow, respectively.

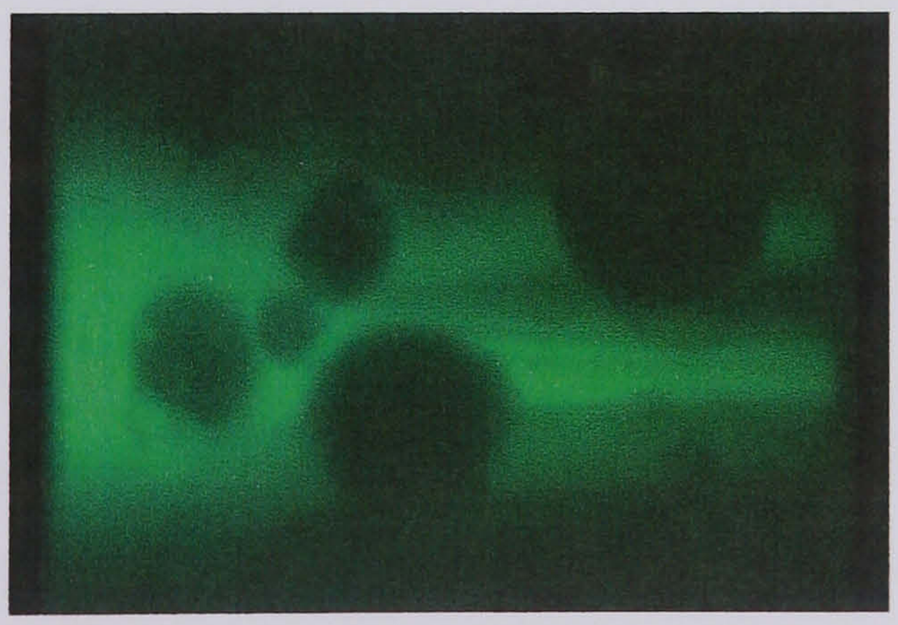


Figure 4.2 O/W dispersed flow at mixture velocity U_m = 0.7 m/s and oil input volume fraction ε^{o}_{input} = 40%.[1]

[1] In this and subsequent Figures in the thesis, the black regions designate the organic phase and the yellowish green regions designate the aqueous phase.

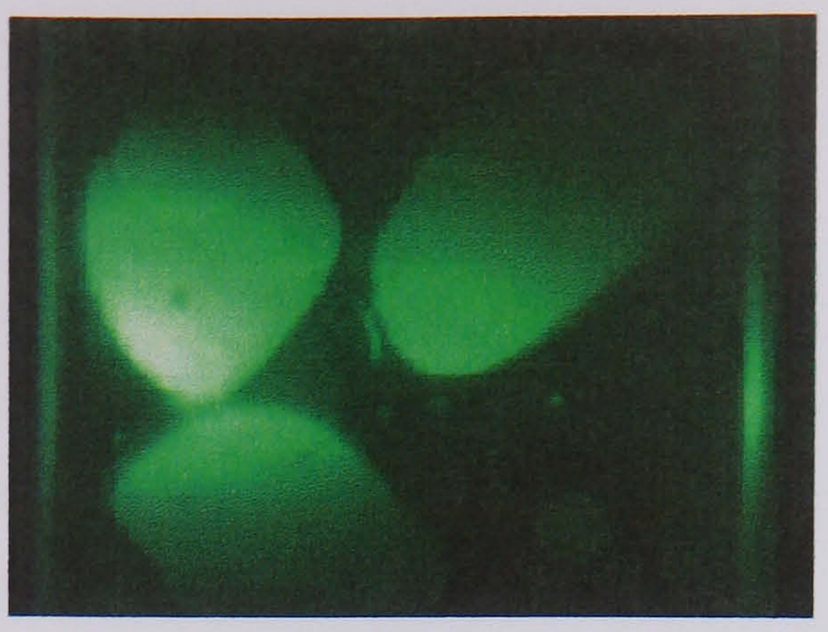


Figure 4.3 W/O dispersed flow at mixture velocity U_m = 0.824 m/s and oil input volume fraction ε^o_{input} = 77.4%.

One phenomenon found in the experiments was that the aqueous phase tended to coat the pipe wall in most experimental cases, even in experiments with very high oil input volume fraction (> 90%). Initially, it was thought that this may have been due to preferential wetting of the test section by the aqueous phase. However, measurements of the contact angles between the fluids and the test section materials were made with the following results: oil/quartz (17°), aqueous phase/quartz (64°), oil/brass (10°) and aqueous phase/brass (84°). These results suggested that the wall should be preferentially wetted by the oil phase. Thus, some other phenomenon must be operating to produce this effect. Joseph *et al.* (1984) has suggested that, in flows of water and highly viscous oils, the less viscous phase (water) will tend to flow adjacent to the wall. In the present experiments, the aqueous phase has a higher viscosity than the oil phase (0.01184 Ns/m^2 for the aqueous phase compared with 0.00162 Ns/m^2 for the oil phase) and the tendency of the wall to be aqueous phase wetted is not obviously consistent with the Joseph hypothesis.

However, Joseph *et al.* (1996) suggested that the case of gas-liquid annular flow (where there is a tendency for the liquid phase to flow at the wall) is actually analogous to his water/viscous oil case. His reasoning is that, in the gas-liquid case, the gas has a higher *effective* viscosity because of its turbulence. Could this argument apply in the present situation?

For the conditions shown in Figure 4.3 the (continuous) oil phase has a superficial Reynolds number of 5690, well into the turbulent region. Thus the effective viscosity of this turbulent core would be higher than that of the aqueous phase and this would,

on Joseph's argument, favour the tendency of the aqueous phase to be present at the wall, as observed.

On the other hand, for the conditions shown in Figure 4.2, the (continuous) aqueous phase has a superficial Reynolds number of 919, well below the onset of turbulence. Thus, in this case, on the Joseph hypothesis, the oil phase with Reynolds number of 2498 would be expected to be present at the wall, which is contrary to observation. Furthermore, the same tendency (i.e. for the aqueous phase to preferentially wet the wall) occurs at even lower velocities (see Chapter 5) which means that the argument relating to turbulent viscosity is unlikely to apply.

The consistent theme throughout these observations (water/viscous oil, viscous aqueous phase/ lower viscosity oil, gas/liquid) is that the phase with *higher density* appears to be the one in contact with the wall. Perhaps the argument has to be a dynamic one.

Consider the case of gas-liquid annular flow. If the liquid phase is initially all in the form of droplets, then radial motions of the drops will cause some of them to penetrate to the wall as results of their inertia and thus form a film there; the original continuous phase (gas) is then no longer in contact with the wall. The role of inertia in the deposition of particles and droplets is discussed, for instance, by Hutchinson *et al.* (1971). For gas-liquid bubbly flow, on the other hand, the bubbles do not have sufficient inertia (because of their low density) to penetrate to the wall, thus leaving the surface wetted by the liquid continuous phase.

Maintenance of a continuous wetting film of the heavier phase at the wall is limited by two types of phenomena:

(1) *Interfacial instability and entrainment.* The film/core interface is subject to instability resulting in wave growth and entrainment of drops from the film into the core. This is certainly the case in gas-liquid flow and results, for high liquid mass fluxes, in most of the liquid being entrained. However, for this case, there is a minimum film flow rate below which entrainment of drops does not occur (Hewitt and Hall Taylor, 1970). Certainly, the present liquid-liquid flow experiments show that entrainment is occurring from the aqueous layer at the wall. Furthermore, as the mixture velocity is increased, the extent of entrainment increases and the wall film becomes thinner and thinner. The existence of a minimum film flow rate, analogous to that for

gas-liquid flow, cannot be established from the present work. Flows classified as oil-continuous (w/o) in the present study (such as that shown in Figure 4.3) are essentially annular dispersed flow with most of the heavier (aqueous) phase entrained.

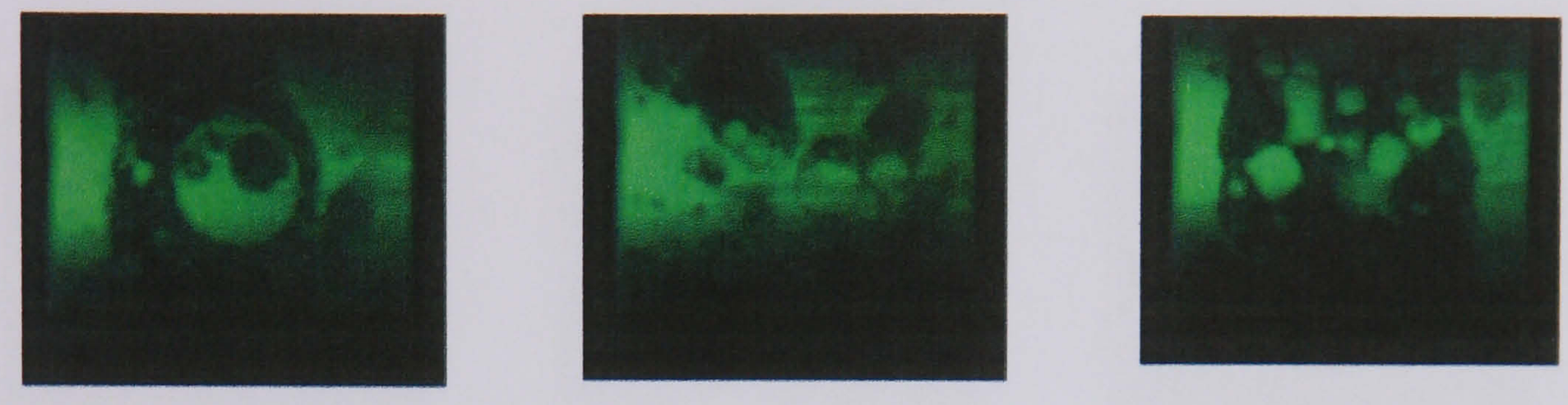
(2) *Stability against de-wetting.* If un-wetted zones ("dry patches") exist on the wall, in the case of an annular-type flow, and the wall is preferentially wetted by the core phase (as in the present w/o flows), then a *minimum wetting rate* of the heavier phase may be required to re-cover the un-wetted zones. This problem was addressed for gas-liquid annular flow by Hewitt and Lacey (1965) who studied the re-covering of an artificially created dry patch on the (acrylic resin) tube wall. They showed that the minimum wetting rate required to re-cover the dry patch decreased with increasing gas flow rate. However, in the absence of a dry zone, the liquid flow rate could be reduced to very small values (well below the minimum wetting rate) before de-wetting occurred. The wetting behaviour of the system will depend, therefore, on the previous history of the flow. These effects are almost certainly relevant to the present (liquid-liquid) case and seem worthy of further investigation.

On the basis of the above discussion, it seems probable that the presence of the aqueous phase at the wall is due to dynamic (inertial) effects related to its higher density. Further investigation (with a larger range of fluids) is required to confirm this and also to investigate minimum wetting rate behaviour in liquid-liquid systems.

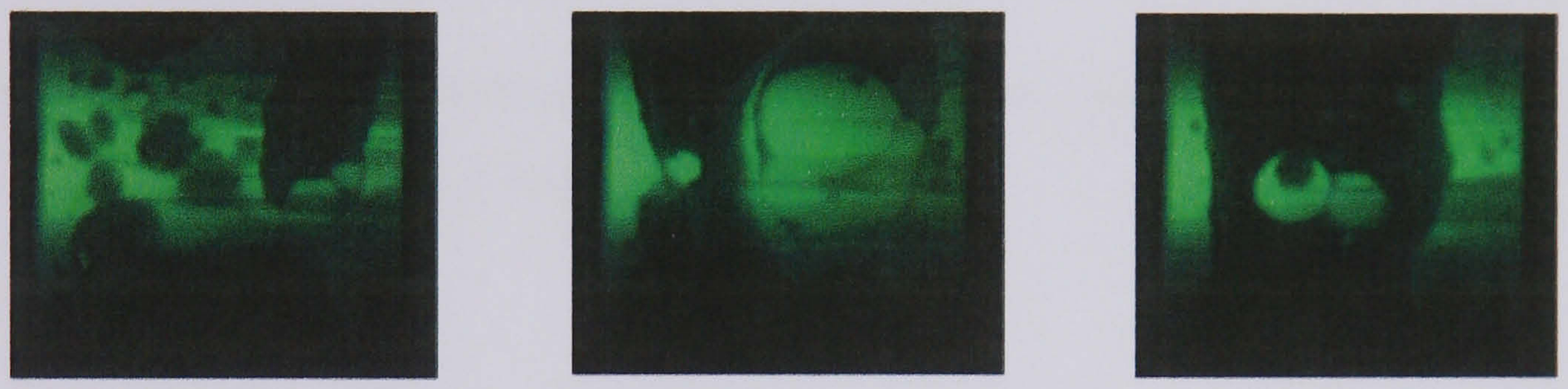
(2) ***Transitional flows.*** The transitional flows observed here represent an unstable mixture of flow regimes that comprise annular flow, slug flow, o/w dispersed flow and w/o dispersed flow. Transitional flow can also be divided into two subgroups, aqueous phase-continuous transitional flow and oil-continuous transitional flow, depending on the input holdup and mixture velocities. However, according to this study there are no clear boundaries to separate these types transitional flow patterns.

Figure 4.4 shows aqueous phase-continuous transitional flow with 48% oil input volume fraction (ε^{o}_{input}) at 1.46 m/s mixture velocity. In this flow pattern, the oil-aqueous phase two-phase flow fluctuates between oil-in-aqueous phase dispersed flow (Figure 4.4 b, d and i) and 'annular' flow (Figure 4.4 a, c and e-h). The flow structure in this flow pattern was very complex; a large number of large oil drops appeared (Figure 4.4 b and d) and the length of some oil drops or 'slugs' could be several or

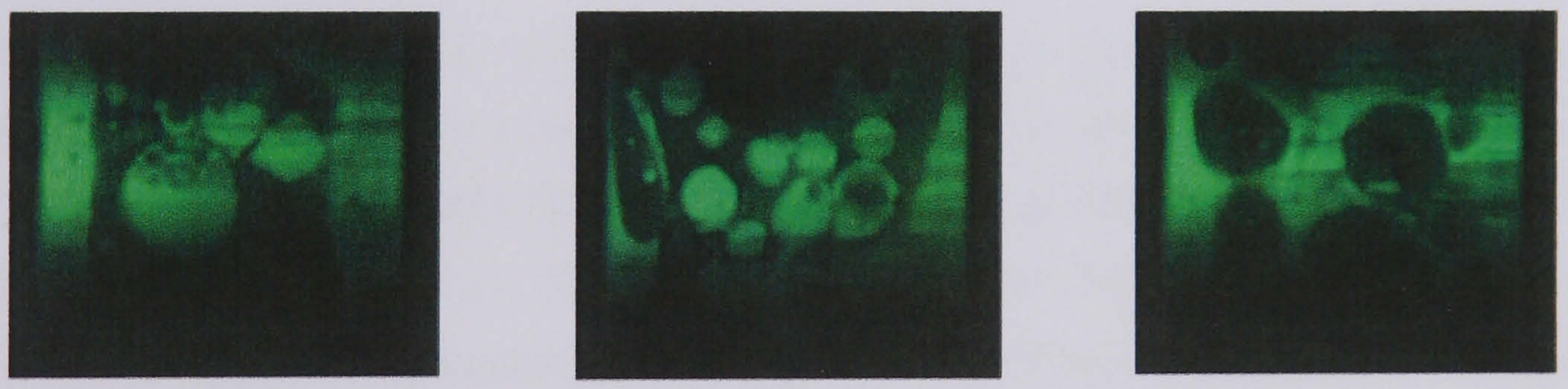
even tens of times the duct equivalent diameter. In this case, the oil acted more like oil 'core' rather than oil drops so that the flow seemed to be an 'annular' flow rather than a dispersed flow. Complex flow structures, such as aqueous drops (with oil droplets inside) in the oil core (Figure 4.4 a and e-h) and oil drops (even with aqueous droplets inside) in the aqueous 'film' (Figure 4.4 e and h), appeared frequently.



(a) 0 s (b) 0.4974 s (c) 0.996 s



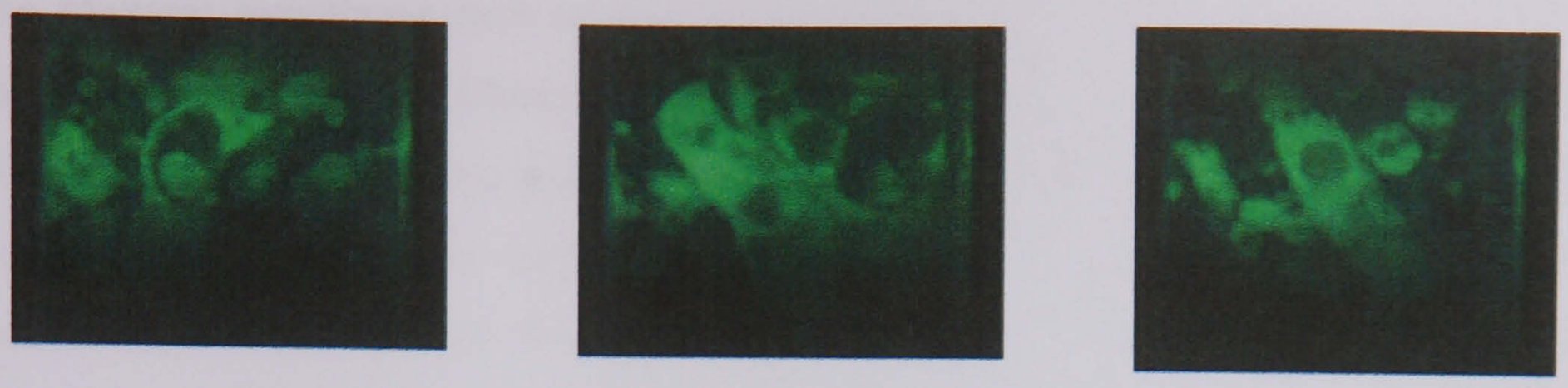
(d) 2.6412 s (e) 2.7566 s (f) 2.8614 s



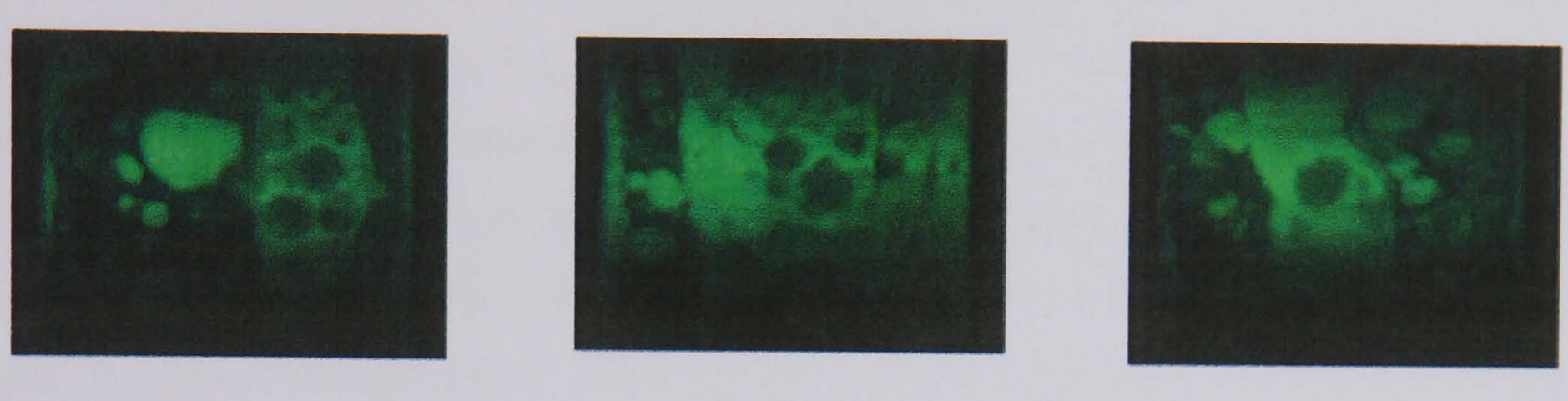
(g) 3.0566 s (h) 3.6386 s (i) 3.9902 s

Figure 4.4 Time series photographs about aqueous phase-continuous transitional flow with mixture velocity U_m = 1.46 m/s and ε^{o}_{input} = 48%.

For the oil-continuous transitional flows, aqueous phase drops also became very large, elongated and deformed into varied shapes (Figure 4.5). A large number of oil droplets were included into the aqueous phase drops. Although no aqueous phase 'core', analogous to the oil 'core' was visualized in aqueous phase-continuous transitional flow, highly distorted and long aqueous drops such as those shown in Figure 4.5 were found in the test section.



(a) 0 s (b) 0.0469 s (c) 0.0585 s



(d) 0.1227 s (f) 0.2474 s (i) 0.5606 s

Figure 4.5 Time series photographs about oil-continuous transitional flow with mixture velocity $U_m = 2.1$ m/s and $\varepsilon^o_{input} = 49\%$.

4.3 Phase Inversion Process

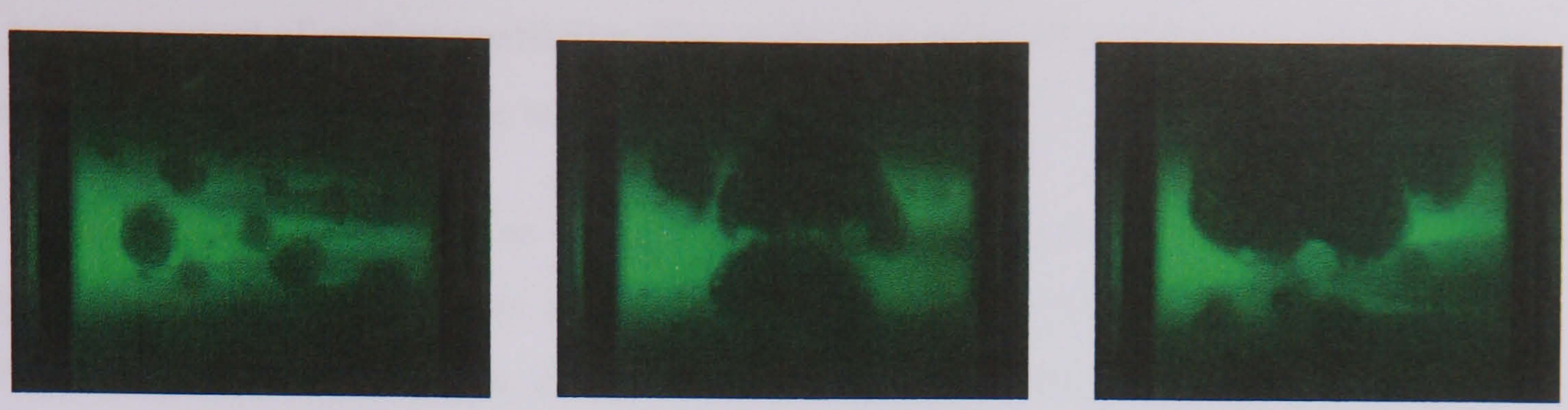
Most experimental studies related to phase inversion in pipe flow have focused on measuring pressure gradient as a function of input water or oil fraction (Arirachakaran *et al.* 1989; Luo *et al.*, 1997; Nädler & Mewes, 1997; Angeli & Hewitt, 1998, 2000 a & b; Soleimani, 1999; Ioannou *et al.*, 2004, Ioannou *et al.*, 2005, Hu, 2004). At high mixture velocities, a sharp peak in pressure gradient appeared, which was considered to correspond to phase inversion (see Figures 2.12- 2.13 and Figure 2.19). The mixture effective viscosity required to give the observed peak in pressure gradient may be calculated (Arirachakaran *et al.*, 1989) (Figure 2.20) and, because pressure gradient in relatively insensitive to viscosity in turbulent flows, an even sharper peak in viscosity is predicted at the presumed phase inversion point. These pressure gradient results are a convincing manifestation of phase inversion but there is a dearth of direct observation of the complex processes occurring.

In the absence of direct observations, a useful approach is to derive statistical models describing the development of droplet breakup, coalescence and drop/drop inclusion (Population Balance Equations, PBE). Such an approach has been pursued, for instance, by Hu (2004) who used the PBE approach to calculate the development of drop size spectra along a pipe starting with a fixed drop size. Phase inversion could then be identified with a

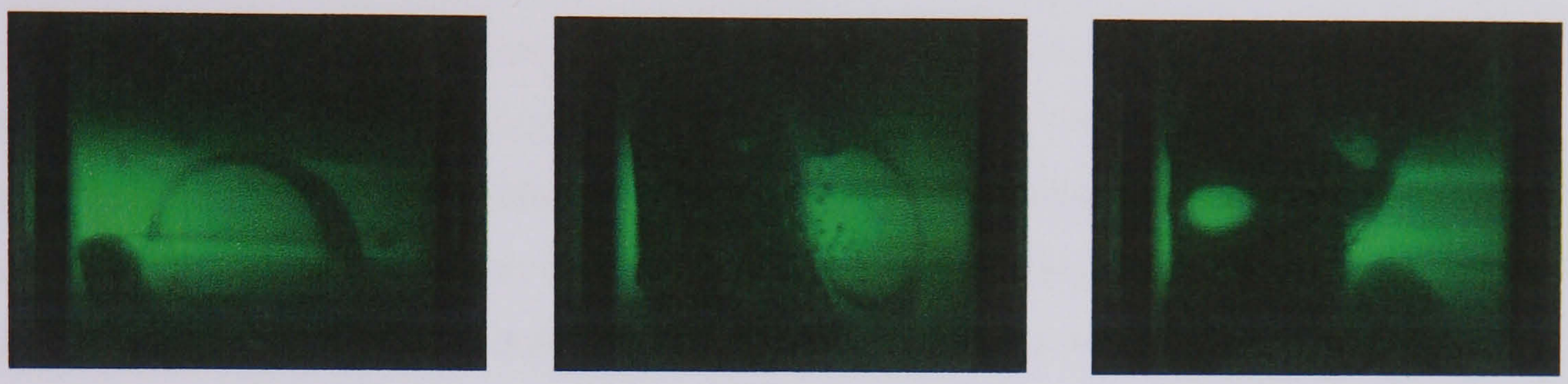
specific physical hypothesis such as the point at which the system free energies of two possible dispersions match. Starting with a w/o dispersion gives a different transition location on this hypothesis than does starting with an o/w dispersion. It was suggested that the region between the two calculated transition locations for inversion bounds the ambivalent region in terms of flow development distance. The position at which phase inversion was predicted to occur shifted towards the entrance with increasing mixture velocity. The present experiments also reveal a range of phase fractions over which the flow pattern is neither clearly w/o or o/w, namely the transitional flow region shown in Figure 4.1. In this region, the flow structure was unstable, varying dynamically between o/w dispersed flow, annular flow and w/o dispersed flow. Thus, phase inversion is not a process occurring suddenly at a fixed phase fraction but, rather, a more diffuse process occurring over a range of phase fractions. Though this is qualitatively in accord with the PBE results, the actual processes occurring are much more complex than those represented in the simplistic models.

In order to observe the full phase inversion process in the present experimental circuit, transient experiments, in which the flow condition passed through the phase inversion region, were carried out. Transient flows were obtained by decreasing of the aqueous phase input fraction (or increasing of the oil fraction). Unfortunately, due to the limitation of the present experimental circuit, the mixture velocity could not be kept constant during the experimental set, thus, as the aqueous phase input fraction decreased, the mixture velocity decreased too.

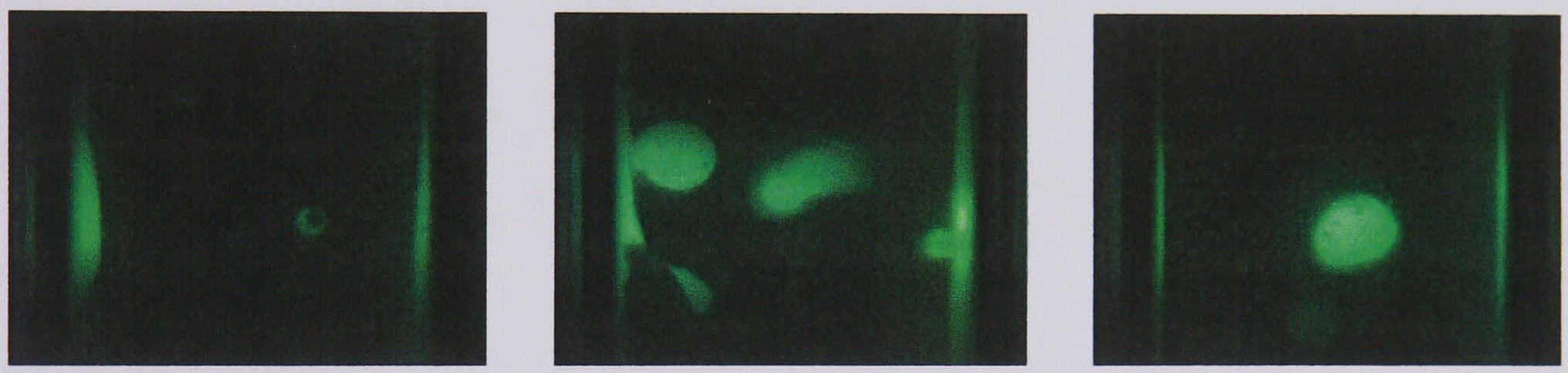
Figure 4.6 presents the whole phase inversion process in a transient flow. At the initial oil input volume fraction (30%), o/w dispersed flow existed. As oil fraction increases, more large oil drops appeared, more aqueous droplets were included into oil drops (Figure 4.6 a-c) and some oil drops grew to the same order of size as the duct (Figure 4.6 e). On further increasing the oil input volume fraction, the large oil drops evolved to form an oil core (Figure 4.6 f) in which aqueous drops appeared. The w/o configuration (or, more strictly, annular dispersed flow with a thin aqueous film remaining at the channel wall) was finally formed as the oil input volume fraction was increased to 82%. As the oil input volume fraction increased, the transient flow crossed the unstable region II (Figure 4.6 d-g) in which o/w, 'annular' and w/o flow appeared alternately.



(a) 0 s (b) 0.036 s (c) 0.098 s



(d) 0.234 s (e) 0.58 s (f) 1.996 s



(g) 2.0214 s (h) 3.1376 s (i) 3.548 s

Figure 4.6 Time series of photographs shown phase inversion process of transient flow at mixture velocity decreased from 1.28 m/s to 0.53 m/s and ε^{o}_{input} increased from 30% to 82%.

4.4 Ambivalent Range

In contrast to the case of agitated vessels, there has been only limited study of the *ambivalent range* in pipe flows. In their experiments, Ioannou *et al.* (2005) found that the phase fraction of the aqueous phase at phase inversion was different depending on which of the two phases was initially continuous, thus identifying a range of phase fraction (essentially an ambivalent range) over which either phase could be continuous, depending on the initial conditions. Brauner & Ullmann (2002) predicted an ambivalent range in pipe flow

by taking account of surface wettibility. This study also predicted a different phase inversion point depending on which phase was initially continuous.

In the present experiments, an unstable transitional flow region is observed as shown in Figure 4.1. The flow pattern data is replotted with oil input fraction as the abscissa in Figure 4.7. When plotted in this form, it will be seen that the unstable range has a qualitatively similar appearance to the ambivalent range in agitated vessels as exemplified in Figure 4.8. However, the ambivalent range in agitated systems is defined by Selker and Sleicher, (1965) as 'a range of volume fractions throughout which either component would remain STABLY dispersed' whereas the unstable range shown in Figure 4.7 is a range in which the identity of the continuous phase (and thus also of the dispersed phase) changes continually in time from one phase to the other. Therefore, in spite of the similar appearance, the unstable range found in the pipe flow experiments is different to the ambivalent range in the agitated systems.

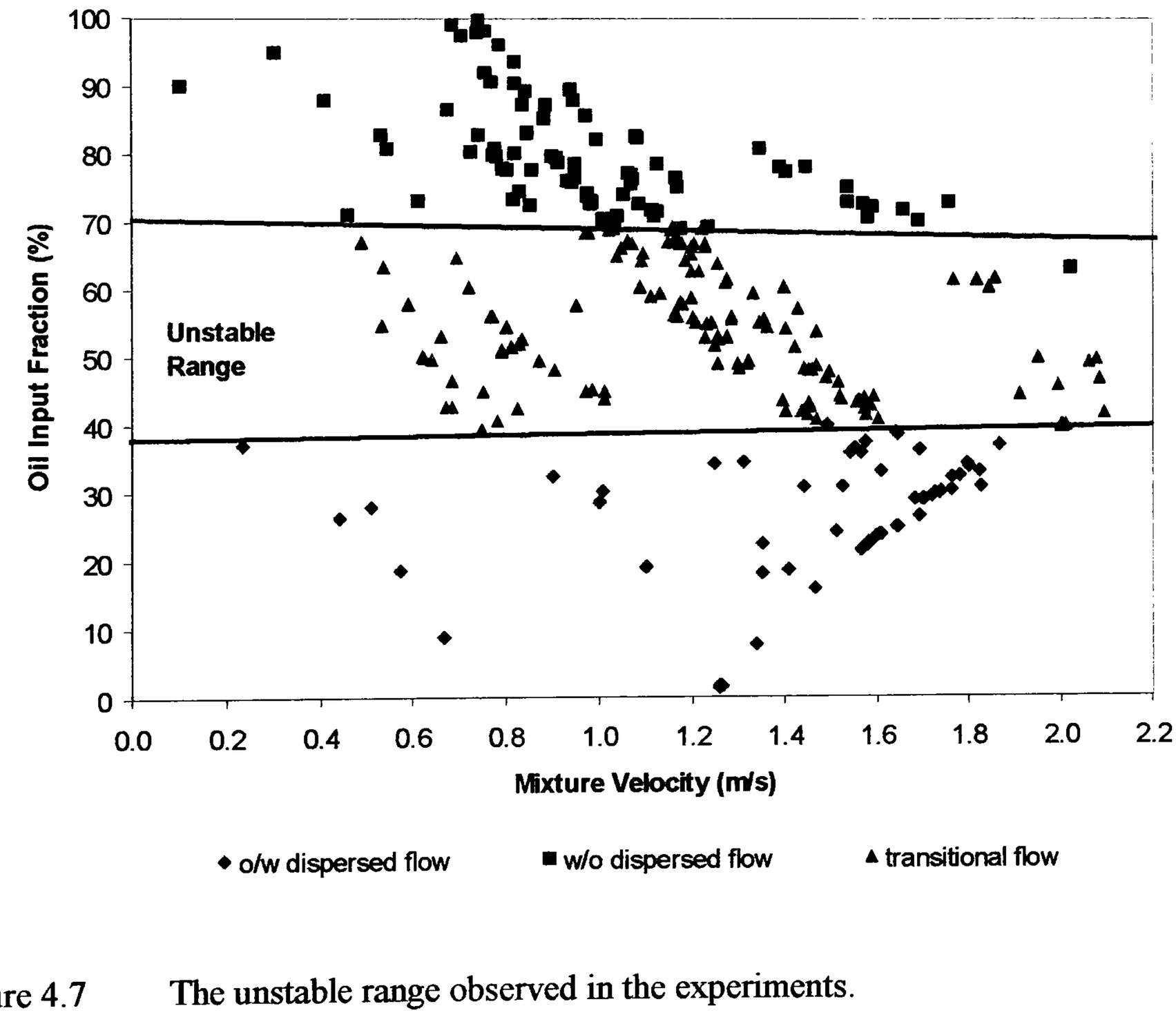


Figure 4.7 The unstable range observed in the experiments.

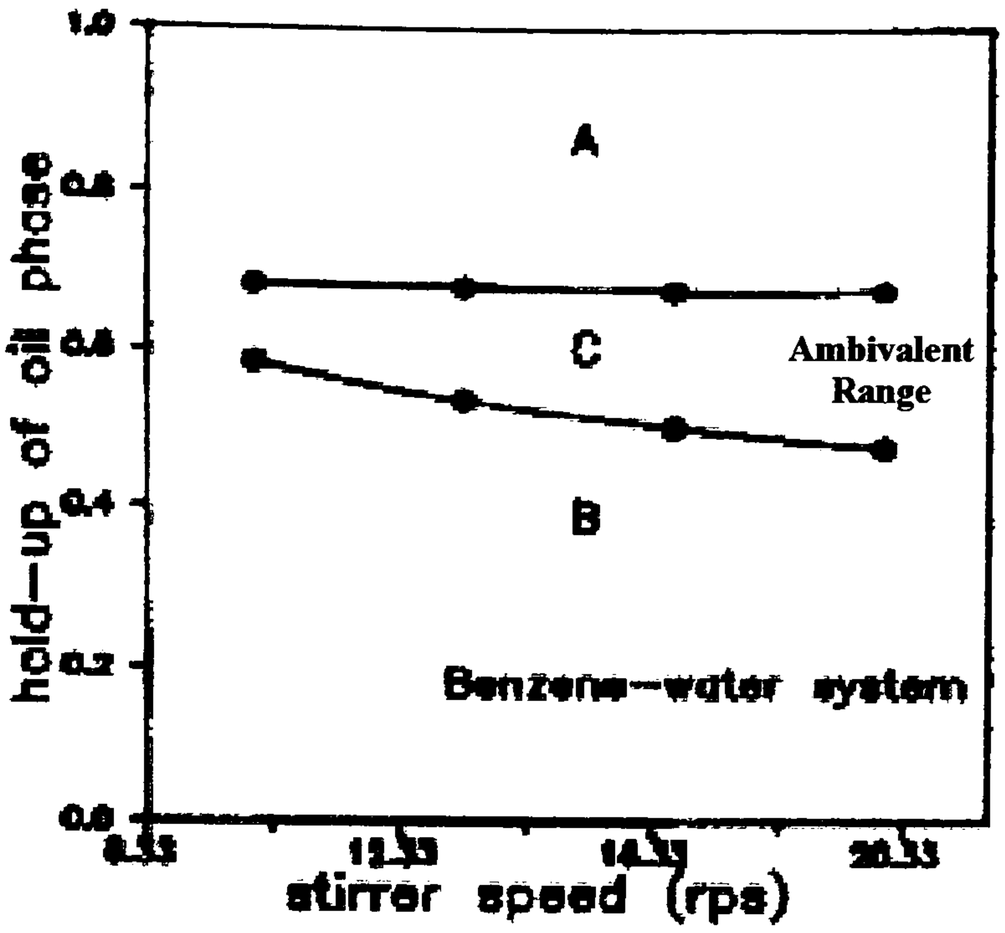


Figure 4.8 The ambivalent range obtained in Benzene-water stirred system by Kumar *et al.* (1991).

A similar unstable region (or phase inversion region) around phase inversion point was also found in the flow pattern maps created by Oglesby (1979), Arirachakaran *et al.* (1989), Nädler & Mewes (1997) and Angeli & Hewitt (2000 a). Arirachakaran *et al.* (1989) called it an intermittent region (details are depicted in Section 2.1.1). It is interesting to note that this intermittent region occurs over a narrow range of water fraction which is independent of the system total flow rate. Oglesby (1979) identified the occurrence of this intermittent flow as manifesting phase inversion.

In the present experiments, the unstable region was somewhat wider than that observed in the previous studies. This may reflect the improved visualization method used in the present study.

4.5 Secondary and Multiple Dispersion

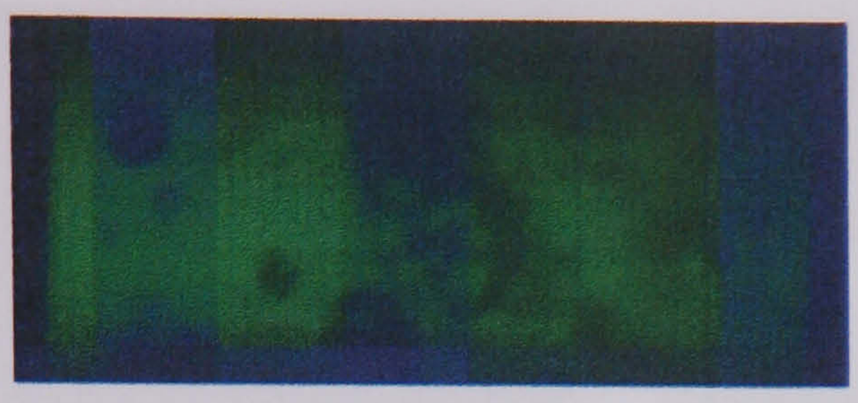
Secondary dispersion has been observed widely in agitated vessels (Rodger *et al.*, 1956; Quinn & Sigloh, 1963; Luhning & Sawistowski, 1971; Pacek *et al.*, 1994 a & b; Pacek & Nienow, 1995; Sajjadi *et al.*, 2002; Liu *et al*, 2005). However, an interesting characteristic of secondary dispersion has been noted, namely that oil droplets in w/o dispersions are much more likely to occur than water droplets in o/w dispersions. For two-phase dispersed pipe flows, very few researchers have reported secondary dispersions. Pal (1993) investigated the pipeline flow of unstable (non-surfactant) and surfactant-stabilized emulsions. It was

observed that phase inversion from w/o to o/w dispersion (with surfactant) involved an intermediate range where an o/w/o secondary dispersion formed (see Figure 2.16); samples of the surfactant-stabilized emulsion were taken from the pipe and diluted with the same continuous medium and examined in a microscope. It was not possible to use a similar technique for the unstable emulsions.

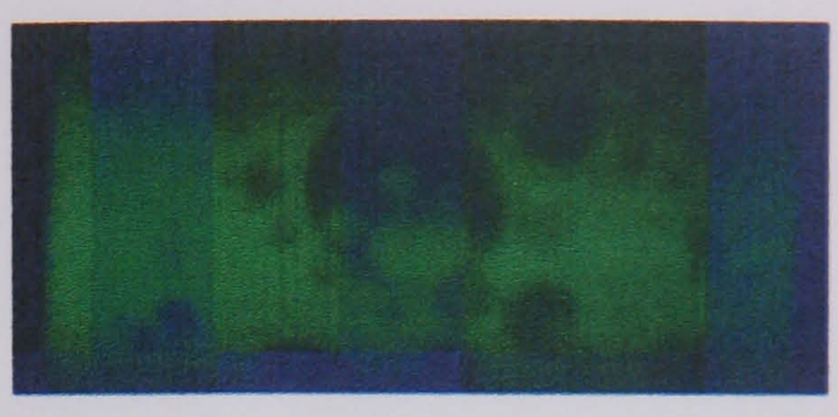
In the present experiments, aqueous phase-in-oil-in-aqueous phase (w/o/w) and oil-in-aqueous phase-in-oil (o/w/o) secondary dispersions were observed at most volume fractions and velocities (Figure 4.9 and 4.10), especially in the unstable range. The phenomenon of the preponderance of o/w/o over w/o/w dispersions in agitated systems (also found in the present work on agitated vessels- see in Chapter 6) was not found in the experiments of pipeline flow. It was observed that, when the flow is in the unstable region, both w/o/w and o/w/o secondary dispersions could appear in the same set of experiments.

In the Pal (1993) experiments, no secondary dispersions were found outside the intermediate range. However, the emulsions for Pal's pipeline flow investigations were prepared in a large stirred tank and then circulated to the pipeline test sections by a centrifugal pump. In contrast, the dispersions in the present experiments were formed by introducing two liquids separately into a T-junction and allowing them to mix naturally by shear forces.

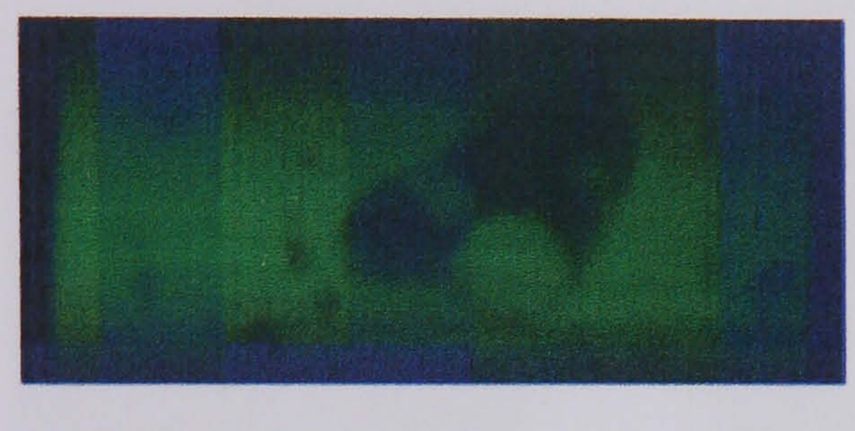
One of the mechanisms observed for the formation of secondary dispersions was by rupture of the aqueous phase annular film as shown in the Figure 4.11. Figure 4.12 shows a case in which several aqueous drops were squeezed by two large coalescing aqueous phase waves; the w/o/w dispersions shown in Figure 4.13 are thought to form in the same way.



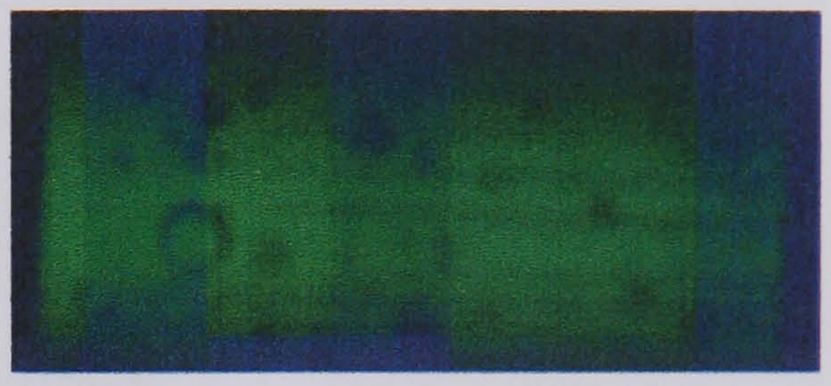
(a)



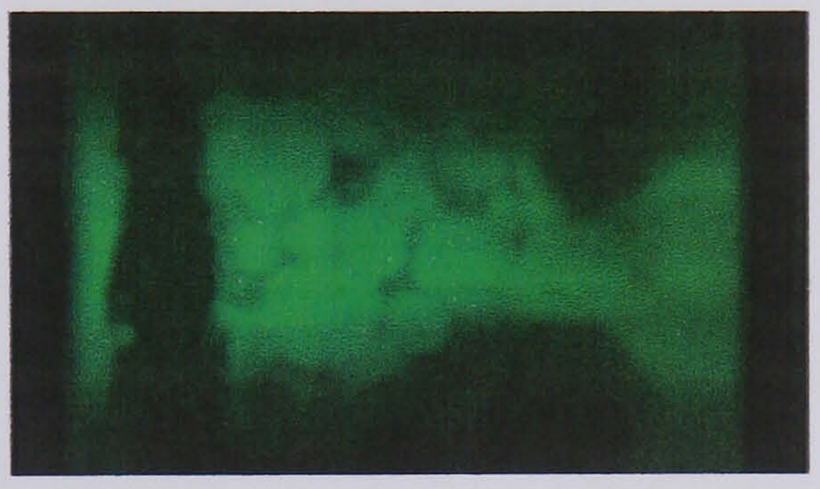
(b)



(c)

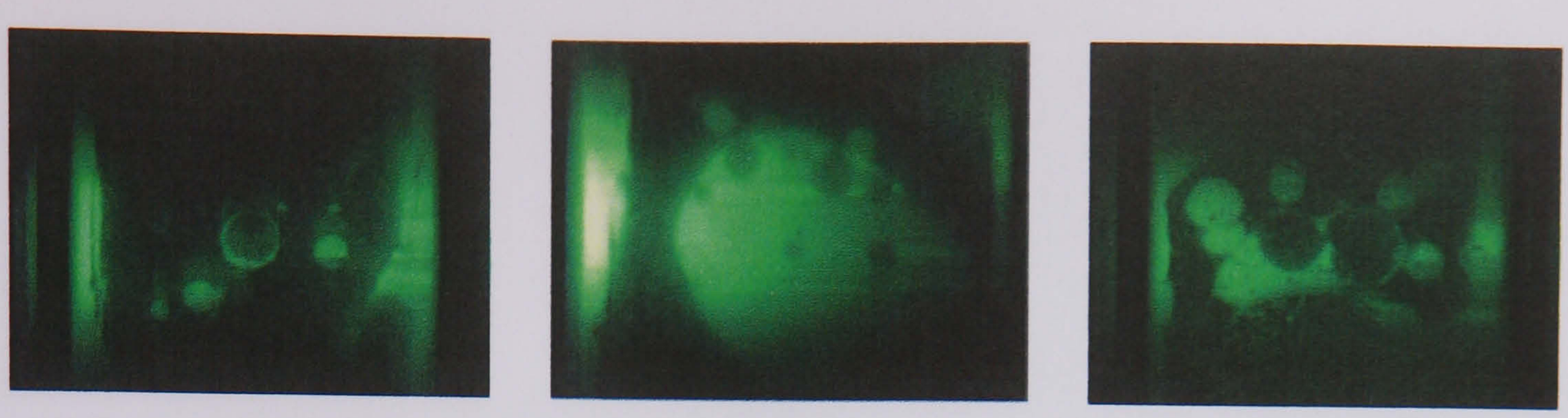


(d)



(e)

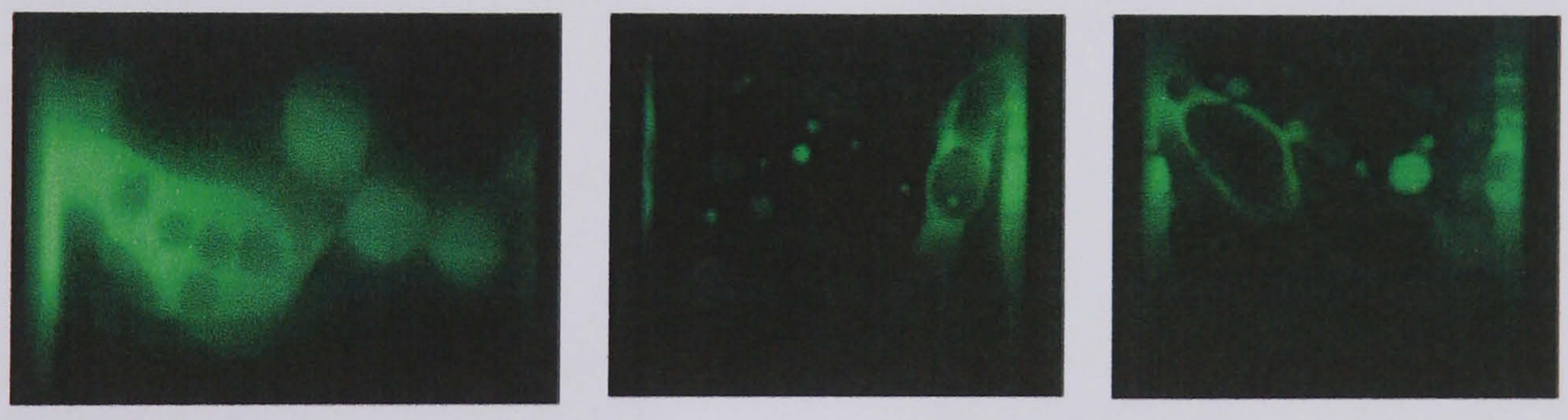
Figure 4.9 W/O/W secondary dispersions; (a) – (d) at mixture velocity U_m = 1.5 m/s and oil holdup ε^o_{input} = 31%; (e) U_m = 1.16 m/s and ε^o_{input} = 67.7%.



(a) (b) (c)

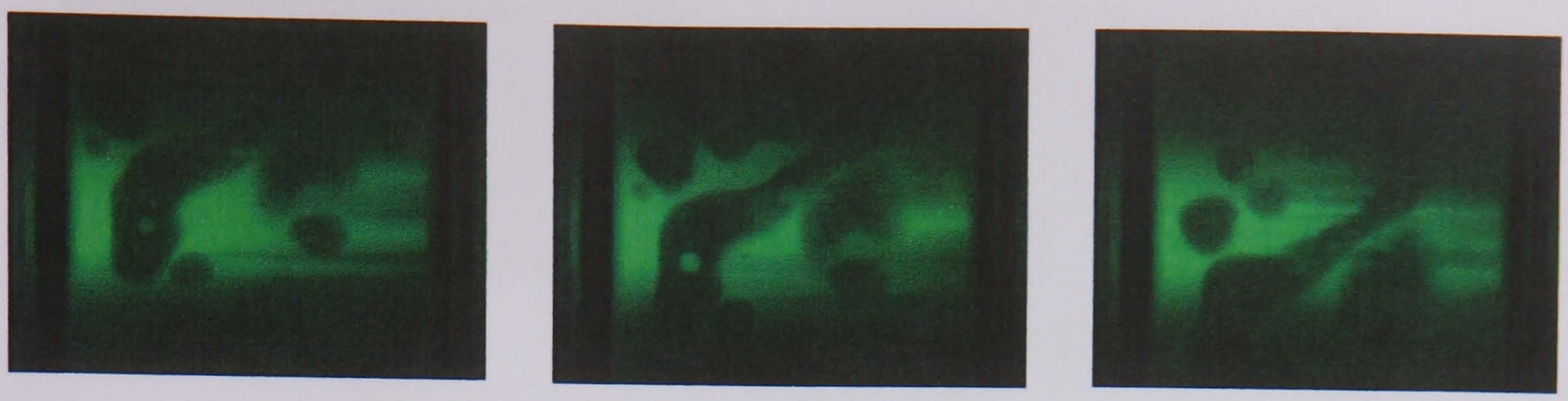
(d) (e) (f)

Figure 4.10 O/W/O secondary dispersions; (a) U_m = 1.3 m/s and ε^o_{input} = 48%; (b) U_m = 1.22 m/s and ε^o_{input} = 55%; (c) U_m = 0.68 m/s and ε^o_{input} = 42%; (d) – (e) U_m = 1.17 m/s and ε^o_{input} = 67%; (f) U_m = 1.34 m/s and ε^o_{input} = 80.9%;

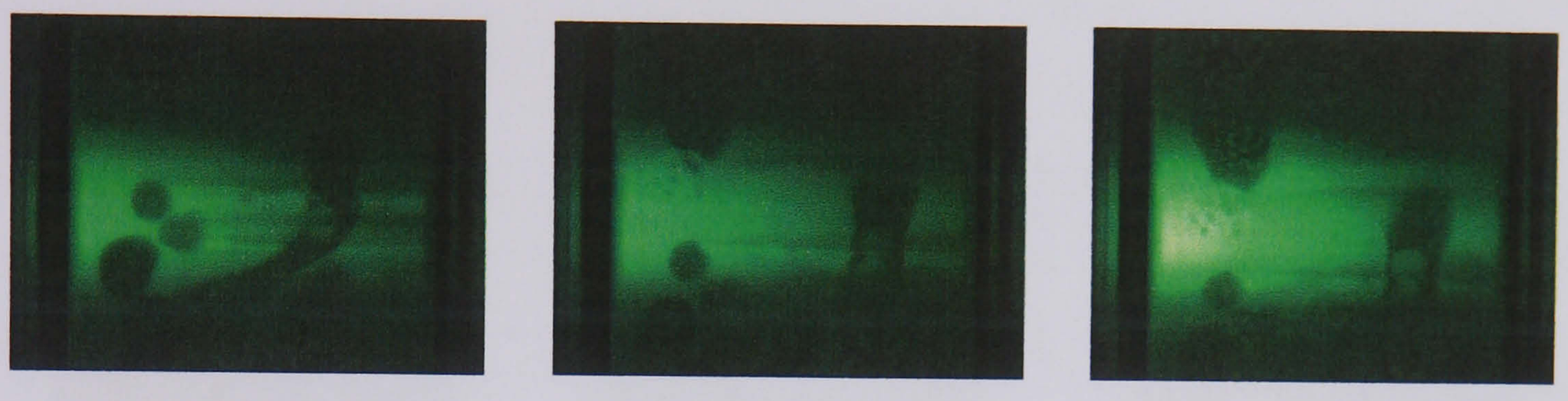


(a) (b) (c)

Figure 4.11 O/W/O dispersions are rupturing from the aqueous films; (a) at U_m = 1.2 m/s and ε^o_{input} = 56%; (b) at U_m = 1.2 m/s and ε^o_{input} = 62.8%; (c) at U_m = 1.22 m/s and ε^o_{input} = 69%.

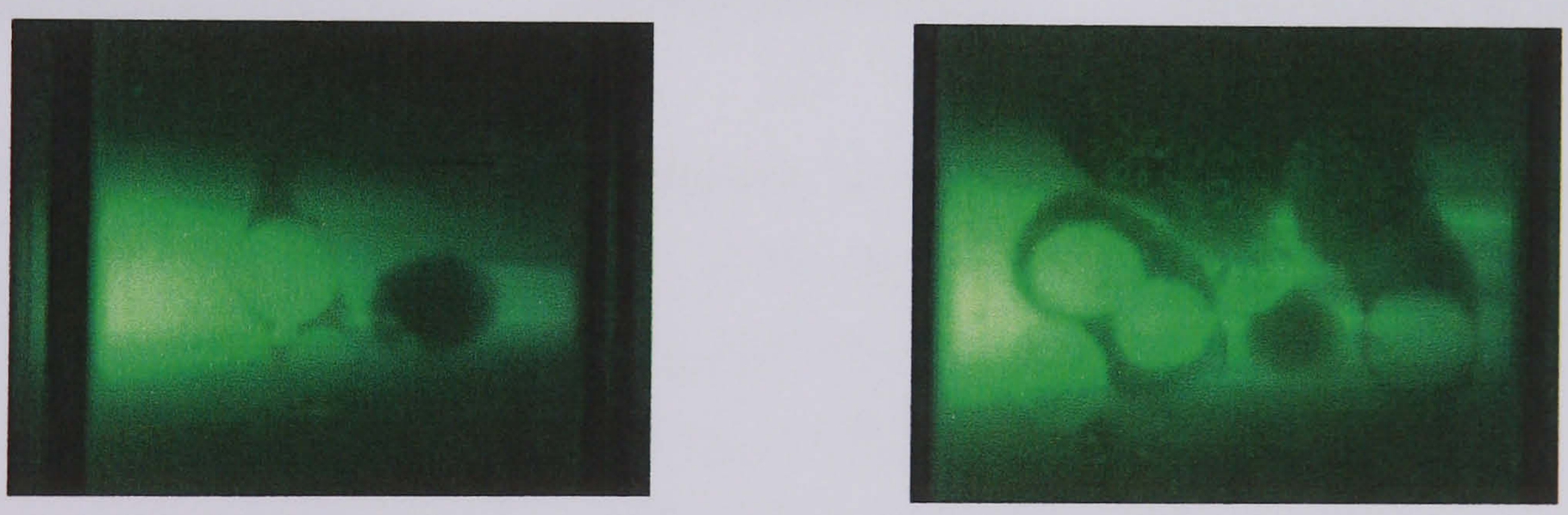


(a) (b) (c)



(d) (e) (f)

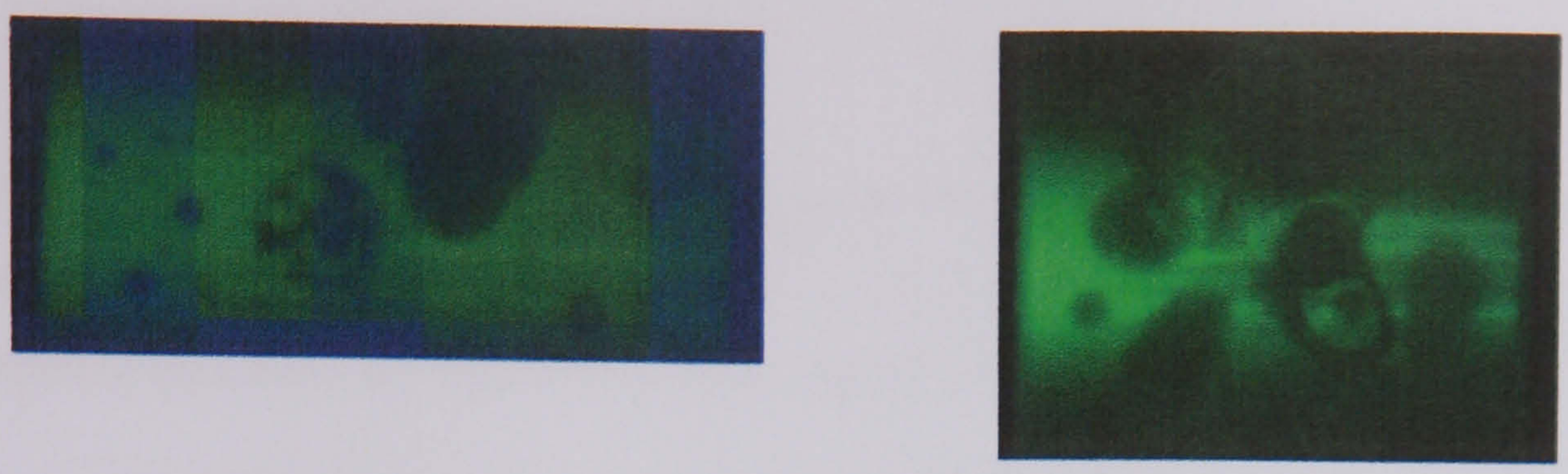
Figure 4.12 Time-series photographs of coalescing process of two aqueous waves including aqueous drop inside oil phase at U_m = 1.46 m/s and ε^o_{input} = 16%.



(a) (b)

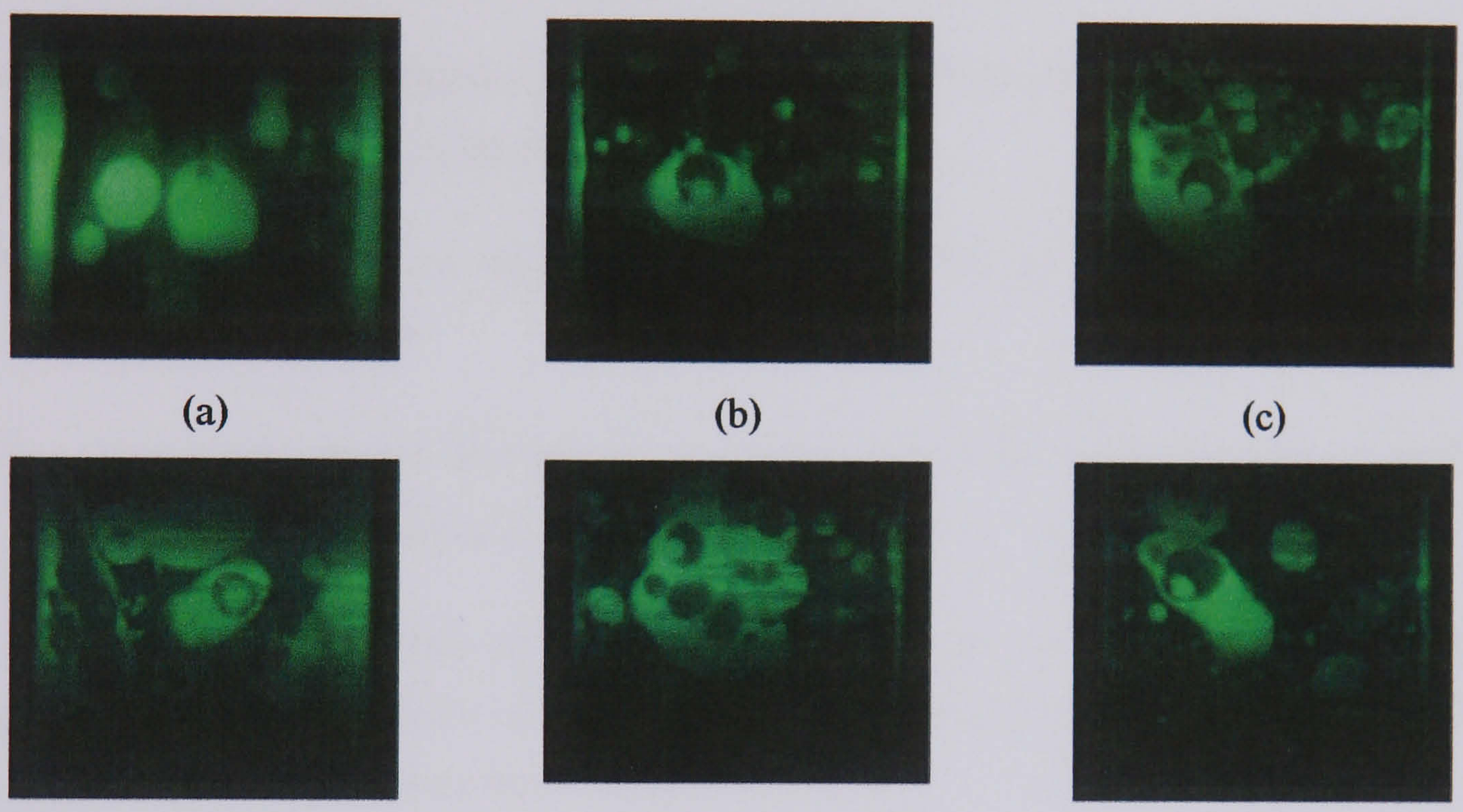
Figure 4.13 W/O/W dispersions are formed by two coalescing aqueous waves; (a) at U_m = 1.02 m/s and ε^o_{input} = 45%; (b) at U_m = 0.68 m/s and ε^o_{input} = 42%.

Some multiple dispersions, both o/w/o/w and w/o/w/o were also found in the experiments (Figures 4.14 and 4.15). The formation of the multiple dispersion was quite similar with that of the secondary dispersion and the droplets included into the host drop were secondary dispersions rather than drops. Figure 4.16 shows an even more complex drop structure.



(a) (b)

Figure 4.14 O/W/O/W Multiple dispersions; (a) at U_m = 1.5 m/s and ε^o_{input} = 31%; (b) at U_m = 0.68 m/s and ε^o_{input} = 42%.



(a) (b) (c)

(d) (e) (f)

Figure 4.15 W/O/W/O Multiple dispersions; (a) at U_m = 1.12 m/s and ε^o_{input} = 59%; (b) at U_m = 1.2 m/s and ε^o_{input} = 62.8%; (c) at U_m = 1.11 m/s and ε^o_{input} = 71.7%; (d) at U_m = 1.85 m/s and ε^o_{input} = 61.8%; (e) at U_m = 1.34 m/s and ε^o_{input} = 80.9%; (f) at U_m = 1.45 m/s and ε^o_{input} = 78.2%.

Figure 4.16 Complex drop structures at U_m = 1.11 m/s and ε^o_{input} = 71.9%.

4.6 Analysis and Discussion

Though the main result of the present experiments has been the observation and recording of the complex flow structures as described in Sections 4.2-4.5, it is also possible to extract quantitative data from the video recordings. Specifically, the images can be analysed to give:

(1) Phase in-situ volume fraction, both with in one image and also averaged over a number of images of the same flow.

(2) Drop section diameter[2], and hence drop section diameter distribution.

Data of this kind were obtained for oil-in-aqueous phase and aqueous phase-in-oil flows and were compared with two methods:

(1) The one-dimensional dispersed flow model of Wallis (1969) for the case of dispersed flow and

(2) A laminar annular flow model for the case where the flow was predominantly annular with an aqueous phase wall film.

Cases were compared with flows which clearly fell into the dispersed and annular categories; if the flows are more complex (such as those shown in Figures 4.9 to 4.15), they clearly could not be predicted by these simplistic models.

4.6.1 Analysis of Data Using One–Dimensional Method

One–dimensional method. Wallis (1969) analysed two-phase pipe flows (including drop flows) by a simple one-dimensional analysis. The objective of the one-dimensional method is to calculate the volume fraction occupied by the respective phases. A key assumption is that the velocity and phase fraction are constant across the pipe. Despite the obvious limitation of this assumption, the model can often be very useful in solving two-phase flow problems.

Suppose we wish to calculate the volume fraction of the channel cross section occupied by the dispersed phase 2 in a mixture of phase 1 and 2 flowing at superficial velocities V_1 and V_2 respectively (the superficial velocity is defined as the total volumetric flow rate of the

[2] In this thesis, it should be emphasized that the measurements were of the diameter of sections through the drops rather than of the drop themselves. No attempt was made to convert the data into actual drop size distributions.

phase divided by the channel cross-sectional area). It is convenient to consider the motion of two phases relative to a plane which is moving at the total superficial velocity V (= $V_1 + V_2$). With respect to this plane, the total volumetric flux (for an incompressible flow) must be zero. From continuity considerations, it can be shown that the volume flux j_{21} (often referred to as a *drift flux*) of component 2 through the plane moving at velocity V is given by:

$$j_{21} = V_2(1-\varepsilon) - \varepsilon V_1 \tag{4-1}$$

The symbol ε represents an average in-situ volume fraction of phase 2. Eq.(4-1) predicts a linear relationship between j_{21} and ε. In fact, Eq.(4-1) represents a line joining the points $\varepsilon = 0, j_{21} = V_2$, and $\varepsilon = 1, j_{21} = -V_1$. The detailed derivation has been described by Wallis (1969), Butterworth & Hewitt (1977) and Hewitt (1978).

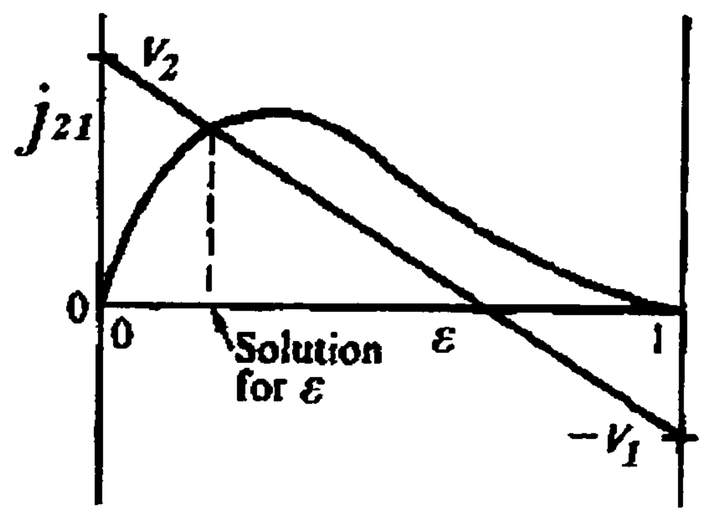
The drift flux j_{21} is also a function of ε, the fluid physical properties and the flow patterns. A suitable functional form suggested by Wallis (1969) is as follows:

$$j_{21} = v_\infty \varepsilon (1-\varepsilon)^n \tag{4-2}$$

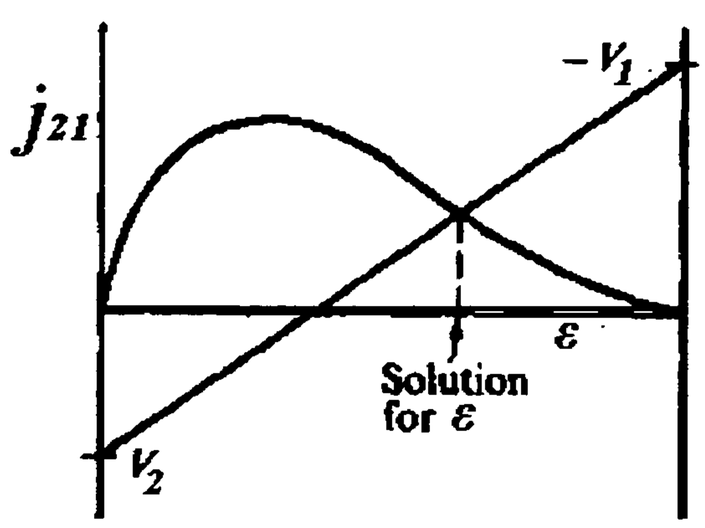
where v_∞ is the terminal velocity of a single dispersed phase element (a drop in the present case) in an infinite fluid. n is an exponent whose value depends on the system (Wallis suggests n=2 for the liquid-liquid system). For a given system, the simultaneous solution of Eqs. (4-1) and (4-2) gives the volume fraction of dispersed phase, ε. This solution can be conveniently obtained by graphical means and the types of solution obtainable are illustrated in Table 4.1.

Table 4.1 Solutions for volume fraction in vertical flow using the one-dimensional analysis method (Butterworth & Hewitt, 1977).

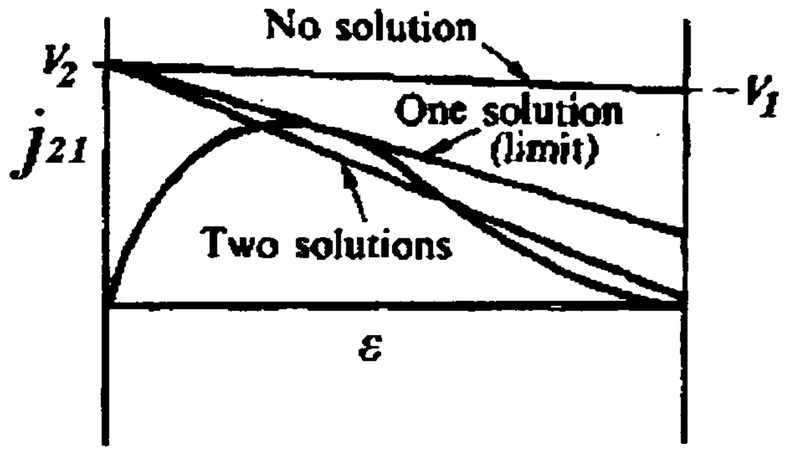
(a) Vertical co-current upward flow. Here, there is only one solution.



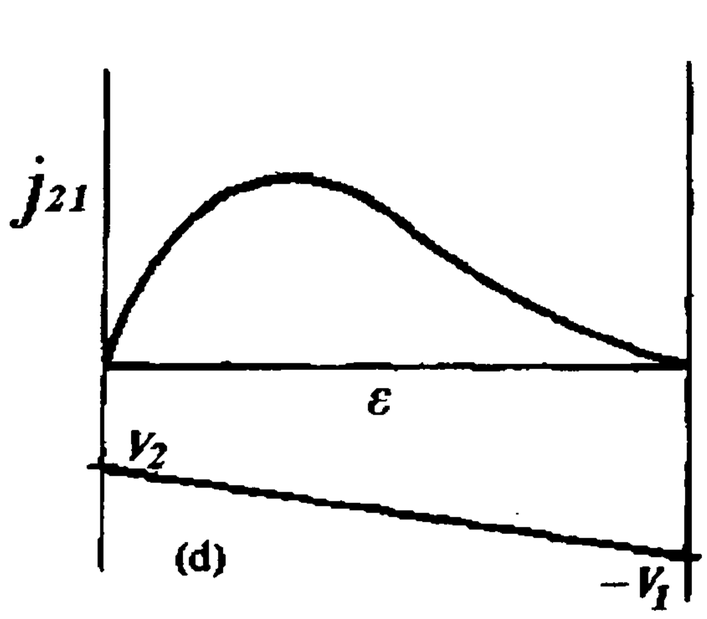
(b) Vertical co-current downward flow. Here, again, there is one solution.



(c) Counter-current flow with component 2 upwards and 1 flowing downwards. For a given component 1 superficial velocity there are two solutions at low component 1 flows. There is also an asymptotic condition of component 1 flow in which there is only one solution and, for high component 1 flows, no solutions are available.



(d) Counter-current flow with component 2 flowing downwards and 1 flowing upwards. There is no solution.



Two experimental cases, one for oil-in-aqueous phase dispersed flow and the other for aqueous phase-in-oil dispersed flow, were analysed using the one-dimensional method described above. The linear relationship between j_{21} and ε based on Eq. (4-1) can be easily obtained using the superficial velocities of the aqueous ($CaCl_2$ solution) and oil phases. To obtain the curve based on the Eq. (4-2), the terminal velocity of a single drop in an infinite fluid (oil drop in aqueous phase or aqueous drop in oil), v_∞, is required. Drops rising or falling freely under gravity in a Newtonian liquid are commonly considered to belong to one of three broad shape regimes: spherical, ellipsoidal, or spherical cap. Grace et al. (1976) showed that a convenient mapping of these three principle regimes, as well as of certain subregimes (e.g., where skirts or wobbling occur), can be obtained by plotting the fluid particles Reynolds number (Eq. 4-3) versus the Eötvös number (Eq. 4-4) with a fluid property group M (Eq. 4-5), as can be seen in Figure 4.17:

$$\mathrm{Re} = \frac{\rho_c d v_\infty}{\mu_c} \tag{4-3}$$

$$Eo = \frac{g \Delta \rho d^2}{\sigma} \tag{4-4}$$

$$M = \frac{g \mu_c^4 \Delta \rho}{\rho_c^2 \sigma^3} \tag{4-5}$$

where ρ_c and ρ_d are the density of continuous and dispersed phase, respectively; μ_c and μ_d are the viscosity of continuous and dispersed phase, respectively; σ is the interfacial tension; g is the acceleration due to gravity; d is drop diameter and $\Delta\rho = \left|\rho_c - \rho_d\right|$.

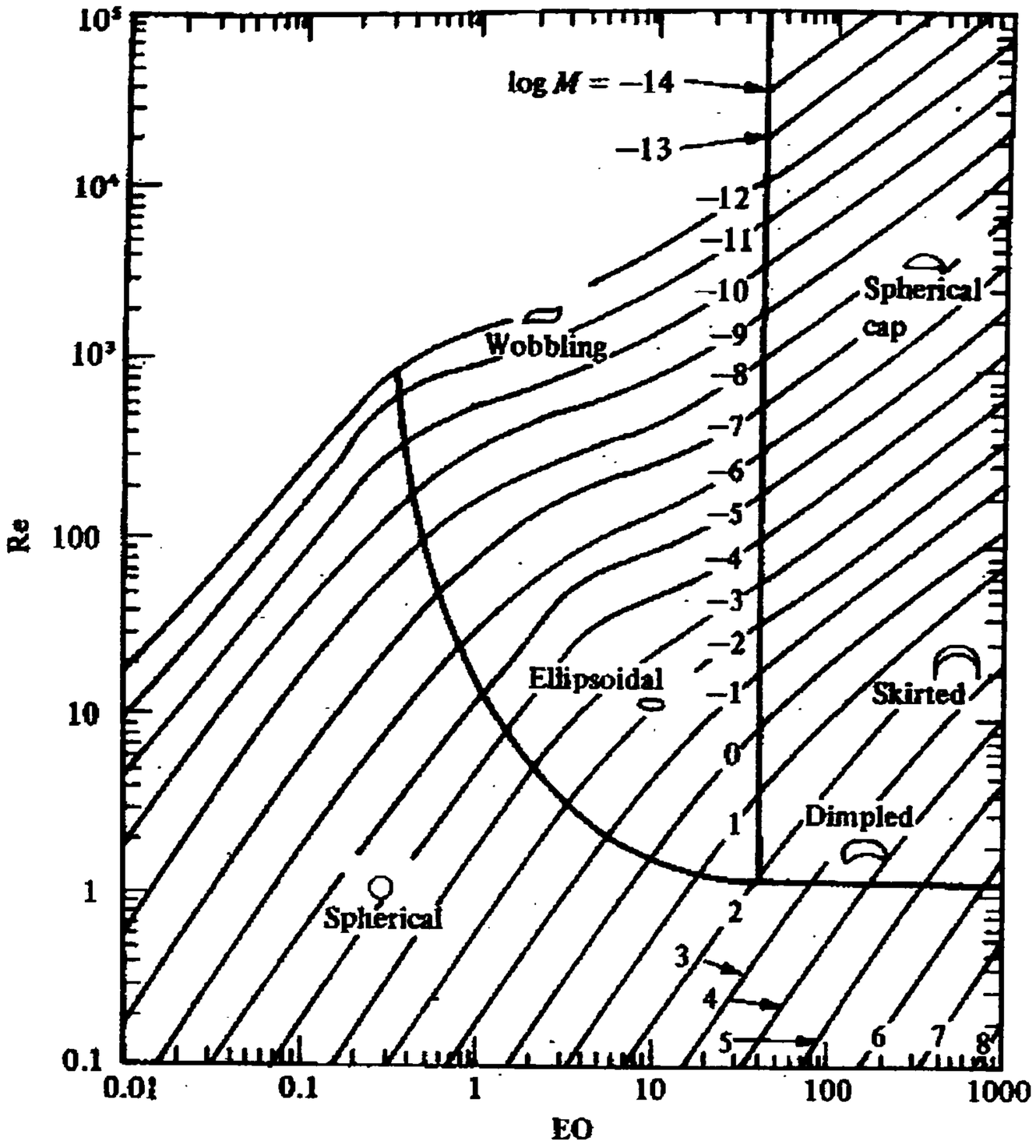


Figure 4-17 Shape regimes and subregimes for liquid drops and gas bubbles rising or falling freely through liquids under gravity (Grace *et al.*, 1976); adapted from Clift *et al.* (1978).

For the spherical or nearly spherical drops at low Reynolds number, Hetsroni (1982) suggests the following expression for the terminal rise or fall velocity:

$$v_\infty = \frac{2}{3}\frac{gr^2\Delta\rho}{\mu_c}\frac{\kappa+1}{3\kappa+2} \tag{4-6}$$

where $\kappa = \mu_d/\mu_c$ is the viscosity ratio, r is the drop radius. For the drops in ellipsoidal regime, the terminal velocity is given by

$$v_\infty = \frac{\mu_c}{\rho_c d}M^{-0.149}(J-0.857) \tag{4-7}$$

where

$$J = 0.94H^{0.757} \qquad (2 < H \leq 59.3) \tag{4-8}$$

$$J = 3.42H^{0.441} \qquad (H > 59.3) \tag{4-9}$$

and the dimensionless group H is defined by

$$H = \frac{4}{3} EoM^{-0.149} \left(\frac{\mu_c}{\mu_w} \right)^{-0.14} \tag{4-10}$$

where $\mu_w = 9 \times 10^{-4}$ Pa s is the viscosity of water. The above method is recommended for systems with M<10^{-3}, Re>0.1, Eo<40 and negligible wall effects.

Oil-in-aqueous phase experimental case. A case of an oil-in-aqueous phase dispersed flow with superficial velocities of V_o = 0.465 m/s and V_w = 1.035 m/s, and input oil volume fraction ε^o_{input} = 31% is analysed here. According to the Eo, Re and M numbers of the experimental system and the shape regimes map (Figure 4.17), the oil drops whose diameter d < 2 mm are in the spherical regime. The terminal rise velocities are therefore calculated from Eq. (4-6). The oil drops whose diameters $d \geq 2$ mm are in ellipsoidal regime and Eq. (4-7) is then applied to obtain the terminal velocities. The liquid physical properties are given in Table 3.1. Figure 4.18 presents the graphical solution of Eqs. (4-1) and (4-2) for the oil-in-aqueous phase dispersed flow in downward direction. The solutions of in-situ oil volume fraction $\varepsilon^o_{in-situ,p}$ for different oil drop diameters are also shown in Figure 4.19.

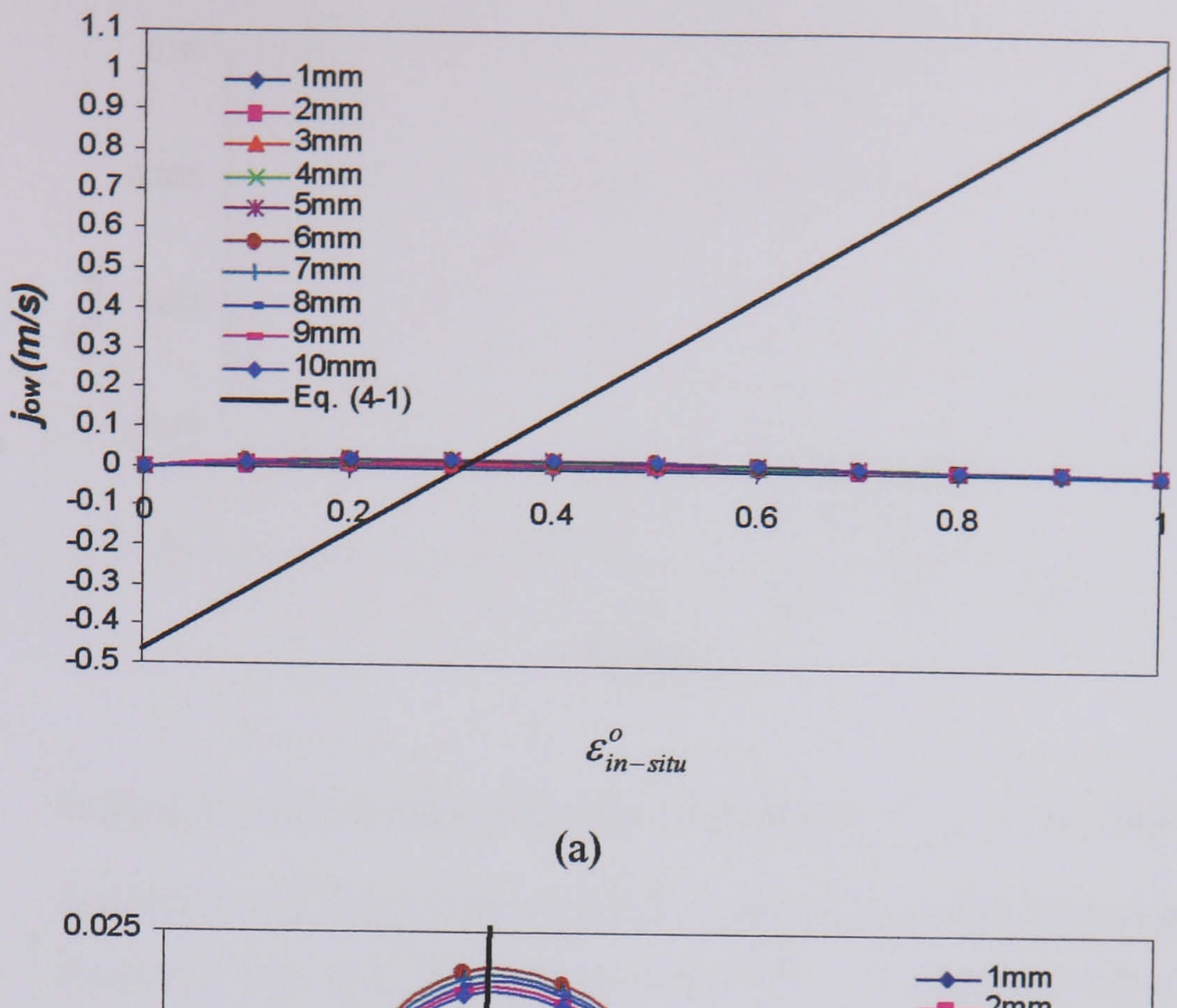


Figure 4.18 Graphical solution of oil in-situ volume fraction $\varepsilon^{o}_{in-situ}$ of Eqs. (4-1) and (4-2) for various drop diameters in the oil-in-aqueous phase dispersed flow with mixture velocity of V_m = 1.5 m/s and input oil volume fraction ε^{o}_{input} = 31%.

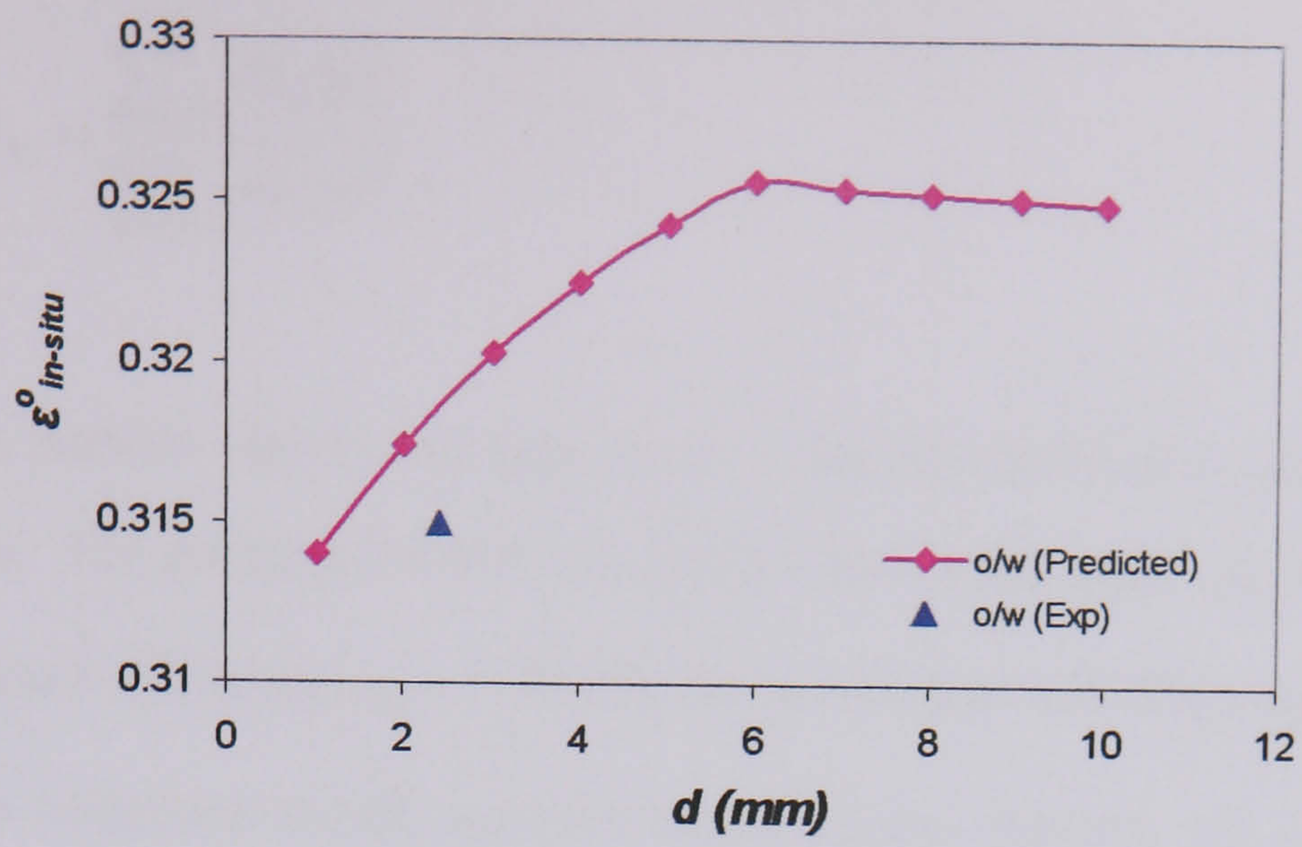


Figure 4.19 Predicted in-situ volume fractions of oil phase $\varepsilon^o_{in-situ,p}$ for different oil drop diameters, calculated from Eqs. (4-1) and (4-2) in the oil-in-aqueous phase dispersed flow with mixture velocity of V_m = 1.5 m/s and input oil volume fraction ε^o_{input} = 31%.

A measured in-situ oil volume fraction ($\varepsilon^o_{in-situ,m}$) can also be obtained by averaging the area fraction covered by oil phase for a number of images obtained in the experiments, as follows:

$$\varepsilon^o_{in-situ} = \frac{1}{N}\sum_{i=1}^{N}\frac{A_{oil,i}}{A_i} \tag{4-11}$$

where A_{oil} is the area occupied by oil phase in one image and A is the total visualised area (see Figure 4.20), N is the number of the analysed images which are randomly selected. In present studies, 30 images are chosen. A typical processed image is shown in Figure 4.20. To analyse the images a MATLAB program was written so as to obtain drop section diameter distribution and volume fraction of each phase; this program is given in Appendix G. For the oil-in-aqueous phase dispersion with superficial velocities of V_o = 0.465 m/s and V_w = 1.035 m/s, and input oil volume fraction ε^o_{input} = 31%, the measured average in-situ oil volume fraction ($\varepsilon^o_{in-situ,m}$) is found to be 31.5%.

For the case analysed, the drop section diameter distribution is given in Figure 4.21. The Sauter-mean diameter can be derived as

$$d_{32} = \frac{\sum_{j=1}^{n} P(j) d_j^3}{\sum_{j=1}^{n} P(j) d_j^2} \tag{4-12}$$

where $P(j)$ is number density of drop group j; for the distribution shown in Figure 4.21, d_{32}^o is 2.4 mm. The predicted in-situ oil fraction calculated from one-dimensional analysis (shown in Figure 4.22), $\varepsilon_{in-situ,p}^o$ = 31.9% for a 2.4 mm oil drop diameter, agrees very well with the measured in-situ aqueous phase volume fraction, $\varepsilon_{in-situ,m}^o$ = 31.5% (▲ in Figure 4.19).



(a) (b)

Figure 4.20 The processed images for obtaining $\varepsilon_{in-situ,m}^o$ in an oil-in-aqueous phase dispersed flow with mixture velocity of V_m = 1.5 m/s and input oil volume fraction ε_{input}^o = 31%; (a) original image; (b) processed black-white image (white represents dispersed phase).

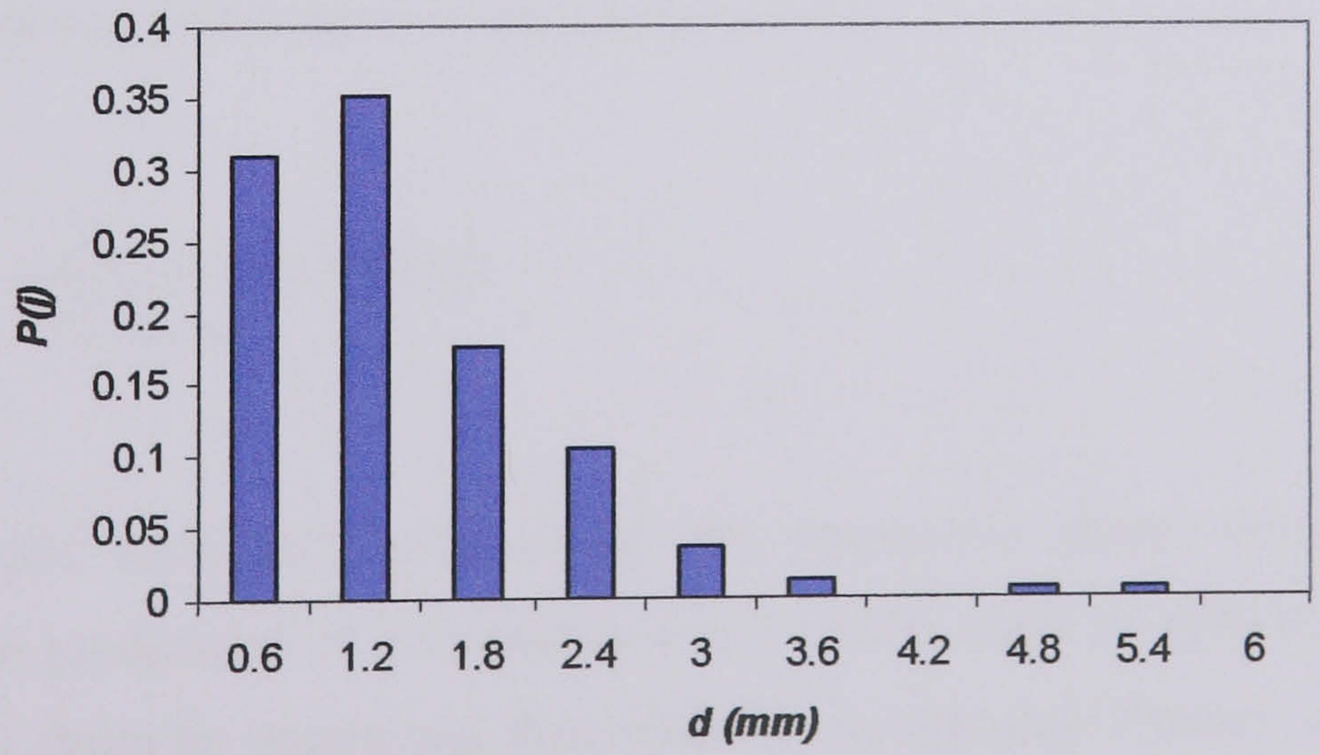


Figure 4.21 The drop section diameter distribution for the oil-in-aqueous phase dispersed flow with mixture velocity of V_m = 1.5 m/s and input oil volume fraction ε_{input}^o = 31%.

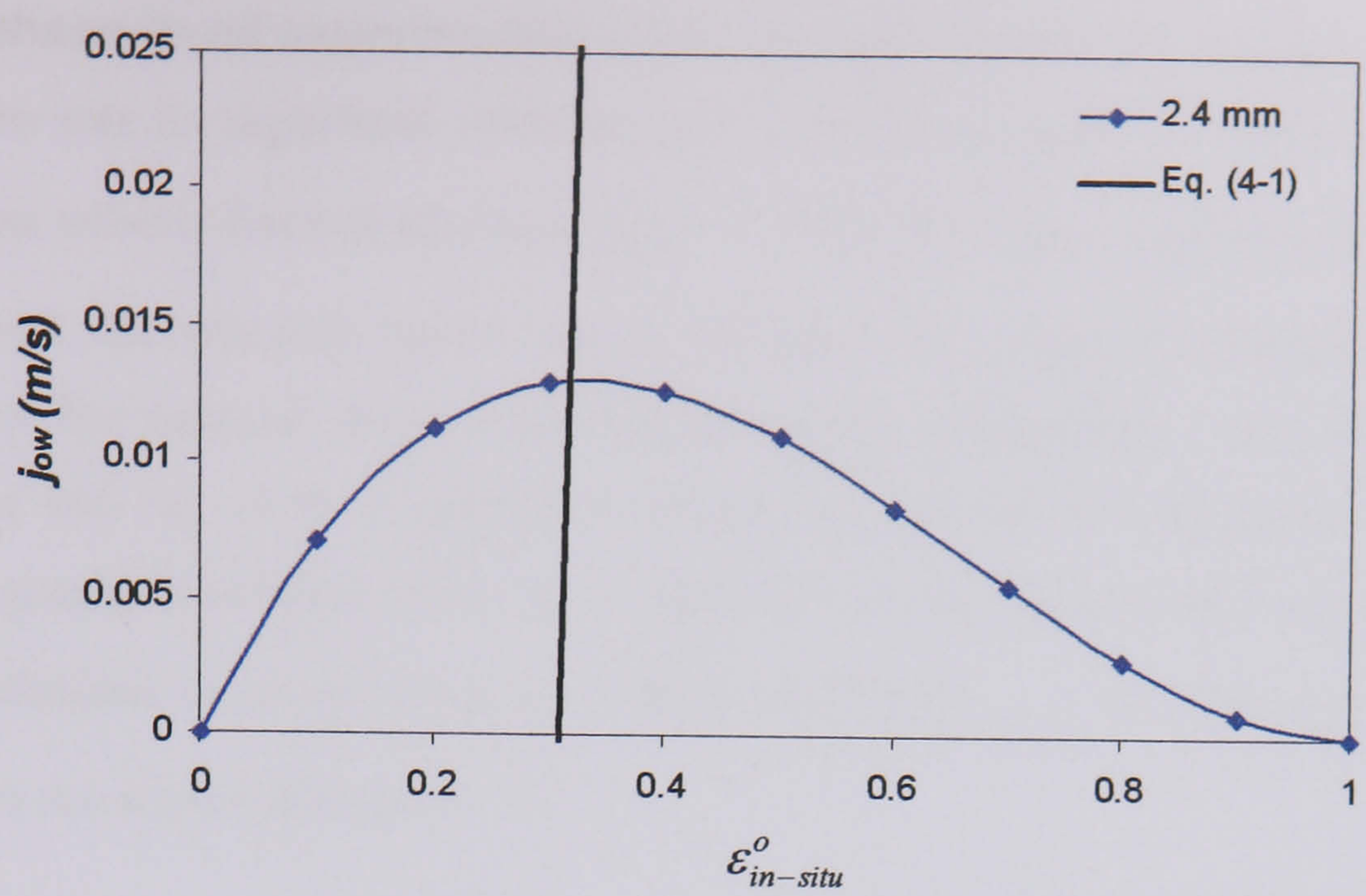


Figure 4.22 Predicted in-situ volume fractions of oil phase $\varepsilon^o_{in-situ,p}$ for d^o_{32} =2.4 mm in the oil-in-aqueous phase dispersed flow with mixture velocity of V_m = 1.5 m/s and oil input volume fraction ε^o_{input} = 31%.

The average oil drop velocity (v_o) is given (using the measured value of $\varepsilon^o_{in-situ,m}$) by

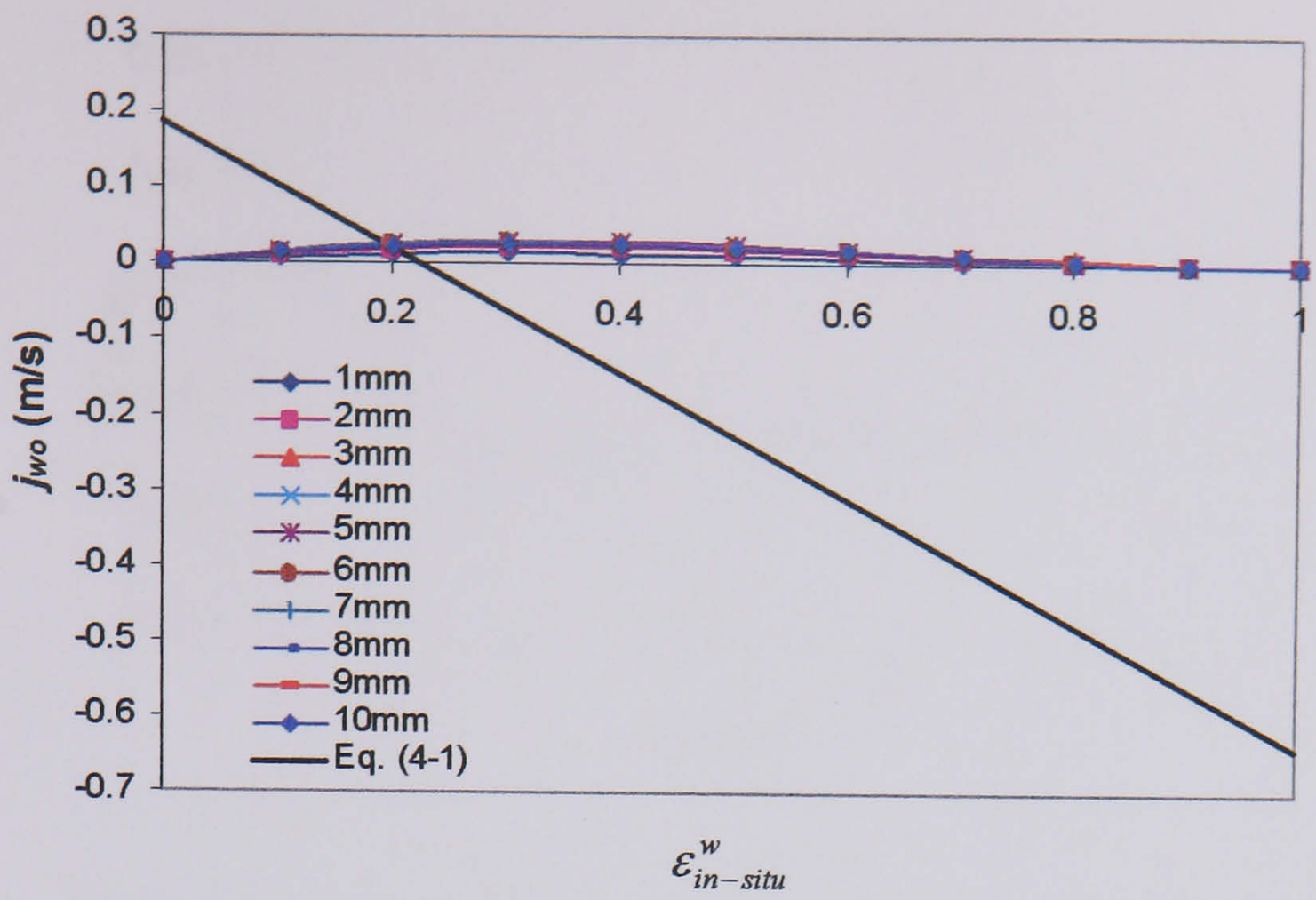
$$v_o = \frac{V_o}{\varepsilon^o_{in-situ,m}} = 1.476 \text{ m/s} \tag{4-13a}$$

and the average velocity of the aqueous phase is given by:

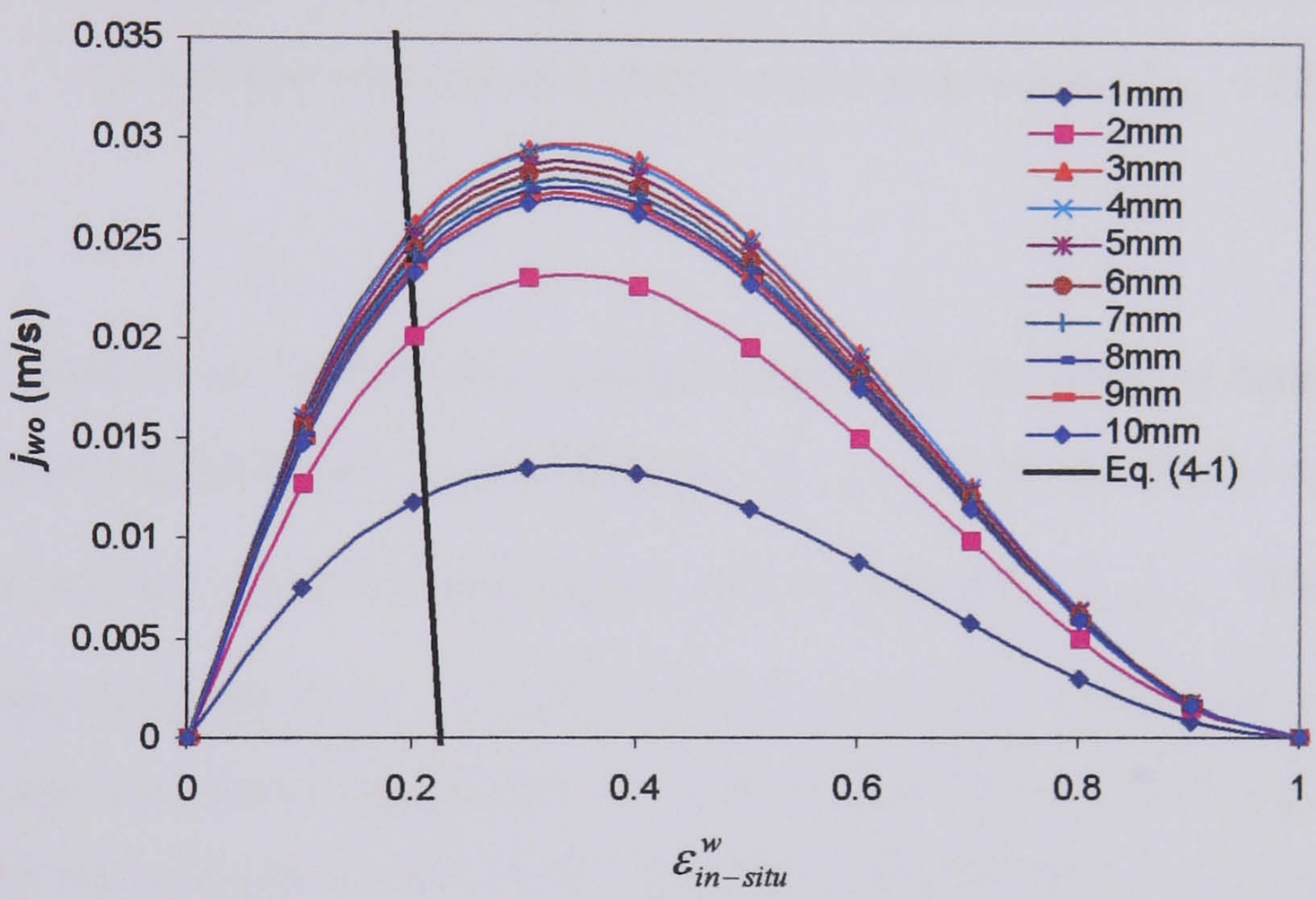
$$v_w = \frac{V_w}{1-\varepsilon^o_{in-situ,m}} = 1.511 \text{ m/s} \tag{4-13b}$$

Thus, the difference between the dispersed and continuous phase velocities is small, consistent with the predictions. A consistency check can be made by determining the actual velocity of the oil drops by measuring their position in successive frames and dividing the displacement by the time elapsed; this method also gave a velocity approximately equal to 1.5 m/s as expected.

Aqueous phase-in-oil experimental case. The case chosen for aqueous phase-in-oil dispersed flow was for superficial velocities of V_w= 0.186 m/s and V_o = 0.638 m/s; the input aqueous phase volume fraction was thus ε^{w}_{input} = 22.6%. For aqueous phase drops diameters less than 1 mm, the spherical regime occurs and Eq. (4-6) is used to calculate the terminal fall velocities. For aqueous phase drops with diameters greater than 1 mm, the ellipsoidal regime occur and Eq. (4-7) is applied to obtain the terminal fall velocities. Figure 4.23 presents the graphical solution of Eq. (4-1) and (4-2) for the aqueous phase-in-oil dispersed flow. The solutions of in-situ aqueous volume fraction $\varepsilon^{w}_{in-situ,\,p}$ as a function of aqueous drop diameter are shown in Figure 4.24.



(a)



(b)

Figure 4.23 Graphical solution of aqueous phase in-situ volume fraction $\varepsilon^{w}_{in-situ}$ of Eq. (4-1) and (4-2) for various drop diameters in aqueous phase-in-oil dispersed flow with the mixture velocity of V_m = 0.824 m/s and the input aqueous phase volume fraction of ε^{w}_{input} = 22.6%.

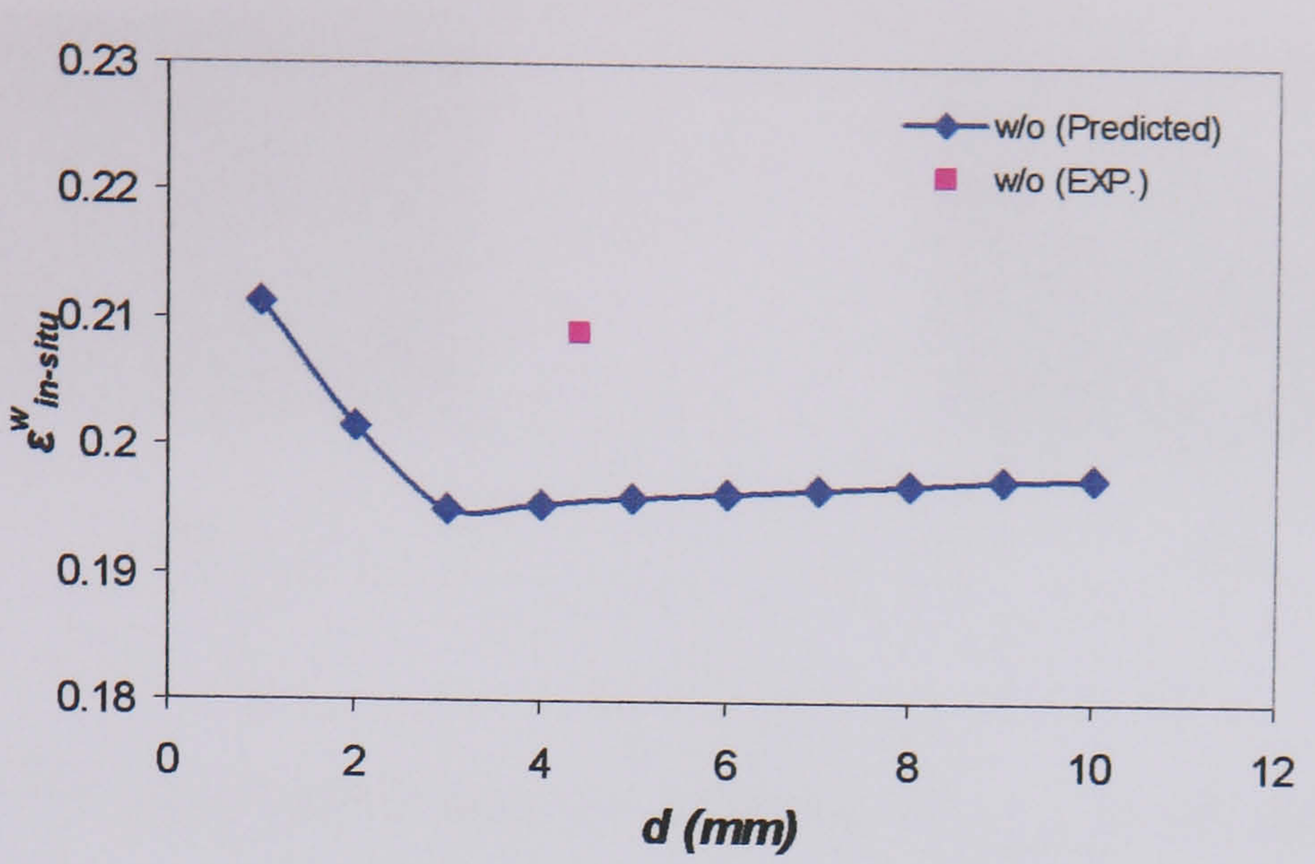
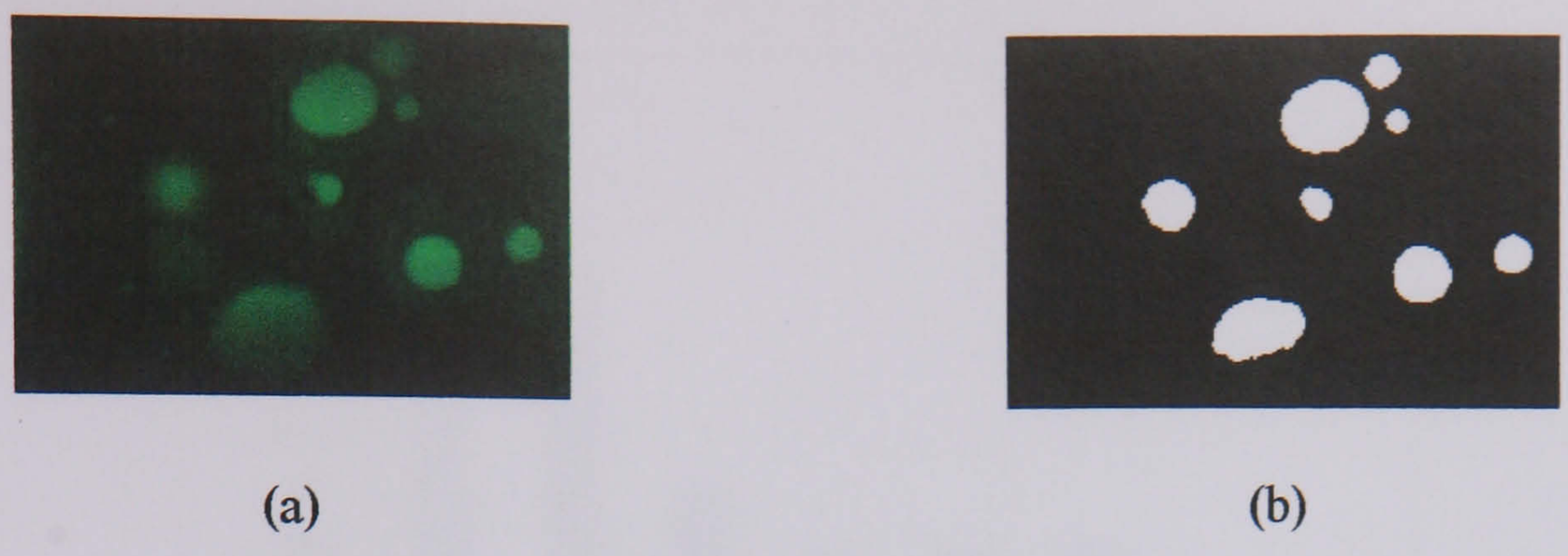


Figure 4.24 Predicted aqueous phase in-situ volume fraction $\varepsilon^{w}_{in-situ,\,p}$ for different aqueous phase drop diameters, calculated from Eqs. (4-1) and (4-2) in aqueous phase-in-oil dispersed flow with the mixture velocity of $V_m = 0.824$ m/s and the input aqueous phase volume fraction of $\varepsilon^{w}_{input} = 22.6\%$.

From the analysis of 30 randomly selected images for the selected case, the average measured aqueous phase in-situ volume fraction, $\varepsilon^{w}_{in-situ,m}$, is 20.9%. Figure 4.25 presents a sample of the original and processed images used in obtaining $\varepsilon^{w}_{in-situ,m}$. The Sauter-mean diameter of aqueous phase drops, d^{w}_{32}, in this case was 4.4 mm. The specific solution to the one-dimensional flow model for this diameter is illustrated in Figure 4.26 and is (of course) consistent with the curve shown in Figure 4.24. The predicted value of in-situ aqueous phase fraction for this diameter, $\varepsilon^{w}_{in-situ,\,p} = 19.6\%$, agrees well with the experimental in-situ aqueous phase volume fraction, $\varepsilon^{w}_{in-situ,m} = 20.9\%$. The drop section diameter distribution for aqueous phase-in-oil dispersed flow is shown in Figure 4.27.



(a) (b)

Figure 4.25 The processed images for obtaining $\varepsilon^{w}_{in-situ,m}$ in an aqueous phase-in-oil dispersed flow with mixture velocity of V_m = 0.824 m/s and input aqueous phase volume fraction ε^{w}_{input} = 22.6%; (a) original image; (b) processed black-white image (white represents dispersed phase).

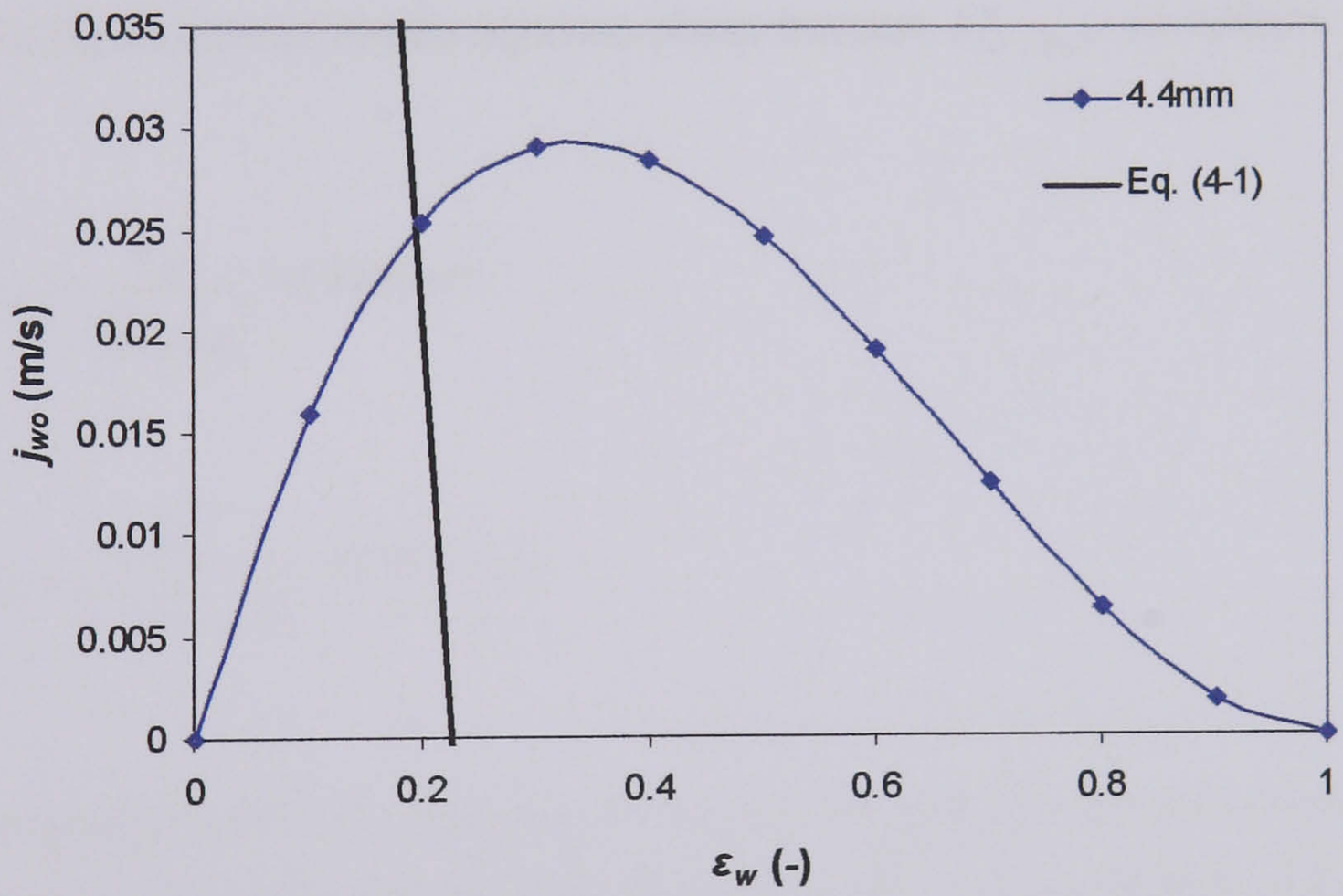


Figure 4.26 Predicted in-situ volume fractions of oil phase $\varepsilon^{w}_{in-situ,p}$ for d^{w}_{32} = 4.4 mm in the aqueous phase-in-oil dispersed flow with mixture velocity of V_m = 0.824 m/s and input aqueous phase volume fraction ε^{o}_{input} = 22.6%.

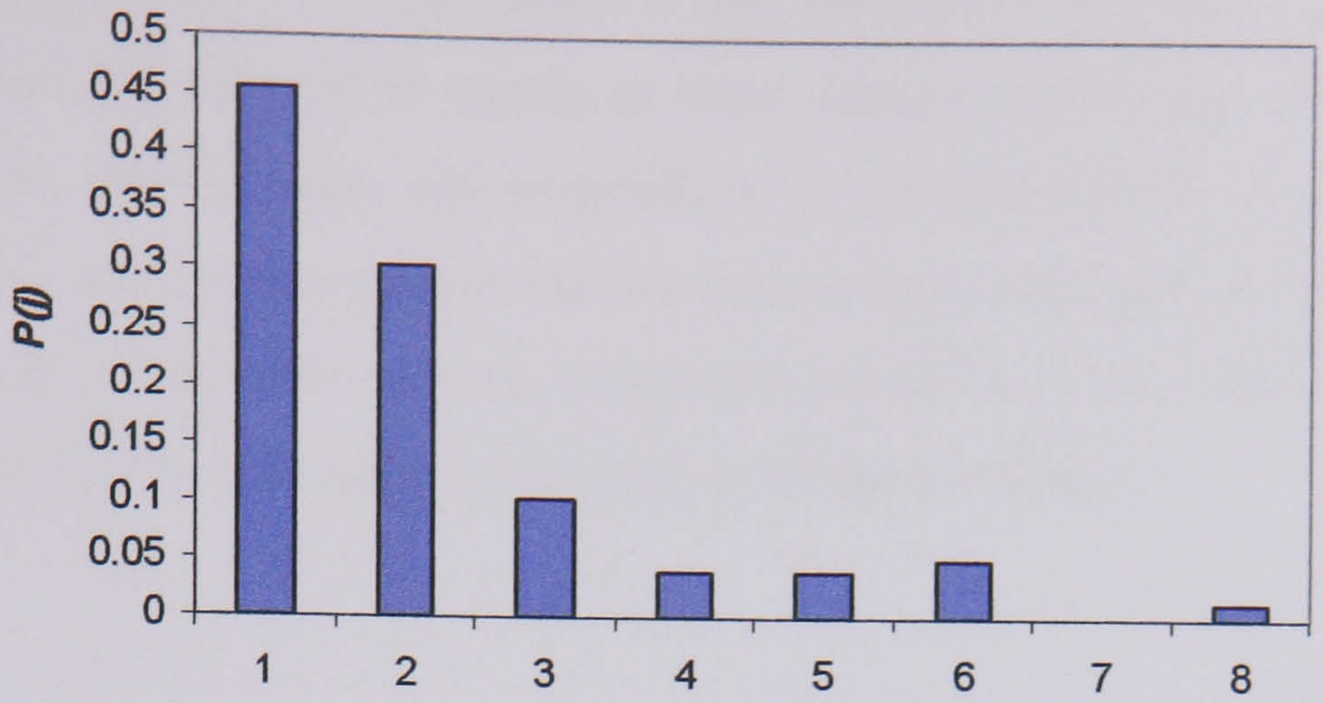


Figure 4.27 The drop section diameter distribution for the aqueous phase-in-oil dispersed flow with mixture velocity of V_m = 0.824 m/s and input oil volume fraction ε^w_{input} = 22.6%.

The average velocities of the aqueous phase drops and of the continuous phase can be estimated from the measured in-situ aqueous phase fraction $\varepsilon^w_{in-situ,m}$ as follows:

$$v_w = \frac{V_w}{\varepsilon^w_{in-situ,m}} = 0.886 \text{ m/s} \tag{4-14a}$$

$$v_o = \frac{V_o}{1-\varepsilon^w_{in-situ,m}} = 0.807 \text{ m/s} \tag{4-14b}$$

Again, the actual value of the velocity of the aqueous phase drops was determined by the measuring drop displacement in successive frames. The mean experimental value of drop velocity was 0.95 m/s, around 7% higher than the value given by Eq. 4-14a. However, part of the aqueous phase holdup is ascribed to the (thin) liquid film and this would make the actual drop velocity somewhat higher as found.

4.6.2 Annular Flow Analysis

As was discussed above, many of the flows visualised were closer to being annular rather than dispersed in nature. It is of interest, therefore, to compare the observed phase fraction with that predicted from an annular flow model. Such a model has been derived and is

described in Section 4.6.2.1; the derivation is for cylindrical geometry, whereas, in the present experiments, the channel is square in cross section. Modelling annular flow in a square cross section channel gives rise to problems in representing the flows in the corner regions; a numerical solution is required and this has not been attempted in the present work. However, comparison of the data with the round tube model on an equivalent diameter basis gives an at least qualitative indication of the success of the prediction.

4.6.2.1 Model and Equations

A model for co-current downward laminar annular flow in circular pipe was developed in this study. The analysis is similar to one derived by Hasson et al. (1974). Though the present analysis is derived by a rather different route, the answers are essentially identical to those given by the Hasson et al. analysis. In the model, it is assumed that there is no drop entrainment of the film phase into the core phase and vice versa and that the core/film interface is smooth (i.e. there is no wave formation). It is further assumed that surface tension has a negligible role and that, therefore, there is no change of pressure across the interface. Figure 4.28 schematically illustrates co-current downward laminar annular flow at steady state, where phase 1 flows in the pipe centre ($r < r_i$) and phase 2 flows in the annulus region ($r_i < r < R$).

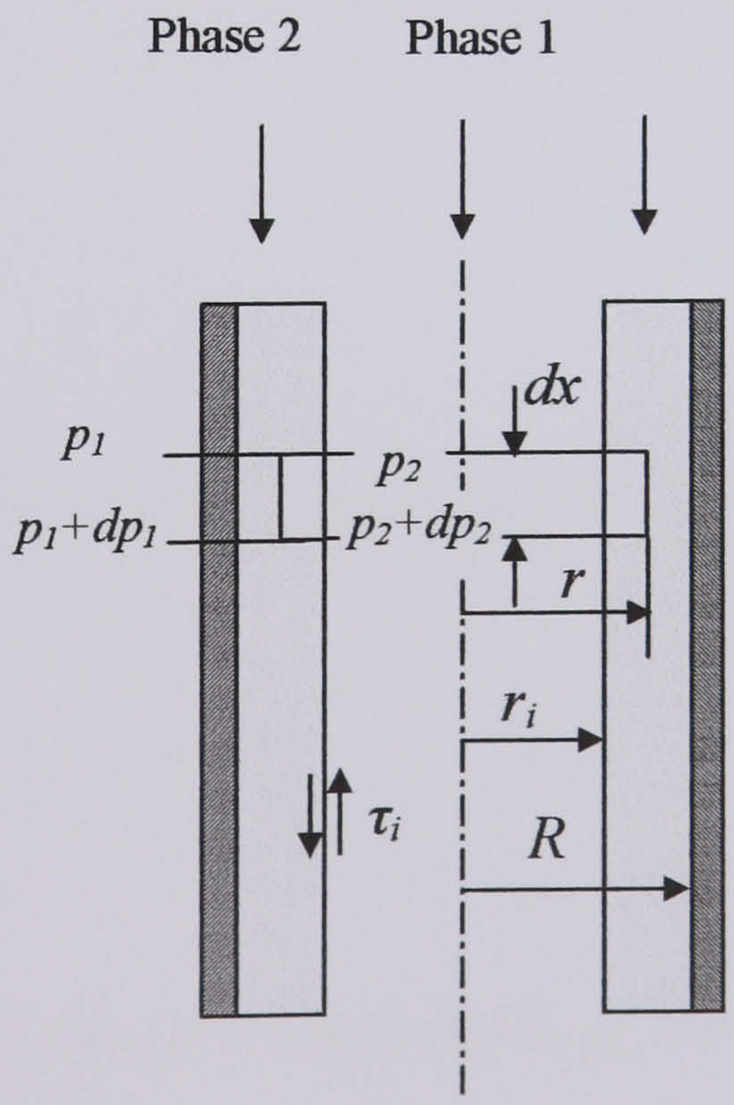


Figure 4.28 The schematic diagram of the co-current downward laminar annular flow.

At steady state for each phase, the Navier-Stokes equation reduces to:

$$0 = -\frac{dp_j}{dx} + \rho_j g + \frac{\mu_j}{r}\frac{d}{dr}\left(r\frac{du_j}{dr}\right) \tag{4-15}$$

where x is the pipe axial coordinate, r is the radial coordinate, p_j is the pressure and u_j is the axial velocity at radial position r for the inner fluid (j = 1) and the outer fluid (j = 2), respectively.

Considering that the flow is symmetrical to the pipe centreline and the velocity of each phase at the interface is equal, the following boundary conditions are derived:

at the centreline ($r = 0$): $u_1 = u_0 \ , \ \frac{du_1}{dr} = 0$ (4-16a)

at the wall ($r = R$): $u_2 = 0$ (4-16b)

at the interface ($r = r_i = aR$): $u_1 = u_2 \ , \ \mu_1 \frac{du_1}{dr} = \mu_2 \frac{du_2}{dr}$ (4-16c)

where u_0 is the centreline velocity, μ_1 and μ_2 are the viscosities of phase 1 and 2.

If P represents the net pressure gradient of the inner fluid, including hydrostatic effects,

$$P = -\frac{dp_1}{dx} + \rho_1 g \tag{4-17}$$

where ρ_1 is the density of phase 1, Eq. (4-15) for phase 1 can then be written as

$$\frac{\mu_1}{r}\frac{d}{dr}\left(r\frac{du_1}{dr}\right) = -P \tag{4-18}$$

Since the pressure gradient is the same in both fluids, $dp_1/dx = dp_2/dx$, Eq. (4-15) for phase 2 thus gives

$$\frac{\mu_2}{r}\frac{d}{dr}\left(r\frac{du_2}{dr}\right) = -P + (\rho_1 - \rho_2)g \tag{4-19}$$

where the last term defines the effect of buoyancy.

The above equations can be written into dimensionless form by defining the dimensionless variables: radius $\hat{r} = r/R$, velocity $\hat{u}_i = u_i/U$ and velocity scale $U = (Q_1 + Q_2)/R^2$, where Q_1 and Q_2 are the volumetric flow rates of inner and outer phases, respectively. The corresponding dimensionless volume flow rate for phase j (j=1 or 2) is expressed as $\hat{Q}_j = Q_j/UR^2 = Q_j/(Q_1 + Q_2)$, which is determined by the input fraction of phase j. Therefore, the following dimensionless equations are obtained:

$$\frac{1}{\hat{r}}\frac{d}{d\hat{r}}\left(\hat{r}\frac{d\hat{u}_1}{d\hat{r}}\right) = -\alpha \tag{4-20}$$

$$\frac{1}{\hat{r}}\frac{d}{d\hat{r}}\left(\hat{r}\frac{d\hat{u}_2}{d\hat{r}}\right) = -\alpha m + \beta m \tag{4-21}$$

with boundary conditions

at the centreline ($\hat{r} = 0$): $\hat{u}_1 = \hat{u}_0$, $\frac{d\hat{u}_1}{d\hat{r}} = 0$ (4-22a)

at the wall ($\hat{r} = 1$): $\hat{u}_2 = 0$ (4-22b)

at the interface ($\hat{r} = a$): $\hat{u}_1 = \hat{u}_2$, $m\frac{d\hat{u}_1}{d\hat{r}} = \frac{d\hat{u}_2}{d\hat{r}}$ (4-22c)

where the dimensionless parameters are the interface position a, the viscosity ratio, $m = \mu_1/\mu_2$ and the dimensionless driving force (α) and buoyancy force (β) are given by:

$$\alpha = \frac{PR^2}{\mu_1 U} = \frac{PR^4}{\mu_1(Q_1 + Q_2)} \qquad \beta = \frac{(\rho_1 - \rho_2)gR^2}{\mu_1 U} = \frac{(\rho_1 - \rho_2)gR^4}{\mu_1(Q_1 + Q_2)} \tag{4-23}$$

Introducing the boundary conditions (Eqs 4-22), the analytical solutions of Eqs. (4-20) and (4-21) can be obtained as follows

$$\hat{u}_1 = \hat{u}_0 - \frac{1}{4}\alpha\hat{r}^2 \tag{4-24}$$

$$\hat{u}_2 = \frac{1}{4}(\alpha-\beta)m(1-\hat{r}^2) + \frac{\hat{u}_0 - \frac{1}{4}\alpha a^2 - \frac{1}{4}(\alpha-\beta)m(1-a^2)}{\ln a}\ln\hat{r} \tag{4-25}$$

where $\hat{u}_0$ is the dimensionless centreline velocity and a is the dimensionless interface radius ($a=r_i/R$). According to the interface boundary condition, $m\frac{d\hat{u}_1}{d\hat{r}} = \frac{d\hat{u}_2}{d\hat{r}}$, $\hat{u}_0$ is then expressed as,

$$\hat{u}_0 = \frac{1}{4}\alpha a^2 + \frac{1}{4}(\alpha-\beta)m(1-a^2) - \frac{1}{2}\beta m a^2 \ln a \tag{4-26}$$

Substituting Eq. (4-26) into Eq. (4-25) gives the velocity of phase 2 as

$$\hat{u}_2 = \frac{1}{4}(\alpha-\beta)m(1-\hat{r}^2) - \frac{1}{2}\beta m a^2 \ln\hat{r} \tag{4-27}$$

Therefore, the dimensionless input volumetric flow rates of each fluid can be obtained by:

$$\begin{aligned}\hat{Q}_1 &= \int_0^a \hat{u}_1 2\pi\hat{r}d\hat{r} = \hat{u}_0\pi a^2 - \frac{1}{8}\pi\alpha a^4 \\ &= \pi a^2\left[\frac{1}{8}\alpha a^2 + \frac{1}{4}(\alpha-\beta)m(1-a^2) - \frac{1}{2}a^2\beta m\ln a\right]\end{aligned} \tag{4-28}$$

$$\hat{Q}_2 = \int_a^1 \hat{u}_2 2\pi\hat{r}d\hat{r} = \frac{1}{8}\pi(\alpha-\beta)m(1-a^2)^2 + \frac{1}{2}\pi a^2\beta m[a^2\ln a + \frac{1}{2}(1-a^2)] \tag{4-29}$$

For given physical properties and a given channel diameter, the physical problem is to find the interface position (a) and the dimensionless driving force (α), these can be obtained

from Eqs. (4-28) and (4-29) for specified values of the viscosity ratio m, the buoyancy term β and the input fractions of the fluids $\hat{Q}_i$, with $\hat{Q}_1 + \hat{Q}_2 = 1$. Equations (18) and (19) have an implicit solution in the form:

$$\hat{Q}_1 = \frac{a^4(2m-1) - 2a^2 m}{a^4(m-1) - m} - \frac{\beta\pi a^4 m}{8} \frac{4m - 1 - 4a^2(2m-1) + a^4(4m-3) + 4(m - a^4(m-1))\ln a}{a^4(m-1) - m} \quad (4\text{-}30)$$

4.6.2.2 Analysis of experimental Annular Flow

The analysis described in Section 4.6.2.2 was applied to the prediction of an annular flow case observed in the present experiments. The case chosen had a mixture superficial velocity (V_m) 0.65 m/s and an oil input volume fraction of 69%. Predictions were made with the model for an equivalent round tube with $R=x/2$ where x is the dimension of the sides of the square channel (x=18 mm). For the current experimental system (where the liquid physical properties can be found in Table 3.1), the viscosity ratio is $m = \mu_1 / \mu_2 = \mu_o / \mu_w = 0.14$; the buoyancy term is $\beta = -152.9$ for mixture velocity $V_m = 0.65$ m/s. The relationships between the interface position a, the dimensionless driving force α and the input volume fractions of the fluids $\hat{Q}_i$, can be obtained according to Eqs. (4-26) and (4-27). The calculated results are shown in Figures 4.29 and 4.30, for a and α respectively as a function of $\hat{Q}_o$. The results for β=0 (i.e. for no density difference between the phases) are also shown for reference. Note that $\hat{Q}_o$ is by definition equal to ε^o_{input}, the symbol used previously for oil input volume fraction.

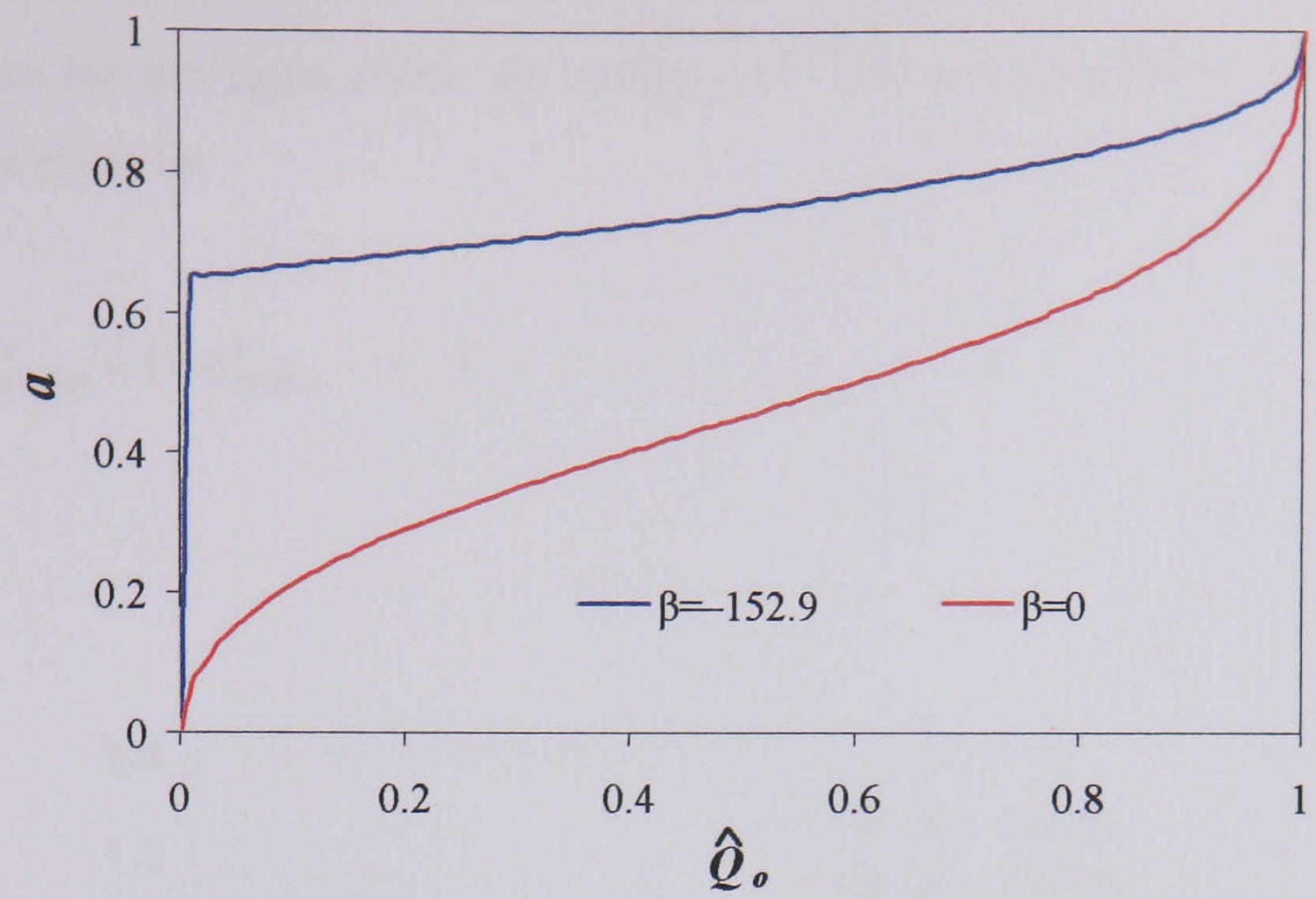


Figure 4.29 The relationship of the interface position, a, and dimensionless oil input volume fraction, $\hat{Q}_o$, with $m = 0.14$ and $V_m = 0.65$ m/s.

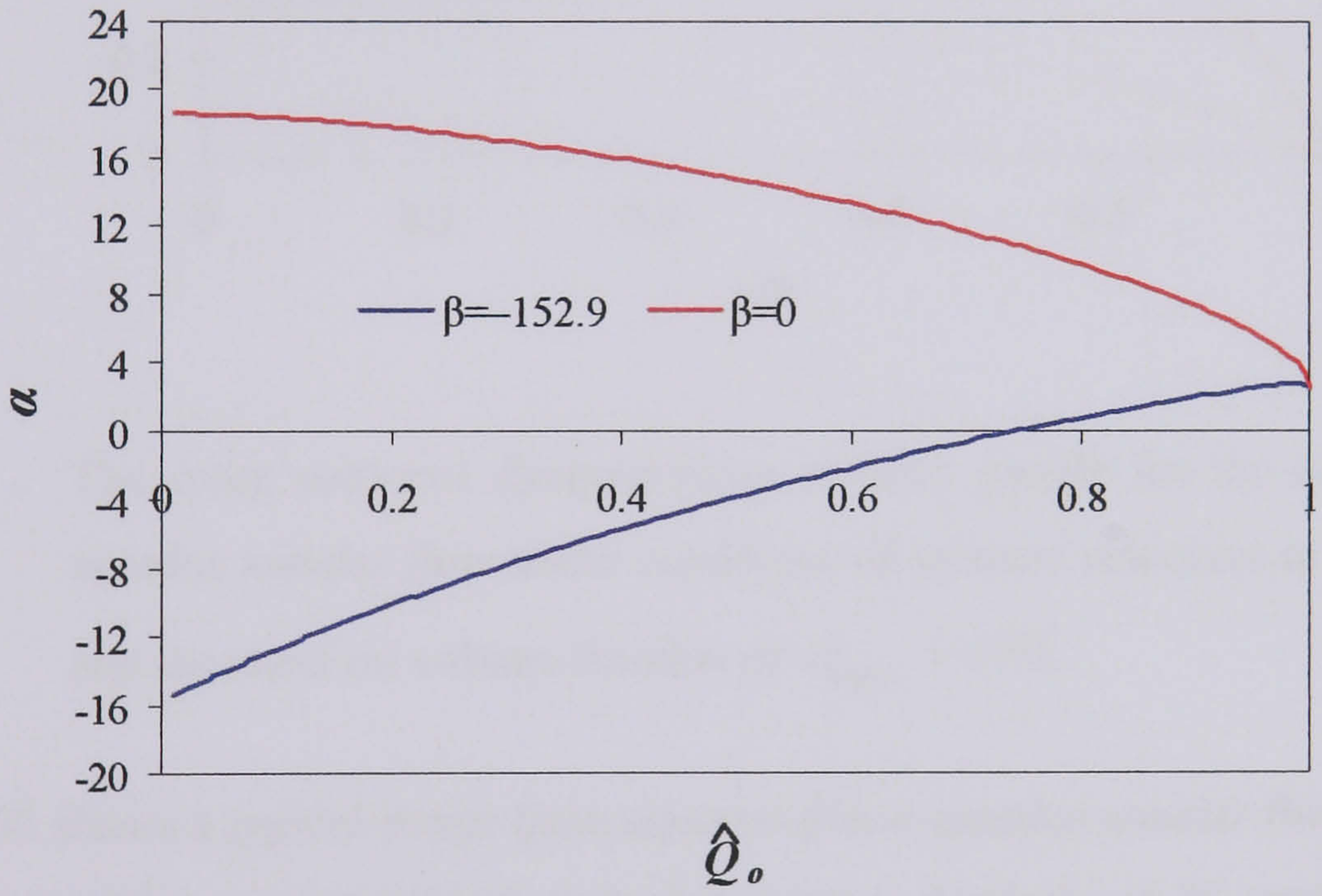


Figure 4.30 The relationship of the dimensionless driving force, α, and the dimensionless oil input volume fraction, $\hat{Q}_o$, with $m = 0.14$ and $V_m = 0.65$ m/s.

For the experimental value of $\hat{Q}_o$ ($=\varepsilon^o_{input}$) of 0.69 a solution for interface position ($a_{predict}$ = 0.79) and dimensionless driving force ($\alpha = -0.76$), are obtained from Figure 4.29 and 4.30 respectively. The cross sectional dimensionless velocity profile is obtained by substituting m,

β , a and α into Eqs. (4-24), (4-26) and (4-27); the resultant plot is shown in Figure 4.31 with the values for β=0 again shown for comparison. The predicted aqueous phase holdup for this case is given by

$$\varepsilon^{w}_{predict} = 1 - a^{2}_{predict} = 0.376 \tag{4-31}$$

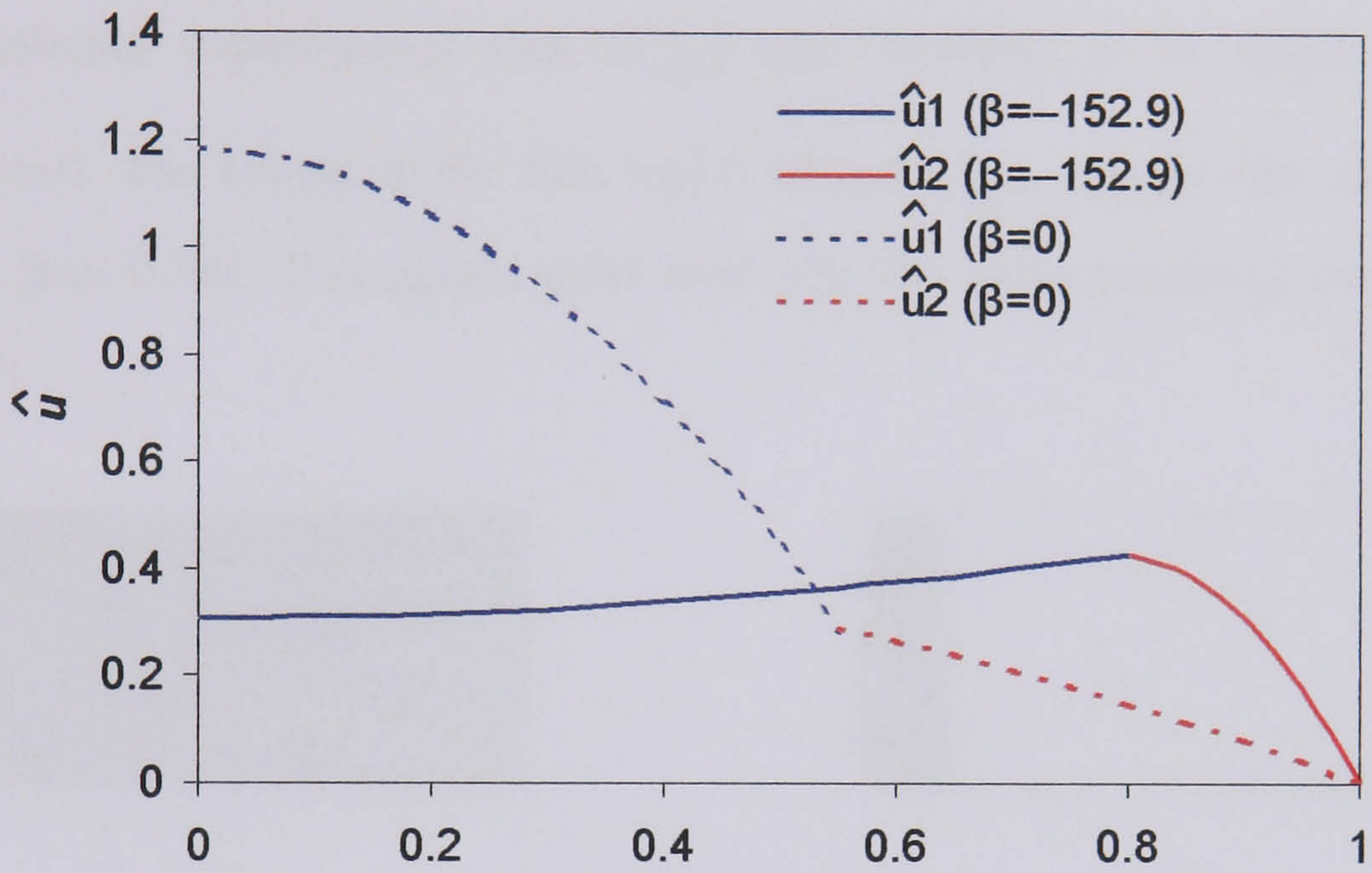


Figure 4.31 The cross sectional dimensionless velocity profile for the aqueous phase-annulus annular flow under conditions of mixture velocities of V_m = 0.65 m/s and the input oil volume fraction of ε^{o}_{input} = 69%.

Figure 4.32 shows a typical image from aqueous phase-annulus annular flow experiments and its corresponding processed black-and-white image. Analysis of 30 randomly selected images taken at the selected experimental conditions for the aqueous phase-annulus annular flow case, the average measured aqueous phase volume fraction in the cross-section plane, ε^{w}_{plane} is found from:

$$\varepsilon^{w}_{plane} = \frac{1}{N}\sum_{i=1}^{N}\frac{A_{w,i}}{A_i} \tag{4-32}$$

where $A_{w,i}$ is the area occupied by the aqueous phase in the ith image and A_i is the area of the whole cross sectional plane in the ith image (A_i is approximately constant but may vary slightly from image to image). N is the total number of images examined. If the liquid layer is assumed to be of constant thickness on all sides of the square duct, then the in-situ aqueous phase fraction $\varepsilon^w_{in-situ}$ can be calculated as:

$$\varepsilon^w_{in-situ} = \varepsilon^w_{plane}(2 - \varepsilon^w_{plane}) \tag{4-33}$$

For the selected experimental case, ε^w_{plane} was measured to be approximately 0.22 (including drops). The holdup in the film was 0.19 and $\varepsilon^w_{in-situ}$ for the film calculated from Eq. (4-33) is then 0.344. This agrees quite well with the value predicted from Eq. (4-31), namely 0.376.



(a) (b)

Figure 4.32 The typical image of aqueous phase-annulus annular flow with the mixture velocity of V_m = 0.69 m/s and input oil volume fraction ε^o_{input} = 69%; (a) original image; (b) processed black-white image (white represents oil phase).

Though the agreement between the annular flow analysis is encouraging, there are a number of factors which would need to be taken into account if the analysis were to be applied to a wider range of cases. These include:

(1) Turbulence. For the case considered the superficial Reynolds number for the aqueous and oil phases are 441 and 4002 respectively. Though the aqueous film is likely to remain laminar, the oil core would be expected to be turbulent (though it is close to transition and the effect of turbulent may not necessarily be manifested). In general, however, turbulence in the film and the core would affect local shear stresses and would need to be taken into account.

(2) Droplet entrainment. Although this case investigated showed little evidence of aqueous phase entrainment into the oil core, many cases would be such that significant drop entrainment occurs and this would need to be taken into account in a more general model. An example of an annular flow with significant entrainment is shown in Figure 4.33(a).

(3) Interface waves. The aqueous phase/oil interface is not usually flat (as assumed in the analysis) but may be covered with waves (as exemplified in Figure 4.33(b)). Such waves would lead to an increase in interfacial shear stress and this would need to be taken into account.

In further work, it may be possible to combine the LIF method with Particle-image Velocimetry (PIV) to evaluate turbulence effects. The LIF images could also be analysed to reveal the extent of droplet entrainment and the interface wave structure, though this has been attempted in the present work.



(a) (b)

Figure 4.33 Annular flow behaviour, (a) entrainment of film phase into core phase, (b) propagation of wave.

4.7 Summary

A novel, non-intrusive dye tracing technique, Laser-induced Fluorescence (LIF), was successfully applied to investigate liquid-liquid dispersed pipeline flow and proved invaluable in demonstrating flow structure in liquid-liquid flows at high dispersed phase fraction. This technique allowed direct visualisation of the dynamic evolution of the dispersion in great detail. Flow structures were revealed which had not been seen (or even been imagined) before!

The one–dimensional method was used to analyse representative cases of oil-in-aqueous phase and aqueous phase-in-oil dispersed flows and the predicted values for volume

fractions occupied by the respective phases are found to agree very well with the experimental values.

An aqueous phase-annulus annular flow was also analysed using a co-current downwards laminar annular flow model. The predicted aqueous phase fraction is in good agreement with the experimental data.

CHAPTER 5

Optical studies of Liquid-liquid Pipe Flows: II. Low Velocities

In Chapter 4, experiments were described in which the "one-through" or "open circuit" configuration of the flow circuit was employed. An alternative (and in many ways preferable) methodology would have been to pump the mixture around a closed circuit and this was tried using a centrifugal pump. However, the high shear in the pump broke the dispersed phase into tiny droplets, uncharacteristic of fully developed flows, and this approach was abandoned for high velocities, and the once-through, open circuit system adopted. However, for lower velocities, a closed-circuit system was employed in which a gear pump was employed. This pump circulated fluid around the circuit at a known volumetric flow rate and, if the pump was operated for some time before the flow was examined using the LIF system, the distribution of the fluids around the circuit would be expected to be reasonably uniform. Furthermore, with the more gentle action of the gear pump, the dispersed phase drops were not broken up excessively and the drops are expected to be more representative of those which would naturally occur at the flow conditions in the experiment. These low velocity, closed circuit experiments are described in the present chapter.

The low velocity experiments provided beautiful LIF pictures of the flow structures and these will be introduced below. As will be seen below, the structures observed at low velocity show many similarities with those seen at high velocity, despite the fact that the

velocities differ by of the order of ten-fold between the two sets of experiments. Obviously, the shear stresses are much lower than these at high velocity and slow "stretching" of fluid ligaments occur which is not seen at the higher flows.

The experimental procedure for the closed-circuit experiments is described in Section 3.5.2.3 which also describes how the phase content of the closed circuit may be adjusted.

In what follows, Section 5.1 describes the experimental results and Section 5.2 discusses the implications of the observations and presents comparisons with the dispersed and annular flow models described in Section 4.6.1 and 4.6.2 respectively. Finally, a short summary is given in Section 5.3.

5.1 Experimental Results

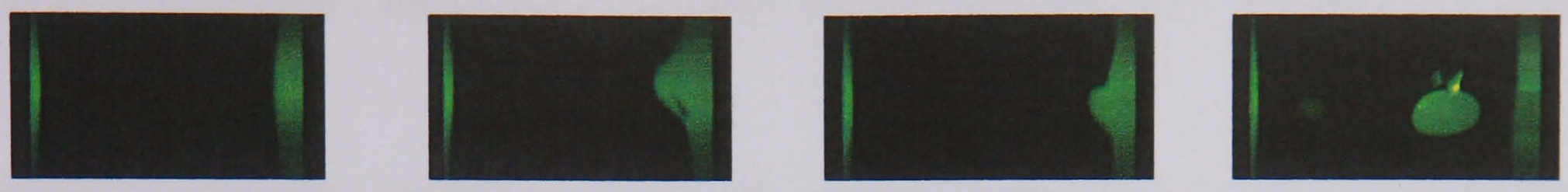
The experiments described here were for a constant volume fraction of the oil phase of 51% and at mixture velocities ranging from 0.0417 to 0.0594 m/s. As will be seen below, this range of velocities (though small) is one in which dramatic changes in flow structure occur.

The results shown in this section were all captured using a high speed video camera operating at 500 frames per second. A total of 1023 frames (full image) or 2730 (split image) were captured for each case. Tests were conducted in the steady state and also in transients following a change in velocity. Such transients occur in the operation of liquid-liquid flow lines and it is important to obtain an insight into regimes occurring during them. In what follows below, Section 5.1.1 describes the results obtained for steady state flow, Section 5.1.2 describes the transients and Section 5.1.3 describes the secondary dispersion.

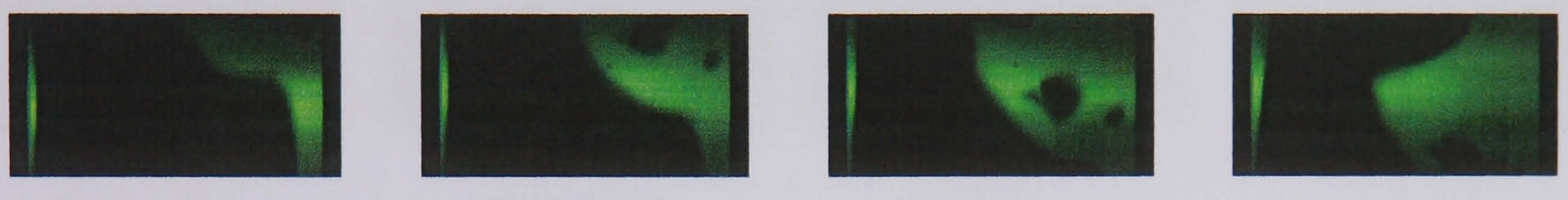
5.1.1 Steady State Flow

Figure 5.1 shows a sequence of images taken from the video obtained for a flow velocity of 0.0417 m/s. For much of the time, the flow was annular with the aqueous phase flowing on the wall. Occasionally, however, wave formation was observed (see examples in Figure. 5.1 b- c and e- l) as well as detachment of drops from the film (see Figure 5.1 d). Wave formation was often accompanied by the entrainment of drops from the core organic phase into the aqueous liquid film (Figure 5.1 g) in addition to the more normal entrainment of the film into the core (Figure 5.1 d). The propagation of a large amplitude wave on one wall

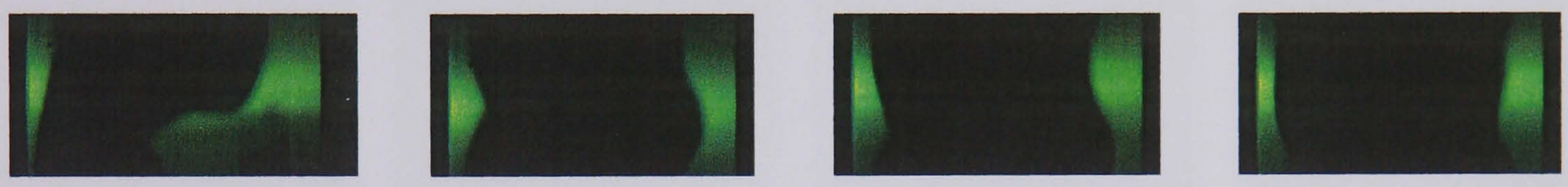
(Figure 5.1 h- l) was also observed to be accompanied by that of a smaller amplitude wave on the opposite wall.



(a) 0.0 s (b) 0.046 s (c) 0.357 s (d) 0.616 s



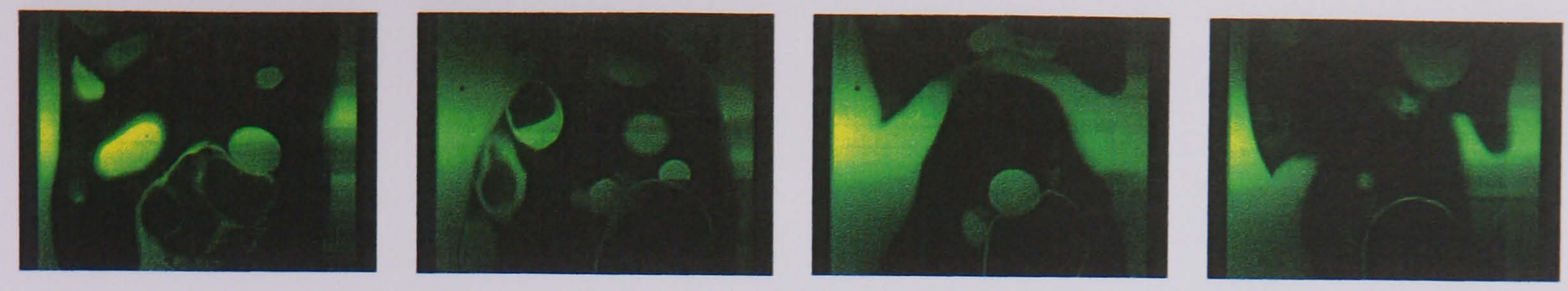
(e) 1.738 s (f) 1.748 s (g) 1.758 s (h) 1.768 s



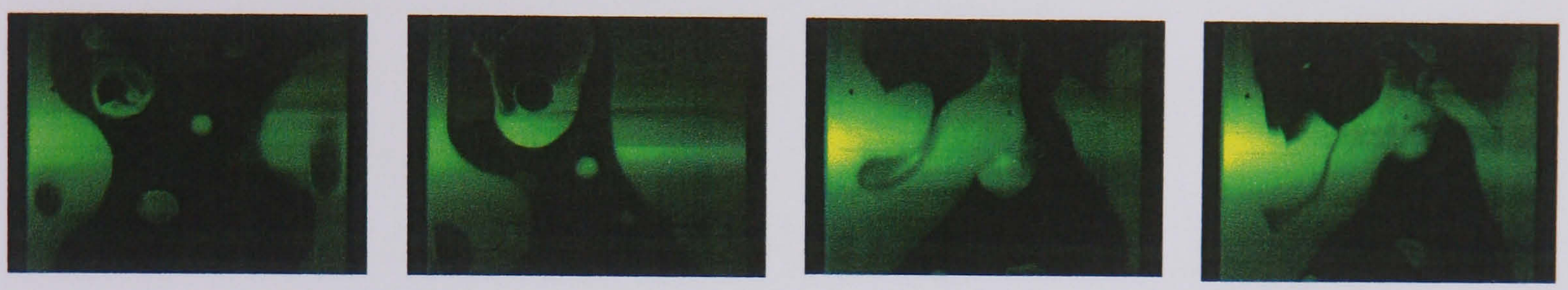
(i) 1.778 s (j) 1.788 s (k) 1.798 s (l) 1.808 s

Figure 5.1 A time-series of photographs taken over 2.046 seconds, showing annular wavy flow (51 % oil holdup). The mixure velocity is 0.0417 m/s.

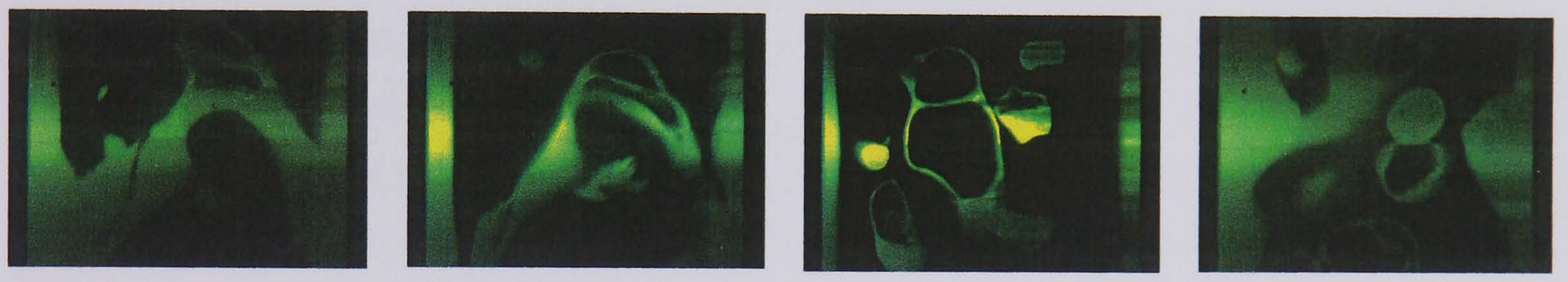
When the mixture velocity was increased to 0.0572 m/s, inter-mixing of the phases increased dramatically as shown in Figure 5.2. Though there was still a tendency for the aqueous phase to concentrate near the wall, occasional bridging of the channel occurred and complex inter-entrainment of the phases took place. The high speed video images demonstrated the wave formation, bridging, bridge breakup and secondary dispersion processes.



(a) 0.0s (b) 0.244 s (c) 0.278 s (d) 0.3 s



(e) 0.632 s (f) 0.744 s (g) 0.952 s (h) 0.964 s



(i) 0.976 s (j) 1.0 s (k) 1.322 s (l) 1.914 s

Figure 5.2 A time-series of photographs of the annular flow with aqueous phase dispersion in the oil core. The mixture velocity is 0.0572 m/s and other parameters are the same as those described in Figure 5.1.

As the flow velocity was increased further, the flow changed to a dispersed flow regime (see Figure 5.3). In this regime, the aqueous phase was continuous over the whole pipe cross section with discrete oil droplets dispersed within it. Due to the still relatively low velocity, most of the oil drops were large and assumed a variety of shapes, including spherical (see Figure 5.3 a), cap-like (see Figure 5.3 b) and even flat (see Figure 5.3 c).

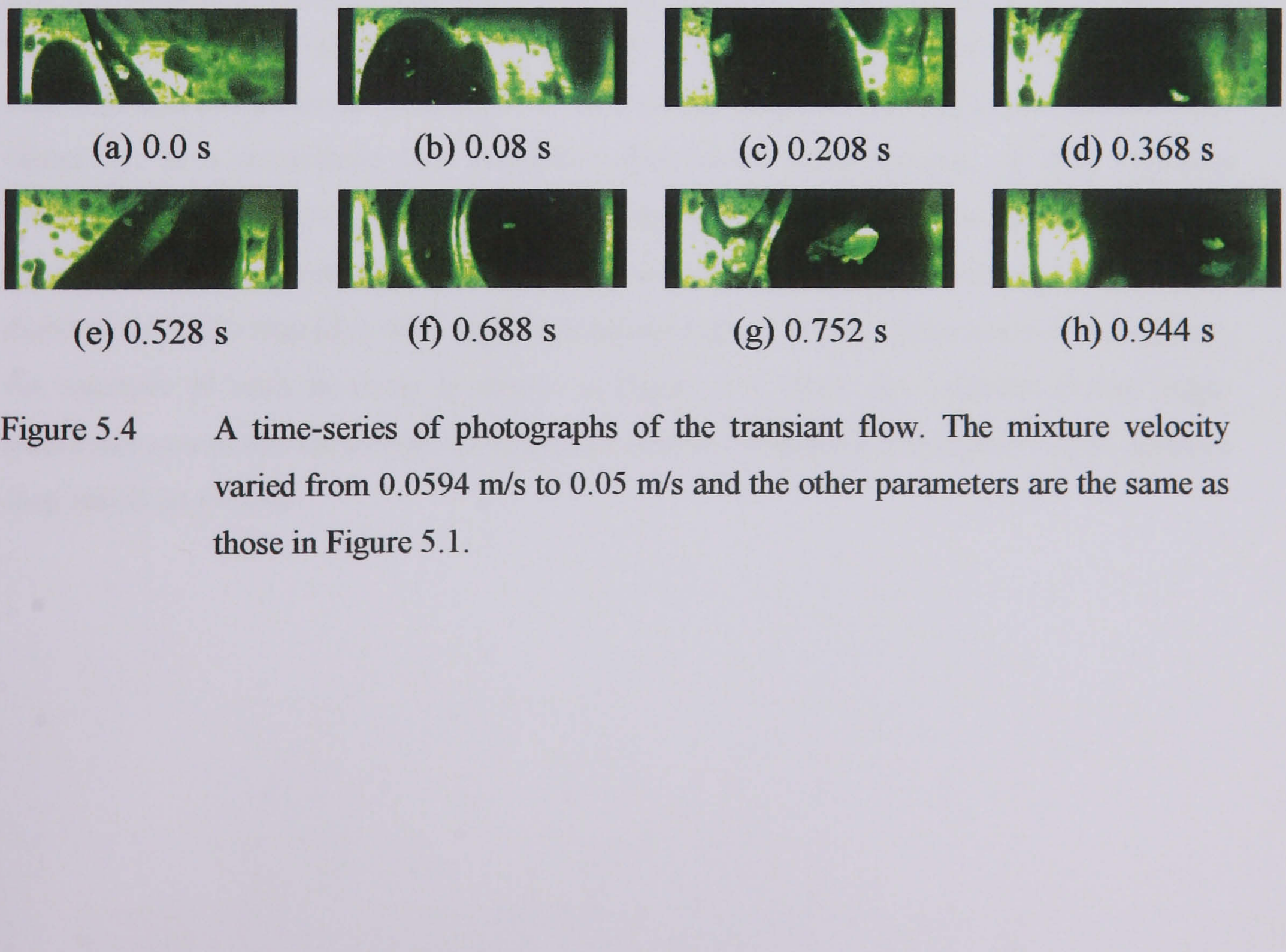


(a) 0 s (b) 0.936 s (c) 2.1 s (d) 2.372 s

Figure 5.3 A time-series of photographs taken over 5.546 seconds, which shows the oil-in-aqueous phase dispersed flow. The mixture velocity is 0.0594 m/s and other parameters are the same with those in Figure 5.1.

5.1.2 Transient Tests

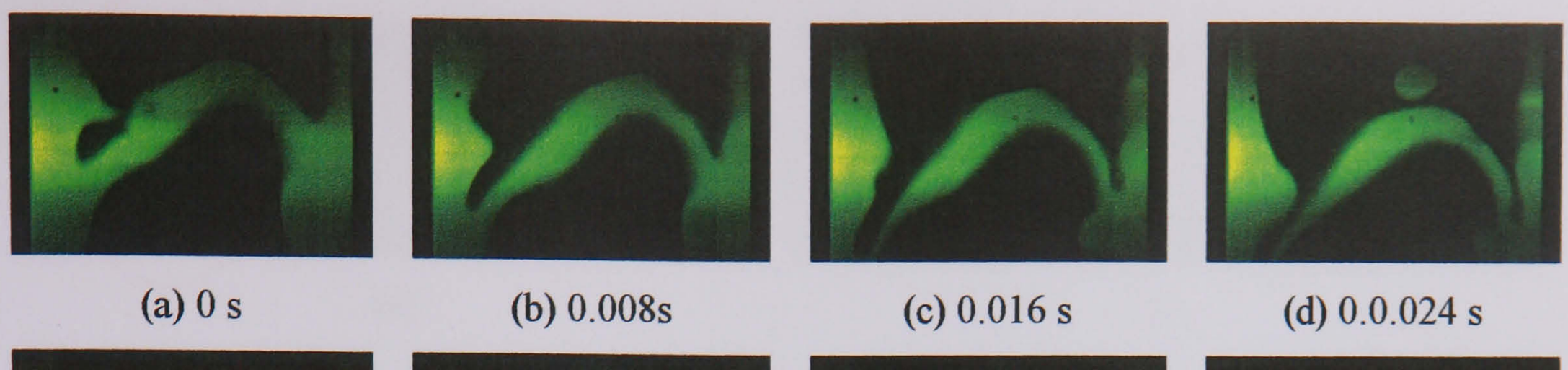
Transient experiments were performed, in which, at the start of the transient, the velocity was decreased by reducing the speed of the gear pump motor. During the transients, the flow structures are more complex than those formed in the steady state. Specifically, the plug or slug flow pattern occurs, though it is not seen in steady state flows over the same range of flowrates. Figure 5.4 presents such a case. In Figure 5.4 (a), an oil-in-aqueous phase dispersed flow initially appeared in pipe. As the velocity decreased, oil drops turn into oil plugs or slugs (Figure 5.4 b-h). During the transient process, some complex flow structures occur frequently, such as several oil slugs travelling side by side (Figure 5.4 f) and, aqueous drop entrainment into a slug (Figure 5.4 g). Figure 5.5 illustrates the coalescence of two slugs after the bridge is broken.



(a) 0.0 s (b) 0.08 s (c) 0.208 s (d) 0.368 s

(e) 0.528 s (f) 0.688 s (g) 0.752 s (h) 0.944 s

Figure 5.4 A time-series of photographs of the transiant flow. The mixture velocity varied from 0.0594 m/s to 0.05 m/s and the other parameters are the same as those in Figure 5.1.



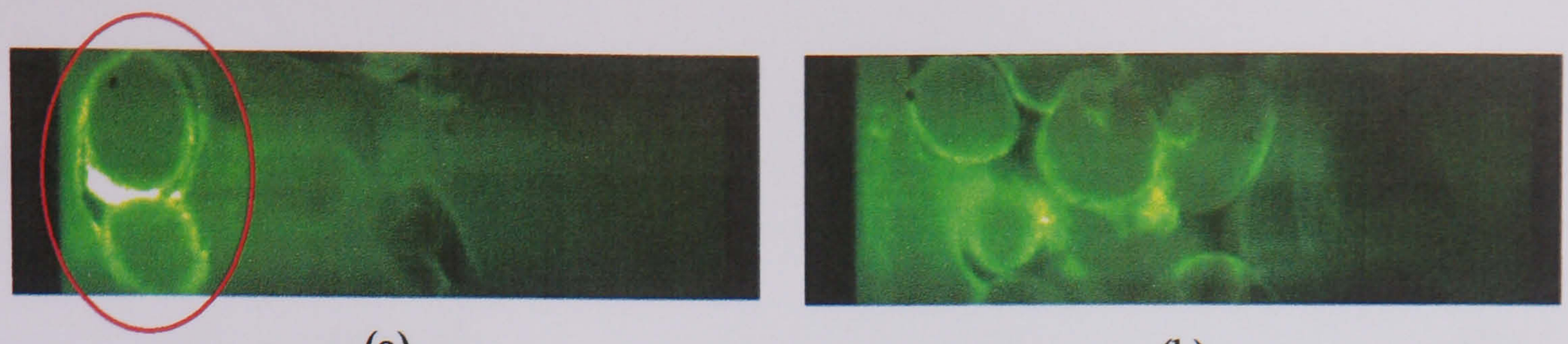
(a) 0 s (b) 0.008s (c) 0.016 s (d) 0.0.024 s

(e) 0.032 s (f) 0.04 s (g) 0.048 s (h) 0.058 s

Figure 5.5 A time-series of photographs showing two oil drops undergoing coalescence. Here, the mixture velocity varied from 0.0572 m/s to 0.05 m/s and the other parameters are the same as those in Figure 5.1.

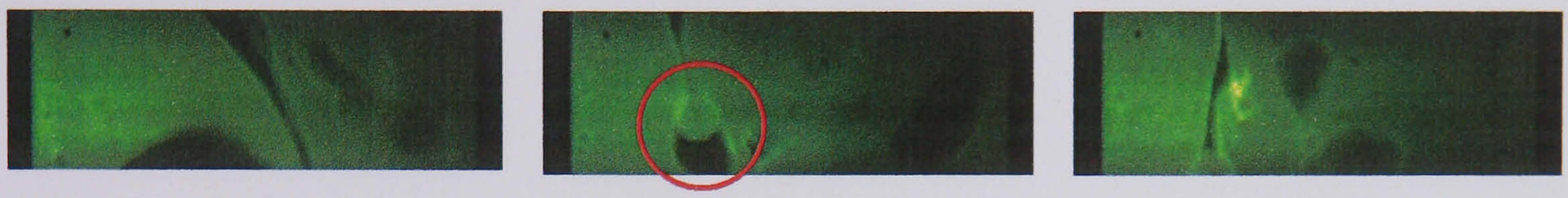
5.1.3 Secondary Dispersion

The results presented in Chapter 4 have demonstrated that the flow structures in vertical flow are very complex, especially in the mixed (or transition) regime, which is accompanied by the formation of secondary dispersions. In the low velocity experiments described in the present Chapter, secondary dispersions were also observed in the mixed and dispersed flow regimes. Examples of an o/w/o and of a w/o/w secondary dispersion are shown in Figures 5.2a (the aqueous phase-in-oil present in the core of the pipe) and Figure 5.6, respectively. Generally, it is considered that secondary dispersions occur because of drop collision (between pairs of drops or between multiple drops) and coalescence or drop deformation. However, in the present experiments our observations indicate that the w/o/w secondary dispersions in the transition flow regime occurred mainly by the coalescence of two waves. An example of such an event is shown in Figure 5.7. Here, the collision of two large-amplitude waves has led to their coalescence and the subsequent entrainment of an aqueous drop inside an oil film.



(a) (b)

Figure 5.6 W/O/W dispersions observed in the transition flow regime and other parameters are the same as those in Figure 5.1.



(a) 0 s (b) 0.05 s (c) 0.072 s

Figure 5.7 The formation of w/o/w dispersion in transient flow, here, the mixture velocity varied from 0.059 m/s to 0.0 m/s and other parameters are the same as those in Figure 5.1.

5.2 Discussions

The flow patterns observed using the closed circuit at low mixture velocity included annular, wavy annular and dispersed flow; these regimes are quite similar to those described in Chapter 4 for the high velocity system.

The one-dimensional drift flux model for dispersed flow and the laminar model for co-current downward annular flow (as described in Chapter 4), are also applied here to predict the in-situ oil holdup. Two flow pattern conditions, which are respectively annular flow (V_m = 0.0417m/s) and annular-dispersed flow (V_m = 0.0572 m/s) with input oil holdup $\varepsilon^o_{input} = 51\%$, are studied and compared with the model predictions. Figure 5.8 shows the calculated in-situ oil holdup ($\varepsilon^o_{prediction}$) for annular and dispersed flow respectively (based a drop size of d=4 mm) at various mixture velocities, together with the measured in-situ oil holdup ($\varepsilon^o_{measured}$). In order to obtain the oil holdup from experimental measurements, 50 images were selected for both annular and annular-dispersed flow cases. Figure 5.9 illustrates an example for the original and processed images for the annular-dispersed flow case.

For annular flow, the in-situ oil holdup ($\varepsilon^o_{in-situ}$) is related to the fraction of the oil phase in the viewing plane by the expressions:

$$\varepsilon^o_{in-situ} = (\varepsilon^o_{plane})^2 \tag{5-1}$$

which is consistent with Eq. (4-32). For dispersed flow, on the other hand, we have:

$$\varepsilon^o_{in-situ} = \varepsilon^o_{plane} \tag{5-2}$$

Calculating $\varepsilon^o_{in-situ}$ for the annular flow case from Eq. (5-1) gives a value $\varepsilon^o_{in-situ,m}$=0.75. this is in good agreement flow model ($\varepsilon^o_{in-situ,p}$=0.82) (see Figure 5.8).

The annular-dispersed flow case lies between the pure annular and the pure dispersed case and the value of ε^o_{plane} was determined as 0.64. This corresponds to values $\varepsilon^o_{in-situ}$ for annular flow of 0.41 (Eq. (5-1)) and to a value of $\varepsilon^o_{in-situ}$ of 0.64 (Eq. (5-2)) for dispersed. These values may be compared with the predicted values (using the methods described in Chapter 4):

$$\varepsilon^o_{in-situ,p} = 0.80 \text{ for annular flow}$$

$$\varepsilon^o_{in-situ,p} = 0.67 \text{ for dispersed flow}$$

and it may be concluded that the flow is more closely represented in this case by the dispersed flow model.

It is interesting to calculate the values of v_w and v_o (the mean in-situ velocities) using Eqs. (4-13a) and (4-13b) for the above cases. The results are as follows:

Superficial velocity (m/s)	Regime assumed	$\varepsilon^o_{in-situ,m}$	v_w (m/s)	v_o (m/s)	v_w/v_o
0.0417	Annular	0.75	0.0817	0.0284	2.88
0.0572	Dispersed	0.64	0.0779	0.0456	1.71

Because of the low superficial flow velocities, v_w/v_o is much greater than observed for high superficial velocities (e.g. v_w/v_o =1.02 calculated from the example high velocity case in Eqs. (4-13a) and (4-13b)).

It seems, from the observations, that the dramatic transition in flow regime between the superficial velocities of 0.0417 m/s and 0.0572 m/s results from the film interfaces becoming unstable leading to wave growth at the interface and drops being torn from the film to make the flow more like a dispersed flow. The mechanisms for these events are being investigated in numerical studies at Edinburgh University in a project linked to the present one.

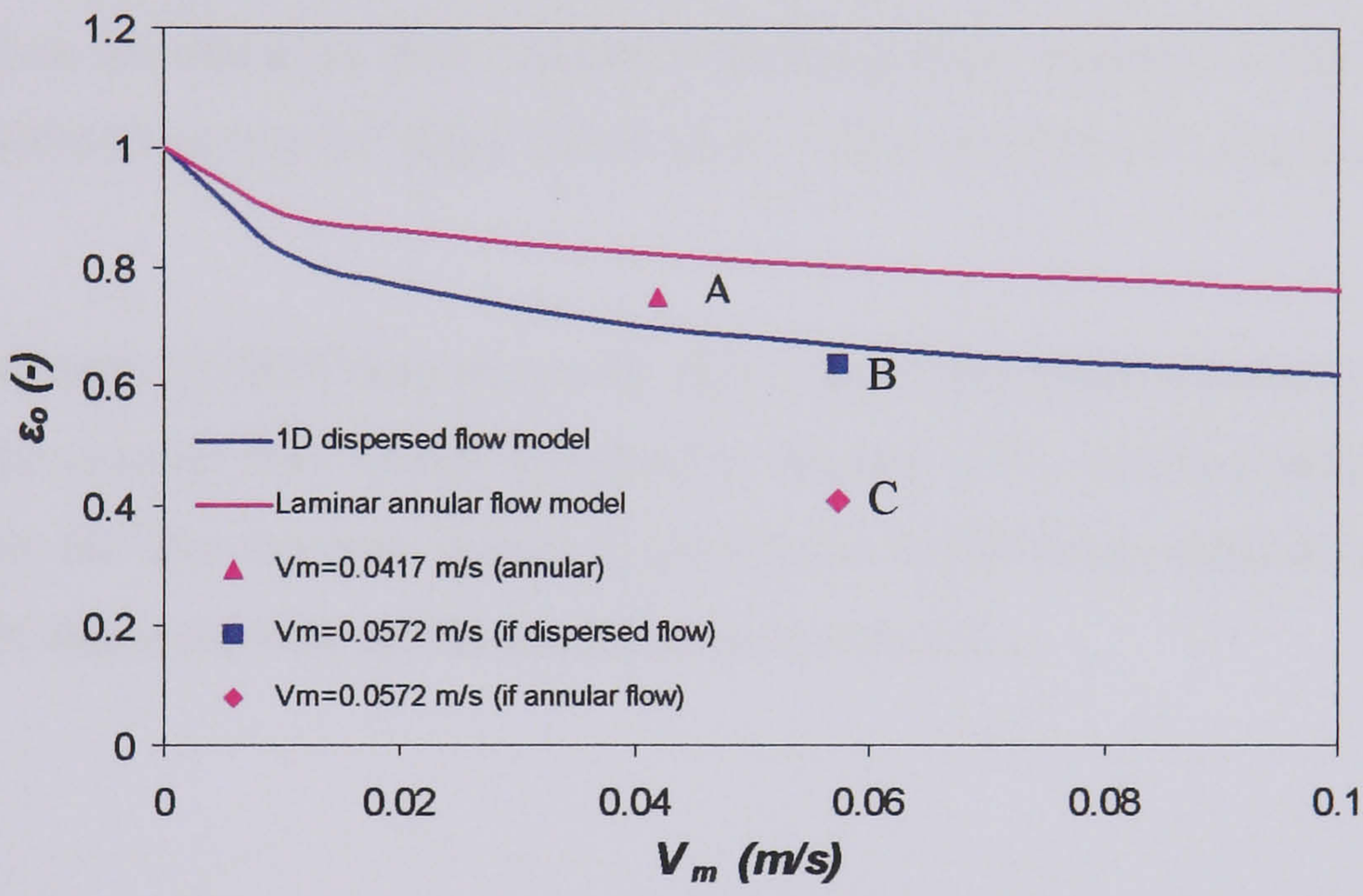
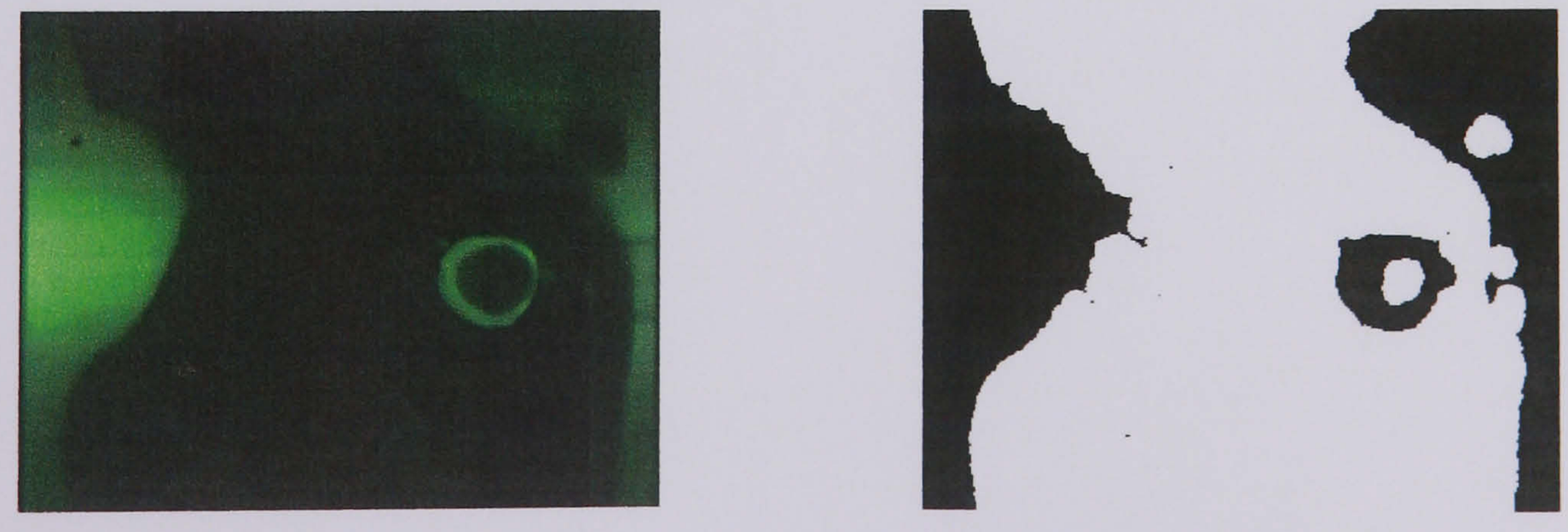


Figure 5.8 The prediction of oil in-situ volume fraction from one dimensional dispersed flow model and laminar annular flow model, in comparisons with the experimental data.



(a) (b)

Figure 5.9 An example image in annular-dispersed flow, (a) original image; (b) processed black-white image (white represents oil phase).

5.3 Summary

In work described in this Chapter, the LIF technique was used to investigate liquid-liquid vertical pipe flow in a closed experimental circuit at very low mixture velocities. The dynamic evolution of annular, mixed and dispersed flows were observed, as well as the associated physical processes such as wave coalescence and the formation of secondary dispersions.

The experimental results presented in this Chapter suggest that as the flow velocity was increased, the flow undergoes a transition from annular to wavy- annular to mixed (or transition), and finally dispersed flow. The results also indicated that secondary dispersions, such as w/o/w and o/w/o, occur in the dispersed core of a mixed flow. It has also been shown that, in transient flow (in which the flow velocity is decreased), the structure of the flow was very complex and the formation of 'slugs' could occur, which resemble the situation in gas-liquid flows.

At the lower velocity (0.0417 m/s) in annular flow, the in-situ phase fraction is in good agreement with the annular flow model described in Section 4.6.2. At the highly velocity (0.0572 m/s), when the flow becomes higher dispersed, the in-situ phase fraction is in good agreement with the dispersed flow model described in Section 4.6.1.

CHAPTER 6

Phase Inversion & Associated Phenomena in a Liquid-liquid Agitated Vessel System

In addition to the pipe flow studies described in Chapters 4 and 5, the laser-induced fluorescence (LIF) technique was also used, in the present work, to study phase inversion process in an agitated vessel and this work is described in the present chapter.

Liquid-liquid dispersions in agitated (or stirred) vessels are frequently employed in the chemical industry for reactions and for solvent extraction. Phase inversion is an important phenomenon in such processes and, in fact, most research work on phase inversion has been carried out in agitated systems. However, the mechanism of phase inversion in agitated vessels is still not clearly understood, hence the present study.

The Chapter is organised as follows. First, the experimental procedure is introduced in Section 6.1. Section 6.2 describes the study of phase inversion at constant stirred speed, which a particular focus on the ambivalent range. Section 6.3 presents results on the dynamic evolution of phase inversion process resulting from an increase in stirred speed. Visualization of the two basic processes in agitated systems, drop breakup and coalescence, is discussed in Section 6.4. Secondary and multiple dispersion and complex flow structures associated with phase inversion, are introduced in Section 6.5. Section 6.6 presents the drop

size distributions before and after phase inversion. A discussion of phenomena associated with phase inversion is presented in Section 6.7. Finally, a short summary is given in Section 6.8.

6.1 Experimental Procedure

In the first series of experiments, the stirred speed was kept constant and the phase fraction changed progressively by adding one or the other of the two phases. In order to determine the hold-up for phase inversion from an aqueous phase-in-oil (w/o) to an oil-in-aqueous phase (o/w) emulsion, the experimental run was started with a w/o emulsion of known dispersed phase holdup at a chosen constant stirrer speed (e.g. 500 rpm). A small volume of aqueous solution was then added to by adding drops from a pipette and the ensuing dispersion dynamics are observed visually using the laser system (see Chapter 3). Following the visual observation of phase inversion from a w/o to an o/w emulsion, the hold up at inversion was determined by dividing the volume of aqueous solution in the vessel by the total volume. The stirrer speed was then determined by counting the number of frames taken for one rotation of the impeller to be executed using the high-speed camera. The error involved in measuring the stirrer speed and volume fractions was estimated to be between 2-5%.

In order to record images of the process of phase inversion, say, from an o/w to a w/o dispersion, the stirrer speed was increased at a fixed phase holdup (e.g. 45% water holdup). The initial emulsion with a given aqueous phase fraction was generated by stirring at a constant lower stirrer speed for several minutes. The whole phase inversion process was recorded at 500 frames/second with the video camera for a time duration of approximately 5.46 seconds. The stages immediately before, during and after phase inversion, however, were recorded at 2000 frames/second. During the experiments, it was found that the initial distribution of emulsion was important for the occurrence of phase inversion. When the speed increases gradually, two things can happen; the emulsion becomes finer or phase inversion happens, and it can also be seen that a less uniform drop size distribution tends to lead to phase inversion.

6.2 Ambivalence Range

The majority of the experiments conducted to investigate phase inversion in liquid-liquid dispersions have demonstrated the existence of an ambivalence region, which corresponds to a range of volume fractions over which either component can be the stable dispersed phase (Selker & Sleicher, 1965; Efthimiadu *et al.*, 1994; McClarey & Mansoori, 1978; Tidhar *et al.*, 1986; Dong & Tsouris, 2001; Deshpande & Kumar, 2003). This region reflects the existence of a hysteresis effect, and, as described in the Literature Review (Section 2.2.1.4), the extent of this range depends on how the dispersion is produced (Arashmid & Jeffreys, 1980). The ambivalence range varies between systems: any factor that influences phase inversion also affects its boundaries. At high levels of turbulence, however, several studies (Tidhar *et al.*, 1986; Brauner & Ullmann 2002; Deshpande & Kumar, 2003) have shown that phase inversion occurs in the absence of hysteresis and the associated ambivalence region, i.e. at a reasonably well defined value of the holdup, which does not depend on the impeller speed or the mixture velocity but solely on the physical properties of the liquids.

In the experiments described here, an ambivalence range was also observed upon variation of the dispersed phase holdup (oil holdup for oil-in-aqueous phase dispersion or aqueous phase holdup for water-in-oil dispersion) while keeping the stirrer speed fixed. This is shown in Figure 6.1 where the variation of the dispersed phase holdup is plotted with stirrer speed. Inspection of Figure 6.1 reveals the hysteresis effect, which accompanies the inversion process. The dispersed phase holdup at inversion clearly depends on whether the experimental run was started from a w/o or an o/w emulsion, being smaller in the former case than in the latter. It can also be seen that the width of the ambivalence range decreases substantially with increasing stirrer speed, resulting from a decrease in the inversion holdup from an aqueous phase-in-oil (w/o) emulsion and increase in inversion holdup from an oil-in-aqueous phase (o/w) emulsion. The w/o and o/w phase inversion transitions occur at nearly the same holdups at above about 1000rpm. The phase inversion holdup appears to change little with stirrer speed beyond a value of 1200 rpm for this set of parameters. These findings are largely in line with those reported in previous experimental studies (Kumar *et al.*, 1991, Norato *et al.*, 1998, Deshpande & Kumar, 2003).

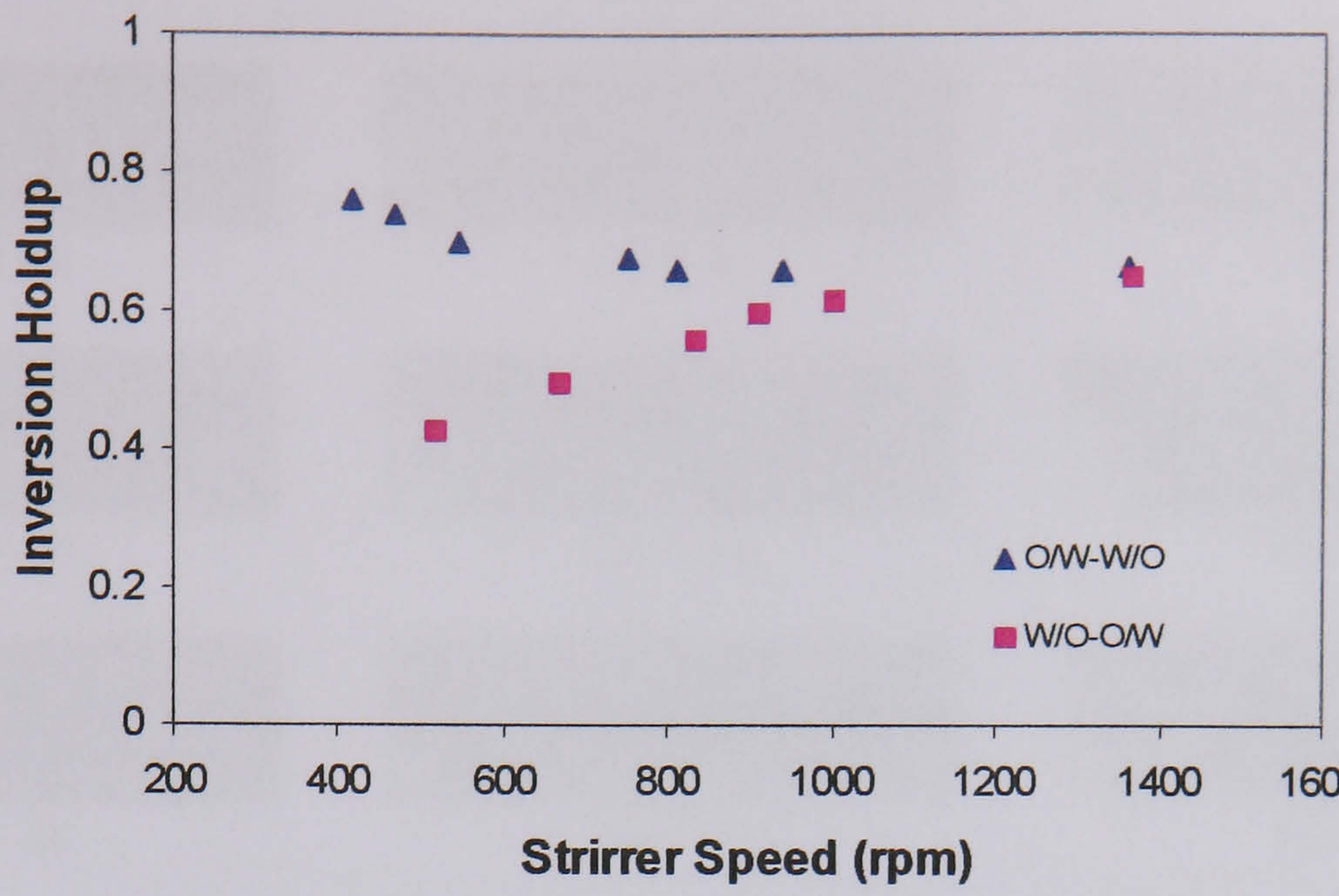


Figure 6.1 Variation of the organic phase holdup with stirrer speed for a 39%wt. $CaCl_2$ solution and Exxol oil showing the ambivalence range.

6.3 Phase Inversion Process

As described in Section 6.1, the phase inversion process was recorded by carrying out transient experiments in which stirred speed was increased and the subsequent behaviour examined. The experimental results are illustrated in Figure 6.2-6.20. It will be noted that the incident laser sheet is attenuated as it passes from left to right across the cell; thus, the brightness (and hence the clarity) of the image reduces across the pictures.

The experimental results shown in Figure 6.2 were for a 45% aqueous fraction case, and started from an emulsion generated by stirring at a stirrer speed of approximately 400 rpm at which an o/w emulsion exists. The stirrer speed was then gradually increased up to a value of 1000 rpm over a period of around 3-4 s. At the higher speeds, a stable w/o emulsion existed. Thus, phase inversion occured during the ramping up of the stirrer speed. For this case, the camera frame rate was set to 500 frames per second and a total of 2730 frames were saved. The camera was started at the same time that the increase in stirrer speed was initiated.



(a) 0.0s



(b) 0.2s



(c) 0.4s



(d) 0.6s



(e) 0.8s



(f) 1.0s



(g) 1.2s



(h) 1.4s



(i) 1.6s



(j) 1.8s



(k) 2.0s



(l) 2.2s



(m) 2.4s



(n) 2.6s



(o) 2.8s



(p) 3.0s



(q) 3.2s



(r) 3.4s



(s) 3.6s



(t) 3.8s



(u) 4.0s



(v) 4.2s



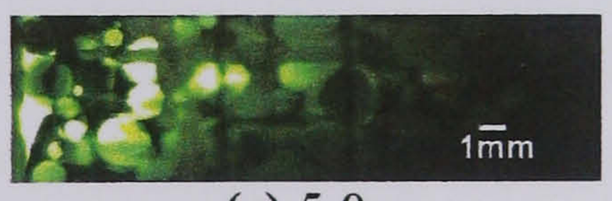
(w) 4.4s



(x) 4.6s



(y) 4.8s



(z) 5.0s



(aa) 5.2s



(ab) 5.4s



(ac) 5.458s

Figure 6.2 A time-series of photographs taken over 5.458 seconds, showing the dynamic evolution of an o/w emulsion (45 % aqueous solution holdup) to a w/o emulsion using the LIF technique.

Figure 6.2 presents photographic evidence of the complicated dynamic situation and associated complex structures, which were observed prior to, during and after the phase inversion had taken place from an o/w to a w/o dispersion. Before phase inversion (see panels a-i), more large oil drops appear (Figure 6.2 g and h). Inspection of panels (j)-(r) of Figure 6.2 reveals that the inversion process became apparent at approximately 1.8s (Figure 6.2 j, in which an elongated oil drop with some water droplets inside appears), and highly prominent at 3.6s (Figure 6.2 s) beyond which a w/o emulsion was observed clearly, as shown in panels (s)-(ac). In addition, a large water drop with oil droplets inside (see left side of Figure 6.2 k-z) is observed, which sticks on the vessel wall, shrinks and releases the oil droplets as phase inversion develops. The whole set of photographs suggests that the phase inversion process is a gradual rather than a catastrophic one, as previously thought. Whether or not phase inversion occurs depends critically upon the stirrer speed and phase holdup. In this case, the stirrer speed was gradually increased so that phase inversion eventually occurs. The results shown are quite reproducible with phase inversion always occurring at around 2 s for the same set of conditions and stirrer ramp-up.

In order to display the details of the transition from one emulsion to the other, Figures 6.3-6.4 show photographic snap-shots of the dynamics before, during and after phase inversion from an o/w (38 % aqueous solution) to a w/o emulsion, respectively. Here, the stirrer speed was increased from 366 rpm to 750 rpm and photographs were taken at 2000 frames/sec with a total of 2730 frames saved. [Note that the group of photos shown in Figure 6.2 illustrated the pre-, during and post-phase inversion periods. The same three stages of phase inversion phenomenon captured at the higher framing rate of 2000 frames per second are shown in Figures 6.3-6.4. 2730 frames have been saved for each photo group]. Prior to phase inversion, the drop sizes become progressively larger due to an increase in the rate of coalescence. During phase inversion, the oil drops deform, elongate and collide with other drops leading to even higher coalescence rates and, consequently, even larger drops are formed (see Figures 6.2 j and k and Figures 6.3 a- f). Direct visualisation of the emulsion evolution showed that phase inversion is directly related to the local drop-size-distribution and does not occur globally. This is demonstrated in Figures 6.3 u and 6.3 ab, in which the co-existence of both w/o and o/w emulsions can be discerned.

These results also show that the dynamic evolution of the emulsion is accompanied by the formation of secondary dispersions, as previously reported in the literature (Pal *et al.*, 1993; Pacek *et al.*, 1994; Pacek & Nienow, 1995; Kumar, 1996; Groeneweg *et al.*, 1998, Yang *et al.*, 2000; Sajjadi *et al.*, 2002; Klahn *et al.*, 2002; Agterof *et al.*, 2003), and multiple-dispersions; which occur during the coalescence of several drops, bringing about the

inclusion of the continuous phase into the newly formed drop. An example of a secondary dispersion is shown in Figure 6.3 (m) during the transition from an o/w to a w/o emulsion. Here, a water drop, corresponding to the dispersed phase after phase inversion, contains a drop of the pre-inversion dispersed phase (oil). At first these water drops are very large, but subsequently either break up due to the prevailing shear field force into smaller drops (see Figure 6.2 s-ac and Figure 6.4) or coalesce and become a continuous phase once again. According to Groeneweg *et al.* (1998), Klahn *et al.*, (2002), Sajjadi *et al.* (2002) and Agterof *et al.* (2003), in addition to break-up and coalescence, escape due to the deformation of the host drops (due to shear) and inclusion of the secondary droplets are two competing processes for secondary dispersions. At steady state, a dynamic equilibrium is reached and the size of multiple drops remains unchanged. On the other hand, a continuous increase in the size of the multiple drops, as effective dispersed phase holdup increases, would eventually lead to phase inversion. The photos shown in Figures 6.2-6.4 provide an experimental corroboration of these suggestions and demonstrate that phase inversion eventually follows when the rate of droplet inclusion dominates that of droplet escape. The formation of secondary and multiple-dispersions is further discussed below. The phenomena observed could be reproduced and the pictures shown are typical of many showing the same effects.



(a) 0s



(b) 0.05s



(c) 0.1s



(d) 0.15s



(e) 0.2s



(f) 0.25s



(g) 0.3s



(h) 0.35s



(i) 0.4s



(j) 0.45s



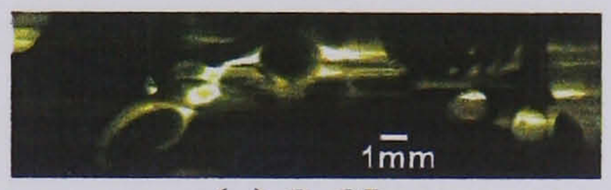
(k) 0.5s



(l) 0.55s



(m) 0.6s



(n) 0.65s



(o) 0.7s



(p) 0.75s



(q) 0.8s



(r) 0.85s



(s) 0.9s



(t) 0.95s



(u) 1.0s



(v) 1.05s



(w) 1.1s



(x) 1.15s



(y) 1.2s



(z) 1.25s



(aa) 1.3s

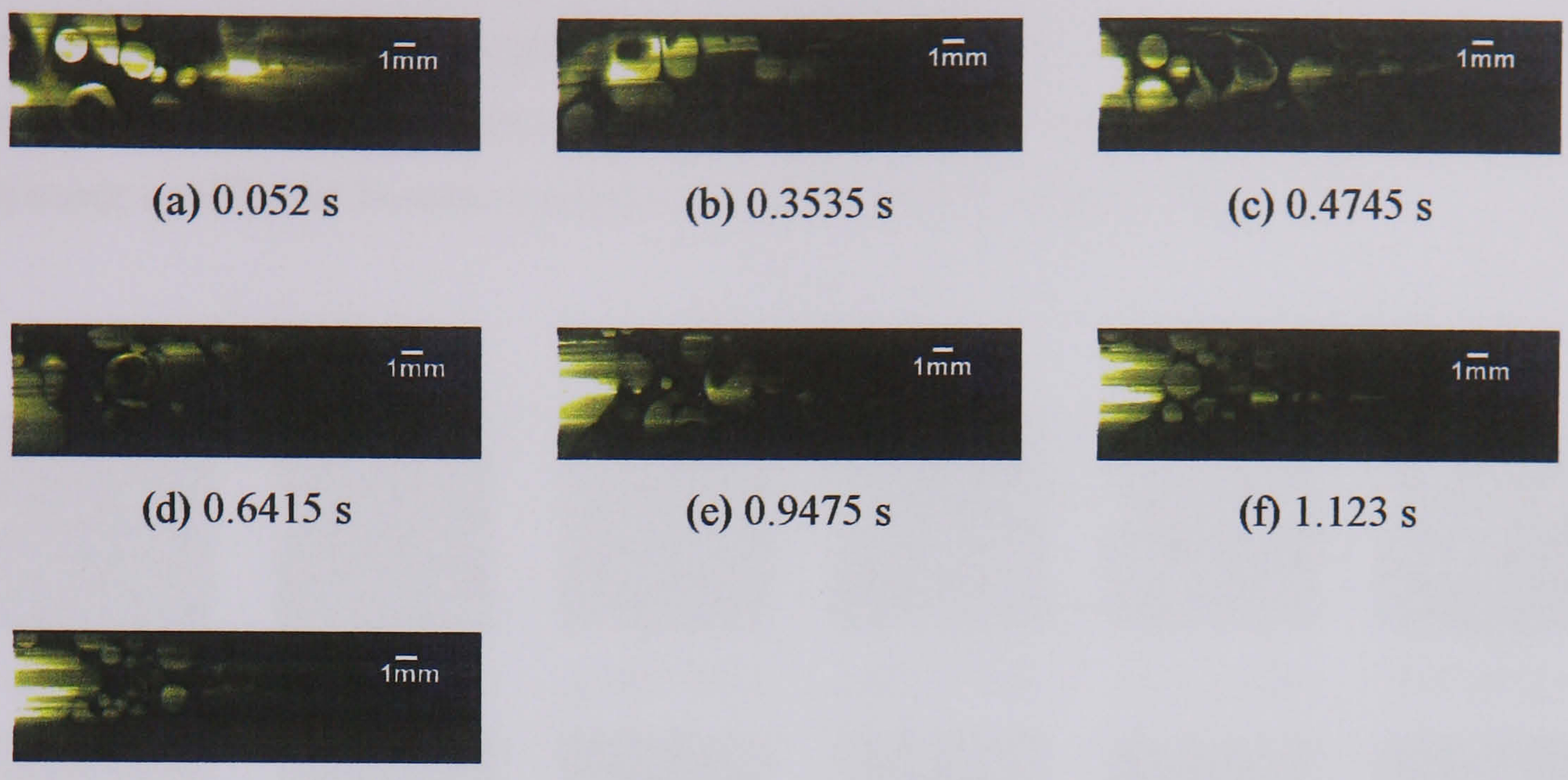


(ab) 1.35s



(ac) 1.365s

Figure 6.3 A time-series of photographs taken over 1.365 seconds, showing the transition from an o/w emulsion (38% aqueous solution holdup) to a w/o emulsion using the LIF technique.



(a) 0.052 s (b) 0.3535 s (c) 0.4745 s

(d) 0.6415 s (e) 0.9475 s (f) 1.123 s

(g) 1.1265 s

Figure 6.4 A time-series of photographs taken over 1.365 seconds, showing the dynamic evolution of the w/o emulsion (38% aqueous solution holdup) resulting from the phase inversion shown in Figure 6.3 using the LIF technique.

6.4 Drop Breakup and Coalescence

Drop breakup and coalescence are two basic processes, which accompany the evolution of turbulent liquid-liquid dispersions. When a steady state dispersion is reached, breakage and coalescence reach a dynamic equilibrium, and they control the steady state drop size distribution. In the absence of such an equilibrium, which may occur following a decrease in the stirrer speed and/or an increase in the dispersed phase holdup, the coalescence rate becomes increasingly dominant over that of break-up, resulting in an overall increase in drop size, which promotes phase inversion. Pacek *et al.* (1994a) postulated that simultaneous break-up of the continuous phase is required to explain the inversion process. By monitoring the change in the full drop size distribution and the mean drop size, they show that both continuous phase break-up to produce droplets-within-drops (i.e. secondary dispersions) and enhanced coalescence of the dispersed phase to give larger drops play a significant role in phase inversion. In the time-series shown in Figures 6.5 and 6.6, which comprise photographs of coalescence and breakup events prior to phase inversion for the same parameters as those used in Figures 6.3-6.4, it can be seen that, before phase inversion, the dispersed drops become relatively large due to high coalescence rates. These large drops then elongate and undergo severe deformation, breakup and coalescence with other drops.

As shown in Figure 6.6, the rate of coalescence appears to dominate that of breakup despite a continual increase in the magnitude of the stirrer speed, ultimately giving rise to phase inversion. After phase inversion, the rate of drop breakup increases, eventually resulting in a dynamic equilibrium between coalescence and breakup, as shown in Figure 6.7.



Figure 6.5 Photographic evidence for the coalescence of two relatively large oil drops before phase inversion for the same parameters as in Figure 6.3.

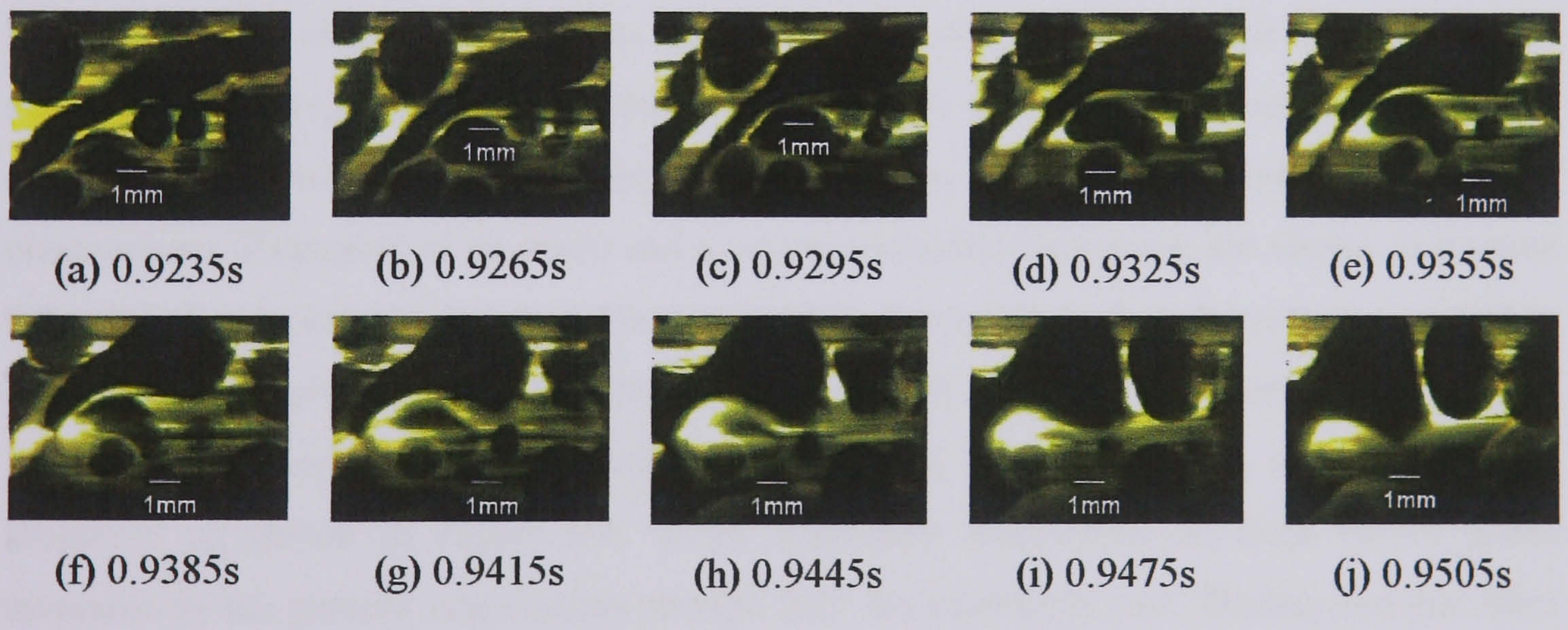
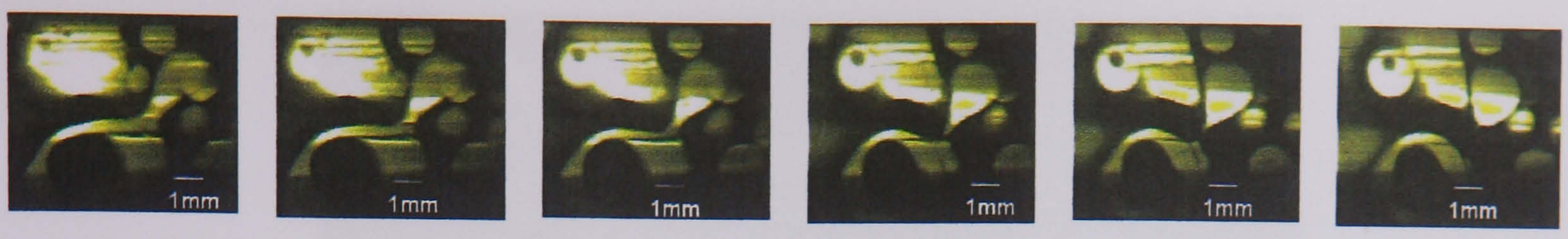


Figure 6.6 A series of photographs showing an elongated oil drop undergoing deformation and breakup. Subsequently, one of the daughter drops is seen to coalesce with neighbouring oil drops before phase inversion for the same parameters as in Figures 6.3.



(a) 0.420s (b) 0.435s (c) 0.450s (d) 0.465s (e) 0.480s (f) 0.495s

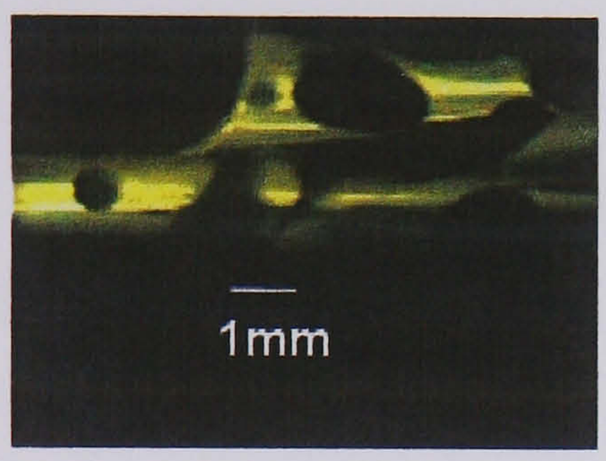
Figure 6.7 A large water drop undergoing breakup after phase inversion. Coalescence of regions of the continuous phase is also visible for the same parameters in Figure 6.4.

6.5 Secondary and Multiple Dispersions

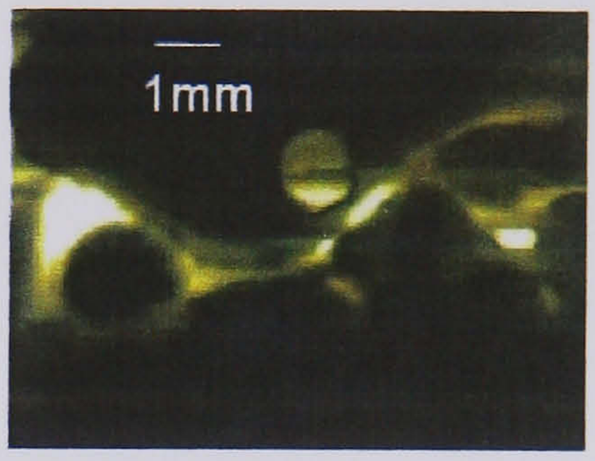
The existence of secondary dispersions (or double emulsions) has been demonstrated by several investigators (Rodger *et al.*, 1956; Quinn & Sigloh, 1963; Luhning & Sawistowski, 1971; Pal, 1993; Pacek *et al.*, 1994 a & b; Pacek & Nienow, 1995; Kumar, 1996; Sajjadi *et al.*, 2002; Klahn *et al.*, 2002; Agterof *et al.*, 2003). These studies have noted that oil droplets in w/o or o/w/o dispersions are much more likely to occur than water-in-oil-in-water or w/o/w dispersions, even in the case of systems with equal phase densities and viscosities. Kumar (1996) suggested that this phenomenon can be explained by noting that oil drops in water experience repulsion due to the overlapping of the electrical double layers leading to low coalescence efficiencies whereas water drops in oils of low dielectric constant do not experience such repulsions and are therefore associated with high coalescence. The relative abundance of o/w/o over w/o/w dispersions has been noted in the present experimental observations. Examples of an o/w/o and a w/o/w secondary dispersion are shown in Figures 6.8 and 6.9, respectively. Pacek & Nienow (1995) claimed that when the system approaches inversion from o/w to w/o, droplets-in-drops are not seen up to inversion and appear immediately afterwards and that droplets of water in drops of oil had never been seen. However, as shown in Figure 6.9, w/o/w secondary dispersions do exist before phase inversion in the present experiments though they are extremely rare. During and just after phase inversion, a large number of the o/w/o secondary dispersions appear. As the stirrer speed is increased following phase inversion, the number of o/w/o secondary dispersions decreases gradually.



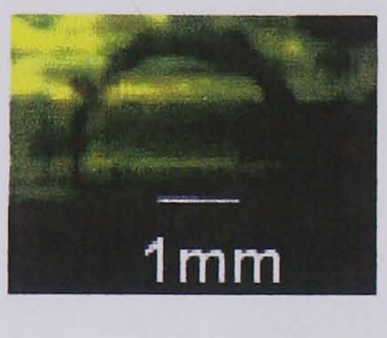
Figure 6.8 An example of an o/w/o secondary dispersion observed after phase inversion had taken place for the same parameters as in Figures 6.3.



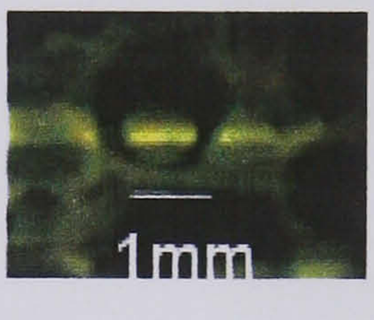
(a)



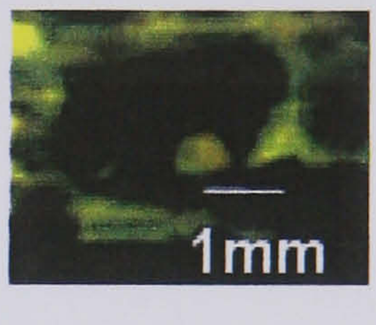
(b)



(c)



(d)

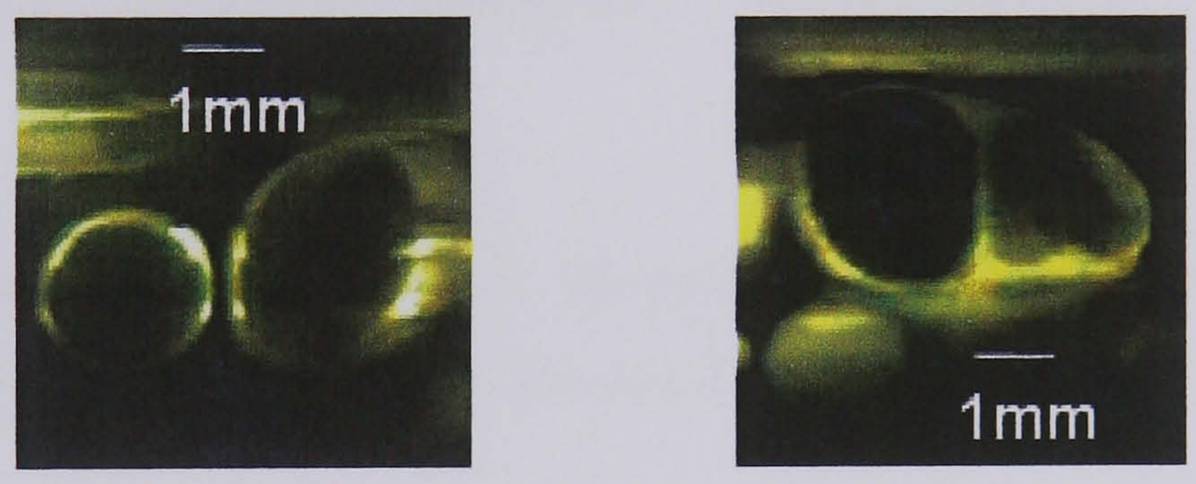


(e)

Figure 6.9 Examples of a w/o/w dispersion observed before phase inversion; (a)-(b) for the same parameters as in Figures 6.3; (c)-(e) for 62% oil holdup at 706 rpm.

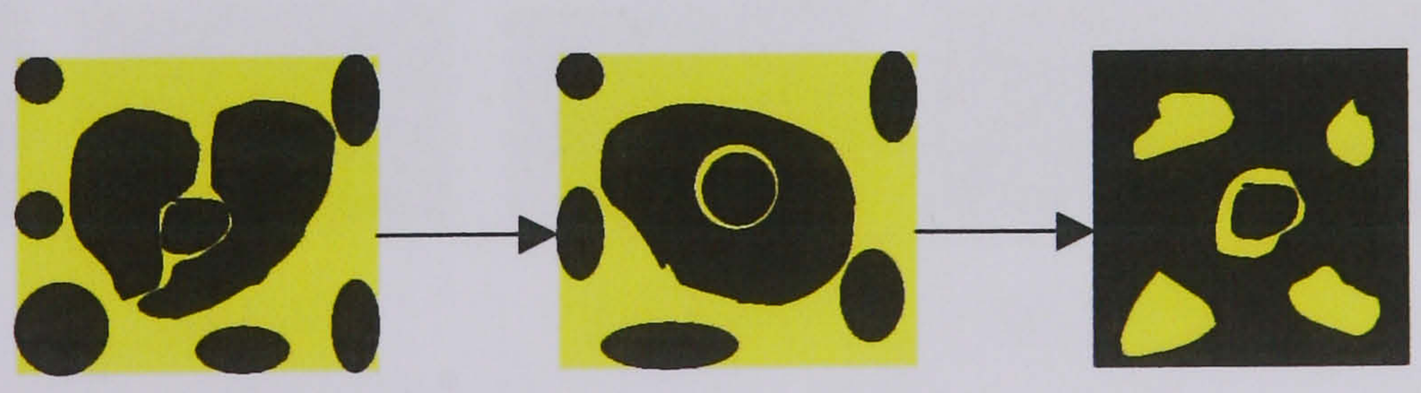
Generally, it is considered that secondary dispersions occur because of drop collision (pairs of drops or multi-drops) and coalescence or drop deformation. At a low dispersed phase holdup, it has been suggested that, during binary-drop coalescence, the continuous phase film which separates the dispersed phase droplets from each other breaks, leading to the formation of small droplets (Davies, *et al.*, 1970; Kumar, 1996; Groeneweg *et al.*, 1998; Sajjadi *et al.*, 2002). On the other hand, the multi-drop collision mechanism becomes progressively more important as the closest packed arrangement between the drops is reached; i.e. near the phase inversion point (Kumar, 1996). Sajjadi *et al.* (2002), on the other hand, proposed a drop deformation mechanism to explain the formation of the larger droplets which are observed in their experiments. They considered that at a low volume fraction of dispersed phase, the collision frequency is very low and the drop coalescence mechanism

cannot significantly contribute to inclusion. The formation of secondary dispersions could occur if large deformation of the dispersed water phase under high shear rate is effected by stirring. When a drop deformation propagates toward the inside of the drop, a thread of oil is formed. The thread gradually breaks into a rather large droplet and a few smaller ones. Our experimental results suggest that when an o/w dispersion inverses to a w/o one, relatively large oil droplets in water drops appear quite often both before and after phase inversion (see for instance Figure 6.10). Clearly, the formation of this kind of secondary dispersion can not be explained by binary-drop coalescence but may be rationalised by considering a multi-drop coalescence process, which is illustrated schematically in Figure 6.11; two large and highly distorted oil drops come together and squeeze a small oil drop between them. The outer drops coalesce and, after phase inversion, the inner oil drop with the water surrounding it appears in the oil continuous phase. Apart from multi-drop coalescence, the process of a larger drop including a small drop is the main reason for the formation of secondary dispersions of this kind.



(a) (b)

Figure 6.10 Photographic evidence for the formation of relatively large oil droplets in water drops for the same parameter as in Figure 6.4.



(a) (b) (c)

Figure 6.11 A schematic illustration of a possible mechanism for the formation of large oil droplets in water drops secondary dispersions following the collision of dispersed phase drops. The yellow and black regions designate the aqueous and organic phases, respectively.

In addition to secondary dispersions, close inspection of the results of the visualisation experiments has uncovered the formation of multi-dispersions such as, for instance, oil-water-oil-water o/w/o/w, an example of which is shown in Figure 6.12. The mechanisms responsible for the formation of these multiple-dispersions are multi-drop coalescence (see Figure 6.11 a-b) and drop inclusion (illustrated in Figure 6.13). In Figure 6.13, an oil drop and the surrounding continuous phase have been engulfed by a larger, deformed oil drop. Following the inclusion of the smaller oil drop and surrounding continuous phase into the larger oil drop, a multiple-dispersion is formed comprising an oil drop inside a water drop, which is inside a larger oil drop that is present within a water continuous phase. Figure 6.13 demonstrates clearly the engulfing process.

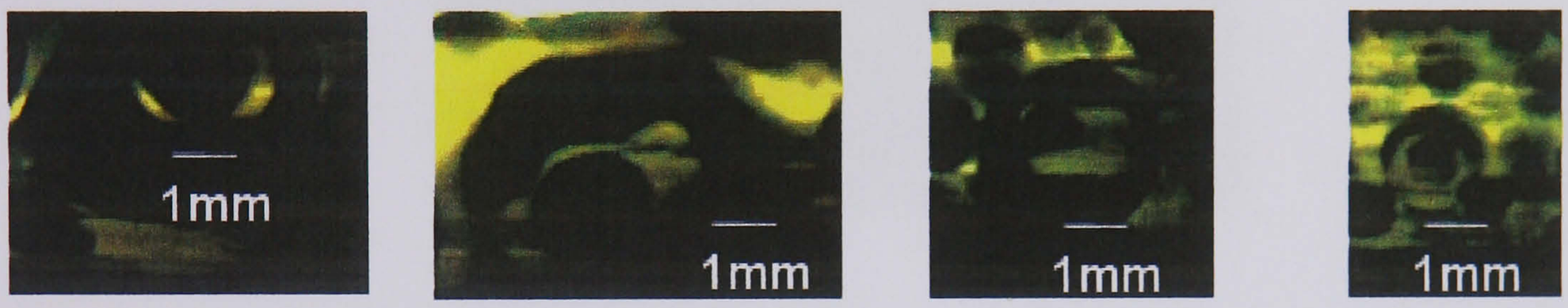


Figure 6.12 Multi-dispersions o/w/o/w. (a)-(b) the same parameters as in Figures 6.3; (c)-(d) 62% oil holdup at 706 rpm.

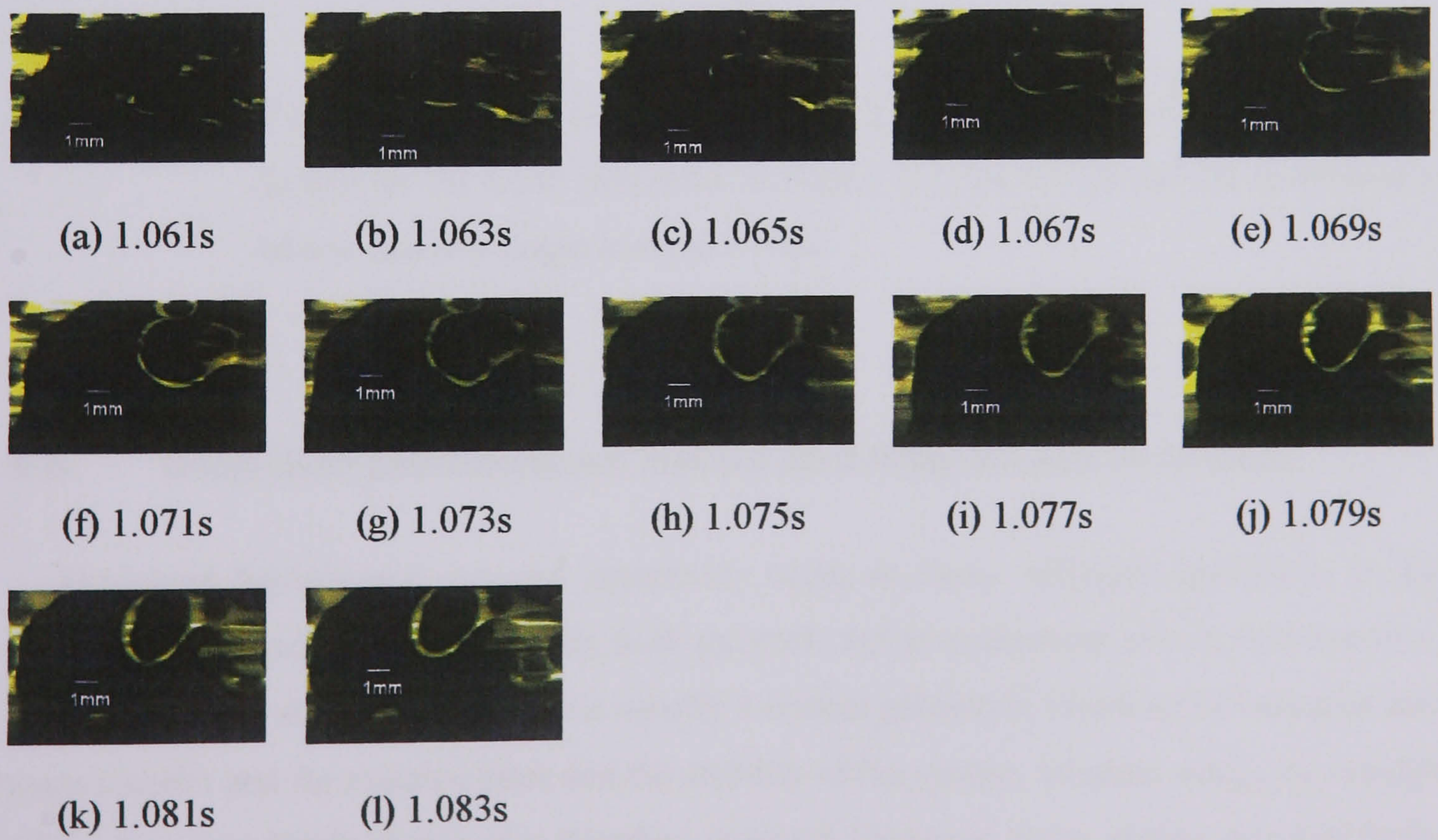
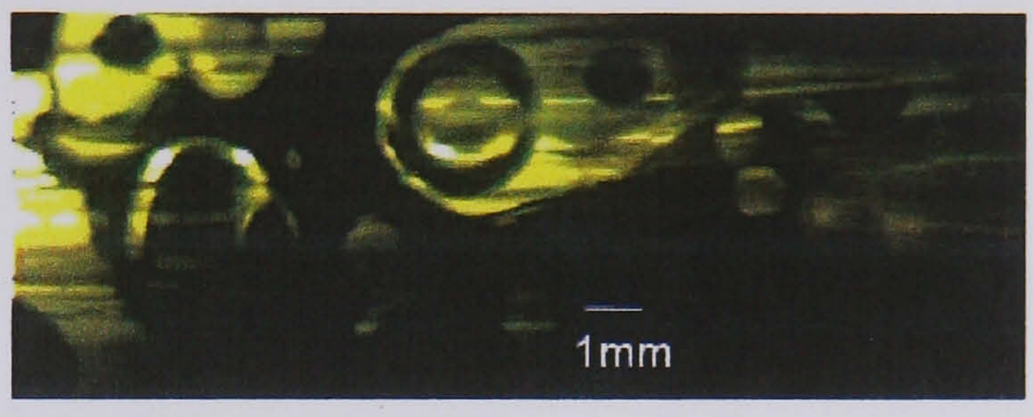


Figure 6.13 A time-series of photographs showing the formation of an o/w/o/w multiple-dispersion for the same parameters as in Figures 6.3.

In addition to the structures already reported, other very complex structures have been visualized using the LIF technique. Examples of these, are shown in Figure 6.14, demonstrate the strongly dynamic situation within the dispersion during the phase inversion process. For instance, Figure 6.14 (b) clearly demonstrates the co-existence of o/w and w/o dispersions, and secondary and multiple dispersions. Thus the emulsion undergoes rapid structural changes during phase inversion, which give way to a more equilibrated situation after its occurrence.



(a)



(b)

Figure 6.14 Complex structures directly visualized to accompany phase inversion of o/w to w/o for the same parameter as Figure 6.3; (a) 1.112s and (b) co-existence of w/o and o/w dispersions at 1.342s.

6.6 Drop Size Distributions Before and After Phase Inversion

Dispersed liquid-liquid systems commonly occur in many different operations in the chemical, food and related industries; both in batch and in continuous stirred tank reactors. In such systems, the mean drop size is usually a critical parameter which influences heat and mass transfer and /or reaction rates and the stability of the system. In many cases, knowledge of the drop size distribution is also therefore required. However, many studies reported in the literature focus on measuring drop size in a dilute system (normally less than 5%) (Mlynek

and Resnick, 1972; Park & Blair, 1975; Sovová, 1981; Tobin & Ramkrishna, 1992; Taweel & Chen, 1996; Sprow 1967; Pacek, 1998).

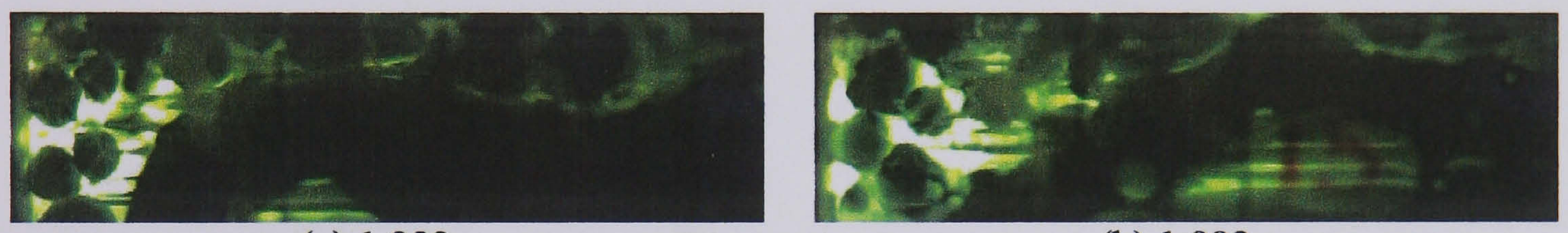
Pacek (1994a and b) and Pacek & Nienow (1995) applied video and capillary techniques to investigate the phase inversion process in a stirred vessel and also obtained drop size distributions at concentrations up to those which cause phase inversion, i.e. ~70%. The principle of the capillary technique is that when a drop is sucked into the capillary, the drop stretches into a slug so that the drop size can be calculated by measuring the length of the slug from its time of passage past light detectors. However, it is found that, for small vessel size at moderate to high concentrations where very wide drop size distributions exist, the video technique seems to be more reliable than the capillary one; and this advantage is enhanced when transients are involved. Consequently, directly sizing drops from video is the technique used in the measurements of the transient process described here.

Sajjadi *et al.* (2002) investigated the dynamic behaviour of drops in oil/water agitated vessel system and the drops sizing was carried out by using a video camera connected to an optical microscope. All measurements were carried out by directly sizing the drops from enlarged photos. The image analyzer was not capable of dealing with highly concentrated dispersions with overlapped drops. Measurements were carried out using only one slide (or two slides) of glass on which a drop of emulsion was placed. It was found that the size of internal oil droplets continuously decreased with time until it reached a steady-state value. The size of multiple water drops showed a minimum as a function of time. After the minimum, the size of multiple water drops either reached a steady-state value or continued enlarging until phase inversion occurred. The time evolution of the size of multiple drops was described in terms of a balance between (a) drop break-up and coalescence and (b) drop escape and inclusion. It was suggested that the inclusion events retarded the initial decrease in the size of multiple water drops with time and increased the drop size after the minimum occurred.

As part of the work described in this thesis, drop section diameter distributions during the whole phase inversion process in the stirred vessel were studied quantitatively by analysing the results for 45% aqueous solution holdup which were shown in Figure 6.2. This set of experiments was started from an initially steady stirrer speed of approximately 400 rpm at which an o/w emulsion exists. The stirrer speed was then gradually increased up to a value of 1000 rpm over a period of around 3-4 s. At the higher speeds, a stable w/o emulsion exists. Thus, phase inversion occurred during the ramping up of the stirrer speed. All measurements were carried out by directly sizing the drop sections from the photos. A total of 418 drops in 54 photos were selected (at about 30 photo intervals) for drop measurement. During the

period from 1.2 s to 3.6 s, phase inversion occurred violently and some extremely large drops appeared and o/w and w/o dispersions were found in the same frame (see Figure 6.15). Thus, the drop section sizes during this period were not measured. Figure 6.16 shows oil drop size distribution of two time periods, 0 s to 0.6 s and 0.6 s to 1.2 s before phase inversion. Water drop section diameter distributions after phase inversion are presented in Figure 6.17. The drop Sauter mean diameters (Eq. (4-12)) of the o/w and w/o dispersions are plotted in Figure 6.18; these values were obtained on the assumption that the drop size and drop section distributions are identical.

From Figure 6.17, it can be seen that as the dispersion approached the phase inversion point, more large oil drops appeared and the drop size distribution became more irregular. The same trend can also be found in the w/o dispersion after phase inversion (Figure 6.17) with more large water drops just after phase inversion occurs.



(a) 1.332 s (b) 1.982 s

(c) 2.324 s (d) 2.73 s

Figure 6.15 Photographs during phase inversion showing the dynamic evolution of an o/w emulsion (45 % aqueous solution holdup) to a w/o emulsion.

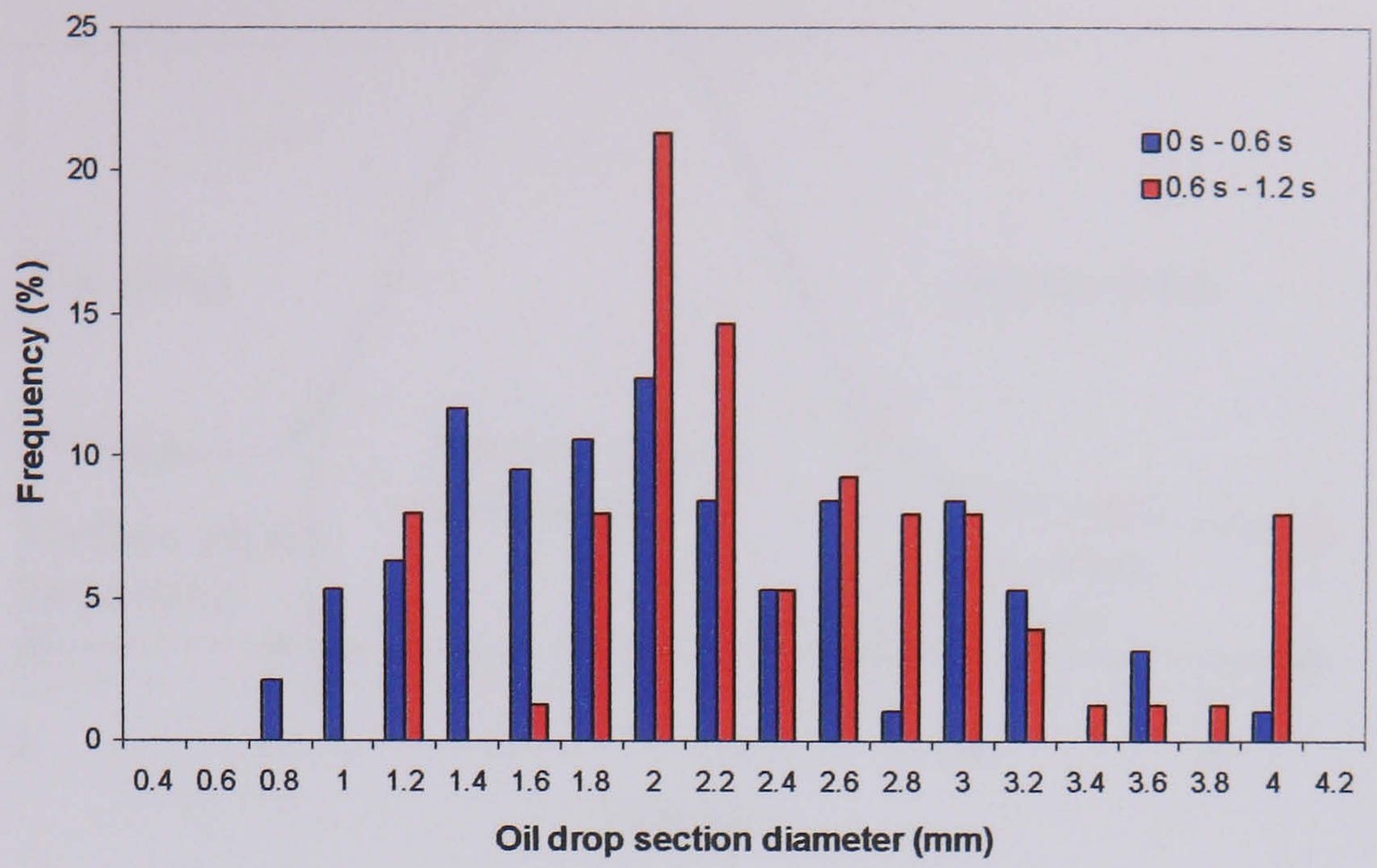


Figure 6.16 Oil drop section diameter distributions before phase inversion.

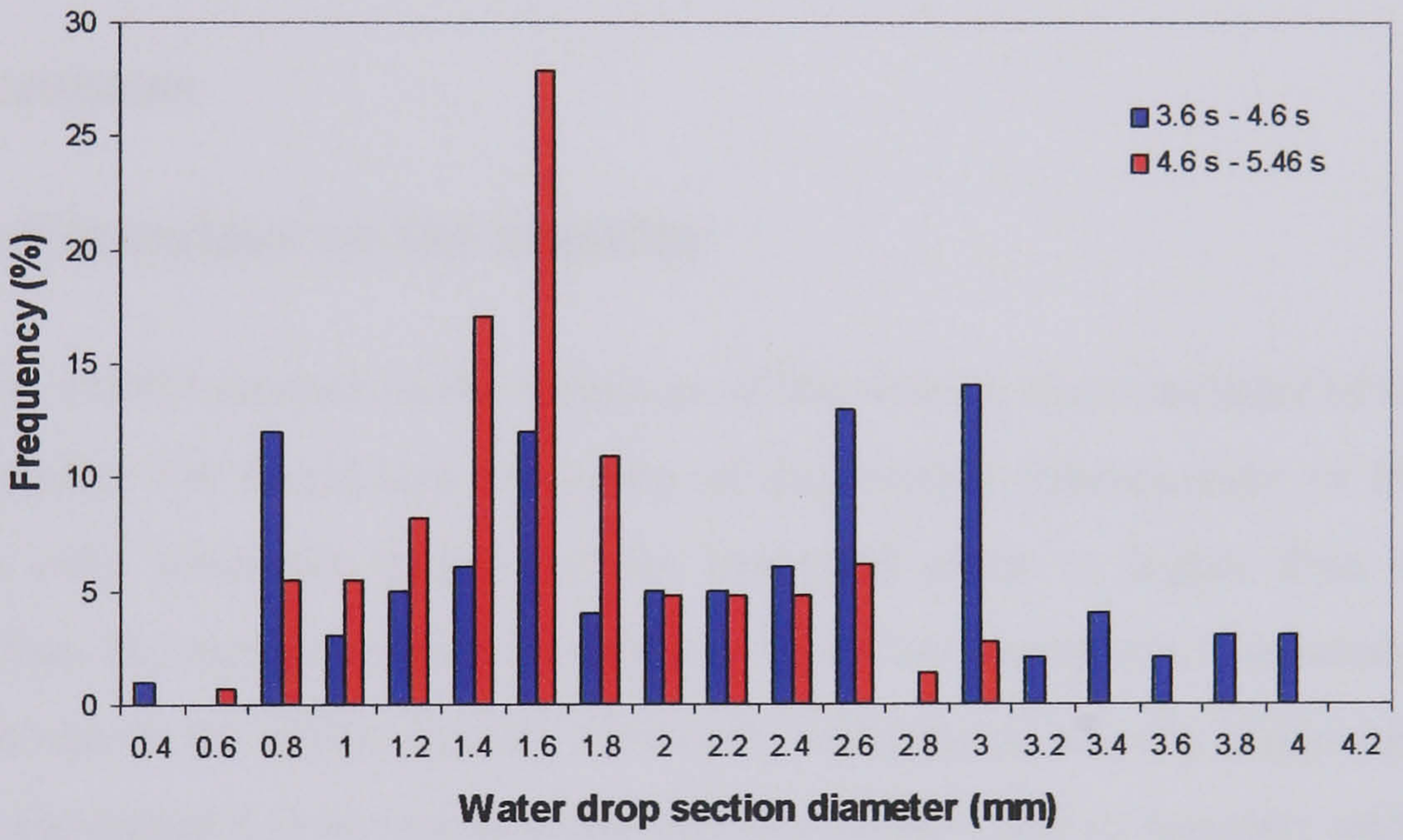


Figure 6.17 Water drop section diameter distribution after phase inversion.

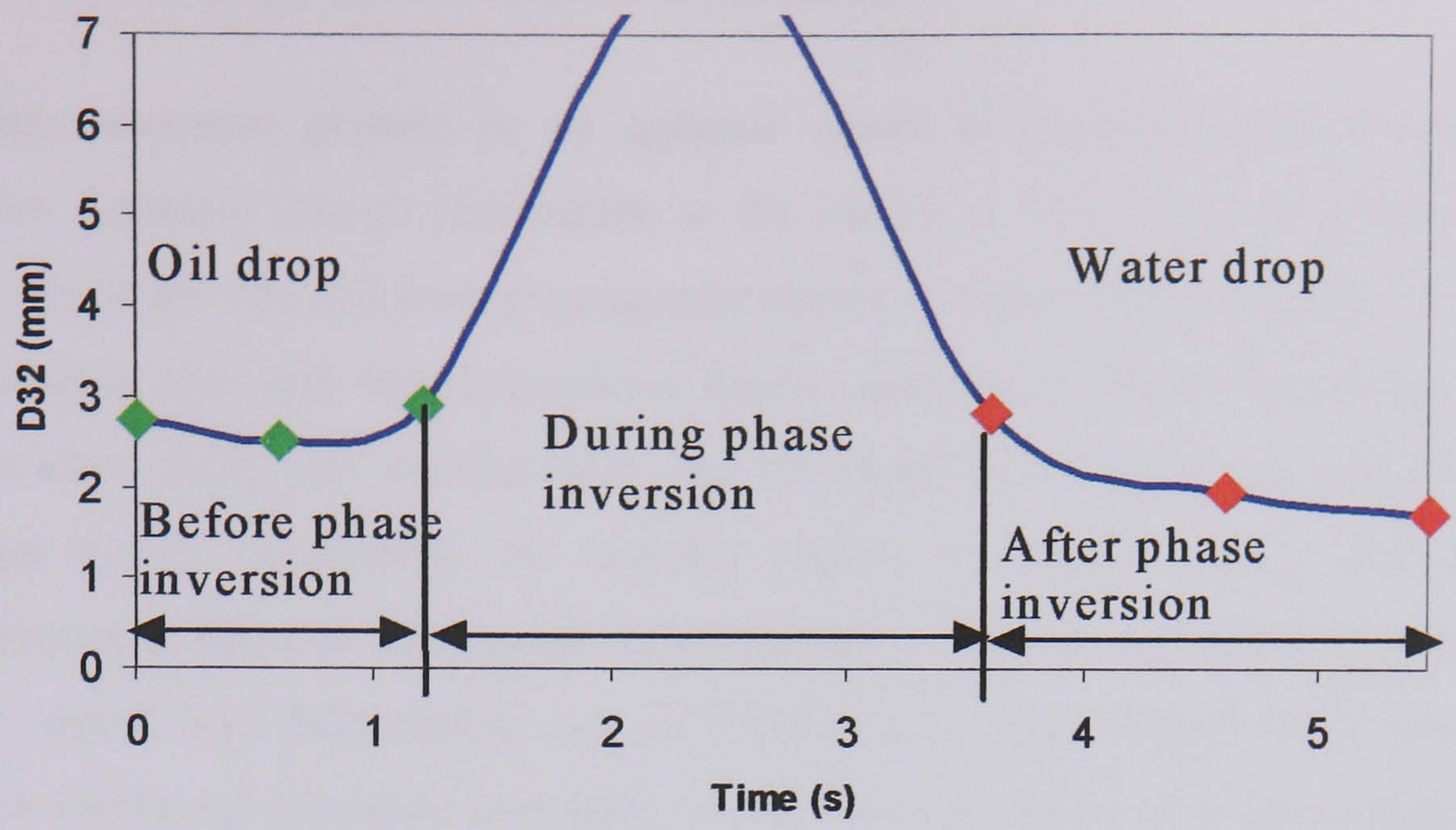


Figure 6.18 The Sauter mean diameter vs. time

6.7 Discussion

6.7.1 Film Formation on the Impeller

Kumar et al. (1991) worked on the influence of the wetting characteristics of the impeller on phase inversion. He found that the effect of the wetting characteristic of the impeller could be felt only when the density of the dispersed phase is higher than that of the continuous phase. He explained this phenomenon by the formation of a dispersed phase film on the impeller due to the higher density. However, when the oil was the dispersed phase, the lower density prevented it from reaching the impeller surface, and so impeller wetting had no effect on the inversion characteristics. However, Kumar et al. (1991) did not provide direct evidence to prove his explanation. In the present experiments, an aqueous phase film can be seen clearly in the water-in-oil dispersion illustrated in Figure 6.19. It is suggested that this film was formed by the coalescence of the aqueous phase on the impeller due to a higher density and then thrown up by the impeller.

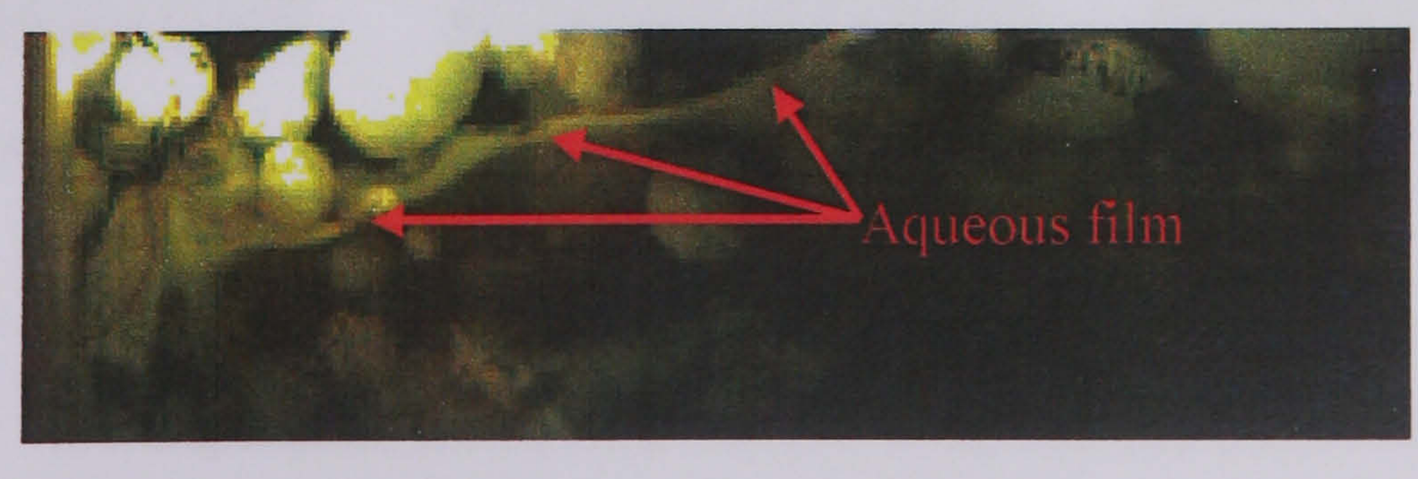
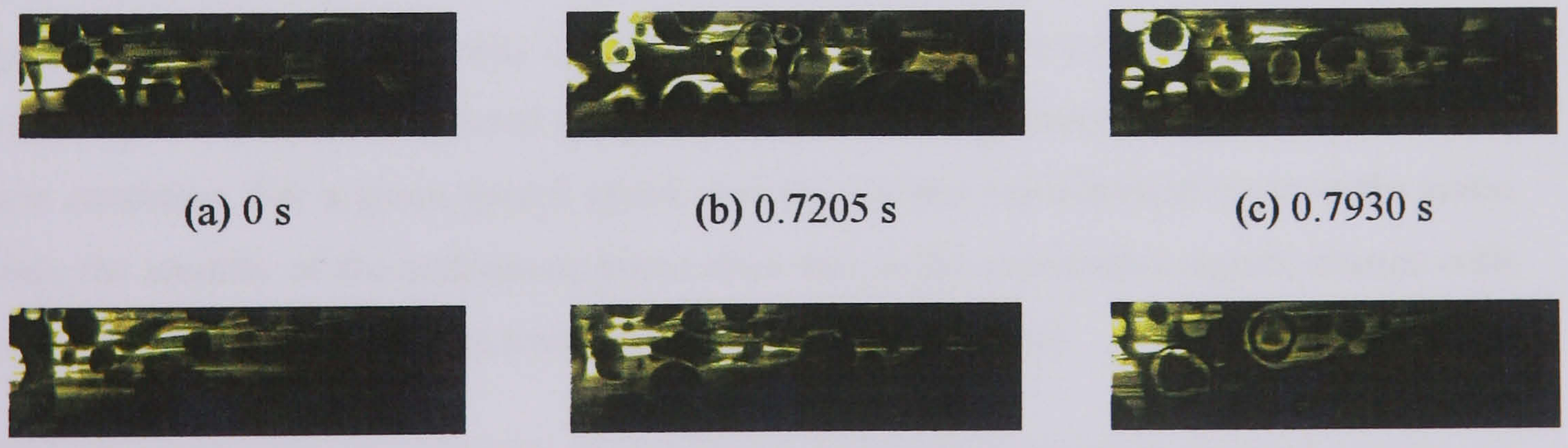


Figure 6.19 Water-in-oil dispersion; 19% aqueous phase holdup and 588 rpm impeller speed.

6.7.2 Local Occurrence of Phase Inversion

Phase inversion process in an agitated vessel is extremely complicated due to the complex turbulent energy distribution in the vessel. A time series of photographs (Figure 6.20), which are selected from photographs shown in Figure 6.3, show that in the same set of experiments, o/w and w/o dispersions appear alternately. Since the photos only show a narrow flow field, this phenomenon can be explained by assuming that phase inversion happens locally. Generally, the impeller region has higher energy and most breakup processes take place in this region. Consequently, coalescence processes occur outside this region. Apart from drop coalescence and breakup processes, droplet inclusions and escaping are two additional important processes during phase inversion. It is found that the formation of secondary dispersions is a dominant mechanism behind phase inversion. Similar to the process occurring in pipe flow experiments; when the systems are close to the phase inversion point or in the phase inversion region, the droplet inclusion process increases rapidly and happens even more frequently than drop coalescence. The inclusion process results in extremely large drops with the continuous phase droplets inside and some host-drops can approach the diameter of the vessel; and so it can be considered that phase inversion happens locally as is also proved by the co-existence of w/o and o/w dispersion (Figure 6.14 b, 6.20 d and 6.21). A similar observation is reported by Chesters and Issa (2004) for pipe flow (see Figure 6.21). At this stage, if the stirrer speed is continuously increased (or decreased) or more dispersed phase is added into the system, phase inversion would occur globally.



(a) 0 s (b) 0.7205 s (c) 0.7930 s

(d) 0.8950 s (e) 0.9890 s (f) 1.1115 s

Figure 6.20 A time series of photographs show that dispersion changes between o/w and w/o dispersions during phase inversion; (a), (d) and (e) o/w dispersions; (b), (c) and (f) w/o dispersions.

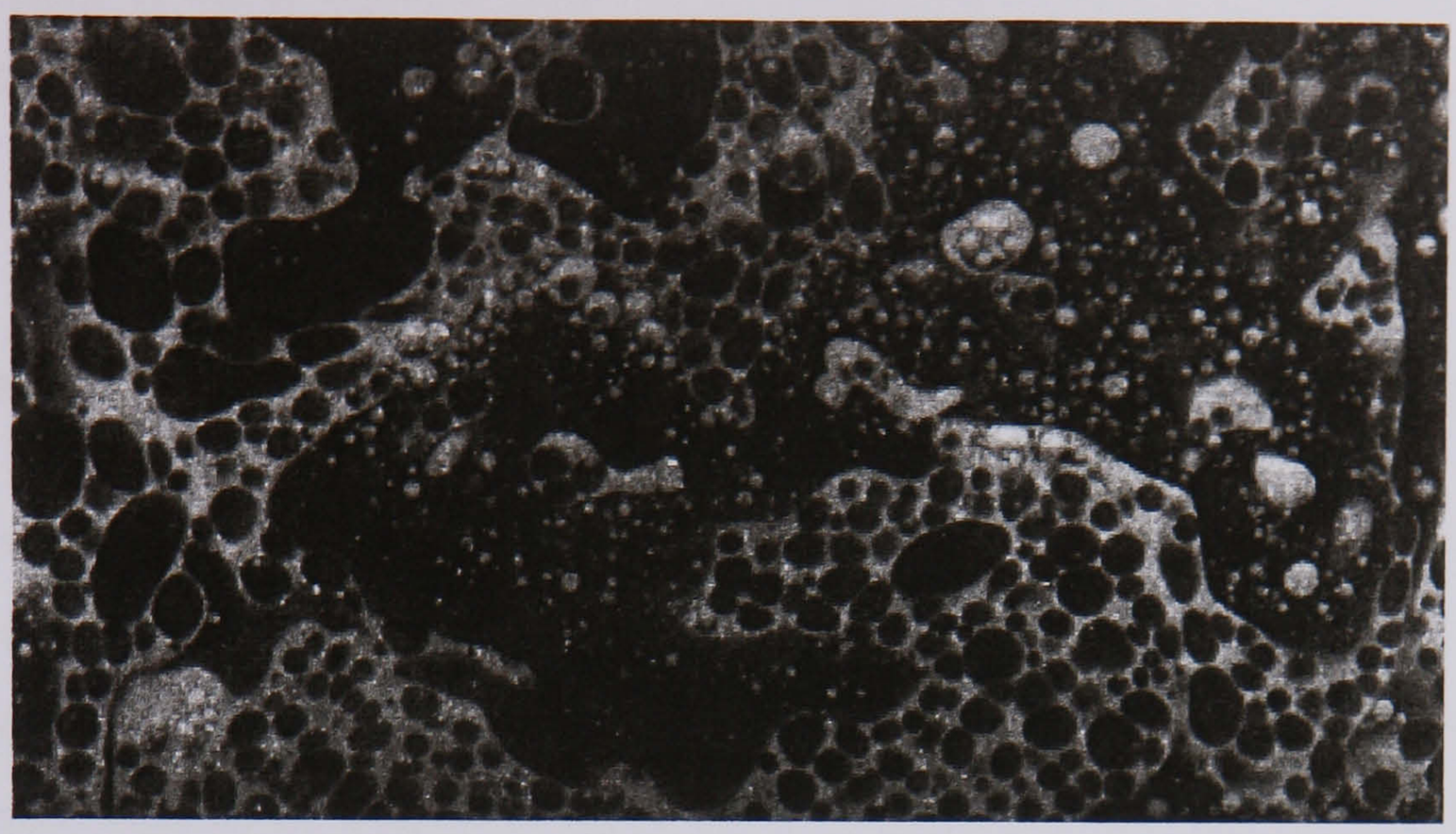


Figure 6.21 Phase inversion in a liquid-liquid system (Chesters and Issa, 2004) (Courtesy of O. Masbernat, ENSIACET, Toulouse)

6.7.3 The Route to Phase Inversion

The phase inversion phenomenon is extremely complex. In both pipe flows and in agitated vessels, there may exist a range of phase fraction in which specification, at a given phase fraction, of flow velocity (in the case of pipe flow) or agitated speed (in the case of an agitated vessel) is not sufficient to specify the identity of the continuous phase.

For pipe flows in this range (called here the "unstable range" - see Figure 4.7), the continuous phase may be either the aqueous phase or the oil phase. The identity of the continuous phase varies from one phase to the other during any given experiment. For the agitated vessel system, the identity of the continuous phase in the ambivalent range depends, at a given phase holdup and stirred speed, on whether the experiment was started in the w/o or o/w condition. For a given stirred speed, and for a given experimental route to the given holdup, the identity of the continuous phase does not, in the ambivalent region, change with time (though it may change with location in the vessel in this case).

Both the unstable region in pipe flow and the ambivalent region in agitated vessels are characterised by the existence of extremely complex structures as shown in the present study. The identity of the continuous phase in both cases clearly depends on the route the system takes to reach the given state. In the case of the agitated vessel, the route is reproducible (i.e. either starting from w/o or o/w and having a fixed stirred speed). In the case of a pipe flow, on the other hand, structures are developed randomly as a result of turbulent fluctuations near the pipe inlet. These structures are then convected along the pipe

(whilst still continuing to develop) but can, in the unstable region, arrive at the observation point in the form of either aqueous phase or oil phase continuous state, with this local state varying with time.

6.8 Summary

The LIF technique has been successfully applied to visualizing phase inversion process in a stirred vessel. The experimental results suggest that phase inversion is a gradual phenomenon rather than a catastrophic one; the process lasts for several seconds and during phase inversion both oil-in-water and water-in-oil dispersions can co-exist. The process may not occur globally but locally being dependent on the local phase distribution. The results also indicate that, during phase inversion, the balance between competing mechanisms such as drop coalescence and breakup, and inclusion and escape of secondary dispersions, constitutes the main deciding factor for whether or not inversion occurs. The structure of the dispersion, which accompanies phase inversion is extremely complex and a large number of secondary dispersions and multi-dispersions appear (including water-oil-water secondary dispersions). The appearance of secondary dispersion is a dominant mechanism behind phase inversion.

CHAPTER 7

CFD Models for Liquid-liquid Dispersed Pipe Flows

As discussed in previous Chapters, dispersed flow is an important flow pattern in liquid-liquid flows. Compared to gas-liquid dispersed (bubbly) flows, which have received considerable attention, the experimental data and theoretical studies involving liquid-liquid dispersed flows have covered only a restricted range of flow configurations and fluid properties. The simulation work on the liquid-liquid dispersed flow is even more limited and most multiphase numerical models are established on the gas-liquid flow system. Computational Fluid Dynamics (CFD) simulations using commercial software (e.g. FLUENT, STAR-CD and CFX) are being in creasingly used in the context of industrial dispersed systems. CFD offers the possibility of calculating velocity, dispersed phase concentration and (in the cases where the dispersed phase has deformable interfaces) the dispersed phase element size distribution (drop size, bubble size).

In earlier work at Imperial College, Soleimani (1999) and Hussain (2004) used the CFX4 code to predict liquid-liquid flows in horizontal pipes. Soleimani (1999) considered fully developed flows and Hussain (2004) considered the flow development case. Comparisions were made, in both studies, between predicted cross-sectional distributions of phase fractions and those measured in the Imperial College TOWER liquid-liquid flow facility using gamma ray tomography. Hussain (2004) used the capability of the CFX 4 code to calculate drop size distributions but no experimental data were available with which to compare the results.

The main objectives of the present work (described in this Chapter and the next) were as follows:

(1) To apply the CFX4.4 code to the predictions of oil-in-water dispersed upwards flow and to compare with experimental data (in this case, some data were available for both phase fraction distributions and drop size i.e. from work reported by Farrar and Bruun, 1996).

(2) To apply the CFX 4.4 code to the prediction of downwards liquid-liquid flow in a square cross section duct as used in the experimental part of the present study. The specific aim was to investigate the role of corner vortices in square duct case.

The CFD work is described in the present and the following Chapter. Thus the present Chapter (Chapter 7) gives details of the bases for the models used in CFX4.4 and the next Chapter (Chapter 8) presents the results of the calculations.The rest of the present Chapter is organized as follows. The CFD governing equations are introduced in Section 7.1. Section 7.2 presents the turbulence models (k- ε model and Reynolds stress model), which will be used in the simulations described in Chapter 8. Boundary conditions are introduced in Section 7.3. Section 7.4 describes the use of the multi-fluid model in conjunction with the MUSIG algorithm (Multiple-Size-Group), which is used to predict the drop size distributions. Finally, the CFD software package (CFX-4.4) is described in Section 7.5. Further detailed information about CFX4.4 is given in the code manual (1999).

7.1 Governing Equations

CFD models are based on the equations of conservation of mass, momentum and initial and boundary conditions. The governing equations for the incompressible liquid are given as follows (vector quantities are indicated in bold)

Continuity:

$$(\nabla \bullet \mathbf{u}) = 0 \tag{7-1}$$

Momentum :

$$\rho \frac{\partial(\mathbf{u})}{\partial t} + \rho \nabla \bullet (uu) = -\nabla p + \nabla \bullet (\mu \nabla u) + S_M \tag{7-2}$$

where, **u** is the velocity vector given by, **u** = [u, v, w], ρ is the mean fluid density and, p is the pressure; μ is the viscosity and S_M is source which includes the overall effect of body force.

7.2 Turbulent Flow and its Modelling

7.2.1 Turbulent Flow

For turbulent flow, firstly, we define the time-dependent flow property φ as the sum of a steady mean component Φ and a time-varying fluctuating component φ' with zero mean value; hence $\varphi(t) = \Phi + \varphi'(t)$. Therefore, the flow variables **u** (hence also u, v and w) and p by the sum of a mean and fluctuating component. Thus

$$\mathbf{u} = \mathbf{U} + \mathbf{u}'; \; u = U + u'; \; v = V + v'; \; w = W + w'; \; p = P + p' \tag{7-3}$$

in the following equations **U** is used to denote the mean velocity, **U** = [U, V, W]. Substituting the equations (7-3) into (7-1) to (7-2), the turbulent flow equations for compressible flows are

Continuity:

$$(\nabla \bullet \mathbf{U}) = 0 \tag{7-4}$$

Momentum:

$$\rho \frac{\partial \mathbf{U}}{\partial t} + \rho \nabla \bullet (\mathbf{UU}) = -\nabla \mathbf{P} + \nabla \bullet (\mu \nabla \mathbf{U}) + \nabla \bullet \mathbf{T} + \mathbf{S_M} \tag{7-5}$$

Where **T** is the stress tensor given by:

$$\mathbf{T} = \begin{pmatrix} \tau_{xx} & \tau_{xy} & \tau_{xz} \\ \tau_{yx} & \tau_{yy} & \tau_{xz} \\ \tau_{zx} & \tau_{zy} & \tau_{zz} \end{pmatrix} \tag{7-6}$$

For an incompressible fluid,

$$\tau_{ij} = -\rho \overline{u_i' u_j'} \tag{7-7}$$

Thus, three normal stresses and six extra shear stresses are given by:

$$\tau_{xx} = -\rho \overline{u'^2} \; ; \; \tau_{yy} = -\rho \overline{v'^2} \; ; \; \tau_{zz} = -\rho \overline{w'^2} \; ;$$

$$\tau_{xy} = \tau_{yx} = -\rho \overline{u'v'} \; ; \; \tau_{xz} = \tau_{zx} = -\rho \overline{u'w'} \; ; \; \tau_{yz} = \tau_{zy} = -\rho \overline{v'w'} \tag{7-8}$$

These extra stresses are termed the Reynolds stresses.

7.2.2 Turbulence Modelling

In performing the time –averaging operation on the momentum equations, we obtain six additional unknowns (the Reynolds stresses), in the time averaged momentum equations. Therefore, turbulence modelling is needed to predict the Reynolds stresses. A turbulence model is a computational procedure to close the system of mean flow equations (7-4) to (7-5) so that a more or less wide variety of flow problems can be calculated. Turbulence models can be put into two broad classes, **eddy viscosity models** and **second order closure models**.

7.2.2.1 Eddy Viscosity Models

The **eddy viscosity models** are based on the presumption that there exists an analogy between the action of viscous stresses and Reynolds stresses on the mean flow. The Reynolds stresses can be written as

$$-\rho\overline{u_i' u_j'} = \mu_t\left(\frac{\partial U_i}{\partial x_j} + \frac{\partial U_j}{\partial x_i}\right) - \frac{2}{3}\rho k\delta_{ij} \tag{7-9}$$

where μ_t is an additional viscosity, call the turbulent or eddy viscosity. The Kronecker delta, δ_{ij} is given by $\delta_{ij} = 1$ if $i = j$ and $\delta_{ij} = 0$ if $i \neq j$. k is the turbulent kinetic energy.

7.2.2.2 k- ε Turbulence Model

The k- ε model uses an eddy-viscosity hypothesis for the turbulence. The transport equations for the turbulence kinetic energy k and turbulence dissipation rate ε are

$$\frac{\partial(\rho\,\mathrm{k})}{\partial t} + \nabla\bullet(\rho\mathbf{U}\,\mathrm{k}) = \nabla\bullet\left(\frac{\mu_t}{\sigma_k}\nabla\mathrm{k}\right) + 2\mu_t E_{ij}\cdot E_{ij} - \rho\varepsilon \tag{7-10}$$

$$\frac{\partial(\rho\varepsilon)}{\partial t} + \nabla\bullet(\rho\mathbf{U}\varepsilon) = \nabla\bullet\left(\frac{\mu_t}{\sigma_\varepsilon}\nabla\varepsilon\right) + C_{1\varepsilon}\frac{\varepsilon}{k}\,2\mu_t E_{ij}\cdot E_{ij} - \mathrm{C}_{2\varepsilon}\rho\frac{\varepsilon^2}{\mathrm{k}} \tag{7-11}$$

where turbulent viscosity $\mu_t = C_\mu\rho\dfrac{k^2}{\varepsilon}$ and $E_{ij} = \dfrac{1}{2}\left(\dfrac{\partial U_i}{\partial x_j} + \dfrac{\partial U_j}{\partial x_i}\right)$.

The equations contain five adjustable constants C_μ, $C_{1\varepsilon}$, $C_{2\varepsilon}$ and the turbulent Prandtl numbers for k and ε, σ_k and σ_ε. The standard k- ε model employs values for the constants that are arrived at by comprehensive data fitting for a wide range of turbulent flows: C_μ =0.09, $C_{1\varepsilon}$ =1.44, $C_{2\varepsilon}$ =1.92, σ_k =1.00, σ_ε =1.30.

Although the k- ε model is presently by far the most widely used and validated, the model also reported not to perform well in a variety of important cases such as (Versteeg and Malalasekera, 1995):

(i) some unconfined flows;

(ii) flows with large extra strains (e.g. curved boundary layers, swirling flows;

(iii) rotating flows;

(iv) fully developed flows in non-circular ducts.

Secondary flows in long non-circular ducts, which are driven by anisotropic normal Reynolds stresses, can also not be predicted owing to the deficiencies of the treatment of normal stresses within the k- ε model.

7.2.2.3 Reynolds Stress Model

The most complex classical turbulence model is the Reynolds stress model (RSM), also called the second-order or second-moment closure model. In Reynolds stress turbulence model, the eddy-viscosity hypothesis is not invoked. Instead, equations are solved for the individual components of the Reynolds stress. The extra Reynolds stress transport equation can account for the directional effects of the Reynolds stress field.

In the differential form of the Reynolds stress model, $\overline{u_i' u_j'}$ satisfies the following equation:

$$\frac{\partial}{\partial t}\rho\overline{u_i' u_j'} + \nabla \bullet (\rho \overline{u_i' u_j'}\,\mathbf{U}) = \nabla \bullet \left(\rho \frac{C_s}{\sigma_{DS}} \frac{k}{\varepsilon} \overline{u_i' u_j'} (\nabla \overline{u_i' u_j'})^T \right) + \mathbf{P} + \phi_{ij} - \frac{2}{3}\rho\varepsilon\delta_{ij} \qquad (7\text{-}12)$$

where σ_{DS} is the turbulent Prandtl number for Reynolds stress.

Here **P** is the shear stress production tensor. **P** is given by:

$$\mathbf{P} = -\rho \left(\overline{u_i' u_j'} (\nabla \mathbf{U})^T + (\nabla \mathbf{U}) \overline{u_i' u_j'} \right) \qquad (7\text{-}13)$$

ϕ_{ij} is the pressure-strain correction given as the following. The pressure-strain is the sum of three parts, a return to isotropy term $\phi_{ij,1}$ a return to isotropy of production term $\phi_{ij,2}$ and a wall reflection term $\phi_{ij,w}$ (Clark and Wilkes, 1988 and CFX-4 manual, AEA Tech. Plc.).

$$\phi_{ij} = \phi_{ij,1} + \phi_{ij,2} + \phi_{ij,w} \qquad (7\text{-}14)$$

where

$$\phi_{ij,1} = -\rho C_1 \frac{\varepsilon}{k} (\overline{u_i' u_j'} - \frac{2}{3} k \delta_{ij}) \tag{7-15}$$

$$\phi_{ij,2} = -C_2 (\mathbf{P} + \frac{2}{3} \rho \overline{u_i' u_j'} \cdot \nabla \mathbf{U} \delta_{ij}) \tag{7-16}$$

$$\phi_{ij,w} = \begin{aligned} &(c_1' \frac{\varepsilon}{k}(\overline{u_l u_m} n_l n_m \delta_{ij} - \frac{3}{2}\overline{u_l u_i} n_l n_j - \frac{3}{2}\overline{u_l u_j} n_l n_i) \\ &+ c_2' \frac{\varepsilon}{k}(\phi_{lm,2} n_l n_m \delta_{ij} - \frac{3}{2}\phi_{il,2} n_l n_j - \frac{3}{2}\phi_{jl,2} n_l n_i))F(x_n) \end{aligned} \tag{7-17}$$

here n_l is the unit normal to the wall, x_n is the normal distance to the wall, and the function F is given by

$$F = \frac{c_w^{\frac{3}{4}} k^{\frac{3}{2}} |J|}{\kappa \varepsilon x_n} \tag{7-18}$$

$|J|$ is Jacobian determinant. The term $\phi_{ij,w}$ is included to account for pressure reflections at the wall since they have a significant effect on the pressure-strain term. The normal stress perpendicular to the wall is well damped, whilst that parallel to the wall is enhanced. The function F can be seen to reduce the effect of the wall correction term with increasing distance from the wall.

The standard values of the constants used in the Reynolds stress model are shown in Table 7.1 below:

C_1	C_2	c_1'	c_2'	C_μ	C_s	$C_{1\varepsilon}$	$C_{2\varepsilon}$	σ_{DS}	σ_k	σ_ε
1.8	0.6	0.5	0.3	0.09	0.22	1.44	1.92	1.0	1.0	1.30

Turbulent kinetic energy k can be found by adding the three normal stresses together:

$$k = \frac{1}{2}(\overline{u_1'^2} + \overline{u_2'^2} + \overline{u_3'^2}) \tag{7-19}$$

As the dissipation appears in the individual stress equations, the equation for ε is still required and has the following form:

$$\frac{\partial}{\partial t}\rho\varepsilon + \nabla \bullet (\rho \mathbf{U}\varepsilon) = \nabla \bullet \left(\rho \frac{C_s}{\sigma_\varepsilon} \frac{k}{\varepsilon} \overline{u_i' u_j'} \nabla \varepsilon \right) - C_{1\varepsilon} \frac{\varepsilon}{k} \rho \, \overline{u_i' u_j'} \cdot \nabla \mathbf{U} - C_{2\varepsilon} \rho \frac{\varepsilon^2}{k} \tag{7-20}$$

Reynolds stress model performs very accurate calculation of the mean flow properties and all the Reynolds stresses for many simple and more complex flows including wall jets, asymmetric channel and non-circular duct flows and curved flows. However, the Reynolds stress model is very complex and by no means as well validated as the *k*-ε model and because of the high cost of the computations it is currently not widely used in industrial flow calculations (Versteeg & Malalasekera, 1995).

7.3 Boundary Conditions

7.3.1 Wall Boundary Conditions for Turbulent Flow

Many of the variables vary rapidly in the near-wall regions of the flow and, instead of using extremely fine grids in these regions, their near-wall behaviour is specified with wall functions. The wall function concept is illustrated below by considering the flow in a fully developed boundary layer over a stationary wall. Near the wall, at y = d say, it is found that the wall shear stress τ is related to the turbulence kinetic energy by

$$\tau^2 = C_\mu \rho^2 k^2 \tag{7-21}$$

A new quantity τ_k is defined such that

$$\tau_k = \rho \, C_\mu^{1/2} \, k \tag{7-22}$$

This may be used to define scaled variables

$$u^+ = \frac{(\rho\tau_k)^{1/2}}{\tau}u \tag{7-23}$$

and

$$y^+ = \frac{(\rho\tau_k)^{1/2}}{\mu}(d-y) \tag{7-24}$$

The scaled velocity component parallel to the wall and in the x direction is

$$u^+ = \begin{cases} y^+ & \text{for } y^+ < y_0{}^+ \\ \dfrac{1}{\kappa}\log(Ey^+) & \text{for } y^+ > y_0{}^+ \end{cases} \tag{7-25}$$

The cross-over point $y_0{}^+$ between the viscous sub-layer and the logarithmic region is the upper root of

$$y_0^+ = \frac{1}{\kappa}\log(Ey^+) \tag{7-26}$$

It is found that von Karman constant $\kappa = 0.4$ and the constant $E = 9.8$ for smooth walls. The equation for the turbulence kinetic energy k is solved in the control volume immediately adjacent to the wall. From this value of the wall shear stress can be obtained. The turbulence dissipation is obtained from the turbulence kinetic energy through the relation

$$\varepsilon = \frac{C_\mu^{3/4}k^{3/2}}{\kappa(d-y)} \tag{7-27}$$

7.3.2 Flow Boundaries

Inlets All variables (velocities, k, ε, temperature, volume fractions and additional scalars) are specified for the inlet and, for the subsonic case, pressure is extrapolated from downstream.

Pressure boundaries Pressure is specified at the inlet and Neumann conditions are applied to the velocities, $\frac{\partial U^i}{\partial n} = 0$. At the outlet, temperature, volume fractions, additional scalars, k and ε are all extrapolated from upstream.

7.3.3 Symmetry Boundary

All variables, at the symmetry boundary, are mathematically symmetric, with thus no diffusion across the boundary, except the component of velocity normal to the boundary and the components of the Reynolds shear stress and Reynolds flux involving the normal velocity which are all anti-symmetric.

7.3.4 Periodic Boundaries

Periodicity is a mathematically simple boundary condition. It ensures that all variables, and hence also all coefficients, have the same value at both ends of the computational or physical domain.

7.4 Multi-phase Flow

For multiphase flows, two basic multi-phase models are available, the multi-fluid model (used in this simulation) and homogeneous model. In the 'multi-fluid' model, there is one solution field for each phase separately. Transported quantities interact via inter-phase transfer terms. The 'homogeneous' model is a simplification of the multi-fluid model. For a given transport process, it assumes that the transported quantities for that process are the same for all phases. In this Section, only the 'multi-fluid' model, which is applied for the calculation described in Chapter 8, is introduced.

7.4.1 Multi-fluid Model

Within the framework of this model, the continuity and momentum equations can be respectively expressed as follows:

$$\frac{\partial}{\partial t}(r_\alpha \rho_\alpha) + \nabla \bullet (r_\alpha \rho_\alpha \mathbf{U}_\alpha) = \sum_{\beta=1}^{N_P} (\dot{m}_{\alpha\beta} - \dot{m}_{\beta\alpha}) \tag{7-28}$$

$$\begin{aligned} &\frac{\partial}{\partial t}(r_\alpha \rho_\alpha \mathbf{U}_\alpha) + \nabla \bullet (r_\alpha (\rho_\alpha \mathbf{U}_\alpha \mathbf{U}_\alpha - \mu_\alpha (\nabla \mathbf{U}_\alpha + (\nabla \mathbf{U}_\alpha)^T))) \\ &= r_\alpha (\mathbf{B} - \nabla p_\alpha) + \sum_{\beta=1}^{N_P} c_{\alpha\beta}^{(d)} (\mathbf{U}_\beta - \mathbf{U}_\alpha) + \mathbf{F}_\alpha + \sum_{\beta=1}^{N_P} (\dot{m}_{\alpha\beta} \mathbf{U}_\beta - \dot{m}_{\beta\alpha} \mathbf{U}_\alpha) \end{aligned} \tag{7-29}$$

where: the subscripts α and β denote the continuous and disperse phases, respectively. N_P, r_α and r_β denote the number of phases and the volume fraction of each phase, respectively; and the volume fractions sum to unity: $\sum_{\alpha=1} r_\alpha = 1$; ρ_α and $\mathbf{U}_\alpha$ are the density and the fluid velocity of phase α, respectively, $\dot{m}_{\alpha\beta}$ is the mass flow rate per unit volume into phase α from phase β, $c_{\alpha\beta}^{(d)}$ are the inter-phase drag terms, which are model dependent and have to be specified empirically; $\mathbf{B}$ is the body force and $\mathbf{F}_\alpha$ are any inter-phase non-drag forces, including the virtual mass force, the lift force, the wall lubrication force and the turbulent dispersion force.

7.4.1.1 Inter-phase Drag

The drag exerted on an immersed body by a moving fluid arises from two mechanisms. The first is due to the viscous surface shear stress, and is called skin friction. The second is due to the pressure distribution around the body, and is called the form drag. The total drag force is most conveniently expressed in terms of the non-dimensional drag coefficient:

$$C_D = \frac{D}{\frac{1}{2}\rho U^2 A} \tag{7-30}$$

here ρ is the fluid density and U its speed. D is the magnitude of the drag force, and A is the projected area of the body in the direction of flow. The **inter-phase drag** terms $c_{\alpha\beta}^{(d)}$ are derived from their relationship with C_D in the following way. The continuous phase is denoted by α and the dispersed phase by β. The area of a single drop projected in the flow direction, A, and the volume of a single drop V are given by:

$$A = \frac{\pi d^2}{4}, \; V = \frac{\pi d^3}{6} \tag{7-31}$$

where d is the volume equivalent mean diameter. The number of drops per unit volume, n_P is given by:

$$n_P = \frac{r_\beta}{V} = \frac{6 r_\beta}{\pi d^3} \tag{7-32}$$

the drag exerted by a single drop on the continuous phase is:

$$D_P = \frac{1}{2} C_D \rho_\alpha A \left|\mathbf{U}_\beta - \mathbf{U}_\alpha\right| (\mathbf{U}_\beta - \mathbf{U}_\alpha) \tag{7-33}$$

hence the total drag per unit volume on the continuous phase is :

$$D_{\alpha\beta} = n_P D_P = \frac{3}{4}\frac{C_D}{d} r_\beta \rho_\alpha A \left|\mathbf{U}_\beta - \mathbf{U}_\alpha\right| (\mathbf{U}_\beta - \mathbf{U}_\alpha) \tag{7-34}$$

comparing Eqs (7-34) and (7-29), it is seen that, $D_{\alpha\beta} = c_{\alpha\beta}^{(d)} (\mathbf{U}_\beta - \mathbf{U}_\alpha)$, and hence :

$$c_{\alpha\beta}^{(d)} = \frac{3}{4}\frac{C_D}{d} r_\beta \rho_\alpha \left| \mathbf{U}_\beta - \mathbf{U}_\alpha \right| \tag{7-35}$$

For a drop of a given shape, undergoing motion in a Newtonian incompressible fluid, C_D depends only on Reynolds number:

$$\mathrm{Re} = \frac{\rho_\alpha U d}{\mu_\alpha} \tag{7-36}$$

where μ_α is the molecular viscosity of the continuous phase.

In the turbulent region (or inertial region) (500 to 1000 $\leq$ Re $\leq$ 1 to 2 $\times$ 10^5), fluid drops become distorted and the distorted drop regime correlation of Ishii-Zuber may be preferred:

$$C_D = \frac{2}{3} Eo^{\frac{1}{2}} \tag{7-37}$$

where Eo is the Eotvos number defined by: $Eo = \frac{g \Delta\rho d^2}{\sigma}$, where $\Delta\rho$ is the density difference between the phases, g is the gravitational acceleration and σ is the interfacial tension.

For high drop concentrations, many of the drag correlations should be modified to allow for the interactions between the drops. The modified drag correlation, due to Ishii & Zuber (1979), is applicable mainly to drops and bubbles. For the Newton and distorted drop regimes, the Ishii & Zuber modification takes the form of a multiplying factor to the drag factor. The factor is given in terms of the volume fraction of the disperse phase (r_β) by:

$$E = \left(\frac{1 + 17.67 f(r_\beta)^{\frac{6}{7}}}{18.67 f(r_\beta)} \right)^2 \tag{7-38}$$

where $f(r_\beta) = \frac{\mu_\alpha}{\mu_m}(1-r_\beta)^{\frac{1}{2}}$. μ_m is the mixture viscosity.

For the spherical cap regime, the Ishii & Zuber modification also takes the form of a multiplying factor:

$$E = (1-r_\beta)^2 \tag{7-39}$$

The influence of the dispersed phase on the turbulence of the liquid phase was taken into account via an additional term proposed by Sato & Sekoguchi, (1975), which allowed the prediction of liquid velocity distributions in two-phase bubbly flow. Sato & Sekoguchi, (1975) subdivided the fluctuation of turbulent velocity into two components: one due to the inherent liquid turbulence independent of the existence of the bubble, (u', v'), and the other due to the additional liquid turbulence brought about by the bubble agitation, (u'', v''); similarly, the shear stress was also split into two components, $-\rho\overline{u'v'}$ and $-\rho\overline{u''v''}$, corresponding to (u', v') and (u'', v''), respectively.

7.4.1.2 Inter-phase Non-drag Forces

In this study, there are three inter-phase non-drag forces to be investigated, the lift force, the wall lubrication force and the turbulent dispersion force. The total force is the sum of all the individual components. All the forces are given in terms of a force per unit volume F_α on the continuous phase; the force on the dispersed phase is equal in magnitude and opposite in sign to F_α . In vertical pipe flow, forces acting perpendicularly to the flow direction (non-drag forces) determine the radial distributions of the dispersed phase. The forces taken into account are: the transverse lift force (Moraga, *et al.*, 1999), the lubrication or wall force and dispersion forces. The model does not consider single bubbles, but the radial distributions of volume fractions.

The lift force

This force is given in terms of the slip velocity and the curl of the continuous phase velocity by:

$$\mathbf{F}_{\alpha} = r_{\beta}\rho_{\alpha}C_{L}(\mathbf{U}_{\beta} - \mathbf{U}_{\alpha}) \times \nabla \times \mathbf{U}_{\alpha} \tag{7-40}$$

here C_L (the lift force coefficient) is 0.5 for inviscid flow round a sphere and can take values between 0.01 and 0.05 for viscous flow.

The wall lubrication force

This force is in the normal direction away from a wall and decays with distance from the wall. The force is given by:

$$\mathbf{F}_{\alpha} = -\frac{r_{\beta}\rho_{\alpha}(U_{\beta} - U_{\alpha})^{2}}{d}\max(0, C_{1} + C_{2}\frac{d}{y_{w}})\mathbf{n} \tag{7-41}$$

where y_w is the distance from the wall and **n** is the normal to the wall. Usually, C_1 takes a value of -0.01 and C_2 takes a value of 0.05. This means the force only exists in the region less than 5 drop diameters from the wall.

The turbulent dispersion force

Drops in a turbulent flow move along fluctuating trajectories as they interact with the turbulent liquid eddies. These fluctuations can disperse the drops. Two-fluid models have accounted for this dispersion by introducing a force proportional to the gradient of the volume fraction in the momentum equations of the dispersed phase (Drew & Passman, 1999; Moraga, *et al*, 2003). The force depends on the amount of turbulence in the continuous phase and the gradient of the volume fraction. The following turbulent dispersion model (Kurul & Podowski, 1990) has been widely used:

$$\mathbf{F}_{\alpha} = -C_{TD}\rho_{\alpha}k_{\alpha}\nabla r_{\alpha} \tag{7-42}$$

where k is the kinetic energy of the turbulence of the continuous phase and C_{TD} is the turbulent dispersion coefficient.

7.4.2 Multiple-size-group (MUSIG) Model

The MUSIG model of Lo (1996) was developed to handle dispersed multiphase flows in which the dispersed phase has a large variation in size. MUSIG provides a framework in which the population balance method together with the break-up and coalescence models can be incorporated into three-dimensional CFD calculations. Olmos *et al.* (2001) used the MUSIG model in conjunction with CFX 4.3 to investigate the bubble size and size distributions in a cylindrical bubble column and achieved good agreement with the experimental data.

In general, the drops in the dispersed phase can be divided into several size groups and each of these size groups can be treated as a separate phase in a multiphase flow calculation. This multiphase flow model therefore has N+1 sets of coupled equations (continuity and momentum) to be solved, where N is the number of size groups. Currently, the MUSIG model is simplified by assuming that all the drops are moving at the same velocity so that it is only necessary to solve one set of momentum equations for all the drops. Therefore, the multiphase approach is reduced to a two-fluid approach with one velocity field for the continuous phase and one for the dispersed phase. The continuity equations of the drop size groups are retained, however, and solved to represent the size distribution.

7.4.2.1 Theory and Modelling of Drop Size Distribution

The continuity equation for the dispersed phase, accounting for the changes in the drop size is given by:

$$\frac{\partial}{\partial t}(r\rho) + \nabla \bullet (r\rho U) + \frac{\partial}{\partial t}(r\rho \dot{d}) = 0 \qquad (7\text{-}43)$$

Changes of drop concentration in time	Convection in physical space	Changes of drop in size

where d is the drop size (diameter), $\dot{d}$ is the rate at which the drop changes its size and r is the volume fraction of the dispersed phase.

The continuity equation for size group i is :

$$\frac{\partial}{\partial t}(\rho r_i) + \nabla \bullet (\rho U r_i) = S_i \tag{7-44}$$

the term S_i is the rate of mass transfer into the size group due to break-up, coalescence, expansion, growth, etc. r_i is the drop volume fraction. Clearly, $\sum_i r_i = r$, or $r_i = r f_i$, where the size distribution of the dispersed phase is therefore defined by the variable f_i. Therefore, the equation can be rewritten as:

$$\frac{\partial}{\partial t}(\rho r f_i) + \nabla \bullet (\rho U r f_i) = S_i \tag{7-45}$$

This equation has the form of the transport equation for the fraction of the drops in size group i of the dispersed phase, f_i. The local Sauter mean diameter can be deduced from $d_s = \frac{1}{\sum_i \frac{f_i}{d_i}}$; and the interfacial area from $A_i = \frac{6r}{d_s}$.

7.4.2.2 Population Balance

Population balance is a well-established method for computing the size distribution of the dispersed phase and accounting for the breakage and coalescence effects. A general form of the population balance equation is:

$$\frac{\partial}{\partial t}(n_i) + \nabla \bullet (U n_i) = B_B - D_B + B_C - D_C \tag{7-46}$$

where the drop number density, n_i, is related to the volume fraction by: $r f_i = n_i v_i$; v_i is the drop volume; B_B and D_B are birth and death rates in the break-up process, respectively; B_C and D_C are the birth and death rates in the coalescence process respectively. So that equation (7-48) becomes:

$$\frac{\partial}{\partial t}(rf_i) + \nabla \bullet (Urf_i) = S'_i \tag{7-47}$$

Equation (7-47) is identical to equation (7-45) above when multiplied by the phase density. Therefore, the link between population balance and CFD via the MUSIG model has been established. To complete the model, the sources ands sinks should be defined due to break-up and coalescence.

7.4.2.3 Break-up Model

Luo and Svenden (1996) developed a theoretical model for the break-up of drops and bubbles in turbulent dispersions. The model is based on the theories of isotropic turbulence and probability but, significantly, the model contains no unknown or adjustable parameters. Binary break-up is assumed. The break-up rate of bubbles (or drops) of volume v_i into bubbles (or drops) of volume $v_i (= v_j f_{BV})$ is expressed as:

$$g(v_j : v_i) = 0.923 f_B (1-r)(\frac{\varepsilon}{d_j^2})^{1/3} \int_{\xi_{\min}}^{1} \frac{(1+\xi)^2}{\xi^{\frac{11}{3}}} e^{-\chi_c} d\xi \tag{7-48}$$

where:

$$\chi_c = \frac{12\left[f_{BV}^{\frac{2}{3}} + (1-f_{BV})^{\frac{2}{3}} - 1 \right]\sigma}{\beta \rho_l \varepsilon^{\frac{2}{3}} d_j^{\frac{5}{3}} \xi^{\frac{11}{3}}} \tag{7-49}$$

in which, f_{BV} is a dimensionless variable describing the sizes of daughter drops or bubbles (the breakage volume fraction), $f_{BV} = \frac{v_1}{v} = \frac{d_I^3}{d^3} = \frac{d_I^3}{d_I^3 + d_{II}^3}$, where d_I and d_{II} are diameters (corresponding to volume v_I and v_{II}) of the daughter drops in the binary breakage of a parent drop with diameter d (corresponding to volume v). Obviously, the value interval for the breakage volume fraction should be $0 < f_{BV} < 1$ ($f_{BV} = 0.5$ meaning equal binary breakage

and f_{BV} = 0 or 1 meaning no breakage). f_B is a coefficient of the model. ξ is the dimensionless size of eddies in the inertial sub-range of isotropic turbulence; r is dispersed liquid volume fraction; d_j is the bubbles or drops diameter; ε is energy dissipation rate; ρ_l is the dispersed fluid density; β is another coefficient; σ is the interfacial tension. χ_c is the critical dimensionless energy for break-up. The f_B is a coefficient of the model.

The birth rate of group i drops due to break-up of larger drops is:

$$B_B = \sum_{j=i+1}^{N} g(v_j : v_i) n_j \tag{7-50}$$

The death rate of group j drops due to break-up to smaller drops is:

$$D_B = g_j n_j \tag{7-51}$$

7.2.4.4 Coalescence Model

The coalescence of two drops is often assumed to occur in three steps. First the drops collide trapping a small amount of liquid between them. This liquid film then drains until the liquid film separating the drops reaches a critical thickness. The film ruptures and the drops join together. The coalescence process is therefore modelled by a collision rate of two drops and a collision efficiency relating to the time required for coalescence (τ_{ij}). Prince and Blanch (1996) considered the collisions resulting from three different mechanisms, turbulence (θ_{ij}^{T}), buoyancy (θ_{ij}^{B}) and laminar shear (θ_{ij}^{LS}). The total coalescence rate is:

$$Q_{ij} = (\theta_{ij}^{T} + \theta_{ij}^{B} + \theta_{ij}^{LS})\eta_{ij} \tag{7-52}$$

where the collision efficiency is:

$$\eta_{ij} = e^{(-t_{ij}/\tau_{ij})} \tag{7-53}$$

The time required for coalescence is:

$$t_{ij} = \left(\frac{r_{ij}^3 \rho_l}{16\sigma}\right)^{\frac{1}{2}} \ln\frac{h_0}{h_f} \tag{7-54}$$

where h_0 is the initial film thickness and h_f is the critical film thickness when rupture occurs; ρ_l is the dispersed fluid density; σ is the interfacial tension; r_{ij} is the equivalent radius given by: $r_{ij} = \frac{1}{2}(\frac{1}{r_i} + \frac{1}{r_j})^{-1}$, where r_i and r_j are the radius of drop i and drop j, respectively.

The contact time of two drops is:

$$\tau_{ij} = \frac{r_{ij}^{2/3}}{\varepsilon^{1/3}} \tag{7-55}$$

In the current model, only the turbulence collision is included. Therefore,

$$Q_{ij} = f_c \theta_{ij}^T e^{(-t_{ij}/\tau_{ij})} \tag{7-56}$$

f_c is a coefficient of the model. The turbulence collision rate is given by:

$$\theta_{ij}^T = S_{ij}[u_{ti}^2 + u_{tj}^2]^{1/2} \tag{7-57}$$

where the collision cross-sectional area of the drop is defined by:

$$S_{ij} = \frac{\pi}{4}[d_j + d_i]^2 \tag{7-58}$$

The turbulent velocity given by:

$$u_{ti(tj)} = 1.4\varepsilon^{1/3} d_{i(j)}^{1/3} \tag{7-59}$$

The birth rate of group *i* drops due to coalescence of group-*j* and group-*k* drops is:

$$B_C = \frac{1}{2}\sum_{j=1}^{i}\sum_{k=1}^{i} Q_{jk} n_j n_k \tag{7-60}$$

The death rate of group *i* drops due to coalescence of group-*i* and group-*j* drops is:

$$D_C = \sum_{j=1}^{N} Q_{ji} n_j n_i \tag{7-61}$$

where N is the number of size groups.

7.5 Introduction to CFX®-4.4

CFD codes are structured around the numerical algorithms that can tackle fluid flow problems. All commercial CFD codes (e.g. CFX®, STAR-CD®, PHOENICS®, etc.) contain three main elements: (i) a pre-processor, (ii) a solver and (iii) a post-processor. The function of each of these elements within the CFX®-4 code is briefly introduces as following.

Pre-processor

Pre-processing consists of the input of a flow problem to the CFX® program. The user activities at the pre-processing stage involve:

1. Definition of the geometry of the region of interest: the computational domain.
2. Grid generation- the sub-division of the domain into a number of smaller, non-overlapping sub-domains: a mesh of control volumes.
3. Selection of the physical and chemical phenomena that need to be modelled.
4. Definition of fluid properties.
5. Specification of appropriate boundary conditions at control volumes which coincide with the domain boundary.

Solver

The numerical solution technique- *the finite volume method* is used in CFX®-4. The numerical algorithm consists of the following steps:

1. Formal integration of the governing equations of fluid flow over all the (finite) control volumes of the solution domain.

2. Discretisation, which involves the substitution of a variety of finite-difference-type approximations for the terms in the integrated equation representing flow processes such as convection, diffusion and sources. This converts the integral equations into a system of algebraic equations.

3. Solution of the algebraic equations by an iterative method.

Post-processor

In this study, CFX®-5 Post has been used mainly to:

1. Domain geometry and grid display;

2. Vector, contours, etc. plots;

3. Colour postscript and data output.

CHAPTER 8

Computational Results for Liquid-liquid Dispersed Flows

This chapter presents the CFD computational results using the CFX®4.4 code. Two simulations were carried out; one for oil-in-water upwards dispersed flow in a circular pipe (Section 8.1) and the other for the oil-in-water dispersed flow in non-circular duct (Section 8.2) matching the experiments described in Chapter 4 and 5.

8.1 CFD Simulations of Oil-Water Dispersed Flow in a Circular Pipe

This section presents the results of the numerical simulations of liquid-liquid flows in a circular pipe and the predictions are compared with the experimental data of Farrar & Bruun (1996). Firstly, a brief account of the experimental setup and conditions are provided; this is followed by a description of numerical method (Section 8.1.1 and 8.1.2 respectively). Calculated results, which include the radial phase distributions and drop size distributions are compared with the experimental data in Section 8.1.3 and a short summary is given in Section 8.1.4.

8.1.1 Experiments

The test facility of Farrar & Bruun (1996) was designed to deliver a mixture of water and kerosene of known composition to the chosen test section by using two pumps; the total mixture flowrate was 185 l/min. The two metered fluids are then mixed in a Y junction, followed by a 90° bend to provide the required vertical flow. A swirl remover and flow conditioning unit as well as a contraction unit are also used with the aim of producing a fully developed two-phase flow at the end of the test section. The circular tube test section was 1.5m long and had a diameter of 78 mm. It consisted of a development length and a measurement section used for detailed hot-film anemometer studies. The hot wire anemometer gave a signal which was different in the respective phases. The fraction of time the probe spent in the oil phase gave the local in-situ oil holdup and the contact times with the oil phase droplets gave local chordal contact length (related to drop size). In the test rig there were, after the swirl remover unit and smooth contraction unit, 17 diameters of straight pipe before the hot-film instrumentation. This was claimed to provide nearly fully developed flow conditions at the measurement position. The majority of the tests were performed over the range 5-30% "volumetric quality" (ε^{o}_{input} [1]) at 5% intervals. At all values of the volumetric quality, measurements were made of the radial profiles of the local volume fraction, mean drop chord length, mean continuous phase velocity and turbulence intensity.

The liquid physical properties were not given by Farrar and Bruun; thus, the following literature values for densities, viscosities and interfacial tension for water and kerosene at 25 °C have been used:

Table 8.1 The physical properties of the two phases.

	Density (kg/m^3)	Viscosity (Ns/m)	Interfacial tension (N/m)
Water	1000	0.0009	0.01
Kerosene	803	0.00162	

8.1.2 Numerical Methods

In order to maximise computational efficiency, the geometry adopted in the simulations was a quarter of the pipe and the whole length of the vertical section (0.078 m diameter and

[1] The "volumetric quality" defined by Farrar and Bruun (1996) is the fraction by volume of the oil phase in the input flow, thus corresponding to ε^{o}_{input} in this current nomenclature.

1.35 m long); the hot film anemometer was located at an axial position X/D of 17 (about 1.32 m away from the entrance of the vertical part). Figure 8.1 shows the mesh generated at the XY plane.

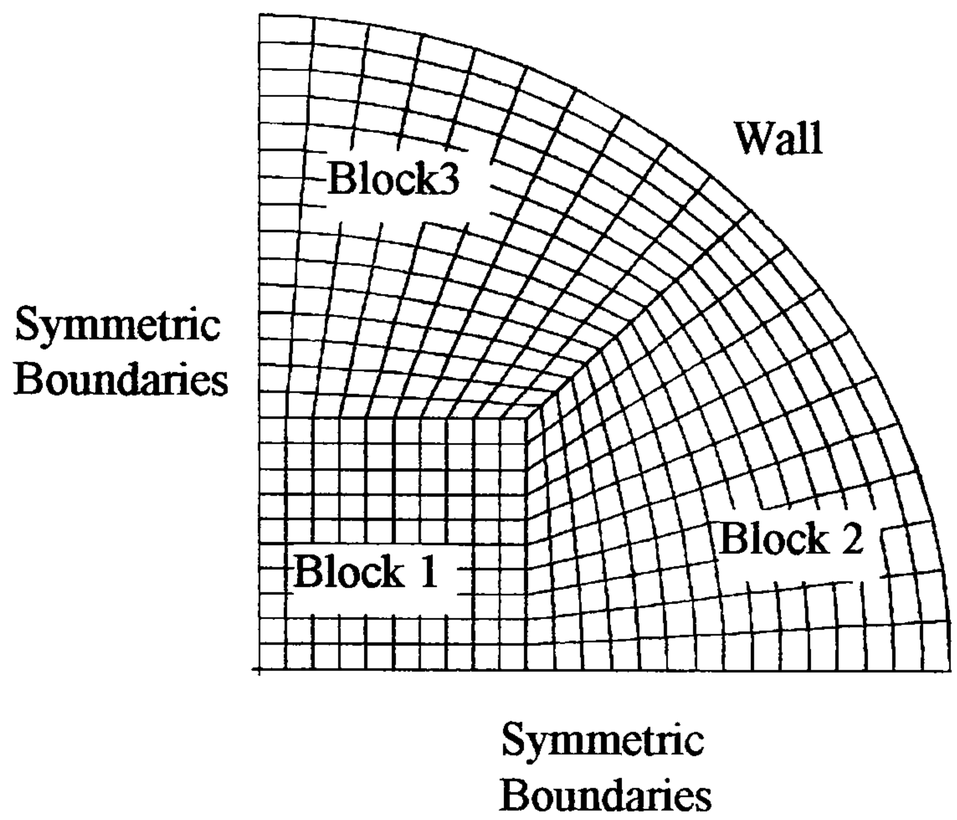


Figure 8.1 Mesh in the XY plane of the quarter tube geometry

To assess the sensitivity of the results to the grid size, a series of tests were carried out. Figure 8.2 (a) shows the calculated results with 100 and 150 grid points in the longitudinal direction. Figure 8.2 (b) shows the wall grid tests which are carried out by changing the number of grids in the radial direction in Block 2 and Block 3. It is seen that the results are very similar. It can thus be concluded that the mesh with 60,000 total grid points (block 1 has 10×10×150 grids in the X, Y and Z direction, respectively, and blocks 2 and 3 have 15×10×150 grids), is sufficient to provide reliable, grid insensitive numerical results.

The calculations achieved convergence after approximately 1000-2000 iterations, taking between 4 and 8 hours on a LINUX workstation having 512 RAM and 1.8GHz Pentium 4 CPU speed. For the boundary conditions, uniform velocities and volume fractions for each phase were specified at the inlet and a pressure boundary ($p = 0.0$) was specified at the outlet. Steady state solutions were then sought.

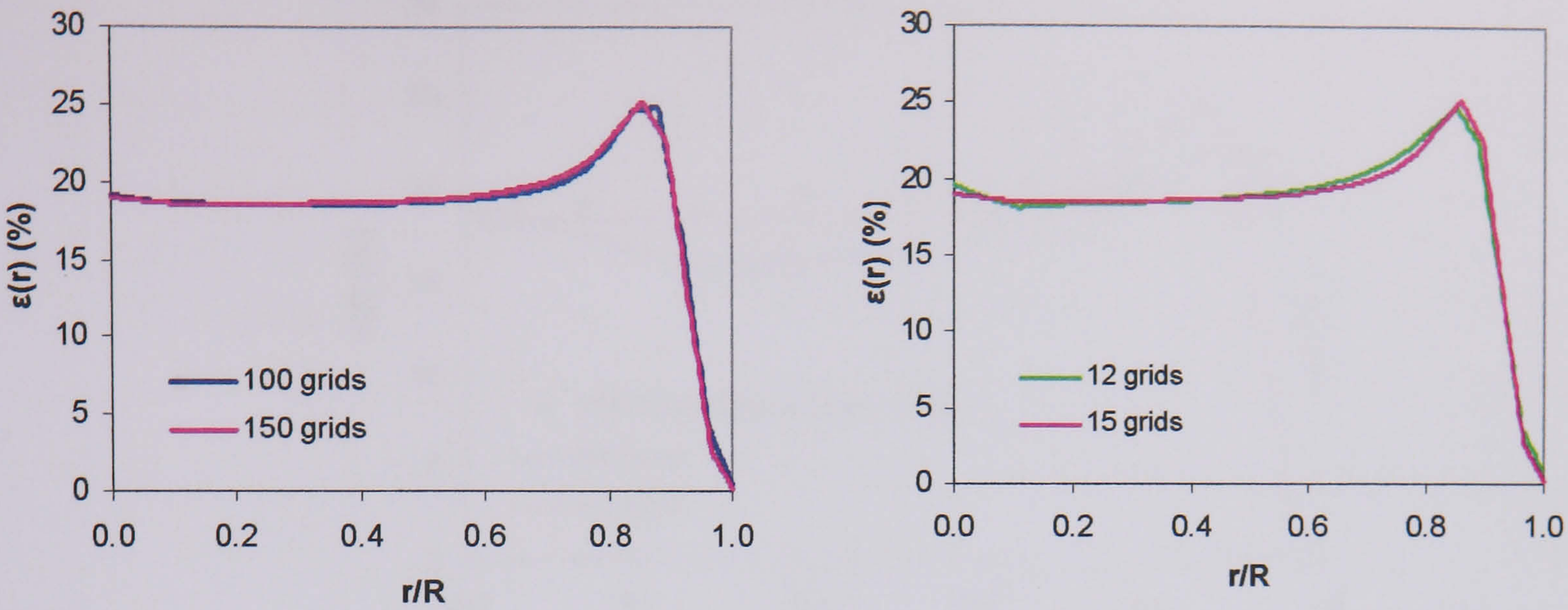


Figure 8.2 Grid sensitivity tests on dispersed phase distributions with ε^{o}_{input} = 20% and the mixture velocity U_m=0.68 m/s; (a) 100 and 150 grids in the longitudinal direction; (b) 12 and 15 grids in radial direction of block 2 and 3. The parameter values are taken as, lift force coefficient C_L = 0.01, the turbulent dispersion force coefficient C_{TD} = 0, break-up coefficient f_B = 0.1 and coalescence coefficient f_C =1.

Two different turbulence models were tested namely the Reynolds Stress (RS) model and the k– ε model. The calculations were carried out using the standard values of the relevant constants as described in Section 7.2.2.

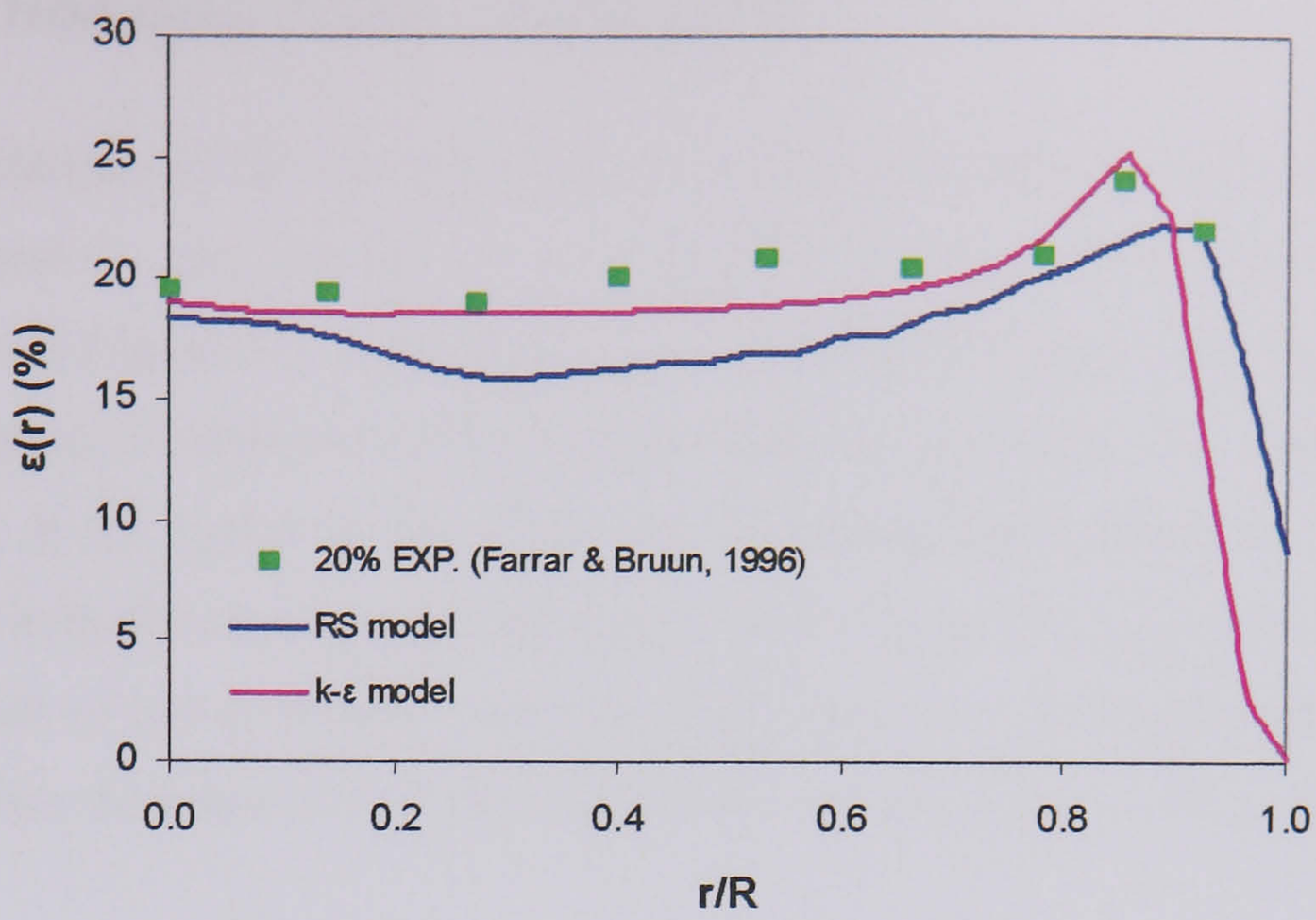


Figure 8.3 Comparisons of experimental dispersed phase distributions, ε(r), with the calculation results using Reynolds stress model and k– ε model for ε^{o}_{input} = 20% and U_m=0.68 m/s.

The CFD predictions of the radial dispersed phase distributions, ε(r), and experimental data shown in Figure 8.3 shows that the prediction using the RS model underestimates the dispersed phase distributions in the region of r/R <0.9. Near the wall, however, the calculated $\varepsilon(r)$ using the RS model is higher than that obtained using the k– ε model. Since the experimental data covered the range of 0< r/R <0.923 only, it is difficult to say which of the two models provides better predictions near the wall. In the region $0 \leq r/R \leq 0.85$, it appears that the k– ε model provides a closer prediction than the RS model. Hence, only the k– ε model was used in further calculations of the Farrar and Bruun (1996) system.

8.1.3 Results Comparison and Discussion

A number of calculations demonstrated that, the coefficient of the non-drag forces (the lift force coefficient, C_L, and the turbulent dispersion force coefficient, C_{TD}) and the coefficients in the break-up and coalescence models, play important roles in the phase distribution near the wall. However, phase distribution, drop size and velocity, are relatively insensitive to these values for $r/R < 0.6$.

8.1.3.1 Non-drag Forces Coefficients

Several calculations at 20% oil volume quality, were performed in order to determine the coefficients C_L and C_{TD} that provide the best agreement between theory and experiments. In Figure 8.4, the experimentally determined $\varepsilon(r)$ profile was compared with the prediction of the CFX calculation for different values of the lift force coefficient, C_L. Inspection of this plot shows that, in the region of r/R < 0.6, the CFX phase distributions are in reasonably good agreement with the experimental results provided C_L is in the range 0.01-0.05. Near the wall where a peak in $\varepsilon(r)$ is observed experimentally, however, good agreement is obtained for $C_L = 0.01$. Thus the value of $C_L = 0.01$ is fixed for the rest of the results given here.

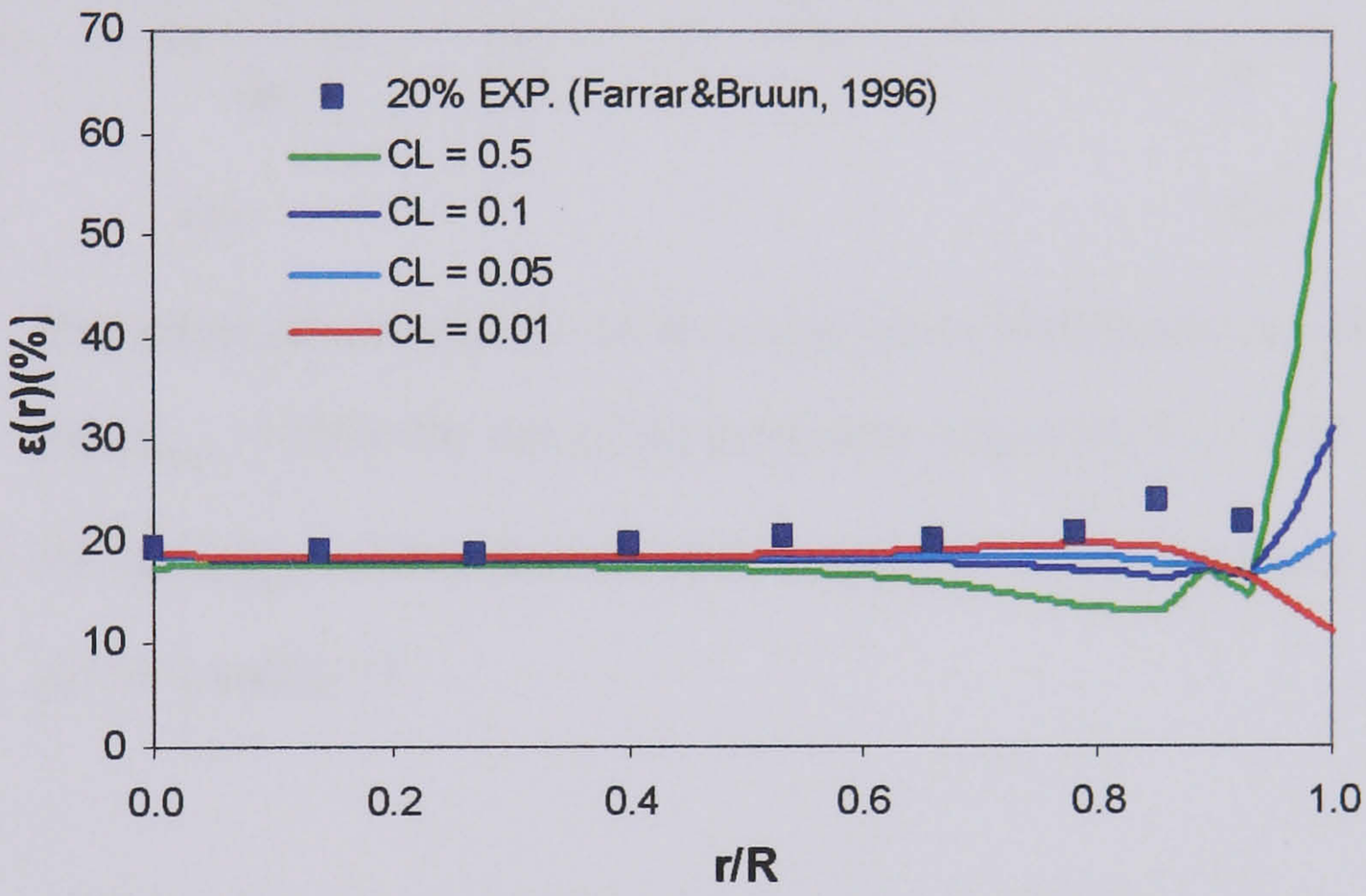
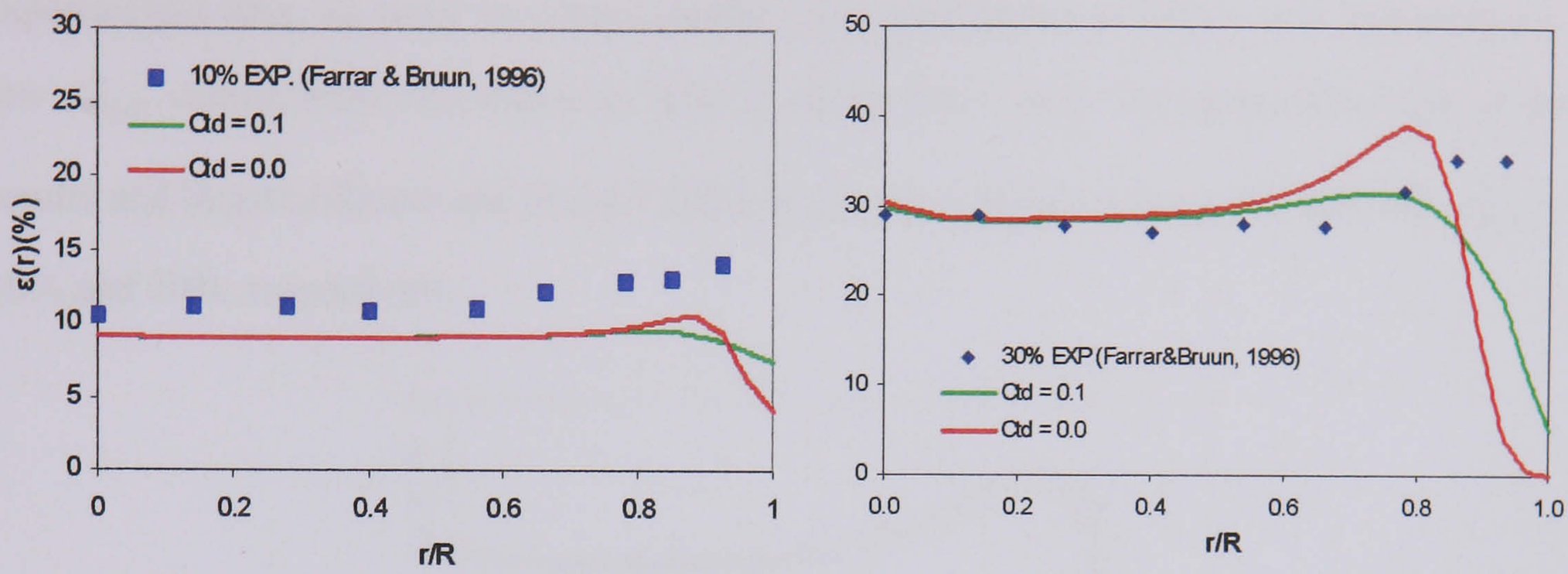


Figure 8.4 The effect of varying C_L on the radial phase distribution with $\varepsilon^o_{input} = 20\%$ and U_m=0.68 m/s. The rest of the parameter values are taken as, the turbulent dispersion force coefficient $C_{TD} = 0$, break-up coefficient $f_B = 0.1$ and coalescence coefficient f_C =1.

The turbulent dispersion force coefficient, C_{TD}, also exerts a significant influence on the phase distributions. The CFX calculations show that large-amplitude peaks in the phase distribution appear for all ε^o_{input} values studied when $C_{TD} = 0$. Conversely, more uniform distributions are obtained when $C_{TD} = 0.1$. The experimental results of Farrar and Bruun (1996), on the other hand, suggest that the dispersed phase fraction profile is rather uniform at low ε^o_{input} but develops a peak near the wall as ε^o_{input} increases. Thus, in order to obtain good agreement with experimental data, C_{TD} has been specified as 0.1 for $\varepsilon^o_{input} < 20\%$ and 0

for $\varepsilon^{o}_{input} \geq 20\%$. The favourable agreement between the CFX predictions and the experimental data is shown in Figures 8.5 (a) and (b) with ε^{o}_{input} = 10% and 30%, respectively.



(a) (b)

Figure 8.5 The effect of varying C_{TD} on the radial phase distribution for U_m=0.68 m/s. (a) ε^{o}_{input} = 10%; the rest of the parameter values are $C_L = 0.01$, $f_B = 1$ and f_C =1. (b) ε^{o}_{input} = 30%; the rest of the parameter values are taken as, $C_L = 0.01$, $f_B = 0.1$ and f_C =1.

8.1.3.2 Break-up and Coalescence Model Coefficients

Drop breakup and coalescence are two important processes which are considered as mechanisms to control drop size distributions. As mentioned previously the MUSIG algorithm in CFX-4 includes the Luo & Svenden (1996) break-up model and the Prince & Blanch (1996) coalescence model, which will be referred to as the 'LS' and 'PB' models, respectively. The predictions of the LS model for air-water systems in pipeline flow have been compared favourably with the experimental results of Hesketh *et al.* (1991 a & b). The PB coalescence model, on the other hand, is valid only for the coalescence of two bubbles and has been only validated against experimental data obtained in a bubble column (Luo & Svenden, 1996). Both models have been developed for dilute dispersions. Nevertheless, two adjustable coefficients (break-up coefficient f_B (see Eq. 7-48) and coalescence coefficient f_C (see Eq. 7-56) for these models have been added to CFX-4.4 to enable their application for the case of liquid-liquid dispersions.

The numerical simulations, however, have indicated that the coalescence coefficient f_C has little influence on the phase distribution, as shown in Figure 8.6. Variation of the break-up coefficient, f_B, on the other hand, does affect the amplitude of the wall peak; the numerical results with small break-up coefficient f_B for $\varepsilon^o_{input} \geq 20\%$ agree well with the experimental data. In order to obtain similar agreement between theory and experiment at low ε^o_{input} values, however, relatively large f_B values were used. The agreement between the results and those of Farrar and Bruun (1996) is shown in Figure 8.7 (a) and (b) with ε^o_{input} = 10% and 20%, respectively.

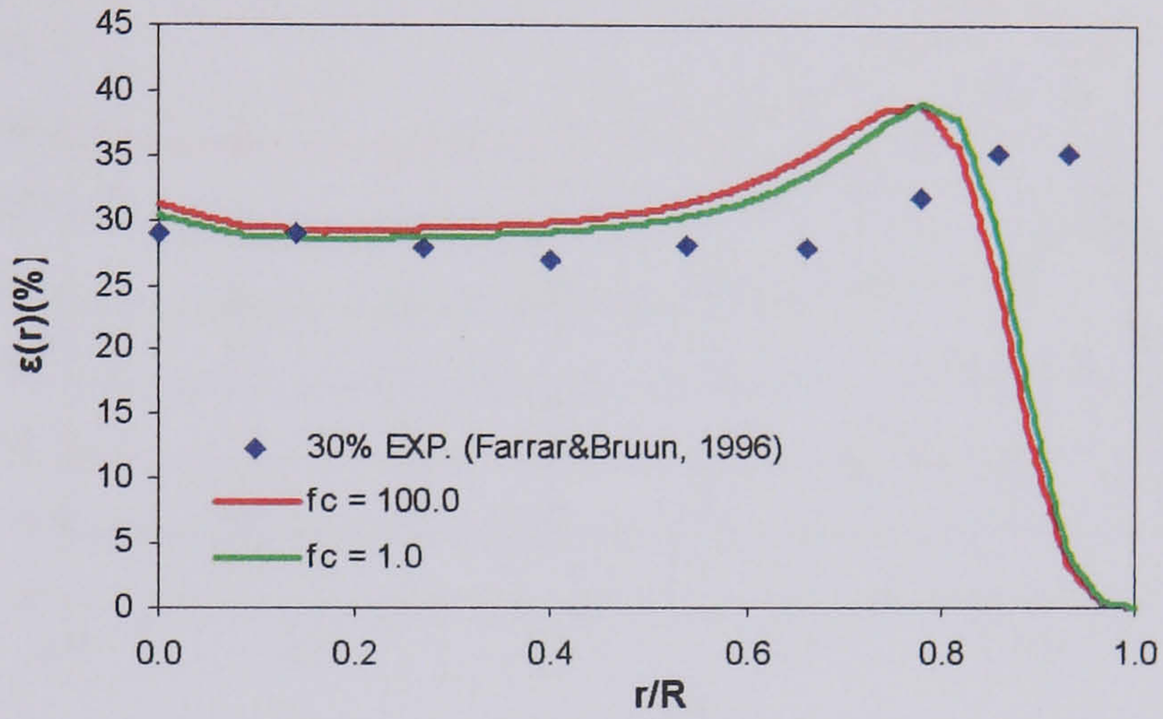
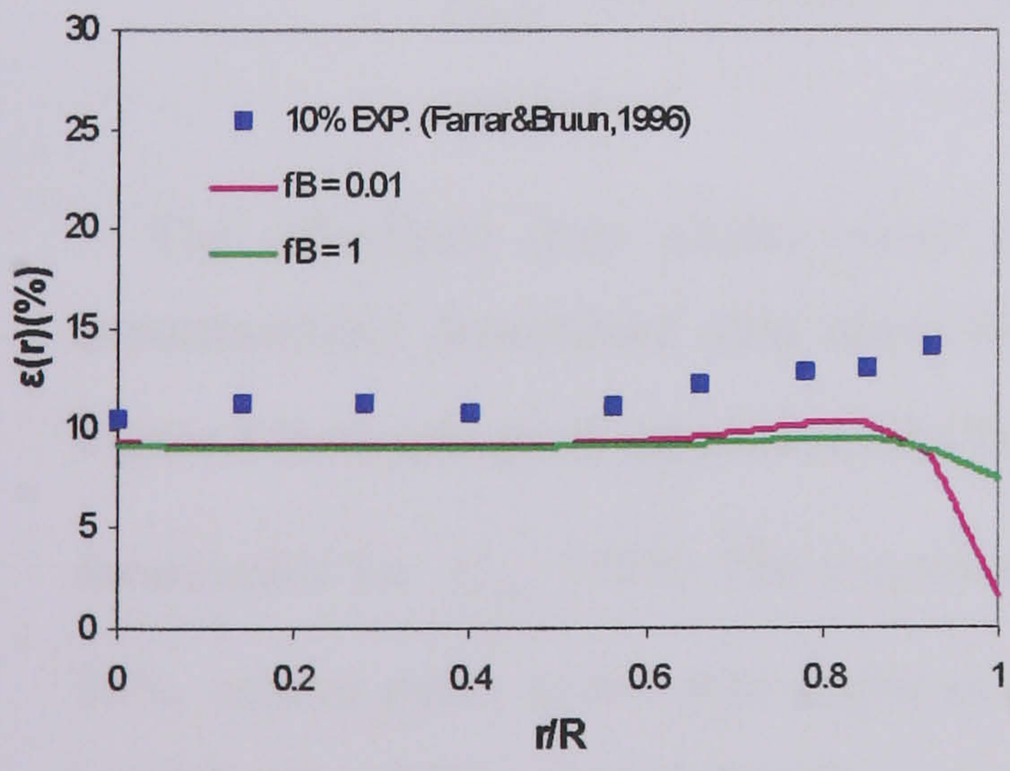
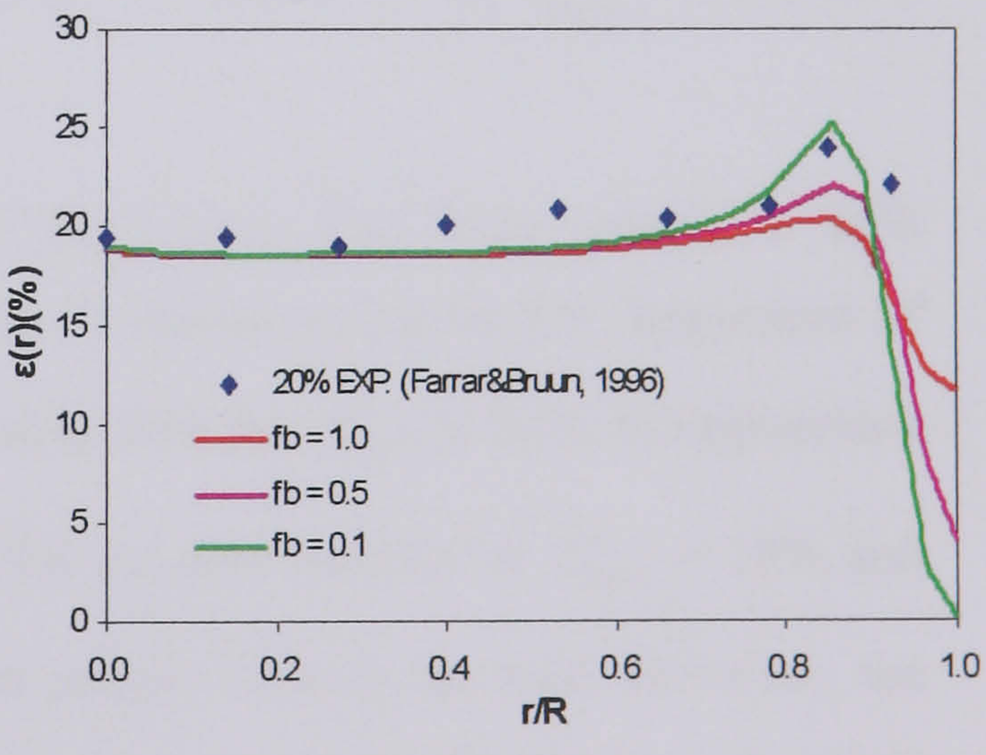


Figure 8.6 The effect of varying f_C on the radial phase distributions with ε^o_{input} = 30% and U_m=0.68 m/s. The rest of the parameter values are taken as, $C_{TD} = 0$, $C_L = 0.01$ and $f_B = 0.1$.



(a)



(b)

Figure 8.7 The effect of varying f_B on radial phase distributions for U_m=0.68 m/s; (a) ε^o_{input} = 10%; the rest of the parameter values are taken as, $C_L = 0.01$, C_{TD} = 0.1 and $f_C = 1$; (b) ε^o_{input} = 20%; the rest of the parameter values are taken as, $C_L = 0.01$, $C_{TD} = 0$ and $f_C = 1$;

Using f_B, C_{TD} and C_L as quality-dependent coefficients, Figure 8.8 shows the CFX-predicted $\varepsilon(r)$ together with experimental data for ε^o_{input} = 5%, 10%, 15%, 20%, 25% and 30% with C_L = 0.01 for all cases. It can be observed that the agreement between the experimental and the calculated phase distribution is reasonably good; the $\varepsilon(r)$ profiles are almost uniform near the centre and exhibit peaks near the wall, which become more prominent with increasing ε^o_{input}. For all volumetric qualities studied, the CFX predictions underestimate the magnitude of the dispersed phase distribution peaks near the wall.

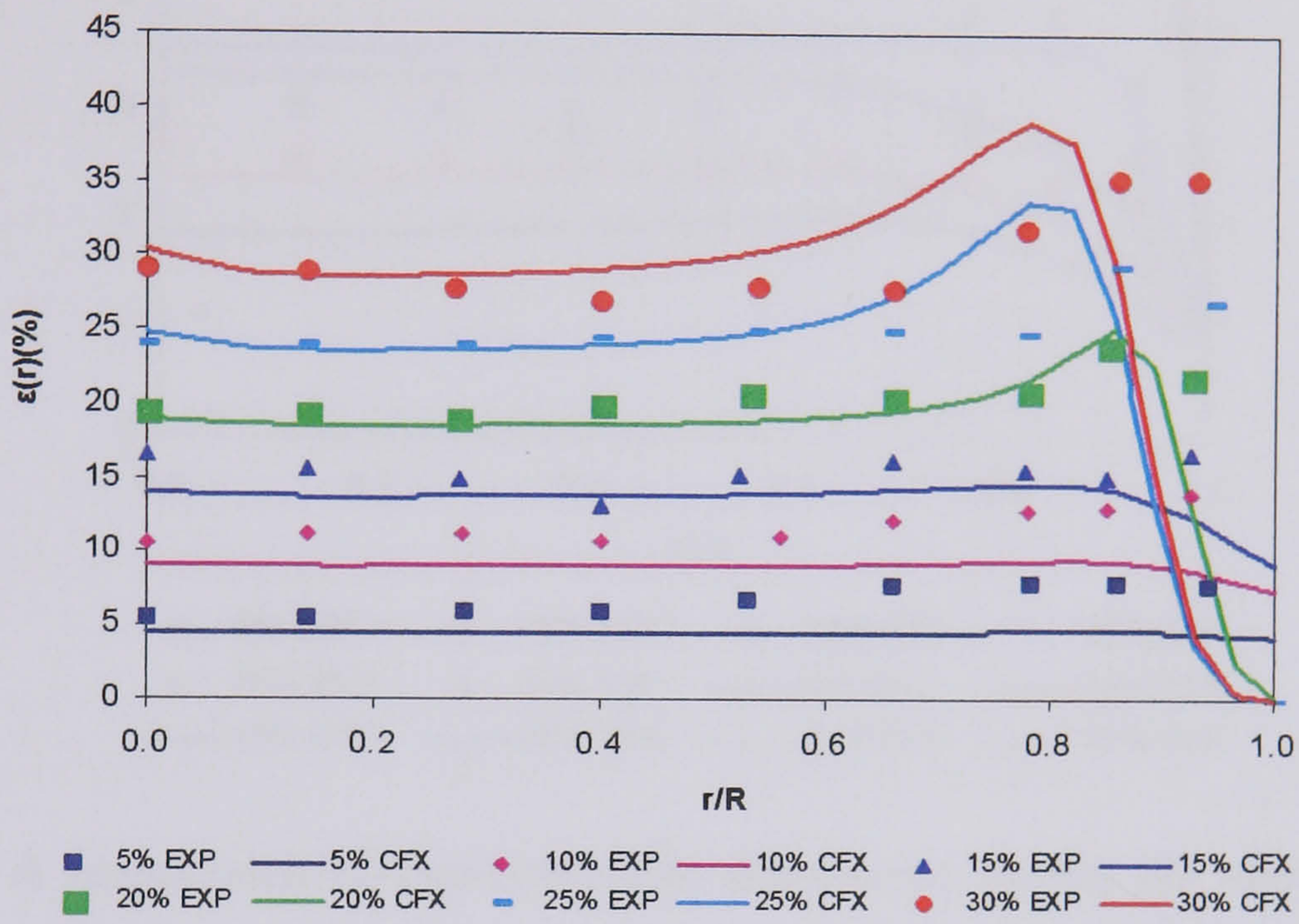


Figure 8.8 Comparison of the CFX-predicted ε(r) with the experimental data of Farrar and Bruun (1996) for U_m=0.68 m/s. C_{TD} = 0.1, f_B = 1.0 and f_C = 1.0 for ε^o_{input} = 5%, 10% and 15%; C_{TD} = 0, f_B = 0.1 and f_C = 1 for ε^o_{input} = 20%, 25% and 30%.

The calculated drop Sauter mean diameters (d_{32}) have also been compared with experimentally determined drop chord lengths; this is shown in Figure 8.9. Inspection of Figure 8.9 reveals good agreement with the experiment data for $\varepsilon^o_{input} \leq 20\%$; the agreement deteriorates for ε^o_{input} >20%. The experimental bubble cut cord lengths, at ε^o_{input} = 25% and 30%, exhibit peaks at the pipe centre and decrease steeply towards the wall. However, the trend for the CFX calculated drop sizes distributions is very similar for all the volumetric quantities: the drop sizes remain essentially uniform at large central region and decrease sharply close to the wall. In fact, the calculated drop sizes for ε^o_{input} > 20% show small peaks near the wall which are similar to those obtained in Figures 8.5-8.8.

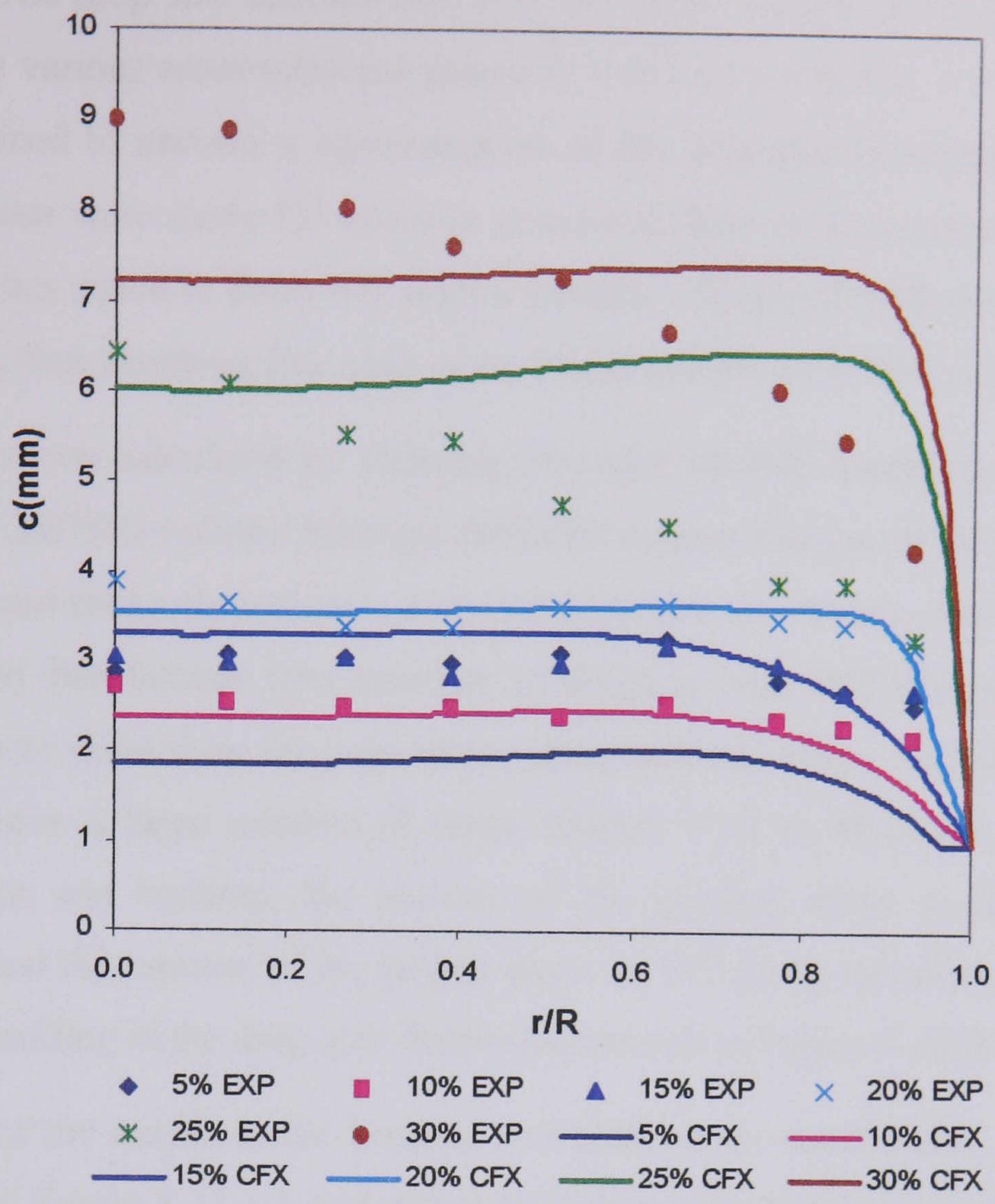


Figure 8.9 A comparison of experimentally determined bubble cut chord length c(r) with drop Sauter mean diameter obtained from the CFX simulations. The rest of the parameters are the same as those in Figure 8.8.

8.1.3.3 Drop Size Distribution

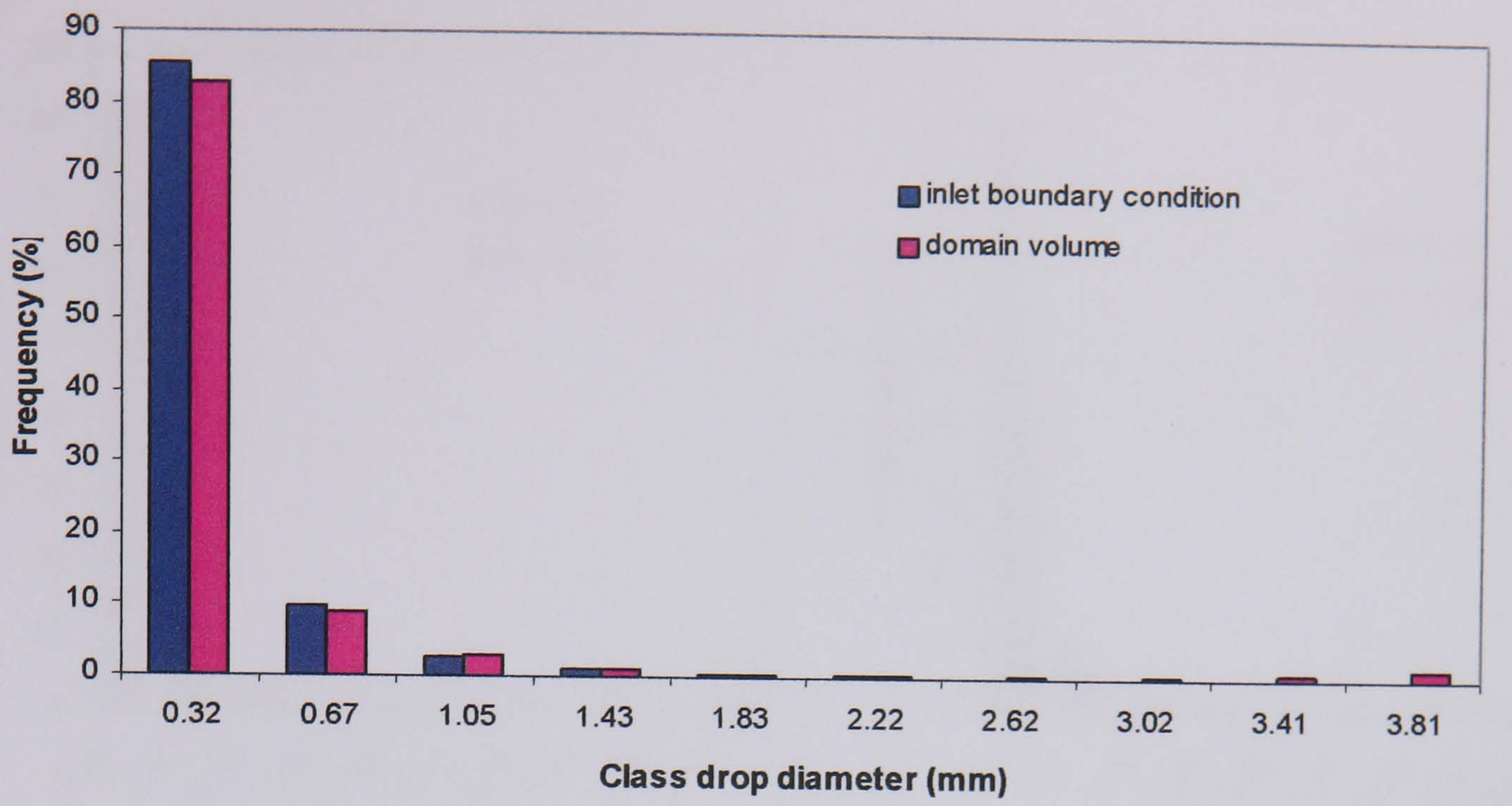
For turbulent dispersed pipe flows, the drops can interact with turbulent eddies in the continuous phase to change the structure of the turbulent flow field and influence parameters such as the pressure gradient. The ability to predict the drop size distribution will therefore lead to better modeling and design of dispersed systems. Furthermore, the knowledge of the dispersed phase size distribution is necessary when subsequent separation of the two phases is considered. However, there is only a limited amount of data for drop size distributions formed during pipeline flow, due to the difficult nature of the experiments involved. So far, the experimental work on drop break-up and coalescence has mainly been conducted in stirred tanks.

To achieve a better understanding of the development of dispersed drops, the drop distributions along the pipe were calculated using the MUSIG algorithm included in CFX-4.4. In the calculations, 10 size groups were used to give a reasonable representation of the

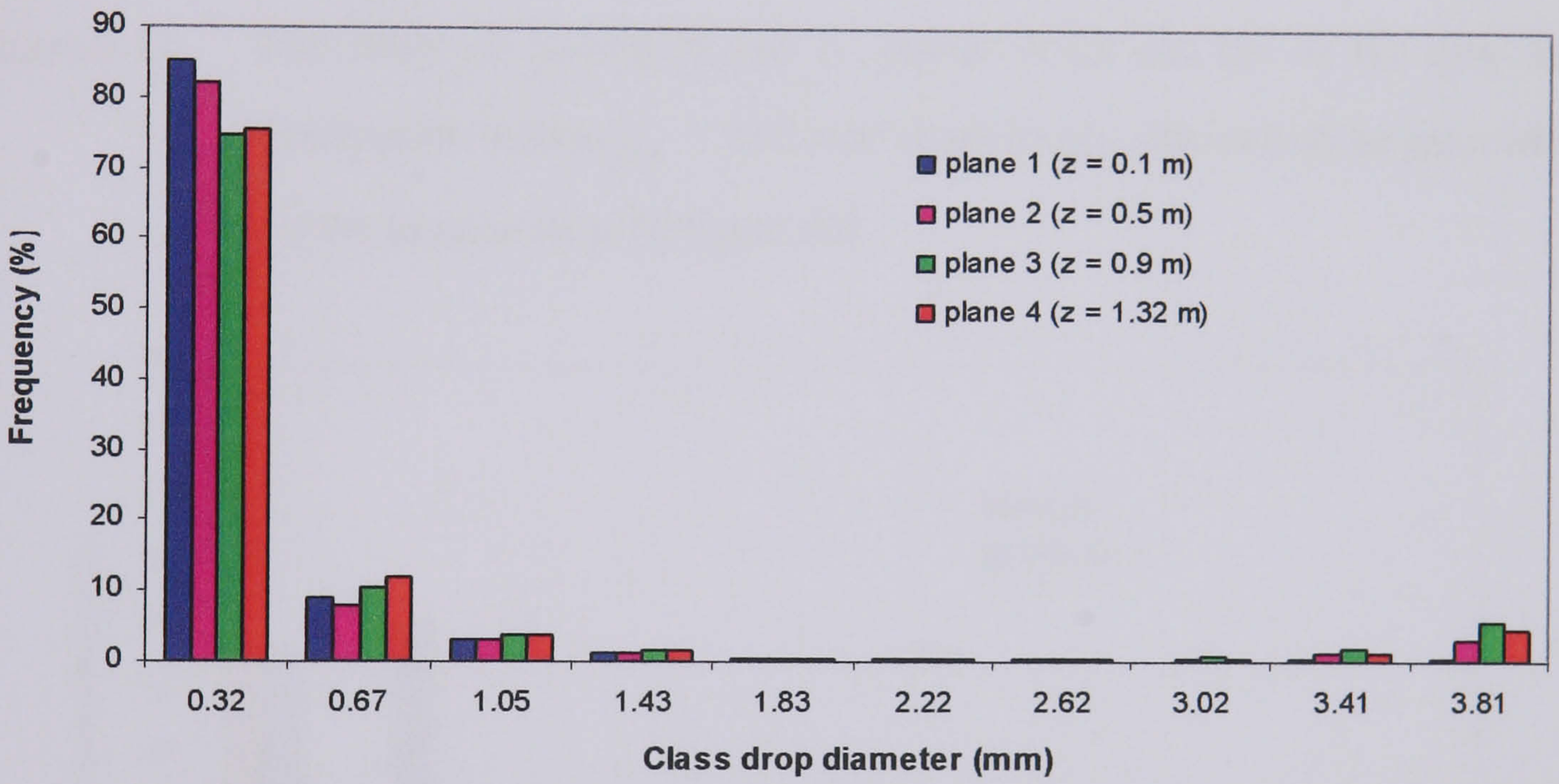
size distributions. The drop size distributions over the entire volume of the pipe as well as distributions across various cross-sectional planes (z = 0.1 m, z = 0.5 m, z = 0.9 m and z = 1.32 m) were obtained to provide a representation of the drop size development along the pipe. The calculations were made for upwards co-current flow of kerosene and water with the physical properties stated in Table 8.1, with a mixture velocity of 0.68 m/s and for a tube diameter of 78 mm, thus matching that used in the Farrar and Bruun (1996) experiments.

Two cases have been calculated by changing the inlet MUSIG boundary conditions. In the first case, equal MUSIG volume fractions (MUSIG volume fraction of size group 1 to 10 = 10%) were used and in the second case, a normal drop size distribution was employed. To derive the drop size distributions (the numbers of drops in each MUSIG group), MUSIG volume fractions were divided by the cube of the class drop diameters. Therefore, the small drop size groups have a large number of drops (Figure 8.10 a). However, as the drops undergo coalescence and breakup, the number of the smallest drops in the first group decreases slightly and the number of the largest drops in 10^{th} group increase along the pipe (plane 1-plane 4) resulting in the drop size distribution shown in Figure 8.10 (b).

The sensitivity of the results to the breakup and coalescence coefficients, f_B and f_C, has also been examined. Figure 8.11 (a) shows that total drop size distributions change slightly for different breakup rates. The coalescence rate, however, has been found to exert a far more significant influence as shown in Figure 8.11 (b), for the smallest and largest drop sizes; with f_c = 100 the drop size distribution develops a distinct U-shaped profile. For the middle drop groups, the influences of the break-up and coalescence coefficients was found to be very weak. Figure 8.12 presents the drop size distributions for different oil volume holdup, and $f_b = f_c = 1$. This plot clearly shows that increasing volume holdup results in the formation of larger drops and a drop size distribution exhibiting a peak at intermediate drop sizes.

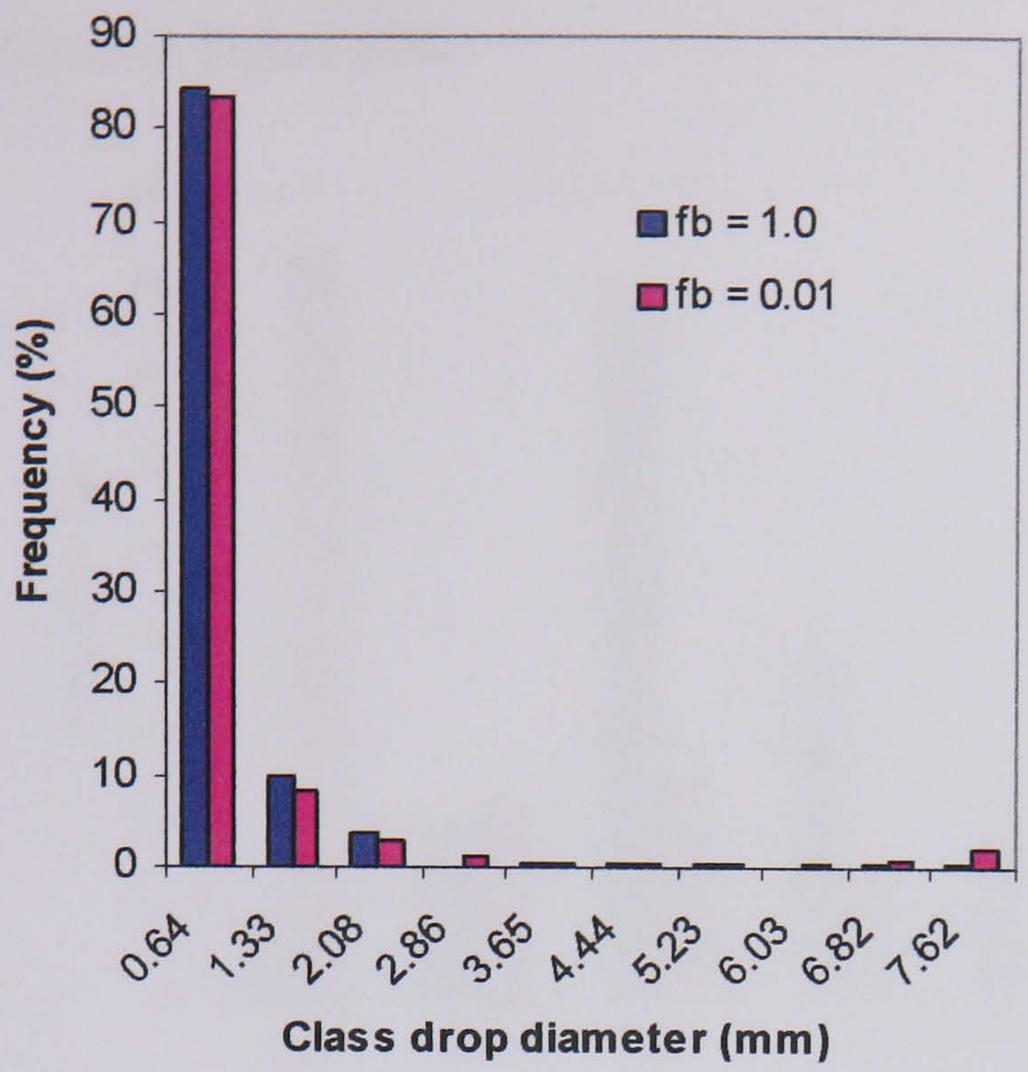


(a)

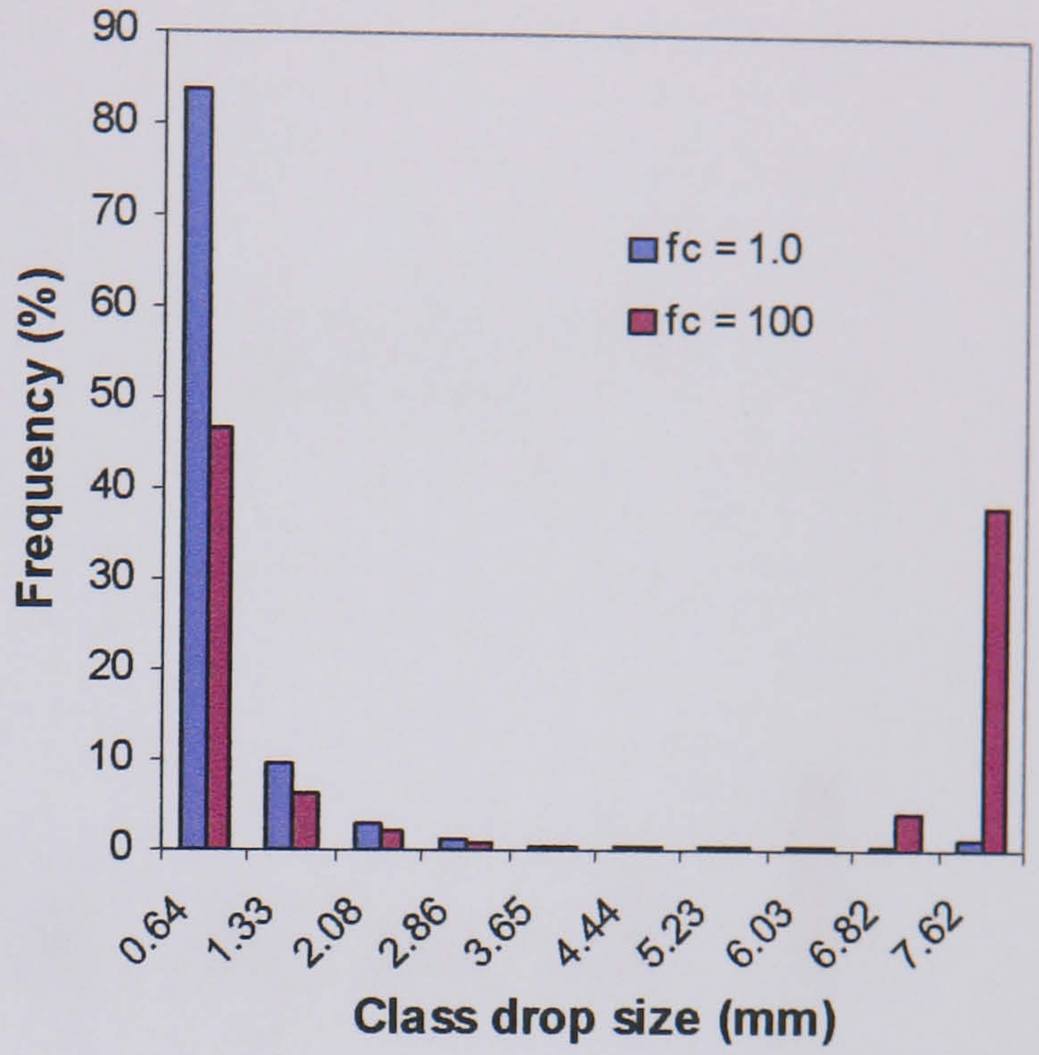


(b)

Figure 8.10 Drop size distributions with ε^{o}_{input} = 20% and U_m=0.68 m/s; (a) at the inlet and the entire volume; (b) at different planes. The rest of the parameters are the same as those in Figure 8.8.



(a)



(b)

Figure 8.11 The effect of varying f_B and f_C, shown in (a) and (b) on the drop size distributions with ε^{o}_{input} = 30% and U_m=0.68 m/s. The rest of the parameters are the same as those in Figure 8.8.

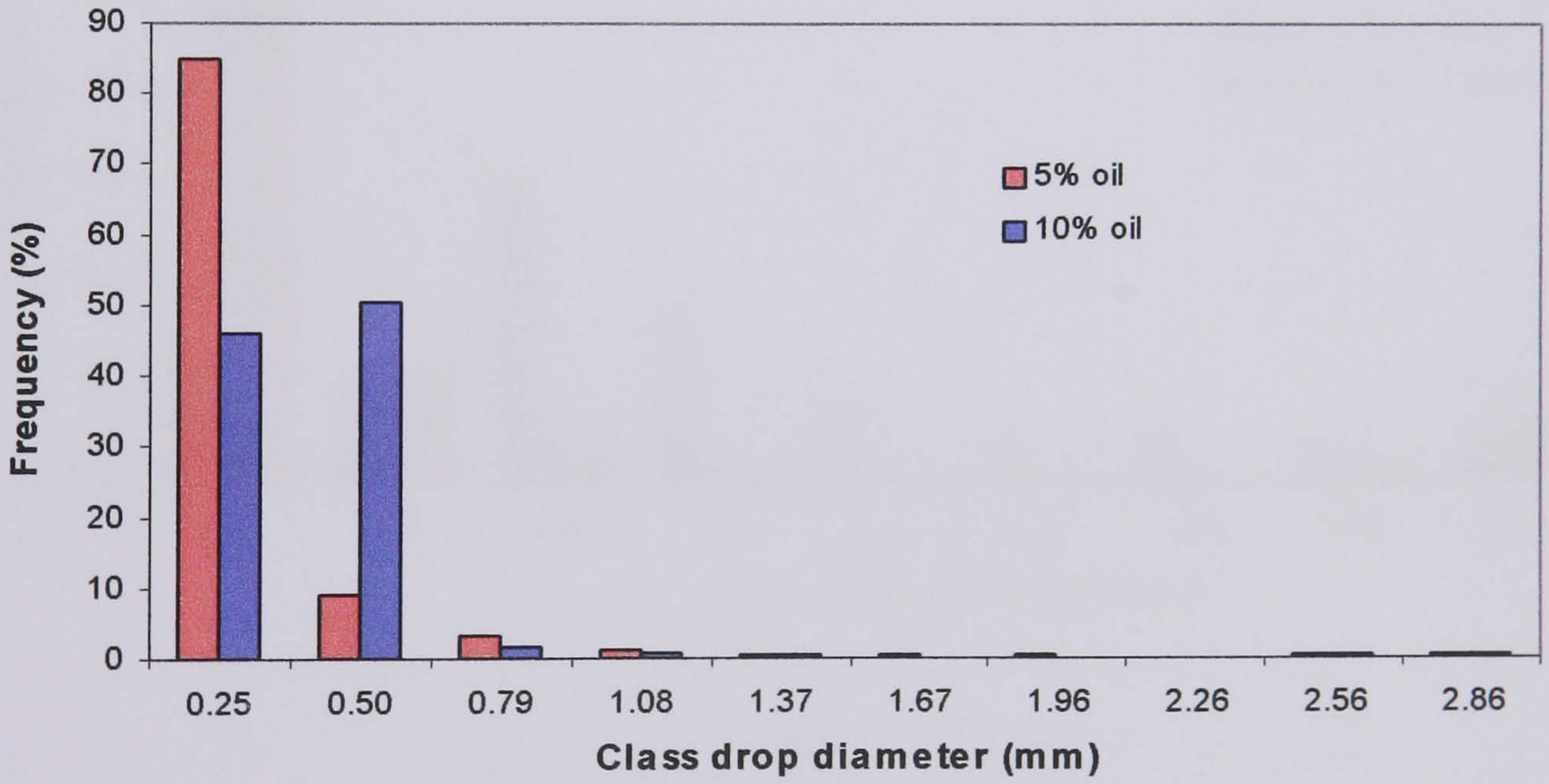
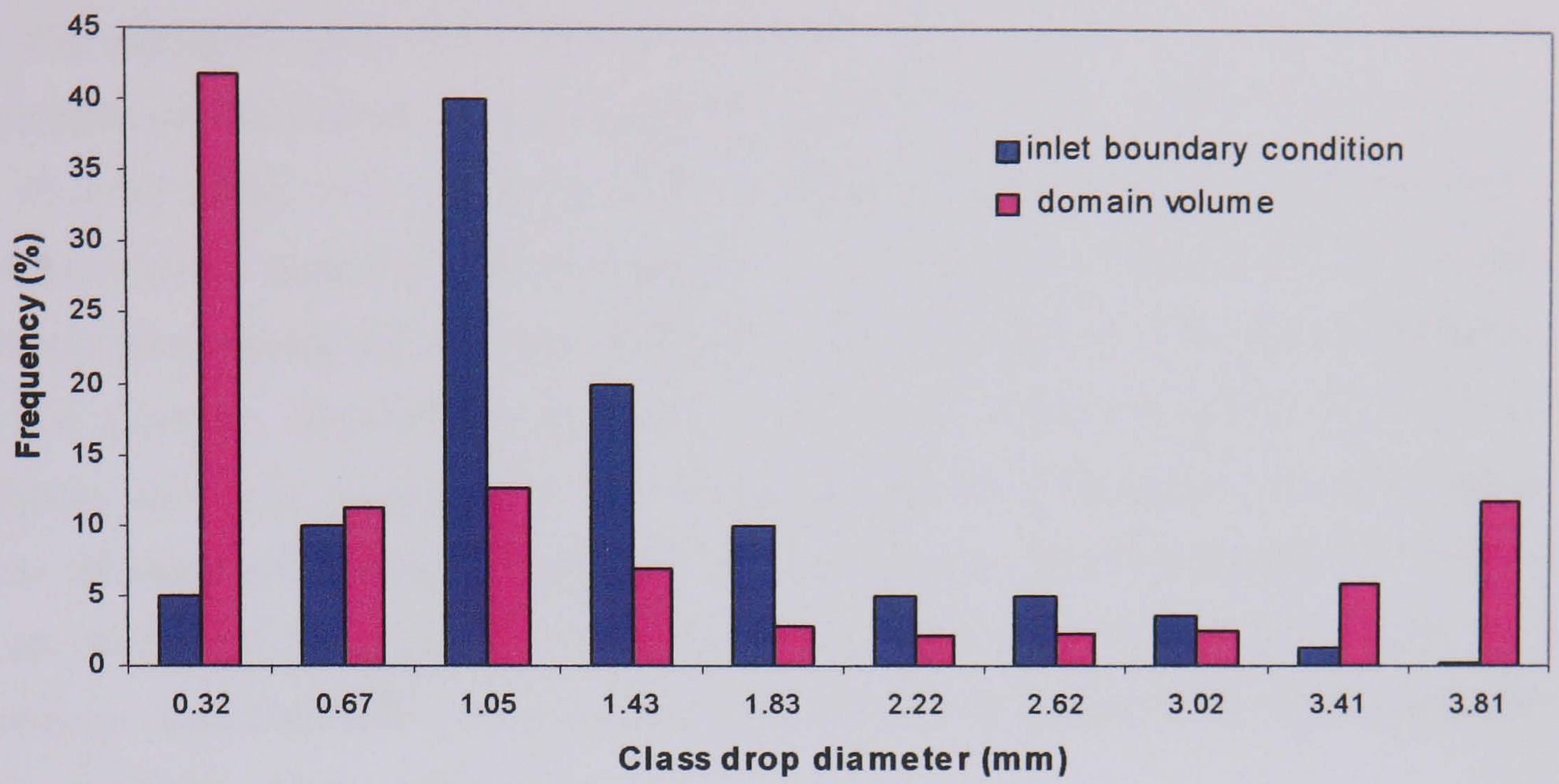


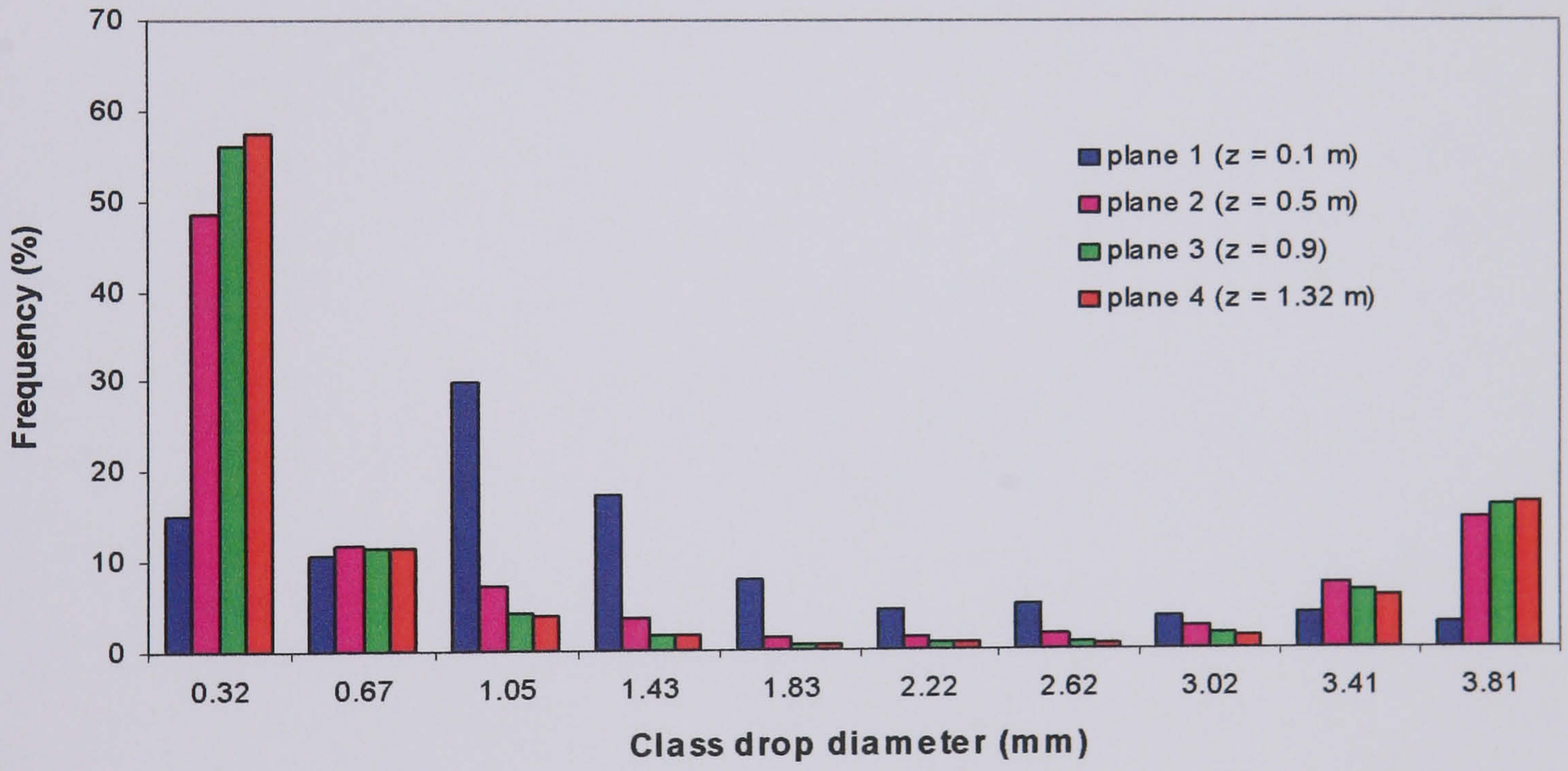
Figure 8.12 Drop size distribution for different oil holdup. The rest of the parameters are the same as those in Figure 8.8.

The results associated with the specification of a normal drop size distribution at the inlet are shown in Figure 8.13. Comparison of Figures 8.10 and 8.13 demonstrates that the results are sensitive to the distribution at the inlet. The sensitivity is maximal near the inlet and decreases along the pipe. The distributions over the whole domain as well as in different

planes along the pipe exhibit U-shaped profiles, which are more pronounced than those shown in Figure 8.10.



(a)



(b)

Figure 8.13 Drop size distributions with ε^{o}_{input} = 20% and U_m=0.68 m/s; (a) at the inlet and the entire volume; (b) at different planes. The rest of the parameters are the same as those in Figure 8.8.

8.1.4 Summary

Commercial software CFX4.4 was used to simulate oil-in-water dispersed upwards pipe flow. The calculated phase distribution and drop size d_{32} for different oil volume fractions were compared with published experimental data (Farrar and Bruun, 1996). Good agreement was obtained using very small lift force coefficients and turbulence dispersed force coefficients in the range 0-0.1. The calculations also demonstrated that the Luo & Svenden (1996) break-up model and the Prince & Blanch (1996) coalescence model can be applied to simulate oil-water dispersed flow; however, for dense dispersed flows, the break-up coefficient should be decreased. It was also found that the coalescence rate had a much greater influence on the drop size distribution than it does on the phase distribution. Finally, the calculations of the drop size distributions showed that the inlet drop boundary size distribution conditions affect the distributions over the whole length of the pipe used in the Farrar and Bruun (1996) experiment.

8.2 CFD Simulations of Oil-Water Dispersed Flow in a Non-circular Duct

In this section, the application of CFD models to oil-in-water dispersed flows in a square cross-sectional duct is described. Subsection 8.2.1 introduces the phenomenon of turbulence-induced secondary flow which appears in non-circular ducts. The implementation of two turbulence models (Reynolds Stress (RS) model and k– ε model), in the prediction of phase distribution and secondary flows is described in Section 8.2.2. The calculated results are shown and discussed in Section 8.2.3. Finally, a short summary is given in Section 8.2.4.

8.2.1 Turbulence-induced Secondary Flow in the Non-circular Duct

Previous experimental work has shown that fully developed turbulent flows in straight non-circular ducts are helical in nature which is not the case in circular pipes. This spiral motion is due to secondary currents which act in the plane normal to the channel walls and generate mean shear stresses to maintain equilibrium between the Reynolds stresses and the pressure gradients in the cross sectional plane. These flows cause the main flow to spiral through the passage and although they are relatively weak compared to the main flow, they have a significant influence on the local mean flow distributions of the axial velocity, wall shear stress and turbulent kinetic energy. Secondary flows of this type are encountered in numerous turbulent flow geometries including triangular and rectangular ducts, eccentric annuli and parallel flow rod bundles. Nikuradse (1926) was probably the first to investigate the differences between flow in circular pipes and square ducts. Quantification of these secondary flows was not reported until Hoagland (1960) devised a hot-wire technique, which was subsequently employed with improved accuracy by Gessner (1964), Gessner and Jones (1965) and Launder and Ying (1972). The secondary velocity components in the cross-section of the duct may be only 1% of the axial velocity, but exert a strong influence on both the overall and local properties of the flow. The most complete description of turbulent flow in square ducts was, however, provided by Brundrett and Baines (1964), who measured the six Reynolds stresses components as well as the three mean velocity components. From an analysis of the transport equation for the mean axial vorticity they deduced that secondary velocities were generated by gradients of Reynolds stresses in the plane of the duct cross-section, and their data showed that the main contribution to the generation term arose from the normal stress gradients. Melling and Whitelaw (1976) measured the details of the axial component of mean velocity and the corresponding normal stress in the developing region of a rectangular duct flow by using a Laser-Doppler anemometer. Experimental data indicated

that the basic pattern of secondary flow was independent of the Reynolds number, but that, with increasing values of the Reynolds number, the flows penetrate the corners and approach the wall (Brundrett and Baines, 1964).

The presence of secondary flows in the corner of the non-circular duct is attributed to the variation of the Reynolds stresses (Gessner, 1973), and cannot be predicted by the standard (or linear) k- ε model, which assumes stress-strain relationships involving an isotropic eddy viscosity. However, for flows with curved streamlines, swirling flow and flows in non-circular ducts additional modelling of the Reynolds stress terms is necessary to account for the anisotropy of the turbulent viscosity. Therefore, application of the linear k- ε models for the effective viscosity can give rise to highly inaccurate predictions for the normal Reynolds stresses which makes it impossible to describe such effects as secondary flows in non-circular ducts. Many efforts have been made to develop calculation procedures for particular non-circular duct that include the turbulence-induced secondary flows in the duct cross plane. These procedures have mainly used the finite difference method for the case of a square duct. The early models of Launder & Ying (1973) and Gessner & Emery (1976) were the first to recognize that as a first order approximation, convective transport of the stresses could be neglected in non-circular duct flows due to the small size of the cross plane velocities and that vorticity production would dominate in the wall regions so that diffusive transport of stress could also be omitted. These simplifications of the Reynolds stress transport equations removed the partial differential stress terms and enabled algebraic relations for the cross plane stresses to be derived.

Speziale (1979, 1981, 1987) developed a nonlinear algebraic Reynolds stress model of anisotropic turbulence. In an algebraic stress model, the assumption of an isotropic eddy viscosity is removed. The differential equations for the Reynolds stresses are simplified to give simple algebraic relationships for each stress component in terms of mean velocity gradients. This model permits inequality of the Reynolds normal stresses, a necessary condition for calculating turbulence-induced secondary flows in non-circular ducts. This model includes transport terms, which are the convective terms that would appear in a Reynolds stress transport equation. By means of an asymptotic expansion, nonlinear k- ε models are obtained which, unlike all such previous nonlinear models, satisfy the requirements of dimensional and tensorial invariance, realizability (i.e. positiveness of the turbulent kinetic energy) and material frame-indifference (form invariant under a change of frame). The nonlinear k- ε model has been used by Lee and Jang (1997) to simulate fully developed turbulent secondary flow in bare rod bundles. Mompean (1998) performed a numerical simulations of the turbulent flow inside a square duct with the nonlinear

turbulence model proposed by Speziale (1987), coupled with the k- ε equations derived using the renormalization group (RNG) theory of Yakhot et al. (1992). Nordsveen (2001) applied the algebraic Reynolds stress (ASM) turbulent model and the generalized Lagrangian mean (GLM) wave field model to model both turbulent- and wave- induced secondary flows in the liquid phase in stratified gas-liquid near horizontal duct flow. An explicit algebraic Reynolds stress model coupled with the k– ε equations has also been used by Belhoucine *et al.* (2004) to simulate the incompressible turbulent flow in a rotating straight duct. Jayanti *et al.* (1990) used the Harwell-Flow3D package to predict the turbulent-induced secondary flow in the duct by using the Reynolds stress model. However, to the present author's knowledge, CFD calculations on the influence of turbulence-induced secondary flows on dispersed two-phase flows have not been reported. This was the reason for the studies reported here; the aim was to assess the likely effects of such secondary flows on the experiments described in Chapters 4 and 5.

8.2.2 Numerical Methods

In all the calculations described below, the lift force coefficient, $C_L = 0.03$; the turbulent dispersion force coefficient, $C_{TD} = 0.1$; the breakup model coefficient, $f_B = 1.0$ and coalescence model coefficient, $f_C = 1.0$.

In order to maximise computational efficiency, the geometry adopted in the simulations was a quarter of a short square cross-sectional channel with the cross section dimension of 0.009 m × 0.009 m and 0.04 m in length which described in Chapter 3. Figure 8.14 shows the CFX mesh of the XY plane. The liquid physical parameters are those of the fluids used in the experimental part of the present work which are summarised in Table 3.1. To assess the sensitivity of the results to the grid size, a convergence test was carried out. Figure 8.15 shows the dispersed phase distribution, ε, and drop Sauter mean diameters, d_{32}, with 2000 grids (20×20×5) and 9000 grids (30×30×10). It is seen that the results are very similar with an average difference of 0.027 and 2.2% in ε and d_{32}, respectively. It can thus be concluded that the mesh with 9,000 total grid points is sufficient to provide reliable and grid insensitive numerical results.

The calculations achieved convergence after approximately 5000 iterations, taking 11 hours on a Digital UNIX 4.0e workstation having 500MHz CPU speed. Since fully developed flows were simulated, the flow domain considered corresponds to only a short part of the actual duct. Therefore, the flow-in and flow-out surfaces were defined as periodic

boundaries and a body force per unit volume (3000 Pa/m) exerted on the flow domain to push the fluids down-wards through the geometry.

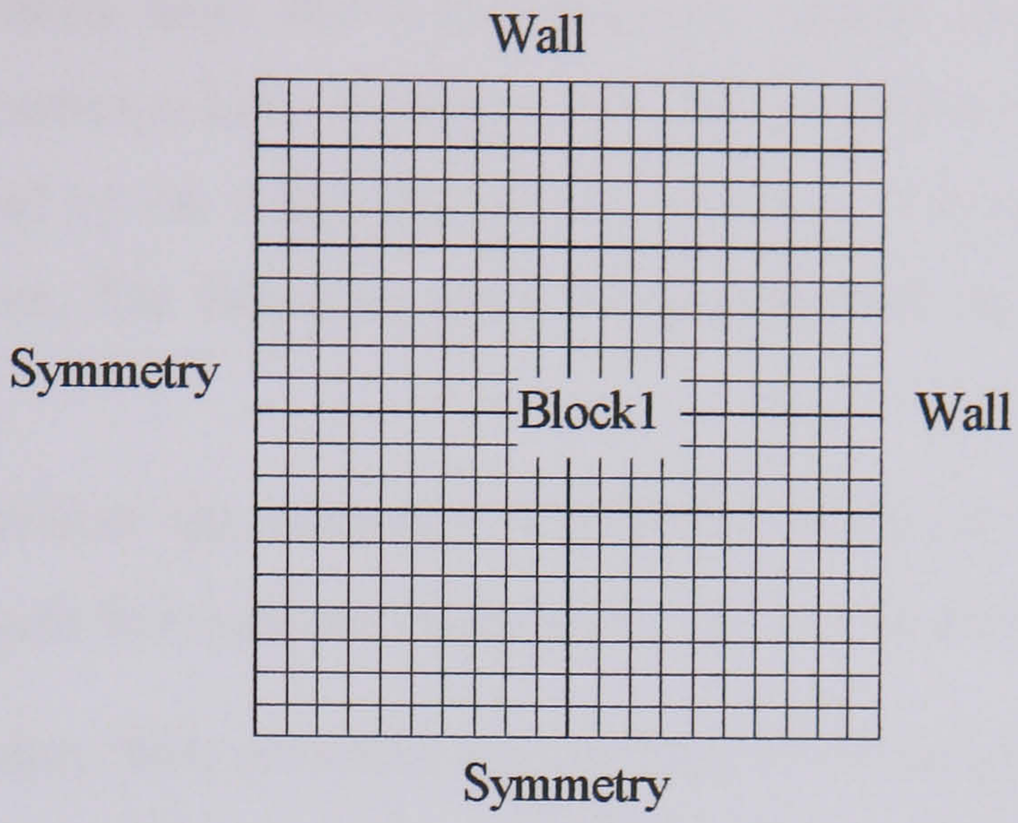
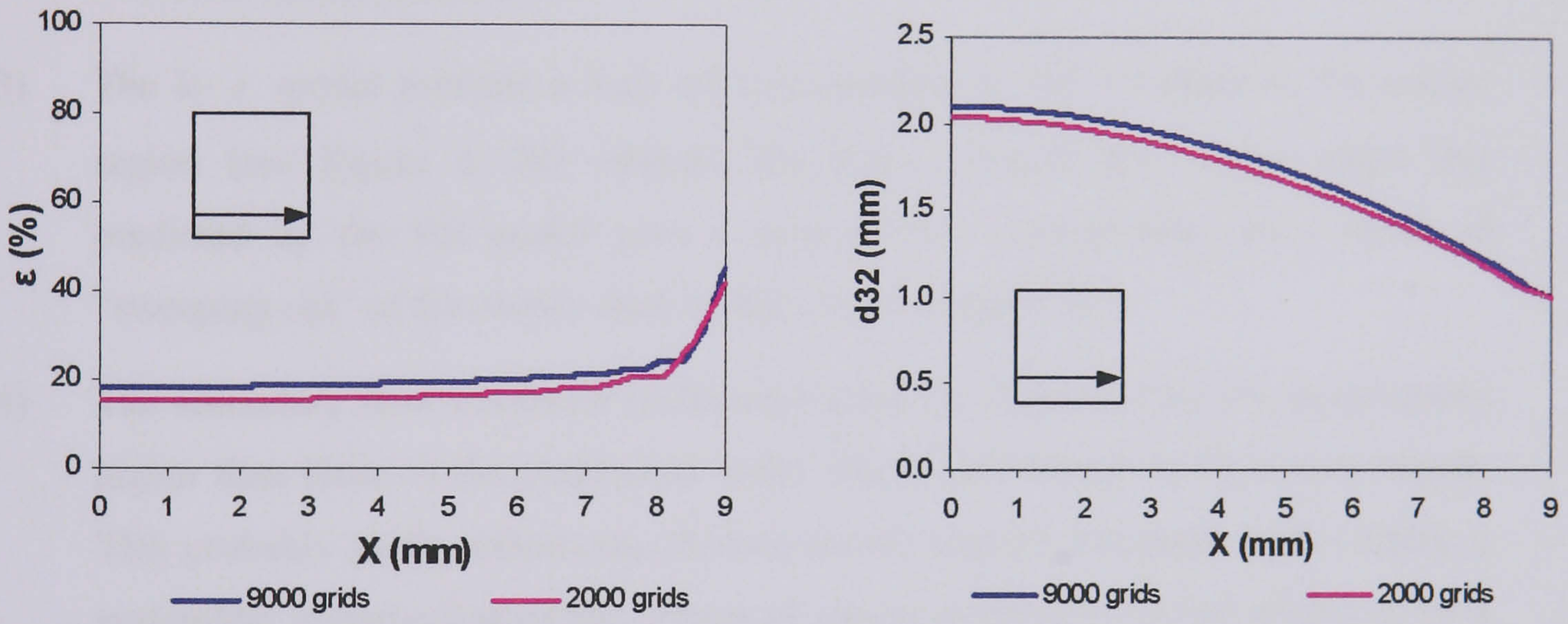


Figure 8.14 Mesh in the XY plane of the quarter tube geometry



(a) (b)

Figure 8.15 Grid sensitivity tests performed for 20% oil input with 2000 and 9000 grids obtained for the plane shown in the panel insets; (a) oil phase distribution; (b) drop Sauter mean diameter.

8.2.3 Calculated Results and Discussions

Two different turbulence models, Reynolds Stress (RS) model and k– ε model, were used. All the values of the constants for both models were set as described in Section 7.2.2 except $C_\mu = 0.065$ in Reynolds stress model due to the wall reflection term (Eq. 7-17) being included. The term proposed by Sato & Sekoguchi, (1975) was also included to take account for the influence of the dispersed phase on the turbulence of the liquid phase.

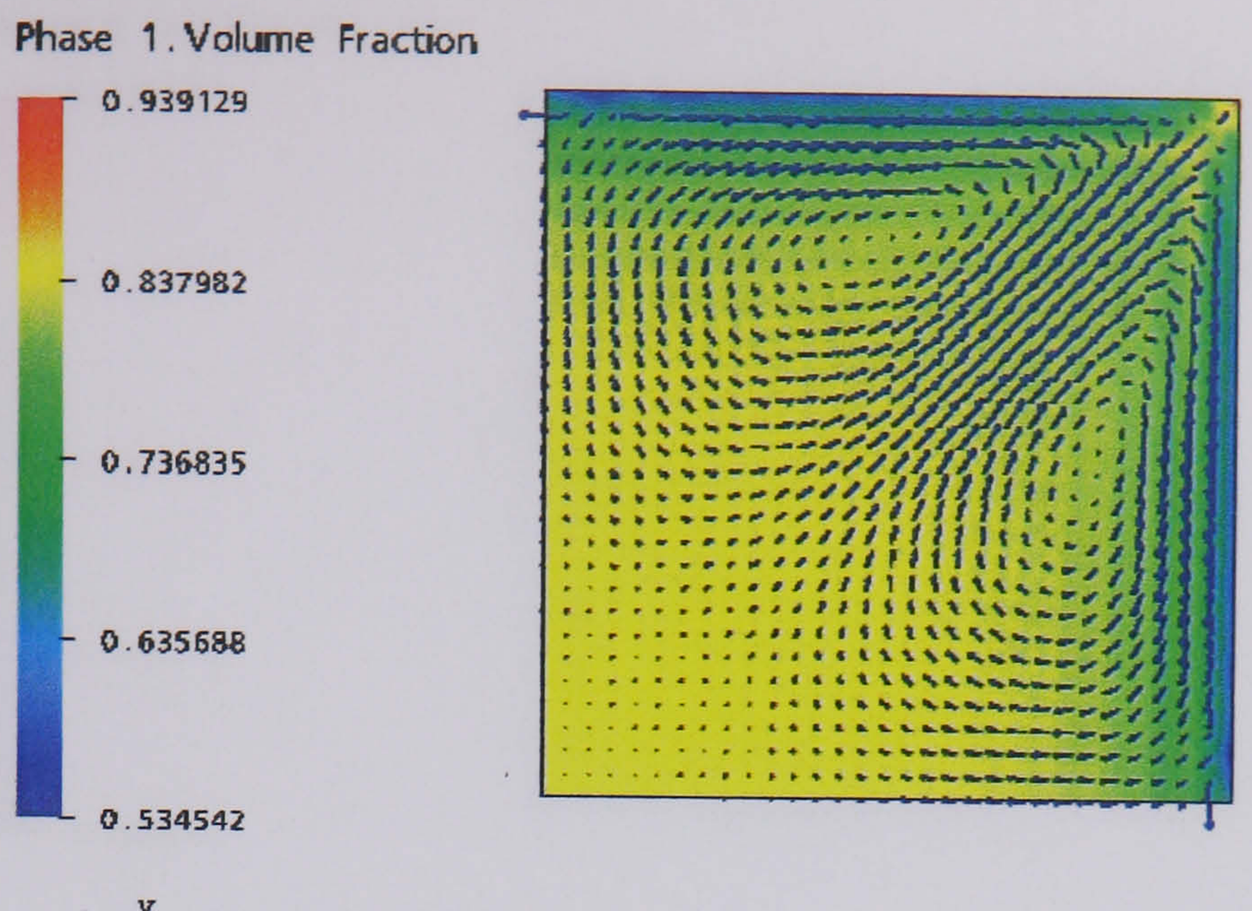
Figures 8.16 to 8.18 show results calculated from the Reynolds stress (RS) and k– ε models for and input oil volume fraction of 20%. Figure 8.16 shows in-situ water volume fraction distributions calculated from the two turbulence models and Figure 8.17 the corresponding oil volume fraction results. In Figure 8.18, the calculated values of in-situ oil volume fraction as calculated by the respective models are plotted along the diagonal and along the side wall as shown. The following main conclusions may be drawn from these results:

(1) The RS model predicts the existence of secondary flows in the corners of the channel whereas such flows are not predicted by the k– ε model, as expected.

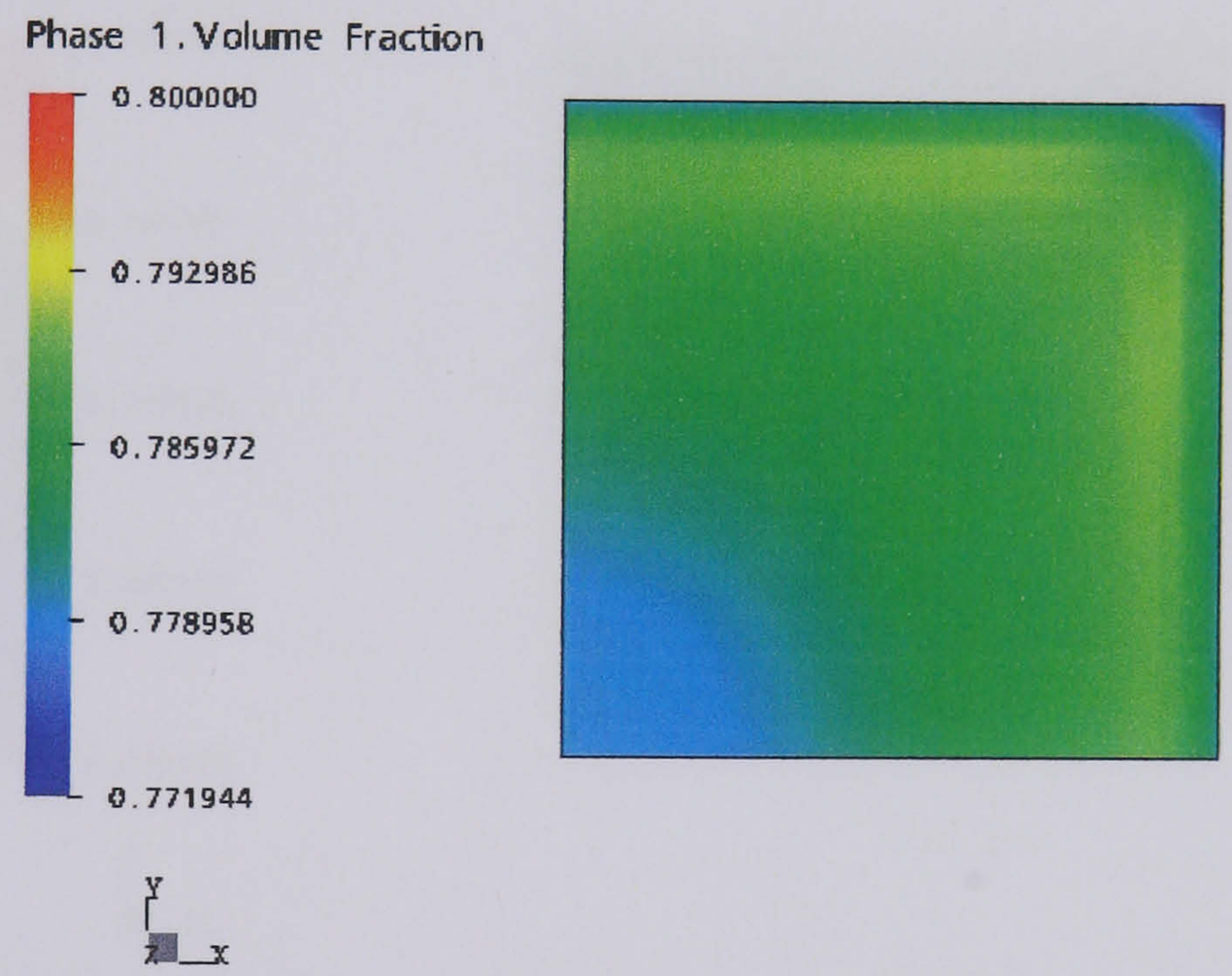
(2) Though the secondary flow velocities are less than 1% of the axial velocities, they can have a significant effect on the phase distributions. Both the RS and k– ε models predict distributions in which the oil concentrations are slightly higher near the wall of the channel. However, the range of variation is much greater in the case of the RS model predictions.

(3) The k– ε model predicts a high oil concentration of the oil phase in the corner region (see Figure 8.17b) whereas the flows towards the corner which are predicted by the RS model give a zone of low concentration as a result of "sweeping out" of the corner zone by the corner-directed flow.

(4) The secondary flow velocities predicted for the oil droplet phase are significantly higher than those of the continuous water phase, particularly in the corner region. This probably partly reflects the choices for the (many) constants in the model; a systematic investigation of the effects of model parameters would appear to be a worthwhile aim for further studies.

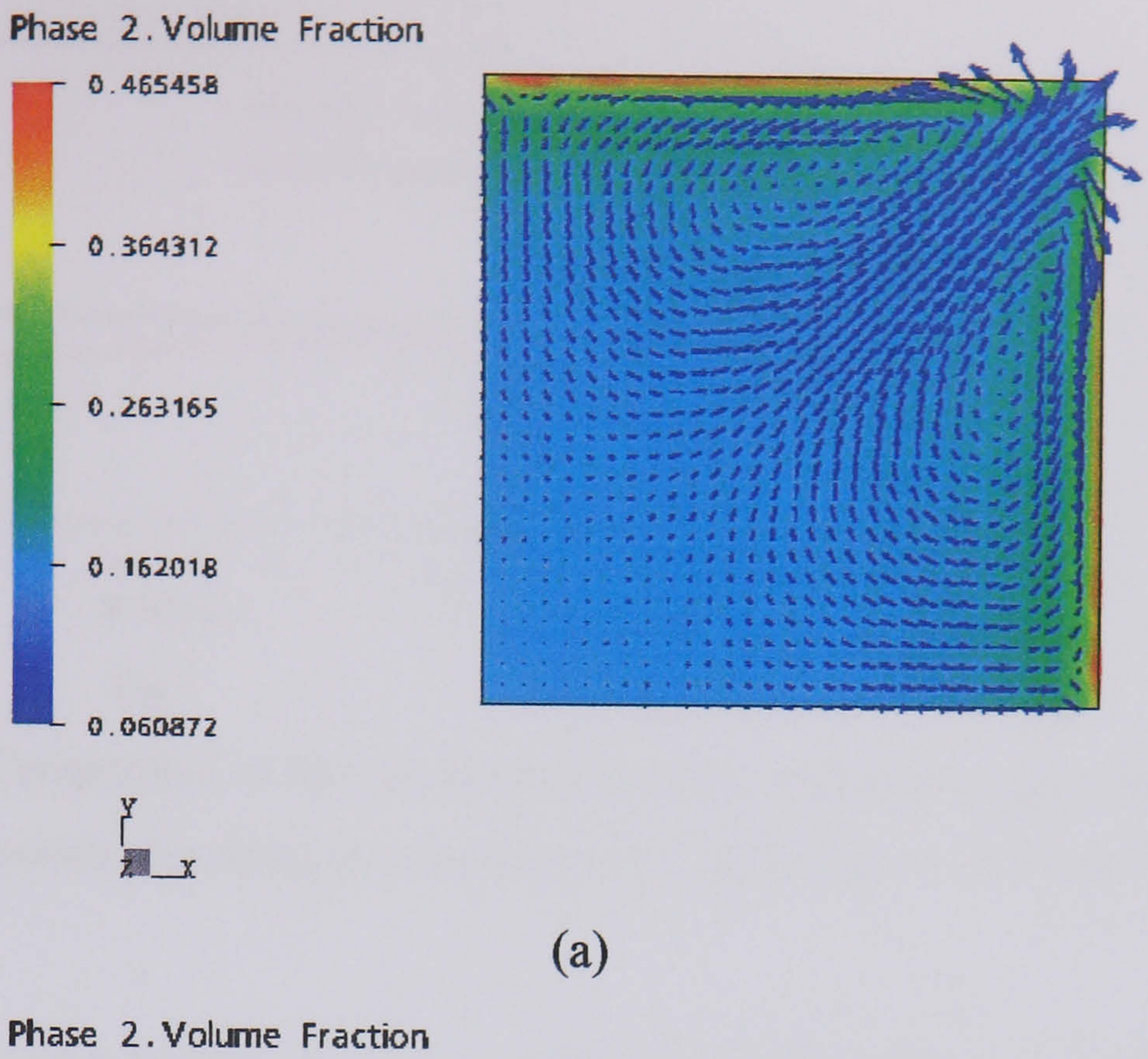


(a)

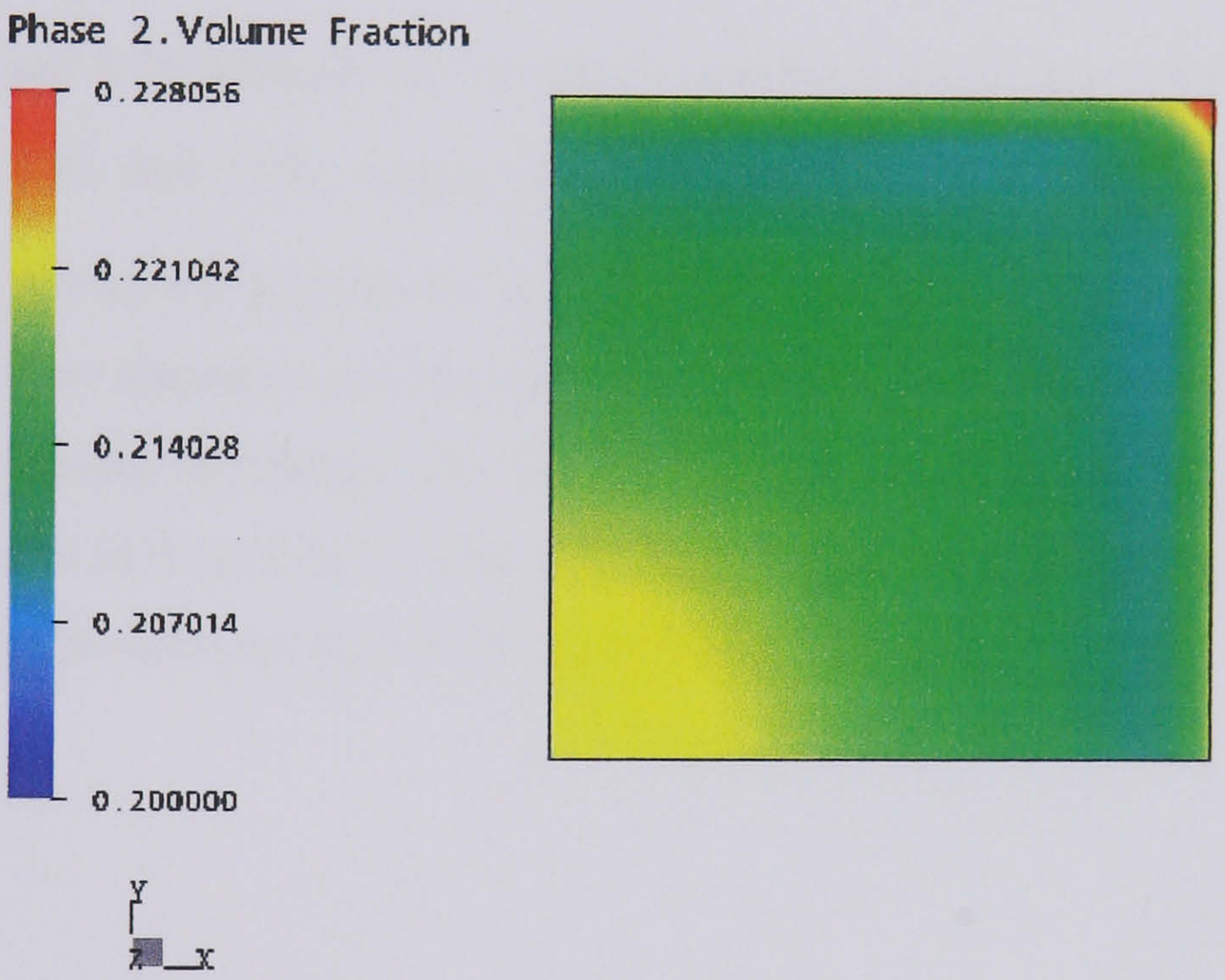


(b)

Figure 8.16 Aqueous (continuous) phase volume fraction profile; (a) Reynolds stress model with secondary flow vectors and (b) k– ε model. Oil input volume fraction ε^{o}_{input} =20%. Calculated mixture velocity U_m= 1.81m/s for k– ε model and U_m= 2.13 m/s for Reynolds stress model.

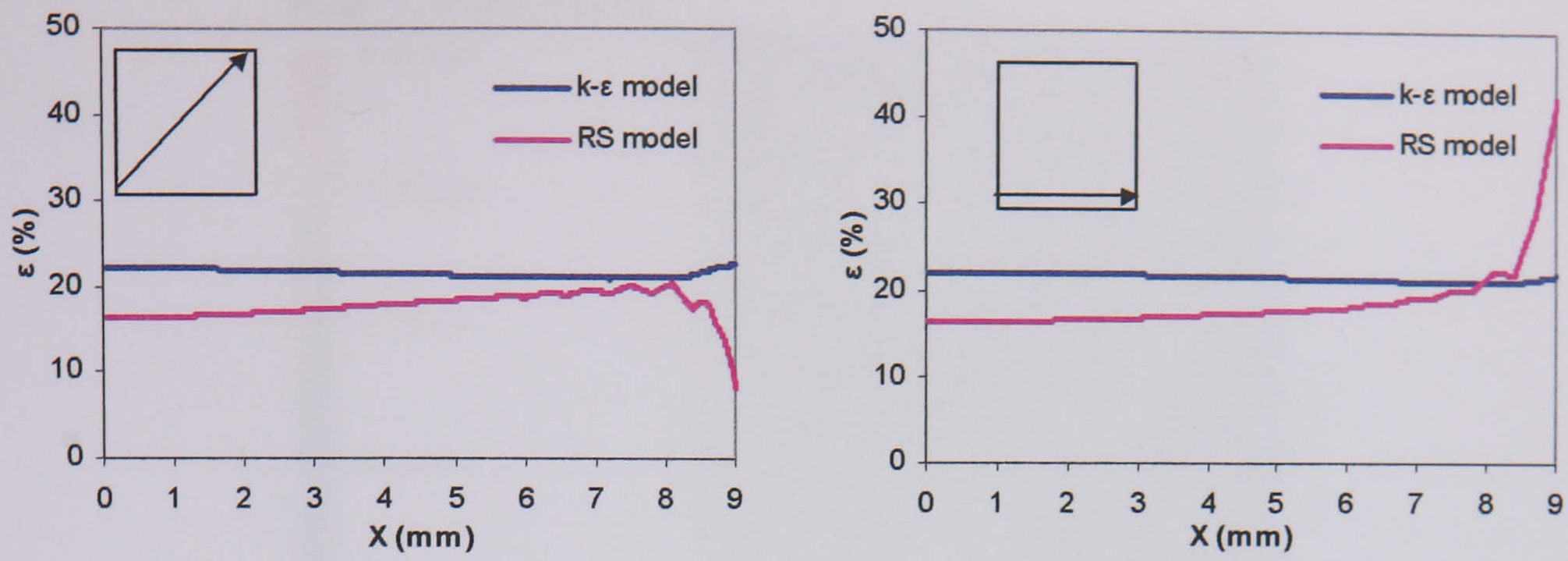


(a)



(b)

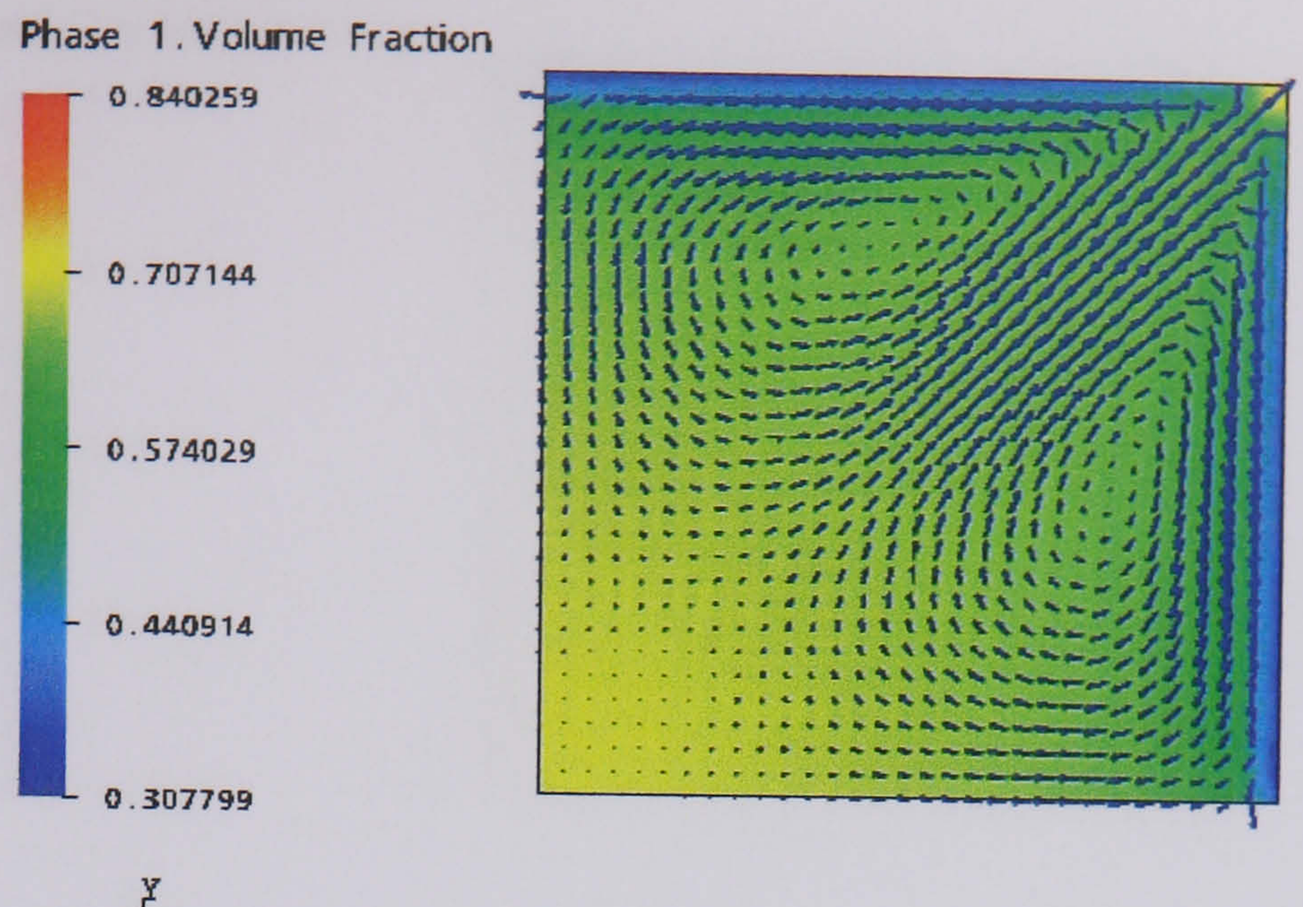
Figure 8.17 Oil volume fraction profile; (a) Reynolds stress model with secondary flow vectors and (b) k– ε model. Oil input volume fraction ε^{o}_{input} =20%. Calculated mixture velocity U_m= 1.81 m/s for k– ε model and U_m= 2.13m/s for Reynolds stress model.



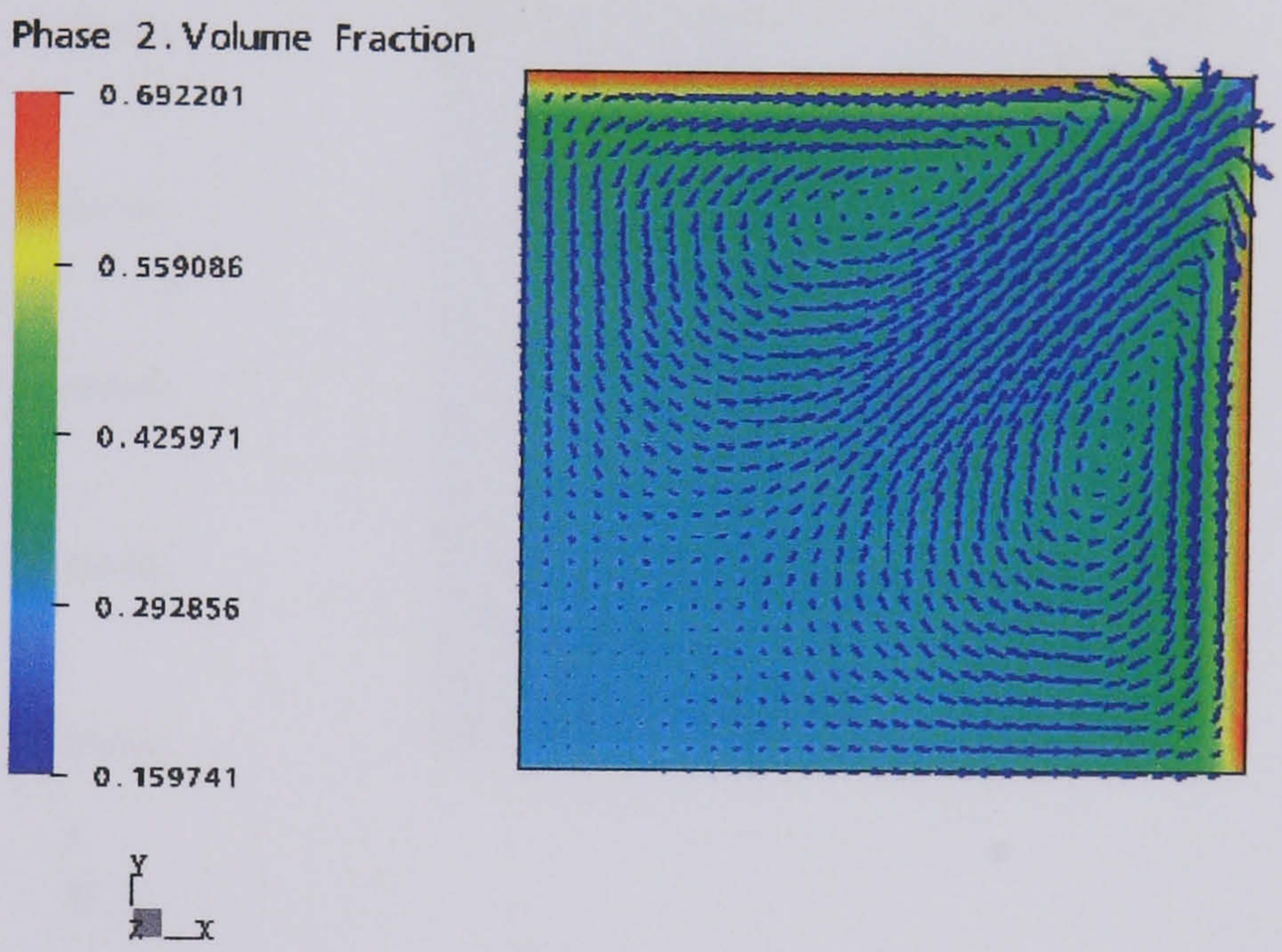
(a) (b)

Figure 8.18 Comparison of the oil volume fractions obtained using different turbulence models; (a) along the diagonal plane; (b) along the side wall (see inset).

Figures 8.19 and 8.20 present the oil phase distribution and secondary flows obtained when ε^{o}_{input} are 30% and 10%, respectively. Comparison of the oil volume distributions shown in Figures 8.16a, 8.17a, 8.19 and 8.20 demonstrates that the strength of the dispersed phase secondary flow increases and the dispersed phase volume distributions become more uniform with decreasing oil holdup. The increase in the non-uniformity of ε with oil holdup is also clearly shown in Figure 8.21. Thus, the secondary flow of the dispersed phase seems to be suppressed as the concentration of dispersed drop increases.

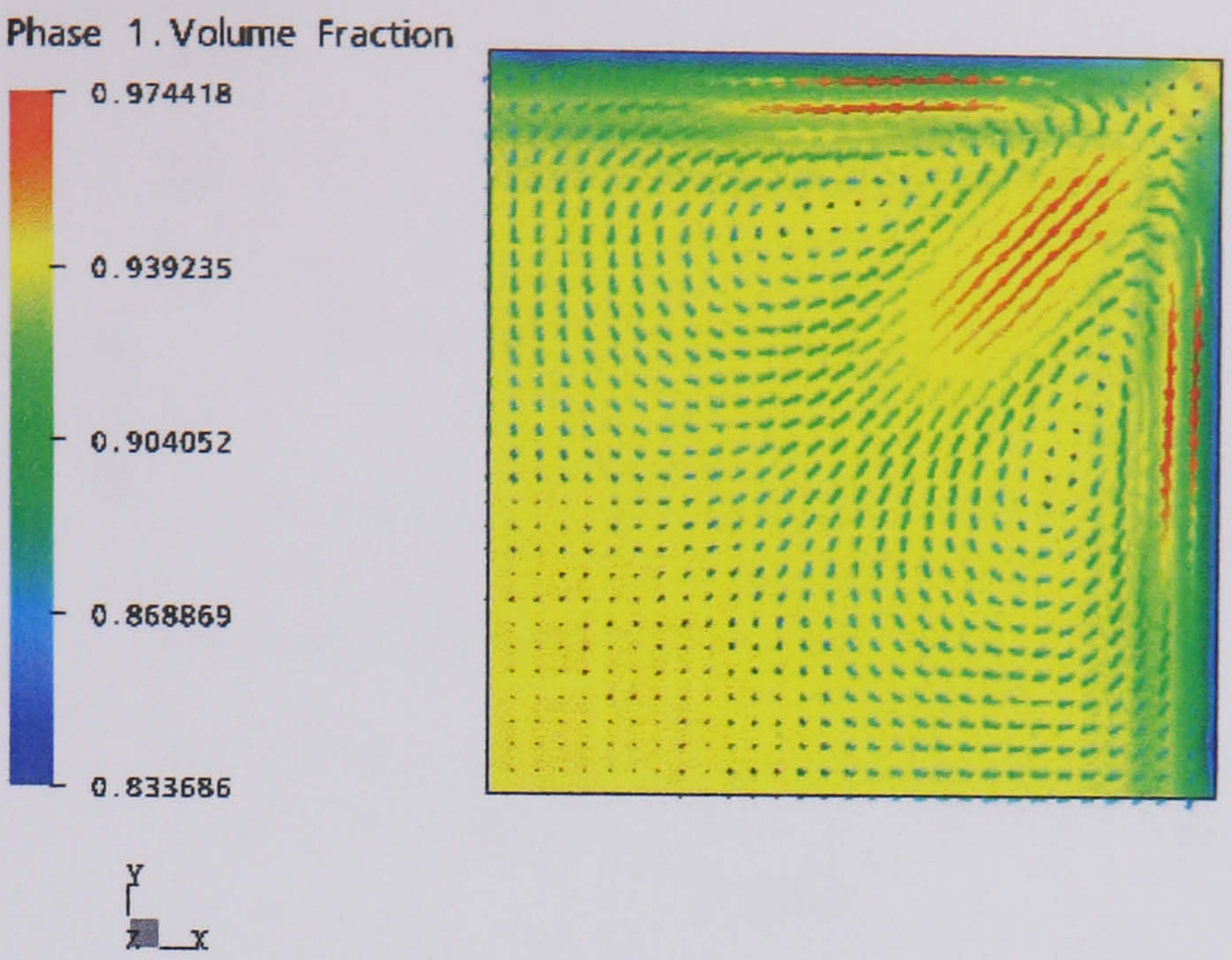


(a)

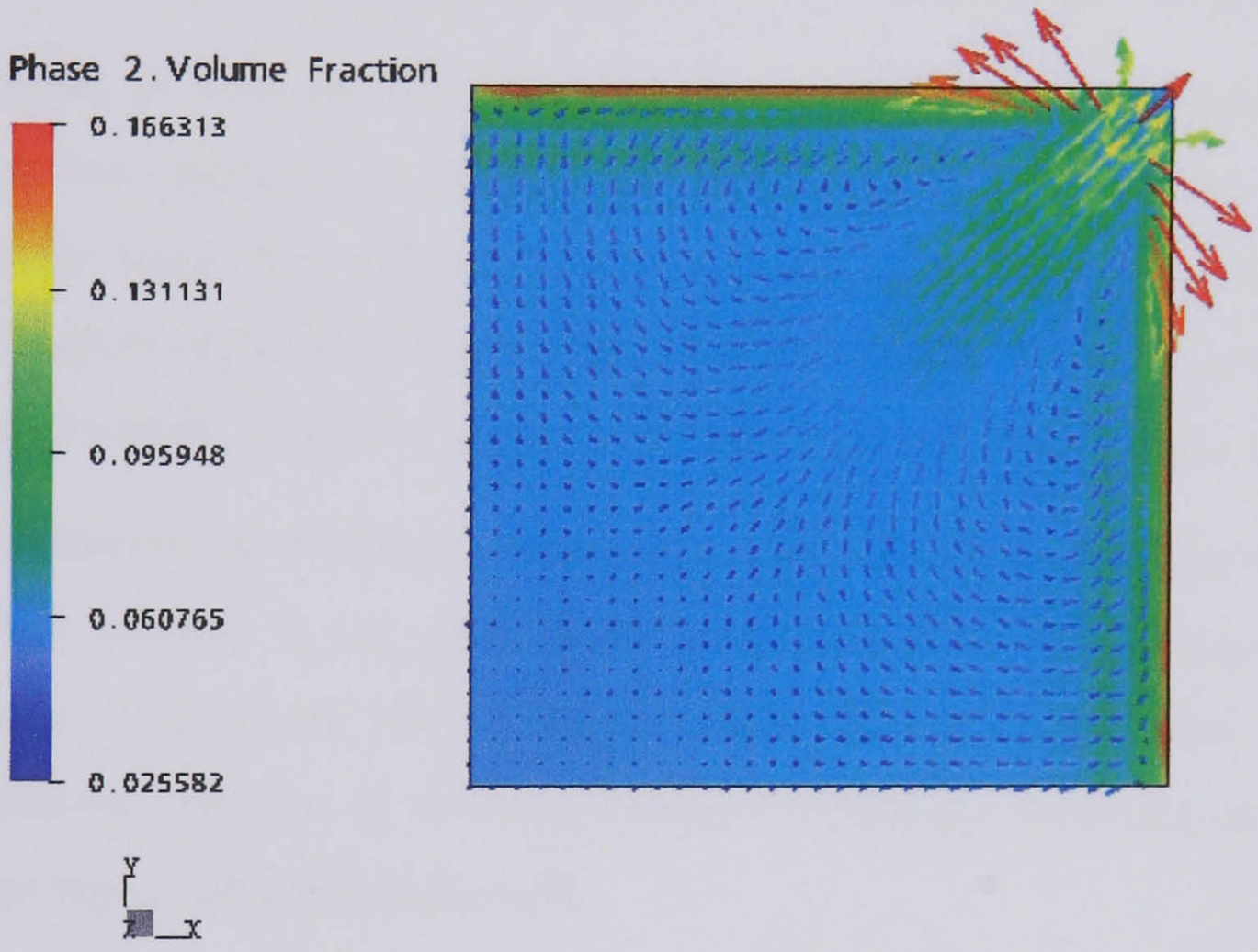


(b)

Figure 8.19 Volume fraction profiles ε^{o}_{input} =30% oil-in-water dispersed flow (a) aqueous phase volume fraction; (b) oil volume fraction. Calculated axial velocity U_m= 2.27 m/s.



(a)



(b)

Figure 8.20 Volume fraction profiles for ε^{o}_{input}=10% oil-in-water dispersed flow; (a) aqueous phase volume fraction; (b) oil volume fraction. Calculated axial velocity U_m= 2.01 m/s.

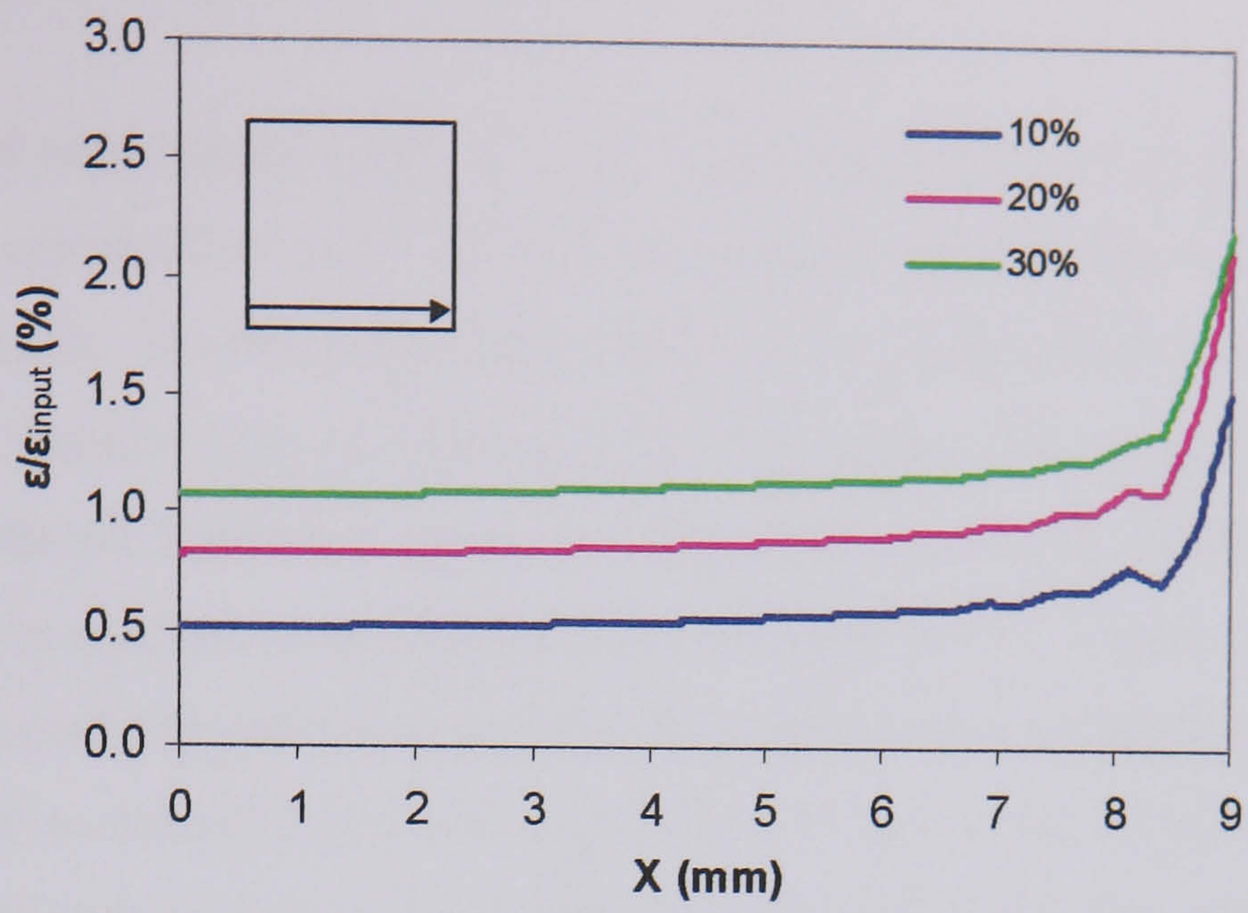


Figure 8.21 Axial variations of the oil volume fraction distribution along the plane indicated in the inset for 10%, 20% and 30% oil input holdup.

It is interesting to compare the trends in phase disptribution calculated here with the visual observations repoarted in Chapters 4 and 5. Direct quantitative comparisons are difficult since the transverse velocities could not be measured in the experiments. Also, because of the nature of the calculations, the mixture velocities were not exactly matched to those in the experiments. However, some quantitative remarks can be made as follows:

(1) The tendency of the (heavier) aqueous phase to wet the wall (probably because of inertial effects) is not reproduced in the models. This is because the models *assume* a dispersed oil-in-aqueous phase mixture throughout, with the model predicting variation of oil concentration but not the existence of a pure aqueous phase region adjacent to the wall.

(2) In the experiments, the view was of a plane passing through the axis of the channel. Results from the calculations indicate that the phase distribution is relatively insensitive to the position of this plane, unless it is immediately adjacent to the wall. This leads more confidence to the intepretation of the results from the square channel (used for optical convenience) as being reasonably representative of the (more normal) circular duct case.

In future work, it may be worthwhile making observations of the corner effects by using LIF method to view a plane adjacent to the (square) channel wall. This would also allow a more accurate assessment of the concentration of the dispersed oil phase in the near-wall region.

8.2.4 Summary

This section reported calculations on the flow of liquid-liquid dispersions down a vertical rectangular duct. The calculations were carried out using a commercially-available CFD software package (CFX4.4). The Reynolds stress (RS) and k-ε models were used to simulate turbulence in this flow. Results indicate that use of the RS model leads to predictions of the expected turbulence-induced secondary flows and the resultant phase distributions in the channel corners; this is in contrast to the results obtained using the k- ε model with which no corner secondary flows could be predicted. Results also indicate that although the secondary flow is relatively weak in comparison to the main flow, it has a significant effect on the phase distribution particularly in the vicinity of the wall. The strength of the secondary flows in the continuous phase were also found to decrease with increasing dispersed phase holdup. The models did not predict the high concentrations of the continuous (aqueous) phase which were observed in the wall region in the experiments.

CHAPTER 9

Conclusions & Recommendations

In this Chapter, the main conclusions from the present experimental and computational work are described in Section 9.1, and the recommendations for the future work are given in Section 9.2.

9.1 Conclusions

9.1.1 Conclusions from Experiments

As mentioned in the Introduction, the experimental work aimed to directly visualize concentrated liquid-liquid dispersed flows. The work described in this thesis was concerned with finding and applying appropriate visualization techniques for the investigation of flow phenomena in liquid-liquid dispersions with particular reference to phase inversion. A novel visualization technique, laser-induced fluorescence (LIF), which has advantage of fast response and quick colour disappearing, was found to satisfy the requirements. In order to obtain the clear images of liquid-liquid flow, especially in concentrated dispersions, the use of two liquids with matched refractive indices is very important to optimize the application of LIF technique. After extensive search and tests, Exxol D80 Oil and 39 wt.% calcium chloride ($CaCl_2$), whose refractive indices match at 1.438 at 25°C, were selected for the

investigations. In addition, the identification of a stable fluorescence dyestuff also played a significant role in the studies; Eosin Y, which emitted strong fluorescence when activated by the laser green light and, more importantly, remained stable in the liquid-liquid system, was selected for the experiments.

The LIF technique was applied to liquid-liquid dispersed systems in pipeline flow and to studying flow structures in an agitated vessel. The major conclusions of the studies were as follows:

[1] Liquid-liquid pipeline flows

Experiments were carried out for downwards liquid-liquid flows in a square cross-sectional duct. The flow circuit used was either a "once-through" system or a recirculating system. The once through system was used for higher mixture velocities (0.1-2.1m/s) and the recirculating system for lower velocities (0.0417-0.0594m/s). In the high velocity tests, a flow pattern map was obtained by plotting the mixture velocity against the oil input holdup. As expected, the oil-in-aqueous phase (o/w) and aqueous phase-in-oil (w/o) dispersed flow were the two main flow patterns. However, an unstable region was also found in the map. In the unstable region, the flow structures were extremely complex and both oil-in-water and water-in-oil dispersions could appear alternately.

Transient flow tests were also carried out with decreasing water fraction and mixture velocities. Since the transient flows cross the unstable range, the dispersed flows, observed through the visualization section, transform from oil-in-water dispersion to water-in-oil dispersion and this transformation could be considered as a phase inversion. Thus, the "unstable region" could also be called a "phase inversion region". When the flow pattern map was plotted as the phase holdup against mixture velocity, the unstable region was very similar to the ambivalent range which is found in plots of holdup against stirrer speed for agitated vessel systems. However, from a phenomenological point of view, these two ranges were different; the ambivalent range in the agitated systems is 'a range of volume fractions throughout which either component would remain STABLY dispersed' (Selker and Sleicher, 1965), whereas the unstable range obtained from the pipe flow experiments is a range in which either component can be the continuous phase, with the identity of the continuous component varying somewhat randomly with time.

In addition, a large variety of w/o/w and o/w/o secondary dispersions and multiple dispersions were observed in the dispersed pipeline flow, especially in flows in the unstable range. Compared with those in the agitated systems, the structures of the secondary

dispersions in the pipeline flow were more complex and varied and the preponderance of o/w/o over w/o/w dispersions in agitated system was not found in the experiments on pipeline flow.

The low velocity experiments (in which the mixture was recirculated using a gear pump) were carried out with a fixed mixture composition and over a range of velocities. They demonstrated a dramatic transition between an annular flow and an annular-dispersed flow as the velocity increased.

Aqueous phase holdups estimated by analysing the LIF pictures for both the high velocity and low velocity experiments were compared with analytical models for annular flow and dispersed flow. Encouraging agreement was obtained when appropriate account was taken of the differences between the vertical and horizontal cross-sectional distributions.

A common feature of all the results was the tendency for the wall to be in contact with the aqueous phase. This was despite the fact that the wetting angle for the surface was much less in the case of the oil phase. It is argued that, in common with gas-liquid annular flow, the heavier (aqueous) phase finds itself at the wall as result of inertial effects. Of course, the wall film can be entrained as drops giving rise to annular dispersed flow at higher velocities.

Though, there exist defects in the experiments due to the limitation of the liquid-liquid flow system, the experimental results prove that the methodology which combines the non-intrusive dye tracing technique, LIF, and refractive indices matching technique is a very powerful tool to investigate liquid-liquid dispersed flows. The dynamic evolution of the dispersion and complex flow structures described in this thesis were observed in great detail for the first time.

[2] Phase inversion in a stirred vessel

The LIF technique with refractive index matched liquids, which proved to be highly effective to investigate concentrated liquid-liquid dispersed pipe flows, was also applied to visualize the phase inversion phenomenon in an agitated vessel. The work provided optical evidence of the dynamic evolution of the dispersion during phase inversion process and clarified the specific issues about phase inversion which were listed in the Introduction (Section 1.2) as follows:

(a) Whether the deciding factor for phase inversion is the enhanced dispersed phase coalescence and/or the formation of secondary dispersions

Though, from the pictures recorded during phase inversion, only a few drop coalescence events were captured, it was still believed that the drop coalescence was

an important process during phase inversion since the drops of the dispersed phase become larger. However, it was found that the formation of secondary dispersions, and the associated inclusion and escape processes, was the dominant mechanism involved in phase inversion. The structure of the dispersion, which accompanied phase inversion, was extremely complex with a large number of secondary dispersions and multi-dispersions appearing (including water-oil-water secondary dispersions).

(b) The time scale of the phase inversion phenomenon

The experimental results suggest that phase inversion was a gradual phenomenon rather than a catastrophic one; the process lasts for several seconds and during phase inversion both oil-in-water and water-in-oil dispersions could co-exist.

(c) Whether phase inversion appears in the whole system globally or locally; whether the appearance of local phase inversion depends on the concentration distribution in the dispersed system

The process occurs locally, dependent on the local phase distribution and local intensity of agitation. However, once phase inversion occurred in a given region of the vessel, this inversion was permanent and the identity of the continuous phase did not change with time (in contrast to the situation for pipe flow). During phase inversion, it was found that the droplet inclusion process increased rapidly and happened even more frequently than drop coalescence. The inclusion process resulted in extremely large drops with the continuous phase droplets inside; some host-drops could be of the same order of size as the diameter of the vessel. The co-existence of w/o and o/w dispersions also proved that phase inversion happens locally. However, if the stirrer speed is further increased (or more of the dispersed phase is added to the system) then the identity of the continuous phase changed throughout the vessel.

(d) Differences in the phase inversion mechanism in pipeline flow and in a stirred vessels, between the case where the system approaches phase inversion from the aqueous continuous side and the case when phase inversion is approached from the oil continuous sides.

As mentioned before, a phase inversion range ("unstable range") rather than a phase inversion point was found in pipeline flows; no differences could be seen in approaching phase inversion from either side. In the unstable region, the identity of the continuous phase fluctuated with time. In the agitated vessel, and in the ambivalent region, the identity of the continuous phase at a given location did not vary with time but did depend on whether the given phase fraction in the vessel was approached from

the aqueous or oil continuous side. Moreover, in the agitated vessel case, the identity of the continuous phase could vary with position in the vessel.

9.1.2 Conclusions from Numerical Calculations

The commercial code CFX 4.4 was used to simulate oil-in-water dispersed flows both in a circular pipe and a non-circular duct. The turbulence in the liquid phase was described using k-ε and Reynolds stress models. The MUSIG algorithm, including break-up and coalescence models, was used to calculate the drop size distribution for the dispersed phase. The conclusions from these numerical studies were as follows:

[1] Oil-in-water dispersed upwards flow in a circular pipe

The calculated phase distribution and drop size d_{32} for different oil volume fractions were compared with the experimental data of Farrar and Bruun (1996) with the following results:

- Good agreement was obtained using a very small lift force coefficient and using turbulence dispersion force coefficients in the range 0-0.1.

- The Luo and Svenden (1996) break-up model and the Prince and Blanch (1996) coalescence model were applied to simulate the oil-water dispersed flow; however, for dense dispersed flows, the break-up coefficient used in the Luo and Svenden model needed to be reduced to well below the default value.

- The coalescence coefficient has more influence on the drop size distribution than on the phase distribution.

- Finally, the calculations of the drop size distributions showed that the inlet drop boundary conditions affected the distributions along the pipe over the region near the inlet.

[2] Oil-in-water dispersed downwards flow in a non-circular duct

The aim of the calculations was to gain a preliminary understanding of the influence of the turbulence-induced secondary flow on the two-phase duct flow. The Reynolds stress model and the k– ε model were used to model the turbulence.

- The Reynolds stress model predicted the turbulence-induced secondary flow successfully and also the influence of secondary flow on phase distribution at the channel corner. As expected, the standard k- ε model could not predict the presence of secondary flows.

- Although the secondary flows were relatively weak compared with the main flow, they had a significant influence on the phase distributions in the liquid-liquid dispersed flow, especially the regions near to the wall.
- As the dispersed phase holdup increased, the secondary flow of dispersed phase seemed to be suppressed.

9.2 Recommendations for the Future Work

Experimental:

The recommendations for the experiments given here include three parts: improvements in the liquid-liquid system, experimental work on liquid-liquid pipeline flows and experiments on dispersions in a stirred vessel.

[1] Improvements of the liquid-liquid system

- Though excellent experimental results obtained by using the selected liquid pair, (Exxol D80 oil and 39% wt. $CaCl_2$ solution), some problems still existed due to the high concentration of $CaCl_2$ (i.e. 39% wt.) needed to achieve the refractive index matching. These problems included crystallisation of $CaCl_2$ and the formation of $CaCO_3$. Thus, it would be better if the 39% wt. $CaCl_2$ solution can be replaced by a less concentrated solution, for example, a mixture of water, glycerol and less concentrated $CaCl_2$ solution.
- It would be very useful if the photochromic dye tracing technique (details in Appendix A) could be combined with the laser-induced fluorescence technique in order to provide the flow structures and velocity profile at the same time.

[2] Liquid-liquid pipeline flows

- The experiments showed that the wall was nearly always wetted by the aqueous phase despite the fact that this had a higher contact angle than did the oil phase. To further investigate the influence of wall material, it is recommended that the copper pipe and quartz cell are replaced by acrylic material and the effect of the wall wettability on the dispersions further investigated.
- It is recommended that the LIF technique be applied to flows in round tubes since these are nearer to practical application than the square ducts used in the present work. Since most pipeline flows are horizontal or near-horizontal, it is recommended

that such studies should give priority to horizontal rather than vertical flows. The LIF technique ideally suited to studying the asymmetry induced by gravity in such horizontal flows. The use of round tubes presents additional chanllenges for the optics; the material used for the visualization sections will need to have a refractive index matched to that of the fluids in the tubes and the outer surfaces of the sections will need to be planar.

[3] Dispersions in stirred vessels

- It is recommended that the LIF technique to the normal round vessel agitated system with impeller and baffles. Again, in this case, it may be necessary to construct the system with matched refractive index material.
- It is recommended that a wider range of fluids should be studied (subject, of course, to the ability to match the refractive indices of the fluid pair chosen).

Computational:

- Due to the limited space in the Work Station in which the simulations for the non-circular duct were calculated, periodic boundary conditions were used for a short geometry; however, it would be interesting to simulate the liquid-liquid flows in the actual geometry as used in the experiments.
- If, as suggested, LIF studies of flow development in horizontal round tubes are carried out, then it would be useful to perform CFD studies to match these data and to make appropriate comparisons between calculated and experimental values.
- In a parallel project to the present one, Edinburgh University are developing Lattice Gas Automato (LGA) methods for predicting liquid-liquid flows. The present data should be compared with such predictions when they become available.

References

A

AEA Technology plc., (1999). CFX-4.4 Documentation, URL http://www-waterloo.ansys.com/cfxcommunity/technotes/ documentation/CFX-4.4/coverall.pdf

Agterof, W.G.M., Vaessen, G.E.J., Haagh, G.A.A.V., Klahn, J.K., J.J.M. Janssen (2003). Prediction of emulsion particle sizes using a computational fluid dynamics approach. *Colloids and Surfaces B: Biointerfaces,* **31**: 141-148.

Angeli, P., (1996). Liquid-liquid dispersed flows in horizontal pipes, *PhD Thesis*, Imperial College London, UK.

Angeli, P., Hewitt, G. F., (1998). Pressure gradient in horizontal liquid-liquid flows, *Int. J. Multiphase Flow*, **24**: 1183-1203.

Angeli, P., Hewitt, G. F., (2000a). Flow structure in horizontal oil-water flow, *Int. J. Multiphase Flow*, **26**: 1117-1140.

Angeli, P., Hewitt, G. F., (2000b). Drop size distributions in horizontal oil-water dispersed flows, *Chem. Eng. Sci.*, Vol. **55**: 3133-3143.

Arashmid, M., Jeffreys, G. V., (1980). Analysis of the phase inversion characteristics of liquid-liquid dispersions, *AIChE J.*, **26**(1): 51-55.

Arirachakaran, S., Oglesby, K.D., Malinowsky, M. S., Shoham, O., Brill, J.P., (1989). An analysis of oil/water flow phenomena in horizontal pipes', Paper SPE 18836, Society of Petroleum Engineers, Oklahoma.

Augier, F., Masbernat, O., Guiraud, P., (2003a). Slip velocity and drag law in a liquid-liquid homogeneous dispersed flow, *AIChE J.*, **49**(9): 2300-2316.

Augier, F., Morchain, J., Guiraud, P., Masbernat, O., (2003b). Volume fraction gradient-induced flow patterns in a two-liquid phase mixing layer, *Chem. Eng. Sci.*, **58**: 3985-3993.

B

Becher, P., (1966). Emulsions: theory and practice. Reinhold Publishing Co., New York.

Belhoucine, L., Deville, M., Elazehari, A. R., Bensalah, M. O., Explicit algebraic Reynolds stress model of incompressible turbulent flow in rotating square duct, *Computers & Fluids*, **33**(2): 179-199.

Born, M., Wolf, Emil, (1964). Principles of optics: Electromagnetic theory of propagation, interference and diffraction of light, Second Edition. Pergamon Press.

Brauner, N., (2001). The prediction of dispersed flows boundaries in liquid-liquid and gas-liquid systems. *Int. J. Multiphase Flow,* **27**: 885-910.

Brauner, N., Ullmann, A., (2002). Modeling of phase inversion phenomenon in two-phase pipe flow, *Int. J. Multiphase Flow*, **28**(1): 55-68.

Brooks, W. B., Richmond, H. N., (1991). Dynamics of liquid-liquid phase inversion using nonionic surfactants, *Colloids and Surfaces*, **58**: 131-148.

Brooks, W. B., Richmond, H. N., (1994). Phase inversion in non-ionic surfactant-oil-water systems – I. the effect of transitional inversion on emulsion drop sizes', *Chem. Eng. Sci.*, **49**(7): 1053-1064.

Brown, G. H. (ed.), (1971). Photochromism. techniques of chemistry, Volume 3, Wiley. New York.

Brundrett, E., Baines, W. D., (1964). The production and diffusion of vorticity in duct flow. *J. Fluid Mech.*, **19**, 375-394.

Butterworth, D., Hewitt, G. F., (1977). Two-phase flow and heat transfer, Oxford University Press.

C

Charles, M. E., Govier, G. W., Hodgson, G. W., (1961). The horizontal pipeline flow of equal density oil-water mixtures, *Can. J. Chem. Eng.*, **39**: 27-36.

Charles, M. E., Redberger, P. J., (1962). The reduction of pressure gradients in oil pipelines by the addition of water: numerical analysis of stratified flow. *Can. J. Chem. Eng.*, **40**: 70-75.

Cheesman, D. F., King, A., (1939). The electrical double layer in relation to the stabilisation of emulsions with electrolytes, *Trans. Far. Soc.*, 241-247.

Chesters, A. K., Issa, R., (2004). A framework for the modeling of phase inversion in liquid-liquid systems, 5th Int. Conference on Multiphase Flow, Yokohama, Japan.

Chiang, C. J., Chen, C. M., (1994). Characteristics of phase inversion in a turbine-type agitator, *J. the Chinese Institute Chem. Engineers*, **25**(6): 367-374.

Clarke, D. S., Wilkes, N S, (1988). The calculation of turbulent flows in complex geometries using an algebraic stress model, AERE R 13251.

Clarke, S. I., Sawistowski, H., (1978). Phase inversion of stirred liquid/liquid dispersions under mass transfer conditions', *Trans. IChemE*, **56**: 50-55.

Clift, R., Grace, J. R., Weber, M. E., (1978). Bubbles, drops and particles, *Academic*, New York.

Couch, G. G., Johnston, K. W., Ojha, M., (1996). Full-field flow visualization and velocity measurement with a photochromic grid method, *Meas. Sci. Technol.*, **7**: 1238-1246.

Coulaloglou, C. A., Tavlarides, L. L., (1977). Description of interaction processes in agitated liquid-liquid dispersions', *Chem. Eng. Sci.*, **32**: 1289-1297.

D

Davies, G. A., Jeffreys, G. V., Smith, D. V., Ali, F. A., (1970). The formation of secondary droplets in a dispersion at a phase boundary, *Can. J. Chem. Eng.*, **48**: 328-329.

Derjaguin, B. V., Laudau, L., (1941). Acta Physicochimica (URSS), **14**:633.

Deshpande, K. B, (2001). Studies on phase inversion, *Msc. Thesis*, Indian Institute of Science Bangalore 560 012 , India.

Deshpande, K. B., Kumar, S., (2003). A new characteristic of liquid-liquid systems-inversion holdup of intensely agitated dispersions, *Chem. Eng. Sci.*, **58**: 3829-3825.

Dickinson, E., (1981). Interpretation of emulsion phase inversion as a cusp catastrophe, *J. Colloid and Interface Sci.*, **84**(1): 284-287.

Dickinson, E., (1982). Thermodynamic aspects of emulsion phase inversion, *J. Colloid and Interface Sci.*, **87**(2): 416-423.

Dong, J., Tsouris, C., (2001). Phase inversion of liquid-liquid dispersions under applied electric fields', *J. Dispersion Sci. and Tech.*, **22**(1): 57-60.

Drew, D.A., Passman, S.L., (1999). Theory of multicomponent fluids, Springer.

Du, H., Fuh, R. A., Li, J., Lindsey, J. S. (1998). PhotochemCAD: a computer-aided design and research tool in photochemistry, Photochemistry and Photobiology, **68**, 141-142.

E

Efthimiadu, I., Kocianova, E., Moore, I. P. T., (1994). Behaviour of concentrated liquid-liquid dispersions in tube flow and in static mixers, *Proc. The 1994 IChemE Research Event*, **2**, 1020-1022.

El-Hamouz, A. M., Stewart, A. C., Davies, G. A., (1995). A study of Kerosene-water dispersions in shear flow through pipes and fittings, *Proc. of the first Int. Sym. Two-phase Flow Modeling and Experimentation, 987-997.*

El-Hamouz, A. M., Stewart, A. C., (1996). On-line drop size distribution measurement of oil-water dispersion using a Par-Tec M300 laser backscatter instrument, *SPE Int.* 36672, 1-14.

F

Fakhr-Din, S. M., (1973). Phase inversion and drop size measurements in agitated liquid-liquid systems, *Ph.D. Thesis*, University of Manchester.

Farrar, B., Bruun, H. H., (1996). A computer based hot-film technique used for flow measurements in a vertical kerosene-water pipe flow, *Int. J. Multiphase Flow*, **22**: 733-751.

Flores, J. G., Sarica, C., Chen, T. X., Brill, J. P., (1997). Investigation of holdup and pressure drop behaviour for oil-water flow in vertical and deviated wells, ETCE-98, Paper no. 10797.

Frantisak, F., Palade de Iribarne, A., Smith, J. W., Hummel, R. L., (1969). Nondisturbing Tracer Technique for Quantitative Measurements in Turbulent Flow, *Ind. Eng. Chem. Fundam.*, **8**(1): 160-167.

G

Gessner, F.B., (1964). Turbulence and mean-flow characteristics of fully developed flow in rectangular channels, *Ph. D. thesis*, Purdue University.

Gessner, F.B., Jones, J. B., (1965). On some aspects of fully developed turbulent flow in rectangular channels. *J. Fluid Mech.*, **23**, 689-713.

Gessner, F.B., (1973). The origin of secondary flow in turbulent flow along a corner, *J. Fluid Mech.* **58**, part 1, 1-25.

Gessner, F.B., Emery, A.F., (1976). A Reynolds stress model for turbulent corner flows. *ASME J. Fluid Eng. 98*, 261-268.

Gilchrist, A., Dyster, K. N., Moore, I. P. T., Nienow, A. W., Carpenter, K. J., (1989). Delayed phase inversion in stirred liquid-liquid dispersions, *Chem. Eng. Sci.*, **44**(10): 2381-2384.

Gillies, R.G., Sun, R., Shook, C.A., (2000). Laboratory investigation of inversion of heavy oil emulsions, *The Canadian J. Chem. Eng.*, **78**: 757–763.

Goldish, L. H., Koutsky, J. A., Adler, R. J., (1965). Tracer introduction by flash photolysis, *Chem. Eng. Sci.*, **20**: 1011-1014.

Govier, G. W., Aziz, K., (1972). The flow of complex mixture in pipes, Robert E. Krieger.

Grace, J.R., Wairegi, T., Nguyen, T.H., (1976). Shapes and velocities of single drops and bubbles moving freely through immiscible liquids, *Trans. Inst. Chem. Eng.*, **54**: 167-173.

Groeneweg, F., Agterof, W. G. M., Jaeger, P., Janssen, J. J. M., Wieringa, J. A., Klahn, J. K., (1998). On the mechanism of the inversion of emulsions', *Chem. Eng. Research & Design, Trans. IChemE (Part A),* **76**: 55-63.

Guilbault, G. G., (1973). Practical fluorescence: theory, methods, and techniques, New York.

Guilinger, T. R., Grislingas, A. K., Erga, O., (1988). Phase inversion behaviour of water-kerosene dispersions, *Ind. Eng. Chem. Res.*, **27**(6): 978-982.

Guzhov, A. I., Grishin, A. D., Medvedev, V. F., Medvedeva, O. P., (1973). Emulsion formation during the flow of two liquids (in Russian). *Neft Khoz*, **8**: 58-61.

H

Hardwick, R., Mosher, H. S., Passailaigue, P., (1960). Photochromic behaviour of 2-(2',4'-Dinitrobenzyl)-Pyridine, *Trans. Faraday Soc.*, **56**: 44-50.

Hasson, D., Mann, U., Nir, A., (1970). Annular flow of two immiscible liquids I. Mechanisms, *Can. J. Chem. Eng.*, **48**:514-520.

Hasson, D., Orell, A. Fink, M., (1974). A study of vertical annular liquid-liquid flow. Part I, laminar conditions, Symp. Multi-Phase Flow System, U. Stratholyde, 2-4 April, Paper No. A5.

Hesketh, R.P., Etchells, A.W., Russell, T.W.F., (1991a). Experimental observations of bubble breakage in turbulent flow, *Ind. Eng. Chem. Res.*, **30**, 835-841.

Hesketh, R.P., Etchells, A.W., Russell, T.W.F., (1991b). Bubble breakage in pipeline flows, *Chem. Eng. Sci.*, **46**, 1-9.

Hetsroni, G, (1982). Handbook of multiphase systems, Hemisphere Publishing Corporation, London.

Hewitt, G.F., Hall-Taylor, N.S., (1970). Annular two-phase flow. Pergamon Press, Oxford.

Hewitt, G.F., Lacey, P.M.C., (1965). The breakdown of the liquid film in annular two phase flow. *Int. J. Heat and Mass Transfer*, **8**, 781-791.

Hewitt, G.F., (1978). Measurement of two phase flow parameters, London ; New York : Academic Press.

Hewitt, G.F., Jayanti, S., Hope, C. B., (1990). Structure of thin liquid films in gas-liquid horizontal flow, *Int. J. Multiphase Flow*, **16**(6): 951-957.

Hinze, J. O., (1955). Fundamentals of the hydrodynamic mechanism of splitting in dispersion processes, *AIChE J.*, **1**(3): 289-295.

Ho, F. C. K., Hummel, R. L., (1970). Average velocity distributions within falling liquid films', *Chem. Eng. Sci.*, **25**: 1225-1237.

Hoagland, L. C., (1960). Fully developed turbulent flow in straight rectangular ducts secondary flow, its cause and effect on the primary flow. *Ph. D. Thesis*, Depatment of Mechanical Engineering, Massachusetts Institute of Technology, USA.

Hope, C. B., (1990). The development of a water soluble photochromic dye tracing technique and its application to horizontal two-phase flows, *Ph.D. Thesis*, Imperial College, University of London.

Howarth, W. J., (1967b). Measurement of coalescence frequencies in agitated tanks, *AIChE J.*, **13**: 1007-1013.

Hu, B., Ioannou, K., Matar, O. K., Hewitt, G. F., Angeli, P., (2004). Theoretical prediction with PBE of phase inversion in dispersed two-phase liquid systems, 3rd Int. Symposium on Two-phase Flow Modeling and Experimentation, Pisa, Italy.

Hu, B., (2004). Phase inversion in highly dispersed liquid-liquid pipe flow. *M.phil/PhD Transfer Report*, University College London.

Hughmark, G. A., (1971). Drop breakup in turbulent pipe flow. *AIChE J.*, **4**:1000.

Hussain, S. A., (2004). Experimental and computational studies of liquid-liquid dispersed flows. *PhD Thesis*, Imperial College London, UK.

Hutchinson, P, Hewitt, G.F., Dukler, A.E., (1971). Deposition of liquid or solid dispersions from turbulent gas streams: A stochastic model. *Chem. Eng. Sci.*, **26**, 419-439.

I

Ioannou, K., Hu, B., Matar, O. K., Hewitt, G. F., Angeli, P., (2004). Phase inversion in dispersed liquid-liquid pipe flows, 5th Int. Conference on Multiphase Flow. Yokohama, Japan.

Ioannou, K., Nydal, O.J., Angeli, P., (2005). Phase inversion in dispersed liquid-liquid flows. *Experimental Thermal and Fluid Science*, 29, 331-339.

Ishii, M., Zuber, N., (1979). Drag Coefficient and relative velocity in bubbly, droplet or particular flows, *AIChE J.* **25**(5) 843-855.

J

Javed, K. H., Thornton, J. D., Anderson, T. J., (1989). Surface phenomena and mass transfer rates in liquid-liquid systems: Part 2', *AIChE J.*, 35(7): 1125-1136.

Jayanti, S., Wilkes, N. S., Clarke, D. S., Hewitt, G.F., (1990). The prediction of turbulent flows over roughened surfaces and its application to interpretation of mechanisms of horizontal annular flow. *Proc. Royal Soc. London A*,**431:** 71-88.

Joseph, D. D., Renardy, M., Renardy, Y., (1984). Instability of the flow of two immiscible liquids with different viscosities in a pipe. *J. Fluid Mech.*, **141**: 309-317.

Joseph, D. D., Bannwart, A. C., Liu, Y. J., (1996). Stability of annular flow and slugging. *Int. J. Multiphase Flow*, 22, 1247-1254.

Juswandi, J., (1995). Simulation of the oil-water inversion process', *MSc. Thesis*, Oklahoma State University.

K

Karabelas, A. J., (1978). Droplet size spectra generated inturbulent pipe flow of dilute liquid/liquid dispersions, *AIChE J.*, 24(2): 170-180.

Kawaji, M., DeJesus, J. M., Tudose, G., (1997). Investigation of flow structures in vertical slug flow, *Nuc. Eng. Des.*, **175**: 37-48.

Kawaji, M., (1998). Two-phase flow measurements using a photochromic dye activation technique, *Nuc. Eng. Des.*, **184**: 379-392.

Klahn, J. K., Janssen, J. J. M., Vaessen, G. E. J., de Swart, R., and W. Agterof, G. M. (2002). On the escape process during phase inversion of an emulsion, Colloids and Surfaces A: Physicochemical and Engineering Aspects, 210(2-3), 167-181.

Kolmogorove, A. N., (1949). On the breaking of drops in turbulent flow, Doklady Akad. Nauk., **66**: 825-828.

Kubie, J., Gardner, G. C., (1977). Drop sizes and drop dispersion in straight horizontal tubes and helical coils, *Chem. Eng. Sci.*, 32: 195-202.

Kumar, S., Kumar, R., Gandhi, K. S., (1991). Influence of the wetting characteristics of the impeller on phase inversion', *Chem. Eng. Sci.*, **46**(9): 2365-2367.

Kumar, S., (1996). On phase inversion characteristics of stirred dispersions, *Chem. Eng. Sci.*, **51**(5): 831-834.

Kurul, N., Podowski, M.Z., (1990). Multi-dimensional effects in sub-cooled boiling. *Proceeding of the 9th heat transfer conference.*

L

Lang, P., Auracher, H., (1996). Heat transfer to nonmiscible liquid-liquid mixtures flowing in a vertical tube, *Experimental Thermal and Fluid Science*, **12**: 364-372.

Laflin, G. C., Oglesby, K. D., (1976). An experimental study on the effects of flow rate, water fraction and gas-liquid ratio on air-oil-water flow in horizontal pipes', *MSc. Thesis*, University of Tulsa.

Launder, B.E., Ying, W.M., (1973). Prediction of flow and heat transfer in ducts of square cross section. *Proc. Institution Mechanical Eng.* **187**, 455-461.

Lavieille, P., Lemoine, F., Lavergne, G., Virepinte, J. F., Lebouche, M., (2000). Temperature measurements on droplets in monodisperse stream using laser-induced fluorescence', *Exp. in Fluids*, **29**: 429-437.

Layfield, R., (2003). Lattice gas automata investigation of phase inversion, Transfer Report of Department of Chemical Engineering, University of Edinburgh.

Lee, K. B., Jang, H. C., (1997) A numerical prediction on the turbulent flow in closely spaced bare rod arrays by a nonlinear k-ε model, *Nuc. Eng. and Des.* 172, 351-357.

Lo, S., (1996). Application of population balance to CFD modeling of bubbly flow via the MUSIG model, *AEA Technology*. AEAT-1096.

Lovick, J., Angeli, P., (2004). Experimental studies on the dual continuous flow pattern in oil-water flows, *Int. J. Multiphase Flow*, **30**: 139-157.

Liu, L., Matar, O. K., Ortiz, E. S., Hewitt, G. F., (2005). Experimental investigation of phase inversion in a stirred vessel using LIF, *Chem. Eng. Sci.*, 60, 85-94.

Luhning, R.W., Sawistowski, H., (1971). Phase inversion in stirred liquid-liquid systems', *Proc. Int. Solvent Extr. Conf., The Hague*, pp. 873-887, Society of Chemical Industry, London.

Luo, Y.S., Chen, T.K., Cai, J.Y., (1997). Frictional pressure loss and phase inversion point for oil-water emulsion in vertical tube, Proceedings of International Symposium on Multiphase Fluid non- Newtonian Fluid & Physico-Chemical Fluid Flows, 3.53-3.58.

Luo, H., Svendsen, H., (1996). Theoretical model for drop and bubble break-up in turbulent dispersions, *AIChE J.*, **42**, 1225-1233.

M

MacLean, D. L., (1973). A theoretical analysis of bicomponent flow and the problem of the interface shape, *Trans. Soc. Rheology*, **17**: 385-399.

Martinez, A. E., Intevep, S. A., Arirachakaran, S., Shoham, O., Brill, J. P., (1998). Prediction of dispersion viscosity of oil/water mixture flow in horizontal pipes. SPE paper 18221.

McClarey, M. J., Mansoori, G. A., (1978). Factors affecting the phase inversion of dispersed immiscible liquid-liquid mixtures, *AIChE Symposium Series*, **74**(173): 134-139.

Melling A., Whitelaw, J.H., (1976), Turbulent flow in a rectangular duct, *J. Fluid Mech.*, **78**, part 2, 289-315.

Mewes, D., Nädler, M., Tokarz, A., (1997). The effect of emulsification on the flow behaviour of two Immiscible liquids in horizontal pipes', *Int. Symp. on Liquid-Liquid Two-Phase Flow and Transport Phenomena*, pp. 97-106, Antalya, Turkey

Mlynek, Y., Resnick, W., (1972). Drop sizes in an agitated liquid-liquid system. *AIChE J.*, **18**(1): 122-127.

Mompean, G., Numerical simulation of a turbulent flow near a right-angled corner using the Speziale non-linear model with RNG K–ε equations, *Computers & Fluids*, **27**(7): 847-859

Moraga, F. J., Bonetto, F. J., Lahey, R. T., (1999). Lateral forces on spheres in turbulent uniform shear flow. *Int. J. Multiphase Flow,* **25**: 1321-1372.

Moraga, F. J., Larreteguy, A. E., Drew, D.A., Lahey Jr., R. T., (2003). Assessment of turbulent dispersion models for bubbly flows in the slow Strokes number limit, *Int. J. Multiphase Flow*, 29, 655–673.

Moran, K., Inumaru, J., Kawaji, M., (2002). Instantaneous hydrodynamics of a laminar wavy liquid film, *Int. J. Multiphase Flow*, **28**: 731-755.

Mosher, H. S., Hardwick, E. R., Ben Hur, D., (1962).Flash-photolysis studies of α- and γ-(2,4-Dinitrobenzyl) pyridine, *J. Chem. Physics,* **37**(4): 904-909.

N

Nädler, M., Mewes, D., (1995). Intermittent three-phase flow of oil, water and gas in horizontal pipes, Proc. 5th Int. Offshore and Polar Eng. Conf., pp. 72–80,

Nädler, M., Mewes, D., (1997). Flow induced emulsification in the flow of two Immiscible liquids in horizontal pipes', *Int. J. Multiphase Flow*, **23**(1): 55-68.

Nienow, A. W., Pacek, A. W., Moore, I. P. T., Homer, J., (1994). Fundamental studies of phase inversion in a stirred vessel, *Proc. Euro. Conf. on Mixing, IChemE Symposium Series*, No. 136, pp.171-178.

Nikuradse, J., (1926). Untersuchungen über die Geschwindigteisverteilung in Turbulenten Strömungen. Thesis, Göttingen, V. D. I.-Forsch. 281.

Norato, M. A., Tsouris, C., Tavlarides, L. L., (1998). Phase inversion studies in liquid-liquid dispersions', *Can. J. Chem. Eng.*, 76: 486-494.

Nordsveen, M., (2001). Wave- and turbulence-induced secondary currents in the liquid phase in stratified duct flow, *Int. J. Multiphase Flow*, **27**, 1555-1577.

O

Oddie, G., Shi, H., Durlofsky, L. J., Aziz, K., Pfeffer, B., Holmes, J. A., (2003). Experimental study of two and three phase flows in large diameter inclined pipes, *Int. J. Multiphase Flow*, **29**: 527-558.

Oglesby, K. D., (1979). An experimental study on the effects of oil viscosity, mixture velocity and water fraction on horizontal oil-water flow, *Msc. Thesis*, University of Tulsa, USA.

Olmos, E., Gentric, C., Vial, Ch., Wild, G., Midoux, N., (2001). Numerical simulation of multiphase flow in bubble column reactors. Influence of bubble coalescence and break-up, *Chem. Eng. Sci.*, **50**: 6359-6365.

P

Pacek, A. W., Moore, I. P. T., Nienow, A. W., (1994a). Video technique for measuring dynamics of liquid-liquid dispersion during phase inversion, *AIChE J.*, **40**(12): 1940-1949.

Pacek, A. W., Nienow, A. W., Moore, I. P. T., (1994b). On the structure of turbulent liquid-liquid dispersed flows in an agitated vessel, *Chem. Eng. Sci.*, **49**(20): 3485-3498.

Pacek, A. W., Nienow, A. W., (1995). A problem for the description of turbulent dispersed liquid-liquid systems, *Int. J. Multiphase Flow*, **21**(2),: 323-328.

Pacek, A. W., Man, C. C., Nienow, A.W., (1998). On the Sauter mean diameter and size distributions in turbulent liquid-liquid dispersions in a stirred vessel, *Chem. Eng. Sci.*, **53**: 2005-2011.

Pal, R., Bhattacharya, S. N., Rhodes, E., (1986). Flow behaviour of oil-in-water emulsions, *Can. J. Chem. Eng.*, **64**: 3-10.

Pal, R., (1993). Pipeline flow of unstable and surfactant-stabilised emulsions, *AIChE J.*, **39**(11): 1754-1764.

Park, H., Hummel, R. L., Ojha, M., (1994). A multi-stage nitrogen laser for the photochromic flow visualization technique, *Meas. Sci. Technol.*, **5**: 1139-1145.

Park, J. Y., Blair, L. M., (1975). The effect of coalescence on drop size distribution in an agitated liquid-liquid dispersion. *Chem. Eng. Sci.*, **30**: 1057-1064.

Pascu, M. L., Moise, N., Staicu, A., (2001). Tuneable dye laser applications in environment pollution monitoring, *J. of Molecular Structure*, 598: 57-64.

Pfennig, A., Schwerin, A., (1998). Influence of electrolytes on liquid-liquid extraction', *Ind. Eng. Chem. Res.*, 37: 3180-3188.

Plegue, T. H., Frank. S. G., Fruman, D. H., Zakin, J. L., (1989). Concentrated viscous crude oil-in-water emulsions for pipeline transport, *Chem. Eng. Comm.*, 82: 111-122.

Popovich, A. T., Hummel, R. L., (1967). A new method for non-disturbing turbulent flow measurements very close to a wall, *Chem. Eng. Sci.*, **22**: 21-25.

Prince, M., Blanch, H. W., (1990).Bubble coalescence and break-up in air-sparged bubble columns, *AIChE J.*, **36**(10): 1485-1499.

Q

Quinn, J. A., Sigloh, D. B., (1963). Phase inversion in the mixing of immiscible liquids', *Can. J. Chem. Eng.*, **41**: 15-18.

R

Reddy, S. R., Fogler, H. S., (1980). Emulsion stability of acoustically formed emulsions, *J. Phys. Chem.*, **84**: 1570-1575.

Rodger, W. A., Trice, Jr., V. G., Rushton, J. H., (1956). The effect of fluid motion on interfacial area of dispersions, *Chem. Eng. Prog.*, **52**(12): 515-520

Russel, T. W. F., Charles, M. E., (1959). The effect of the less viscous liquid in the laminar flow of two immiscible liquids. *Can. J. Chem. Eng.*, **37**: 18-24.

Russel, T. W. F., Hodgson, G. W., Govier, G. W., (1959). Horizontal pipeline flow of mixture s of oil and water. *Can. J. Chem. Eng.*, **37**: 9-17.

S

Sajjadi, S., Zerfa, M., and Brooks, B. W., (2002). Dynamic behaviour of drops in oil/water/oil dispersions', *Chem. Eng. Sci.*, **57**: 663-675.

Sato, Y., Sekoguchi, K., (1975). Liquid velocity distribution in two-phase bubbly flow. Int. J. Multiphase Flow, 2: 79-95.

Selker, A. H., Sleicher, Jr., C. A., (1965). Factors affecting which phase will disperse when immiscible liquids are stirred together, *Can. J. Chem. Eng.*, **43**: 298-301.

SenGupta, A. K., Papadopoulos, K. D., (1998). Stability of concentrated colloids: the controlling parameters, *J. Colloid and Interface Sci.*, **203**: 345-353.

Serizawa, A., Kataoka, I., (1992). Dispersed flow, Proc. 3 Int. Workshop on Two-phase Flow Fundamentals, June 15-19, London, UK.

Simmons, M. J. H., Azzopardi, B. J., (2001). Drop size distributions in dispersed liquid-liquid pipe flow, *Int. J. Multiphase Flow*, **27**: 843-859

Soleimani, A., (1999). Phase distribution and associated phenomena in oil-water flows in horizontal tubes, *PhD Thesis*, Imperial College London, UK.

Sovová, H., Breakage and coalescence of drops in a batched stirred vessel-II. Comparison of model and experiments, *Chem. Eng. Sci.*, **36**(9):1567-1573.

Speziale, C. G., (1979). Invariance of turbulence closure models. *Phys. Fluids*, **22**: 1033-1037.

Speziale, C. G., (1981). Some interesting properties of two-dimensional turbulence, *Phys. Fluids*, **24**:1425-1427.

Speziale, C. G., (1987). On non-linear k-l and k- ε models of turbulence, Journal of Fluid Mechanics, 178, 459-475.Sovová, H., (1981). Breakage and coalescence of drops in a batched stirred vessel - II. comparison of model and experiments, *Chem. Eng. Sci.*, **36**(9): 1567-1573.

Sprow, F. B., (1967). Distributions of drop sizes produced in turbulent liquid-liquid dispersion. *Chem. Eng. Sci.*, **22**: 435-444.

T

Taweel, A. M., Chen, C., (1996). A novel static mixer for the effective dispersion of immiscible liquids. *Trans. IChemE*, 74 Part A: 445-450.

Tezock, M. C., (1993). Some aspects of crossflow hydrodynamics on distillation trays. *Ph.D. Thesis*, Imperial College, University of London.

Thom, R., (1989). Structural stability and morphogenesis, (D. H. Fowler, Transl.), Addison-Wesley, Redwood City, CA.

Thornton, J. D., Anderson, T. J., (1981). Surface renewal phenomena in liquid-liquid droplet systems with and without mass transfer, *Int. J. Heat Mass Transfer*, **24**(11): 1847-1848.

Thornton, J. D., Anderson, T. J., Javed, K. H., Achwal, S. K., (1985). Surface phenomena and mass transfer interactions in liquid-liquid systems, *AIChE J.*, **31**(7): 1069-1076.

Tidhar, M., Merchuk, J. C., Sembira, A. N., Wolf, D., (1986). Characteristics of a motionless mixer for dispersion of immiscible fluids-. phase inversion of liquid-liquid systems, *Chem. Eng. Sci.*, **41**(3): 457-462.

Tobin, T., Ramkrishna, D., (1992). Coalescence of charged droplets in agitated liquid-liquid dispersions, *AIChE J.*, **38**(8): 1199-1205.

Tobin, T., Ramkrishna, D., (1999). Modeling the effect of drop charge on coalescence in turbulent liquid-liquid dispersion, *Can. J. Chem. Eng.*, 77:1090-1104.

Trallero, J. L., (1995). Oil-water flow patterns in horizontal pipes. *PhD Thesis*, The University of Tulsa, Tulsa.

Tsouris, C., Tavlarides, L. L., (1994). Breakage and coalescence models for drops in turbulent dispersions, *AIChE J.*, **40**(3): 395-406.

V

Vaessen, G. E. J., Stein, H. N., (1995). The applicability of catastrophe theory to emulsion phase inversion, *J. Coll. Interface Sci.*, **176**: 378-387.

Vaessen, G.E.J., Visschers, M., Stein, H.N. (1996). Predicting catastrophic phase inversion on the basis of droplet coalescence kinetics. Langmuir, 12: 875–882.

van Voorhis, J. J., Cartmell, J. V., Hsieh, P. Y., (1969). Surface activity of some merocyanines and spiropyrans at liquid-liquid interfaces, *J. Colloid Interface Sci.*, **33**(1): 8-15.

Versteeg, H. K., Malalasekera, W., (1995). An introduction to computational fluid dynamics: the finite volume method, Harlow: Langman

W

Wallis, G. B., (1969). One-dimensional two-phase flow, McGraw-Hill, New York.

Ward, J. P., Knudsen, J. G., (1967). Turbulent flow of unstable liquid-liquid dispersions: drop sizes and velocity distributions, *AIChE J.*, **13**(2): 356-365.

Y

Yakhot, V., Orszag, S. A., Thangam, S., Gatski, T. B. and Speziale, C. G., (1992). Development of turbulence models for shear flows by a double expansion technique, *Physics of Fluids A*, **4**: 1510-1520.

Yang, Z.Z., Xu, Y.Z., Zhao, D.L. and Xu, M., (2000). Preparation of waterborne dispersions of epoxy resin by the phase-inversion emulsification technique. 1. Experimental study on the phase inversion process, *Colloid Ploym Sci.*, **278**: 1164-1171.

Yeh, G. C., Haynie, Jr., F. H., Moses, R. A., (1964). Phase-volume relationship at the point of phase inversion in liquid dispersions', *AIChE J.*, **10**(2): 260-265.

Yeo, L. Y., Matar, O. K., Perez de Ortiz, E. S., & Hewitt, G. F. (2000) 'Phase inversion and associated phenomena', *Multiphase Sci. and Tech.*, **12**(1), 51–116.

Yeo, L. Y., Matar, O. K., Perez de Ortiz, E. S., Hewitt, G. F., (2002a). Simulation studies of phase inversion in agitated vessels using a monte carlo technique', *J. Colloid and Interface Sci.*, **248**: 443-454.

Yeo, L. Y., Matar, O. K., Perez de Ortiz, E. S., Hewitt, G. F., (2002b). A simple predictive tool for modeling phase inversion in liquid-liquid dispersions, *Chem. Eng. Sci.*, **57**: 1069-1072.

Yeo, L. Y., Matar, O. K., Perez de Ortiz, E. S., Hewitt, G. F., (2002c). A description of phase inversion behaviour in agitated liquid-liquid dispersions under the influence of the Marangoni effect, *Chem. Eng. Sci.*, *57*: 3505-3520.

Yeung, A., Moran, K., Masliyah, J., Czarnecki, J., (2003). Shear-induced coalescence of emulsified oil drops, *J. Colloid and Interface Sci.*, **265**(2): 439-443.

Z

Zalzal, P., Ojha, M., Ethier, C. R., Cobbold, R. S. C., Johnston, K. W., (1994). Visualization of transitional pipe flow using the photochromic tracer method', *Phys. Fluids*, **6**(6): 2003-2010.

Zerfa, M., Sajjadi, S., Brooks, B. W., (1999). Phase behaviour of non-ionic surfactants-p-xylene-water systems during the phase inversion process, *Colloids and Surfaces A*, 155: 323-337.

Zerfa, M., Sajjadi, S., Brooks, B. W., (2001). Phase behaviour of polymer emulsions during the phase inversion process in the presence of non-ionic surfactants, *Colloids and Surfaces A*, **178**: 41-48.

Zolotorofe, D. L., Scheele, G. F., (1970). Photochromic dye tracer measurements of small liquid velocities, *Ind. Eng. Chem. Fundam.*, 9(2): 291-293.

Appendix A Photochromic Dye Tracing

As mentioned in Chapter 3, photochromic dye tracing (PDT) is a non-intrusive dye tracing technique and has been applied to investigate velocity fields in single-phase and two-phase (gas-liquid) flows. Therefore, some tests were performed in the present work to investigate the application of this technique to liquid-liquid dispersed flow. In the event, the LIF technique was chosen rather than PDT. However, the PDT method has the advantage of allowing the velocity of the fluid (for example, the continuous phase fluid) to be determined whereas, with the LIF method, only the motion of the interfaces can be observed. Thus, to form a starting point for future work on PDT, this Appendix gives the background and a summary of the development work done in the present project.

A.1 The Mechanism of Photochromic Dye Tracing

The photochromic dye tracing (PDT) technique is based on light activation of photochromic dye material dissolved in transparent test fluids. In general, a photochromic dye can be activated instantaneously by one or several pulses of ultraviolet light; a coloured trace is generated in a localised volume of solution and extends up to the fluid interfaces. The dye position can then be monitored with time in order to provide a visual description of the flow. The advantages of a photochromic dye tracing technique is that it does not suffer from the limitations of conventional tracer techniques, in that it is non-intrusive and that it does not create a significant local density difference for the tracer.

Photochromism can be defined on an operational basis to be 'a reversible change of a single chemical species induced in one or both directions by absorption of electromagnetic radiation between two forms, A and B, having different absorption spectra ' (Brown, 1971). In general, the following reaction takes place:

$$A\,(\lambda^1) \xleftrightarrow{h\nu} B(\lambda^2)$$

where A can be a molecule or an ion and B a single chemical species (or more than one species) in its ground electronic state providing that it recombines to give A. λ^1 and λ^2 are wavelength characteristic absorption spectra unique to A and B. Figure A.1 illustrates a

typical graphical representation of the cyclic response of the photochromic compound to activating radiation. Excitation radiation is applied at time t_1 causing the relative amounts of *B* molecules to *A* molecules to rise until steady-state is achieved. This intermediate state between *A* and *B* might possibly be a metastable ground state. At time t_2 when the excitation radiation is removed, the *B* molecules revert back to *A* molecules via the reverse reaction.

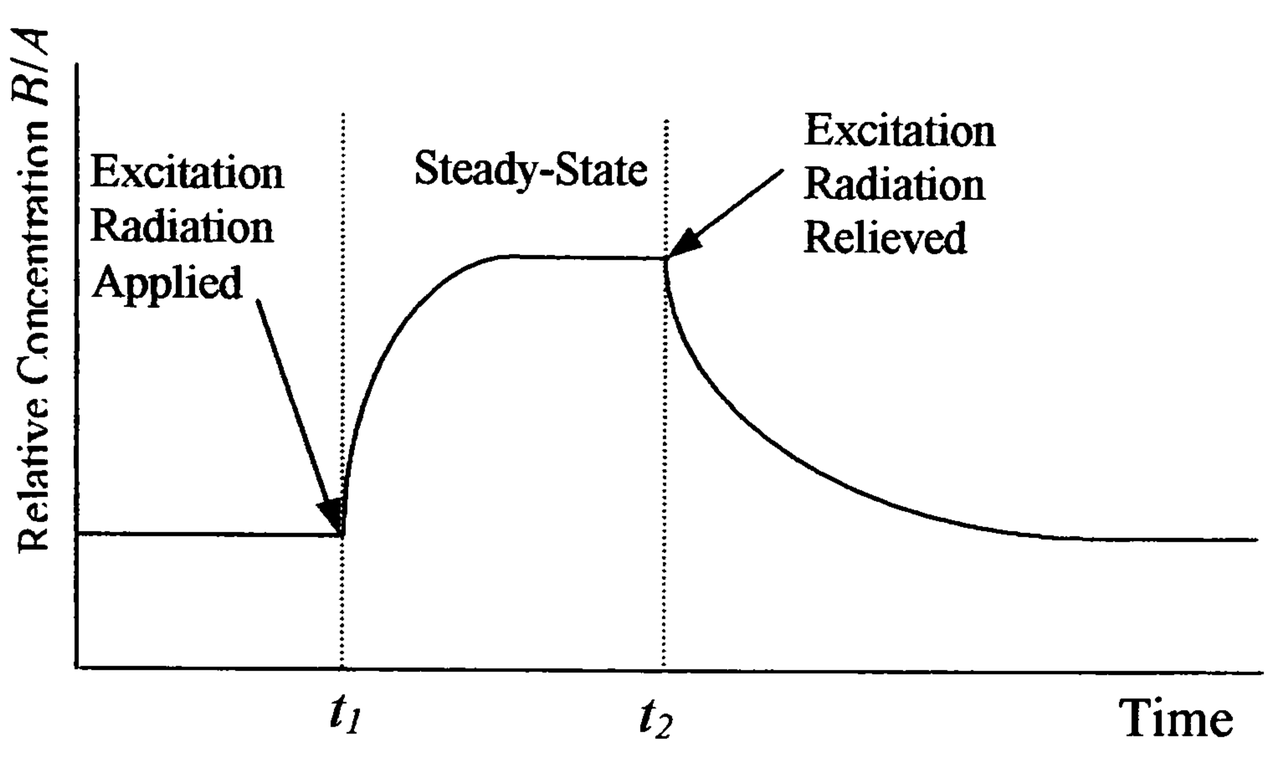


Figure A.1 Typical Behaviour of Photochemical Compound (Brown, 1971)

The most common photochromic molecules have a colourless or pale yellow form A and a coloured form B (e.g., red or blue). For example, solid photochromic *spiropyrans,* which have been studied extensively, or their solutions (in ethanol, toluene, kerosene, etc.), are colourless or weakly coloured. Upon UV irradiation, they become coloured. The coloured solutions fade thermally to their original state; in many cases, they can also be decolourised (bleached) by visible light. The UV-induced change from A to B (the forwards reaction) can take place in times of the order of a few nanoseconds. The backwards reactions (from B to A) is thermally induced and takes place spontaneously, over timescales up to several seconds. An example of the change in absorption spectrum arising from the photochromic reactions in is shown in Figure A.2. In photochromism, the reaction is reversible. Should the reaction be irreversible, then that reaction applies to ordinary photochemistry rather than photochromism.

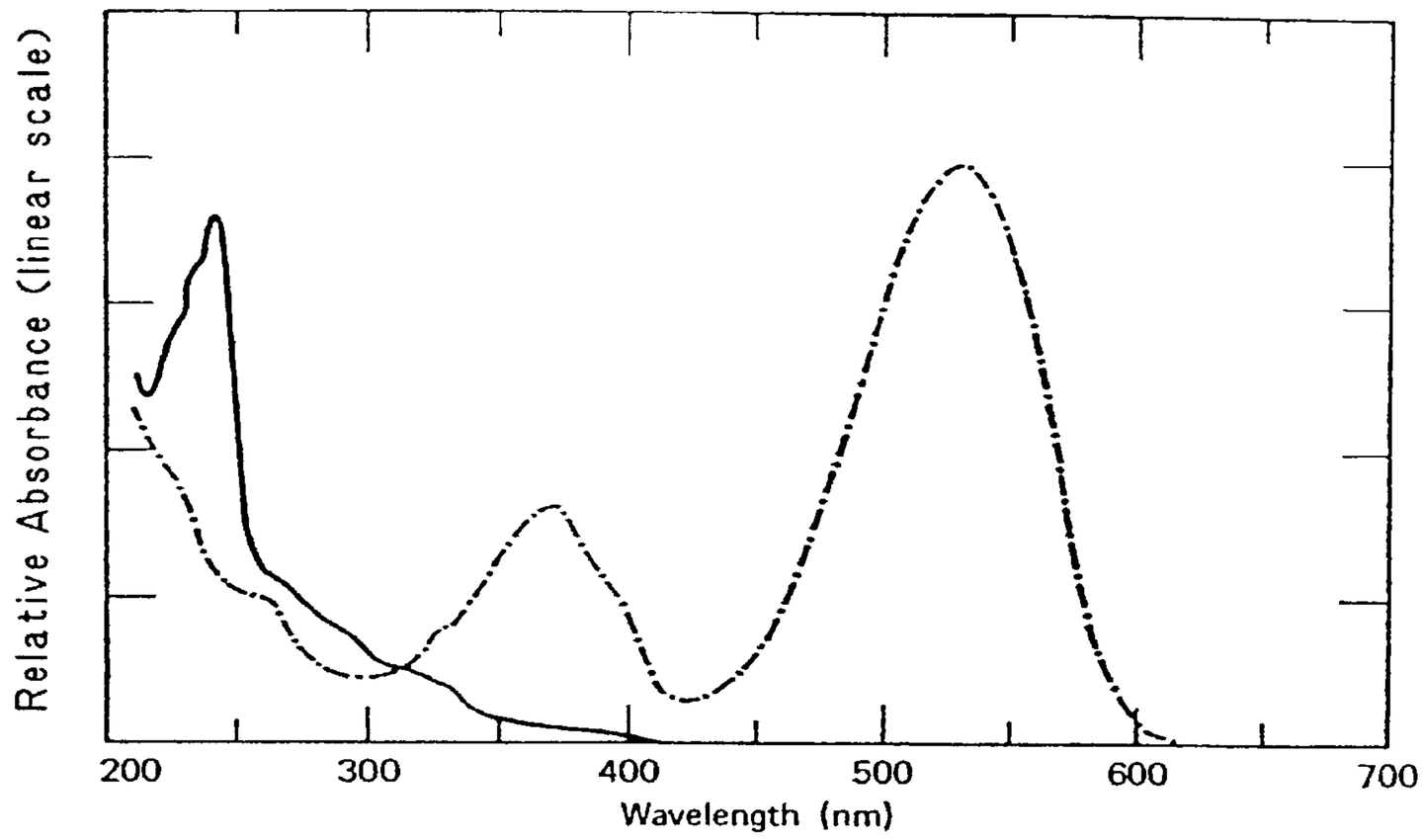


Figure A.2 Absorption Spectra of Coloured (Dotted Line) and Colourless (Solid Line) Solutions of 5,7-DiChloro-6-NitroBPS in Ethanol at 20°C (Brown, 1971)

A.2 Application of Photochromic Dye Tracing to Flow Visualisation

The photochromic phenomenon was discovered as early as 1899; however, the first researchers who utilized this technique to study the velocity of laminar flow, were Goldish et al. (1965). A clear, yellow light-sensitive liquid was used as fluid, and when the fluid was exposed to high intensity illumination would immediately change its colour to a dark, permanent blue. However, strictly speaking, due to its irreversible property, this was not a photochromic reaction. In addition, the drawback with the Goldish et al. method was that the solution required a substantial amount of irradiation time in order to secure a colour transformation.

Popovich and Hummel (1967) carried out the first application of a true photochromic reaction to study the viscous sublayer in turbulent pipe flow. They used a 0.1% by weight dilute solution of 2-(2,4-dinitro-benzyl)-pyridine (DNBP) in 95% ethyl alcohol as the photochromic dye (Hardwick *et al.*, 1960). Using a parabolic mirror to focus the light from a xenon flashtube, the solution was made to undergo the following tautomeric shift (Figure A.3):

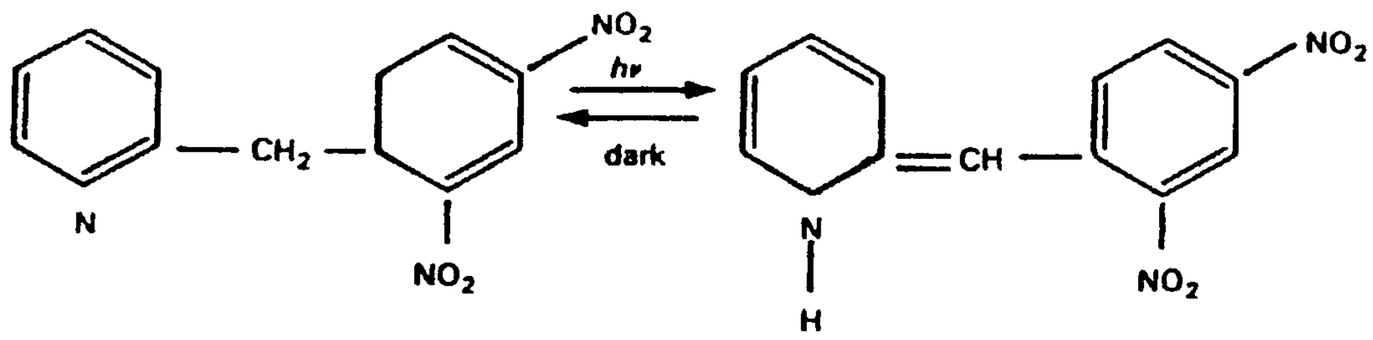


Figure A.3 DNBP – Tautomeric shift

A dark blue trace was produced from the initial pale yellow solution in less than 3 μs (Mosher *et al.*, 1962) and reverts back to its original pale yellow form in a couple of milliseconds after the exposure has stopped. Later, Frantisak *et al.* (1969) used a pulse ruby laser rather than the flashtube and a high speed ciné camera (10,000 fps) to study turbulent flow conditions. Ho and Hummel (1970) used this refined method and a 35mm still camera to study the velocity distributions of falling liquid films.

However, Zolotorofe and Scheele (1970) noted that the disadvantage of using DNBP was that its lifetime after irradiation was extremely short, rendering it unsuitable for low velocity investigations. They proposed the use of 1,3,3-trimethylindolino-6'-nitrobenzopyrylospiran (TMINBPS, otherwise referred to as TNSB, or spiropyran). Upon irradiating with ultraviolet radiation, TNSB is converted in the forward reaction via heterolytic cleavage (i.e. the breaking of the carbon-oxygen bond in the spiropyran ring) to yield a merocyanine dye structure as follows (Figure A.4):

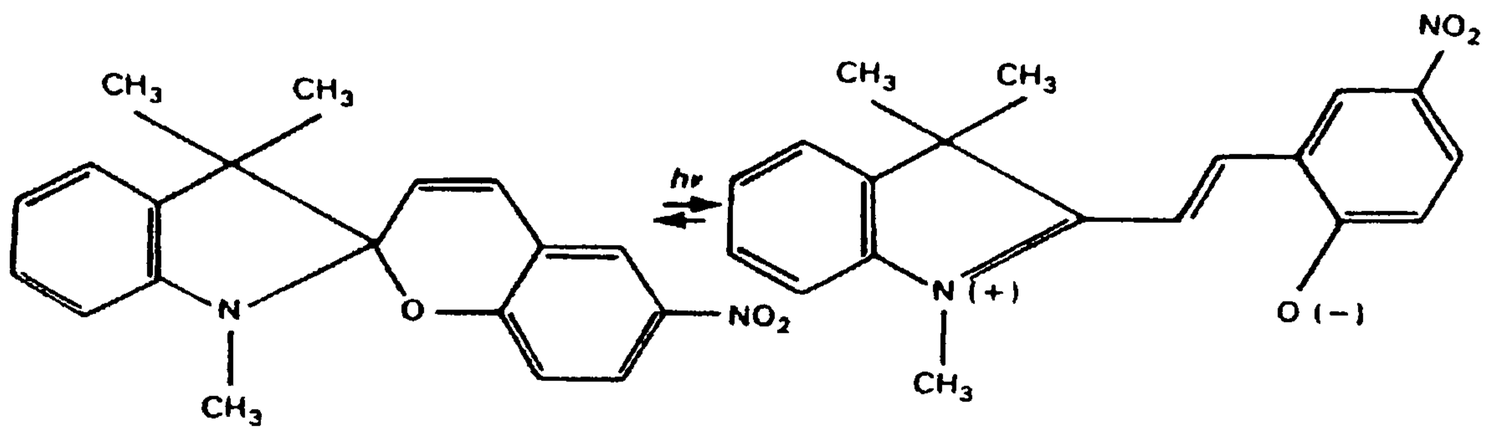


Figure A.4 TMINBPS-Heterolytic cleavage

TNSB has been found to produce colour changes in various solvents such as benzene, toluene, xylene, acetone, etc., with the colours of the unexcited and excited states depending on the solvent used. Since the laminar velocity distribution investigations by Zolotorofe and Scheele (1970), numerous flow visualisation studies have been carried out using TNSB (Park *et al.*, 1994; Zalzal *et al.*, 1994; Couch *et al.*, 1996; Kawaji *et al.*, 1997; Kawaji, 1998; Moran *et al.*, 2002).

However, all the photochromic dyes mentioned above are soluble only in organic liquids. Actually, most fluid flow applications involve aqueous based systems and the majority of previous measurements and experimental data have been obtained for water systems. Hewitt et al. (1990) carried out a feasibility study to develop a water-soluble photochromic dye, Acid Magenta (monomethyl), otherwise known as Acid Violet 19. The structure of Acid Violet 19 is given in Figure A.5. In solution, the dye is in the coloured ionic form and hence

has to be bleached by adding sulphite anions to render it colourless. However, Hope found that on bleaching the dye, the acidity of the solution increased causing the sulphite to combine with oxygen to form sulphate. The loss of sulphite thus resulted in the solution reverting to its original ionic coloured form. Phosphate buffers were thus added to stabilise the pH of the solution at around pH 5-7. Hope used the dye in laminar and turbulent single-phase flow velocity measurements as well as for the analysis of velocity profiles in a variety of two-phase gas-liquid flow regimes such as stratified flow, annular flow and slug flow.

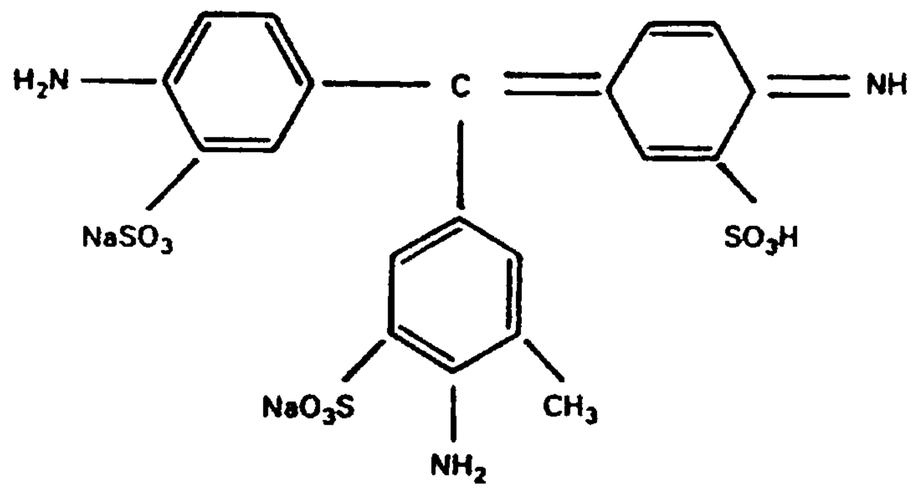


Figure A.5 Structure of Acid Violet 19 (Acid Magenta – Monomethyl Magenta)

The surface dynamics and surface renewal phenomena of hemispherical quasisteady-state pendant aqueous droplets immersed in toluene were studied by Thornton and Anderson (1981), Thornton *et al.* (1985) and Javed *et al.* (1989). In their work, Thornton *et al.* used a ferric dye similar to that used by Goldish *et al.* (1965) but with a different chemical composition, allowing it to be developed rapidly, unlike the dye used by Goldish *et al.* Thornton *et al.* did not use TMINBPS because they claimed that the local colour change it produces at the liquid-liquid interface was accompanied by a severe disturbance in the form of an initial eruption toward the light source. This was attributed to a decrease in the interfacial tension on exposure to ultraviolet light as reported in the work of van Voorhis *et al.* (1969). For this case, the extent of the decrease was largely dependent upon the degree of solubility and the concentration of the dye in the organic liquid. As a result the high-pressure fluid within the droplet erupted through the region of low-pressure fluid. Recently, TMINBPS has also been used to visualise the flow hydrodynamics in distillation trays (Tezock, 1993).

A.3 The Trial Experiments using Photochromic Dye Tracing

The criteria for finding the liquid pair for liquid-liquid dispersed flow investigations are the same as those considered in Chapter 3. After extensive searches, 1,1,2-

trichlorotrifluoroethane (Freon 113) and 13.9 wt.% sodium chloride solution (16.1 g NaCl in 100 ml H_2O) were selected for further investigations using a photochromic dyestuff.

Table A.1 Physical Properties of the Selected Liquid Pair.

	1,1,2-Trichlorotrifluoroethane	13.87% Sodium Chloride Solution
Specific Gravity (20°C)	1570 kg/m^3	1117 kg/m^3
Viscosity (25°C)	0.00067 Ns/m	0.0014 Ns/m
Boiling Point	47°-48°C	-
Melting Point	-35°C	-
Flash Point	None	-
Solubility in Water	-	357 g/l
Surface Tension (20°C)	0.0182 N/m	0.0584 N/m
Refractive Index (25°C)	1.3571 1.3582 (with dye)	1.3575 1.3581 (with dye, bleach & buffer)
Interfacial Tension (20°C)	~ 6 N/m	

Two photochromic dyes, a photochromic spiropyran dyestuff (1', 3', 3'-trimethylindoline-6-nitrobenzospiropyran (TNSB) which is soluble in organic phases) and Acid Violet 19 (Acid Magenta Monomethyl) which is an aqueous soluble dye, were tested.

Spiropyran produces a dark blue colouration upon ultraviolet irradiation whereas Acid Violet 19 gives a magenta colour. Acid Violet 19 was first bleached with potassium sulphite (K_2SO_3) and sodium metabisulphite ($Na_2S_2O_5$) to give a colourless (or yellowish) solution before use. The dye/bleach solution must then be buffered using equal proportions of sodium dihydrogen orthophosphate (NaH_2PO_4) and disodium hydrogen orthophosphate (Na_2HPO_4) to increase the stability of the dye. The relative bleach and buffer concentrations to be used have been optimised and are given by Hewitt et al. (1990), see Table A2. The photochromic dyestuffs tests are shown in Figure A.6. Figure A.6 (a) and (b) indicate that higher penetration produces lower contrast, and *vice versa*.

However, after several single-phase flow experiments (Figure A.7) using the aqueous system (Acid Violet 19 plus bleach and buffer), white and black solid suspended material was observed in the liquid. In the light of consultation with the Department of Chemistry, the black material is probably copper sulfide where the copper is oxidized to Cu (I) and the

bisulfide reduced to sulfides. The white precipitation is probably a Cu (I) salt of the remaining ions.

Table A.2 Photochromic Dyestuffs

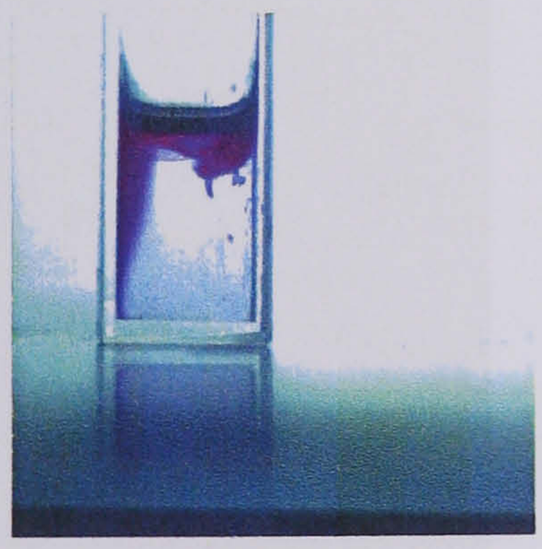
Liquids	**Organic Phase**	**Aqueous Phase**	
Dyestuffs	TNSB	Acid Violet 19	
Concentrations	0.005% by weight	0.1g/litre of solvent	
Bleach		K_2SO_3	1.2 g/litre of solvent
		$Na_2S_2O_5$	0.48 g/litre of solvent
Buffer		NaH_2PO_4	1.136 g/litre of solvent
		Na_2HPO_4	14.357 g/litre of solvent



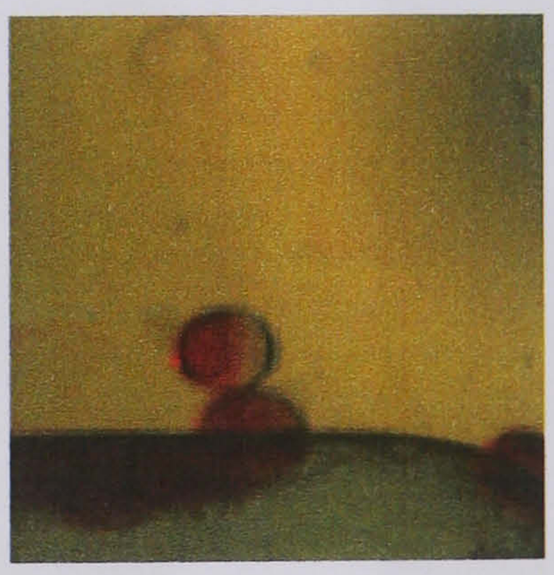
(a)



(b)



(c)



(d)

Figure A.6 Aqueous and organic phase dyestuffs test (static); (a) aqueous phase with 0.1% Acid Violet 19; (b) aqueous phase with 1% Acid Violet 19; (c) organic phase with TNSB; (d) aqueous solution (upper) and Freon 113 (lower and drops) with photochromic dyestuff-TNSB

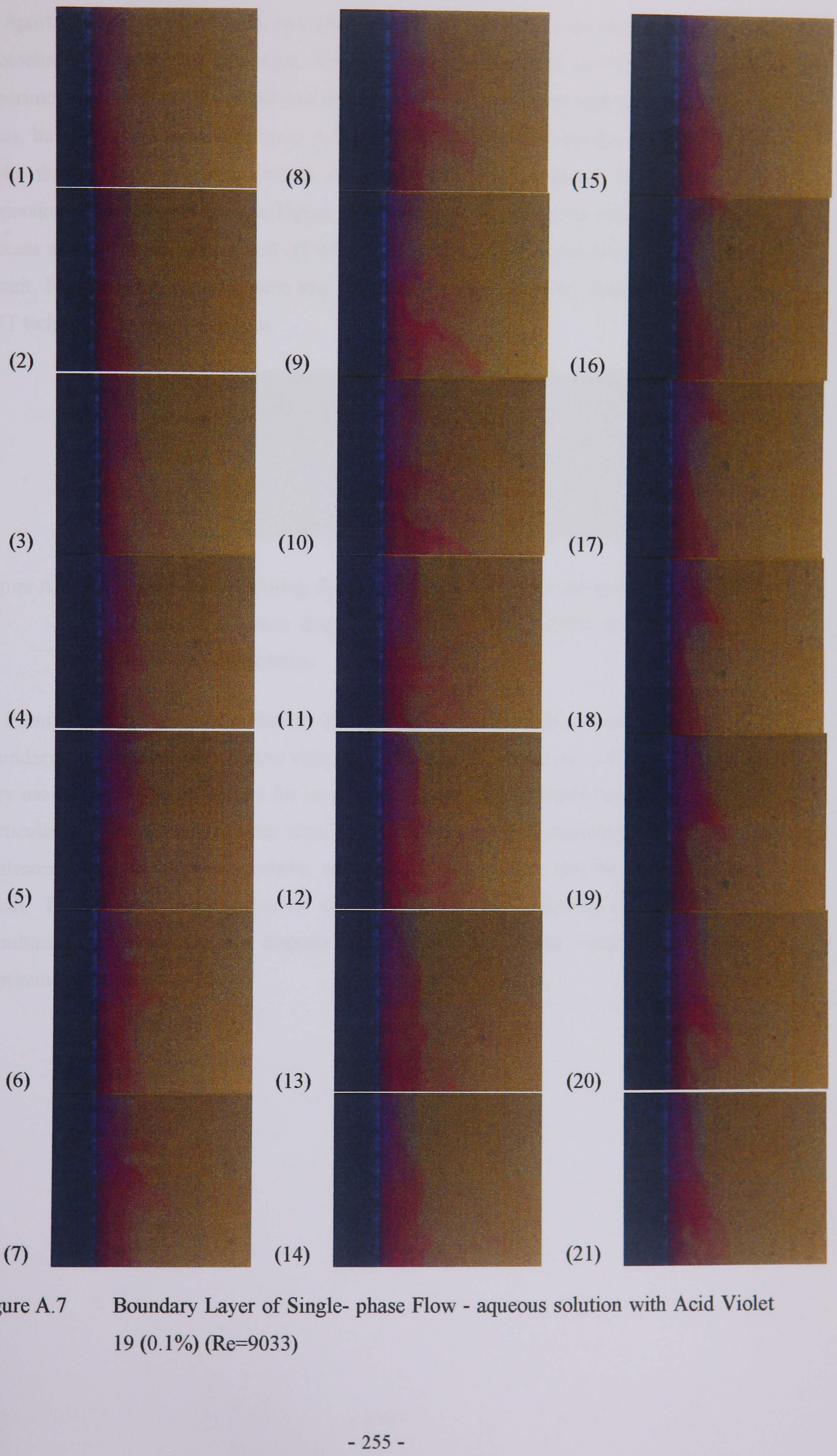


Figure A.7 Boundary Layer of Single- phase Flow - aqueous solution with Acid Violet 19 (0.1%) (Re=9033)

Apart from single-phase tests, two-phase dispersed flow tests were also performed using photochromic dye tracing technique. The two liquids were Freon and NaCl solution. The experimental circuit for this liquid pair had to be air-tight due to the high volatility of Freon. Thus, bubbles (black spots in Figure A.8), which were generated by the centrifugal pump, broke the matched refractive indices of two liquids and obstructed the images of the dispersions. The image shown in Figure A.8 was captured during the two-phase separation process after the pump was turned off when most bubbles had accumulated at the top of the circuit. Nevertheless, the drop size and phase distribution could be obtained by using the PDT technique for the dispersions.



Figure A.8 The dispersion during the separation process after the pump turned off; the red region is Freon drop with activated TNSB (25% holdup) and yellow region is NaCl solution.

From Figure A.7, it is seen that the PDT technique can provide visualization of the wall boundary flow pattern and the flow velocity profile. At the same time, LIF is proved to be a very useful experimental method for investigating concentrated liquid-liquid dispersions. In particular, properties such as drop sizes and phase distribution, secondary dispersion, drop coalescence and breakup mechanisms, and even phase inversion may be observed in great detail. Therefore, a combination of these two techniques provides the possibility of simultaneously visualizing the dispersion characteristics and the velocity profile of the continuous phase.

Appendix B Properties and Preparation of the Liquid pair Used in the LIF Experiments

B.1 Refractive Indices

Exxol D80 Oil and 39 wt.% calcium chloride *($CaCl_2$)*, whose refractive indices are matched at 1.438 at 25°C, were chosen for the laser-induced Fluorescence experiment described in this thesis. An ABBE refractometer was used to determine the refractive index of the liquids. The refractive indices of aqueous calcium chloride solution as a function of temperature and concentration are shown in Figure B.1-B.2.

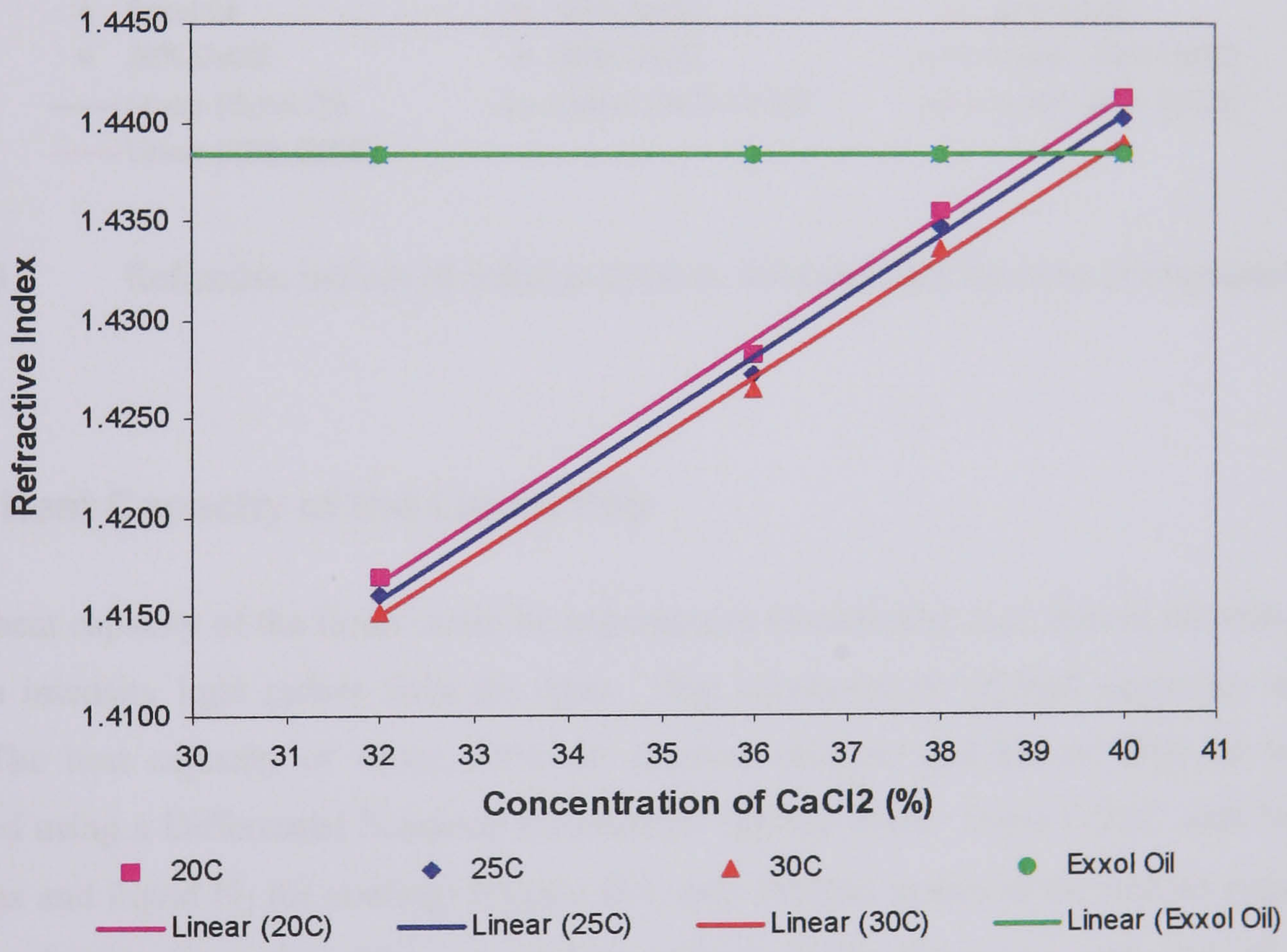


Figure B.1 Refractive indices of calcium chloride solution as a function of concentrations at 20°C, 25°C and 30°C compared with that of Exxol oil at 25°C.

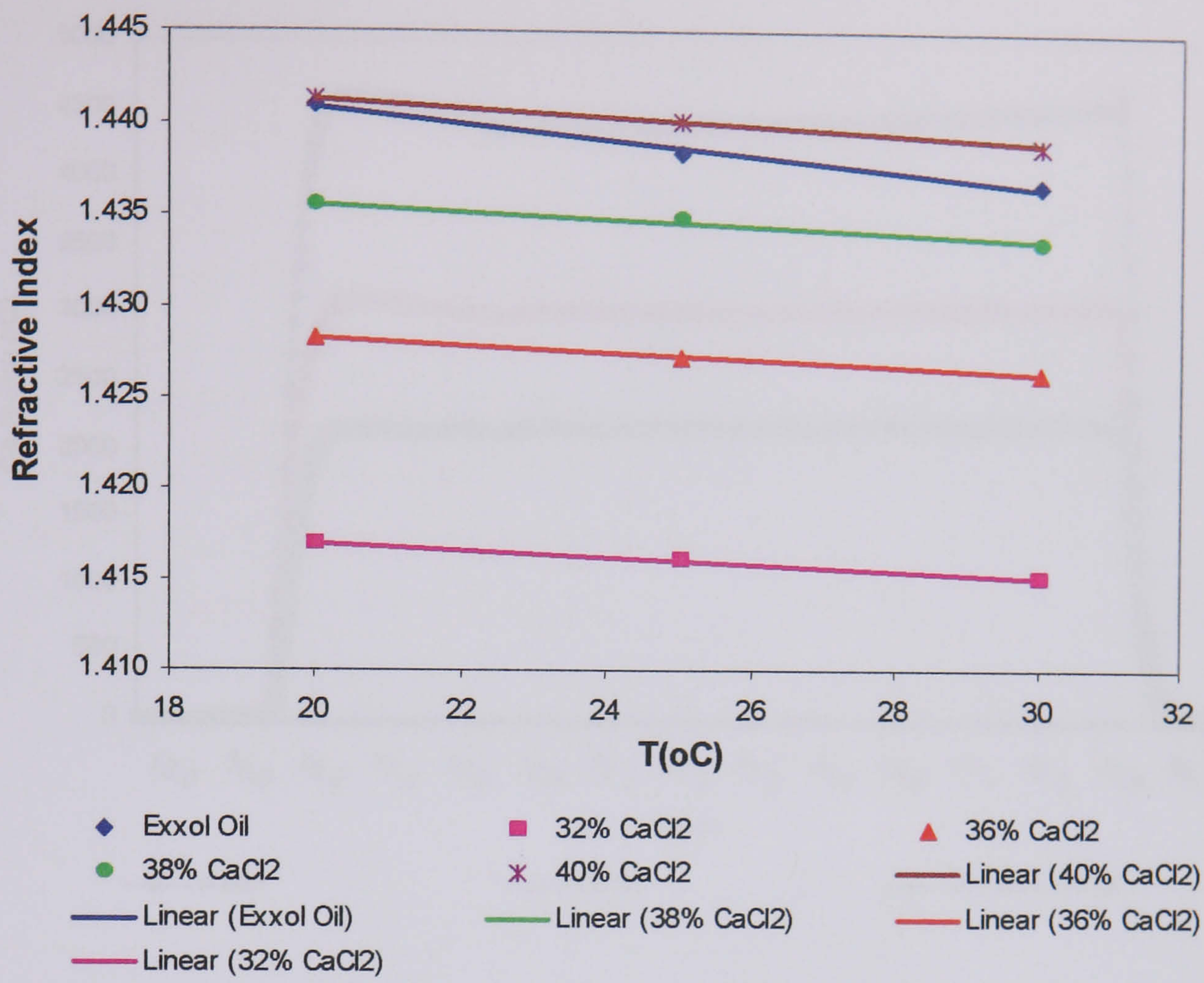


Figure B.2 Refractive indices of calcium chloride solutions as a function of temperature.

B.2 Heat Capacity of the Liquid Pair

The heat capacity of the fluids could be important in determining their themal response to the high intensity light pulses from the laser. Thus measurement of heat capacities were made. The heat capacity of water, 39% wt. calcium chloride and Exxsol D80 oil were measured using a Differential Scanning Colorimeter (Perkin Elmer, Pyris 1 DSC with N_2 as purge gas and liquid N_2 for cooling) (Figure B.4; note that the values in the platean regions are the relevant ones, the rising and falling values at the beginning and end of the measurements are not releavant). It was found that the 39 % wt. $CaCl_2$ solution has a much lower heat capacity than that of water but higher than the heat capacity of oil. It is concluded that the difference in heat capacities of the fluids used were smaller than that between oil and water and that differences in the rate of heating were unlikely to be significant.

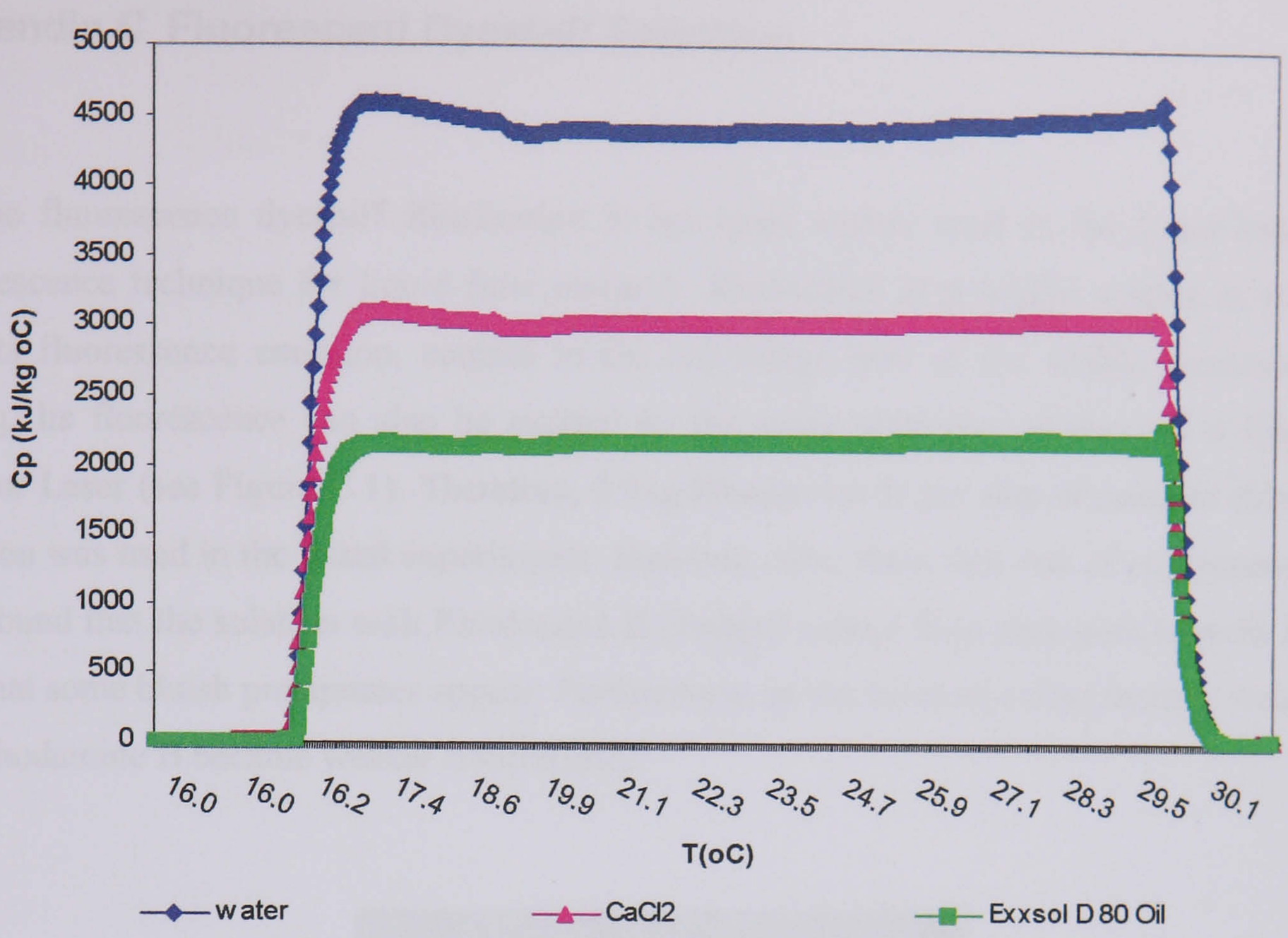


Figure B.3 The heat capacity of water, 39% wt. calcium chloride and Exxsol D80 oil

B.3 The Procedure for Making the 39% wt. $CaCl_2$ solution

Pure calcium chloride is very expensive and it is more economical to prepare the aqueous solution from calcium chloride dehydrated ($CaCl_2 \cdot 2H_2O$) crystals (99% purity) which was purchased from Sigma-Aldrich Ltd. To make up the calcium chloride solution of 39% concentration 107.3g of the dehydrated calcium chloride was added per 100ml of distilled water. The process of dissolving $CaCl_2 \cdot 2H_2O$ crystal is exothermic and therefore the crystal had to be added slowly and carefully. Since the target concentration (39%) is very near to that for saturation at room temperature, the solution was continuously stirred by a magnetic stirrer and regularly cooled by a cold-water bath. In addition, due to the high concentration, there is less 'free' water left to dissolve the fluorescence dye. Therefore, in order to dissolve more dye into the solution, the dye should be added into water before adding calcium chloride. The fluorescence dye solution (i.e. a 5%Eosin Y solution in water, Appendix C) was therefore fed in using a pipette (15 drops in 3 litres water). The cooled solutions were left overnight for some undesired red precipitates (dyestuff) to settle out before being further filtered.

Appendix C Fluorescent Dyestuff Selection

The fluorescence dyestuff Rhodamine B has been widely used in the Laser-Induced Fluorescence technique for liquid flow research. Rhodamine B is highly soluble in water, and its fluorescence emission, centred in the red-orange part of the visible spectrum, is strong. Its fluorescence can also be excited by the green light (λ=510.6nm) of a Copper Vapour Laser (see Figure C.1). Therefore, 0.01g Rhodamine B per litre of calcium chloride solution was used in the initial experiments. However, after these first sets of experiments, it was found that the solution with Rhodamine B changed colour from dark pink to weak blue and that some bluish precipitates appear. Furthermore, as the solution colour became weaker, the Rhodamine B became weaker fluorescence.

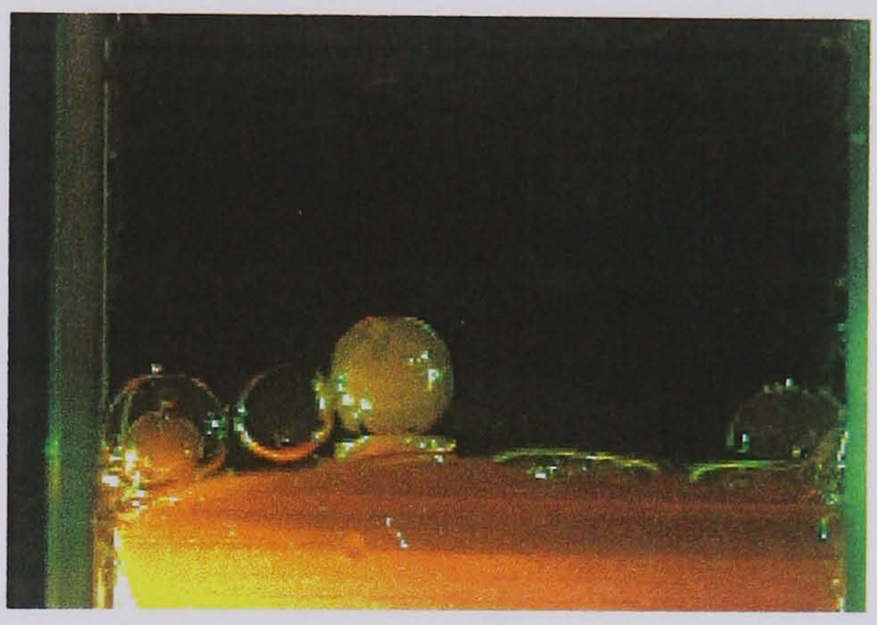


Figure C.1 Rhodamine B Test in Two-phase Static liquids. Exxol Oil (upper) and Water (lower and drops) with Rhodamine B.

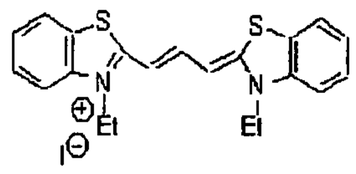
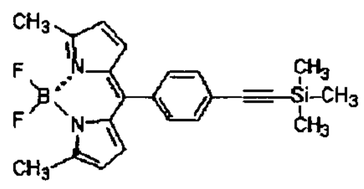
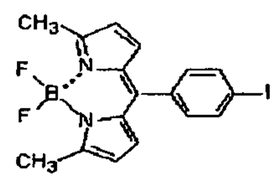
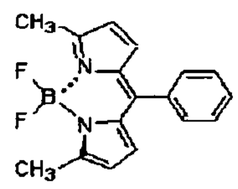
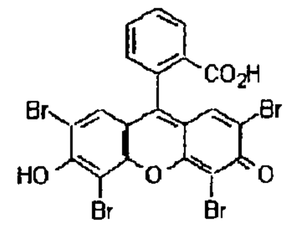
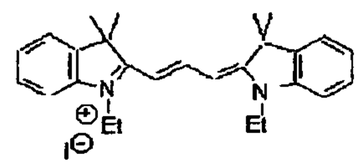
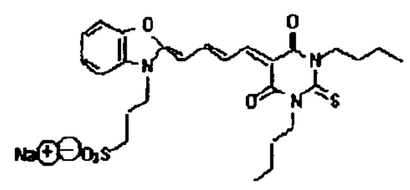
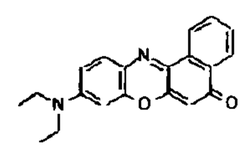
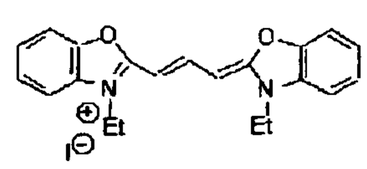
After analysis, it was found that the Rhodamine B reacted with the copper tube and that the bluish precipitates were Cu^{2+} ions. The reaction changed the pH of the solution and furthermore, switched the excitation (or absorption) wavelength of the fluorescence dye towards shorter wavelength. Consequently the colour of the solution became weaker as the running time increased.

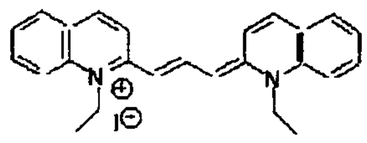
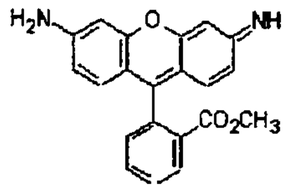
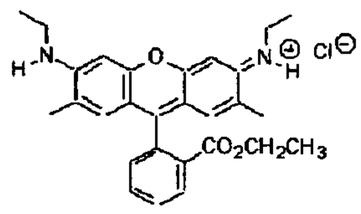
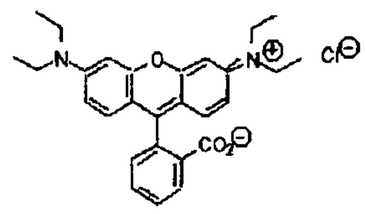
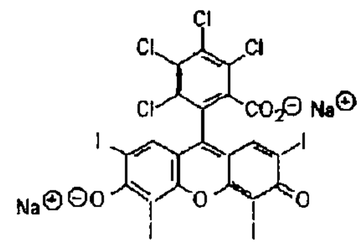
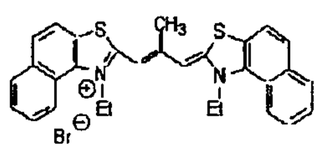
An acid and its conjugate base exhibit different spectroscopic properties. The influence of the acid-base dissociation phenomena on absorption spectra is the basis of acid-base indicator behaviour. Clearly, therefore, the fluorescence spectra of molecules containing acidic or basic functional groups are expected to be pH-dependent. A sudden change in the pH of an aqueous solution ('pH jump') useful for kinetic study, can be achieved by pulsed laser excitation of a solute molecule that undergoes a fast proton transfer reaction in the excited state populated by the laser pulse.

The inorganic ion thus combined with a non-fluorescent organic ligand to form a highly fluorescent metal chelate. The $CuCl_2$ probably combined with the N^+-$(C_2H_5)_2$ group in the Rhodamine B (see Table C1).

It was necessary, therefore, to find a new fluorescence dye for the experimental work described in this thesis. Initially, the fluorescence dyestuffs in Table C.1 were selected according to the absorption wavelength (see criteria 2 in Section 3.3.2.1).

Table C.1 Fluorescence dyestuffs.

	Symbol	Extinction coefficient [a] (solvent)[b]	
		510.6nm	578.2nm
C3-thiacyaninedye		33325 (ethanol)	24708 (ethanol)
Dimethyl BDPY-TMSCC		41696 (toluene)	75 (toluene)
DimethylBDPY		50591 (toluene)	0 (toluene)
DimethylBDPY-phenyl		36107 (toluene)	0 (toluene)
Eosin Y (Acid Red 87)		**59524 (ethanol)**	**12 (ethanol)**
Indocarbocyanine (C3) dye		83696 (methanol)	2229 (methanol)
Merocyanine 540		34316 (ethanol)	44443 (ethanol)
Nile Red		37334 (Dioxane)	1867 (Dioxane)
Oxadicarbocyanine (C5) dye		17112 (ethanol)	226663 (ethanol)

Pinacyanol iodide		8133 (methanol)	45736 (methanol)
Rhodamine 123		84665 (ethanol)	0 (ethanol)
Rhodamine 6G		52227 (ethanol)	160 (ethanol)
Rhodamine B		36231 (ethanol)	2346 (ethanol)
Rose bengal (Acid Red 94)		19997 (ethanol)	14648 (ethanol)
Stains all		12052 (ethanol)	94914 (ethanol)

a: the extinction coefficients are measured by R. A. Fuh, 1995 [H. Du, R. A. Fuh, J. Li, A. Corkan, J. S. Lindsey, "PhotochemCAD: A computer-aided design and research tool in photochemistry," *Photochemistry and Photobiology,* 68, 141-142, 1998].

b: the solvents which the dyestuff were dissolved.

Some dyes, such as Rhodamine 123, Rhodamine 6G, Nile Red, Eosin Y (from Sigma-Aldrich Ltd), were selected to test. The samples of the fluorescence dyestuffs were tested in following way:

(1) Is the dye soluble in water or Exxol oil?

(2) If it is soluble in water, is it soluble in the calcium chloride (40% wt.) solution?

(3) Does it react with the calcium chloride solution?

(4) Does it corrode the pipe material- copper?

The following procedures were followed to find suitable dyestuffs:

1. A small amount of each of these dyes was added to 100ml distilled water and 100ml oil. Each sample was stirred by the magnetic stirrer and left overnight. From this test, it was found that all the dyes, except Nile Red, were soluble in the water. Nile Red dissolved in the Exxol oil and appeared yellow in colour.

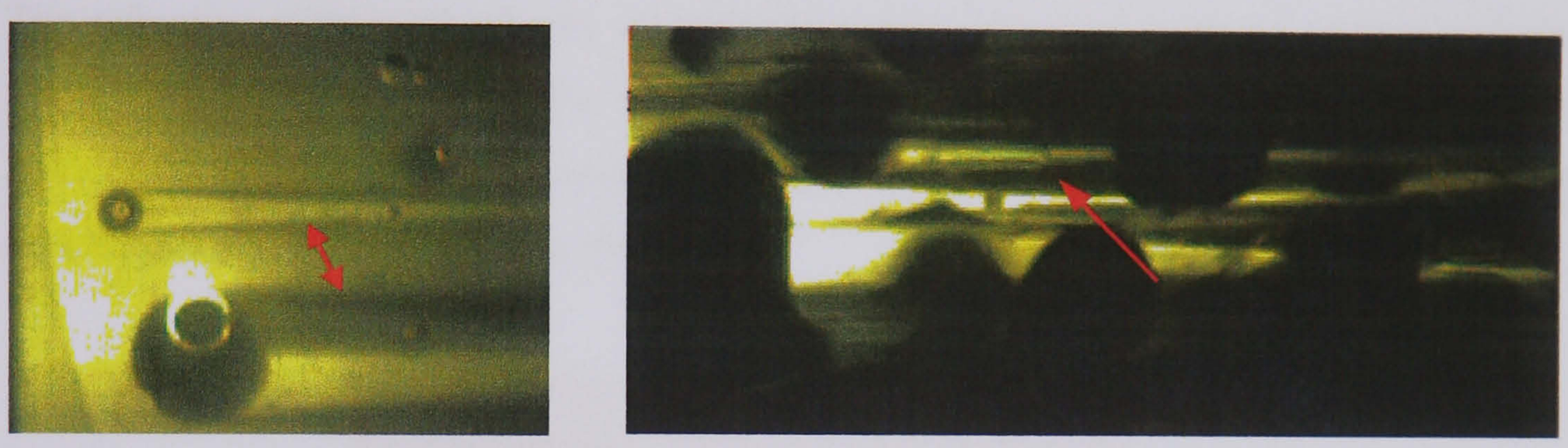
2. For the aqueous soluble dyes, the next test was to see whether they would dissolve in the 39%wt. calcium chloride solution and whether they would react with calcium chloride. None of the samples reacted with calcium chloride. However, Rhodamine 6G and Rhodamine 123 were not soluble in such a highly concentrated solution (near saturation). At the same time, after 5% wt. Eosin Y water solution was added to the 39% calcium chloride solution, some red precipitates appeared. It was found that the red precipitates were Eosin Y which were 'salted out' due to the high concentration. However, some Eosin Y did dissolve into the solution. From this test, Rhodamine 6G and Rhodamine 123 were eliminated.

3. The next stage was to test the remaining dye samples (Eosin Y and Nile Red) to establish whether they would corrode the copper tube. A sample of the copper tube was therefore put into each solution, stirred vigorously, and left overnight. Three days later, no bluish precipitate appeared in the two beakers.

After these tests, Eosin Y and Nile Red were found to be suitable for the aqueous and oil phase in the present studies.

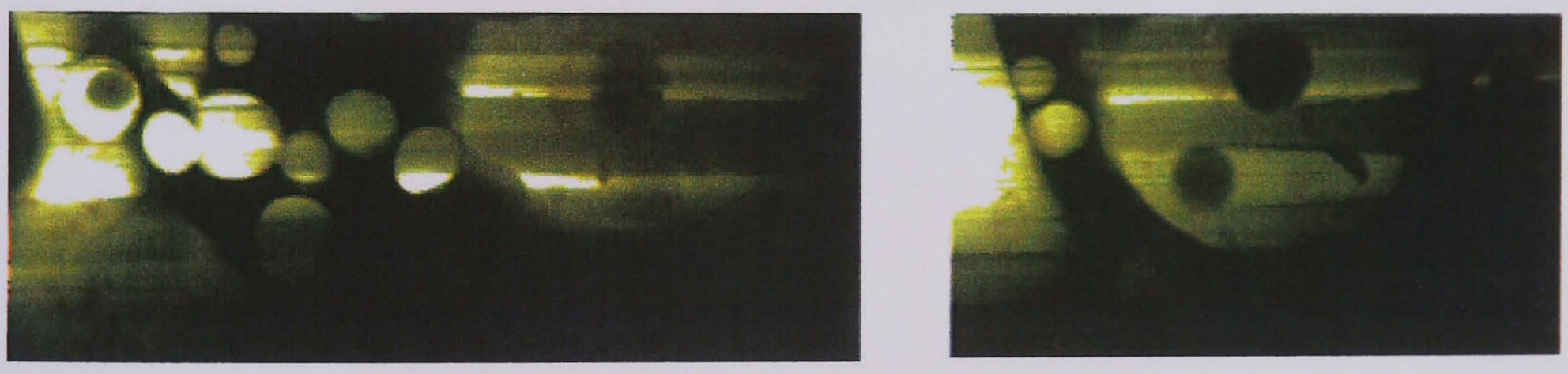
Appendix D Light Diffraction and Reflection

In many of the LIF photographs of the oil-in-water dispersions (with the laser light entering from left), it was found that all oil drops had apparent 'tails' (see Figure D.1). This phenomenon was also seen in water-in-oil dispersion (Figure D.2). Obviously, the black tails were not oil 'traces' which had been left in aqueous solution. There is instead another explanation.



(a) (b)

Figure D.1 'Oil tail' in oil-in-water dispersions (a) in the pipe; (b) in agitated vessel.



(a) (b)

Figure D.2 'Oil tail' in water-in-oil dispersions in agitated vessel.

The "tail" effect is an optics phenomenon caused by light refraction. Drops in the liquid can act as concave or convex lenses depending on the refractive indices of the two liquids. If there is no difference in refractive index, then this lens effect would not exist. Though the refractive indices of the fluids were carefully matched, small differences could still occur. As shown in Appendix B, the refractive index of calcium chloride solution changes with the temperature and the concentration of calcium chloride in a predictable way. In some cases, the calcium chloride solutions were diluted by traces water 'trapped' in the rig or the vessel

so that the refractive indices of the solutions decreased slightly. Consequently, in these cases, the oil would have a slightly higher refractive index than the calcium chloride solution. The oil drops in the calcium chloride solution, therefore, act as a convex lenses. The light is thus slightly bent by these oil lenses. From a calculation of the electromagnetic fields surrounding a particle was carried out for the present author by Prof. Alan Jones (Department of Chemical Engineering, Imperial College London. Private Communication, December 2003) and it was found that the tail appearing after the particle is very similar to those shown in the experimental photographs.

In Professor Jones' calculation, the particle size was 100 microns at visible wavelengths. The refractive indices of oil and calcium chloride solution are assumed to be 1.442 and 1.440, respectively and thus, the relative refractive index (ratio of refractive indices) is 1.0014. Figure D.3 shows the energy of the electromagnetic fields surrounding a particle with the particle represented as a red circle.

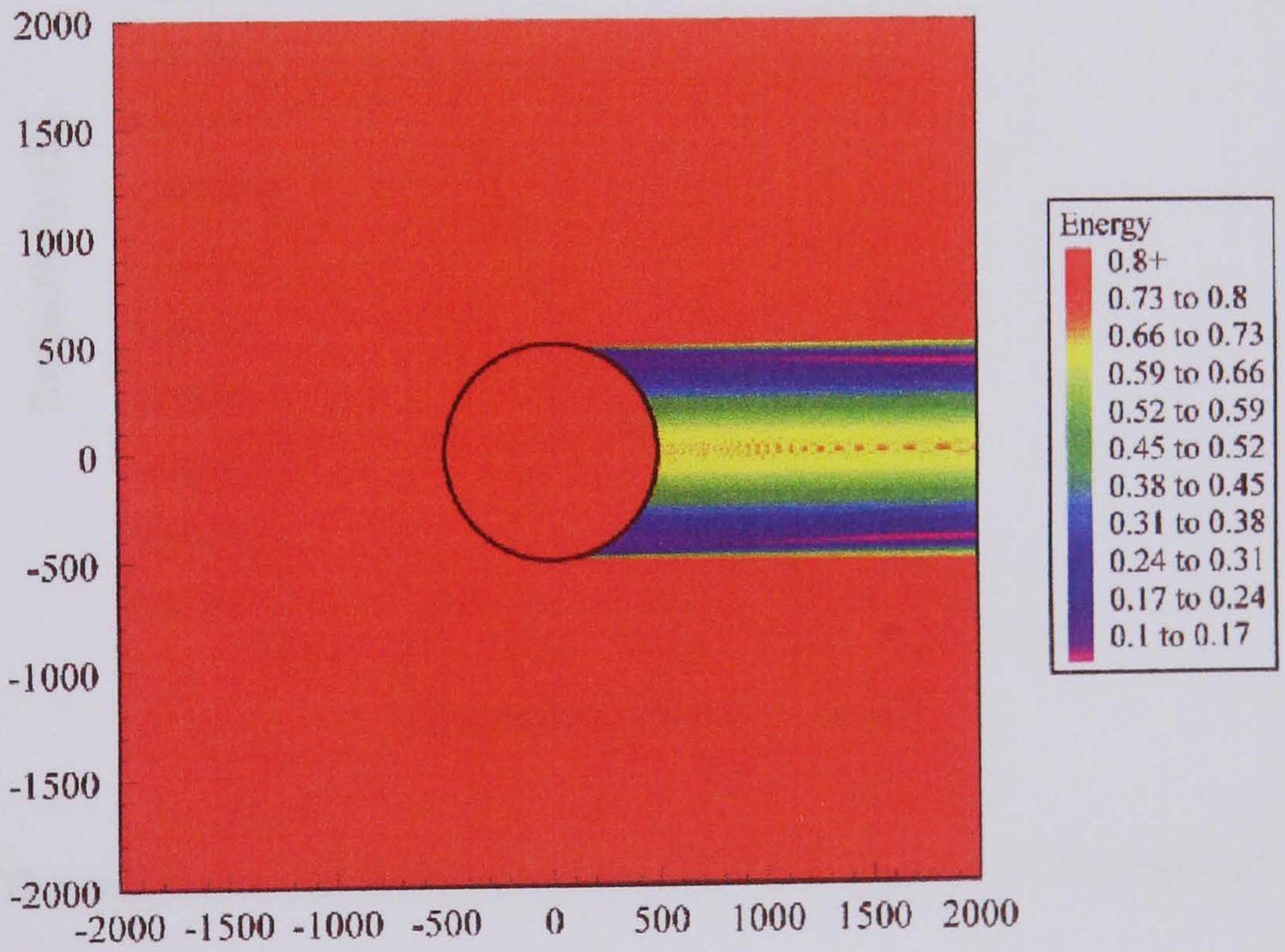


Figure D.3 The electromagnetic fields surrounding a particle by Prof. Alan Jones (December, 2003).

Any slight difference between the refractive indices of the liquid pair would also cause light loss due to reflection (Born and Wolf, 1964). The reflection loss (or reflectivity), and hence the ratio of reflection over incidence, can be calculated as a function of refractive indices by the following expression:

$$R(m_2) = \left|\frac{m_1 - m_2}{m_1 + m_2}\right|^2 = \left|\frac{\frac{m_1}{m_2} - 1}{\frac{m_1}{m_2} + 1}\right|^2 \qquad \text{(D-1)}$$

where R is the reflectivity and m_1 and m_2 are the refractive indices of the continuous and dispersed phases, respectively.

The reflection loss (%) in the calcium chloride solution and oil dispersed system is shown in Figure D.4, in which the refractive index of oil was assumed to be 1.438. It is found that the reflection loss is very small compared with the attenuation of the light caused by the absorption of the fluorescence dye.

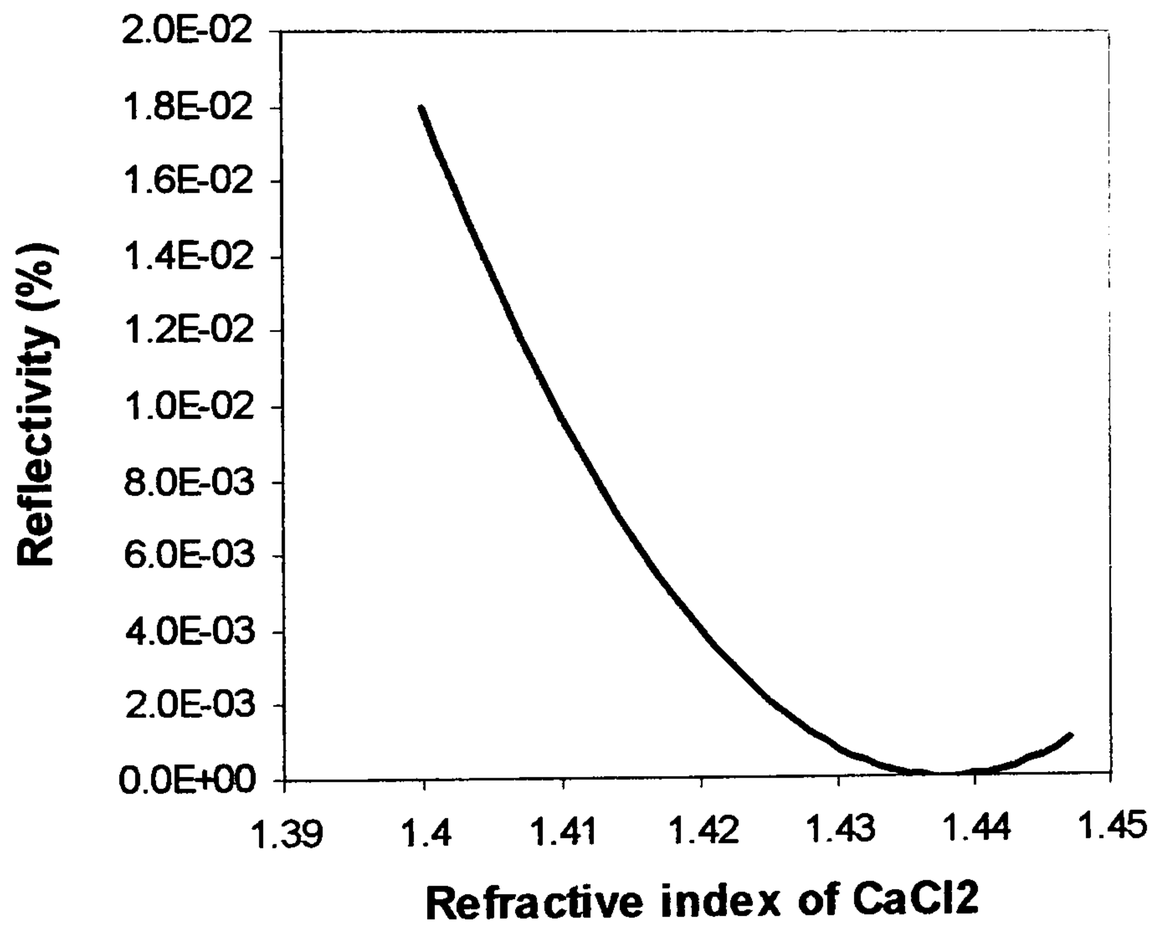


Figure D.4 The reflection loss in the calcium chloride solution and oil dispersed system.

Appendix E Preliminary Experimental Circuits and Results

One of the most difficult problems in the work on pipe flows described in this thesis was that of designing a flow circuit which was sufficiently compact to be mounted in the (small) laser laboratory and which gave representative flows. The solutions finally adopted were a once-through system for the higher liquid velocities (see Chapter 4) and a recirculating circuit (with a gear pump) for lower velocities (see Chapter 5). However, the approach to these designs was evolutionary and this Appendix describes the successive steps towards the final design. Finally, an alternative design (not actually used in the present experimental work) is described.

E.1 The 1st experimental Circuit

The 1st experimental circuit shown in Figure E.1 was a simple and partially open system that was designed to test the photochromic dye tracing technique. The circuit included:

- One pump [1] to mix the two liquids and circulate the mixture in the circuit;
- A copper vessel [2] (about 1 litre in volume) with an inlet at the bottom, an outlet on the side and a cover;
- Test section [3] (described in Chapter 3);
- An air-vent valve [4].

This experimental circuit was applied for the single-phase flow study (NaCl solution with Acid violet 19, bleach and buffer) (shown in Figure A.7). However, it was found that Freon evaporated quickly from the partially open vessel and also the bleach and buffer reacted with the copper (details in Appendix A.3.1). Consequently, this circuit did not used for further investigations.

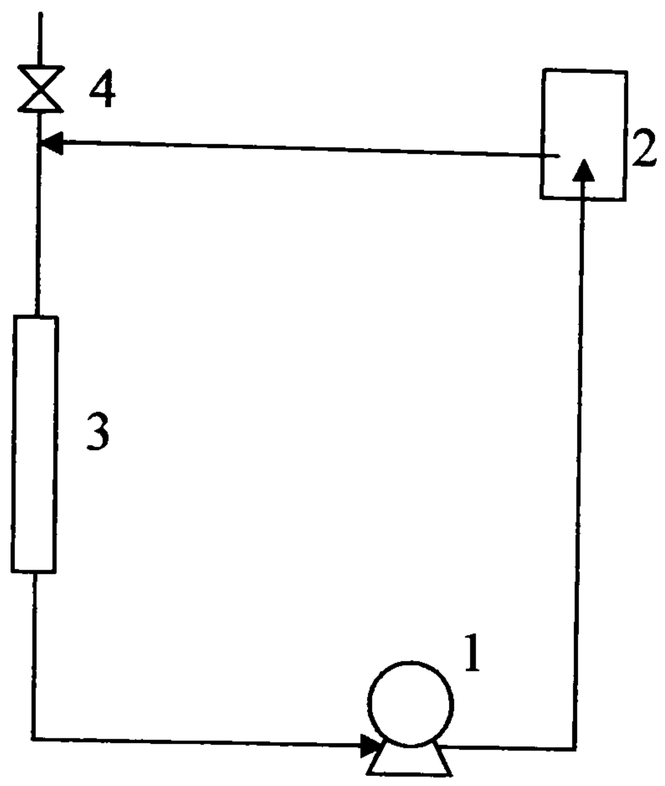


Figure E.1 The schematic description of the 1st experimental circuit.

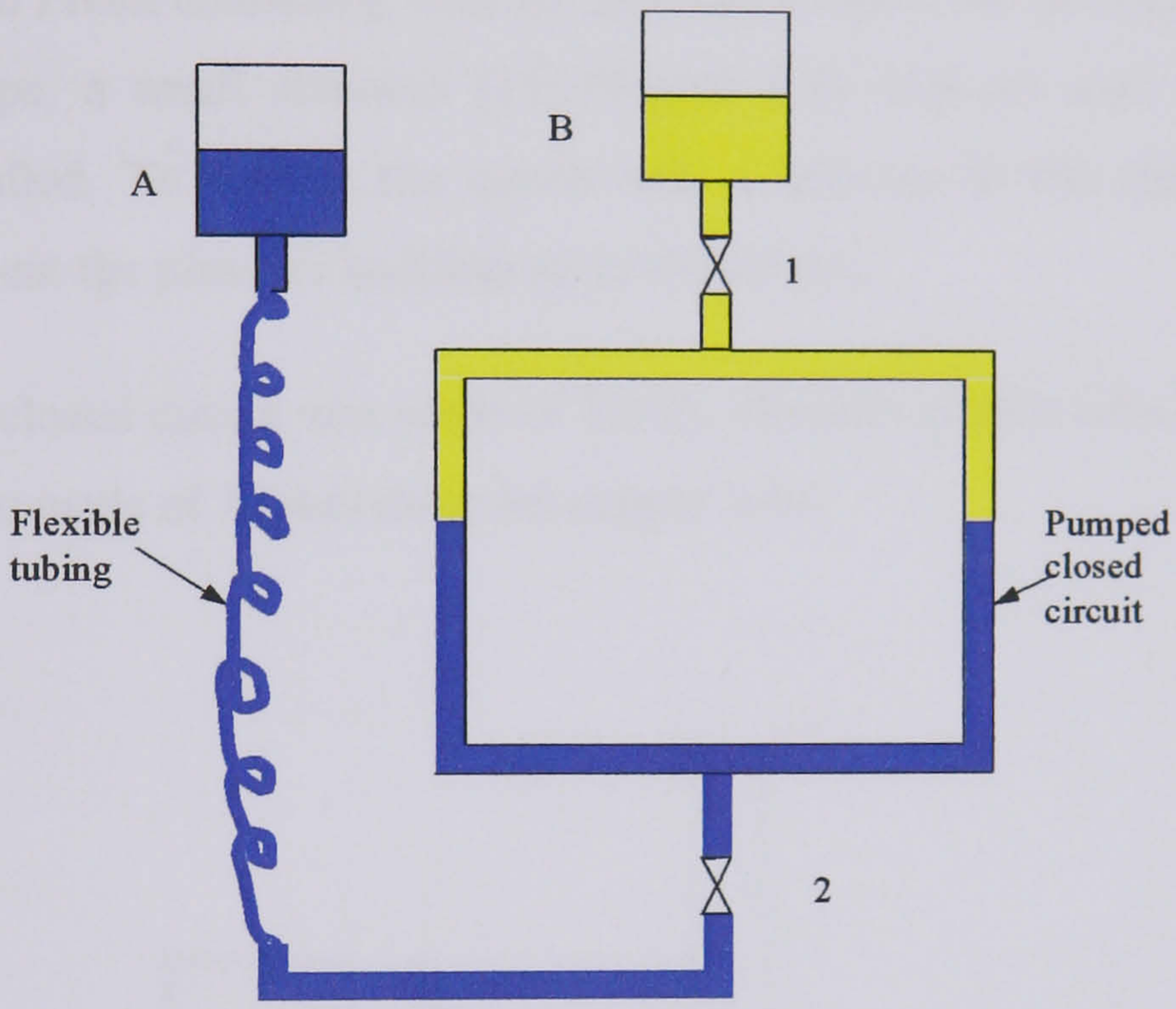
E.2 The 2nd Experimental Circuit

E.2.1 The objective and design of the 2nd experimental circuit

The objective of the 2nd flow circuit was to produce a liquid-liquid mixture of known composition (i.e. known phase fractions of light and heavy phases) which could be pumped through the optical cell so that its structure could be observed by photochromic or fluorescence techniques. The aim was to achieve a well mixed liquid-liquid mixture by continuously circulating it around a pumped closed circuit, with the centrifugal pump in the circuit acting as a mixer for the fluids. It is recognized that this method may not give a flow structure which is exactly the same as those that would occur if the fluid mixing occurred solely as a result of natural turbulence. Nevertheless, it was believed initially that the structure would be a reasonable representation of the true situation (particularly bearing in mind the straight channel length of 20 equivalent diameters upstream of the optical section).

The main problem with using a pumped closed circuit is that of achieving precise phase compositions in the fluid. The solution to this problem is illustrated schematically in Figure E.2. Suppose that the two fluids are in transparent, graduated containers A and B respectively, with container A having the heaver fluid. The pumped closed circuit can be filled with either fluid by opening either valve 1 or valve 2. It should also be noted that there were additional valves, not shown in this diagram, that release any air contained in the circuit during the filling process. After filling, the amount of the filling fluid in the circuit can be determined from the change in level of the filling liquid in the graduated container holding

that fluid. By opening the other valve (for example valve 1 if the circuit had been filled with the lighter fluid), the second fluid can be introduced into the circuit. The amount introduced is controlled by moving the graduated container A up or down (since it has a flexible connection to the circuit, as shown in Figure E.3). The amount of the second fluid in the circuit can be determined from the changes in levels in the graduated containers. Once the required amounts of fluid have been introduced into the circuit, valves 1 and 2 (Figure E.2) are closed and, when pumping is initiated, the result is a liquid-liquid mixture of known composition.



Figue E.2 Operating Principle of the 2nd flow Circuit.

The constructed experimental circuit is shown in the Figure E.3 and includes:

- A pump [1], manufactured by Grundfos Pump Ltd.;
- A 4 litre vessel [2] acting like vessel A in Figure E.2;
- A 0.5 litre graduated [3] whose bottom has been cut off and glued onto a glass tube with a stopper. (This cylinder is equivalent to container B in Figure E.2);
- A 3-meter PVC flexible [5] tubing to connect vessel [2] and the closed circuit. In addition, the flexible tube allows vessel [2] to move up and down;

- A shell-tube heat exchanger [9], which is designed to remove the heat which is generated by the pump and transferred to the mixing liquids;

- Valves, [4], [6], [7] and [8], to adjust the liquid fraction.

- An orifice plate [10], constructed to BS 1042: 1993, together with a differential pressure transducer (Validyne) to measure the flowrate of the mixture. A homogeneous mixture model was used in converting the differential pressure to a flowrate.

- Due to the high volatility of Freon, the circuit was designed as a closed loop to avoid Freon contacting with air. In order to allow the air trapped in the circuit to escape, a small chamber [11] (Figure E.4) with an auto air vent valve was installed. To protect the quartz cell, a bellows in the chamber was used to prevent the pressure building up in the circuit.

Most of the closed circuit was made of 22mm diameter copper tube, though the air vent and drain part are made of 15 mm diameter copper tube.

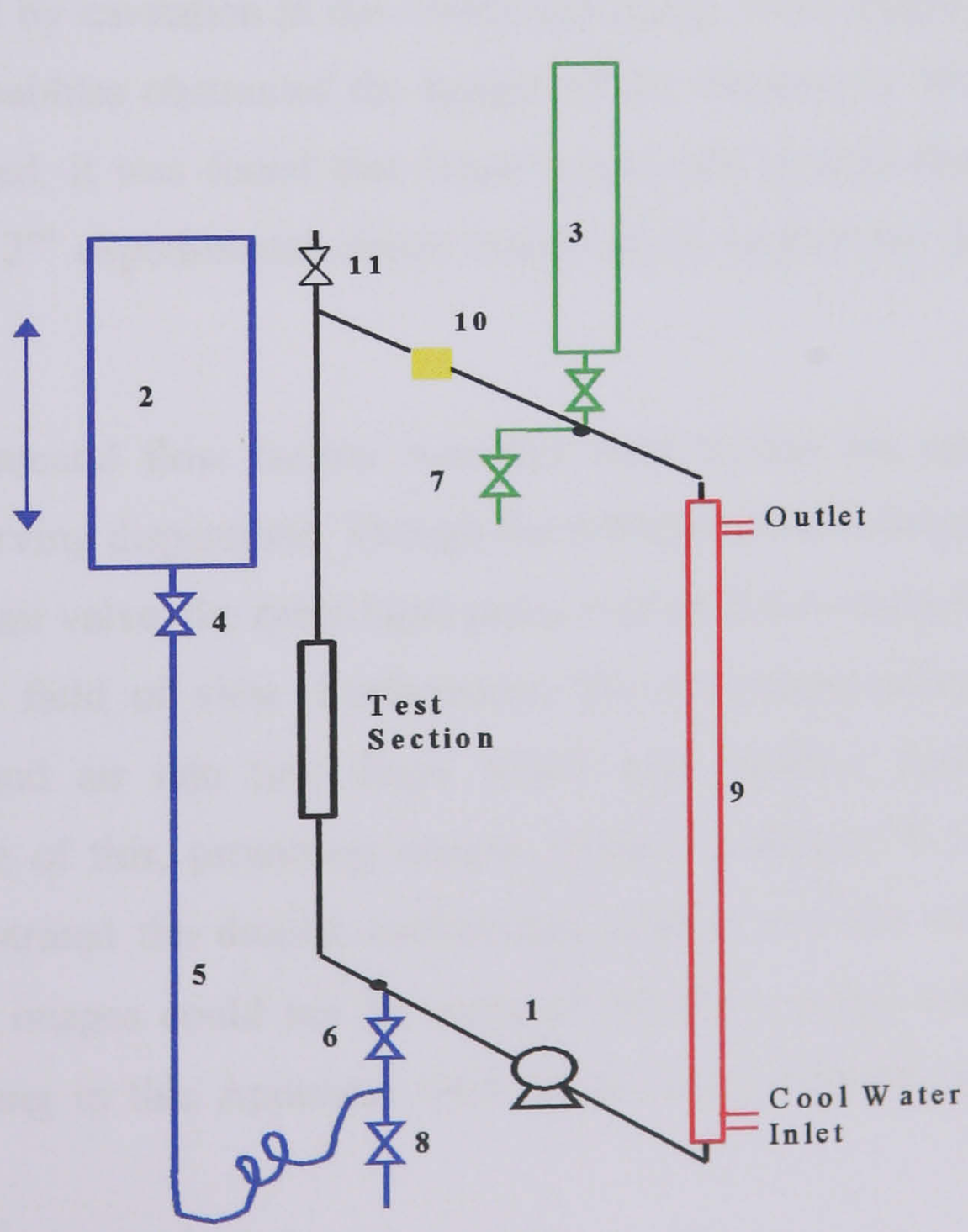


Figure E.3 Schematic description of the 2nd experimental circuit.

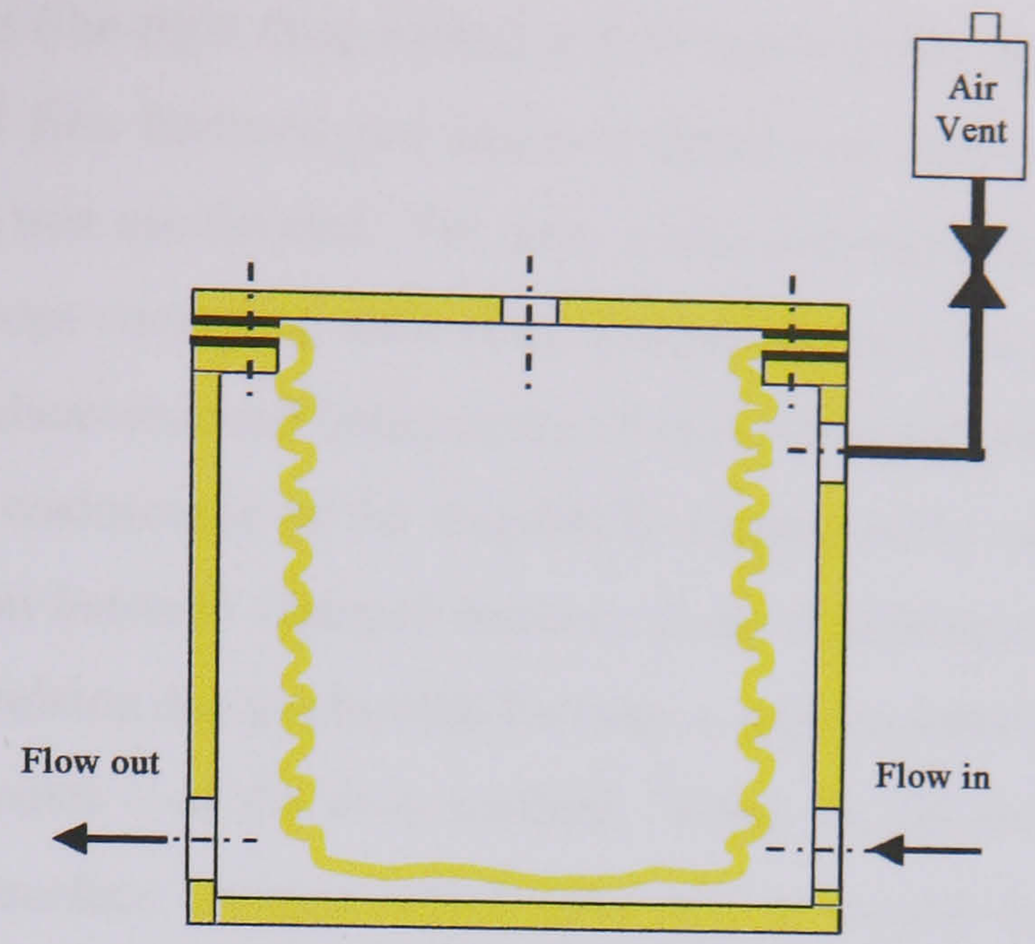


Figure E.4 The chamber with a bellows.

E.2.2 Experimental results using the 2nd experimental circuit

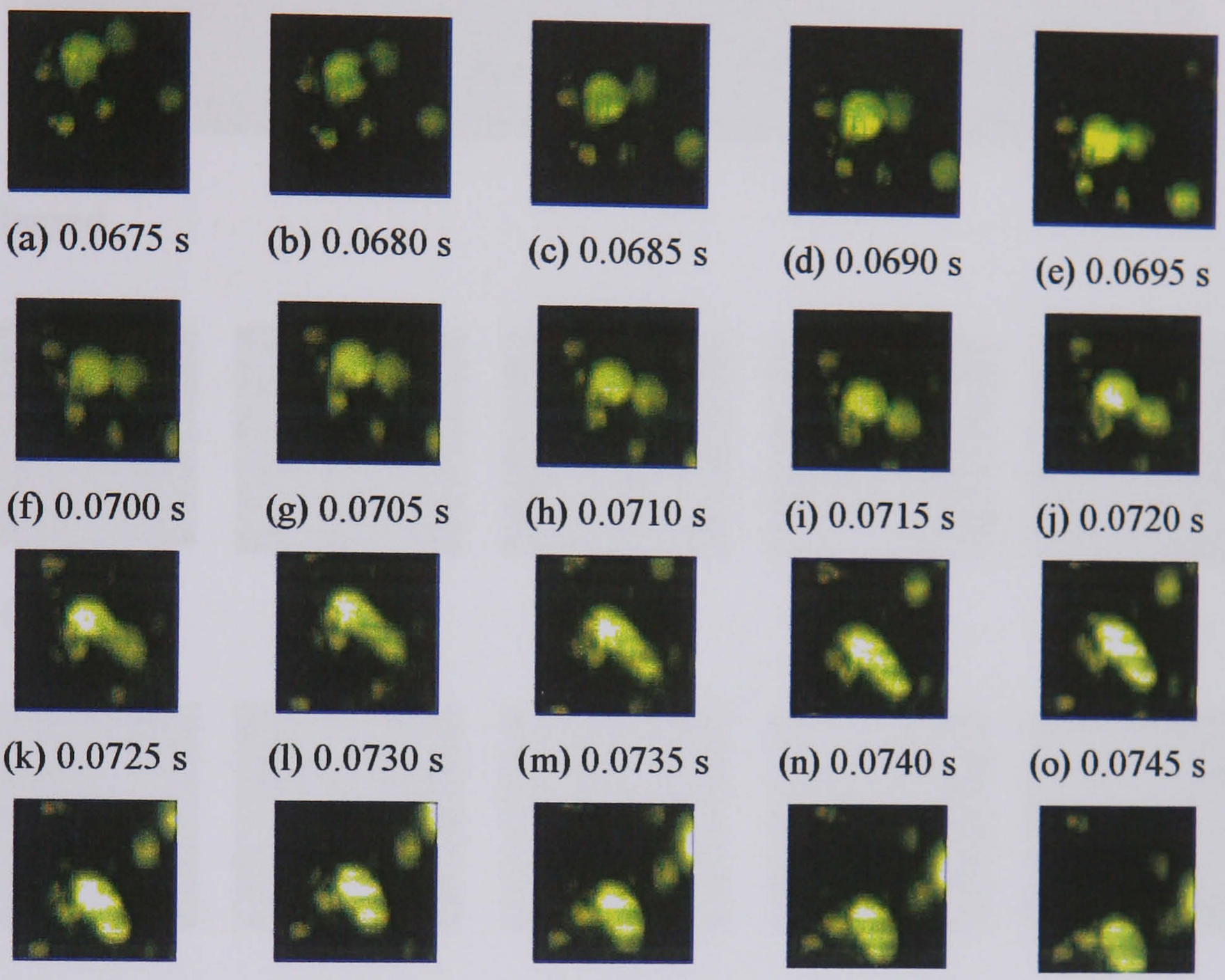
The 2nd experimental circuit was initially used to perform experiments using photochromic dye (see Figure A.8). As mentioned in Appendix A, air bubbles, which were probably generated by cavitation in the centrifugal pump, were trapped in the experimental circuit. These air bubbles obstructed the images of the dispersions. When the auto-air vent system was installed, it was found that Freon evaporated quickly through the vent valve. Consequently, the 2nd experimental circuit could not be applied for the photochromic dye tracing technique.

The 2nd experimental flow facility was also used to test the application of the LIF technique for observing dispersions. Though the problem of air entrapment was reduced by installing the auto air valve, the centrifugal pump still tended to produce cavitations bubbles which entered the field of view. Furthermore, the centrifugal pump impeller broke the dispersed phase and air into tiny drops which were smaller than the camera's pixel resolution. In spite of this, promising images (shown in Figures E.5-E.8) were obtained, which clearly illustrated the droplet coalescence process and the existence of secondary dispersions. Clear images could not be obtained when the pump was fully running. The photographs showing in this Appendix were taken in the transient period after the pump start-up.

Two kinds of coalescence are shown in Figure E.5 to Figure E.7; one was shear-induced coalescence (Figure E.5) and the others were 'head-on' coalescence (Figure E.6 and E.7). The two aqueous drops in Figure E.5, which are located close to the wall, approached along

the different centre lines (the right drop moved at 0.78 m/s velocity and the left drop at 0.58 m/s). Therefore, the oil film between two aqueous drops was torn by the shear force and process of coalescence was accelerated. The time series photographs show that the whole process from the two drops contacting each other to coalescence took only 0.005s. Yeung *et al.* (2003) investigated shear-induced coalescence of emulsified oil drops and suggested that in a "stable" emulsion, coalescence of the droplets is suppressed by two main mechanisms: (i) electrostatic repulsion between charged surfaces in an electrolyte (i.e., the double-layer force), and (ii) steric repulsion due to physical barriers— such as adsorbed layers of colloidal particles or macromolecules —at the drop surfaces. When the oil drops suspend in water, they possess negative surface charges which give rise to double-layer repulsive forces between the drops. According to conventional DLVO theory, the magnitude of this repulsion (based on the measured zeta potential) is more than sufficient to prevent coalescence of the droplets. Yeung *et al.* (2003) found that when two such drops were brought together on direct (i.e., "head-on") approach, coalescence was rarely observed. Upon oblique approach, in which lateral shearing was introduced, however, the same drops were seen to coalesce readily.





(a) 0.0675 s (b) 0.0680 s (c) 0.0685 s (d) 0.0690 s (e) 0.0695 s

(f) 0.0700 s (g) 0.0705 s (h) 0.0710 s (i) 0.0715 s (j) 0.0720 s

(k) 0.0725 s (l) 0.0730 s (m) 0.0735 s (n) 0.0740 s (o) 0.0745 s

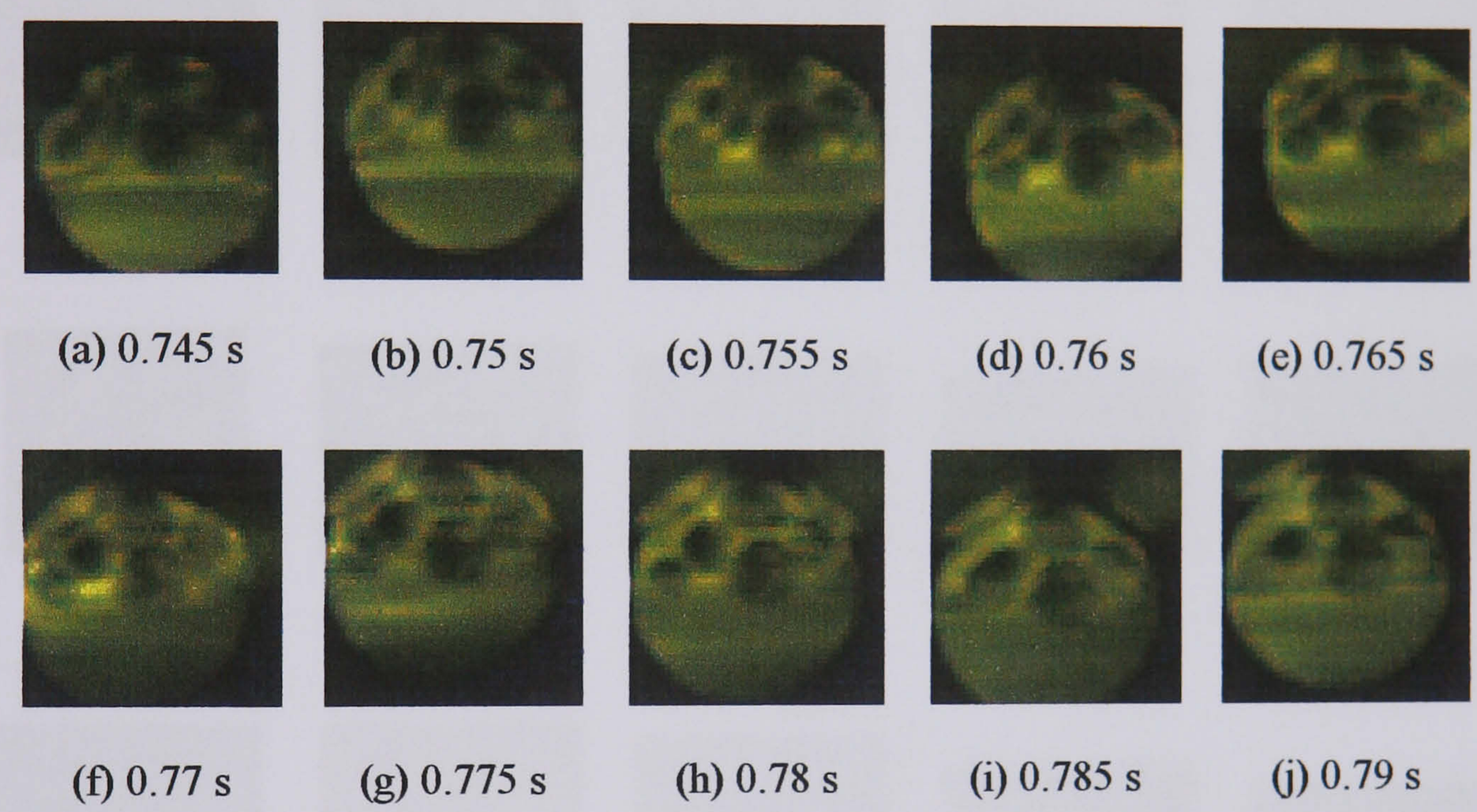
(p) 0.0750 s (q) 0.0755 s (r) 0.0760 s (s) 0.0765 s (t) 0.0770 s

Figure E.5 The process of two aqueous drops (with activated Eosin Y) coalescence during transient period after the pump start-up; in this and subsequent Figures, the yellowish green and black regions designate the aqueous and organic phases, respectively.

'Head-on' coalescences were also found between two oil droplets in water host-drops (Figure E.6 and E.7). However, compared with shear-induced coalescence, 'head-on' coalescence took a significantly longer time to occur. It can be seen in Figure E.7 that the aqueous film between two oil droplets became 'S' shaped firstly and then an oil bridge formed after the film drained. In simple shear flow, it was suggested by Klahn *et al.* (2002) that the external flow around the host-drop would generate elliptic streamlines inside the host-drop. Therefore, it was suggested that the internal flows in the aqueous host-drops gave rise to the occurrence of the 'head-on' coalescences shown in Figure E.6 and E.7, whereas the 'head-on' coalescence described in the paper of Yeung *et al.* (2003) were performed in static liquid.



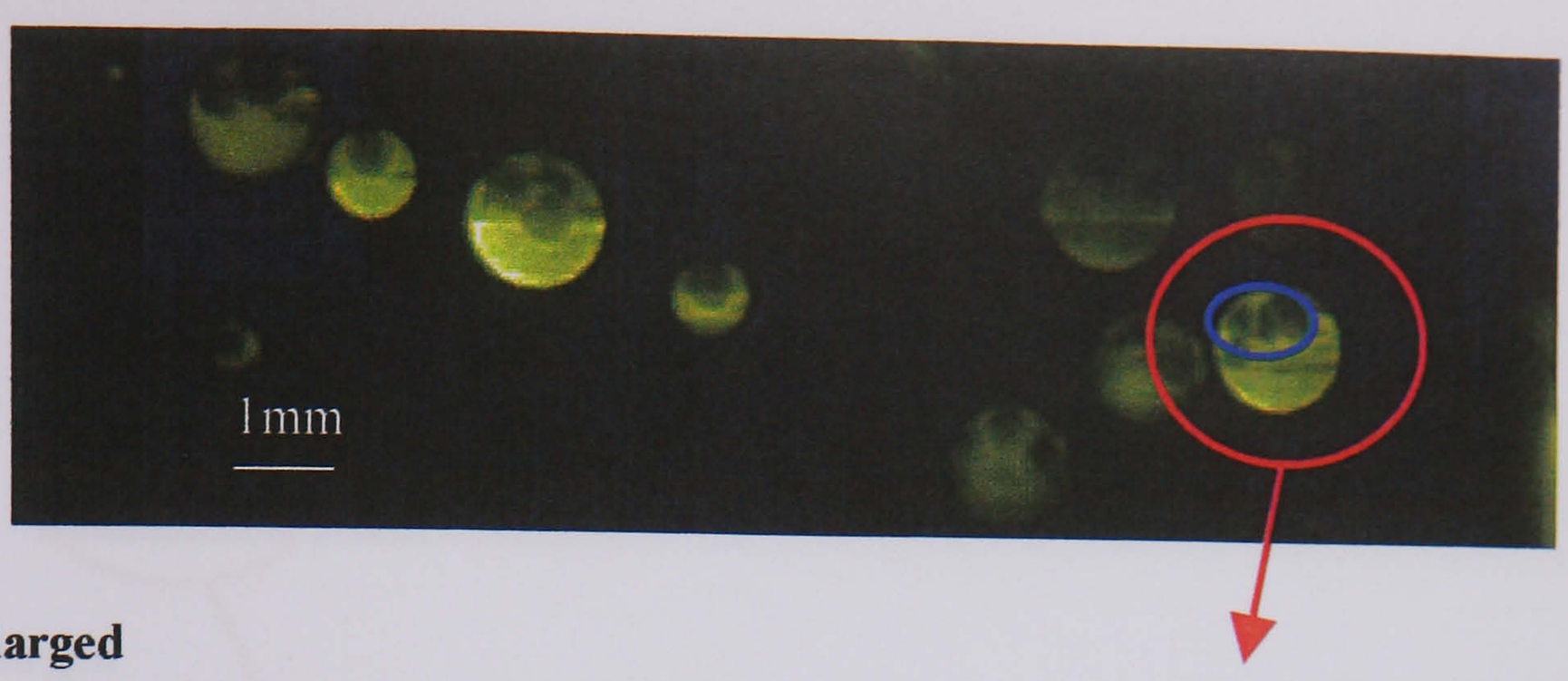
Enlarged



(a) 0.745 s (b) 0.75 s (c) 0.755 s (d) 0.76 s (e) 0.765 s

(f) 0.77 s (g) 0.775 s (h) 0.78 s (i) 0.785 s (j) 0.79 s

Figure E.6 Time series photographs of two oil-droplets coalescence, during transient period after the pump start-up. The drop moved at 0.0375 m/s.



Enlarged

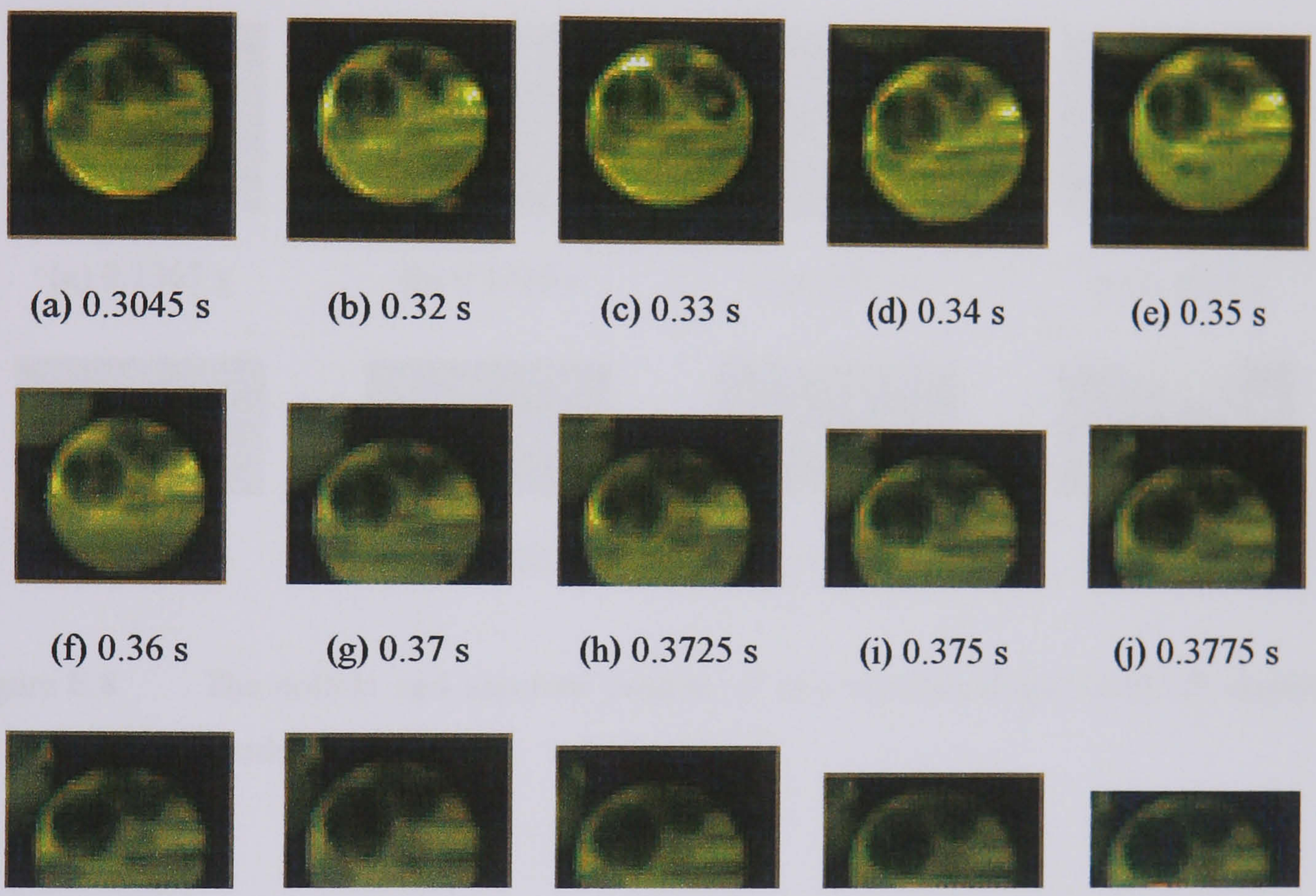
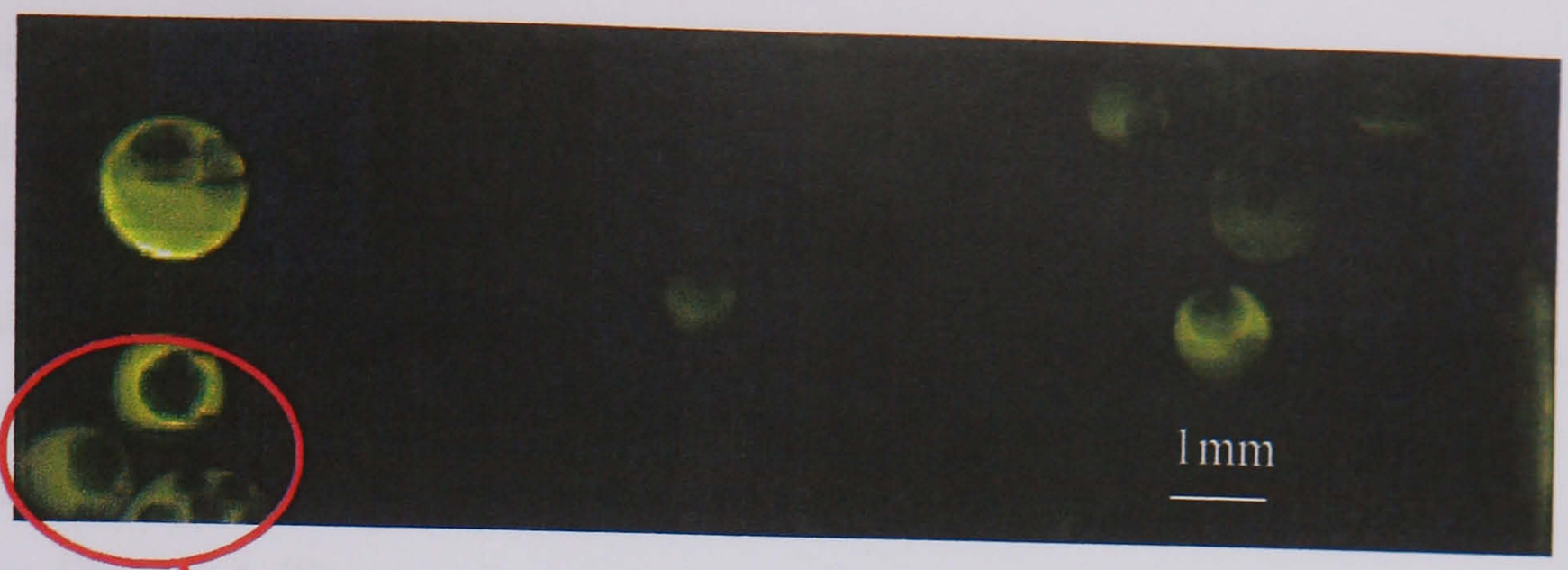
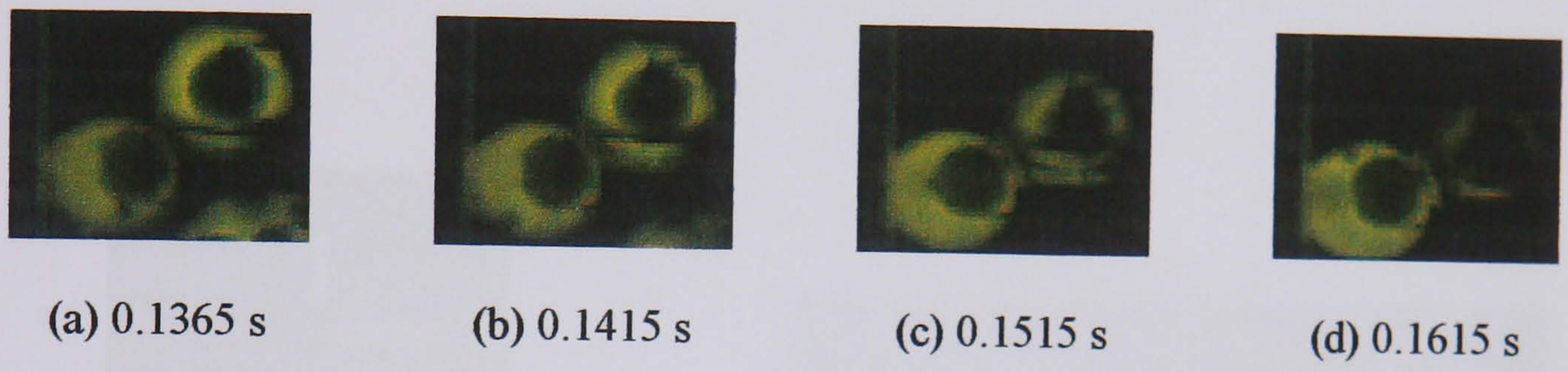


Figure E.7 Time series photographs of two oil-droplets coalescence, during transient period after the pump start-up. The drop moved at 0.03125 m/s.

Oblique approachs of two drops did not always lead to coalescence. Figure E.8 showes two aqueous drop colliding obliquely but the lateral shearing was not strong enough to tear the oil film so that the right hand drop then bounced away.





(a) 0.1365 s (b) 0.1415 s (c) 0.1515 s (d) 0.1615 s

(e) 0.1665 s (f) 0.1765 s (g) 0.1865 s (h) 0.1915 s

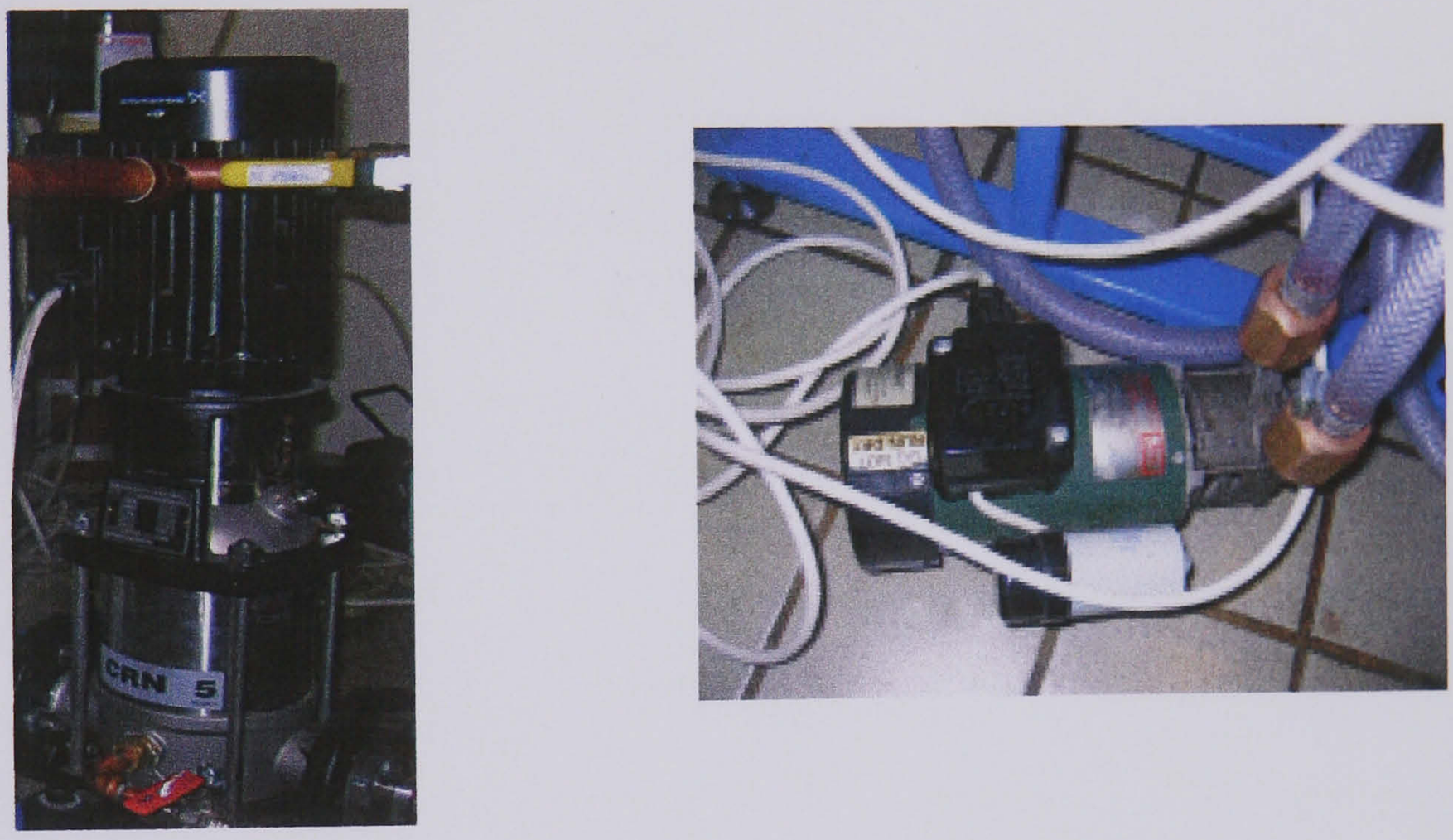
Figure E.8 The collide and separate process of two aqueous drops (with oil droplets inside).

E.3 The 3rd Experimental Circuit

The 3rd experimental circuit was identical to that used in the present experiments (and described in Chapter 3 and 4) except that, in the 3rd experimental circuit, the pump for the aqueous phase was identical with the pump for oil phase (Figure E. 9 a).

Before the liquid-liquid experiments were performed, tap water was used to test the circuit and few air bubbles were found. However, when actual liquid-liquid mixture was used in this circuit, the images were not clear as expected (Figure E.10). Several minor modifications were then implemented to determine the causes of the problem. Finally, it was found that, since the aqueous phase tank was relatively small compared with the pump circulation rate, bypass flow of the liquid caused very strong turbulence within the tank. The turbulence of flow drew the air into the liquid and, due to the very high viscosity of the aqueous phase, the air did not have enough time to escape. In addition, the CO_2 in the air

reacted with the Cl^- in the $CaCl_2$ solution to generate the $CaCO_3$ particles. Two routes were considered to solve this problem: one was to replace the pump for the aqueous phase by a relatively small pump (Figure E.13 b). The second solution investigated was to design an experimental circuit without any pumps. The use of the smaller aqueous phase pump was found adequate and this formed the basis of the final (4^{th}) experimental circuit which is described in detail in Chapter 3. This final circuit was used for the high velocity experiments described in Chapter 4. The circuit without pumps was not implemented but, for the record and with possible future implementation in mind, it is described in Appendix F.



(a) (b)

Figure E.9 (a) The Grandfos pump for the aqueous phase in the 3^{rd} experimental rig; (b) The pump for the aqueous phase in the 4^{th} experimental rig.

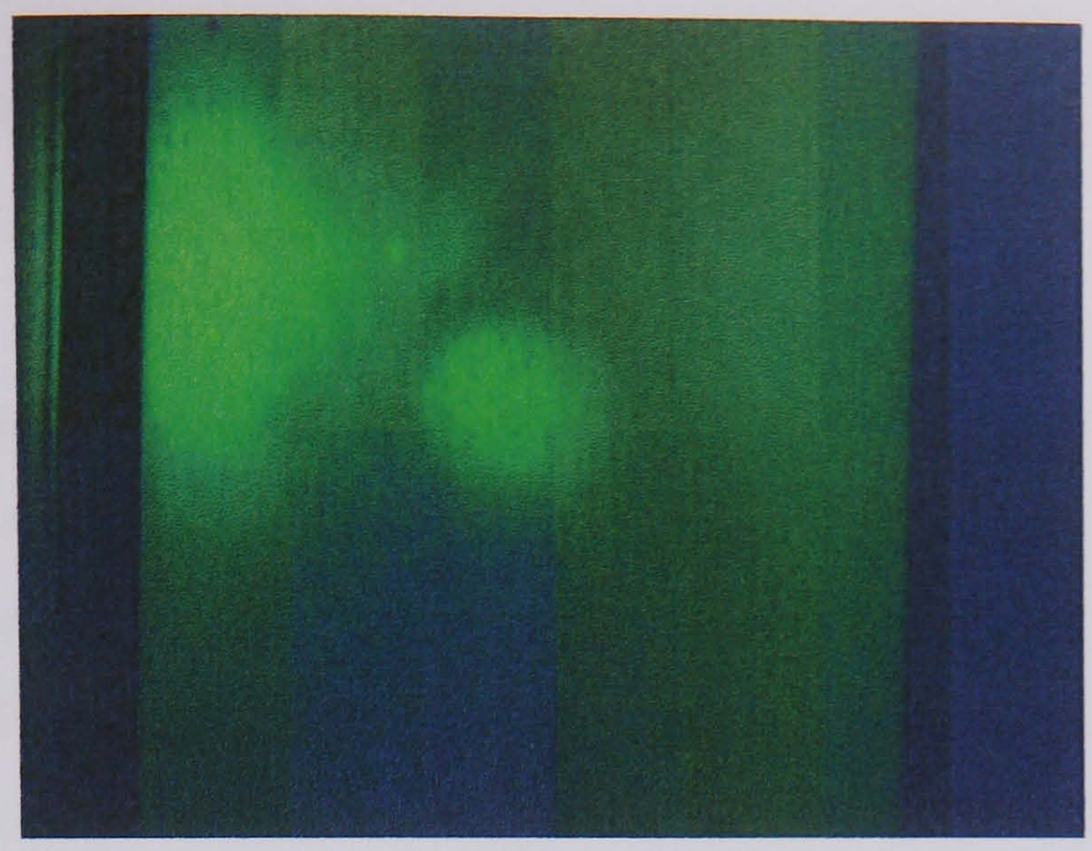


Figure E.10 Liquid-liquid dispersed flow using the 3rd experimental circuit.

Appendix F Proposed Experimental Circuit

A persistent problem with the pumped circuit described in Appendix E was that of cavitation induced by using a smaller pump for the aqueous phase but this meant that the aqueous phase velocity was limited (though sufficient for the experiments done). A better solution in the longer term would be address the safety problems involved in mounting the laser system in the Imperial College London flow facility. However, if high velocities were required on the smaller scale, a pump-free circuit could possibly be used, employing gas pressure to push the liquids through the test section. Design work on such a system was carried out and, though the system was not implemented, a brief description is given here for further reference. Figure F.1 presents a schematic representation of the experimental circuit which includes: two pressure-resistant vessels, [1] for the aqueous phase and [1'] for the oil phase; two on/off valves, [2] and [2']; two needle valves to control the flowrates of each phase, [3] and [3']; two flowmeters, [4] and [4']; two non-return valves, [5] and [5']; the test section, [6]; a separator, [7]; a drain valve, [8]; and a Nitrogen gas bottle, [9].

This experimental circuit was also designed for once-trough experiments. Two needle valves [3] and [3'] would be set to a certain position before experimental runs and the flowrates [4] and [4'] would be recorded by the flow measurement system. In order to avoid the Nitrogen gas being absorbed into the liquids, the gas bottle [9] would only be opened during the experimental runs.

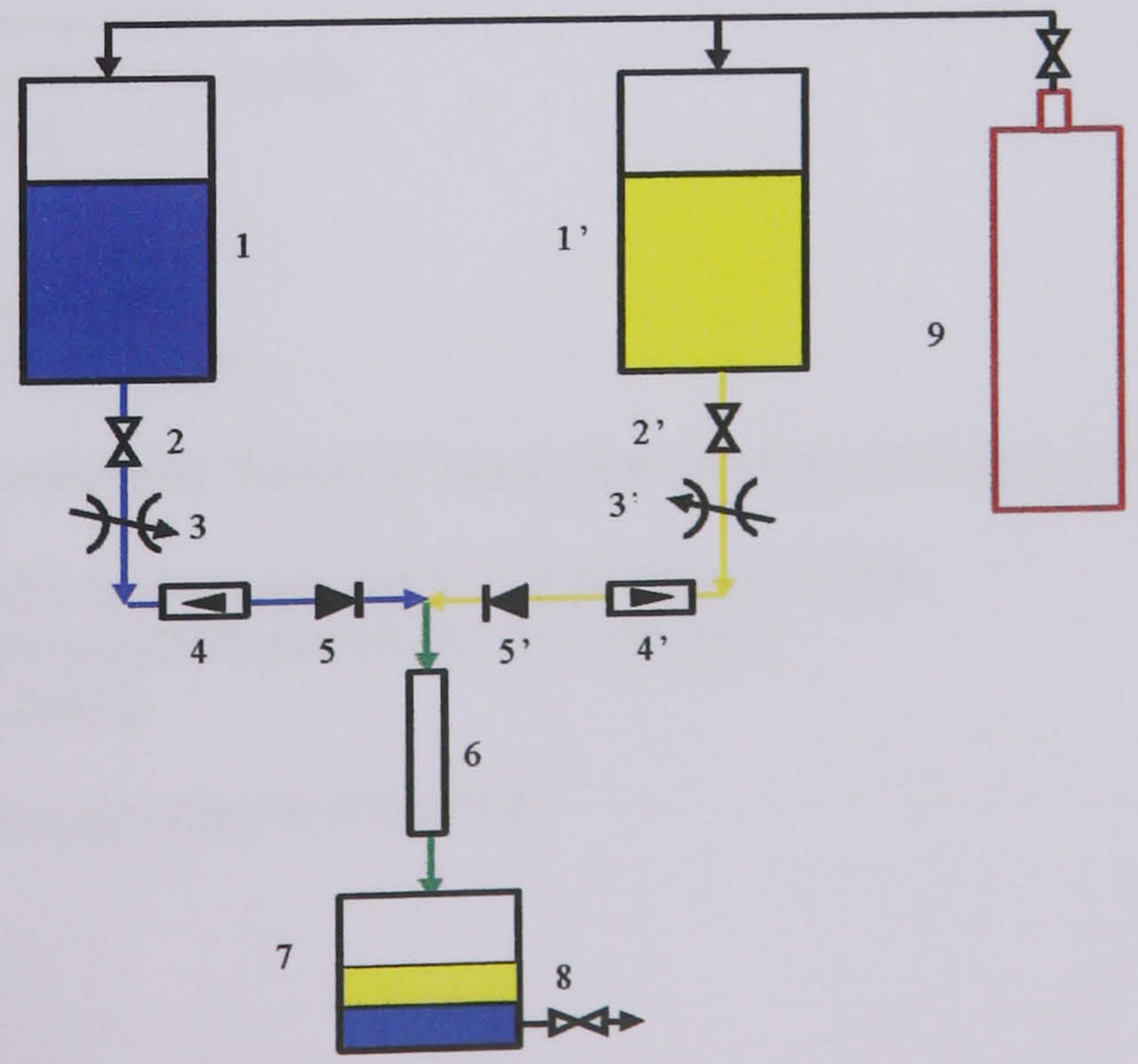


Figure F.1 The schematic description of the proposed experimental circuit.

Appendix G In-situ Phase Volume Fraction and Drop Size Measurement Program

The code listed here is to obtain the in-situ phase volume fraction and drop size by analysing the photographs of liquid-liquid dispersed flows. This program was developed using MatLab 5.6.

```
close all;
clear all;
clc;
img=imread('9746_7310.jpg');
img0=img;
threshold=1.1;  %input parameter, changing with different exp. set-up
%figure,imshow(img);
img=img(:,:,2);
width=240;
height=100;
img1=imcrop(img,[42,80,width,height]);   %crop picutre [leftupX,leftupY,width,
height]
img0=imcrop(img0,[42,80,width,height]);

%figure, imshow(img1);
subplot(4,1,1),imshow(img1);
img1=imcomplement(img1);          % for oil in water dispersion.
img2 = imopen(img1,strel('disk',2,0));   %10 can satisfy most drops, make it small
for small drop
%img2 = imadjust(background, stretchlim(background), [0 1]);
%figure, imshow(img2);
img2=img1;
level=graythresh(img2);
%bw=im2bw(img,level*0.9);
bw=im2bw(img2,level*threshold);
%figure,imshow(bw);

subplot(4,1,2),imshow(img2);
subplot(4,1,3),imshow(bw)
subplot(4,1,4),imshow(img0)

fraction=bwarea(bw)/(width*height);  %volume fraction of drops over the whole
picture
[labeled,numdrops] = bwlabel(bw,4);% Label components.
dropdata = regionprops(labeled,'basic');%drop data
alldrop=[dropdata.Area];
for i=1:numdrops
   dropsize(i)=(alldrop(i)*4/pi)^0.5*24/512;
end
fraction
```

Appendix H Location of Files on CD

A compact disk (CD) is attached to this thesis for future reference. The following table lists the contents of this CD.

Table G.1 Location of files on CD

Case	Contents	Location
Experimental work		
Movies of Chapter 4	movie_4_1.jpeg- movie_4_2.jpeg	/Movie/Chapter_4
Movies of Chapter 5	movie_5_1.jpeg	/Movie/Chapter_5
Movies of Chapter 6	movie_6_1.jpeg- movie_6_2.jpeg	/Movie/Chapter_6
CFD modelling		
Circular pipe	FC, GEO	/cfx/round
Non-circular duct	FC, GEO, F	/cfx/square

Key:

GEO – Geometry file

FC – Command file

F – Fortran file

BIBL. IN.